Advances in Electrochemical Science and Engineering

Volume 4

Advances in Electrochemical Science and Engineering

Distribution:
VCH, P. O. Box 101161, D-69451 Weinheim, Federal Republic of Germany
Switzerland: VCH, P. O. Box, CH-4020 Basel, Switzerland
United Kingdom and Ireland: VCH, 8 Wellington Court, Cambridge CB1 1HZ, United Kingdom
USA and Canada: VCH, 220 East 23rd Street, New York, NY 10010-4606, USA
Japan: VCH, Eikow Building, 10-9 Hongo 1-chome, Bunkyo-ku, Tokyo 113, Japan

ISBN 3-527-29205-5 ISSN 0938-5193

Advances in Electrochemical Science and Engineering

Volume 4

Edited by Heinz Gerischer and Charles W. Tobias

Contributions from

P. Allongue, Paris
P. C. Searson, Baltimore
T. Iwasita, F. C. Nart, Bonn, Sao Paolo
Z. Galus, Warsaw
Z. Samec, T. Kakiuchi, Prague, Yokohama
P. Tatapudi, J. M. Fenton, Storrs

Editors:
Prof. Dr. Heinz Gerischer†
Fritz-Haber-Institut der MPG
Faradayweg 4–6
D-14195 Berlin

Prof. Charles W. Tobias
Dept. of Chemical Engineering
University of California
Berkeley, California 94720, USA

Published jointly by
VCH Verlagsgesellschaft mbH, Weinheim (Federal Republic of Germany)
VCH Publishers Inc., New York, NY (USA)

Editorial Director: Dr. Thomas Mager
Production Manager: Claudia Grössl

Library of Congress Card No. applied for

A catalogue record for this book is available from the British Library

Deutsche Bibliothek Cataloguing-in-Publication Data
Advances in electrochemical science and engineering :
Weinheim ; Basel (Switzerland) ; Cambridge ; New York, NY : VCH
ISSN 0938-5193
Erscheint unregelmäßig. – Aufnahme nach Vol. 1 (1990)
Vol. 1. (1990) –

Printed on acid-free and low-chlorine paper

Composition: K + V Fotosatz GmbH, D-64743 Beerfelden
Printing: strauss offsetdruck GmbH, D-69509 Mörlenbach
Bookbinding: Wilh. Osswald + Co., 67433 Neustadt
Printed in the Federal Republic of Germany

Preface

The chapters in this volume address challenging problems associated with the observation and interpretation of anodic dissolution of semiconductors, electrode reactions in nonaqueous solvents, and charge-transfer across the interface between two immiscible electrolytes. In-situ FTIR spectroscopy of surface reactions, and a review of electrochemical methods of pollution abatement complete the range of timely topics included.

Phillipe Allongue addresses the special problems associated with the interpretation of images obtained by Scanning Tunneling Microscopy for in-situ characterization of the topography, reactivity, and reaction dynamics of dissolving semiconductor surfaces. Applications of novel methods such as Scanning Tunneling Spectroscopy, and Tip Current Voltammetry, to the study of chemical and electrochemical dissolution, corrosion, and passivation are included.

Charge-transfer processes involving electrochemical reactions offer unique opportunities for the control of atomic scale structure, including pore formation. Peter Searson discusses recent advances in understanding the interaction of silicon surfaces with fluoride ions, processes on which the most important methods for surface modification and fabrication are based.

Teresa Iwasita and F. C. Nart provide a valuable perspective on the foundations, capabilities, and limitations of in-situ infrared external reflection spectroscopy of electrode surfaces, with emphasis on Fourier Transform instruments. In addition to the description of underlying principles and instrumentation, selected examples are given of the monitoring and interpretation of spectra of various species adsorbed at electrochemical interfaces.

Zbigniew Galus relates equilibrium potentials and kinetic parameters of electrode reactions in pure and mixed nonaqueous solvents to relevant properties of the media involved. Available experimental data are interpreted in the light of most recent theoretical models, with indication of difficulties, sources of inaccuracies, and needs for future work.

The interfacial structure and charge-transfer mechanism of two immiscible electrolyte solutions, as revealed by the kinetics of the charge-transfer processes, is the subject of Chapter 5 by Z. Samec and T. Kakiuchi. Theoretical and experimental advances made over the last 10 to 15 years in the study of ion- and electron transfer are systematically and critically reviewed.

Principles and applications of electrochemical remediation of industrial discharges are presented by Pallav Tatapudi and James M. Fenton. Essentials of direct and indirect oxidation and reduction, membrane processes, electrodialysis, and treatment of gas streams, and of soils, are complemented by discussions of electrode materials, catalysts, and elements of reactor design.

Heinz Gerischer*
Charles W. Tobias

* Completed his share of the editorial work before his death in August 1994.

Contents

List of Contributors

Philippe Allongue
Laboratoire de Physique des Liquides
et Electrochimie
UPR 15 du CNRS Associé à
l'Université P.&M. Curie
4 Place Jussieu, Tour 22
F-75005 Paris
France

James M. Fenton
Department of Chemical Engineering
and Pollution Prevention Research
and Development Center
University of Connecticut
Storrs, CT 06269-3222
USA

Zbigniew Galus
Department of Chemistry
The University of Warsaw
ul. L. Pasteura 1
02-093 Warsaw
Poland

Teresa Iwasita
Institute for Physical Chemistry
University of Bonn
Römerstraße 164
D-53179 Bonn
Germany

T. Kakiuchi
Department of Physical Chemistry
Yokohama National University
Tokiwadai 156, Hodogaya-ku
Yokohama 240
Japan

F.C. Nart
Institute for Physics and Chemistry
of São Carlos
University of São Paulo
Brazil

Zdenek Samec
The J. Heyrovský Institute
of Physical Chemistry
Dolejškova 3
18223 Prague 8
Czech Republic

Peter C. Searson
Department of Materials Science and
Engineering
The Johns Hopkins University
Baltimore, MD 21218-2689
USA

Pallav Tatapudi
Department of Chemical Engineering
and Pollution Prevention Research
and Development Center
University of Connecticut
Storrs, CT 06269-3222
USA

Advances in Electrochemical Science and Engineering
Edited by Heinz Gerischer and Charles W. Tobias

Scanning Tunneling Microscopy of Semiconductor Electrodes

Philippe Allongue

Laboratoire de Physique des Liquides et Electrochimie, UPR 15 du CNRS,
Associé à l'Université P. & M. Curie, 4 Place Jussieu, Tour 22,
F-75005 Paris, France

Contents

List of Symbols

A	Richardson's constant (120 A/cm^2 K^2)
E_c	energy of the conduction band minimum at the surface
E_v	energy of the valence band maximum at the surface
E_{gap}	energy of the band gap of the semiconductor
E_o	energy of the reference electrode versus the vacuum level
e	elementary charge
i_{ph}	photocurrent at the semiconductor
i_{th}	thermionic current
i_T	tunnel current
i_F	Faradaic current on the tip
i_t	tip current (in the electrolytic environment $i_t = i_T + i_F$)
Φ	work function of the sample
Φ_T	tunnel barrier
Γ	normalized contuctance
K	decay length for tunneling
Q_s	charge at the surface of the semiconductor
Q_{sc}	space charge in the semiconductor
Q_H	counter charge in solution
N_D, N_A	doping concentration of donors or acceptors in the semiconductor
n_s, p_s	density of electrons and holes at the surface
N_s	density of states on the sample surface
N_t	density of states at the tip extremity
s	tip-to-sample separation
$T(E)$	tunnel probability
U_{fb}	flat band potential of the electrode
U_{ph}	photovoltage
U_s	sample bias (quoted versus the reference potential)
U_t	tip bias (quoted versus the reference potential)
U_T	tunnel bias ($U_T = U_s - U_t$ in the electrolytic environment)
V_b	band bending in the semiconductor
V_H	potential drop in the Helmholtz layer
χ	electron affinity of the semiconductor
w	thickness of the space charge layer in the semiconductor
ε	dielectric constant

Abbreviations

AFM	Atomic force microscopy
BEEM	ballistic electron emission microscopy
FFT	fast Fourier transform
LDOS	local density of states
MBE	molecular beam epitaxy
MIS	Metal/Insulator/Semiconductor
PL	photoluminescent
PSL	porous silicon layers
SECM	scanning electrochemical microscopy
SPM	scanning probe microscopy
SPV	surface photovoltage
STM	scanning tunneling microscopy

STS	scanning tunneling spectroscopy
TCV	tip current voltammetry
UHV	ultrahigh vacuum
ULSI	Ultra large scale Integration
UPD	underpotential deposit
WKB	Wentzel Kramers Brillouin

1 Introduction

Studies of semiconductor surfaces in ultrahigh vacuum (UHV) have had a great impact on the early development of scanning tunneling microscopy (STM). The first surface structure resolved at an atomic level was indeed the 7×7 unit cell on Si(111) [1, 2] and scanning tunneling spectroscopy (STS) was also first successfully attempted at semiconductor surfaces [2]. Later, the search for a local characterization of carrier transport at interfaces of semiconductors gave rise to several other microscopy techniques derived from STM. For an overview of STM and its applications the reader is referred to the series of books edited by Gütherodt and Wiesendanger [3–5], as well as the book edited by Strocio and Kaiser [6] which covers applications of STM more specific to semiconductors. The proceedings of the conferences *STM'91* and *STM'93* may also provide snapshots of the state-of-the-art of achievements [7]. The first textbook about STM has now been published [8].

In the electrolytic environment, scanning probe microscopes have rapidly demonstrated their capability for in-situ topographic imaging of any type of electrochemical interface (including insulators with the AFM). In-situ characterization of surface reactivity and reaction dynamics is accessible with an unprecedented resolution which gives a new dimension to electrochemistry. So far, studies have mostly concerned metal electrodes. In particular, spectacular results have been achieved with single crystals of noble metals showing that surface properties can now be analyzed on an atomic or molecular basis at the solid/liquid interface. The reconstruction of the three low-index faces of gold, the structure of adsorbed layers and that of UPD (UnderPotential Deposit) layers of various metals on Au, Pt and Ag have been extensively studied at an atomic level [9, 10]. On a mesoscopic scale, real-time imaging is becoming almost a new routine tool for studies of interfacial reactions [11–14].

There have been relatively few in-situ STM studies of semiconductor electrodes although there should be a great interest for this kind of interface. Semiconductor technology involves very different electrochemical treatments of surfaces whose high quality and simplicity still surpass those of certain dry processes. The number of wet steps is expected to increase in microelectronics because mask patterns become more complex owing to an increasing circuit complexity and density of components. The characterization of topography and chemistry of surfaces down to the nanometer scale, after etching, selective etching, surface cleaning, and oxide stripping, therefore becomes fundamental. In that respect in-situ scanning probe microscopes are ideal tools to yield a better understanding and control of such processes. Several groups

have recently imaged silicon surfaces with the resolution of atomic-scale defects, such as monoatomic steps [15–20]. Individual atoms have also been resolved on the same material [16, 17, 19, 20], and silicon is the only material for which dissolution could be observed in real time and at an atomic level [19, 20]. Individual atoms have also been resolved on the (111) and (110) faces of germanium [21]. Though flat surfaces of layered materials are easy to prepare and are normally weakly reactive, InSe is the only layered material which has been imaged in situ at an atomic level [22]. All other substrates, and particularly III–V compounds, have still not been imaged with a high resolution.

We are at the frontier between two generations of STM studies in semiconductor electrochemistry, and it seemed time to review the current status of in-situ scanning probe investigations of such systems. The first investigation of the contact semiconductor/electrolyte was published in 1987, shortly after the advent of STM; until very recently the aim was mostly to image different substrates or evaluate various types of experiments. In the last couple of years searches have really begun for physical, chemical or kinetic information from STM images of semiconductor electrodes. In such studies the preparation of surfaces is a key question since the surface must be flat initially in order to perform long-standing high-resolution imaging of structural defects and to follow their eventual transformation during interfacial processes.

After a short introduction to tunneling in Sec. 2, special attention is given in Sec. 3 to operating conditions on semiconductors because these are not as trivial as for metals and may raise experimental problems. Questions related to in-situ spectroscopic characterization are addressed in the following section. Section 5 reviews in-situ as well as ex-situ studies (in UHV or in air after treatment of the surface in solution) according to the materials and electrochemical reactions involved. Silicon electrodes are treated separately, mostly in relation to electrochemical etching and porpous layer formation. The two final sections outline perspectives and draw general conclusions. Details related to instrumentation and tip preparation are not discussed here unless they are specific to semiconductors. They are reviewed in [9]. Experimental aspects of in-situ AFM are not presented either, because the immersion of the surface in an electrolyte raises no specific problem. The theory and other applications of AFM are discussed elsewhere [3, 4].

2 The Tunneling Junction

2.1 General Equations in Vaccuum

This section recalls very briefly the basic concepts necessary for the discussion. Electron tunneling has been established for several decades in vacuum [23] as well as in solid-state structures [24]. Quantum mechanics predicts that electrons can flow between two conductors separated by a distance of the order of 20 Å. The energy diagram of a tunneling junction is sketched in Fig. 1 a. From the Bardeen tunneling

formalism it can be shown that the tunneling current is proportional to the following integral:

$$i_T \propto \int_0^{-eU_T} N_s(E) N_t(E - eU_T)\, T(E, U_T)\, dE \tag{1}$$

where E is the energy of tunneling electrons with respect to the Fermi level of the sample and U_T is the tunnel bias. $T(E, U_T)$ is the tunnel probability, and $N_s(E)$ and $N_t(E - e\,U_T)$ are the densities of states at the surface of sample and tip respectively. In the WKB approximation the transmission coefficient is given by:

$$T(E, U_T) = \exp\left[-Ks\,(\Phi - E + eU_T/2)^{1/2}\right] \tag{2}$$

where $K = 2\,(2m^*/\hbar^2)^{1/2}$. Φ is the sample work function, m^* is the effective mass of electrons, $\hbar = h/2\,\pi$ and s is the tip-to-sample separation. Assuming that the density $N_t(E - eU_T)$ is a constant in Eq. (1) and using further the fact that $T(E, U_T)$ is maximal either for electrons at the Fermi level of the sample with a tip positive (for $U_T > 0$ this means that $E = 0$) or for electrons at the Fermi level of the tip with a tip negative (for $U_T < 0$ this means that $E = -eU_T$), the current i_T appears to be proportional to the following expression:

$$i_T(U_T) \propto N_s(U_T) \exp\left(-Ks\sqrt{\Phi_T}\right) \tag{3}$$

with $\Phi_T = \Phi - |eU_T/2|$. Equation (3) is **a posteriori** justified by the fact that there seems to be no defined dependence of STM images on the metal used for the tip. Numerically, with $\Phi_T = 4 - 5$ eV, the decay length is $K \sim 1$ Å^{-1}, which means that the tunneling current i_T decreases by one order of magnitude if s is increased by 1 Å. This is the origin of the extreme vertical resolution of the scanning tunneling microscope.

2.2 Tunneling at the Solid/Liquid Interface

If the tunnel junction of Fig. 1 a is simply immersed in an electrolyte, the polarization between the tip and the sample will promote an electrolysis. A bi-potentiostat is necessary to ensure real tunneling between the sample and the tip. Such a device, classically used in electrochemistry, enables to split the tunnel junction into two solid/liquid interfaces, *independently* polarized against a reference of potential (Fig. 1 b). Using this configuration, also referred to as the four-electrode configuration and introduced very early by several groups, it is possible to avoid any electrochemical transfer between the sample and the tip [25, 26]. The reference potential is an electrode whose potential is well defined and constant with respect to the vacuum level. The sample is biased against the reference electrode to monitor reactions at the surface, just as in a classical electrochemical cell. The tip potential is adjusted

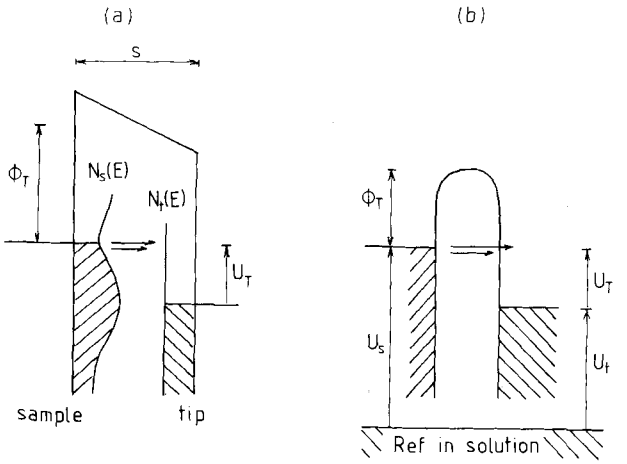

Fig. 1. Energy diagram of a tunneling junction. (a) In UHV: U_T is the tunnel bias. (b) In the electrolytic environment: U_s and U_t are set independently against the reference potential in solution (four-electrode configuration); the tunnel voltage is $U_T = U_t - U_s$. See text for other symbols.

independently of that of the sample to *nullify* the faradaic current at its extremity. The potentiostat regulates the potential of an auxiliary electrode, also called the counter electrode, so as to prevent any current flow in the circuitry of the reference electrode. The counter electrode therefore collects all the electrochemical current issued from the sample and the tip collects only tunneling electrons when its potential is properly adjusted. Usually the tunnel bias $U_T = U_s - U_t$ depends on the sample bias U_s, because the tip potential U_t is generally constant.

Within the conditions described above, barrier height measurements show that tunneling in liquids looks very similar to tunneling in UHV. Figure 2 presents the variation of the tip current flowing between an n-Si(111) electrode and a tungsten

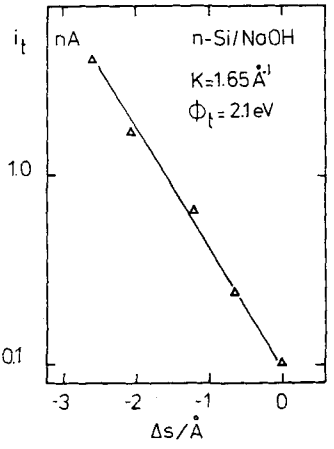

Fig. 2. Variation of log i_t vs. Δs at the n-Si(111)/NaOH/tungsten tip junction. The tunnel barrier is 2.1 eV, as derived from the slope. This is ~1 eV below the value calculated from the energy diagram (after [20]).

tip in NaOH as a function of the tip-to-sample separation (more precisely, its variation Δs) [20]. The exponential dependence is in accordance with pure electron tunneling (see Eq. (3)), in spite of an electrochemical current as large as 150 $\mu A\,cm^{-2}$ on the sample. The tunnel barrier derived from the slope of the plot is $\Phi_T \sim 2.1$ eV ($K \sim 1.65$ $Å^{-1}$), which is about 1 eV smaller than expected from the calculated energy diagram of the junction [20]. Values of $\Phi_T \sim 2$ eV have also been reported on gold in acidic solutions [25], again about 1 eV smaller than those measured in UHV. Very recent detailed measurements confirm this tendency with well-prepared Au(111) in different solutions and solvents [27]. Bingelli et al. [28], in contrast, have reported tunnel barriers as small as 0.2 eV on polycrystalline silver.

Various theories have been published on the immersed tunnel junction. Schmickler and Henderson [29] describe the metallic surface and the tip respectively as a semi-infinite and a spherical jellium, and treat the liquid as a dielectric. Within this model the effect of the solution is mostly a lowering of the potential energy barrier due to screening of electrostatic interactions by the dielectric constant ε. In their calculation the authors consider the solvent's optical dielectric constant ($\varepsilon = 1.88$ for water) rather than its static dielectric constant ($\varepsilon = 80$ for water) since the interactions between the tunneling electrons and the molecules of solvent have a length scale in the ångström range. Transferring electrons interact only with the electronic polarization of solvent molecules (orientational and vibrational modes are considered to be too slow compared with the speed of tunneling electrons). Saas and Gimzewski [30] postulated that spontaneous or induced orientational polarizations of solvent molecules generate short-lived microscopic intermediate traps which assist tunneling and explain the small tunnel barriers measured by Bingelli et al. [28]. The relevance of this later approach, which is subject to the significance of barrier measurements performed on rough surfaces,[1] has been discussed recently by Sebastian and Doyen [31]. Including fluctuations of the polarization in their calculation, these authors find a weak temperature dependence of the tunnel barrier which confirms the minor dynamical role of the liquid, in agreement with Schmickler and Henderson's assumption [29]. The transit time of tunneling electrons estimated by Sebastian and Doyen is $\sim 10^{-15}$ s, which is indeed much shorter than the time needed for the solvent molecules to rearrange. Calculations nevertheless show that thermal fluctuations in the polarization can reduce the effective barrier to nearly 1.5 eV, independently of the difference of work functions.

The very recent data of Pan et al. [27] are quite interesting since they underline the influence of dipoles of water molecules in the tunneling gap. Measurements in aqueous solution indeed show that electrons tunneling out of the tip into the substrate electrons do see a tunnel barrier which is nearly 0.5 eV larger than when they tunnel in the reverse direction (for the small tunnel bias used, no difference should be detected). Keeping the tunnel voltage constant, it is observed that the tunnel bar-

[1] On rough surfaces small values of Φ_T may be easily explained by tunneling from the side of the tip. The presence of several mini-tips is a second problem, common to rough and flat surfaces. Both effects introduce artefacts in the determination of Φ_T because the distance s is ambiguously defined in Eq. (3). To exclude such artefacts one should verify the resolution of the tip before and after measurements, and preferably perform measurements on flat portions of surfaces.

rier also decreases when the sample and tip bias are both made more positive, which is quite opposite to expectations (the effect is best seen with the tip negative to the sample). Lastly, regardless the electrochemical bias of the sample (versus the reference), a sharp dip is found around zero tunnel bias in aqueous solutions (no dip is seen in nonpolar solvents). The authors propose that the tunnel barrier includes a correction term due to an induced polarization of a cluster of molecules in the tunneling gap. The size of the cluster (ca. 30 molecules) seems too big, however, with respect to the tunneling gap, which suggests that some refinement of the theory is necessary.

3 STM of Semiconductors

3.1 The Semiconductor/Electrolyte Junction

The semiconductor/electrolyte contact has been extensively investigated since the 1970s. A recent review [32] and text books [33, 34] furnish details of the theory and applications of semiconductor electrodes. Below are given only some elements necessary for the discussion. Phenomenologically the liquid junction behaves more or less like a solid-state Schottky diode, with the electrolyte playing the role of the metal layer.

At equilibrium, when Fermi levels are equal the contact on both sides of the interfacial distribution of charges is that shown in Fig. 3a: Q_{sc} is the space charge in the semiconductor and extends over a distance w of several hundred nanometers, since the density of electronic charges available in the solid is several orders of magnitude

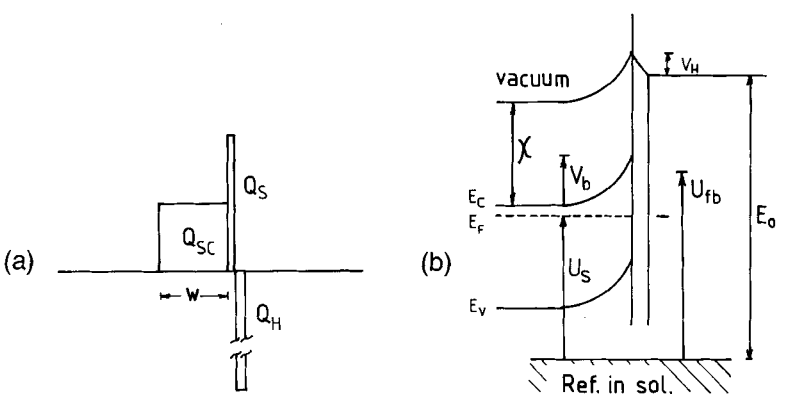

Fig. 3. Distribution of charge (a) and energy diagram (b) for the n-type semiconductor/electrolyte interface: U_{fb} is the flat band potential and V_b the band bending. The energy difference E_0 depends on the reference electrode in solution. $E_0 = -4.5$ eV for the NHE. See text for other symbols.

smaller than that in solution (typically 10^{16} charges/cm^3 in the solid against 10^{20} charges/cm^3 in the solution), which corresponds to immobile ionized dopants because each transferred electronic charge leaves one ionized atom. Q_{sc} is positive in an n-type electrode. Q_s is a charge localized at the surface, arising for instance from surface states and adsorbates. Q_H is an ionic counter charge in the Helmholtz layer (thickness ~ 3 Å) which compensates $Q_{sc}+Q_s$. The corresponding potential distribution at the interface is shown in Fig. 3b. Inside the semiconductor the potential drop, also referred to as the band bending, V_b, is a potential barrier to majority carriers. Its thickness w varies as $(V_b/N_D)^{1/2}$. Any change of the potential U_s is distributed according to $\Delta U_s = \Delta V_b + \Delta V_H$. In many situations, however, the surface energy levels are fixed against the levels in solution ($\Delta V_H \sim 0$ when the charge Q_s is independent of the bias) and the density n_s of majority carriers at the surface is monitored by the sample bias, according to the Boltzmann relationship

$$n_s = N_D \exp(-eV_b/kT)$$

with

$$V_b = U_s - U_{fb}$$

The full determination of the energy diagram is achieved by measuring the flat band potential U_{fb}, which can be performed by various methods [35]. The bottom of the conduction-band is given by:

$$E_c = -E_o - eU_{fb} + e\Delta V_{fc}$$

where

$$\Delta V_{fc} = kT \ln(N_c/N_D)$$

and N_c is the density of states at the conduction band minimum and N_D the doping concentration. E_o makes the correspondence between the normal hydrogen electrode (NHE) and the zero of energies ($E_0 = -4.5$ eV [36]).

$$E_v = E_c - E_{gap}$$

U_{fb} represents the potential which must be applied to the electrode to flatten the bands. This situation is scarcely achieved at liquid contacts because of the existence of interface states. The position of band edges of a semiconductor results from many parameters including electron affinity (χ), formation of surface bonds with ligands from the solution, adsorption of species from the liquid phase, and the presence of surface states, which all contribute to Q_s. Figure 4 gives the position of band edges of a selection of materials at pH = 0 (see also [37, 38]). It indicates, for instance, that the potential drop in the Helmholtz layer amounts to $V_H \sim -0.5$ V in the case of GaAs ($\chi \sim 4.1$ eV [39]). This corresponds to a charge Q_s of the order of 10^{13} elemental charges/cm^2 for a Helmholtz capacitance of 10 μF/cm^2.

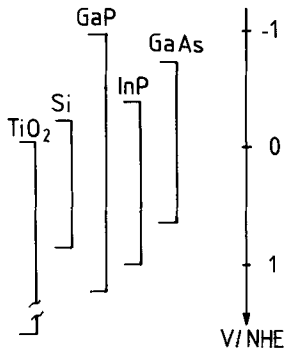

Fig. 4. Position of band edges of some classical materials at pH = 0 (after [77]).

In aqueous solutions U_{fb} shifts by -0.06 V/pH unit for many materials. The generally accepted reason is specific adsorption of OH^- or H^+ ligands, especially on materials forming oxide or hydride layers, which is the case for III–V compounds, Ge, Si, and oxides, for instance. Specific adsorption means that a chemical bond is formed according to a reaction of the type

$$S_0 + H_3O^+ \leftrightarrows S_0 - H^+ + H_2O$$

or

$$S_0 + H_2O \leftrightarrows S_0 - OH^- + H^+$$

with S_0 a surface atom. Any displacement of this equilibrium modifies the potential drop across the Helmholtz layer according to a Nernstian equation. U_{fb} may also shift with the applied bias as soon as the charge Q_s is modified at the surface (one speaks of band "unpinning"). This occurs for instance when the electronic occupation rate of surface states is affected by the bias (as the Fermi level crosses their energy level). Experimentally, the band edges of single crystals are generally pinned under depletion conditions.

The carrier transport properties of the interface are summarized in Fig. 5. Typical $i-U$ curves (top) and corresponding energy diagrams (bottom) are shown for an n-type electrode. In darkness a rectifying behavior is observed at positive bias because the surface is depleted of electrons (diode-like behavior). At cathodic bias the band bending is reduced and electrons are emitted over the barrier (thermionic process). Illumination of the surface with light of energy larger than the band gap generates electron-hole pairs. If the band bending is sufficiently large, the electron-hole pairs are separated by the electric field in the space charge region, and the minority carriers reach the surface. The intensity i_{ph} of the photocurrent is normally proportional to light intensity in such conditions because each photogenerated carrier is transferred to solution. At less positive voltages photocarriers recombine with majority carriers in bulk and/or surface traps, which decreases the photocurrent. The photovoltage U_{ph} is the difference between the rest potentials in darkness and under illumination.

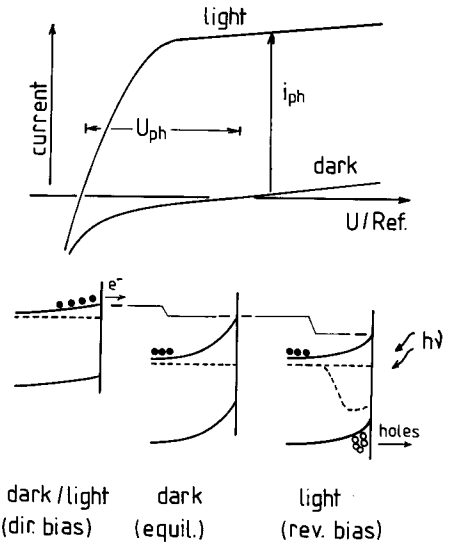

Fig. 5. Typical $i-U$ curves of an n-type semiconductor electrode in darkness and under illumination. The band diagrams illustrate the shift of the band edges with illumination (right) and at cathodic bias (left).

To summarize, the semiconductor/electrolyte interface presents two types of currents: in the dark this is a current of majority carriers whereas the photocurrent is a current of minority carriers. The same reactions can be monitored at n- and p-type electrodes but under different conditions. Hole accumulation corresponds to corrosion, since holes are trapped in surface bonds. Electron accumulation is generally not destructive for the surface unless cathodic reduction leads to decomposition. The band diagrams of Fig. 5 indicate that a downward shift of the flat band potential is expected at an illuminated n-type electrode. At negative bias, conversely, the shift is upward since electrons are accumulated in a thin surface layer (metallic-like behavior).

3.2 Conditions for Imaging Semiconductors

Figure 6 compares the situation for imaging a semiconductor in vacuum and in the electrolytic environment. The ideal image of the tunnel junction in vacuum is that shown in the top diagrams. With the tip negative, electrons are injected into the conduction band (Fig. 6a); with the tip positive, valence band electrons are tunneled into the tip (Fig. 6b). The situation with flat bands in vacuum is in fact not correct because tunnel voltages generally exceed the value of the band gap. In the absence of electronic states at the surface of the semiconductor, the tunnel junction behaves like an ideal Schottky contact with no pinning of the Fermi level. The tip *locally* promotes a band bending in the sample to screen the outward electric field [40]. Conversely, in the presence of a large density of electronic states at the surface, the tunnel voltage drops mainly in the gap between the tip and the surface because the surface

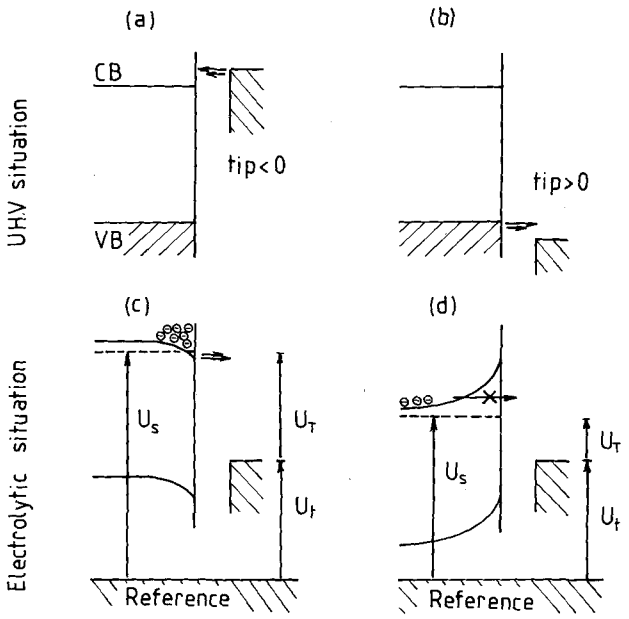

Fig. 6. Comparison between tunneling conditions on a semiconductor in vacuum (top) and in the electrolytic environment (bottom). In vacuum empty states (a) and occupied states (b) are imaged with a negative and positive tip respectively. In the liquid the position of band edges is *fixed* with respect to the tip Fermi level: a cathodic bias stabilizes the tip above the n-type electrodes and occupied states are imaged in (c). Under depletion the tip comes into contact (d). Arrows refer to the direction of tunneling electrons.

has metallic-like behavior. The charge in surface states causes a *uniform* band bending in the semiconductor and no tip-induced effect is expected.

To summarize tunneling on low doped materials in vacuum requires that the diode be forward biased ot that extremely small tunnel currents be used under reverse polarization [41]. Using highly doped materials (with doping up to $10^{19}\,cm^{-3}$) is therefore preferable to avoid the question of the potential drop in the solid and to allow imaging at positive and negative tunnel bias on the same sample.

In the liquid environment the situation is different from that described above. Highly doped electrodes are often avoided because they present an enhanced reactivity with the solution. The sample and tip biases are set independently with respect to levels in solution and the position of the band edges of the semiconductor is fixed with respect to the tip Fermi level (U_t is indeed generally fixed within a narrow potential window). It follows that the situation is often the one shown in Fig. 6, with the tip Fermi level located in the band gap. In this situation, maintaining the tip at a constant height above the surface requires that the n-type electrode be cathodically biased so as to provide a sufficiently large density of electrons (Fig. 6c). The stability of this situation is governed by the sample bias and not by the tip bias since the position of the tip Fermi level is not critical here, unless it is outside the band gap.

Conversely, the tip comes into contact with the surface when the semiconductor is under depletion because free carriers are blocked in the bulk in Fig. 6d. The critical role of band bending for tunneling was identified very early by Itaya and coworkers with n-TiO_2 [42], n-ZnO [43] and n-Si [44]. With p-type samples, accumulation of majority carriers is not suitable for detailed STM imaging since holes corrode the surface at a high rate, unless reduced species from a redox system capture the holes to prevent corrosion.

Accumulation of majority carriers at the surface is however not the only possibility for tunneling. At a depleted surface, even with the tip Fermi level located in the band gap, tunneling may be possible under certain conditions. This is shown in Fig. 7. With a low-doped n-type electrode (Fig. 7a) tunneling at anodic bias requires illumination to create free holes in the valence band and tunnel electrons from the tip into the valence band of the sample. At a highly doped electrode, electrons can directly tunnel electrons from the tip into the conduction band through the space charge layer (Fig. 7b). Illumination is not necessary. The corresponding situations with a depleted low-doped electrode and a highly doped p-type electrode are shown in Fig. 7c and d.

It must be borne in mind that if the situations above extend the potential range for imaging they are associated with an electrochemical current, which may be critical. At n-type electrodes illumination or electron emission from the valence band into the conduction band causes corrosion by generating holes at the surface (Fig. 7, top) at the surface. With p-type semiconductors the situation is conversely

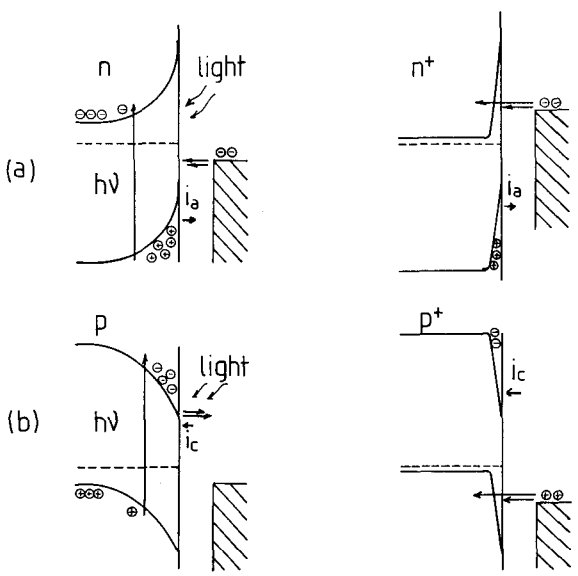

Fig. 7. Stable conditions for tunneling at a depleted n- (a) and p-type (b) electrode. Low-doped materials (left) require light of energy greater than the band gap. At the highly doped substrate (right) the thin space charge region can be tunneled. Electrochemical currents on the sample are i_a (anodic) and i_c (cathodic). Situations in (a) are associated with corrosion.

ideal since electrons arrive at the surface in Fig. 7c and d and no corrosion is expected.

In summary, in-situ STM is quite different from tunneling in vacuum. Long-standing imaging is preferable under accumulation at n-type and under depletion at p-type electrodes. The choice of the metal for the STM tip is an alternative way to gain flexibility for in-situ imaging. Tips made of noble metal are potentially interesting since the wide window of potential with no electrochemical current may allow imaging regardless of the sample voltage when the tip Fermi level reaches the conduction or the valence band of the electrode. Such a situation has been reported effective on n-MoS_2 with a Pt-Ir tip sufficiently negative to tunnel electrons directly into the conduction band [45, 46]. With a very positive Pt-Ir tip-tunneling out of the valence band of p-Si(111) has also been reported [17]. Tunneling from the valence band at a low-doped n-type electrode in darkness has not been used, to our knowledge. Though there is no physical impossibility, such conditions require extremely small tunneling currents, which are very difficult to obtain in-situ (in vacuum this situation is also avoided).

3.3 Topography and Electronic Contours

Equation (3) indicates that the STM tip does probe the density of electronic contours rather than the surface topography in terms of a hard-sphere model [47]. Electronic contours generally coincide with atoms on metals. With semiconductors the interpretation of images is not trivial because electrons are located in bound states (dangling bonds on clean surfaces in UHV, chemical bonds between surface atoms and ligands in liquids) whose density and occupation can vary from one atom to another.

Figure 8 illustrates this effect in the case of cleaved GaAs(110) [48]. Empty states (tip negative) appear as round spots and a rectangular unit cell can be defined in image (a). With a positive tip, image (b) shows that occupied states appear conversely as elongated chains, parallel to the $[1\bar{1}0]$ direction, with a unit cell identical in size to the first image. In Fig. 8c, the superposition of images (a) and (b) shows, however, that the two unit cells are shifted with respect to each other by a fraction of an ångström, demonstrating that only one-half of the complete (1×1) unit cell of the GaAs(110) surface is imaged at each of the biases. Filled states are located on As atoms and empty ones on Ga atoms because a partial transfer of electron occurs from a Ga atom to the next neighboring As atom (As is more electronegative than Ga) [49].

Clean surfaces of semiconductors do not exist in contact with liquids because dangling bonds react with ligands from the solution to form stable new chemical bonds. This contrasts with metals, for which the structure of the clean surface can be found in vacuum and in liquids, when specific adsorption does not take place. Figure 9 is an image of occupied states on clean Si(100)-2×1 after adsorption of a fraction of a monolayer of water [50]. The remaining clean surface consists of parallel rows whose orientation is rotated by 90° between two adjacent terraces (Fig. 9a). The (2×1) unit cell arises from the formation of Si dimers because this stabilizes the

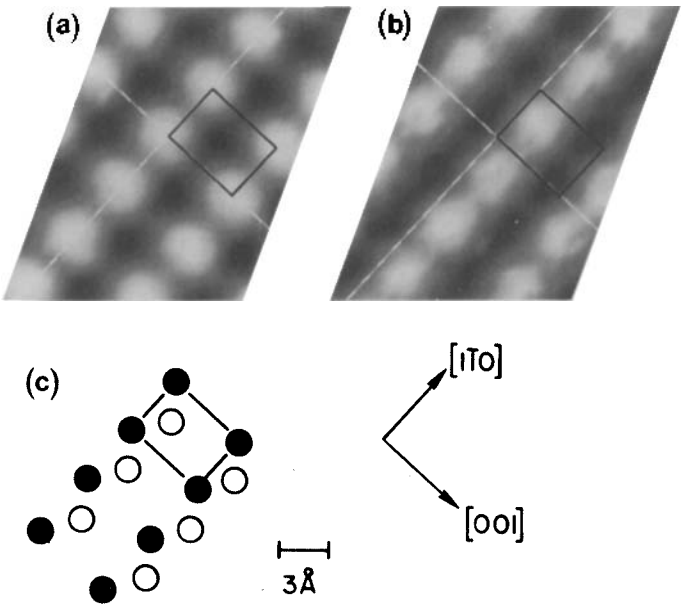

Fig. 8. Constant current images on cleaved GaAs(110): (a) empty (Ga atoms) and (b) occupied (As atoms) states. (c) Superposition of images showing the complete surface lattice (after [48]).

surface by leaving a single unpaired electron per surface atom instead of two at the ideally unreconstructed (100) surface. Adsorption of water molecules is dissociative and leads to the saturation of dangling bonds on a dimer according to the reaction

$$\geq {}^{\bullet}\mathrm{Si}-\mathrm{Si}^{\bullet}\leq + H_2O \rightarrow \overset{H}{\geq}\mathrm{Si}-\mathrm{Si}\overset{OH}{\leq}$$

with

$$\geq {}^{\bullet}\mathrm{Si}-\mathrm{Si}^{\bullet}\leq$$

representing a dimer with one unpaired electron on each Si atom and two bonds to the lattice. The density of states on Si–H and Si–OH bonds is smaller than on dangling bonds $Si^{\bullet}$, which explains why the depressed (i.e., darker) regions in Fig. 9a correspond to regions where adsorption occurred. At an atomic level, Fig. 9b shows that the (2×1) structure is preserved in accordance with IR spectroscopy [51]. Whether H and OH ligands are located on the *same* dimer remains an open question, however, because ligands are not completely immobile [50].

The structure of semiconductor surfaces under bulk solution can generally not be extrapolated from adsorption studies in UHV. For instance, Si(100) oxidizes in pure water with time and the surface is not simply saturated by Si–H and Si–OH

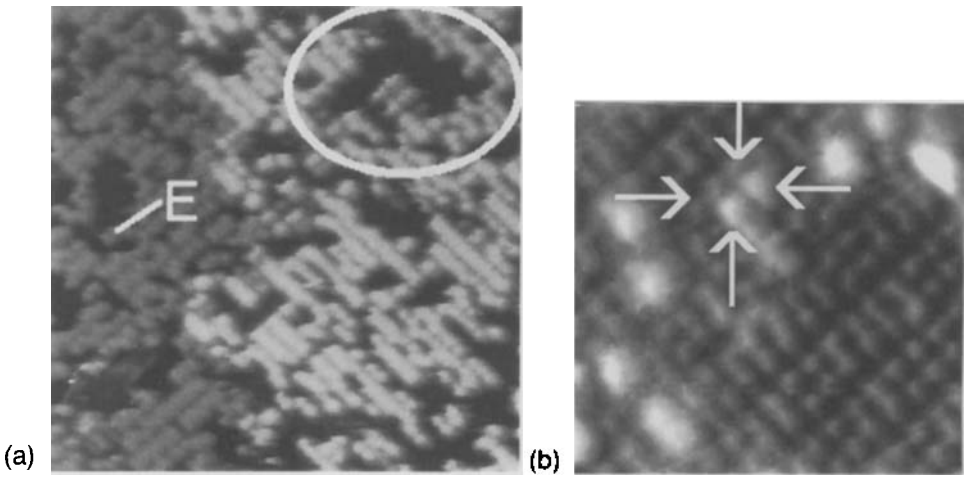

Fig. 9. (a) 180 Å × 180 Å STM image showing the empty states on Si(100)-2×1 after adsorption of 0.8 L H_2O. Bright spots are dangling bonds and dark regions are places where Si–H and Si–OH bonds have formed. (b) High-resolution image showing some Si dimers with H and OH bound (after [50]).

bonds. The composition of the solution is also an important parameter. In fluoride solutions the Si(100) corrodes and is finally covered with one monolayer of H atoms forming a (2×1) structure. (1×1) domains also exist because vertical dihydride modes are resolved in IR spectra [52].

Probing in situ the bias dependence of images seems difficult because of the restrictions concerning the polarization of the tip. Empty states are also short-lived. At a given bias, charge density effects can yet be observed. As an example, Fig. 10 shows an in-situ high-resolution STM image taken on n-Si(111) in NaOH. Occupied states are imaged since the sample is in accumulation [20]. Although the surface is known to be mainly terminated with Si–H bonds in this solution (see Sec. 5), few isolated atomic-size white spots are visible, and the atomic corrugation in the profile of Fig. 10 shows that they are nearly 0.8 Å higher than Si–H bonds. These spots presumably correspond to Si–OH bonds created during a polarization phase close to the rest potential. Within a hard-sphere model Si–OH bonds should appear higher than Si–H bonds by only 0.3 Å. The fact that they protrude excessively suggests that oxygen enhances locally the density of states (in constant-current imaging the tip-to-sample separation must increase when the density of states increases; see Eq. (3)). A similar effect is observed in the case of oxygen adsorption on GaAs in UHV [53]. The envelope of the profile of Fig. 10 is here almost flat apart from the protrusion, contrary to observations in UHV, because the negative charge on the ligand is efficiently screened by charges from the solution and by accumulation of free conduction electrons. In the UHV oxygen adsorbates induce locally an electrostatic potential (i.e., a band bending) in GaAs [53].

On metals and in the liquid environment, Magnussen et al. [60] have also found an electronic effect when imaging ordered layers of hydrogensulfate ions on Au(111).

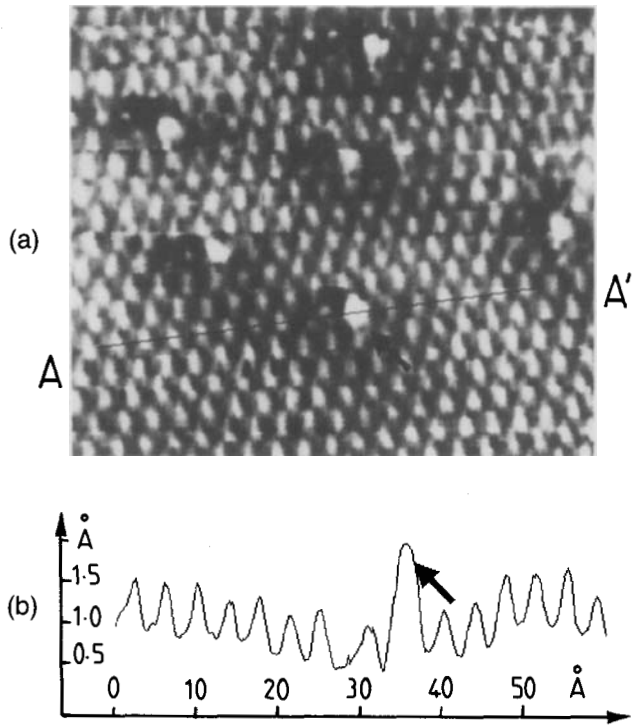

Fig. 10. High-resolution 72 Å × 62 Å in-situ STM image of n-Si(111) in NaOH after a short polarization period close to the rest potential. Imaging was performed at $U_s = -1.5$ V/SCE. The surface is mostly H-terminated but atomic-size white spots correspond to isolated Si–OH bonds (P. Allongue, unpublished image).

Layers appear differently according to tunneling conditions. Examples of the bias dependence of images at metallic substrates, even in vacuum, remain nevertheless rather scarce; carbon adsorption on Al(111) is one of the few. The effect is again a local variation of the charge density which modifies the electronic contour on nearest- and next-nearest-neighbor Al atoms [61]. Controlling the tip chemistry is another method of imaging adsorbates on metals. Ruan et al. [62] have, for instance, distinguished oxygen atoms from Cu atoms on Cu(110) by reversibly chemisorbing oxygen on the apex of a tungsten tip.

4 Spectroscopic Characterization

In vacuum, scanning tunneling spectroscopy (STS) has already opened new possibilities of studying the energy distribution of states at an atomic level. Owing to the necessity of scanning the tip potential over several volts, true spectroscopy has still not

been applied in liquids. After a brief review of tunneling spectroscopy, illustrated in one example, in-situ spectroscopic approaches to surface electrodes are discussed and the potential of in-situ STS is examined.

4.1 Ex-Situ Scanning Tunneling Spectroscopy

The bias dependence of STM images originates from the *spatial* distribution of states at the surface (see Fig. 8). The *energy* distribution can be derived from STS. It is easy to demonstrate from Eq. (3) that the normalized conductance $\Gamma = (di_t/i_t)/(dU_T/U_T)$ is proportional to $N_s(E)$, the local density of states (LDOS) at the surface of the sample, provided that the tip-to-sample distance s is constant and $N_t(E)$ does not vary. The difficult question of the influence of the tip has been investigated recently.[2] Experimentally, STS is performed by scanning the voltage during U_T while the feedback loop is *interrupted* briefly. Measurements must be sufficiently fast to probe a defined site.

Figure 11 compares the LDOS and surface structures of two Si(111) surfaces [54]. After cleavage, the clean surface is (2×1) reconstructed with π-bonded chains of Si atoms. This is accounted by the rows visible in the large-scale and high-resolution STM images (left). On this surface the STS spectrum shows two peaks, which have been explained theoretically by the existence of bonding and antibonding states at the surface [55]. These states are due to partial charge transfer between dangling bonds on atoms forming dimers [56]. After treatment in HF the surface becomes unreconstructed and ideally (1×1), as shown by the high-resolution STM image on the right. IR spectroscopy has determined that the surface is terminated by one monolayer of Si–H bonds [57]. The corresponding LDOS becomes featureless over nearly 1 eV (see spectrum on the right), showing that surface states are removed from the band gap of Si. The H-terminated Si surface is the prototype of passivated semiconductor surfaces. Electronically this surface presents the lowest surface recombination velocity ever reported [58]. Chemically the monolayer of H atoms is also relatively inert and resists oxidation over hours at ambient [59] or in acidic solution [15, 17, 44]. These unique properties come from the fact that each dangling bond is saturated by an H atom and that the topmost Si atoms retain their bulk position (Si–H bonds are nonpolar).

STS can be performed in air, especially on materials unreactive to the surroundings, such as TiO_2 [63, 64], Fe_2O_3 [63], FeS_2 [65] and n-WSe_2 [66]. GaAs [67] could also be studied by STS in air after stabilization of the surface with a sulfur treatment (see Sec. 5.2). On WSe_2, Fan and Bard [66] combined STS with sample illumination

[2] Using low-temperature STM operating at 4 K, the contribution of the tip to Γ could be determined in the case of Fe adsorbed on Pt(111) because the tip could be positioned on a defined point for a long time. After deconvolution the true distribution of states was obtained (see M. F. Crommie, G. P. Lutz, D. M. Eigler, Phys. Rev. B 48 2851 (1993). The main features of the distribution were however resolved without deconvolution.

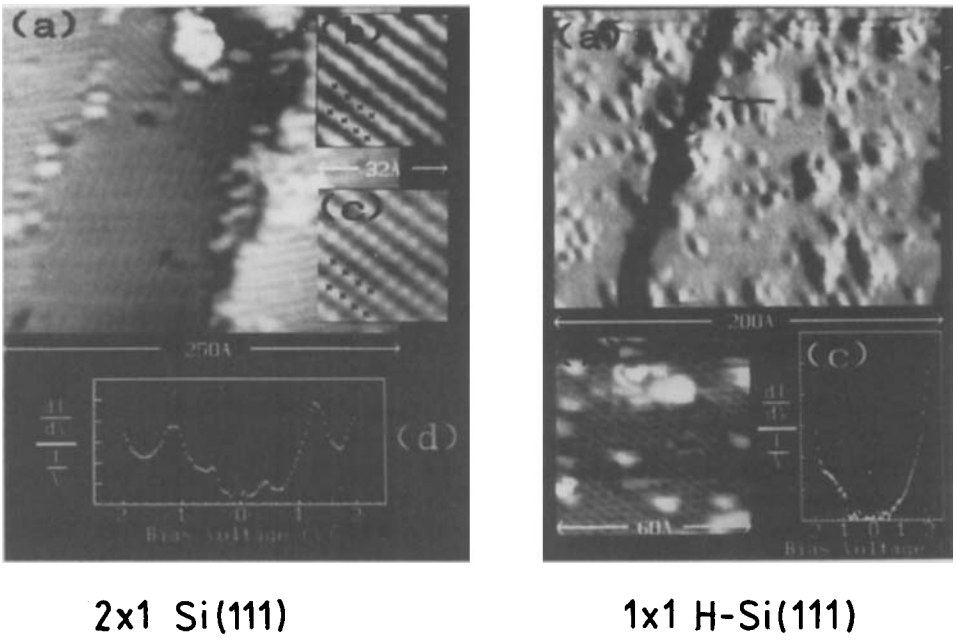

Fig. 11. Comparison between STM and STS results obtained on cleaved 2×1-Si(111) (left) and NH_4F-treated 1×1-H–Si(111) (right) surfaces. STS spectra are shown together with a large-scale STM image and one or two atomically resolved STM images in each case. Note that the H-termination of the surface removes the states which exist in the band gap of the 2×1 surface after cleavage (after [54]).

and demonstrated that recombination centres are localized at steps. STS has been also resolved spatially and coupled to topographic images by several groups [6]. Using this approach Wolkov and Avouris [68] could characterize and analyze the reactivity of the different Si adatoms of the 7×7 unit cell on a Si(111) surface upon adsorption of ammonia. Though difficult, STS is now an established method which confers a chemical sensitivity to STM.

At metallic surfaces, STS spectra are generally not as structured as at semiconductors. This probably explains why STS has had much less impact upon metals [69]. STS has nevertheless been successfully attempted on Au(100), Au(111) and Pd(111) [70–72]. On Au(111), imaging the surface near the surface state gives a better contrast [73]. On Ni(100), islands of NiO were detected by STS [2]. Very nice results have recently been obtained on Al(111) after adsorption of various species [74]. Hasegawa and Avouris [75] have imaged on reconstructed Au(111) the standing wave pattern formed by the electron density. Such a phenomenon, observed at steps or around adsorbates, stems from interferences between the incident and the reflected wave functions of electrons in 2-D states on this surface.

4.2 In-Situ Spectroscopic Investigations

According to Sec. 3, the characterization of interface states at semiconductor electrodes is a key question since these states influence the behavior of the interface [76, 77]. The many different techniques of characterization have been reviewed [35, 76, 77] for the solid/liquid interface. True STS has not been applied until now. In first attempts to derive energy information the sample voltage was scanned to avoid problems with the electrochemical current at the tip extremity. The possibility of scanning the tip bias is discussed later.

4.2.1 Tip Current Voltammetry (TCV)

This technique, thus named by Carlsson et al. [78], consists in recording the tip current as a function of the potential of the sample. TCV can be applied with the regulation loop of the tunnel current active or not. Though the terminology "tip current voltammetry" is rather confusing, because the tip potential is *fixed*, we use it in the following to conform with published work.

With Feedback Loop Active

This approach has been applied to GaAs [78–81], GaP [78, 82] and CdS [80]. Examples of TCV obtained with various n-type GaAs electrodes are presented in Fig. 12. Results are redrawn from [80]. According to the principle of TCV, imaging is possible in regions of potential where the tip current is equal to its pre-set value as indicated by horizontal arrows. A negative tip current means that electrons are flowing out of

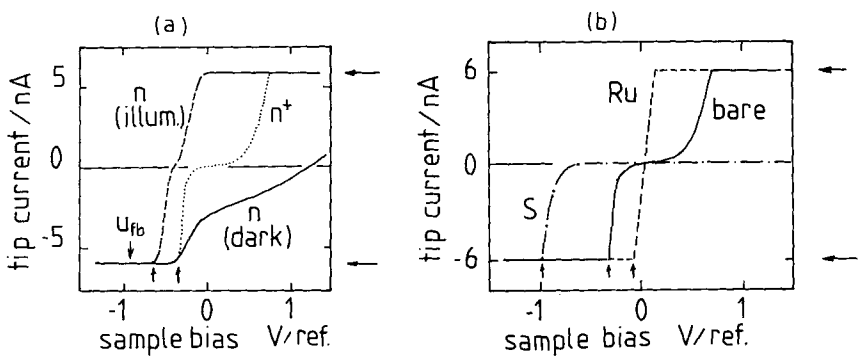

Fig. 12. Example of TCV recorded with the feedback loop active on n-GaAs electrodes. (a) Effect of the doping level: the n- and n^+-GaAs (10^{18} cm^{-3}) samples contact $HClO_4$. (b) Effect of the surface treatment on n^+-GaAs: Ru deposition and sulfide coating. A negative tip current means that electrons flow out of the sample. Horizontal and vertical arrows indicate the pre-set current and transition potentials U_s^0. The reference of potential is Ag/AgCl (redrawn from [80]).

the sample. Starting from cathodic bias U_s, where tunneling is stable, the regulation loop forces the tip into contact with the surface above a certain potential U_s^0 (see vertical arrows) because the band bending becomes too large: this is the so-called "contact mode" introduced by the authors. The z-voltage undergoes variations of several tens of volts [42, 44, 82], which seems very large.[3] The tip either travels downward over such a large distance that it should completely plunge into the surface or it retracts too far for allowing tunneling.

TCV is a rapid method for evaluating stable tunneling conditions, and observations fit the general principles exhibited in Fig. 7 as far as the effect of the doping level is concerned for tunneling at anodic bias (Fig. 12a). After various surface treatments of n^+-GaAs, TCVs display remarkable modifications (Fig. 12b). After electroless deposition of a thin film of Ru, the TCV resembles that of a metallic electrode, with a sharp transition from $i_t < 0$ to $i_t > 0$. The treatment in ammonium sulfide hampers tunneling at anodic bias and shifts U_s^0 negatively, apparently in accordance with a passivation of electronic states by the sulfur layers on GaAs [83].

The above observations point to the question of whether TCV really yield information regarding the surface states. At the bare surface of GaAs, the distribution of electronic states in GaAs is shown in Fig. 13a [84]. There are two surface states located about 0.4 eV above the valence band and labeled "CORR. STATES" because these have been identified as intermediate states in the corrosion of GaAs. The state EL2 is a bulk defect, well known in GaAs, whose origin is not completely identified. The two other band diagrams in Fig. 13 correspond to the situation where electrons *begin* to tunnel from the tip into GaAs (see Fig. 12a). The position of the band edges is taken from [80, 84].

At the illuminated lightly doped sample (Fig. 13b) holes accumulate at the surface, in the valence band, and in surface states, which shifts the flat band potential shifts downward by ~ 0.2 V [85]. Electrons tunneling out of the tip can enter the solid either in the valence band or in the corrosion states. That TCV, recorded with a tip Fermi level located between surface states and E_v, is identical to the ones Fig. 12a [78] shows that the anodic branch is not related to the distribution of surface states. At the highly doped electrode (Fig. 13c) tunneling is most likely assisted by the bulk state EL2, as the band diagram suggests. The space charge layer is indeed too thick at this energy even for a doping level of 10^{18} cm^{-3} (w is 100 Å). In both cases observations are not related to surface levels.

No metal-induced surface state is necessary to explain the new behavior after Ru coating (Fig. 12c). The simplest interpretation is that the surface becomes metallic through electronic coupling between small metal clusters forming the film above a critical density [77], in analogy with observations reported in the case of Au on GaAs in vacuum [86]. The impossibility of tunneling at anodic bias after passivation of GaAs in $(NH_4)_2S$ is also not related to a reduced density of surface states. Recent studies have indeed shown that the sulfide coating does not suppress surface states but rather pins the Fermi level at a lower position in the band gap [87]. The new be-

[3] This value roughly corresponds to a vertical motion of the tip by several hundreds of ångströms in the z-direction with usual piezo elements of sensitivity 20 Å V^{-1}.

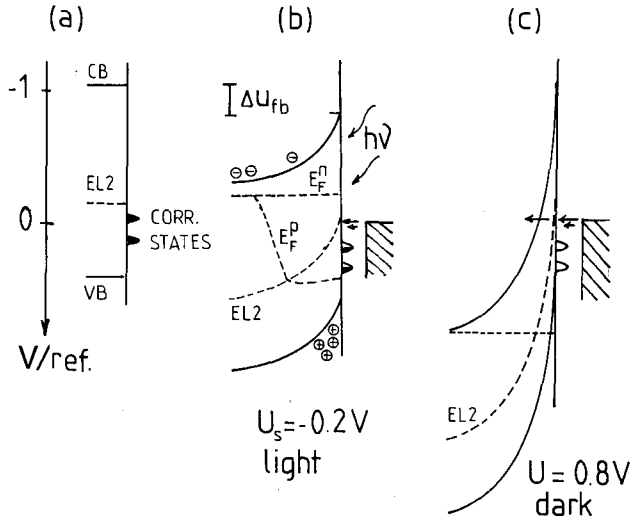

Fig. 13. Band diagrams corresponding to the onset of "anodic" branches of TCV of Fig. 12(a). The distribution of states is taken from [84]: EL2 = $E_c - 0.85$ eV is in the bulk and the two surface states labeled "CORR. STATES" are located 1 eV and 1.15 eV below E_c. U_{fb} is taken from [80]. In the highly doped sample tunneling is assisted by EL2.

havior of the passivated surface probably stems from the formation of some thick layer whose poor adhesion [88] may hinder tunneling with the sample.

The discussion above shows that TCV can be reasonably interpreted in the framework of known electronic states. The direct determination of interface states from TCV seems difficult because the dependence of U_s^0 with the tip potential [78, 81] finds no simple explanation within a simple one-dimensional energy diagram. Tip-induced local modifications of the band diagram of the semiconductor may exist (see Sec. 4.2.3) which complicates the determination of energy levels. The experimental dependence of U_s^0 on the pre-history of the electrode [78, 81] stem probably from changes in the position of band edges [89, 90].

With Feedback Loop Interrupted

This technique has been used by Tomita et al. [44]. The tip is maintained at a constant height during scanning of U_s, by opening the regulation for the tip current for a short time. Figure 14 shows results in the case of n-Si(111) in acidic medium, after etching in HF so as to produce an H-passivated surface [58]. As soon as U_s is positive relative to U_{fb}, accumulation of electrons stops and the tip current decreases. A plateau is seen before the current finally drops to zero. This behavior, ascribed by the authors to the presence of surface states in the upper part of the band gap [44], might very well be explained differently since the H-terminated Si surface is free of surface states according to Fig. 11. Within a simple Schottky diode description of

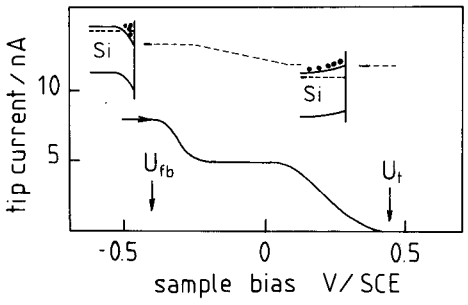

Fig. 14. Example of TCV recorded with the feedback interrupted on n-Si(111) in H_2SO_2 (after [44]). The broken line is a speculated sweep of band edges with bias.

the tunnel junction, the tip current is proportional to n_s, the density of free electrons at the surface, and its decrease reflects the decrease of n_s with increasing band bending V_b when the potential becomes more positive. In this context, the plateau in Fig. 15 is indicative of a positive shift of band edges, as the dotted lines between band diagrams illustrate, because the Si is initially in accumulation at cathodic bias [20]. It would be interesting to test the technique on other materials where surface states are undoubtedly present.

Tip-Induced Potential Distribution

This section addresses the interpretation of energy diagrams of the tunnel junction. There is some evidence that a one-dimensional approach such as that in Fig. 13 is not always correct because Fig. 12 suggests that tunneling is possible, with the feedback loop active, at a low-doped semiconductor depleted by a band bending as large as ~ 0.4 V. A rapid estimate of the local current shows that this should not be possible. In fact, excluding tunneling through the space charge layer (its thickness is ~ 1000 Å at this bias) electrons must first jump over the barrier (thermionic process) and then tunnel into the tip. The thermionic current is given by:

$$i_{th} = A^* T^2 \theta \exp(-eV_b/kT) \tag{4}$$

with A^* the Richardson constant (~ 8 A cm^{-2} T^{-2} for GaAs) and θ the surface area from which electrons are collected before emission into the tip.

If one assumes, as in Fig. 15 a, a one-dimensional band diagram and that tunneling electrons are collected from the sample within a disk of diameter 100 Å, which is already larger than the radius of the tip, the current i_{th} is *several orders of magnitude smaller* than typical tunnel currents in the nanoamp range. To reach a thermionic current of 1 nA locally, the surface θ must be a disk of diameter in the micrometer range. An explanation in terms of surface diffusion of carriers seems insufficient.

The simple evaluation above suggests that the surface barrier is not the ideal one shown in Fig. 15 a and we speculate that the tip induces a potential well at the surface. The modified band diagram is presented in Fig. 15 b. Away from the tip, the po-

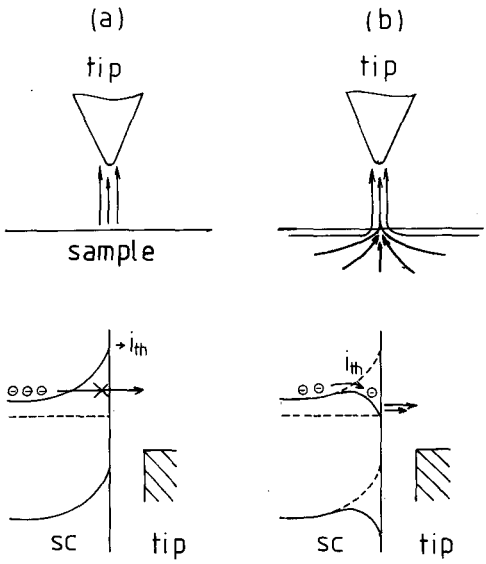

Fig. 15. Schematic lines of current between a depleted semiconductor and a tip, according to two hypotheses. (a) The surface is an equipotential and electrons are collected from a small disk under the tip. (b) Case where the tip induces a three-dimensional potential. The profile of bands under the tip is the solid line. Away from the tip, the broken-line profile is the one in (a). In this case lateral conduction of carriers is possible in $i_{th} \sim i_t$ (see Eq. (4)).

tential in the space charge layer is quadratic as usual (broken-line profile). Close to the tip the profile of bands is inverted under the surface (solid line). The potential barrier seen by electrons in the semiconductor is locally reduced by the positive charge at the tip extremity, in analogy with the modulation of the potential in MOS structures when fixed charges are localized in the oxide layer[4] [91]. The size of the disk θ in Eqn. (4) is related to the screening distances of the potential pocket under the tip, typically the Debye length toward the bulk of the substrate, and the width of the space charge layer (a few 100 nm) laterally, since this potential well allow lateral conduction of electrons.

Tip-induced effects are expected to be less important and even to disappear at highly doped materials and also when majority carriers are accumulated at the surface. It should be noted that images are experimentally featureless when extreme tunneling conditions such as those described at the beginning of this section are used.

4.2.2 In-Situ Spectroscopy

We refer here to techniques where the tip potential is scanned within limits of low faradaic currents. The tip insulation is critical. The results presented below are preliminary observations made by our group. No other results have been published, to our knowledge.

[4] An array of positive point charges on a n-type semiconductor creates potential pockets whose depth and spatial extension depend on certain conditions defined in [91]. With a single point charge the same effect is expected.

With Feedback Loop Active (Pseudospectroscopy)

This first approach has been used to study the interface between Si(111) and a dilute NH_4F solution of pH 4 [16]. In Fig. 16 sharp transitions (potential U_t^0) are observed at n-Si except when it is biased too cathodically. U_t^0 follows the bias sample. At p^+-Si, U_t^0 shifts negatively with illumination.

The coincidence between U_t^0 and U_s stems from the "metallic-like" behavior of n-type Si by accumulation of electrons ($U_{fb} \sim 0$ V/Pd−H; the flat band of n-Si almost coincides with the rest potential of the electrodé [92]). When U_t is negative relative to U_s, electrons tunnel from the tip into the conduction band of n-Si. For $U_s = -0.6$ V, the excursion of U_t is too small to reach the transition potential where the tip Fermi level crosses the Fermi level of n-Si. In the case of p^+-Si, which is depleted of holes at the surface by a band bending of ~ 1.3 V at $U_s = -0.7$ V, electrons must tunnel through the space charge region, from the valence band into the conduction band, and then from the surface into the tip when $U_t > U_s$ (Fig. 16b). Under illumination, the accumulation of photoelectrons at the surface shifts the position of band edges negatively and the transition potential is displaced by the same quantity indicating that U_t^0 is related to the potential where the tip crosses the conduction band edge ($E_c \sim -0.25$ V). Electrons tunnel out of the tip into the conduction band before crossing the thin space charge layer. No surface state is involved in observations: this is consistent with Fig. 11b. In this example the interpretation of results is fairly simple because surface states are not involved.

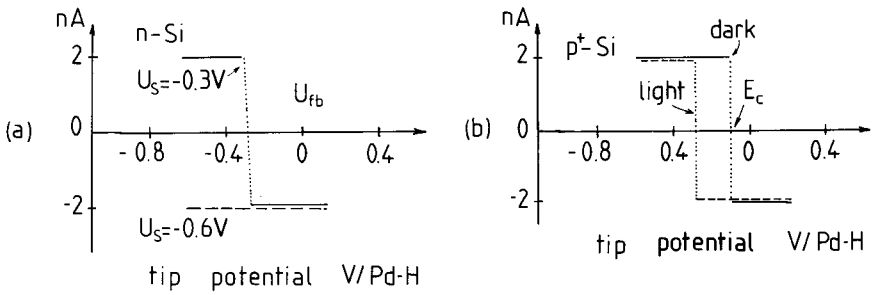

Fig. 16. $i_t - U_t$ curves recorded with feedback loop active at n- and p^+-Si(111) in NH_4F, pH = 4. The sample bias is as indicated in (a). For p^+-Si $U_s = -0.7$ V in darkness and under illumination. When $i_t < 0$ electrons flow out of the sample (after [16]).

In-Situ STS (Feedback Loop Interrupted)

Results obtained with n-GaAs in NaOH are presented in Fig. 17. True in-situ STS measurements, plotted in the form of $i_t - U_t$ curves, are solid lines. Since in tunneling mode the tip current is the sum $i_T + i_F$, with i_T the tunnel current, the faradaic component i_F has been determined by retracting the tip far away from the surface (dotted line). The shape of STS curves is very similar to curves obtained in ex-situ

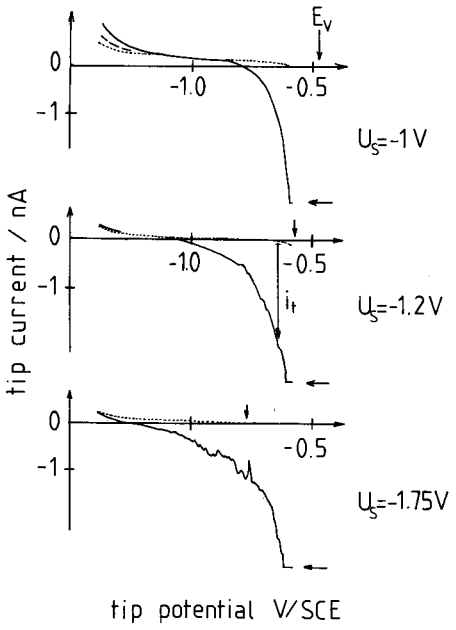

Fig. 17. Actual in-situ STS results obtained at the interface n-GaAs/NaOH. Solid lines represent the sum $i_t = i_F + i_T$. Dotted lines correspond to $i_t = i_F$ and are recorded with the tip retracted. The bias of the sample is as indicated. Vertical arrows correspond to the position of the valence band maximum at the surface. When $i_t < 0$, electrons flow out of the sample (P. Allongue, unpublished work).

experiments with an n-type semiconductor because the faradaic current i_F was carefully kept very small over the potential excursion.

The tip current drops abruptly for $U_s = -1$ V because the tip Fermi level is in the band gap of GaAs, in its lower portion. The current decreases further in the gap as the tip bias is scanned negatively (i.e., it enters more deeply into the band gap). With more negative sample bias, hydrogen evolution starts and the flat band of GaAs is shifted negatively [89]. The decrease of the tip current accordingly becomes smoother and smoother, as the two curves show. The approximate position of the valence band edge is shown in the Figures.

The results of Fig. 17 are encouraging and demonstrate that real STS is feasible in situ, with some care. The principal complications with respect to vacuum are twofold.

1. $i_t - U_t$ curves include an electrochemical component which needs being subtracted, even if it remains small.
2. The rate for scanning U_t cannot be very large because the large tip capacitance will dominate (in the experiment presented, the scan rate only a few volts per second). The capacitive current might perhaps be compensated in the input of the i/V converter [6].

To improve the dynamics of the results one should also record $i_t - U_t$ curves at different tip-to-sample separations, as suggested by Feenstra [86].

5 Studies of Electrochemical Reactions at Semiconductor Electrodes

Dissolution and metal deposition are the two major reactions which have been studied by in-situ scanning probe microscopy. The rate of electrochemical reactions can be affected by tip shielding, especially for reactions controlled by diffusion (mass transport is hindered in the close proximity of the tip). The effect manifests itself by reaction overpotentials larger than expected, for instance to observe deposition under the tip. Shielding is less important for slower reactions or with increasing scan size of images. The influence of the tip is not a simple problem and some reports indicate that the rate of reactions is enhanced instead of being reduced. Tip-induced modifications of reaction rates can be detected by observing whether the topography of the surface significantly changes with the size of scans.

5.1 Silicon Substrates

The technology of silicon is now extremely well controlled, as evidenced by the increasing integration of ULSI circuits. The use of short interconnected active components and more recently the discovery of photoluminescent porous layers of Si [93] further widen the future applications of silicon to high-speed electronics and possibly to integrated optoelectronic devices. Electrochemical processing of Si wafers (cleaning, etching, etc.) has gained tremendous interest in recent years and the surface topography and chemistry of this material can be controlled at an atomic level by appropriate surface treatments. Atomically flat Si surfaces, in particular, can be prepared by exposure to fluoride solutions of appropriate pH [57, 94–96].

It has been established that one monolayer of Si–H bonds is left on the surface of Si after treatment in fluoride solutions. A recent review [94] on that topic gives historical notes and detailed information about the chemistry and topography of hydrogenated Si surfaces at an atomic level. Chabal's group developed IR spectroscopy and performed theoretical calculations (by means of ab-initio cluster calculations) to such an extent that atomic-size inhomogeneities and imperfections could be identified on H/Si(111) and (100) surfaces [95, 96]. The recent advent of STM has provided a unique complement to IR investigations.

The Si–H termination passivates the surface electronically (the density of states is very low, as Fig. 11 shows) and prevents oxidation over several hours in air [59] and acidic liquids [15, 17]. Most of scanning probe characterizations have been performed ex-situ, in air, in a liquid which does not react with the surface, or in UHV, after processing the surface in various fluoride solutions. The dissolution process has been observed also in-situ and in real time.

5.1.1 Ambient Imaging

Though resistant to oxidation in air, HF-treated Si surfaces seem unstable under the STM tip. The large tunnel bias (~ 2 V) necessary to image the surface induces chemical modifications underneath the tip, probably with the help of adsorbed water. Direct writing with a resolution of 20–30 nm has been reported on hydrogenated Si surfaces by applying a tunnel voltage larger than necessary for imaging [97, 98]. Figure 18a shows a pattern written on Si(111) by this method. Dark regions are depressed by more than 1 nm in STM images and the measured work function is locally lower [97], which suggests either the removal of some material or oxide formation since regions of lower work function should appear to protrude in constant-current mode imaging; see Eq. (3). AFM imaging could help in elucidating the exact nature of surface modifications by discriminating topographic from electronic effects. The dimensions of patterns depend on the value of the tunnel voltage, duration of treatment and composition of the ambient atmosphere. With increasing O_2 partial pressure in an O_2/N_2 atmosphere the depth of patterns increases, suggesting that oxygen incorporation does occur locally [97]. Barniol et al. [99] have reported that high tunnel voltages are not necessary to create such depressed regions. At large voltage they formed mounds, in contrast to the report of Dagata et al. [97]. Enhanced oxidation of the surface at fluoride sites is the authors' explanation for samples which were not rinsed in water after HF treatment.

The results above point to the difficulty of high-resolution ambient imaging of hydrogenated silicon. Besocke et al. [100] nevertheless presented good-quality large-scale STM images of Si(100) with steps visible after extended tip scanning. One view of the surface is shown in Fig. 18b. The measured step height of 4 Å, is however surprising and might be indicative of the formation of biatomic steps. In other sequences the authors showed that step edges migrate under the tip while the surface smoothens. Hsiao et al. [101] studied the roughness of Si(111) after exposure to 40% ammonium fluoride (NH_4F). The authors started with a surface covered by an oxide layer and had to thin it down before STM imaging. The surface looked porous

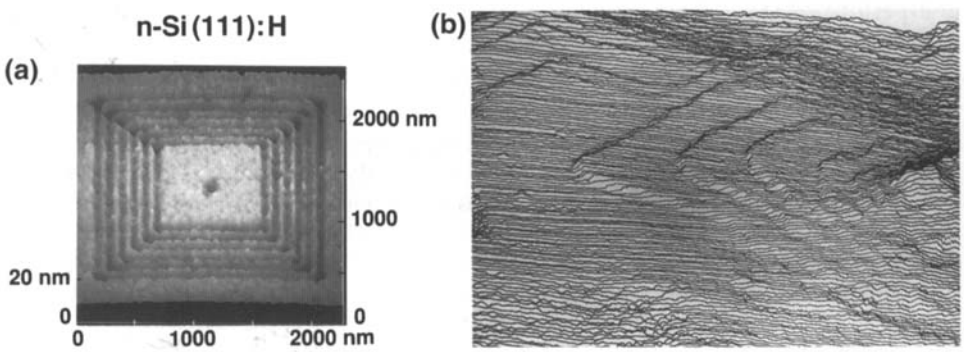

Fig. 18. STM images of Si in ambient conditions. (a) Pattern generated by the tip on Si(111) etched in HF (after [98]) and (b) image showing the resolution of atomic steps on Si(100) (after [100]).

before complete removal of the oxide layer by NH_4F (the surface was still hydrophilic). For longer etchings silicon itself was then imaged (the surface was hydrophobic) with a minimum roughness of 1.4 Å obtained after 1–2 min of etching. At longer exposures pillars 200 Å high were formed and their size could be decreased by addition of $NaCNBH_3$ in solution. This surface topography, with high aspect ratio structures, is probably due to the fact that the surface was chemically oxidized just prior to final etching. The interface between Si and SiO_2 is indeed *rough* [102] and etching in NH_4F has the tendency to increase the relief. A flat Si/SiO_2 interface, obtained by thermal oxidation in dry O_2 with subsequent annealing should be preferred [103].

Atomic resolution has been also achieved in air. Jungblut et al. [104] imaged Si(100) surfaces after electrochemical treatment including anodic oxidation and anodic oxide dissolution in dilute NH_4F solution of pH 4.5. The surface was very rough on a large scale. High-resolution images were very noisy but (1×1) and (2×1) domains could apparently be resolved after image processing. Using AFM, Kim and Lieber [105] resolved the (1×1) structure after etching Si(111) in HF/NH_4F solutions of pH 5–8 without surface processing. The quality of AFM images was much better than that of STM images, probably because AFM imaging involves no electric field. AFM imaging of Si in air is not easy with a high resolution, however. The force applied to the cantilever is critical for the resolution in air. Capillary forces due to some layer of moistures stick the tip on the surface and may result in surface damaging as sometimes evidenced by depressed squares on enlarged scans. The tip may also degrade on hard surfaces such as the surface of Si. Non contact mode AFM sems to allow better resolution on a large scale. Vatel et al. [106] showed that annealing Si(100) in hydrogen reduces to 1 Å the roughness of HF-treated wafers. Monoatomic steps and flat terraces were resolved by the same authors after epitaxial growth of Si on the same substrates and also on MBE Si(100) layers [107]. Susuki et al. [108] imaged by AFM Si(111) prepared in vacuum so as to produce a Si(111)-(7×7) surface before thermal oxidation and observation in air. On a large scale the morphology is characteristic of that observed on clean (7×7) Si surfaces in vacuum, with large flat terraces and step bunching [109].

5.1.2 Silicon Etching

In-situ IR spectroscopy has proved that the surface of Si is exclusively covered by Si–H bonds when it contacts fluoride solutions [110] or strong bases [20, 111]. Ex-situ IR spectroscopy [57] and more recently ex-situ scanning probe microscopy [17, 20, 112, 113] have also shown that the topography of Si depends critically on the pH of fluoride solutions. These results have prompted many studies to elucidate the mechanism of etching.

Ex-Situ UHV Investigations

Hessel et al. [112] imaged Si(111) after etching in NH_4F solutions of increasing pH, and rapid transfer of the samples into a UHV chamber. Images paralleled very well

IR spectroscopic results by showing that the surface becomes atomically smoother with increasing pH, in accordance with the sharpening of the absorption IR stretching mode of vertical Si–H monohydrides on Si(111) observed at intermediate pH [57]. Itaya et al. [17] obtained similar STM results by transferring p-Si etched samples into dilute sulfuric acid where the Si–H surface was chemically stable at cathodic bias. The rough surface observed after etching in acidic HF reflects the fingerprint of the Si/SiO_2 interface since Si is scarcely etched[5]. Using a spinning technique, Pietsch et al. [113] studied the very initial stages of Si(111) etching in buffered NH_4F, after removal of the oxide layer in acidic HF. Figure 19a shows that a large density of triangular etch pits is created after only 0.1 s of exposure. Pits grow laterally until adatoms on top of terraces are removed; large and atomically flat terraces with large triangular pits are observed after 4 min on a perfectly oriented surface. On a sample slightly tilted (by 0.2°), Figure 19b shows that 3 min of etching in buffered NH_4F preserves the initial stepped surface structure because Si etching occurs according to a step flow process (similar images are obtained for longer exposures) [112]. The authors have found that terrace edges move six times faster than etch pits on terraces.

The long-range structure of monoatomic steps strongly depends on the crystal miscut. As expected from the coordination of step edge atoms, monohydride-terminated steps dominate on precisely oriented samples [113] and steps are either rectilinear or jagged, on surfaces slightly tilted in $[\bar{2}11]$ and $[\bar{1}\bar{1}2]$ respectively [112]. Figure 19c shows, however, that step-to-step interactions may stabilize dihydride-terminated steps on a (111) sample tilted by 2°, in $[\bar{1}\bar{1}2]$ [113]. Steps are perfectly linear, and regularly spaced, in this image; terraces are also defect-free, in contrast to those seen on better-oriented surfaces (Fig. 19b), because the lateral migration of narrow steps is too fast to allow the nucleation and growth of etch pits. Along the same lines, the results concerning the etching of Si(100) in NH_4F are quite instructive since they show that the atomic coordination is not the sole parameter governing the etch rate. Figure 19d is a large-scale image of Si(100) after etching in NH_4F [115]. Pyramids and flat portions are visible. There are *c.* 10^{12} pyramids/cm^2 presenting (111) microfacets and a height of 20 Å; (100) terraces represent about 60% of the surface exposed to solution. This surface structure is little affected at longer exposure, implying that the (100) face is rather unexpectedly stable compared with the (111) face. The reason is apparently a 2×1 reconstruction of the (100) face, as suggested by the strings resolved in the area with enhanced contrast of Fig. 19d. Though Si–H monohydrides are threefold-coordinated on the reconstructed (100) face and on the (111) face, the etch rate of the (100) surface is slightly faster because the Si–H are strained on the (100) face.

At an atomic level (100)–H surfaces are 2×1 reconstructed [115] (see above). (111) faces have the ideal (1×1)–H arrangement after treatment in buffered NH_4F [105, 116, 117] or in hot water [118]. The 1×1–H/Si(111) surface has been imaged in dilute H_2SO_4 [17] and in NaOH [20] (although etching proceeds in the latter case). Etching in 1% HF apparently leaves (111) terraces covered by Si trihydrides

[5] The etch rate of Si(111) is about 0.3 Å min^{-1} in 48% HF [114].

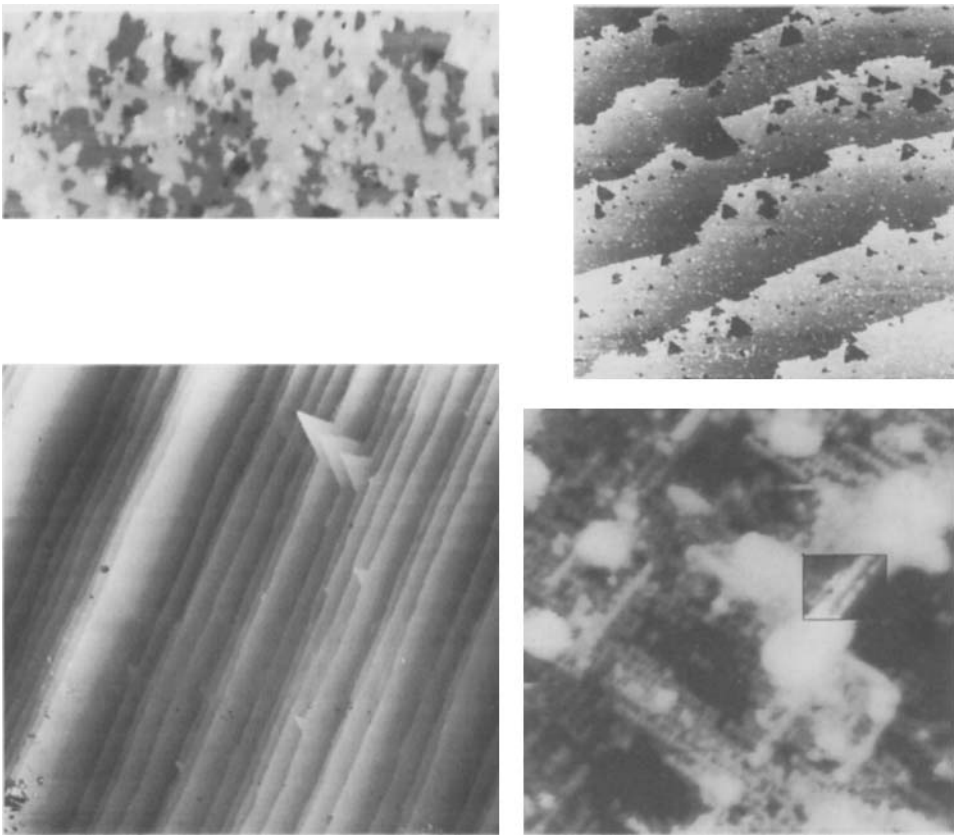

Fig. 19. Ex-situ (UHV) STM images taken on Si after removal of the chemical oxide in HF and final etching in 40% NH_4F. (a) Precisely oriented (111) sample after a 0.1 s etching (1400 Å × 600 Å). (b) Slightly misoriented (111) sample toward $[\bar{2}11]$ after 3 min of etching (5000 Å × 5000 Å). (c) Same as (b), but on a surface misaligned by 2° in $[\bar{1}\bar{1}2]$ (3000 Å × 3000 Å). (d) (100) face after 10 s of etching (240 Å × 240 Å). Images (a) and (c) are taken from [113], image (b) from [112], and image (d) from [115].

[118]. Figure 20a presents two atomic models for the $-SiH_3$ termination, which fit the threefold symmetry with 2.2–2.3 Å interatom spacing found in STM images (for Si–H monohydrides on Si(111), 3.8 Å is expected). Large domains of this structure are found on images which showed also fuzzy regions, perhaps because of some species mobile at the surface (the sample was not rinsed), a feature which recalls also the observations of Kim and Lieber [105]. In some places, however, atomic-scale STM images display very complex and disordered atomic structures, an example of which is shown in Fig. 20b. The different sites labelled G1 to G3 in the image have been interpreted by the authors as being sites at the boundary between the two domains of $-SiH_3$ in Fig. 20a since the $-SiH_3$ cannot rotate freely at the surface (domains are rotated by 30°).

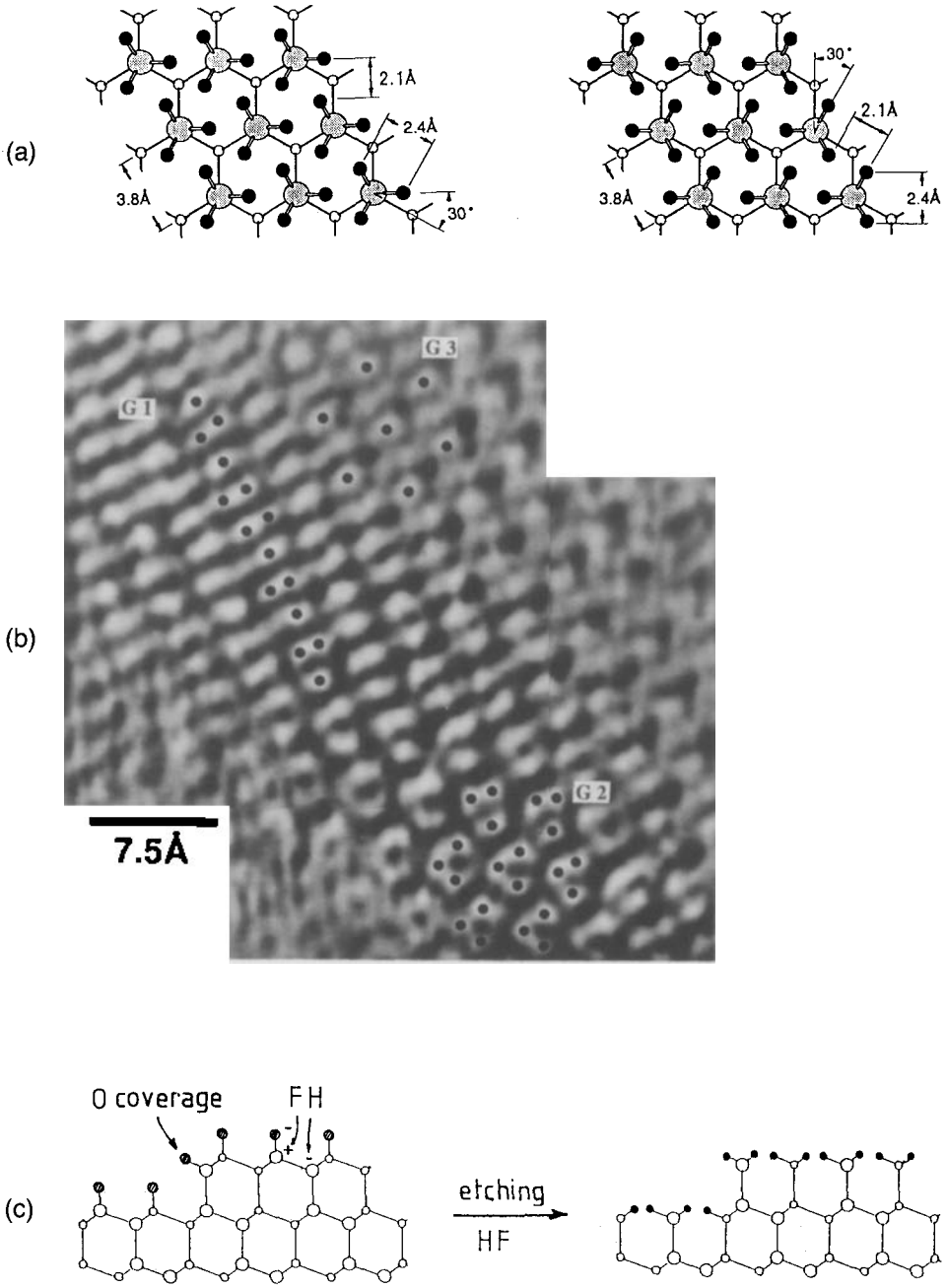

Fig. 20. (a) Atomic model for the trihydride termination of Si(111) after etching in 1% HF (after [118]). (b) UHV-STM image of Si(111) showing a boundary between the two domains of $-SiH_3$ in (a) (after [118]). (c) Hypothetical Si/SiO_2 interfacial structure explaining trihydride formation upon etching in HF (see text).

The existence of $-SiH_3$ species only once bound to the surface is surprising and a mechanism of formation is difficult to imagine. To reach a trihydride termination one must speculate that the structure of the Si/SiO_2 interface is that in Fig. 20c and that the topmost $\equiv Si-O$ groups can be removed by breaking the three $Si-Si$ bonds underneath by HF, similarly to the mechanism described in Fig. 28. This involves important steric problems and lattice stresses, however, since the length of $Si-Si$ bonds is 2.35 Å against ~2.2 Å for the hard-sphere diameter of HF molecules[6] during disruption of bonds; it is surprising that no pitting occurs, as it is observed at higher pH. The very slow etch rate of Si and the short exposure (30 s) of the surface to the 1% HF solution with no subsequent rinsing are perhaps key parameters for $-SiH_3$ formation.

In-Situ Investigations

Silicon has been imaged in aqueous solution over the entire range of pH. Studies in dilute sulfuric acid [15, 17, 44] are regarded below as ex-situ investigations since no etching reaction is taking place in this solution. The following paragraphs are concerned with real-time observation of Si(111) etching in NH_4F [18, 19] and in NaOH solutions [16, 20]. It is worth noticing that Sueh-Lin et al.[7] have recently published images of Si(100) etching in dilute NH_4F, showing that (111) facets are formed after long exposure to solution. The authors achieved also atomic resolution showing the (1×1)-H-Si(100) square lattice in initial stages of etching.

Allongue et al. [16, 119, 123] used in-situ STM to image n-Si(111) in dilute NH_4F solutions of different pH. High-resolution imaging was difficult, probably because the geometry of tungsten tips is easily and seemingly irreversibly modified by reaction with fluoride-containing solutions if the potential is not properly chosen, as has been reported by Yau et al. [19]. Pt-Ir tips might be more adequate than tungsten tips in these solutions. The large-scale images of n-Si(111) presented in Fig. 21 nevertheless confirm the statements of the preceding section, with a gradual change of the surface topography with the pH. At pH 4 the surface is rough, in the subnanometer range, whereas flat, smooth terraces are seen at pH 8. Multiple steps are seen in the image. Images are very stable with time, indicating that the etching is stopped at cathodic bias. Yau et al. [19] observed n-Si(111) in 1% HF with or without hydrogen peroxide (H_2O_2) added. In the first solution, atomic resolution showing the (1×1) structure was observed, which contrasts with the SiH_3 species resolved by Morita et al. [118] and is a confirmation that trihydride species are not stable in solution. Addition of peroxide (2%) accelerates the dissolution and improves the surface structure on a larger scale. Flat terraces separated by monoatomic steps[8] could then

[6] The diameter has been estimated as twice the $H-F$ bond length (1.1 Å).

[7] See Sueh-Lin et al., Appl. Phys. Lett. 66, 766 (1995), which appeared during the final stage of publication and could not be included in this chapter.

[8] On Si(111) steps of 3.1 Å correspond to the distance between two (111) planes and contain two layers of Si atoms. The terminology monoatomic step is taken here for simplification in the following.

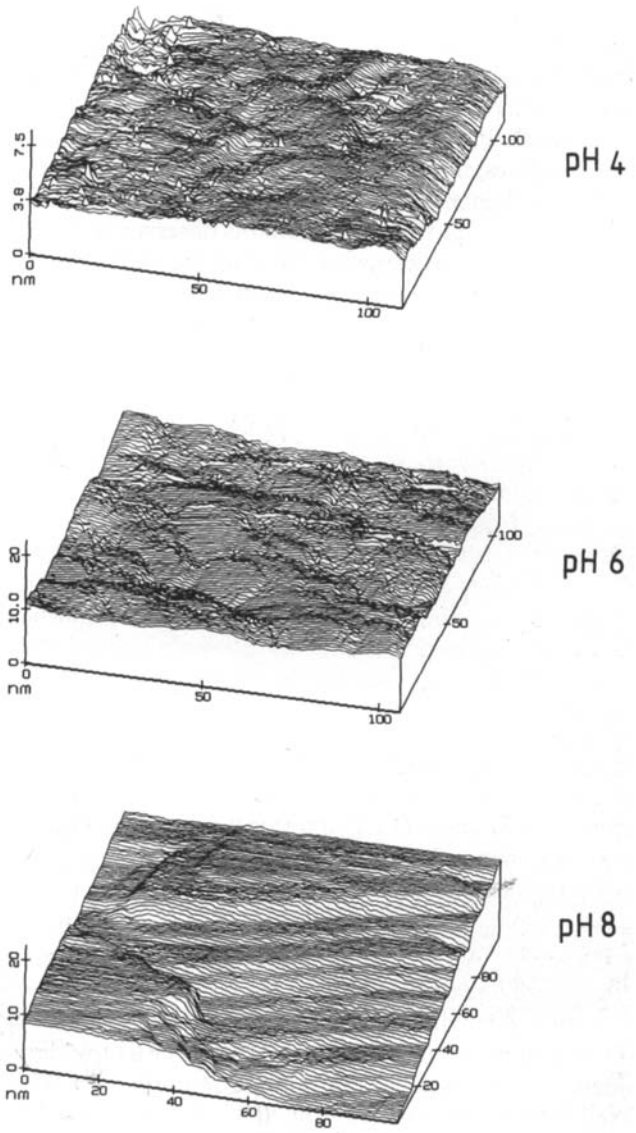

Fig. 21. *In-situ* STM images taken on negatively biased n-Si(111) in contact with dilute NH_4F solutions of different pH, as indicated (after [123b]).

be seen in 1% HF due to anisotropic etching by H_2O_2 molecules, which preferentially disrupt surface bonds at step edge atoms for steric reasons. In buffered NH_4F the anisotropy stems from a different reaction path involving water molecules as chemical dissolution agent and F^- ions as catalysts. An electrochemical component also exists in this case [123b].

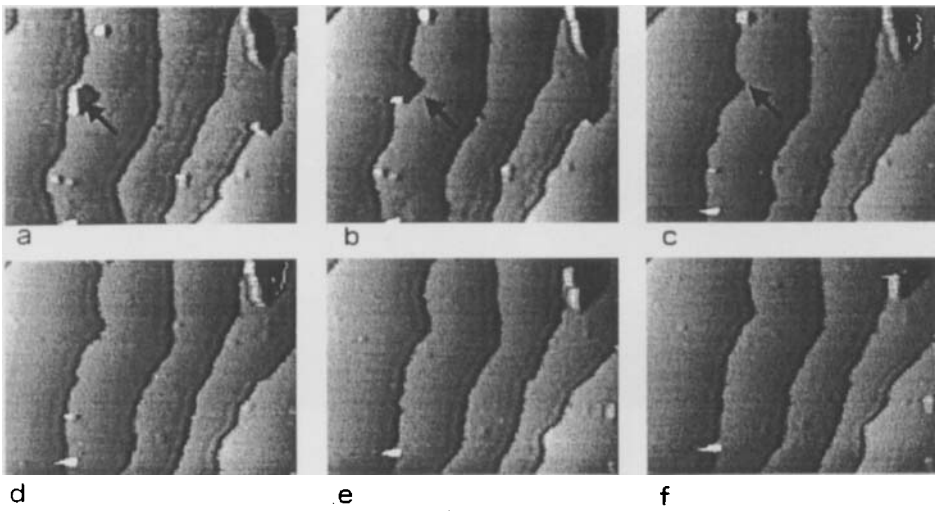

Fig. 22. Sequence of in-situ STM images showing n-Si(111) etching in 2 M NaOH ($U_s = -1.65$ V/SCE, $i_s = -150\ \mu A/cm^2$). Frames are 1270 Å × 935 Å and were recorded 45 s apart. In image (f) the hatched area is the surface of terraces removed during the sequence. Its value divided by the surface area under observation is used to calculate the local etch rate (after [20]).

In NaOH the resolution of images was much better than in fluoride solutions. In-situ high-resolution images revealed first that the surface was terminated by a monolayer of Si–H bonds because it was again (1 × 1) unreconstructed (see Fig. 10) [18, 20, 120]. This surface chemistry, unexpected in an alkaline solution, has been confirmed recently by in-situ IR spectroscopy [111]. On a larger scale the potential dependence of Si(111) etching has been followed in real time with the resolution of atomic-scale defects. Figure 22 presents a sequence of in-situ images showing that the dissolution is almost stopped by hydrogen evolution. There only remains a slow lateral migration of step edges (3.1 Å high) visible toward the right of the images, which illustrates the perfect anisotropy of the dissolution at that potential. Step edge atoms are indeed preferentially removed, as shown by the removal of a pre-existing etch pit between images (a) and (c). No new etch pit is nucleated during the entire sequence. Decreasing the H_2 evolution current increases the speed at which steps migrate and the rate of nucleation of 3.1 Å-deep etch pits. For potentials near and positive relative to the rest potential, long-standing imaging becomes impossible [20], in accordance with Sec. 3. Surface transformations have nevertheless been resolved with a special approach in which a first image of the surface is recorded at cathodic bias, a short positive potential pulse applied to the sample while the feedback loop and tip scanning are interrupted, before the second image is at the initial negative potential. For a pulse length of 3 s at the rest potential, pronounced and homogeneous pitting of terraces is observed in Fig. 23. Pits are almost triangular in the initial stages and remain one bilayer deep (3.1 Å). At more anodic bias, in the initial stages of

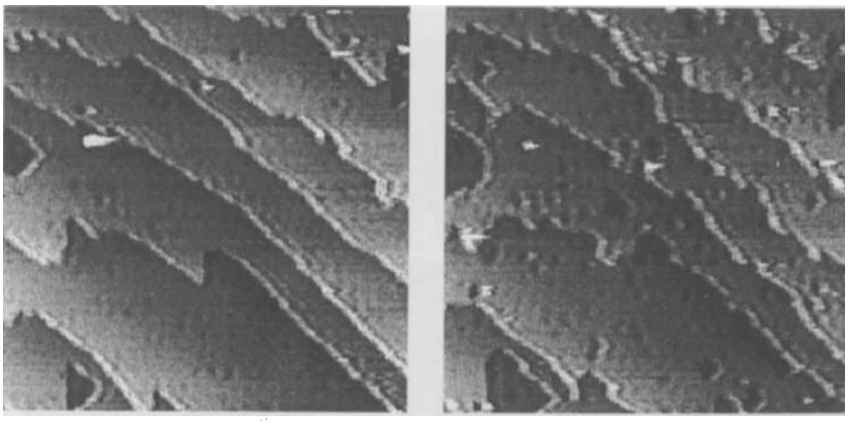

Fig. 23. In-situ STM images showing the surface of n-Si(111) before and after 3 s of polarization at the rest potential in NaOH. Frames are 1400 Å × 1400 Å. See text for the experimental procedure (after [20]).

oxide growth, i.e., in the passivation region of the $i-U$ curve, one finds a greater density of small round pits (about 20 Å in diameter).

Addition of a small quantity of surfactant such as Triton substantially modifies the foregoing observations [120]. Figure 24 presents one sequence of images obtained at an intermediate cathodic potential. Long-standing imaging is possible close to the rest potential and the etch rate is reduced by a factor of nearly 3. Compared with pure NaOH, under similar electrochemical conditions of hydrogen evolution, the main feature of the modified solution is a slower pitting of flat terraces. Whenever pitting occurs this is in the vicinity of atomic-scale defects (etch pits or terrace edges) and a more anisotropic etching process is achieved by reduction of surface pitting [120]. Observations have been interpreted in terms of formation of a self-assembled micelle layer or Triton molecules[9] standing normally to the surface, with the hydrophilic tail of the molecule facing the solution and the hydrophobic hydrocarbon chain in contact with the hydrophobic H-terminated Si surface. This configuration protects the silicon surface by repelling water away from it, except close to atomi-scale defects where the order of the layer is disrupted, leaving access to the surface to reactants. Triton molecules being only physisorbed at the surface (no chemical bonding with the surface can be expected) the (1×1) H-termination of Si(111) is still seen in high-resolution images [120]. These results show that ideal flat surfaces can be prepared in solutions other than those of fluoride. They also emphasize the utility of in-situ STM imaging as a unique tool to select additives and demonstrate that extended atomic-scale defects are already critical with respect to the protection.

[9] The developed structure of Triton X-100 is $(CH_3)_3CCH_2C(CH_3)_2-C_6H_4-(OCH_2CH_2)_nOH$ with $n = 9-10$.

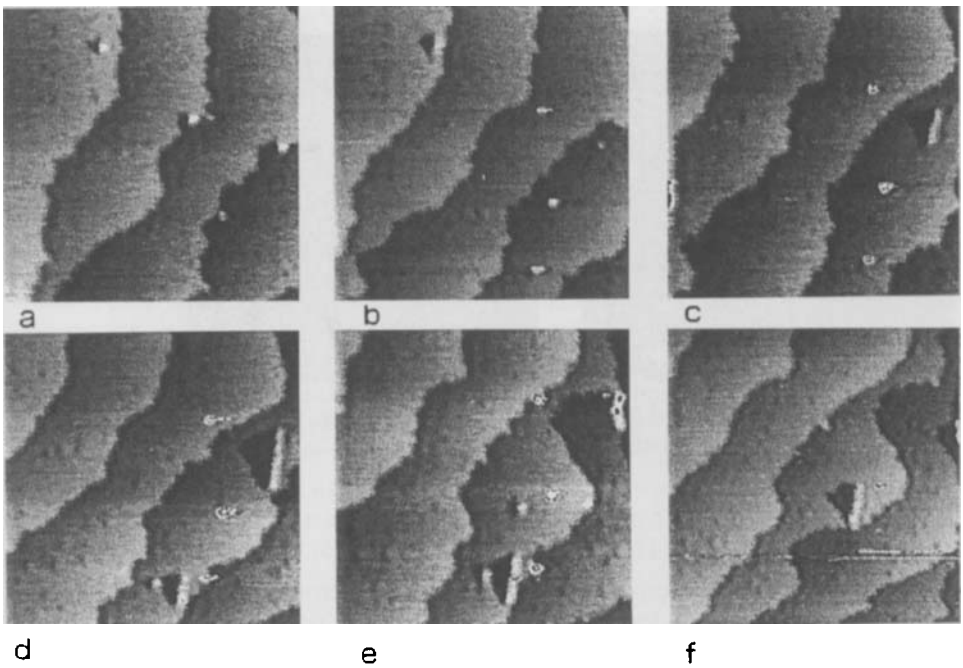

Fig. 24. Same as Fig. 22 but after addition of 10^{-5} M of Triton ($U_s = -1.65$ V/SCE, $i_s = -50\ \mu A/cm^2$). Frames are 1400 Å × 1400 Å (after [120]).

Addition of sulfide species is another method of modifying the etching process [119]. For a concentration in the millimolar range, the etch rate of Si(111) is decreased by a factor of 10 for comparable electrochemical conditions. Figure 25a shows that an ordered layer of sulfur species is adsorbed, presumably on the top of Si–H bonds. On a larger scale, terraces show regions depressed by 1.45 Å, which is smaller than normal step height and indicates that the surface is only partially covered by the sulfide layer (Fig. 25b). Pitting is naturally reduced in this solution because the surface is protected at an atomic level. At anodic bias the adlayer probably desorbs, because $i-U$ curves of n-Si electrodes are independent of the presence of sulfide species [119].

In addition to the visualization of topographic transformations, sequences of in-situ images yield a measure of the local kinetics of the reaction. The etch rate of Si has been evaluated in [20] by using the expression $R = (\Delta S/S)\, h/\Delta t$, with $\Delta S/S$ the surface area of terraces removed per cm^2 of electrode in one sequence, h the step height (3.14 Å) and Δt the time elapsed. The quantity $(\Delta S/S)h$ in fact represents the volume of material which has been removed per cm^2 of electrode, because the dissolution occurs layer by layer. The experimental determination of ΔS is sketched in Fig. 22f, in which the hatched area represents ΔS. In other sequences ΔS includes the surface of eventual pits. The bias dependence of the etch rate and the current voltage curve are shown in Fig. 26 for n-Si(111) in a 2 M NaOH solution [20].

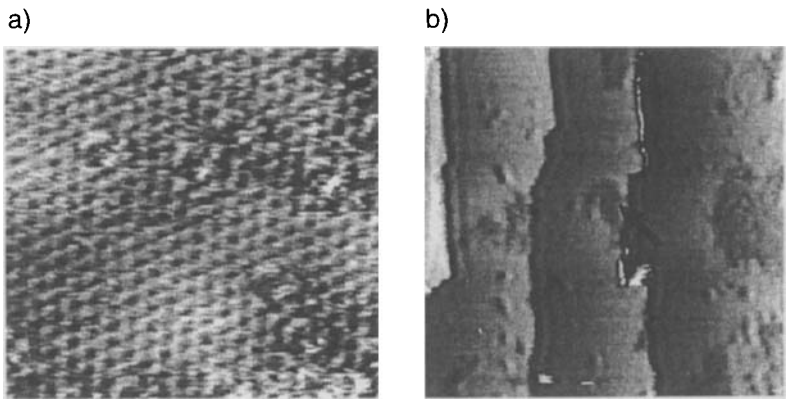

Fig. 25. (a) High-resolution and (b) large-scale in-situ STM images taken on n-Si (111) in a sulfide solution. Frames are respectively 64 Å×60 Å and 1424 Å×1420 Å (P. Allongue, unpublished work).

Although the results correspond to etch rates on a microscopic scale, the curve fits remarkably well the bias dependence of etch rates derived from macroscopic measurements such as material losses. Note that etch rates of a few ångströms per minute are an upper limit to follow surface transformations by STM unless the microscope is especially designed for fast large-scale imaging. Recently, the comparison of experimental sequences of images with simulated ones, according to the Monte-Carlo method, has allowed the quantitative determination of etching rates at the atomic level on Si [121].

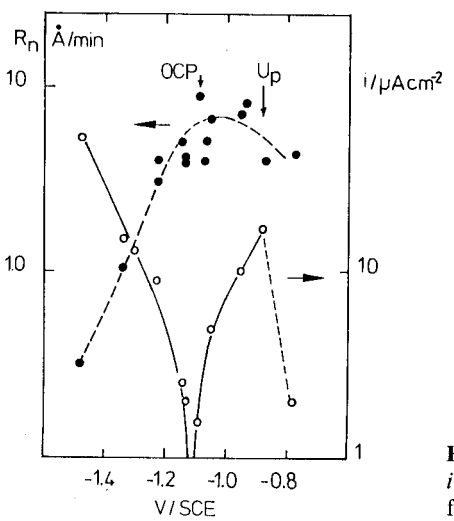

Fig. 26. Bias dependence of the etch rate (●) and $i-U$ (○) curve of Si(111) in 2 M NaOH as derived from sequences of STM images (after [20]).

Mechanism of Dissolution

Allongue et al. [122] and Gerischer et al. [123] have recently published models describing, at a molecular level, the etching of silicon in strong bases and in fluoride solutions respectively. They are shown in Figs. 27 and 28 respectively for NaOH and acidic HF.

In NaOH the dissolution of Si can follow a chemical and an electrochemical route (Fig. 27, top and bottom paths respectively). The chemical path represents 90% of the dissolution [122]. This route underlines the role of water molecules in the dissolution of Si at high pH in accordance with the weak dependence of the etch rate with respect to the OH^- concentration. Hydroxyl ions are catalysts of the reaction and do not react directly. This is consistent with the fact that Si etching in boiling water also produces atomically flat Si(111) surfaces, as has been made evident by IR absorption spectroscopy [124] and UHV-STM observations [117]. In this case the temperature is sufficient to overcome the activation energy since no OH^- ion is available. The remarkable anisotropy of Si etching in strong bases stems from the fact that the chemical route represents about 90% of the dissolution and begins with a hydrolysis step in Fig. 27 [122]. The hydrolysis of Si–H bonds by water molecules

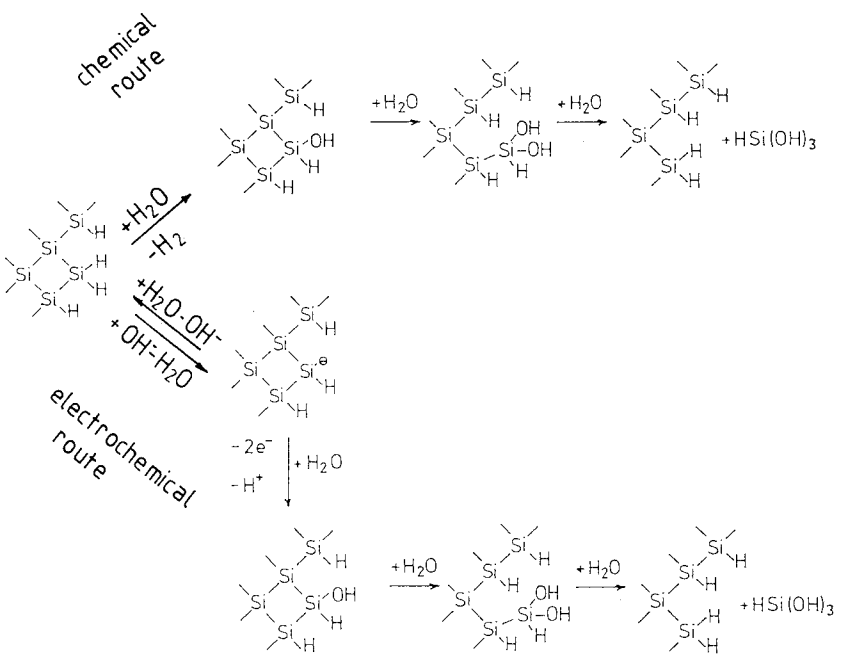

Fig. 27. Molecular model for the etching of Si in strong bases. In NaOH two routes are possible for the hydrolysis step. The chemical one (top route) dominates at the rest potential. The H-termination persists despite dissolution because the initial steps are rate-determining. $HSi(OH)_3$ is further oxidized to $Si(OH)_4$ which liberates another H_2 molecule (after [122]).

is evidently easiest at steps especially at kink sites where steric hindrance is minimal and surface bonds also are more flexible than on terraces (water molecules must come in close contact with Si–H bonds). Though a chemical etch rate should not display much bias variation, there is no contradiction between the nature of the reaction and the results of Fig. 26 as it is exposed in [122]. At anodic bias the rate of formation of Si–OH bonds increases and a thin oxide layer is built by condensation of Si–OH bonds which stops etching since SiO_2 is slightly soluble in NaOH.

Though negligible, the electrochemical route is nevertheless critical with respect to the surface topography. This route is responsible for the pitting on terraces, as Fig. 23 shows [122]. This is because the electrochemical hydrolysis of the Si–H bonds is a two-step process initiated by an acid-base dissociation of the Si–H bond which avoids steric problems by liberating a terrace site to form a silanol group which is then removed (Fig. 27, bottom). Additives may reduce the formation of etch pits (see Figs. 24 and 25).

In fluoride solutions etching begins also with the formation of a Si–OH bond, as in NaOH, with the difference that the electrochemical route becomes proportionally more important than the chemical one with decreasing pH [123 b]. The silanol group may be also rapidly transformed into a Si–F bond and F^- ions are probably catalyst of the reaction at intermediate pH. Two electrons are thermally excited, from activated states into the conduction band, in the electrochemical process [123 a]. As discussed above this path is more isotropic than the chemical path in NaOH and the uptake of the electrochemical reaction as the pH decreases, it represents about 80% and 50% in NH_4F solutions of pH 4 and pH 8 respectively [123 b, 128], which fits the results of Figs. 19 and 21, where the atomically flat terraces seen at pH 8 become atomically rough at lower pH. In acidic diluted HF, the 'chemical etching' is almost exclusively electrochemical in nature showing that the terminology 'chemical etching' is rather misleading here. The reaction is the one described in Fig. 28 (top). The step with formation of the Si–OH bond has been omitted, since they are short lived. Under illumination photogenerated holes are first captured in Si–H bonds and a single electron is injected in the second stage of Si–F bond formation. For one photohole one electron is produced which is in accordance with photocurrent multiplication factors of 2 [125]. Molecular hydrogen is formed in a homogeneous reaction in solution, since the dissolution product $HSiF_3$ corresponds to Si with valence 2. which explains that it still evolves at anodic bias [126]. Hydrogen evolution is also observed in NaOH.

In all solutions, after formation of the Si–X bond with X = OH or F, the final steps are exclusively chemical and involve water and possibly undissociated HF, but only at low pH for the later. These steps are faster since the Si–Si back bonds are weakened by the large difference in electronegativity between Si and the ligand X. In HF these steps are similar to those of the model of Trucks et al. [127] who considered that etching stops after completion of the coverage by Si–H bonds. The description in Fig. 28 shows how etching may still proceeds even though at a limited rate. At intermediate pH, water is again the main reactant [123 b]. The persistence of the H-termination, which contradicts thermodynamics since Si–F and Si–OH bonds are more energetic than Si–H bonds, simply means that the initial substitution Si–H → Si–X is rate determining in the reaction of dissolution. This is a kinetic problem which stems from the unpolar character of Si–H bonds.

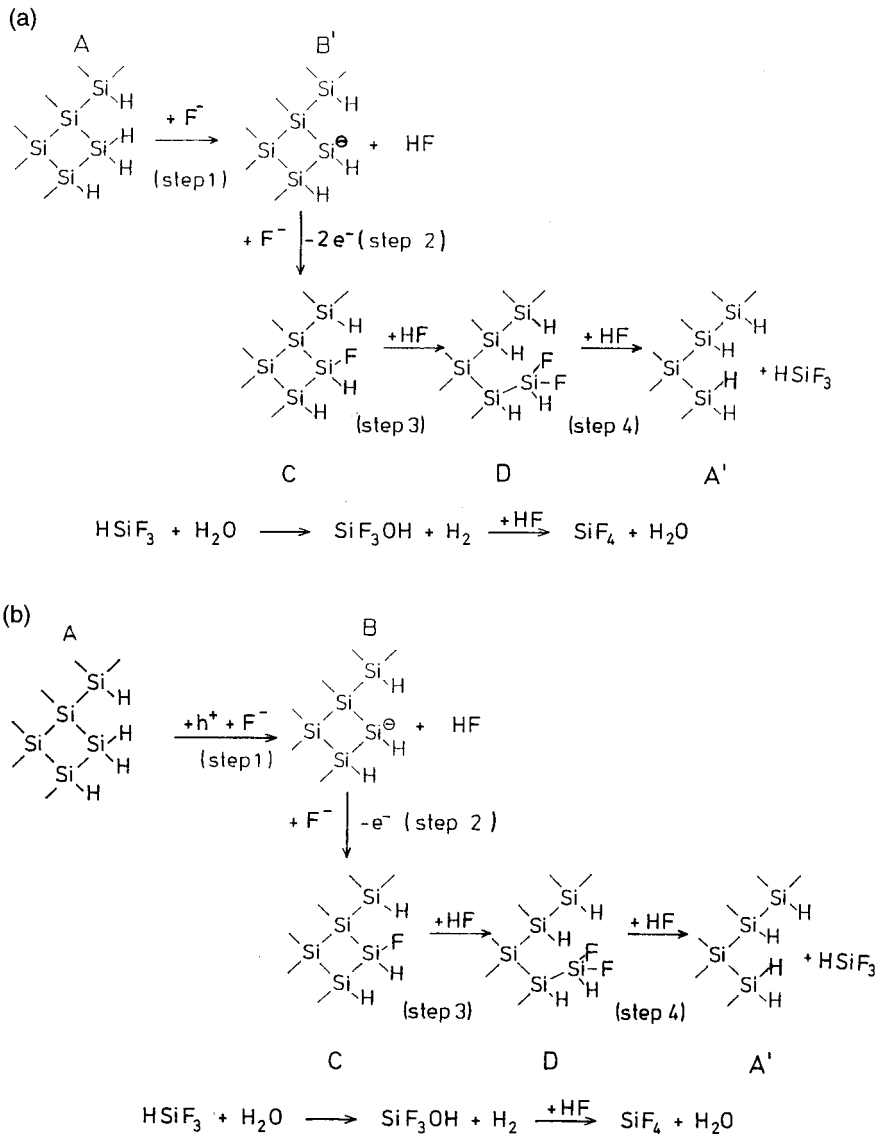

Fig. 28. Molecular models for Si etching in acidic HF: (a) Electrochemical route under 'chemical etching' condition. (b) Dissolution initiated by holes, here under illumination at n-Si (after [123a]).

In summary, the two models of Figs. 27 and 28 provide new insights into the pH dependence of the surface topography of Si(111) in fluoride solutions (see Fig. 21). With increasing pH the uptake of the chemical reaction with water enhances the anisotropy of the dissolution since the chemical route depends critically on the atom coordination in contrast to the electrochemical one [122, 123b].

5.1.3 Porous Silicon

As opposed to the situation described in the previous section, where etching was performed at the rest potential and the aim was for ideally smooth Si surfaces, porous silicon layers (PSLs) are formed at anodically biased p-Si in fluoride-containing solutions. Light or a large anodic bias is necessary at n-Si. Surprisingly, deep and almost unidirectional pores can be electrochemically grown on flat crystalline Si surfaces over thicknesses of several tens of micrometers. The morphology of the layers (shape, size of pores, interconnection of pores) depends on many parameters, including solution composition, current density, doping level, type of conduction, surface orientation [129], and even UV illumination [130]. PSLs are intensely photoluminescent (PL) in the visible range (typically at 650 nm) beyond a critical porosity of 85%. Below this value the PL intensity decreases rapidly and becomes orders of magnitude lower for flat Si. These observations have been interpreted as an effect of quantum confinement in nanostructures composing the skeleton of PSLs. Calculations predict that the gap becomes direct below a critical size (2–4 nm) of Si particles. Despite many investigations the mechanism of formation and the origin of the photoluminescence are still not clearly elucidated and remain open questions [93].

In the context of PSL studies, local probe microscopes are difficult to operate ex situ for several reasons. The Si skeleton is fragile and easily destroyed, especially by AFM tips. The resistivity of layers ($>10^9\,\Omega$ cm) is also a problem for tunneling. Only thin layers can be imaged [131]. Typically layers cannot exceed 20–50 nm in thickness to keep the tunneling gap larger than the layer resistance [132]. Surface modification occurs under the tip at large tunnel bias (several volts) and this has been used to write patterns on the surface [133]. The tip geometry is critical to image such rough surfaces. Amisola et al. [134] could not obtain a correlation between the size of surface features and PL properties by using ambient AFM on highly porous layers, whereas Enachescu et al. [132] were able to show close correlation between STM images and PL properties of layers. The reason is that STM tips usually have a better resolution than AFM tips. George et al. [135] compared porous layers grown in HF/H_2O at anodic bias and in $HF/HNO_3/H_2O$ with no bias applied. In this latter solution PSL formation arises from the injection of holes from the solution whose injection rate depends mainly on the concentration of HNO_3, which is the oxidizing agent. PSLs formed in this way have been also called "stain films". Ambient AFM images show columnar features for the first type of layer, whereas a smoother morphology (between larger pores) is observed on the other type of film.

Houbertz et al. [136] have studied the very initial stages of PSL formation in 40% NH_4F, though PSL is generally prepared in mixtures of 48% HF and water or ethanol. Figure 29 shows ex-situ UHV-STM images of highly doped n-Si(111) after 30 s of anodic polarization. Starting from ideally flat surfaces, prepared at the rest potential as in Fig. 19b, images show that the size and density of pores depend on the bias applied. Pores are ~500 Å in diameter and ~10 Å in depth at low overvoltage as in image (a). At more anodic bias, pores are more open, presumably because one reaches the transition region between PSL formation and electropolishing [93]. Atomic steps are still seen in images confirming that the skeleton of the PSL is actually crystalline. Using different techniques of preparation, Enaschescu et al.

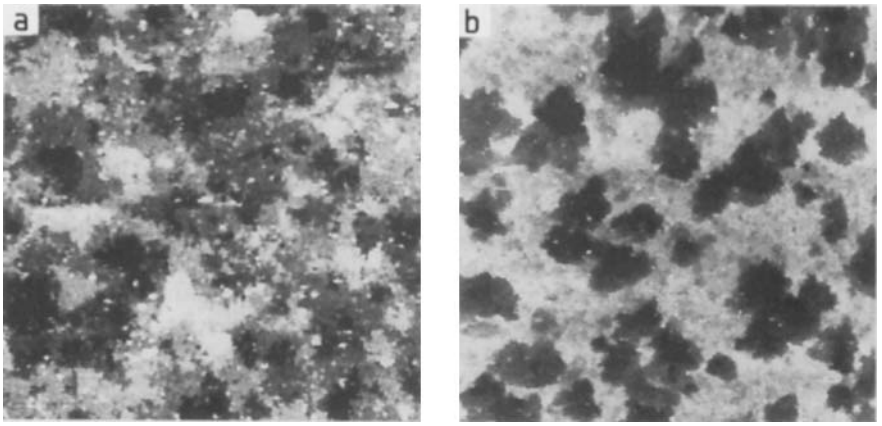

Fig. 29. Ex-situ (UHV) STM images recorded on anodically biased Si(111). (a) 30 s etch at 0 V/SCE (porous layer formation) and (b) 30 s etch at 0.6 V/SCE (transition region before electropolishing). Frames are 0.35 μm×0.35 μm (after [136]).

[132, 133, 137, 138] have observed by UHV-STM a correlation between the morphology of thicker porous layers (20–50 nm) and photoluminescence properties. The top of the layer consists of hills and valleys whose characteristic size must be decreased to the nanometer range to obtain intense PL which fits general assumptions about quantum confinement [93]. Effective barrier imaging may be interesting. This shows finer structures than topographic imaging because the most conductive regions dominate in constant-current mode [132].

The (opto)electronic properties of PSL were also studied with STM: $i_T - U_T$ curves taken on PSL display the rectifying behavior of the substrate (p-type material in [132]). A surprising inversion of conductivity at the surface, detected by STS, was reported in another paper [134]. Dumas et al. [131, 139] have performed photon mapping by injecting low-energy electrons from the tip (negative) into the substrate. Figures 30a and b compare STM and the corresponding photon-emission images made on a photoluminescent p-type PSL. The photon image is obtained by photon counting with a photomultiplier. The principle of the technique recalls cathodoluminescence as it was described some years ago with GaAs/GaAlAs heterostructures [140]. Tunneling electrons penetrating the layer recombine with holes and photons are radiatively emitted locally with a mean energy corresponding to the gap of the substrate. For PSL the light energy is about 2 eV (see Sec. 6). Photon emission requires the porosity of the layer to be >85%, in accordance with the general concept of quantum confinement. No photon emission is obtained on flat Si, which excludes inverse photoemission as a light-emitting process. The cross-section in Fig. 30c demonstrates a strong correlation between protrusions and photon counts [131]. The origin of the contrast image has not been elucidated. One possibility is that the conservation of parallel momentum of ballistic electrons (as in BEEM; see Sec. 6.3) tends to focus light emission [140].

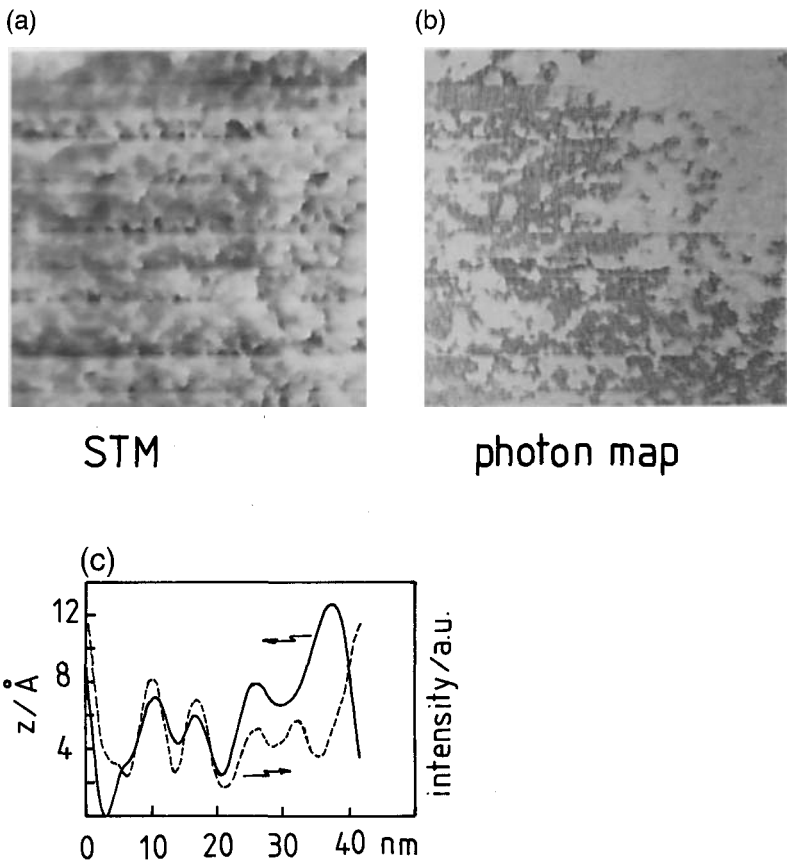

Fig. 30. Topographic STM image (a) and photon map (b) recorded on p-type 85% PSL (after [131]). (c) Profiles showing the correlation between the surface topography and the intensity of emitted light (after [139]).

In-situ investigations of PSL have been performed only very recently. Yau et al. [141] have published in-situ STM observations of p-Si(100) in 1% HF after anodization. Ex-situ AFM results are similar to those described above, with surface damaging observed. In-situ STM images had to be collected at cathodic bias because of a loss of resolution at anodic bias (surprisingly, the potential was however only weakly cathodic with respect to the low doping level of the substrate). Originally relatively flat, the (100) surface roughens after anodization with well-defined crystallographic trenches running along the $[1\bar{1}0]$ direction and V grooves, whose side walls are apparently (111) facets. Images confirm that the anodic dissolution of Si is anisotropic in fluoride-containing solutions. The relation between pore formation and orientation of features needs however being further investigated since it is known that pores preferentially grow in the (100) direction [93]. Observations might be related to a too strong anodization which opened pores.

In-situ studies of PSL should offer further perspectives. In the first place the initial stages of the layer formation could be studied with the technique used in Fig. 23. "Ex-situ" topographic imaging of PSL, in sulfuric acid for instance, might also be easier than in UHV since the necessary tunnel voltage is expected to be smaller in the liquid environment (about 1 V against 3–5 V in UHV). Free carriers are indeed available in PSL immersed in solution whereas carriers seem localized in dried layers, according to recent IR absorption investigations [142]. Photoemission could also be studied in situ, with two aims. The first is conventional cathodoluminescence as in UHV, by injection of electrons from the tip into the conduction band of an n-type PSL for instance. The other possibility is localized electroluminescence (EL) by electrogeneration of a strongly oxidizing redox agent (e.g., $S_2O_8^{2-}$ which is reduced to SO_4^{2-} with formation of the hole-injecting species SO_4^- [143, 144]) at the extremity of the tip, in a way similar to that performed by scanning electrochemical microscopy (SECM; see Sec. 5.2).

5.2 Materials other than Silicon

Principally two other classes of materials have been studied by in-situ STM and AFM: the III–V compounds and layered materials. In-situ atomic resolution has been obtained on p-InSe by Uosaki and Kuomina [22]. Semiconductor oxides have not been studied since the early work of Itaya and Tomita on TiO_2 [42] and ZnO [43]. STS [63, 64] and atomic resolution [64] have however been recently reported in air on TiO_2. Kepler and Gewirth [21] could resolve in-situ individual atoms on Ge(111) and (110) electrodes. That in-situ atomic resolution was obtained by AFM on Ge [21] and InSe [22] opens new possibilities for electrochemical studies since the sample bias is less subject to constraints of polarization. Photoeffects, induced by the laser beam need nevertheless being avoided.

Studies of pyrite and related substrates are surprisingly missing from the list above. They should also be very good candidates for in-situ imaging since they are very stable to oxidation and present interesting electronic properties. RuS_2 [145], for instance, shows a remarkable bias dependence of images in air which deserves to be exploited in situ as model electrodes for investigating surface reactivity at an atomic level. As an example, Fig. 31 presents filtered STM images of occupied and empty states on cleaved RuS_2(100) in air [145]. Occupied states are distributed in two patterns: intense spots on zigzag chains correspond to S atoms forming the topmost layer and smaller spots in a square arrangement correspond to Ru atoms, in agreement with the crystallography of this material. A similar STM image is found on FeS_2 [146]. Empty states on RuS_2 present a more complex distribution which is still not completely elucidated [145].

5.2.1 Surface Preparation

The resolution of atomic-scale defects in STM images requires surfaces as flat as possible to start with. Scanning probe microscopy has improved our knowledge concern-

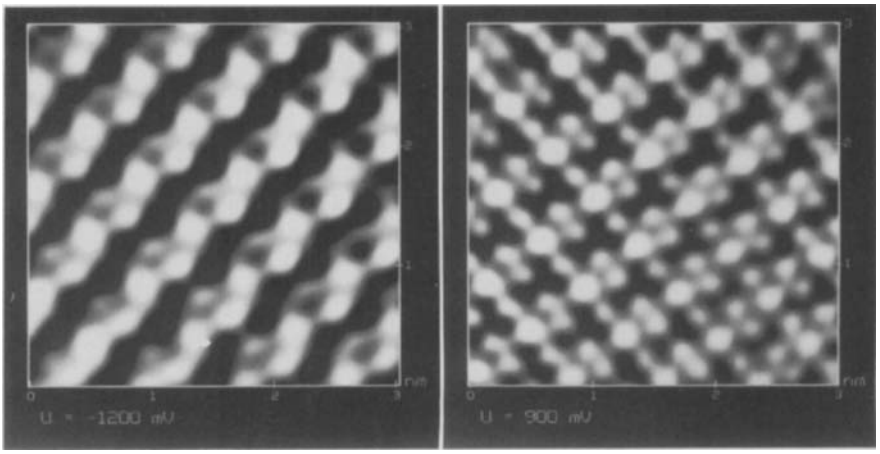

(a) (b)

Fig. 31. FFT-filtered STM image of occupied (a) and empty (b) states on RuS_2 [145].

ing surface preparation in vacuum. This step is appropriate to STM and AFM studies even if this aspect seems frustrating. Obtaining flat surfaces by chemical treatment and keeping them ideal in solution are intrinsically interesting aims and require improved understanding of the chemical reactivity of surfaces. In that respect the recent progress in the preparation of Si surfaces (the best-known material) explains the achievement of good in-situ resolution on these surfaces. Each material raises new problems, which explains why many of them, especially compound materials, have still not been imaged with a high resolution.

The surface of III–V compounds looks generally rough, as in Fig. 32a, which shows the earliest in-situ image of a semiconductor electrode [147]. The highly doped p^+-GaAs ($N_A > 10^{19}\,cm^{-3}$) sample was simply imaged under the solution in a two-electrode configuration (tunneling occurs through the space charge layer). A similar roughness is found after etching in $HCl-HNO_3$ [151]. Robach et al. [148] have recently shown that the roughness of InP(100) can be significantly decreased by growing a chemical native oxide layer in HNO_3 and dissolving it in HF. This result belongs to a more general technique in which flat surfaces are obtained by growing an oxide layer in such a way that the interface between the semiconductor and the oxide is flat, and then removing the oxide *selectively* without corroding the substrate. In the case of Si, thermally grown oxides are better candidates than chemically formed oxides to attain atomically flat surfaces [102]. Using epitaxial MBE (Molecular Beam Epitaxial) layers of III–V materials seems better than using polished wafers since extremely flat (100) GaAs surfaces layer may be prepared with only two to three layers exposed [149]. Figure 32b is an STM image of a MBE n-GaAs(100) layer etched in dilute Na_2S. This surface shows defined crystallography with terraces and steps, like a multivicinal surface. The question will however remain to keep it structured when it contacts an aggressive solution.

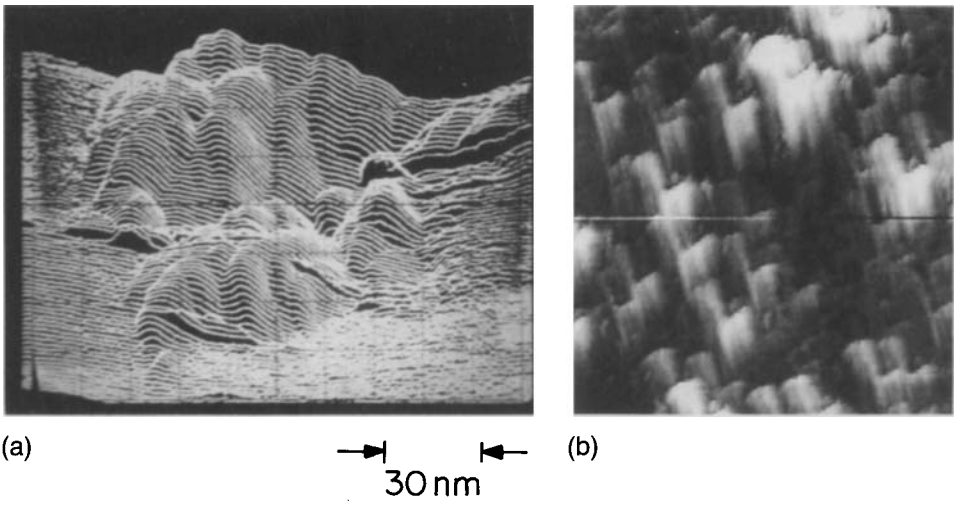

Fig. 32. In-situ STM images of GaAs(100): (a) p^+-GaAs ($>10^{19}\,cm^{-3}$) in KOH within a two-electrode configuration (after [147]). (b) MBE n-GaAs layer in dilute Na_2S. Size 3000×3000 Å (P. Allongue, unpublished)

Flat surfaces are easy to prepare with layered materials. There have yet been only few in-situ studies, the resolution has been not as good as expected, with the exception of InSe [22]. Steps and pit formation have been reported on MoS_2 [45]. Cleaved pyrite and related material such as RuS_2 also give nice flat and stable surfaces [145, 146].

5.2.2 Corrosion and Passivation Studies

Corrosion of III–V Compounds

In-situ images have never reached the resolution of atomic-scale defects on these surfaces, except in Fig. 32b and in the AFM work of Koinuma and Uosaki [151], who followed the anodic photodissolution on n-GaAs(100) in diluted HCl and found that the surface smoothens with time, an effect which is perhaps related to oxide formation induced by tip shielding. Atomically resolved images surprisingly showed the arrangement of the (111) face although they should correspond to facets 54.7° off the initial plane. Eriksson et al. [79] and Carlsson et al. [82] have imaged n-GaAs(100) in NaOH by STM under potential control. Under illumination, sequences of images showed dramatic changes because the surface was dissolved with a current density as high as $150\,\mu A\,cm^{-2}$, which is equivalent to the removal of ~ 20 ML min^{-1}. Topographic changes between two images were too fast to be analyzed. Much slower dissolution rates must be monitored (see the discussion of Si in Sec. 5.1). In darkness no topographic change was observed within the scale used. This is in contrast to the report of Thundat et al. [150], who observed that the sur-

face, initially rough, had the tendency to smoothen after repeated scanning. STM imaging also became difficult with time, suggesting that an oxide layer is formed under the tip due to the high electric field. That the same effect was seen by in-situ AFM [151] rather suggests that the oxide growth under the tip might also be related to tip-induced reaction shielding and not the electric field.

Local corrosion and nanolithography have been performed by STM. Nagahara et al. [152] wrote features as small as 20 nm in linewidth on n^+-Si(100) and p^+-GaAs within a two-electrode configuration (the counter electrode had to be disconnected). The rate at which grooves form depends on the size of images and almost stops above a critical scan size. The tip was surprisingly in tunneling mode at a bias 1.4 V positive with respect to the semiconductor. Using the fact that no etching was observed on n-Si in H_2SO_4, where SiO_2 is stable, the authors postulated field-induced oxide growth beneath the tip, followed by chemical removal of this oxide (by HF) as the mechanism of feature etching. This mechanism remains nevertheless unclear because Sugimura et al. [153] reported that Ti is anodized under the tip when the substrate is positively biased. Under the tunneling conditions described in [152] the substrate is negative and cathodic reduction was expected instead of oxide formation. Since Si and GaAs do not decompose cathodically, writing might proceed as follows. In the case of Si, tunneling probably occurs from the valence band, with free carriers supplied by bulk recombination. For tip currents as large as 1 nA the rate of bulk recombination is certainly insufficient and bound valence electrons are involved in tunneling. This will lead to local corrosion. At p-GaAs, Fermi level pinning is very likely. Here the positively charged tip reduces the band bending locally, which promotes enhanced corrosion in the vicinity of the tip.

Using SECM, Bard and coworkers [154, 155] could form etch spots and real in-situ lithography on n-GaAs. Figure 33a is an SEM view of three etched holes. The principle of SECM lithography is explained in Fig. 33b. In a strongly oxidative solution, holes can be injected into the valence band of n-GaAs, according to the reaction $ox^+ \rightarrow red + h^+$. In the vicinity of the tip the generated reduced species (red) diffuse rapidly to the tip. If the reverse reaction $red \rightarrow ox^+ + e^-$ is monitored at the tip extremity, by adjusting its potential, the ox^+ ions may diffuse back to the surface (the tip is an ultramicroelectrode approached to ~ 1 μm from the surface). This creates a loop locally and enhances etching as the tip comes closer to the surface. This procedure is referred to as the "positive feedback mode" of SECM. Far from the tip, hole injection (i.e., etching) occurs uniformly. This technique of lithography takes advantage of the *increased* etch rate underneath the tip. At p-GaAs, etching was generally not observed because injected holes are removed from the surface by the electric field (see Fig. 33b). p-GaAs could however etched by electrogenerating bromine at the tip since in that case the dissolution is chemical and involves no hole injection. Patterns with a submicrometric resolution have been generated using the SECM. SECM has also been used to etch or deposit metal locally on various types of substrates [154–158].

Note that the value of the redox potential is critical. If the redox potential lies in the band gap of the semiconductor, monitoring the reaction $red \rightarrow ox^+ + e^-$ at the tip will not help for lithography. As the tip comes closer to the surface the reaction stops (negative feedback). This behavior, characteristic of insulating electrodes,

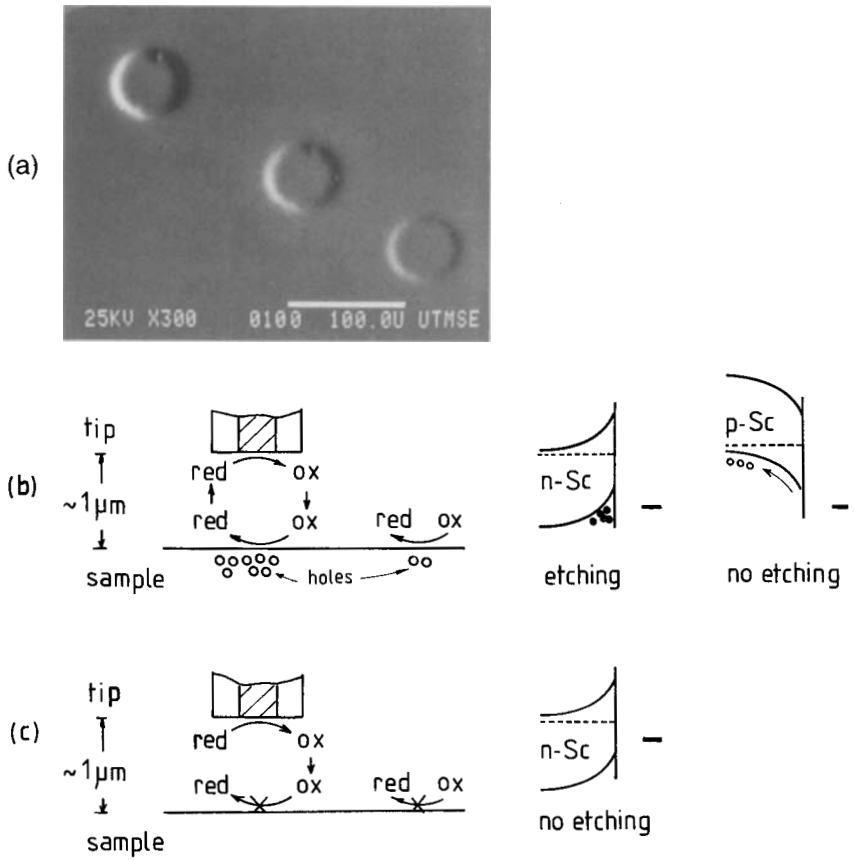

Fig. 33. Lithography on GaAs by SECM. (a) SEM image showing holes etched in n-GaAs (after [154]). (b), (c) Principles of SECM lithography: in (b) the very oxidative solution enables lithography of n-GaAs by enhanced corrosion under the tip (positive feedback mode of SECM). At p-GaAs no etching can be expected. In (c) the less oxidative solution makes lithography impossible since holes are not injected in the electrode (negative feedback is observed).

has been observed with n-GaAs in solutions of lower pH because U_{fb} shifts downward. The situation is shown in Fig. 33c.

Passivation of III–V Compounds

The passivation of III–V compounds remains a challenging problem for microelectronics but has still received no answer as efficient as the H-termination of Si. The increase of the photoluminescence intensity and lifetime after treatments in sulfide solutions have recently attracted much attention [67]. Dagata et al. [160] have compared, by STM/STS in the ambient atmosphere, the passivation of GaAs in $(NH_4)_2S$

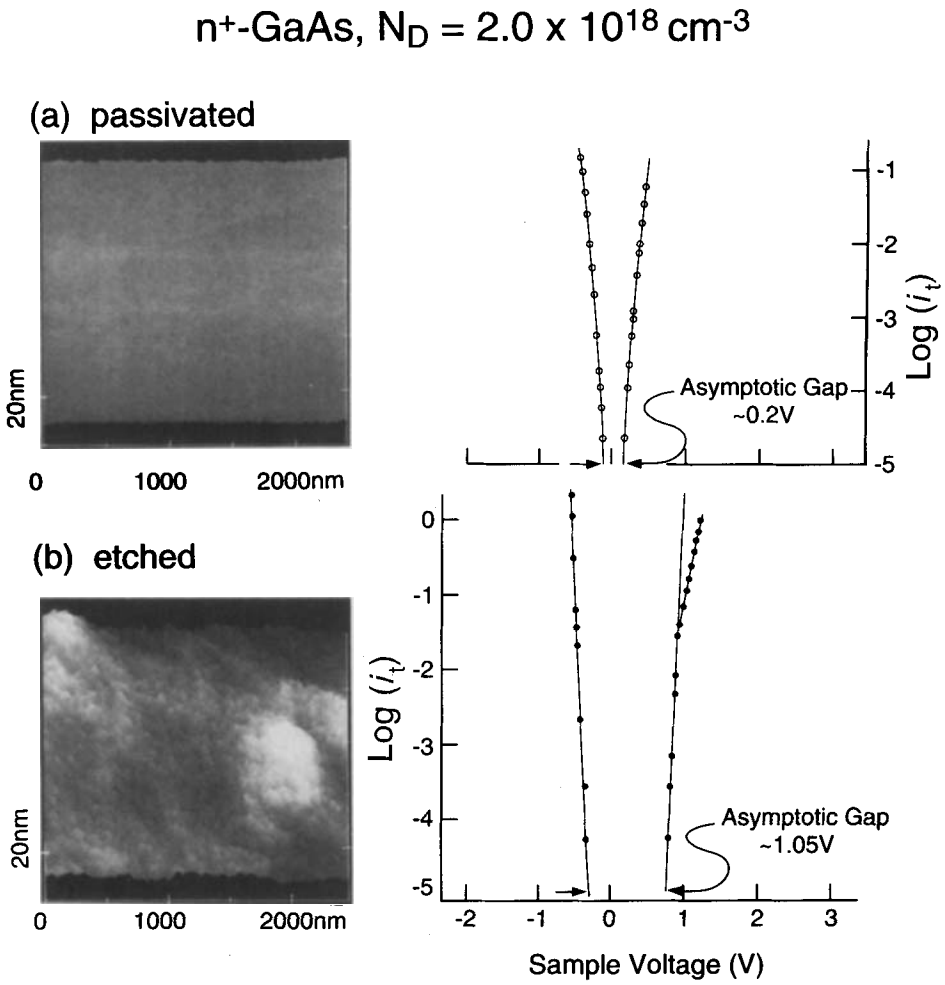

Fig. 34. STM images (left) and spectroscopy results, plotted as log $i_T - U_T$ curves (right), of GaAs in the ambient atmosphere. The surface is coated with sulfide in (a) and simply etched in (b) (after [67]).

and $P_2S_5/(NH_4)_2S$. The second treatment stabilizes the surface over hours in air by formation of an oxide monolayer between the sulfide layer and GaAs [161]. The coating does not degrade under the tip. The same solution also stabilizes the surface of InP [162]. Figure 34 compares results obtained with GaAs cleaved in a mixture of $NH_4OH/H_2O_2/H_2O$ and treated or not with $P_2S_5/(NH_4)_2S$. The surface looks smoother after passivation if it is not rinsed in deionized H_2O. Increasing the rinsing time increases the roughness of the surface [161, 163]. Rinsing in methanol preserves the passivation layer [163]. The smoothing effect might nevertheless be related to electronic effects since AFM images look equally rough [164]. The STS results of

Fig. 34 are presented as $i_T - U_T$ curves. Without sulfide treatment a 1.05 eV band gap is resolved, whereas the gap shrinks completely after passivation. Though results seem in line with a passivation of electronic surface states by the sulfide treatment, since no band gap is resolved on clean GaAs(110) in vacuum [53][10], one may wonder whether the results of Fig. 34a are not related to the overlayer instead of the substrate. Recent studies have indeed shown that the density of states is not reduced after sulfur coating [87], in contrast to initial assumptions [86]. Moreover, thermal desorption of the sulfide layer opens a band gap [164], as in Fig. 34b, which is consistent with the existence of the monolayer of oxygen at the interface between GaAs and the layer [161]. In vacuum a wide band gap is also found locally at places where oxygen is adsorbed on clean GaAs(110) [53].

The role of the P_2S_5 in the passivating solution seems very important to the interfacial chemistry and to STM imaging. The dip in the $P_2S_5/(NH_4)_2S$ mixture leads to the formation of a Ga_xO_y phase at the very surface of GaAs and an As_xO_y phase on top of the layer [164]. This layer is stable under the tip. Without P_2S_5 the surface of GaAs is conversely terminated by a sulfur layer while the excess arsenic is removed by formation of a compound As_xS_y [165]. Sulfur being only physisorbed [166] and the sulfide layer poorly adhesive [160]. STM imaging is impossible also because the overlayer degrades under the tip [68]. The As_xS_y phase also oxidizes in air [88], which is another factor that is unfavorable to tunneling. Formation of oxide clusters underneath the layer might also contribute to tip instability.

This kind of problems seems to be less dramatic when imaging the surface in-situ as Fig. 32b shows. The interesting point in this image is the anisotropic shape of structures which are parallel [1$\bar{1}$0] and suggest a complete restructuring of the initial surface, due to etching in the sulfide solution. Moreover sequences of images show a preferential attack of structures at their narrowest extremity, which indicates a chemical dissolution and also that the surface is probably terminated by one short of atoms (probably Ga one bound to S species). Atomic resolution has, however, not been achieved yet on this surface.

Dissolution of Layered Materials

Sakamaki et al. have STM-imaged n-MoS_2 in various solutions [45]. Using a negatively polarized Pt-Ir tip for tunneling electrons into the conduction band, the sample could be imaged regardless of its bias and photoinduced corrosion could be followed at anodic bias. In dehydrated acetonitrile no reaction occurred but addition of water traces induced the formation and anisotropic growth of etch pits on a large scale. With KI added, the surface is stabilized. In HCl, corrosion occurs at surface defects.

[10] The clean GaAs(110) surface presents no surface states in the band gap as derived from conductance $\Gamma(U_T)$ measurements. When spectroscopic results are plotted in the form shown in Fig. 34, however, no band gap is resolved because dopant-induced bulk states contribute to tunneling [53].

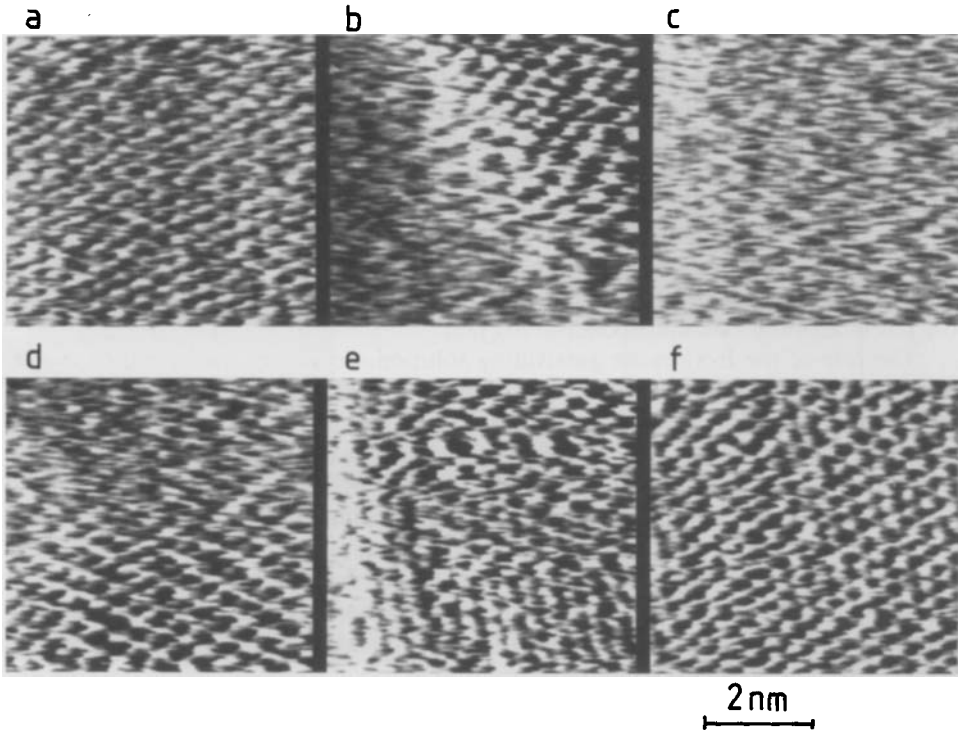

Fig. 35. Sequence of high-resolution in-situ AFM images of p-InSe showing the formation of an insoluble Se layer as the bias becomes anodic. The potential is scanned positively between images (a) and (d). The potential is scanned negatively afterwards and atoms are visible again in (f) (after [22]).

By AFM, Uosaki et al. have imaged p-InSe in acidic medium [22] and in air [167]. Figure 35 shows that the topmost layer of atoms (presumably Se) can be resolved at potentials cathodic relative to the rest potential, just as in air. When the potential is anodic of the open circuit, images become noisier by formation of insoluble oxidized Se layer (In is dissolved as $InOH^{2+}$) [22]. Returning the potential to negative values restores atomic resolution. Prolonged anodic polarization makes however the Se layer too thick to be dissolved at cathodic bias and atoms are not seen any more.

Layered materials have often been used for atomic-scale modifications in air. Garcia [168] removed single atoms from WSe_2 by moving the tip closer to the surface by 5 Å (feedback loop open) and ramping the tip potential. Huang et al. [169] simply used a positive pulse instead of a ramp to modify SnS_2 and MoS_2. Parkinson and coworkers [170, 171] have shown that many of these substrates are etched layer-by-layer during prolonged STM or AFM imaging. Capillary interactions between the tip and samples (there is always a layer of adsorbed water on these surfaces in air) are thought to be the origin of this phenomenon. The authors found that point defects are necessary to start etching.

5.2.3 Metal Deposition

Metal deposition under potential control has been studied mostly on metallic substrates with STM [9]. Nichols et al. [172] showed that three-dimensional Cu deposition on Au single crystals preferentially starts at defects (monoatomic steps, dislocations). Addition of organic molecules modifies the film growth into an almost two-dimensional process [173, 174]. The very little that has been done on semiconductors is still at a mesoscopic level. For experimental reasons, studying the *initial* stages of the formation of films is not easy on semiconductor electrodes. Tunneling must be possible where deposition does not occur and, according to the energy diagram of Fig. 6, this implies favorable conditions on an n-type electrode since imaging is not always stable close to the rest potential. AFM seems more relevant here. However, unlike working with noble metals, performing repetitive experiments by stripping the deposit will be always impossible since this will corrode the substrate by the same time.

Thundat et al. [150] have deposited Ni on Ge under potential control. A thin Ni layer is first formed before island growth starts, presumably because Ni germanide forms. Eriksson et al. [175] have studied Sn deposition on n-GaAs and Phaner et al. [176] compared films of Au obtained by evaporation and electroless deposition on GaAs. Hydride formation on Ge has been investigated by Kepler and Gewirth by in-situ AFM and STM [21]. Close to the rest potential, atoms could be resolved on Ge(111), as Fig. 36 shows. Long-range images showed reversible dendritic cathodic growth/anodic removal of hydride species. The rectangular-shaped features in images correspond to spikes (the authors demonstrated that tip imaging was responsible for this apparent shape by showing that the geometry of features changed with the geometry of tips). The growth of features was enhanced under the STM tip.

Local deposition is interesting in technology, and several studies show that this can be performed with in-situ scanning probe microscopes. On graphite Li et al. [177] applied short anodic pulses (6 V during 50 μs) and induced deposition by formation of a nucleation site during the first 5 μs with the counter electrode disconnected. Figure 37a shows a train of silver pillars grown by this method. This technique works on graphite because a defect site must be created prior to deposition [178]. Figure 37b displays a series of dots of copper deposited on Au single crystals by Ulmann et al. [179] within a standard four-electrode configuration. Controlled deposition is performed by covering the tip with copper from the solution and releasing it on the surface by touching the surface briefly with the tip. This approach offers the advantage of being less specific to the sample and should be applicable also with semiconductors, provided stable tunneling is possible at a potential where no metal deposition occurs. The size of clusters is adjustable with both techniques.

On semiconductors illumination is a supplementary parameter for deposition. Thundat et al. [150] used light-assisted deposition to grow Au dots on n^+- and p^+-GaAs. The tip was retracted from the surface by a few hundreds of ångströms and its potential pulsed by 4 V anodically. The counter electrode was disconnected for deposition, an arrangement which is similar to the configuration of a scanning electrochemical microscope. With p-GaAs, gold dots with a diameter of $0.1-1$ μm were deposited under the tip with a tip positive relative to the redox potential of the

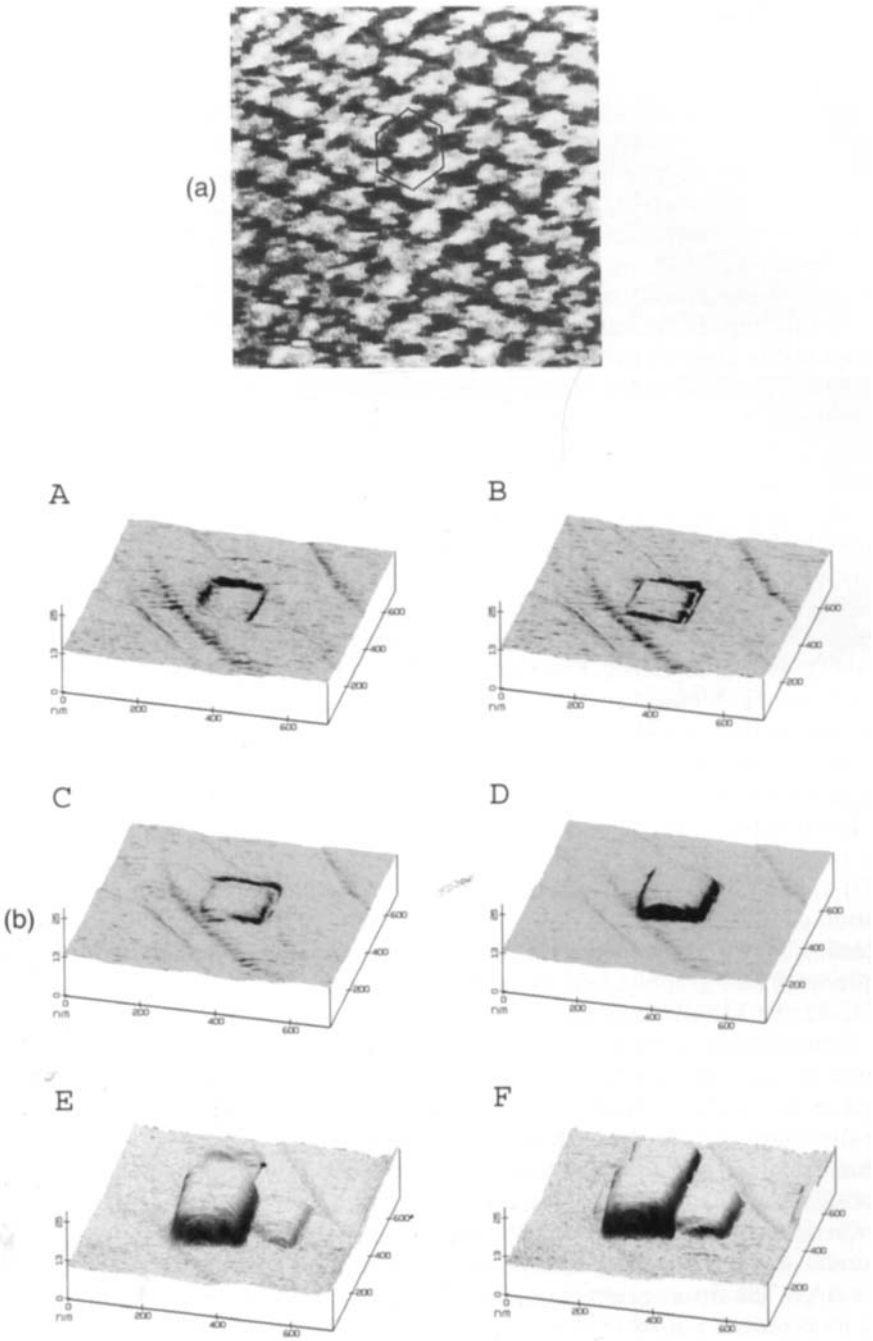

Fig. 36. High-resolution in-situ AFM image of Ge(111) in H_2SO_4 (a) and time sequence of images (b) showing the growth of a hydride layer. The regular rectangular shape of features, which should be dendrites, is due to tip imaging (after [21]).

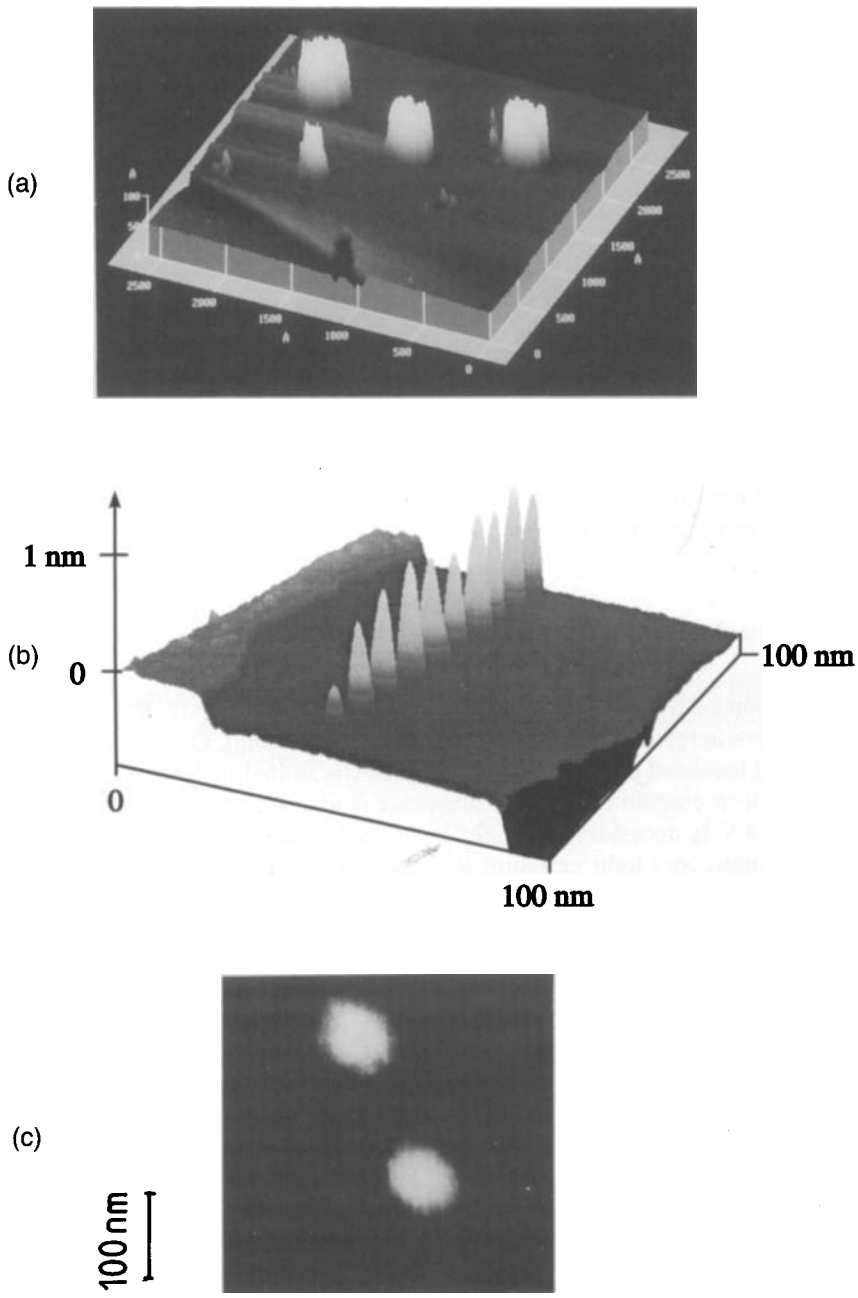

Fig. 37. Localized tip-induced in-situ metal deposition: (a) Ensemble of Ag pillars deposited on graphite (after [177]). (b) Train of Cu dots deposited on Au (after [179]). (c) Au dots grown on p-GaAs at positive tip and with light. Size is 500 Å × 500 Å (after [150]).

Au solution ($V_{redox} = -1$ V/SCE). An example of such dots is shown in Fig. 37c. According to the authors the mechanism of deposition involves the screening of the positive charge on the tip by formation of a local depletion layer in p-GaAs (the ionized dopant in the semiconductor is negative). This allows electron-hole pair separation, electrons being driven to the surface, and deposition occurs by reduction of Au ions at the conduction band edge (the conduction band minimum is $E_c = -1.15$ V which is negative relative to the redox potential). At n-GaAs, conversely, local corrosion occurs under the tip and annular deposition is observed around the tip because holes arrive at the surface. Maskless deposition on a nanometer scale is also possible with SECM, as has been shown on metals by Bard and coworkers [156].

6 Further Perspectives

This section briefly describes several methods addressed to the study of carrier properties at interfaces with semiconductors in UHV. We also examine the possibility of applying this approach in situ.

6.1 Photon Emission

This application of STM has been introduced recently [180, 181]. It uses the tip as a source of low-energy electrons which recombine in the solid. On metals, excitement of tip-induced localized plasmon modes via inelastic tunneling is the accepted mechanism for photon emission [180]. Fluorescence is also a possible mechanism [181]. A bias of 3–4 V is necessary and light is emitted in the visible range.

On semiconductors light emission is induced by injection of electrons into the conduction band and subsequent band-to-band radiative recombination with holes (Fig. 38a). The process is reminiscent of electroluminescence or cathodoluminescence and works with p-type substrates only (at n-type specimens no hole is available at the surface). Tunnel biases of ~1.5–2 V are necessary in the case of GaAs, for instance. Figure 38b is a photon map of a GaAlAs/GaAs multiquantum well obtained by Alvarado et al. [140]. The white stripes are regions where photons are emitted and correspond to the GaAs layers. The lateral resolution is about 1 nm and is limited by the diffusion distance of minority carriers. In Sec. 5.1 we have seen an example of the application of this technique in the case of porous silicon layers.

In-situ photoemission seems possible with semiconductors since tunneling out of a Pt-Ir tip into the conduction band of certain materials has been reported (see Sec. 3). The large biases used in UHV are in fact not necessary in the liquid since the band edges of the semiconductor are almost fixed with respect to the vacuum level, which is often not the case in vacuum (see Sec. 3). In the case of porous silicon, using liquid interfaces seems promising and easier than in vacuum (see Sec. 5.1.3). In the liquid environment the main problem will certainly be the collection of photons within a difficult geometry due to the electrochemical cell.

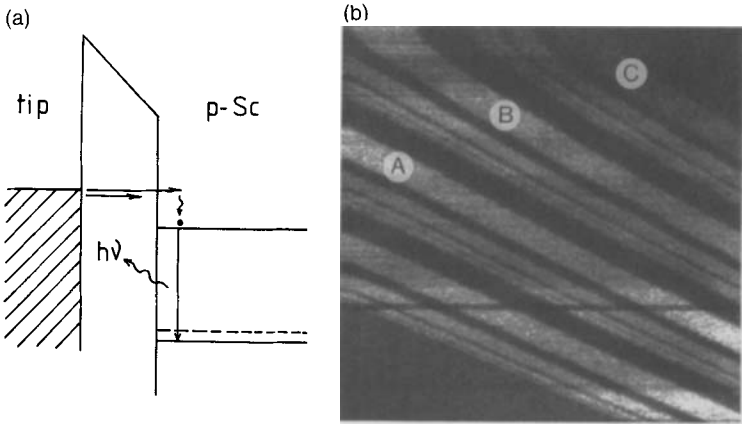

Fig. 38. Photon emission at a semiconductor. (a) Principle of the process at a p-type semiconductor. (b) Photon map taken on a GaAlAs/GaAs multiquantum well. Electrons are injected into GaAlAs and recombine in p-GaAs, from which light is emitted (after [140]).

6.2 Surface Photovoltage (SPV) Measurements

Under illumination and at the free potential, the band bending of the semiconductor decreases because photogenerated minority carriers are driven to the surface. The photovoltage is the difference

$$\Delta U_{ph} = |E_F\,(\text{light}) - E_F\,(\text{dark})|$$

If minority carriers recombine with majority carriers at surface defects, variations of ΔU_{ph} are expected locally. A similar mechanism occurs at Schottky photodiodes and results in energy losses for solar cells. SPV measurements are addressed to the study of recombination centres. The technique, introduced by Kuk et al. [182] and Hamers and Markert [183], combines STM with optical irradiation of the surface and necessitates two feedback (FB) loops [183]. The first FB loop (FB1) regulates the tunnel current just as for normal topographic imaging (Fig. 39a). The second feedback loop (FB2) is interrupted during imaging. To measure the SPV the system FB1 is interrupted briefly, so as to maintain the tip at a defined height above the surface, and the system FB2 is simultaneously activated. This regulation applies a voltage U to the sample in order to nullify the photocurrent flowing between the tip and the surface. The SPV is the difference $U\,(\text{light}) - U\,(\text{dark})$. Spatial resolution of SPV is possible.

Figure 39(b) shows the empty states on a Si(111)-7×7 surface with a point defect visible in the middle [182]. In the SPV image the point defect corresponds to a dark region (low SPV), with a much larger lateral dimension than the crystallographic defect. Recombination takes place at a distance of up to 40 Å from the defect. In an-

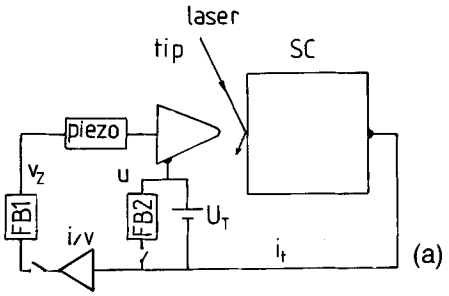

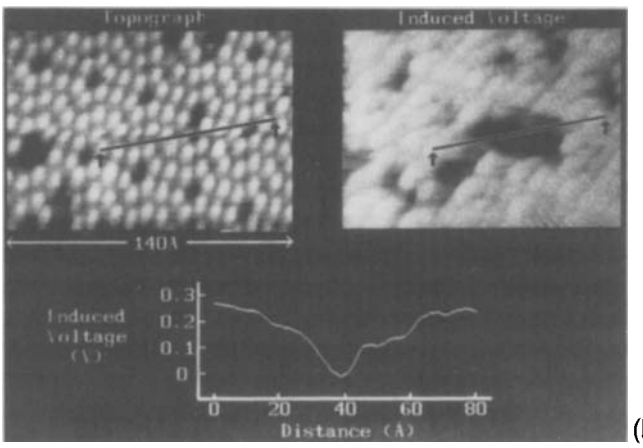

Fig. 39. Surface photovoltage measurements. (a) Principle of the technique: the two feedback systems FB1 and FB2 are alternately active. FB1 serves for topography and FB2 adds a potential u to U_T so as to nullify i_t. The SPV is $U_{light} - U_{dark}$. (b) STM (left) and SPV (right) images taken on Si(111)−7×7. Low-SPV (dark region) corresponds to point defects in (a) (after [182]).

other publication Cahill and Hamers [184] found that the atomic-scale variations of the SPV were dependent on tunneling conditions (bias and tip current). On a negatively biased n-Si(100) sample and for a sufficiently large tunnel current, the light intensity dependence of the SPV agrees with thermionic emission of majority carriers in the semiconductor. Decreasing the current increases the SPV because the band bending increases with an MIS approach of the tunnel junction. This reduces, however, the spatial variations. Cahill and Feenstra [185] found a similar behavior with Si(111)-2×1. With the tip negative, the SPV increases at defects on n-Si and decreases at p-Si, implying that surface states are locally charged by tunneling electrons [184, 185]. It could be estimated that the carriers injected into surface states were collected over a disk of radius 16 μm at n-Si and 2 μm at p-Si [185].

Dark regions in Fig. 39b correspond to regions where no charge accumulates. At an interface these regions would be electrically inactive (no charge transfer taking place). Numerically the observation of Fig. 39 means that $\sim 10^{12}$ point defects/cm^2

are sufficient to quench the photovoltage over the entire surface by overlapping of electrically inactive regions. This simple evaluation explains why a concentration of ca. 10^{12} recombination centres/cm^2 is an upper limit above which the performance of photodiodes decreases.

In-situ SPV measurements seem possible with minor modifications: (1) the tip potential (versus the reference) is set at a value close to the rest potential of the semiconductor in darkness (this must be compatible with the electrochemical response of the tip), and (2) the tip current is quenched by adjusting the sample voltage (versus the reference) with the second feedback system. With p-type materials the method seems more obvious than with n-type specimens, since illumination promotes surface electrons. At n-type materials SPV measurements will induce corrosion since holes are driven to the interface. If absolute measurements of the SPV seem difficult, because they depend on the adjustment of the tip potential, differential measurements appear accessible to experiment.

6.3 Ballistic Electron Emission Microscopy (BEEM)

Ballistic electron emission microscopy has been developed by Bell, Kaiser and coworkers [40, 186] to probe the electronic imperfections and carrier transport at *buried* interfaces [187, 188]. The principle of the technique is presented in Fig. 40a. The sample is covered with a metallic layer 20–30 Å thick and electrons tunnel into the metal at a large bias (typically 2 V): in this way hot electrons are injected ballistically from the sample into the conduction band of the semiconductor. Only a few percent of the electrons penetrate ballistically into the semiconductor without being thermalized in the metal layer or reflected at the metal/semiconductor interface. Electrons must indeed enter the semiconductor within a cone angle of a few degrees for parallel momentum conservation.[11] The spatial resolution of BEEM is therefore in the nanometer range. Ballistic electrons are collected at the ohmic contact on the rear side of the sample and BEEM images correspond to the spatial variations of the collector current i_c. Dark regions in BEEM images are indicative of defects where electrons are blocked by oxide clusters, for instance, or scattered on defects and point charges, since the collection efficiency decreases there. The electrical effect presumably extends over distances larger than the physical size of inhomogeneities if they are mesoscopic. Figure 40b compares the STM and BEEM images taken at a Au/GaAs Schottky contact [186]. The BEEM image displays dark regions presumably connected with oxide clusters, whereas the STM topography exhibits no specific feature. The technique enables a quick diagnosis of the homogeneity of the interface and is also applicable in ambient conditions [67]. The constraints on tip polarization for in-situ BEEM are similar to those in photon emission experiments.

[11] At metal/semiconductor contacts the cone angle $\theta \simeq 5°$ since $\tan\theta = V_{th}/V_f$, with V_{th} is the thermal velocity of electrons (10^7 cm s^{-1}) and V_f is the velocity of electrons at the Fermi surface in the metal (10^8 cm s^{-1}) [189]. In BEEM θ should be even smaller since ballistic electrons have a greater kinetic energy than electrons in the metal.

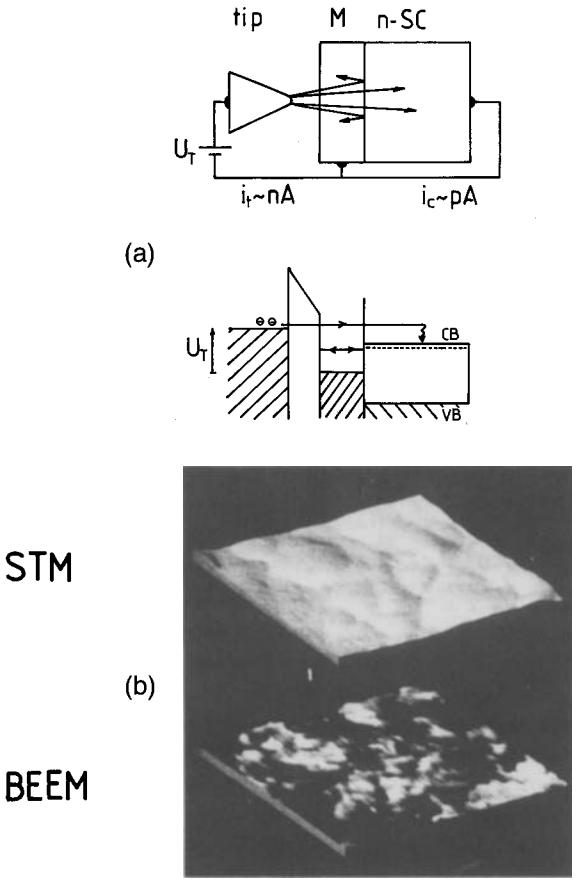

Fig. 40. Ballistic emission electron microscopy. (a) Electrons are tunneling at a high voltage out of the tip into the thin metal layer. A small fraction of hot electrons ballistically penetrate the sample. They are collected at the rear ohmic contact of the sample. (b) STM (top) and BEEM (bottom) images of an Au/GaAs Schottky contact. Dark regions in BEEM correspond to areas with no collector current i_c (after [186]).

7 General Conclusions

High-resolution scanning probe microscopy (SPM) studies require flat surfaces at an atomic level. The preparation of flat surfaces is essential and is not a minor problem. This necessitates advanced understanding of surface reactivity and chemistry: success has been obtained with silicon because systematic ex-situ studies of surface topography have been conducted by several groups. A good surface preparation is certainly more difficult with compound semiconductors because the different elements may dissolve at different rates.

It has been emphasized that STM is sensitive to topography convoluted with the electronic density of states. Spectroscopic characterization of surface states by STM is a challening field of research to be intensified for a better understanding of the chemical reactivity of interfaces. There are still fundamental effects which could be clarified definitively by direct observation. The characterization of transport properties, as demonstrated in Sec. 6, is complementary to STM and STS, and the combination of several techniques should provide a comprehensive description of charge transfer at electrodes.

Although in-situ AFM has been much less used than STM, the technique must be combined with STM, especially on chemically inhomogeneous and structured surfaces, since AFM only responds to topography and avoids the convolution with electronic effects. Problems specific to STM have mostly been related to polarization of the sample, as shown in Sec. 3. They do not apply to AFM imaging, which is an interesting point in favor of this microscopy. AFM presents other difficulties; for example, the laser beam used for detection may be a problem with semiconductors by inducing parasitic photoeffects on large-scale images. At present the most serious limitation of AFM is certainly the quality of the tip, whose geometry and resolution are still not as good as that of STM tips, even if atomic resolution has been reported in some papers. The resolution of monoatomic steps is necessary in studies of surface processes and this remains difficult by AFM.

Acknowledgements. I wish to dedicate this chapter to Professor H. Gerischer. I will always remember the great scientist he was as well as the generous man he used to be during my stay at the Fritz Haber Institute. I am pleased to thank A. J. Bard, R. J. Behm, H. Brune, Y. J. Chabal, J.-N. Chazalviel, H. Collel, V. Costa-Kieling, J. A. Dagata, Ph. Dumas, M. Enaschescu, S. Eriksson, A. A. Gewirth, U. Memmert, F. Ozanam, R. M. Penner, G. J. Pietsch, K. Uosaki, R. Ulmann, and O. Vatel for valuable discussions and preprints of their work. Thanks are also due all authors who kindly supplied original images of their work for this chapter. The author's stay at the Fritz Haber Institut, where the STM work was initiated, has been supported by a grant from the Alexander von Humboldt Foundation and a Max Planck Gesellschaft fellowship.

References

1. G. Binnig, H. Rohrer, Ch. Gerber, E. Weibel, Phys. Rev. Lett. 50, 120 (1983).
2. G. Binnig, H. Rohrer, IBM J. Res. Dev. 30, 355 (1986).
3. R. Wiesendanger, H.-J. Güntherodt (eds.), Scanning Tunneling Microscopy I, Springer Series in Surface Sciences, Vol. 20, Springer Verlag, Berlin (1992).
4. H.-J. Güntherodt, R. Wiesendanger (eds.), Scanning Tunneling Microscopy II, Springer Series in Surface Sciences, Vol. 28, Springer Verlag, Berlin (1992).
5. H.-J. Güntherodt, R. Wiesendanger (eds.), Scanning Tunneling Microscopy III, Springer Series in Surface Sciences, Vol. 29, Springer Verlag, Berlin (1993).
6. J. Strocio, W. J. Kaiser (eds.), Scanning Tunneling Microscopy, Methods of Experimental Physics, Vol. 27, Academic Press, Boston (1993).

7. P. Descout, H. Siegenthaler (eds.), 10 years of STM, Proc. 6th Int. Conf. on STM, Interlaken (1991), in Ultramicroscopy 42–44 (1992); C. Bai, R. Colton and Y. Kuk (eds.) Proceeding of the 7th Int. Conf. on STM, Beijing (1993), J. Vac. Sci. Technol., B12 n°3 (1994).
8. C. J. Chen, Introduction to Scanning Tunnelling Microscopy, Oxford University Press, Oxford (1993).
9. H. Siegenthaler, IBM J. Res. Dev. 30, 7 (1986).
10. H. Siegenthaler, A. A. Gewirth (eds.), Nanoscale Probes of the Solid/Liquid Interface, NATO ASI Series, Kluwer Academic Publishers, to be published.
11. F. F. Fan, A. J. Bard, J. Electrochem. Soc. 136, 166 (1989).
12. S. A. Hendricks, Y. T. Kim, A. J. Bard, J. Electrochem. Soc. 139, 2818 (1992).
13. B. J. Cruikshank, A. A. Gewirth, R. M. Rynders, R. Alkire, J. Electrochem. Soc. 139, 2828 (1992).
14. R. S. Robinson, J. Power Sci. 40, 149 (1992).
15. R. Houbertz, U. Memmert, R. J. Behm, Appl. Phys. Lett. 58, 1027 (1991).
16. P. Allongue, V. Kieling, H. Gerischer, Poster presented at the conference STM'91, Interlaken (1991).
17. K. Itaya, R. Sugawara, Y. Morita, H. Tokumoto, Appl. Phys. Lett. 61, 2535 (1992).
18. P. Allongue, H. Brune, H. Gerischer, Surf. Sci. 275, 414 (1992).
19. S. Lin Yau, F. F. Fan, A. J. Bard, J. Electrochem. Soc. 139, 2825 (1992).
20. P. Allongue, V. Kieling, H. Gerischer, J. Electrochem. Soc. 140, 1008 (1993).
21. K. D. Kepler, A. A. Gewirth, Surface Sci. in press.
22. K. Uosaki, M. Koinuma, J. Electroanal. Chem. 357, 301 (1993).
23. R. Fowler, L. Nordheim, Proc. Roy. Soc. A119, 173 (1928).
24. L. Esaki, Phys. Rev. Lett. 109, 603 (1957).
25. J. Wiechers, T. Twomey, D. M. Kolb, R. J. Behm, J. Electroanal. Chem. 248, 451 (1988).
26. P. Lustenberger, H. Rohrer, R. Christoph, H. Siegenthaler, J. Electroanal. Chem. 243, 225 (1988).
27. J. Pan, T. W. Jing, S. M. Lindsay, J. Phys. Chem. 98, 4205 (1994).
28. M. Bingelli, D. Carnal, R. Nyffeneger, H. Siegenthaler, H. Rohrer, J. Vac. Sci. Technol. B9, 1985 (1991).
29. W. Schmickler, D. Henderson, J. Electroanal. Chem. 290, 283 (1990).
30. J. K. Saas, J. K. Gimzewski, W. Haiss, K. H. Besoke, L. Lackey, J. Phys. Condens. Matter 3, S 121 (1991); J. K. Saas, J. K. Gimzewski, J. Electroanal. Chem. 308, 333 (1991).
31. K. L. Sebastian, G. Doyen, Surf. Sci. Lett. 290, L703 (1993).
32. H. Gerischer, Electrochem. Acta 35, 1677 (1990) and references therein.
33. S. R. Morrison in: Electrochemistry at Semiconductor and Oxidized Metal Electrodes, Plenum Press, New York (1980); idem, in: Chemical Physics of Surfaces, Plenum Press, New York (1978).
34. H. Gerischer in: Physical Chemistry: An Advanced Treatise, H. Eyring, D. Henderson, W. Jost (eds.), Academic Press, New York (1970), Ch. 5.
35. J.-N. Chazalviel, Electrochim. Acta 33, 61 (1988); idem, Electrochim. Acta 35, 1545 (1990).
36. H. Gerischer, W. Ekardt, Appl. Phys. Lett. 43, 383 (1983).
37. H. Gerischer in: Photovoltaic and Photoelectrochemical Solar Energy Conversion, NATO ASI Series B, Physics, F. Cardon, W. P. Gomes, W. Dekeyser (eds.), Plenum Press, New York (1981), Vol. 29.
38. See H. O. Flinkea (ed.) Semiconductor Electrodes, Studies in Physical and Theoretical Chemistry, Vol. 55, Elsevier, Amsterdam (1988), for a review of the electrochemistry of most semiconductors.
39. Handbook of Chemistry and Physics, 67th ed., CRC, Cleveland (1986/87).
40. L. D. Bell, W. J. Kaiser, M. H. Hecht, F. J. Grunthaner, Appl. Phys. Lett. 52, 278 (1988).
41. M. Tabe, M. Tanimoto, Appl. Phys. Lett. 58, 2105 (1991).
42. K. Itaya, E. Tomita, Chem. Lett. 285 (1989).
43. K. Itaya, E. Tomita, Surf. Sci. Lett. 219, L515 (1989).

44. E. Tomita, N. Matsuda, K. Itaya, J. Vac. Sci. Technol. A8, 534 (1990).
45. K. Sakamaki, K. Hinokuma, K. Hashimoto, A. Fujishima, Surf. Sci. Lett. 237, L383 (1990); K. Hinokuma, K. Sakamaki, A. Fujishima, Bull. Chem. Soc. Jpn. 63, 2713 (1990).
46. K. Sakamaki, K. Hinokuma, A. Fujishima, J. Vac. Sci. Technol. B9, 944 (1991).
47. J. Tersoff, Haneman, Phys. Rev. B31, 805 (1985).
48. R.M. Feenstra, J.A. Strocio, J. Vac. Sci. Technol. B5, 923 (1987); R.M. Feenstra, J.A. Strocio, J. Tersoff, A.P. Fein, Phys. Rev. Lett. 58, 1192 (1987).
49. J. Tersoff, R.M. Feenstra, J.A. Strocio, P.A. Fein, J. Vac. Sci. Technol. A6, 497 (1988).
50. L. Andersohn, U. Köhler, Surf. Sci. 284, 77 (1993).
51. H. Ibach, H. Wagner, D. Bruchmann, Solid State Commun. 42, 457 (1982); J.A. Schaefer F. Stucki, D.J. Frankel, W. Göpel, G.J. Lapeyre, J. Vac. Sci. Technol. B2, 359 (1984).
52. P. Dumas, Y.J. Chabal, P. Jakob, Surf. Sci. 269/270, 867 (1992).
53. J. Strocio, R.M. Feenstra, J. Vac. Sci. Technol. B6, 1472 (1988); R.M. Feenstra, J. Strocio, J. Vac. Sci. Technol. B5, 923 (1987).
54. R.S. Becker, G.H. Higashi, Y.J. Chabal, A.J. Becker, Phys. Rev. Lett. 65, 1917 (1990).
55. K. Pandey, Phys. Rev. Lett. 47, 1950 (1981).
56. J.A. Strocio, R.M. Feenstra, A.P. Fein, Phys. Rev. Lett. 57, 2579 (1986).
57. P. Jakob, Y.J. Chabal, J. Chem. Phys. 95, 2897 (1991).
58. E. Yablanovitch, D.L. Allara, C.C. Chang, T. Gmitter, T.B. Bright, Phys. Rev. Lett. 57, 249 (1986).
59. U. Neuwald, A. Feltz, U. Memmert, R.J. Behm, Appl. Phys. Lett. 60, 1307 (1992).
60. O. Magnussen, J. Hageböck, J. Hotlos, R.J. Behm, Faraday Discuss. 94 (1993).
61. H. Brune, J. Winterllin, G. Ertl, R.J. Behm, Europhys. Lett. 13, 123 (1990).
62. L. Ruan, F. Besenbacher, I. Stensgaard, E. Laegsgaard, Phys. Rev. Lett. 70 4079, (1993).
63. S.E. Gilbert, J.H. Kennedy, Langmuir 5, 1412 (1989).
64. F.F. Fan, A.J. Bard, J. Phys. Chem. 94, 3761 (1990).
65. F.F. Fan, A.J. Bard, J. Phys. Chem. 95, 1969 (1991).
66. F.F. Fan, A.J. Bard, J. Phys. Chem. 97, 1431 (1993).
67. J.A. Dagata, W. Tseng, Appl. Phys. Lett. 62, 591 (1993).
68. R. Wolkow, Ph. Avouris, Phys. Rev. Lett. 60, 1049 (1988).
69. Y. Kuk, p. 17 of [4].
70. Y. Kuk, P.J. Silverman, J. Vac. Sci. Technol. A8, 289 (1990).
71. W.J. Kaiser, R.C. Jakelevic, Surf. Sci. 181, 55 (1987).
72. M.P. Everson, R.C. Jakelevic, J. Vac. Sci. Technol. A8, 3662 (1990).
73. M.P. Everson, R.C. Jakelevic, W. Shen, J. Vac. Sci. Technol. B9, 891 (1991).
74. H. Brune, Ph. D. Thesis, Freie Universität Berlin (1992).
75. Y. Hasegawa, Ph. Avouris, J. Vac. Sci. Technol., B12, 1447 (1994).
76. R.A. Batchelor and A. Hamnett in: Modern Aspects of Electrochemistry, B.E. Conway, T.H. White, J. O'Bockris (eds.) Plenum Press, New York, Vol. 22, Chap. 3 (1992).
77. P. Allongue in: Modern Aspects of Electrochemistry, B.E. Conway, T.H. White, J. O'Bockris (eds.), Plenum Press, New York, Vol. 23, Chap. 4 (1992).
78. P. Carlsson, B. Holmström, H. Kita, K. Uosaki, Surf. Sci. 237, 280 (1990).
79. S. Eriksson, P. Carlsson, B. Hölmström, K. Uosaki, J. Electroanal. Chem. 313, 121 (1991).
80. K. Uosaki, M. Koinuma, Faraday Discuss. 94 (1993).
81. S. Eriksson, P. Carlsson, B. Holmström, K. Uosaki, J. Electroanal. Chem. 336, 57 (1992).
82. P. Carlsson, B. Holmström, H. Kita, K. Uosaki, J. Electroanal. Chem. 283, 425 (1990).
83. E. Yablanovitch, C.J. Sandroff, R. Bhat, T. Gmitter, Appl. Phys. Lett. 51, 439 (1987).
84. P. Allongue, Ber. Bunsenges. Phys. Chem. 92, 895 (1988).
85. P. Allongue, S. Blonkowski, E. Souteyrand, Electrochim. Acta 37, 781 (1992).
86. R.M. Feenstra, Appl. Surf. Sci. 56–58, 104 (1992) and references therein.
87. A.M. Green, W.E. Spiecer, J. Vac. Sci. Technol. A11, 1061 (1993).
88. M.S. Carpenter, M.R. Melloch, B.A. Cowans, Z. Dardas, W.N. Delgass, J. Vac. Sci. Technol. B7, 845 (1989).

89. P. Allongue, H. Cachet, Solid State Commun. 55, 49 (1985).
90. K. Schröder, R. Memming, Ber. Bunsenges. Phys. Chem. 89, 935 (1985).
91. J. Levine, Surf. Sci. 10, 313 (1968).
92. P. Allongue, unpublished data.
93. For reviews see R.L. Smith, S.D. Collins, J. Appl. Phys. 71, R1 (1992); P.C. Searson, J.M. Masaulay, S.M. Prokes, J. Electrochem. Soc. 139, 3373 (1992).
94. G.S. Higashi, Y.J. Chabal in: Handbook of Semiconductor Wafer Cleaning Technology, W. Kern (ed.) Noyes Publications, Park Ridge (1993) Ch. 10, p. 433, and references therein.
95. Y.J. Chabal, A.L. Harris, K. Raghavachari, J.C. Yully, Int. J. Modern Phys. B7, 1031 (1993).
96. Y.J. Chabal, J. Mol. Struct. 292, 65 (1993).
97. J.A. Dagata, J. Schneir, H.H. Harary, C.J. Evans, M.T. Postek, J. Bennett, Appl. Phys. Lett. 56, 2001 (1990).
98. J.A. Dagata, J. Schneir, H.H. Harary, J. Bennett, W. Tseng, J. Vac. Sci. Technol. B9, 1384 (1991).
99. N. Barniol, F. Perez-Murano, X. Aymerich, Appl. Phys. Lett. 61, 462 (1992).
100. K.H. Besocke, M. Teske, J. Frohn, J. Vac. Sci. Technol. A6, 408 (1988).
101. G.S. Hsiao, J.A. Virtanen, R.M. Penner, Appl. Phys. Lett. 63, 1119 (1993).
102. P. Jakob, P. Dumas, Y.J. Chabal, Appl. Phys. Lett. 59, 2968 (1991).
103. G.J. Pietsch, U. Köhler, O. Jusko, M. Henzler, P.O. Hahn, Appl. Phys. Lett. 60, 1321 (1992).
104. H. Jungblut, D.J. Müller, M. Aggor, H.J. Lewerenz, Electrochim. Acta 38, 1367 (1993); poster presented at the 44th ISE meeting, Berlin (1993).
105. Y. Kim, C.M. Lieber, J. Am. Chem. Soc. 113, 2333 (1991).
106. O. Vatel, S. Verhaverbeke, H. Bender, M. Caymax, F. Chollet, B. Vermeir, P. Martens, E. Andre, M. Heyns, Jpn. J. Appl. Phys., submitted.
107. O. Vatel, R. Petri, P. Brault, E. Andre, Ph. Dumas, F. Salvan in: Proc. STM'93, Beijing (1993), in J. Vac. Sci. Technol., to be published.
108. M. Susuki, Y. Homma, Y. Kudoh, N. Yabumoto, Jpn. J. Appl. Phys. 32, 1419 (1993).
109. B.S. Swartzentruber, Y.-W. Mo, M.B. Leeb, M.G. Lagally, J. Vac. Sci. Technol. A7, 2901 (1989).
110. A. Venkateswara Rao, J.N. Chazalviel, F. Ozanam, J. Electrochem. Soc. 138, 153 (1991).
111. J. Rappich, H.J. Lewerenz, H. Gerischer, J. Electrochem. Soc., 141, L187 (1994).
112. H.E. Hessel, A. Feltz, U. Memmert, R.J. Behm, Chem. Phys. Lett. 186, 275 (1991).
113. G.J. Pietsch, U. Köhler, M. Henzler, J. Appl. Phys. 73, 4797 (1993); idem, Chem. Phys. Lett. 197, 346 (1992).
114. S.M. Hu, D.R. Kerr, J. Electrochem. Soc. 114, 414 (1967).
115. U. Neuwald, H.E. Hessel, A. Feltz, U. Memmert, R.J. Behm, Surf. Sci. Lett. 296, L8 (1993).
116. G.S. Higashi, R.S. Becker, Y.J. Chabal, A.J. Becker, Appl. Phys. Lett. 58, 1656 (1991).
117. Y. Morita, K. Miki, H. Tokumoto, Appl. Surf. Sci. 60/61, 466 (1992).
118. Y. Morita, K. Miki, H. Tokumoto, Appl. Phys. Lett. 59, 1347 (1991); idem, Ultramicroscopy 42–44, 922 (1992); idem, Jpn. J. Appl. Phys. 30, 3570 (1991).
119. P. Allongue, V. Kieling, H. Gerischer, to be published.
120. P. Allongue, V. Bertagna, V. Kieling, H. Gerischer, J. Vac. Sci. Technol., B12, 1539 (1994); P. Allongue, V. Kieling and H. Gerischer, J. Phys. Chem. (1995), in press.
121. P. Allongue and J. Kasparian, Microsc., Microanal., Microstruct. 5, 257 (1994).
122. P. Allongue, V. Costa-Kieling, H. Gerischer, J. Electrochem. Soc. 140, 1019 (1993).
123. H. Gerischer, P. Allongue, V. Costa-Kieling, Ber. Bunsenges. Phys. Chem. 97, 753 (1993); P. Allongue, V. Kieling and H. Gerischer, Electrochim. Acta, in press, issue of the 6th Int. Fischer Symp., Karlsruhe (1994).
124. S. Watanabe, N. Nakayama, T. Ito, Appl. Phys. Lett. 59, 1458 (1991); idem, Jpn. J. Appl. Phys. 32, 3420 (1993).
125. H. Gerischer, M. Lübke, Ber. Bunsenges. Phys. Chem. 91, 394 (1987).
126. J. Stumper, L.M. Peter, J. Electroanal. Chem. 309, 325 (1991).
127. G.W. Trucks, K. Raghavachari, G.S. Higashi, Y.J. Chabal, Phys. Rev. Lett. 65, 504 (1990).

128. V. Costa-Kieling, Ph.D. Thesis, Technical University of Berlin (1993).
129. R. Herino, G. Bomchil, K. Barla, C. Bertrand, J.L. Ginoux, J. Electrochem. Soc. 134, 1994 (1987); V. Lehmann, H. Föll, J. Electrochem. Soc. 137, 653 (1990).
130. A. Kux, F. Müller, F. Koch in: Mater. Res. Soc. Symp. Proc. 283, 311 (1993).
131. Ph. Dumas, M. Gu, C. Syrykh, F. Salvan, J.K. Gimzewski, O. Vatel, A. Hallimaoui in: Optical Properties of Low Dimensional Silicon Structures, D.C. Bensahel et al. (eds.) Kluwer Academic, p. 157 (1993).
132. M. Enaschescu, E. Hartmann, A. Kux, F. Koch in: Proc. ICPS-21, Beijing (1992), p. 1439.
133. M. Enaschescu, E. Hartmann, A. Kux, F. Koch, J. Luminesc., in press.
134. G.B. Amisola, R. Behrensmeier, J.M. Gallian, F.A. Otter, F. Navamar, N.M. Kalkoran, Appl. Phys. Lett. 61, 2595 (1992); idem, J. Vac. Sci. Technol. B11, 1788 (1993).
135. T. George, M.S. Anderson, W.T. Pike, T.L. Lin, R.W. Fathauer, K.H. Jung, D.L. Kwong, Appl. Phys. Lett. 60, 2359 (1992).
136. R. Houbertz, U. Memmert, R.J. Behm, Appl. Phys. Lett. 62, 2516 (1993).
137. M. Enaschescu, E. Hartmann, F. Koch, Appl. Phys. Lett. 64, 1365 (1994).
138. M. Enaschescu, E. Hartmann, F. Koch, J. Vac. Sci. Technol., submitted.
139. Ph. Dumas, M. Gu, C. Syrykh, J.K. Gimzewski, I. Makarenko, A. Hallimaoui, F. Salvan, Europhys. Lett., submitted; M. Gu, C. Syrykh, A. Hallimaoui, Ph. Dumas, F. Salvan, J. Luminesc., in press (1993).
140. S.F. Alvarado, Ph. Renaud, D.L. Abraham, Ch. Schönenberger, D.J. Arent, H.P. Meier, J. Vac. Sci. Technol. B9, 409 (1991); Ph. Renaud, S.F. Alvarado, Phys. Rev. B44, 6340 (1991).
141. S.L. Yau, M. Arendt, A.J. Bard, B. Evans, C. Tsai, J. Sarathy, J.C. Campbell, J. Electrochem. Soc. 141, 402 (1994).
142. V. Dubin, F. Ozanam, J.N. Chazalviel in: Optical Properties of Low Dimensional Silicon Structures, D.C. Bensahel et al. (eds.), Kluwer Academic Publishers (1993) p. 163; V. Dubin, F. Ozanam, J.N. Chazalviel, J. Luminesc. 57, 61 (1993).
143. P.M.M.C. Bressers, J.W.J. Knapen, E.A. Meulenkamp, J.J. Kelly, Appl. Phys. Lett. 61, 108 (1992); E.A. Meulenkamp, P.M.M.C. Bressers, J.J. Kelly, Appl. Surf. Sci. 64, 283 (1992).
144. L.T. Canham, W.Y. Leong, M.I.J. Beale, T.I. Cox, L. Taylor, Appl. Phys. Lett. 61, 2563 (1992).
145. E. Collel, M. Bronold, S. Fiechter, H. Tributsch, Surf. Sci. Lett. 303, L361 (1994); E. Collel, N. Alonso-Vante, poster at the 44th ISE meeting, Berlin (1993).
146. D. Siebert, W. Stocker, Phys. Stat. Sol. A134, K17 (1992).
147. R. Sonnenfeld, J. Schneir, B. Drake, P.K. Hansma, D.E. Aspnes, Appl. Phys. Lett. 50, 1742 (1987).
148. Y. Robach, M. Phaner, C. de Villeneuve, L. Porte, Appl. Phys. Lett. 61, 2551 (1992).
149. E.J. Heller, M.G. Lagally, Appl. Phys. Lett. 60, 2675 (1992).
150. T. Thundat, L.A. Nagahara, S.M. Lindsay, J. Vac. Sci. Technol. A8, 539 (1989).
151. M. Koinuma, K. Uosaki, J. Vac. Sci. Technol., B12, 1543 (1994) and K. Uosaki, presentation at the 6th Int. Fischer Symposium, Karlsruhe (1994).
152. L.A. Nagahara, T. Thundat, S.M. Lindsay, Appl. Phys. Lett. 57, 270 (1990).
153. H. Sugimura, T. Uchida, N. Kitamura, H. Masuhara, Appl. Phys. Lett. 63, 1288 (1993).
154. D. Mandler, A.J. Bard, Langmuir 6, 1489 (1990).
155. C.W. Lin, F.R. Fan, A.J. Bard, J. Electrochem. Soc. 134, 1038 (1986).
156. O.E. Hüssel, D.H. Craston, A.J. Bard, J. Vac. Sci. Technol. B6, 1873 (1988); idem J. Electrochem. Soc. 136, 3222 (1989).
157. D. Mandler, A.J. Bard, J. Electrochem. Soc. 136, 3143 (1989).
158. Y.M. Wuu, F.R. Fan, A.J. Bard, J. Electrochem. Soc. 136, 885 (1989).
159. D.O. Wipf, A.J. Bard, J. Electrochem. Soc. 138, 469 (1991).
160. J.A. Dagata, W. Tseng, J. Bennett, J. Schneir, H.H. Harary, Ultramicroscopy 42–44, 1288 (1992).
161. J.A. Dagata, W. Tseng, J. Bennett, J. Schneir, H.H. Harary, Appl. Phys. Lett. 59, 3288 (1991).
162. P. Moriarty, G. Hughes, Ultramicroscopy 42–44, 956 (1992).

163. P. Moriarty, B. Murphy, G. Hughes, J. Vac. Sci. Technol. A11 1099, (1993).
164. J.A. Dagata, private communication.
165. C.J. Sandroff, M.S. Hedge, C.C. Chang, J. Vac. Sci. Technol. B7, 841 (1989).
166. J. Shin, K.M. Geib, C.W. Wilmsen, Z. Lillienthal-Weber, J. Vac. Sci. Technol. A8, 1894 (1990).
167. K. Uosaki, M. Koinuma, J. Appl. Phys. 74, 1675 (1993).
168. R.G. Garcia, Appl. Phys. Lett. 60, 1960 (1992).
169. J.L. Huang, Y.E. Sung, C.M. Lieber, Appl. Phys. Lett. 61, 1528 (1992).
170. E. Dewalski, B.A. Parkinson, J. Am. Chem. Soc. 114, 1661 (1992).
171. B.A. Parkinson, J. Am. Chem. Soc. 112, 798 (1990).
172. R.J. Nichols, D.M. Kolb, R.J. Behm, J. Electroanal. Chem. 313, 109 (1991).
173. N. Batina, T. Will, D.M. Kolb, Faraday Discuss. 95 (1994).
174. R.J. Nichols, C.E. Bach, H. Meyer, Ber. Bunsenges. Phys. Chem. 97, 1012 (1993).
175. S. Eriksson, P. Carlsson, B. Holmström, K. Uosaki, J. Electroanal. Chem. 337, 217 (1992).
176. M. Phaner, G. Stremdoerfer, Y. Wang Li, J.R. Martin, C. de Villeneuve, L. Porte, J. Electrochem. Soc. 138, 874 (1991).
177. W. Li, J.A. Virtanen, R.M. Penner, Appl. Phys. Lett. 60, 1181 (1992); idem, J. Phys. Chem. 96, 6529 (1992).
178. R.M. Penner, private communication.
179. R. Ulmann, T. Will, D.M. Kolb, Chem. Phys. Lett. 209, 238 (1993).
180. R. Berndt, J.K. Gimzewski, R. Schlitter, Ultramicroscopy 42–44, 355 (1992).
181. J.H. Coombs, J.K. Gimzewski, B. Reihl, J.S. Sass, R.R. Schlittler, J. Microsc. 152, 325 (1988).
182. Y. Kuk, R.S. Becker, P.J. Silverman, G.P. Kochanski, Phys. Rev. Lett. 65, 456 (1990); idem, J. Vac. Sci. Technol. B9, 545 (1991).
183. R.J. Hamers, K. Markert, Phys. Rev. Lett. 64, 1051 (1990).
184. D.G. Cahill, R.J. Hamers, J. Vac. Sci. Technol. B9, 564 (1991).
185. D.G. Cahill, R.M. Feenstra, J. Vac. Sci. Technol. A11, 792 (1993).
186. L.D. Bell, W.J. Kaiser, M.H. Hecht, F.J. Grunthaner, J. Vac. Sci. Technol. B7, 945 (1989).
187. A.M. Milliken, S. Manion, W.J. Kaiser, L.D. Bell, M.H. Hecht, Phys. Rev. B46, 12826 (1992).
188. W.J. Kaiser, M.H. Hecht, R.W. Fathauer, L.D. Bell, E.Y. Lee, L.C. Davis, Phys. Rev. B44, 6546 (1991).
189. E.H. Rohderick, Metal Semiconductor Contacts, Clarendon, Oxford (1980).

Advances in Electrochemical Science and Engineering
Edited by Heinz Gerischer and Charles W. Tobias

The Surface Chemistry of Silicon in Fluoride Electrolytes

Peter C. Searson

Department of Materials Science and Engineering,
The Johns Hopkins University, Baltimore, MD 21218-2689, USA

Contents

List of Symbols

C_H	double layer capacitance
C_{HF}	concentration of HF
ΔU_{sc}	change in band bending
F_H	electric field at Helmholtz double layer
F_s	electric field at silicon surface
i_v	hole current
N_A	acceptor concentration
N_D	donor concentration
N_{red}, N_{ox}	concentration of reduced and oxidized states
N_V	density of states in valence band
p_0	equilibrium hole concentration
p_s	surface hole concentration
q	electronic charge
t_c	time at which pore front penetrates wafer
$U_{applied}$	applied potential
U_{fb}	flat band potential
U_H	potential drop across the Helmholtz layer
U_{sc}	potential drop across the space charge layer
d_H	double layer width
ε_H	dielectric constant of the Helmholtz double laye
ε_s	dielectric constant of silicon surface
ψ	distance from pore front; screening length

Abbreviations

cb	conduction band
HREELS	high resolution electron energy loss spectroscopy
LEED	low-energy electron diffraction
STM	scanning tunneling microscopy
vb	valence band

1 Introduction

Technological applications for high-purity silicon include the microelectronics industry, microfabrication, photovoltaics, sensors, detectors, and photocatalysis. These applications are derived from properties such as the ability to form an insulating oxide layer by chemical or thermal treatment, an optical band gap in the infrared, long minority carrier diffusion length, and the relatively low cost of high-quality crystals. The ability to modify the structure and properties of silicon surfaces on an atomic scale by contact with a liquid offers a number of unique opportunities both for the fundamental study of these surfaces and for surface processing under ambient conditions. Many of these techniques are analogous to vacuum processes; however, the silicon/electrolyte interface is unique in allowing control of a wide range of surface processes, including chemical and electrochemical reactions. Recent advances in surface modification and processing techniques based on semiconductor/liquid junctions have demonstrated that the structure and chemistry of silicon surfaces can be controlled on very short length scales.

The interaction of silicon surfaces with fluoride ions represents the most important method for surface modification. Examples of processes involving interaction with F^- include: oxide removal, hydrogen passivation, reactive ion etching, porous silicon formation, electropolishing, and chemical etching. Chemical etching of silicon in HF solutions is important for oxide removal and in the formation of stabilized silicon surfaces by hydrogen passivation. Recent work has resulted in dramatic advances in the understanding of the relationship between etching processes and atomic-scale structure. Advances in selective etching based on orientation-dependent etch rates have led to widespread use of wet chemistry in microfabrication.

The optical properties of porous silicon have given rise to renewed interest in the processes leading to pore formation and the relationship between the structure and characteristic properties of porous layers. Indeed, porous semiconductors may be considered a new class of materials, since pore formation is not limited to silicon and has been observed for a wide range of compound semiconductors.

In this chapter the current advances in the understanding of fluoride interactions with silicon surfaces are discussed. The mechanism of reactions at liquid junctions under open-circuit conditions and in the presence of an applied potential are compared.

2 Open-Circuit Etching of Silicon

2.1 Micromachining

Open-circuit, or chemical, etching of semiconductors is widely applied in microelectronic device technology. As a processing tool, chemical etching is used for polishing (isotropic etching), shaping (anisotropic etching), and surface modification. Etching

is also used as a technique for characterization of structural and compositional defects at semiconductor surfaces. Sequential photoetching in conjunction with capacitance measurements is used as a technique for determination of doping profiles. The fundamental reactions controlling open-circuit etching processes are usually electrochemical in nature, involving both oxidation and reduction reactions. In this case oxidation of the semiconductor and reduction of the oxidant occur at spatially separated microscopic sites on the surface.

For silicon, most etching solutions contain an oxidizing agent such as HNO_3 and a complexant such as HF. The HF increases the solubility of the oxidation products and minimizes precipitation reactions that tend to slow the reaction rate. For the HF/HNO_3 system at high HF concentrations, anodic dissolution is the rate-limiting process and the etching reaction is dependent on dopant concentration, surface structure, and crystal orientation. In this case, kinetic differences in surface properties may lead to anisotropic etching or pore formation. For low HF concentrations, oxide dissolution is the rate-limiting process and the etching reaction is controlled by mass transport. As a result the reaction is independent of surface properties and the etching is generally isotropic.

Anisotropic etching of silicon is routinely used in the fabrication of three-dimensional structures [1, 2]. These microfabrication techniques take advantage of orientation-dependent etch rates where the planes of lowest etch rate, usually the (111) planes, act as etch stops for the dissolution process [3, 4]. In electrolytes such as KOH, the etch rates of the (100) and the (110) planes may be more than two orders of magnitude faster than those of the (111) planes. In buffered NH_4F solutions, etch rate enhancements as high as 15 have been reported for the (100) plane in comparison with the (111) surface [5].

Table 1. Surface density and number of dangling bonds for ideally terminated, unreconstructed silicon surfaces as a function of crystal orientation.

Plane	Atom density (cm^{-2})	Dangling bonds per atom	Dangling bond density (cm^{-2})
(100)	6.78×10^{14}	2	1.36×10^{15}
(110)	9.59×10^{14}	1	0.959×10^{15}
(111)	7.83×10^{14}	1	0.783×10^{15}

The lattice parameter of silicon is 5.43 Å.

Although the relative etch rates for different orientations are well known, the mechanisms of etching are not well understood. In some solutions, such as those containing NH_4F, the relative etch rates follow the dangling bond density (see Table 1). It is generally assumed that atom removal is thermally activated so that the relatively small differences in dangling bond density for different orientations can result in large differences in etch rates. Other proposed mechanisms have focused on effects such as steric hinderance to explain the relative etch rates of different crystal planes.

2.2 The Composition of Chemically Etched Silicon Surfaces

2.2.1 Hydrogen Passivation: Si–H

The formation of ultraclean and oxide-free surfaces is important in the fabrication of high-quality electronic devices. In some cases stabilization of the surface is also important; for example, the Si(111) surface is unstable in vacuum and reconstructs to a lower-energy configuration, e.g. Si(111) 7×7. In the last few years, a variety of experimental techniques have been used to investigate the nature of the interaction between silicon surfaces and HF solutions and, in particular, the structure and properties of the hydrogen-terminated surface.

Hydrogen passivation of silicon surfaces has been used for many years in device fabrication as a means for providing a stable, oxide-free surface. Considerable attention has been given to electrochemical and chemical processes that could offer a simple alternative to vacuum techniques for surface passivation. The structure of silicon surfaces in ultrahigh vacuum is dependent on crystal orientation and hydrogen coverage [6–8]. For example, at low coverages monohydrides (Si–H) are observed on the Si(100) 2×1 surface, whereas at higher coverages, transformation to the Si(100) 1×1 surface is correlated to the formation of dihydrides ($Si-H_2$). The presence of dihydrides is also observed on the Si(111) 7×7 surface.

Although it has been known for more than 20 years that HF treatments can passivate the silicon surface, it has been recognized only recently that the raction between silicon and HF produces a hydrogen-terminated surface [9, 10] as opposed to one terminated by fluorine. Historically the Si–F surface was assumed to be more stable since the Si–F bond energy of 550 kJ mol^{-1} (8 eV) is much larger than the Si–H bond energy of 290 kJ mol^{-1} (4 eV) [11]. It is now recognized that kinetic parameters play an important role in determining the surface chemistry and favor the hydrogen-terminated surface. As described below, the Si–F surface is unstable since the large difference in electronegativity between Si and F results in polarization of the Si–Si backbonds that become easily attacked by HF. The HF molecule inserted into the backbond leads to the formation of a fluoride dissolution intermediate and a hydrogen-terminated surface. In contrast, the Si–Si backbonds of the Si–H surface have a much higher activation energy for reaction with HF and are highly stable under most conditions.

In addition to satisfying dangling bonds, hydrogen passivation influences many properties of silicon surfaces. For example, the hydrogen-passivated surface is generally hydrophilic and easily wetted in aqueous solutions. The interaction between hydrogen and donor or acceptor species results in a change in resistivity; this effect is more pronounced in the case of p-type silicon [12]. There is also evidence that the H atoms induce surface defects into the lattice [13].

The procedure for preparing atomically smooth, hydrogen-terminated silicon surfaces involves a number of steps: removal of hydrocarbon contamination, formation of a uniform oxide, oxide removal, etching of the silicon surface, and the formation of the passivation layer. The uniformity of the oxide is important in developing a smooth surface at the Si/SiO_2 interface.

The most widely used chemical oxidation treatment is the so-called RCA etch [14, 15]. This process involves sequential immersion steps designed to remove organic and inorganic contaminants, respectively:

1. $H_2O/H_2O_2/NH_4OH$ (5:1:1–7:2:1 by volume) at 75–85 °C for 10–20 min.
2. $H_2O/H_2O_2/HCl$ (5:1:1–7:2:1 by volume) at 75–85 °C for 10–20 min.

In addition to removal of organic contaminants, this process provides a relatively uniform oxide of about 15 Å in thickness and a smooth silicon/oxide interface. A variation of this procedure is the acidic Piranha etch in H_2SO_4/H_2O_2 (4:1 by volume) at 100 °C. Reviews of the composition and structure of the oxides formed by these techniques can be found in the literature [16–18]. In general, the basic peroxide etches have been shown to give higher surface roughness than the acidic versions [16]. Other cleaning procedures, such as ultraviolet-ozone cleaning [16, 18], have also been used to remove hydrocarbon contamination prior to oxide removal in HF solutions.

The structure and morphology of hydrogen-passivated silicon surfaces are dependent on the crystal orientation and pH of the HF solution. Since the number of hydrogen ligands per silicon atom is related to the atomic co-ordination, analysis of the $Si-H_x$ stoichiometry at the surface can give information on the surface structure. For example, silicon monohydride (Si–H) is characteristic of an ideally terminated, unreconstructed Si(111) surface, denoted by Si(111):H (1×1). Detection of dihydride ($Si-H_2$) and trihydride ($Si-H_3$) groups on a Si(111) surface gives an indication of the concentration of atomic-scale roughness. As discussed below, the structure of the surface is dependent on the pH of the electrolyte. At very low pH, the silicon surface is relatively unreactive and the structure corresponds to that of the silicon/oxide interface prior to oxide removal. Both step and terrace sites are stable at low pH and there is no modification of the surface morphology. In contrast, at higher pH, steps are unstable and step recession results in the formation of relatively large regions of ideally terminated terraces. As a result, the surface morphology is determined by the rate of step recession and hence by the pH of the solution.

Infrared absorption spectra for Si(100) and (111) treated in HF of pH < 4 reveal the presence of mono-, di-, and tri-hydrides at the surface [9, 20–23], showing that the silicon surface is stabilized by the hydrogen passivation layer but is atomically rough. For a (111) surface, di- and tri-hydrides are considered defect modes since they are indicative of atomic-scale roughness. For Si(100) surfaces treated with HF, regions of microscopic (111) facets have been observed [22], illustrating that the (111) planes exhibit the slowest etch rates and are highly stable. A detailed discussion of the possible configurations of surface hydride groups at silicon surfaces can be found in [16]. These results have been confirmed by a range of experimental techniques, including scanning tunneling microscopy (STM) and low-angle electron diffraction (LEED).

Morita et al. [24] have reported ultrahigh vacuum STM images showing regions of SiH_3 termination on a Si(111) surface after treatment in 1% HF solution, suggesting that there are relatively large domains of the surface that are atomically rough. Tomita et al. [25] have reported on in-situ scanning tunneling microscopy of

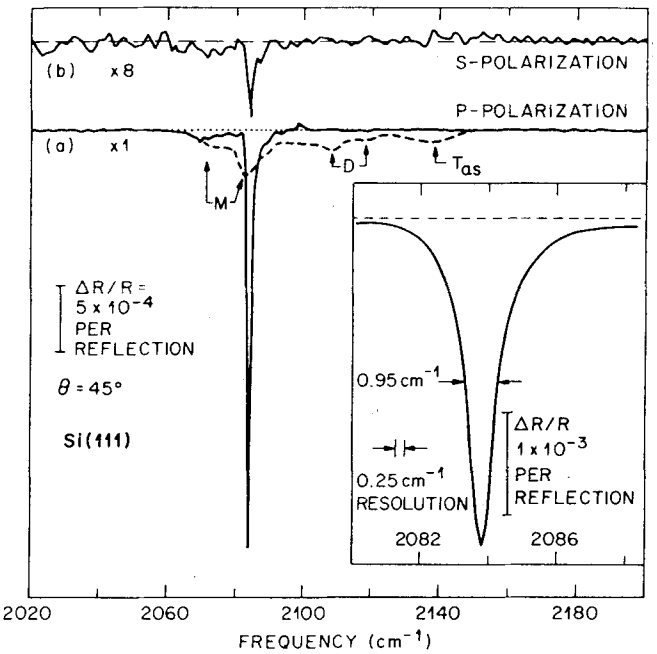

Fig. 1. Internal reflection spectra for HF-treated Si(111) surfaces. (a) Surface treated with buffered HF, pH 9–10 (solid curve), dilute HF (H_2O/HF 100:1) (broken curve); (b) s-polarization spectrum for surface treated with buffered HF, pH 9–10. Inset: high-resolution spectrum for Si(111) treated with buffered HF, pH 9–10 [20].

hydrogen-passivated p-Si(100) surfaces in H_2SO_4 solutions. The passivated surfaces formed by treatment in 1% HF solution were reported to be stable at negative potentials where the p-type silicon surface is reverse-biased and the hydrogen evolution reaction provides a hydrogen overpressure. After etching in dilute HF, the surfaces were characterized by large step heights.

Recent work has shown that etching of Si(111) at higher pH in NH_4F solutions leads to domains of atomically smooth, monohydride-terminated surface. These surfaces are atomically smoother than Si(111) surfaces etched in acidic HF solutions [20, 22, 26, 27] or exposed to hydrogen under ultrahigh vacuum conditions [28]. Figure 1 shows internal reflection spectra of HF-treated Si(111) surfaces; for etching in buffered HF, pH 9–10, a single, sharp monohydride line is observed [20], indicating that the surface is dominated by the ideally terminated Si(111):H (1×1) structure. Infrared spectra shown in Fig. 2 illustrate that subsequent rinsing in water of a Si(111) surface treated with buffered HF of pH 5.0 further increases the monohydride line and decreases the intensity of dihydride defect modes. This effect is thought to be related to removal of ionic species, such as F^-, remaining on the surface after the etching process [21].

The presence of the Si(111):H (1×1) structure has also been confirmed by LEED and scanning tunneling microscopy of the etched surfaces in ultrahigh vacuum [29].

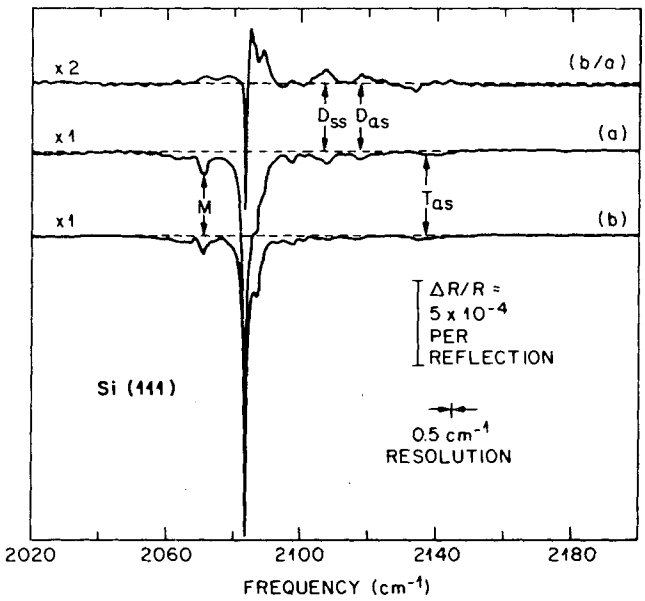

Fig. 2. Internal reflection spectra for HF-treated Si(111) surfaces. (a) Surface treated with buffered HF, pH 5.0; (b) subsequently rinsed in water; (b/a) difference spectrum showing a decrease in intensity of dihydride defect modes (D_{ss} and D_{as}) and an increase in the intensity of the monohydride mode (M) [20].

Figure 3 shows an STM image of a region of the Si(111):H (1×1) surface after immersion in NH_4F. The hexagonal arrangement of the surface is clearly seen with a spacing of 3.8 Å, close to the expected lattice spacing of 3.84 Å for the (111) orientation. Itaya et al. [30] have reported atomic-resolution STM images of p-type Si(111):H (1×1) surfaces in H_2SO_4 after open-circuit etching in NH_4F.

Ideally terminated Si(111):H (1×1) surfaces are reported to be stable toward contamination in air or vacuum. The levels of carbon and fluorine on these surfaces have been shown to be less than 1% of a monolayer [21, 31]. Exposure of the ideally terminated monohydride surface to low-energy electrons in vacuum desorbs the surface hydrogen and the surface reconstructs to Si(111) (2×1) [32].

2.2.2 Mechanism of Open-Circuit Etching

Phenomenologically, the dependence of the surface structure on pH can be explained in terms of the relative etch rates for the oxide and silicon. In general, the etch rate of SiO_2 is one or two orders of magnitude faster than for crystalline silicon. In addition, etching of the oxide is isotropic whereas etching of the hydrogen-terminated surface is anisotropic. Preferential etching of the hydrogen-terminated surface at step sites leads to the formation of (111) facets. Typical etch rates for

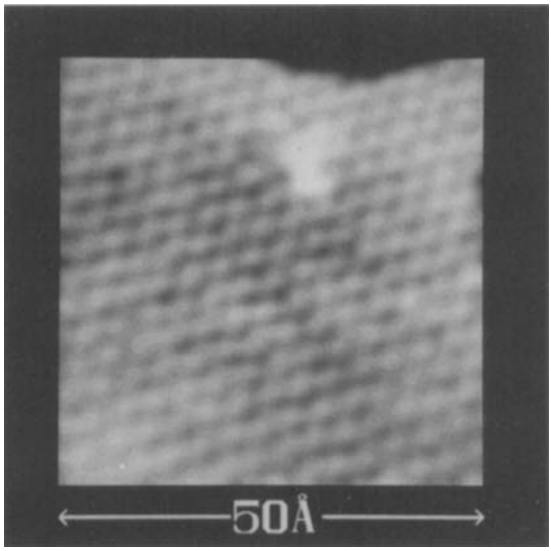

Fig. 3. STM image of the Si(111):H (1×1) structure in ultrahigh vacuum after immersion in NH_4F. The transition from light to dark corresponds to a height change of 0.5 Å and the lattice spacing is 3.8 Å [29].

SiO_2 are in the range 1 – 100 Å s^{-1}, depending on the HF concentration, pH, and temperature [33 – 35]. In concentrated HF, although the etch rate of the oxide is fast, the hydrogen-terminated surface is etched at very slow rates and hence the microscopic roughness of the Si/SiO_2 interface is essentially frozen into the surface. An etch rate of 0.005 Å s^{-1} has been reported for n-Si(111) in 48 wt.% HF [33]. Even in dilute HF, the etch rate of silicon is relatively slow, on the order of 0.013 Å s^{-1} [33], in comparison with the oxide [34], and the surface remains atomically rough. However, as the pH is increased further, the etch rates for weakly coordinated atoms increase, resulting in observable changes in the surface morphology. This effect is discussed in more detail below. Typical etch rates are given in Table 2.

As described above, the limiting flatness of the surface is related to the smoothness of the Si/SiO_2 interface before etching and the kinetics of step recession. Thermal oxidation, as opposed to chemical treatment (e.g., RCA clean), results in a smoother interface region so that subsequent treatment of Si(111) in buffered HF

Table 2. Etch rates for Si and SiO_2 in HF and NH_4F solutions [33 – 35].

Substrate	Electrolyte	Etch rate (Å s^{-1})
n-Si(111) 2 Ω cm	48 wt.% HF	0.005
n-Si(111) 2 Ω cm	2 wt.% HF, pH 3.5	0.013
SiO_2 (electrochemically grown on n-Si(111))	0.1 M NH_4F, pH 4.5	0.5
SiO_2 (electrochemically grown on p-Si(111))	0.1 M NH_4F, pH 4.5	0.8
SiO_2 (thermally grown)	1 M HF	1.0
SiO_2 (thermally grown)	10 M HF	20

(pH > 8) results in large regions of ideally terminated Si(111) : H (1×1) surface, limited only by the miscut of the wafer [36]. The morphological dependence of the surface induced by immersion in HF is related to the relative etch rates for different surface sites [37]. The (111) surface is relatively unreactive so that the final surface morphology is related to the kinetics of dissolution of other orientations and the time of exposure. With increasing pH, the overall etch rate increases and the surface roughness decreases.

On immersion of an oxide-covered silicon surface in HF, the initial process is oxide removal for which the overall reaction is:

$$SiO_2 + 6\,HF \rightarrow 2\,H^+ + SiF_6^{2-} + 2\,H_2O \tag{1}$$

This reaction proceeds through HF insertion into the Si–O bonds of the oxide. Polarization of the Si–O bond is thought to decrease the activation energy for this process, resulting in strong coulombic attraction between the H atom in the HF molecule and the O atom in the Si–O bond and between the F atom and the Si in the Si–O bond [9, 16, 38]. Fluorine termination of the exposed silicon surface is expected to be the final step of oxide removal. Conversion of the fluorine-terminated surface to one terminated by hydrogen is thought to be related to attack of the Si–Si backbonds by HF molecules resulting from polarization of the surface Si–F bond [9, 16, 38]. This process is shown schematically in Fig. 4 [38].

Molecular orbital calculations for chemical reactions involving the insertion of HF molecules into Si–Si backbonds support this hypothesis [38], as shown in Table 3. From these calculations it can be seen that the Si–Si backbonds for the hydrogen-terminated surface exhibit a 1.6 eV activation barrier and hence are rela-

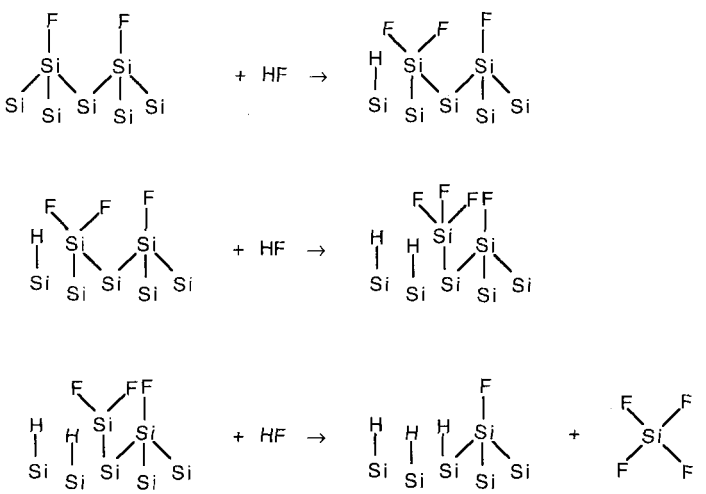

Fig. 4. Schematic illustration of the final stage of chemical etching in HF solutions where Si–F is converted to Si–H. Note that the HF molecule is inserted into the Si–Si backbond due to polarization of the Si–F bond. Adapted from [37].

Table 3. Calculated activation barriers for chemical insertion of HF molecules into Si–Si backbonds [38].

Reaction	Activation energy (eV)
(1) $H_3Si-SiH_3+HF \rightarrow$ intermediate $\rightarrow SiH_4+SiH_3F$	1.6
(2) $H_3Si-SiH_2F+HF \rightarrow$ intermediate $\rightarrow SiH_4+SiH_2F_2$	1.0

tively stable to attack by HF (reaction (1)). However, the activation energy for HF insertion if one of the Si–H ligands is exchanged for Si–F (reaction (2)) is reduced to 1 eV. For a thermally activated process, the rate constant for the reaction of HF with Si–H would be expected to be about three orders of magnitude slower than for the Si–F surface [38].

Since the overall etch rate increases with increasing pH, it has been suggested that smoothening of the surface is related to attack of $Si-H_2$ at step sites. Further evidence comes from the observations that hydrogen gas is evolved from Si(100) and vicinal Si(111) surfaces during etching in NH_4F where the step density is relatively high, but not from an ideally terminated Si(111) surface [37].

Hessel et al. [154] have demonstrated that the smoothening process occurs through a step flow mechanism. Ultra-high vacuum scanning tunneling microscopy was used to characterize the step configurations on Si(111) surfaces miscut to give steps parallel to the [110] direction. Surfaces immersed in HF solutions at low pH were atomically rough and the steps poorly resolved showing that the etching process was very slow. Surfaces immersed in HF buffered to pH 8, however, were atomically smooth with well resolved monatomic steps. STM images of the surfaces revealed two contributions to the smoothening process. The first component was related to recession of the steps resulting from the wafer miscut. The second component was related to the formation of triangular etch pits of monatomic height on the (111) terraces, with the edges corresponding to monohydride-terminated [110] steps. The density of these features was independent of position, consistent with the random nucleation of a vacancy resulting from the removal of a monohydride-terminated terrace atom. The size of these features increased progressively from an ascending step to descending step demonstrating that they are eventually annihilated by the motion of the descending step on the terrace. From analysis of the dimensions of the triangular features, the velocity of the steps was estimated to be about six times faster than the growth velocity of the etch pits on the terraces. These experiments clearly demonstrate that the smoothening process in neutral and weakly alkaline HF solutions is controlled step recession that occurs through the removal of dihydrideterminated kinks on monohydride-terminated terraces. The fast removal of trihydride- and dihydride-terminated atoms results in large Si(111):H (1×1) terraces and (111) microfacets formed by monohydride terminated steps. The rate limiting step for this process is either the removal of monohydride-terminated step atoms (creating dihydride-terminated kink sites) or the removal of a monohydride-terminated terrace site (vacancy formation).

A key issue at present is related to the role of OH^- in the etching process. Watanabe et al. [21] have shown that Si(111) surfaces dipped in 1.5% HF followed

by immersion in boiling water also exhibit strong monohydride lines with less than 0.5% defect density. Infrared absorption measurements indicate that dihydrides may be attacked preferentially in deionized water [20, 21], as shown in Fig. 2 [20]. These results suggest that the smoothening process occurs through a reaction with OH^-, and that the etching process can proceed through reaction of HF with Si–Si backbonds polarized by Si–F or Si–OH surface groups; this process is discussed in more detail in Sec. 4.7. The ligand exchange reactions Si–H → Si–F or Si–H → Si–OH are electrochemical processes and can only occur under open-circuit conditions if coupled with a suitable reduction reaction.

Possible reactions involving OH^- or H_2O with Si–H groups include [39]:

$$Si_{bulk} \equiv Si^*-H + OH^- \rightarrow Si_{bulk} \equiv Si^*-O^- + H_2 \quad (2)$$

$$Si_{bulk} \equiv Si^*-H + H_2O \rightarrow Si_{bulk} \equiv Si_{bulk}Si^*-OH + H_2 \quad (3)$$

where Si* represents a surface site triply coordinated to the bulk lattice. Note that reactions (2) and (3) involve the formation of molecular hydrogen. These surface groups can then be attacked by HF:

$$Si_{bulk} \equiv Si^*-OH^- + HF \rightarrow Si_{bulk} \equiv Si^*-F + OH^- \quad (4)$$

$$Si_{bulk} \equiv Si^*-OH + HF \rightarrow Si_{bulk} \equiv Si^*-F + H_2O \quad (5)$$

Reactions (4) and (5) are analogous to HF insertion into Si–O bonds during oxide dissolution and are expected to be relatively fast. Reactions (2) and (3) are expected to be slow so that the surface remains hydrogen-terminated during the etching process [20, 37, 40]. The Si–Si backbonds of the Si–F surface groups are then attacked by HF insertion. Jakob et al. [37] have suggested an overall reaction of the form:

$$[Si]_{4-n}\,Si-H_n + OH^- + H_3O^+ + 4\,HF \rightarrow (4-n)\,Si-H + SiF_4 + 2\,H_2O + n\,H_2 \quad (6)$$

where [Si] represents bulk silicon sites that become hydrogen-terminated after removal of the surface $Si-H_n$ groups. This model of the reaction mechanism suggests that direct reaction of OH^- with surface silicon atoms occurs at weakly coordinated sites.

Smoothening of the Si(111) surface in NH_4F is associated with a decrease in the kink density and straightening of the steps, as shown schematically in Fig. 5. At pH 8, steps are rearranged into staircase-like features, creating monohydride-terminated facets [37]. Jakob et al. [37] have estimated the relative etch rates of adatom, kink, and step sites from infrared absorption spectra of atomically flat and stepped (111) surfaces, as shown in Table 4.

In summary, oxide layers on silicon surfaces are chemically dissolved in HF leading to the formation of an atomically rough hydrogen-terminated surface. At (111) surfaces, relatively large domains of ideally terminated Si(111):H (1×1) can be formed by subsequent immersion in buffered HF of pH 8–9. The smoothening process is controlled by the rate of step recession at the surface.

Table 4. Relative etch rates for silicon surface sites during etching in buffered HF [37].

Site	Relative etch velocity
$v_{step}/v_{terrace}$	20 – 50
v_{kink}/v_{step}	50 – 100
v_{adatom}/v_{kink}	10 – 100

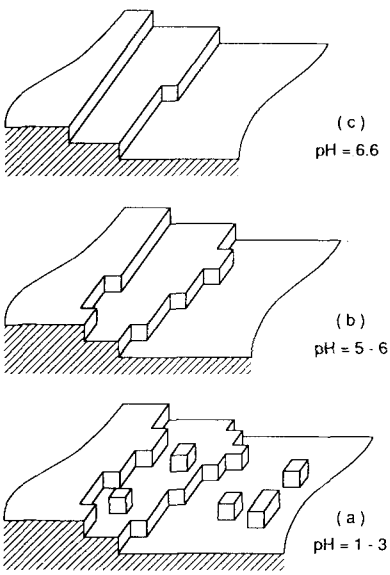

Fig. 5. Schematic illustration of the dependence of surface morphology on pH [38].

2.2.3 Hydrogen Absorption in Silicon

In general, discussions of the hydrogen-passivated silicon surface consider an atomically sharp interface between the silicon substrate and the hydrogen passivation layer. Hydrogen can exist in silicon in atomic or molecular form. In addition, hydrogen may be trapped at specific sites in the crystal lattice or bound to dangling bonds at defects such as vacancies [38]. Hydrogen passivation of interband bulk states is also well known. In many cases, trapping is thought to be related to chemically induced reconstructions at defect sites.

The transport properties of hydrogen in silicon are complicated by trapping processes and molecule formation. For single-crystal silicon with low defect concentration ($< 10^{12}\,cm^{-3}$), diffusion coefficients on the order of $10^{-11}\,cm^2\,s^{-1}$ have been measured [41].

3 The Silicon/Gas Interface

3.1 Silicon/Fluorine

The etching of silicon in the gas phase exhibits many of the same features as etching in solutions. Etching occurs when a gas reacts with the solid surface to form a volatile reaction product. For the case of silicon, etching is usually performed by reaction with a gas-phase fluorine compound. Enhancements of the etch rate are obtained with the addition of energetic ions or electrons (reactive ion etching), a process widely used in device fabrication. Although the atomic processes involved in gas-phase etching are not well understood, many of the features observed are similar to electrochemical etching.

Silicon can be isotropically etched in XeF_2 according to the overall reaction:

$$2\,XeF_2\,(g) + Si\,(s) \rightarrow SiF_4\,(g) \tag{7}$$

The etching rate at room temperature is proportional to the XeF_2 pressure, with rates as high as $12\,nm\,s^{-1}$ at 1.4×10^{-2} Torr [42]. This etch rate corresponds to an equivalent etching current of about $7\,mA\,cm^{-2}$ on a (100) surface and assuming a dissolution valence of 2.

Although the product of the etching process is gaseous SiF_4, the dissolution reaction in XeF_2, Eq. (7), proceeds through the formation of an interfacial fluorosilyl (SiF_x) layer at the surface [42–47]. The reaction sequence involves dissociative adsorption of F^- and Xe from XeF_2 although the Xe is subsequently desorbed from the surface [42]. The initial desorption reaction is followed by the the formation of an SiF_x layer where the silicon atoms are sequentially oxidized to the tretravalent state. Finally, the reaction product, SiF_4, is desorbed from the surface. The reaction sequence can be summarized according to:

$$XeF_2\,(g) \rightarrow (XeF_2)_{ads} \tag{8a}$$

$$(XeF_2)_{ads} \rightarrow 2\,F^-_{ads} + Xe\,(g) \tag{8b}$$

$$(SiF_x)_{ads} + (4-x)\,F^-_{ads} \rightarrow (SiF_4)_{ads} \tag{8c}$$

$$(SiF_4)_{ads} \rightarrow SiF_4\,(g) \tag{8d}$$

For very low doses of XeF_2 (50 L), monolayer coverage of SiF is observed with small amounts of SiF_2 and SiF_3, thought to be related to adsorption of these species at steps on the surface. Under these conditions, the adsorbed F atoms terminate any dangling bonds with the formation of SiF groups. At higher doses of XeF_2, the etching process is characterized by the formation of an SiF_x layer on the order of seven monolayers in thickness and distinct from the silicon substrate [47, 48]. In the fluorosilyl layer, SiF, SiF_2, SiF_3, and SiF_4 species have been observed [47]. At low

doses of XeF_2 (50 mTorr for 5 min), the SiF_x layer is dominated by SiF_3 although at higher doses (4 Torr for 5 min) significant amounts of SiF_4 are trapped in the layer. This result suggests that the $Si^{III} \rightarrow Si^{IV}$ step is the slowest in the oxidation sequence and that desorption of SiF_4 is fast, analogously to the final step in chemical etching.

The dependence of the etch rate on the XeF_2 flux suggests that the adsorption (8a) and dissociation (8b) steps control the reaction rate. The sequential oxidation of the silicon-forming SiF_x species and the subsequent desorption of SiF_4 are apparently fast in comparison with the dissociative adsorption process.

The mechanism of the etching process is thought to be related to the surface hole concentration, with an initial oxidation step according to [49]:

$$Si(s) + F^-_{ads} + h^+(vb) \rightarrow SiF_{ads} \tag{9}$$

The negative surface charge induced by the F^- species is balanced by a corresponding hole concentration in the silicon. Experimentally, the dependence of etch rate on dopant concentration is in the order:

$$n^+ > p^+ > n,\ p \tag{10}$$

This dependence of etch rate on dopant type and concentration is identical for the case of pore formation in silicon by etching in aqueous HF solutions, as discussed in Sec. 4.3, and is thought to be related to the space charge layer formed at the surface [49].

In reactive ion etching, the presence of energetic ions or electrons can significantly enhance the etch rate. This enhancement is thought to be related to the formation of surface active (damage) sites that increases the dissociation rate of XeF_2 on the silicon surface. In addition, it is worthwhile to note that although silicon reacts with XeF_2, SiO_2 surfaces can only be etched in the presence of energetic particles [e.g., 50].

The gas-phase reaction of silicon with F_2 has also been studied [51]. Based on gravimetric measurements, the reaction rate was found to be linear with F_2 partial pressure in the range of 2–50 Torr, with a reaction order of ≈ 1.

3.2 Silicon/Water Interactions

In-situ spectroscopic measurements have shown that water is dissociatively chemisorbed onto reconstructed silicon surfaces in ultrahigh vacuum at room temperature [52–54]:

$$2Si(s) + H_2O(g) \rightarrow SiH_{ads} + SiOH_{ads} \tag{11}$$

George and coworkers [55] have shown that reaction (11) also occurs on porous silicon surfaces at ambient temperatures. At higher temperatures, however, the SiOH groups are no longer stable and decompose with oxide formation according to:

$$SiH + Si_2SiOH \rightarrow 2\,SiH + SiOSi \tag{12}$$

At 377 °C, the Si–H concentration reaches a maximum because of complete conversion of SiOH to SiH. At temperatures above 377 °C, hydrogen is desorbed from the surface, allowing reaction of the exposed surface sites with water and leading to further oxide formation.

4 Anodic Dissolution of Silicon in HF

4.1 HF Chemistry

Detailed mechanistic analysis of any reaction in HF is complicated by the presence of multiple fluoride species. In relatively dilute solutions, HF, H^+, F^-, and HF_2^- need to be considered [35, 56–58]. The equilibria and rate constants for these species are given in Table 5. Figure 6a and b shows the relative concentrations of HF, HF_2^-, and F^- as a function of pH calculated for 1 M and 10 M total fluoride concentration, respectively. As can be seen from these figures, at low pH HF molecules are the dominant species whereas at high pH F^- dominates. At intermediate values of pH, fluoride electrolytes are dominated by HF_2^- with a maximum mole fraction at about pH 3.

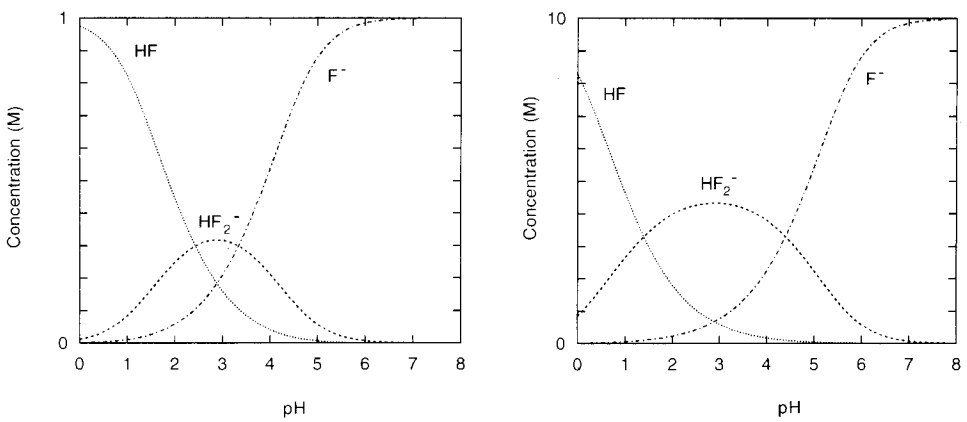

Fig. 6. Molar concentrations of HF, HF_2^-, and F^- calculated for (a) 1 M and (b) 10 M total fluoride concentration from rate constants at 25 °C.

Table 5. Equilibria and rate constants (25 °C) for HF solutions [56–58].

Equilibrium	K (mol s^{-1})
$HF \leftrightarrow H^+ + F^-$	1.3×10^{-3}
$HF_2^- \leftrightarrow HF + F^-$	0.104

The increase in etch rate of SiO_2 with decreasing pH is related to the concentration of molecular HF and is independent of F^- concentration. As described in Sec. 2, the reaction of HF molecules with Si–O bonds is relatively fast because of the highly polar character of the Si–O bond.

4.2 Electrochemistry of Pore Formation in Silicon

Historically, the first reports of porous silicon layers were by Uhlir [59] and Turner [60]. These authors reported on the electropolishing of silicon and noted that under certain conditions a porous layer was formed at the silicon surface. The first models for porous layer formation assumed that the layer was formed on the silicon substrate by a deposition process thought to involve the reduction of divalent silicon to amorphous Si via a disproportionation reaction in solution [61]. Subsequently, Theunissen [62] showed that the porous structure was the result of a selective etching process within the silicon, contradicting the silicon deposition model.

The two fundamental issues related to porous layer formation are the mechanism of the dissolution reaction and the processes controlling the morphology of the porous layer. Although the overall reaction is well characterized, many aspects of the reaction mechanism remain unresolved.

The current-voltage curves for silicon in HF solutions are characterized by three distinct regions, as shown in Fig. 7. At low potentials the current increases sharply with potential, whereas at more positive potentials, beyond a characteristic current peak, the current is relatively large (typically $>10\,\text{mA cm}^{-2}$) and increases weakly with increasing potential. This latter region is the electropolishing region. Between these two potential domains is a transition region where features of both pore formation and electropolishing are observed. The low-potential region corresponds to a region of anisotropic etching characterized by pore formation whereas the higher-potential region is characterized by isotropic etching (electropolishing).

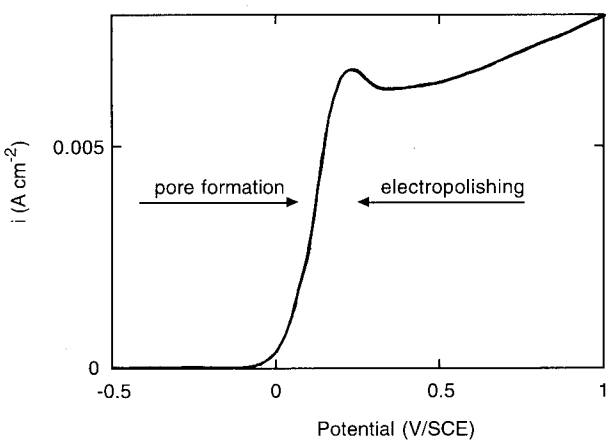

Fig. 7. Steady-state current-voltage curve for p-Si(100), $N_A = 3\times10^{15}\,\text{cm}^{-3}$ in 0.05 M (1wt.%) HF.

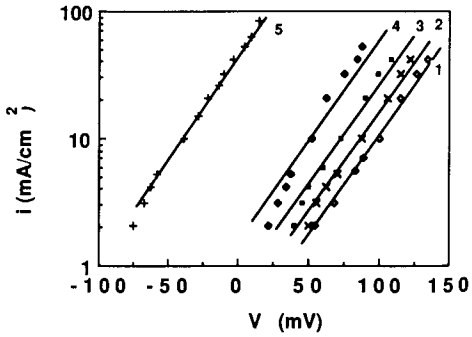

Fig. 8. Plots of log i vs. $U_{applied}$ for p-Si(100): potential in volts vs. Ag/AgCl [65].
(1) $N_A = 2.5\times10^{15}\,cm^{-3}$
(2) $N_A = 2.5\times10^{16}\,cm^{-3}$
(3) $N_A = 1.3\times10^{17}\,cm^{-3}$
(4) $N_A = 8.0\times10^{17}\,cm^{-3}$
(5) $N_A = 1.0\times10^{19}\,cm^{-3}$

In the pore formation regime, the dissolution current increases exponentially with applied potential for p-type silicon and heavily doped n-type silicon [61, 63–66]. The potential range over which this exponential behavior is observed is dependent on dopant concentration and HF concentration. The exponential current-potential curves are characterized by a slope of 60 mV (kT/q) on a plot of the logarithm of the etching current versus applied potential, as can be seen in Fig. 8 [65].

The interfacial electrochemical reaction during pore formation is characterized by a reaction order of 1.0 with respect to HF concentration, C_{HF}, [60, 64], as shown in Fig. 9. The dissolution current at the limit of the exponential region is plotted as

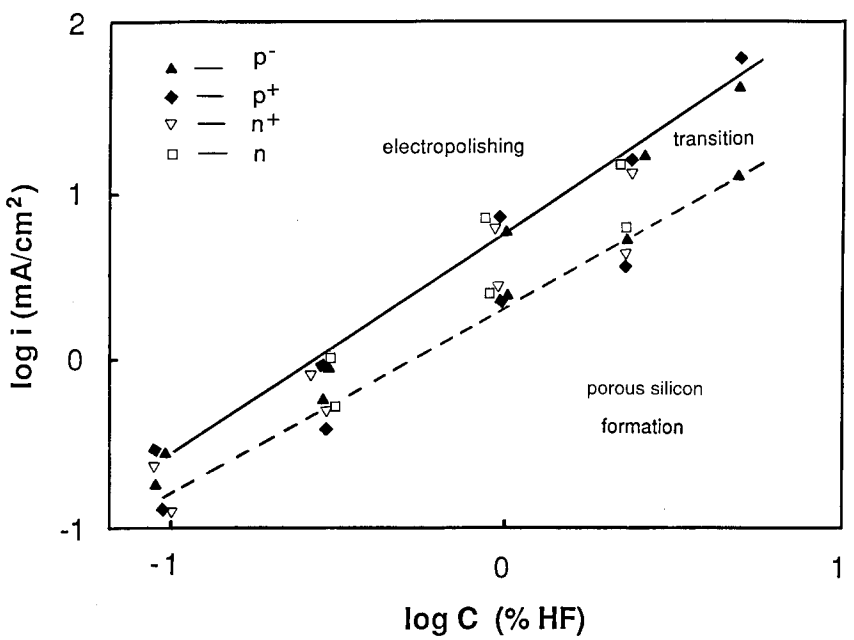

Fig. 9. Plots of log i vs. log C_{HF} for Si(100): n, $N_D = 1\times10^{17}\,cm^{-3}$; n^+, $N_D = 2\times10^{19}\,cm^{-3}$; p, $N_D = 1\times10^{15}\,cm^{-3}$; p^+, $N_D = 1\times10^{19}\,cm^{-3}$ [64].

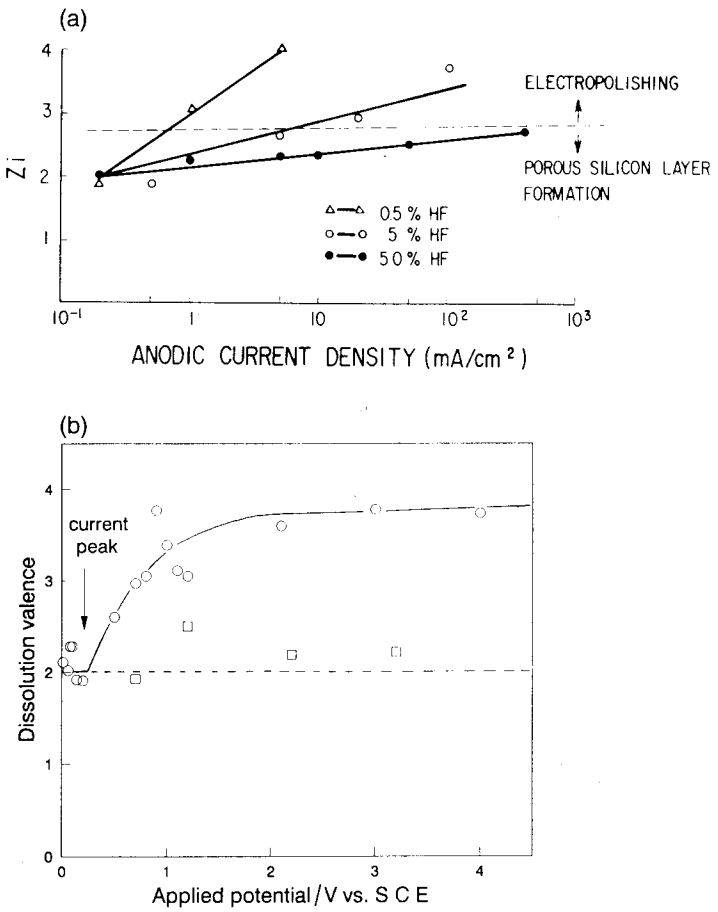

Fig. 10. (a) Dissolution valence versus current density for p-Si(111), 0.02 Ω cm, as a function of HF concentration [63]. (b) Dissolution valence vs. applied potential for (○) p-Si(100), 0.075–0.125 Ω cm, (□) n-Si(100) 0.375–0.625 Ω cm, under illumination [67].

a function of HF concentration for four different dopant concentrations, N_D, showing that the limit of the pore formation region is independent of dopant concentration. Figure 9 also shows that the pore formation region is extended as the HF concentration is increased. For example, in 10 M HF pore formation occurs up to current densities on the order of 100 mA cm^{-2}.

The effective valence for dissolution increases from a value of about 2 at low current density to a value of 4 in the electropolishing domain [59–63, 67–69], as shown in Fig. 10a [63] and Fig. 10b [67]. While gravimetric determinations may be subject to a number of errors derived from oxide formation and hydrogen adsorption, these data show that the dissolution process associated with pore formation, in the absence of illumination, proceeds through interfacial charge transfer reaction involving two

charge carriers per silicon atom. The final reaction products for the pore formation process are SiF_6^{2-} ions and molecular hydrogen [59, 60].

For the dissolution of silicon in fluoride electrolytes where two electrons are transferred per silicon atom, it is generally assumed that the first step in the reaction sequence is hole capture:

$$X^0 + h^+ \rightarrow X^I \tag{13}$$

where X^0 represents a surface silicon atom and X^I represents a dissolution intermediate. This notation is used since hole capture may occur at surface sites with different bonding configurations. In addition, electrochemical reactions involving ligands may occur with no change in the formal oxidation state of the silicon atom. In the second electrochemical step, hole capture by X^I competes with electron injection into the conduction band to form the intermediate X^{II}:

$$X^I + h^+(vb) \rightarrow X^{II} \tag{14}$$

$$X^I \rightarrow X^{II} + e^-(vb) \tag{15}$$

Finally, X^{II} reacts to form the dissolution product SiF_6^{2-} through a sequence of chemical steps involving HF and coupled with hydrogen evolution.

The reaction steps given by Eqs. (13)–(15) represent a general framework for silicon dissolution in fluoride electrolytes. The nature of the X^I and X^{II} intermediates and the chemical reactions are dependent on solution chemistry and dopant type and are discussed in more detail in subsequent sections.

4.3 Potential Distribution at the Si/HF Interface

For n-type silicon in the dark, where dissolution occurs at potentials positive to the flat band potential, the etching current density during pore formation is associated with strong band bending. Under these conditions, holes can be created at the surface by the formation of an inversion layer by tunneling of valence band electrons into the conduction band [70]. Tunneling occurs in regions where the curvature of the pore front is sufficiently small for the local field to exceed the breakdown field for silicon of 3×10^5 V cm^{-1}. Initial hole capture with the formation of the intermediate X^I according to Eq. (13) is expected to be the slow step in the etching reaction [71]. This process is shown schematically in Fig. 11. The second electrochemical step, Eq. (14), can occur through three possible pathways: by hole capture, thermal excitation, or tunneling into the conduction band. Thermal excitation is thought to control the photomultiplication effect observed during the dissolution of n-type silicon under illumination [71].

For the case of pore formation in p-type silicon where the holes are the majority carriers, silicon dissolution occurs at much lower potentials than for n-type silicon. Both hole capture and electron injection have been suggested for the second elec-

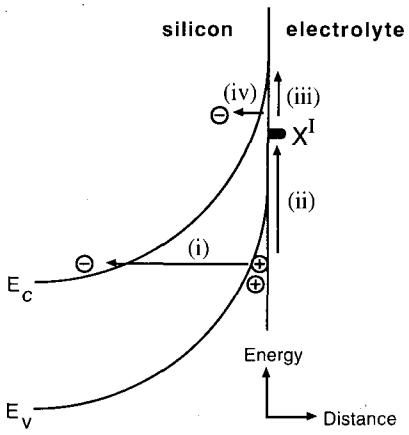

Fig. 11. Energy-level diagram for the etching of n-type silicon in the dark. Holes are generated by tunneling of electrons from the valence band into the conduction band (i). The first electrochemical step is hole capture resulting in the formation of the intermediate X^I (ii). The second electrochemical step can occur through hole capture (ii), thermal excitation into the conduction band (iii), or tunneling into the conduction band (iv) [70].

trochemical step although the band bending at the surface, discussed later in this section, suggests that hole capture is more likely. The mechanism of dissolution is discussed in more detail in Sec. 4.7.

Although the dissolution process results in the formation of a porous structure, electrode impedance measurements [72, 73] have shown that the etching process is not limited by mass transport, even for thick porous silicon layers [74]. Figure 12 shows a plot of potential as a function of time during pore formation in p-Si(100), $N_A = 5 \times 10^{19}$ cm^{-3} (0.003 Ω cm) in HF (49 wt.%) – C_2H_5OH solution (1 : 1 by volume). After an initial transient the electrode potential remains constant with time until the pore front reaches the backside of the wafer, at which time a sharp change in the potential is observed. The formation of self-supporting porous membranes [74] by electrochemical etching and drying in supercritical fluids suggests that this technique may be used to fabricate semiconductor xerogels.

These results illustrate the fact that mass transport effects in the pores are not significant. Figure 13 shows a plot of the reciprocal of the time at which the pore

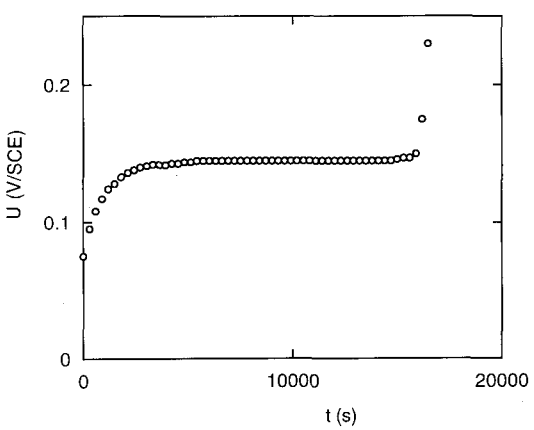

Fig. 12. Plot of potential versus time during pore formaton in p-type Si(100), $N_A = 5 \times 10^{19}$ cm^{-3} (0.003 Ω cm) in HF (49 wt.%) – C_2H_5OH solution (1 : 1 by volume); wafer thickness = 350 μm [74].

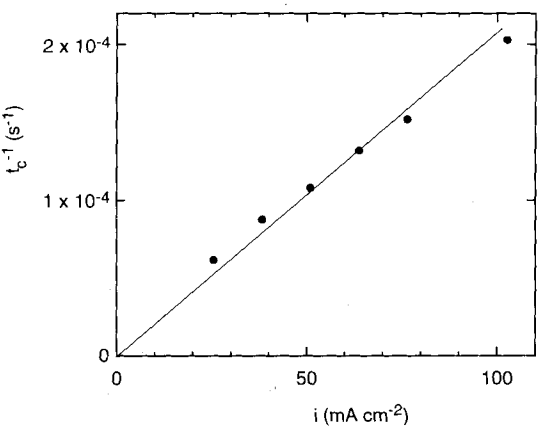

Fig. 13. Plot of the reciprocal of the time at which the pore front penetrates the wafer, t_c, as a function of etching current density [74].

front penetrates the wafer, t_c, as a function of etching current density. The linear relationship implies that the velocity of the pore front, and hence the porosity, are independent of etching current in the measured range. The small deviation from linearity at higher current densities suggests that mass transport may be important for high growth velocities. A small effect of mass transport in the electrolyte has been reported by Lehmann for the the etching of n-Si under illumination [68].

During anodic dissolution, the applied potential is partitioned between the space charge layer in the semiconductor, U_{sc}, and the Helmholtz double layer, U_H:

$$U_{applied} = U_{sc} + U_H \tag{16}$$

as shown in schematically in Fig. 14. The fraction of potential drop across the space charge layer is dependent on dopant concentration and etching conditions. The exponential dependence of the etching current on applied potential may be derived from either space charge layer control (U_H constant) or Helmholtz layer control (U_{sc} constant), corresponding to Schottky junction or Tafel behavior, respectively. During dissolution, if the space charge capacitance is smaller than the Helmholtz layer capacitance then a small change in the applied potential ($\Delta U_{applied}$) will lead

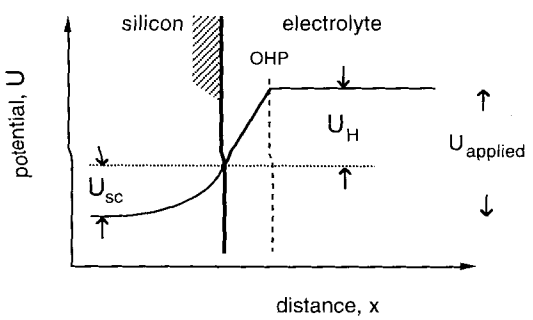

Fig. 14. Schematic illustration of the potential distribution at the silicon/electrolyte interface.

to an equivalent change in the band bending (ΔU_{sc}) and hence, for the case of p-type silicon, to a change in the surface hole concentration. In this case the rate constants for any surface reactions are unchanged since U_H remains constant. For the case where a change in $U_{applied}$ results in a corresponding change in U_H, the band bending and hence the surface carrier concentration remain constant. As a result the kinetics of the etching reaction are given by the potential dependence of the electrochemical rate constants.

Analysis of the etching reaction [75] has shown that space charge layer control (i.e., U_H constant) would be expected to give a slope of 60 mV on a plot of $U_{applied}$ versus log (i), as seen experimentally, whereas for Helmholtz control either one or two linear regions with slopes greater than 60 mV would be obtained. Stability analysis of pore formation also supports this conclusion since instabilities only tend to propagate when the rate-limiting step is in the receding phase, i.e., bulk silicon. Helmholtz layer control would be expected to result in smoothening of the interface.

In the pore formation regime, the Helmholtz layer potential may be considered constant for a given dopant concentration and HF concentration, independently of the etching current. Experimentally it is observed that the current-voltage curves are shifted to more positive potentials with increasing acceptor concentration, as shown in Fig. 7. This behavior can be explained by the dependence of the Helmholtz potential on acceptor concentration [65]. As described above, the same trend is observed in the relative rates of isotropic etching of silicon in XeF_2. At the interface between the space charge layer and the Helmholtz layer:

$$\varepsilon_s F_s = \varepsilon_H F_H \tag{17}$$

where ε is the dielectric constant and F is the field at the silicon surface (subscript s) and the Helmholtz layer (subscript H), respectively. The potential drop in the Helmholtz layer is given by:

$$U_H = F_H \delta = \frac{\varepsilon_s}{\varepsilon_H} F_s d_H = \frac{\varepsilon_s F_s}{C_H} \tag{18}$$

where d_H is the double layer width and C_H is the double layer capacitance. The field strength at the silicon surface, assuming an abrupt junction at a planar interface [76], is given by:

$$F_s = \sqrt{\frac{2qN_A}{\varepsilon_s}\left(U_{sc} - \frac{kT}{q}\right)} \tag{19}$$

Substituting Eq. (19) into Eq. (18):

$$U_H = \frac{1}{C_H}\sqrt{2q\varepsilon_s N_A\left(U_{sc} - \frac{kT}{q}\right)} \tag{20}$$

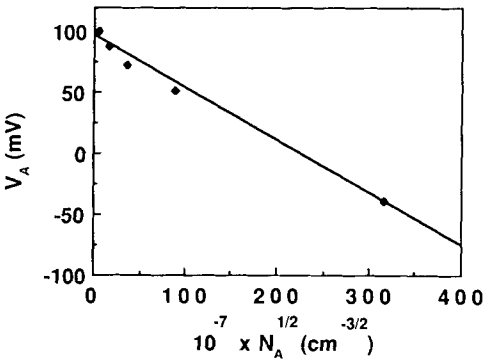

Fig. 15. Plot of electrode potential versus the square root of the acceptor concentration [65].

From this equation, it can be seen that the Helmholtz potential is expected to increase with the square root of the acceptor concentration. This result, shown in Fig. 15, has been confirmed by Gaspard et al. [65].

The exponential dependence of the current on applied potential for p-type silicon and highly doped n-type silicon in the pore formation regime can be analyzed using the Gerischer model of the semiconductor/electrolyte interface [77]. In the absence of surface states, the hole current for a p-type semiconductor is given by:

$$i_v = k_v^+ \cdot + p_s \cdot N_{red} - k_v^- \cdot N_v \cdot N_{ox} \tag{21}$$

where N_{ox}, N_{red} are the concentration of oxidized and reduced species, respectively, p_s is the surface hole concentration, and N_v is the density of states in the valence band. The surface hole concentration, p_s, is given by:

$$p_s = p_0 \exp\left(-\frac{q\Delta U_{sc}}{kT}\right) \tag{22}$$

where p_0 is the equilibrium hole concentration and ΔU_{sc} is the potential drop in the semiconductor. For a decomposition reaction, N_{red} corresponds to the concentration of surface active sites. Assuming that the Helmholtz potential is constant and taking $p_0 \approx N_A$, the dissolution current can be written as:

$$i_{diss} = k' \cdot N_A \cdot \exp\left(-\frac{U - U_{fb}}{kT/q}\right) \tag{23}$$

where U_{fb} is the flat band potential. Equation (23) predicts an exponential dependence of the etching current on applied potential with a characteristic slope of 60 mV on a plot of log (i) versus U, which is analogous to the situation for a solid-state Schottky junction at forward bias. This behavior has been reported for a limited number of semiconductor/electrolyte systems in the presence of suitable redox couples [73]. For the limiting case of thermionic emission, the current flow across the

interface is controlled by majority carrier supply. For the case of p-type silicon, this corresponds to the rate at which holes are transported to the interface. However, at a liquid junction it is very difficult to provide a means to extract majority carriers at this rate and, even for redox couples with large rate constants, the current-voltage curves may be shifted from the thermionic emission limit. In this case the exponential dependence of the current on voltage is related to the majority carried concentration at the interface as the band bending is decreased from depletion toward the flat band potential.

Figure 16 shows a plot of log (i) versus $U_{applied}$ for p-type silicon in 0.05 M HF showing that the exponential region occurs at a potential within about 0.5 V of the flat band potential [75]. The flat band potential was determined from impedance measurements to be 0.15 V (SCE) [73]. As the potential is increased from the open-circuit potential, the magnitude of U_{sc} is decreased and the surface hole concentration increases exponentially according Eq. (22). In this model, the first step in the reaction sequence given by Eq. (13), for the case of p-type silicon and highly doped n-type silicon, can be thought of in terms of the probability of a surface silicon atom reacting with an electronic hole.

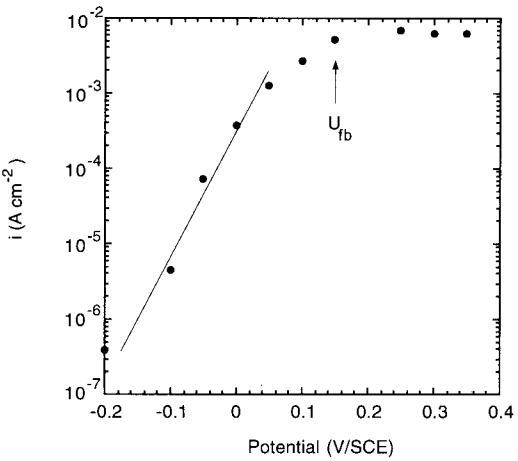

Fig. 16. Plot of log i versus $U_{applied}$ for p-Si(100), $N_A = 3 \times 10^{15}$ cm^{-3} in 0.05 M HF, showing that the exponential region occurs at potentials within about 0.5 V of the flat band potential [75].

For p-type silicon, the surface hole concentration is expected to be uniform over the surface as long as there is no change in the position of the band edges. As suggested by Lehmann and Goesele [78], if the silicon is etched so that small filaments are formed with dimensions on the order of tens of ångstroms, then enlargement of the bandgap will lower the probability of a mobile hole populating these regions. As a result, the surface hole concentration will be highest at the pore tips and negligible in the interpore regions, resulting in stable pore propagation. The reaction rate is proportional to the local hole concentration at the pore tips and not limited by hole transport [78] since the rate constant for electrochemical reactions are too slow for this situation to occur [71]. Figure 17 shows an energy scheme for pore formation in p-type silicon [79].

Electrical impedance measurements for silicon etching in HF have been used to analyze the potential distribution at the interface [72, 73, 75, 79, 80]. Analysis of these data has resulted in insight into the kinetics of the dissolution process and the potential distribution at the silicon/HF interface. The characteristic features of the

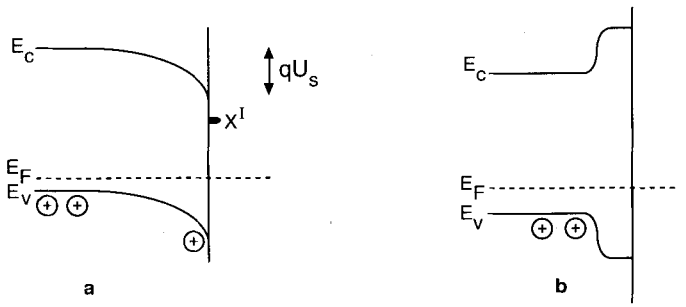

Fig. 17. Energy scheme for pore formation in p-type silicon. At the pore base, the surface hole concentration is in quasi-equilibrium and increases exponentially as the Fermi level is lowered toward the flat band condition (a). In the regions between the pores the minimum feature size is determined by enlargement of the band gap due to quantum confinement; holes are excluded from these regions, as shown in (b) [79].

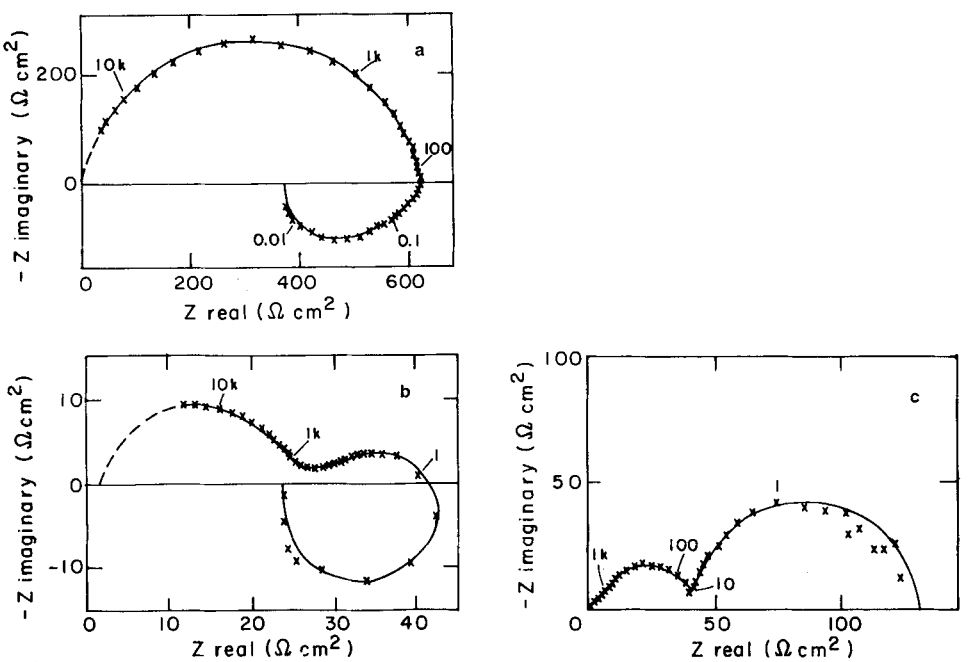

Fig. 18. Complex plane plots of the electrode impedance for p-Si(100), $N_A = 3 \times 10^{15}\,cm^{-3}$ in 0.05 M HF at: (a) −0.05 V (SCE); (b) 0.15 V (SCE); and (c) 1.0 V (SCE). These potentials correspond to pore formation, the transition region, and electropolishing, respectively [72].

impedance of the silicon/HF interface are illustrated in Fig. 18 for the case of p-Si(100), $N_A = 3 \times 10^{15}\ cm^{-3}$, in 0.05 M HF.

The complex plane plots in Fig. 18 illustrate the characteristic components of the impedance response for p-type silicon and heavily doped n-type silicon in the absence of illumination. In the region of pore formation where $dU/d \log (i) = 60$ mV, the impedance response is characterized by an inductive loop at low frequencies and a capacitive loop at higher frequencies, as shown in Fig. 18a. In the transition region, a second capacitive loop is observed related to oxide formation at the surface (Fig. 18b). At more positive potentials in the electropolishing domain (Fig. 18c) only the two capacitive loops are seen.

Figure 19 summarizes the energetic schemes for n-type and p-type silicon in 0.05 M HF in the pore formation regime [73]. For n-type silicon in the dark, a depletion layer is formed at the interface and the electrode capacitance follows Mott-Schottky behavior. As the potential is increased and the band bending becomes sufficiently large, the etching current also increases [81]. Holes are generated through tunneling of valence-band electrons into the conduction band [70]. For p-type silicon, a depletion layer capacitance can also be observed close of the open-circuit potential [73]. In this potential region, the impedance response is characterized by two capacitive loops with the higher-frequency loop corresponding to the depletion layer capacitance. As the potential is increased, the band bending is reduced and the current increases exponentially with potential as described above. In this region, the impedance response shown in Fig. 18a is observed.

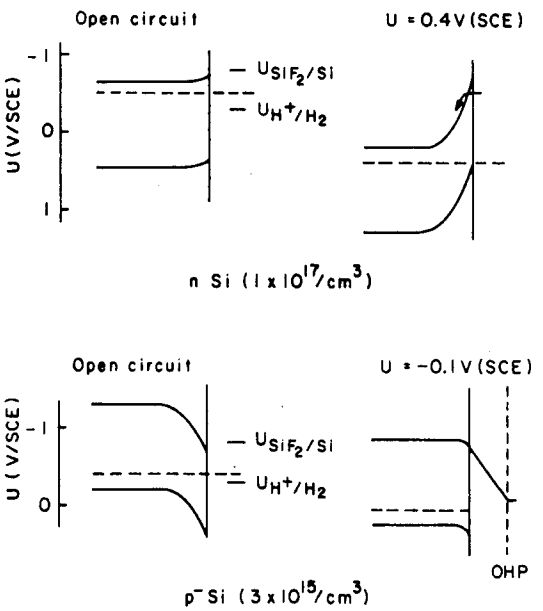

Fig. 19. Energy schemes for n-type and p-type silicon in 0.05 M HF [73].

The current-voltage curves and electrode impedance measurements, shown in Figs. 16 and 18, are consistent with a reaction scheme given by Eqs. (13)–(15) in which two electrochemical steps are followed by chemical oxidation [75, 82]. The initial electrochemical step is assumed to be hole capture at a surface site with two Si–Si backbonds. in the second electrochemical step, hole capture by X^I competes with electron injection into the conduction band by thermal excitation to form an X^{II} intermediate. Since the surface hole concentration is relatively large, injected electrons recombine with holes, leading to an anodic current [75]. It has been shown theoretically [75] that reaction (15) gives rise to the characteristic inductive loop in the complex plane plots (Fig. 18). At sufficiently low potentials, below the critical current for electropolishing, X^{II} is further oxidized to the dissolution product SiF_6^{2-} through a sequence of chemical steps involving HF. The mechanisms are discussed in more detail in Sec. 4.7.

4.4 Pore Morphology in Silicon

The selective dissolution of silicon in HF solutions results in the formation of a porous structure with a characteristic morphology dependent on the dopant type and concentration, the applied voltage, and the electrolyte composition. For n-type silicon, illumination also influences the pore morphology in the near-surface region. The depth of this modified layer is dependent on the absorption coefficient at the illumination wavelength. The physical properties of these structures span a wide range with typical pore dimensions of about 30 Å up to 1 μm or more, and average porosities in the range of 0.1–0.9, depending on etching conditions. The morphological trends reported for all porous silicon layers can be summarized as follows.

1. Pores grow preferentially in the ⟨100⟩ directions, independently of the surface orientation.
2. Steady-state pore growth is characterized by a depth-independent morphology (constant porosity); a transient region may been seen in some cases at the surface and large morphology changes are seen for etching of n-type silicon under illumination.
3. The interface between the porous layer and the silicon bulk is generally smooth on the length scale of the pore dimensions.
4. The pores are distributed randomly on the surface and are uniformly spaced.
5. For n-type silicon, the pore walls exhibit a preferred orientation, whereas for p-type silicon the pores are generally polygonal in cross-section.
6. For n-type silicon the pores do not grow into each other, but for p-type silicon the pores are interconnected.

Based on these characteristics, porous silicon may be described as a random array of channel-like pores or etch tunnels growing in ⟨100⟩ directions. For the case of n-type silicon these channels are isolated from each other and, for etching in the dark, the pore spacing is approximately equal to the depletion layer width at a planar surface [83–86]. For the case of p-type silicon the channels are interconnected. The

morphology is determined primarily by the dopant concentration in the silicon and, to a lesser extent, by the etching conditions. In many cases, the growth velocity of the pore front is proportional to the etching current density, indicating that the average porosity is independent of current, as shown in Fig. 13.

Although the range of morphologies exhibited by porous silicon structures has been identified, detailed analysis of these structures is not complete, especially for low-doped p-type silicon, and surprisingly few electron microscopy studies have been reported in the literature [68, 83, 87–93]. Electron and X-ray diffraction techniques have been used to show that the silicon that constitutes the porous structure is single-crystal and maintains the crystallographic orientation of the original silicon wafer, although some lattice distortion and small amounts of misorientation have been reported, especially for porous layers formed in p-type silicon [94–97].

Figure 20 shows a transmission electron microscope image of a porous layer formed in 0.1 Ω cm n-Si(100) in HF (49 wt.%)–C_2H_5OH (2:3 by volume) at 50 mA cm^{-2}. Many of the characteristic features of porous layers are illustrated in this figure. The primary pores are highly directional and spaced relatively uniformly. The interface between the pores and the bulk silicon is very smooth, at least down to length scales on the order of the pore dimensions. The porous structure exhibits a hierarchy of characteristic dimensions [83, 89]. The primary pores are about 80 nm in size and propagate in the [100] direction from the (100) surface [83], as shown in Fig. 20. The average pore spacing of 330 nm is approximately equal to the depletion layer width at a flat surface [83]. This figure also shows secondary pores of approximately 20 nm in size propagating laterally from the primary pores. These side pores are, in turn, decorated with pores which are < 10 nm in size, giving rise to a dendritic-like structure. In addition, it is seen that the pores do not grow into each other.

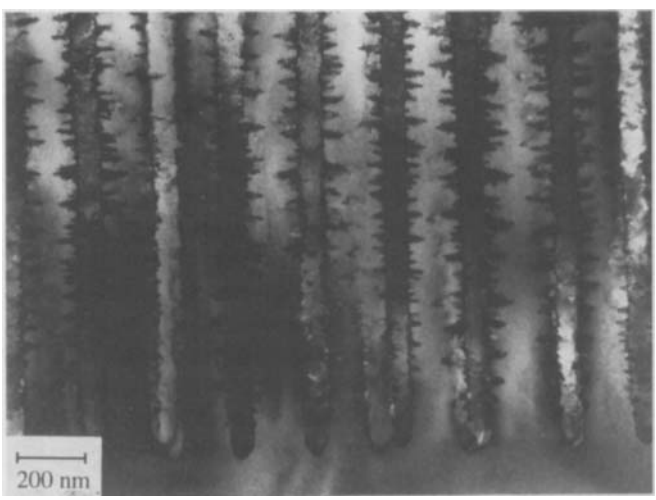

Fig. 20. Transmission electron microscope image of the cross-section of a porous layer formed in n-Si(100), 0.1 Ω cm, in HF (49 wt.%) – C_2H_5OH (1:1 by volume) at 50 mA cm^{-2} [83].

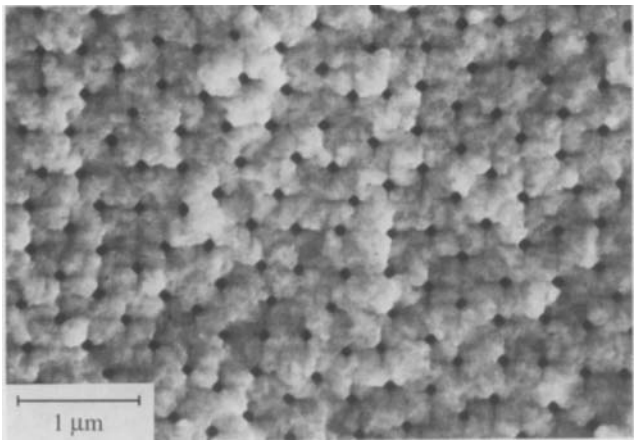

Fig. 21. Secondary electron plan view of the porous layer in Fig. 20 showing that the primary pores are square in cross-section and defined by the (011) planes. The secondary pores are seen to propagate from the corners of the primary pores in the ⟨010⟩ directions [83].

Figure 21 is a plan view of the same structure showing that the primary pores are square in cross-section and defined by the {011} planes. The secondary pores are seen to propagate from the corners of the primary pores in the ⟨010⟩ and ⟨001⟩ directions. The density of the primary pores from Fig. 21 is $9.0\times10^{8}\,\mathrm{cm}^{-2}$ and from the average pore size, the primary pores represent 7.3% of the plan area. Based on calcula-

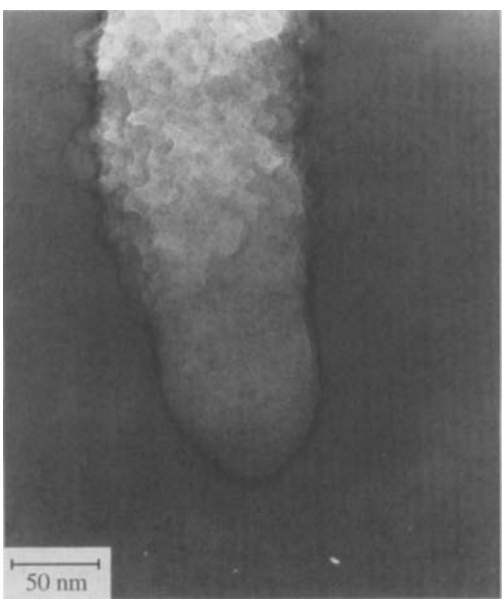

Fig. 22. Transmission electron microscope image of the porous layer in Fig. 20 showing an individual pore [83].

tion of the autocorrelation function, each pore has five nearest neighbors, suggesting that the pores are distributed randomly.

Figure 22 depicts a higher-magnification transmission electron microscope image of the porous layer in Fig. 20, showing an individual pore in which the pore tip is similar to the shape of etch pits formed in Si(100). The pore tip is a four-sided, inverted pyramid defined by (111) planes corresponding to the planes of slowest etch rate. At a constant applied potential, the etching process drives this structure into the bulk of the silicon. Figure 23 shows a schematic illustration of pore orientation in n-type silicon [83].

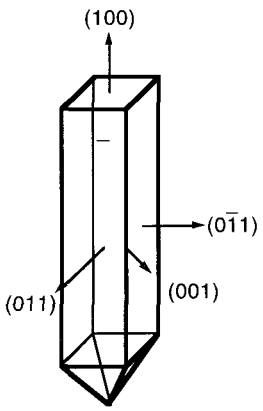

Fig. 23. Schematic illustration of pore orientation in n-type silicon.

The crystal structure of the silicon has a strong effect on the pore growth. Pores propagate preferentially in the ⟨100⟩ directions so that for a (100) oriented surface the primary pores propagate in the [100] direction, as seen in Fig. 20. For a (100) surface the primary pores propagate in the [100] and [010] directions, and for a (111) surface pore propagation is in the [100], [010], and [001] directions from the surface. The directionality of pore growth has been observed for n-type silicon and highly doped p-type silicon and remains to be established for low-doped p-type silicon.

Figure 24 shows a plan view image of a porous layer formed in p-Si (100), 0.001 Ω cm in 10 M HF at 100 mA cm^{-2} [94]. The primary pores are highly oriented and channel like, propagating perpendicular to the surface in the [100] direction. The pores are polygonal in cross-section and do not exhibit any obvious anisotropy. The pores are packed closely together with interpore regions of silicon on the order of 100 Å and a pore density of 2×10^{10} cm^{-2}.

The dependence of pore morphology on dopant type and concentration can be summarized as follows:

1. Low-doped p-type silicon: the porous layer is composed of an interconnected network of nanometer-size silicon ligaments with porosities on the order of 40–60% and pore dimensions less than 100 Å [87, 88, 90, 92, 94, 98, 99]. At the present time, the detailed morphology of these porous structures has not been resolved.

2. Highly doped p-type silicon: the pores propagate in the [100] direction and are polygonal in cross-section, with pore diameters in the range 10 – 100 nm depending on the etching current density. The pores are interconnected [79].
3. n-Type silicon: the pores are characterized by a square cross-section, with typical dimensions of 100 nm or less [68, 83, 84]. For a pore propagating in the [100] direction the walls are defined by the {011} planes. The side pores propagate from the corners of the main pores in the ⟨010⟩ and ⟨001⟩ directions. For low donor concentrations, the pore dimensions can be above 1 μm [83, 84].
4. Heavily doped n-type silicon: channel-like pores propagate in the [100] direction. The pores are typically 10 nm or smaller in diameter and do not exhibit the characteristic anisotropy of low donor concentrations. These structures are similar to those seen in highly doped p-type silicon.

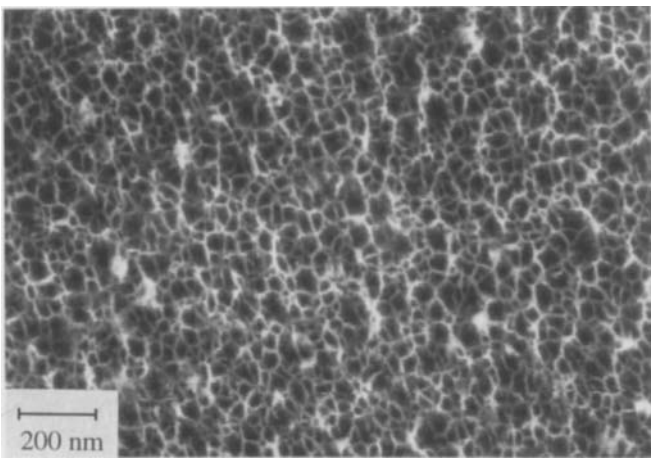

Fig. 24. Plan view secondary electron image of a porous layer formed in p-Si(100), 0.001 Ω cm in 10 M HF at 100 mA cm^{-2} [83].

The minimum dimensions for feature sizes in porous silicon may be limited by quantum confinement [78]. Depending on the local geometry, as the feature sizes in the porous layer are reduced to dimensions on the order of 40 – 50 Å enlargement of the bandgap will tend to prevent free charge carriers from being transported into these regions, as shown in Fig. 17b. As a result, characteristic feature sizes of less than about 40 Å would not be expected. For n-type silicon in the dark, depletion layer width is much larger than the dimensions for bandgap enlargement to be significant, so that the interpore spacing is determined by the screening length.

Porous layers have also been formed in polycrystalline silicon [100]. The presence of the grain boundaries in the polysilicon gives rise to a unique morphology. Depletion of majority carriers from the grain boundaries inhibits pore growth in these regions, while voids are observed adjacent to the boundaries. Smaller pores are seen in the grain interiors.

4.5 Other Methods of Pore Formation in Silicon

Although most work related to pore formation in silicon has involved electrochemical etching of silicon in HF solutions, porous silicon layers have also been formed by chemical etching and by spark erosion in vacuum.

The formation of porous layers in silicon by chemical etching in HF/HNO_3 solutions was first reported at about the same time as electrochemical etching [101 – 104]. These so-called stain etch films are characterized by rough or porous surfaces, typically < 500 Å in thickness. Recent work has shown that these stain etch films exhibit strong visible photoluminescence, similar to the emission observed from electrochemically etched porous silicon layers.

The conditions for the formation of stain etch films are similar to the case for chemical etching of silicon in HF or NH_4F, except for the the addition of an oxidizing agent. As for any open-circuit process, the etching involes coupled oxidation and reduction reactions. For the HF/HNO_3 case, these are thought to be:

$$X^0 \rightarrow X^{II} + 2\,e^- \tag{24}$$

$$NO_2 + e^- \rightarrow NO_2^- \tag{25}$$

The reduction reaction is coupled with the chemical reaction:

$$HNO_3 + HNO_2 \leftrightarrow 2\,NO_2 + H_2O \tag{26}$$

Archer [102] used ellipsometry to monitor the growth of stain etch films in HF/HNO_2 solutions and observed a parabolic rate law showing that the process is diffusion-limited. In view of the relatively recent understanding of hydrogen passivation, it is worthwile noting that Archer [102] performed vacuum annealing measurements on stain etch films and observed desorption of hydrogen and water with no evidence of fluorine, carbon, or nitrogen. Archer suggested that the surfaces of the porous stain etch films were composed of silicon hydrides, SiH_x.

The significant differences in the properties of the stain etch films in comparison with electrochemically formed films can be explained in terms of the band bending at sites on the surface sustaining the oxidation and reduction reactions, as shown in Fig. 25. Assuming that the Schottky junction model for the silicon/electrolyte interface is applicable, the rate of the reduction reaction for p-type silicon is expected to be independent of applied potential and only dependent on barrier height and concentration of electron acceptors (e.g., NO_2). From Fig. 25, it can be seen that the rate of the silicon etching reaction is exponentially dependent on the applied potential in forward bias. For a fixed applied potential, large differences are expected in the etch rate as a function of acceptor concentration because of shifting of the flat band potential. The thickness of films formed in n-type silicon is relatively independent of donor concentration, as would be expected for a hole-limited process in reverse bias. In agreement with this model, illumination of the surface increases the growth rate of films in n-type silicon and has a relatively small effect on films formed in p-type silicon.

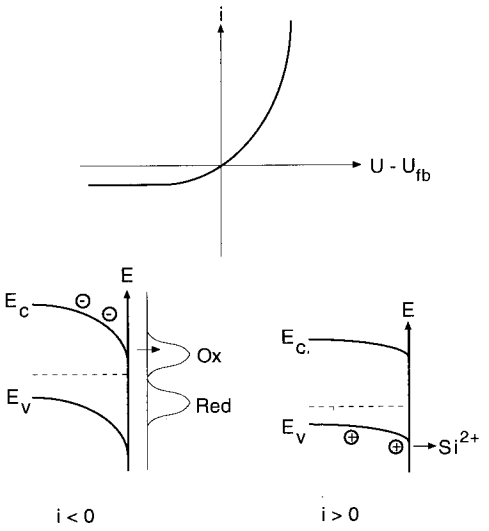

Fig. 25. Energy-level model for the chemical etching of silicon based on mixed-potential theory.

Since morphologically rough surfaces are created by open-circuit etching, it can be assumed that the areas sustaining the oxidation and reduction reactions become spatially fixed during the etching process. Regions where the reduction occurs would remain unetched, and these sites would be expected to be close to the original surface. The area ratio of the unattacked regions to the etched regions is expected to be strongly dependent on the dopant concentration. For example, a surface with a fast etch rate would need to be coupled to a large area sustaining the reduction reaction and hence the porosity would be low.

Recent work has shown that porous films can also be formed by open-circuit etching of n- and p-type Si in $NaNO_2$/HF and CrO_3/HF [105, 106], p-type Si in HF/HNO_3/CH_3COOH [107], and n-Si photoetched in anhydrous or aqueous HF/O_2 [108]. In all cases except for etching in CrO_3/HF solutions, these chemically etched films exhibited visible photoluminescence. In 1960 Gee [109] reported on irreversible visible luminescence from stain etch films during oxidation in H_2SO_4.

Hummel and Chang have shown that porous films can also been formed by a spark erosion technique [110]. The morphologies of these porous films exhibit less anisotropy than electrochemically formed porous structures although the pores propagate perpendicular to the surface. The growth rates of about 0.3 nm s^{-1} are much slower than those of electrochemically formed porous layers. Porous layers formed in air and under nitrogen exhibited visible photoluminescence similar to the emission spectra obtained from electrochemically grown porous layers.

4.6 Surface Chemistry of Silicon/HF Interfaces With an Applied Potential

4.6.1 Electrochemically Prepared Si(111):H (1×1) Surfaces

In Sec. 2.2, the interactions between silicon surfaces and HF under open-circuit conditions were discussed. Hydrogen passivation of silicon surfaces can also be carried out electrochemically [27]. The approach involves the formation of an oxide layer by thermal, chemical, or electrochemical oxidation followed by immersion in NH_4F solution at constant potential. Figure 26 shows a dark current transient for n-type Si(111) with a 70 Å oxide layer immersed in 0.2 M NH_4F at 0.5 V (SCE). During the initial stages of immersion the oxide layer is chemically dissolved and no current is observed. The current peak observed after oxide removal is associated with smoothening of the surface, analogous to the open-circuit etching of silicon in NH_4F. The charge determined from the area under the transient corresponds to removal of 2.6 monolayers, assuming a tetravalent dissolution reaction. At the current peak, the surface is characterized by OH and SiO_x species with small amounts of Si–H and $Si-H_2$. After the current transient, LEED [110] and HREELS [27] spectra suggest that the surface is converted to the Si(111):H (1×1) structure. Bitzer et al. [27] have suggested that the lateral smoothening of the Si/SiO_2 interface occurs through reaction of Si–OH until an ideally terminated monohydride surface is formed.

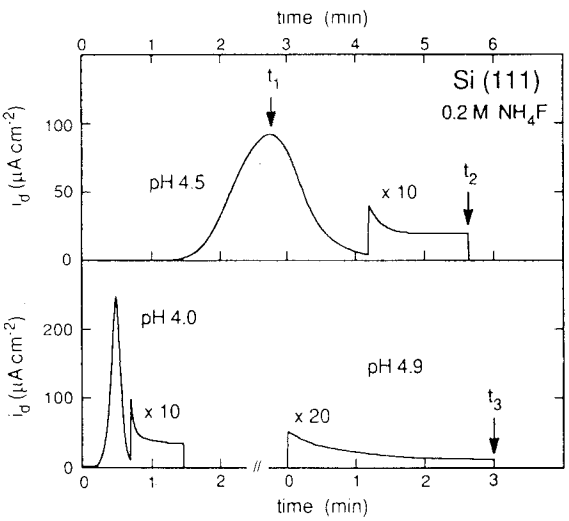

Fig. 26. Dark current transient for n-type Si(111) in 0.2 M NH_4F at 0.5 V (SCE). During the initial stages of immersion the 70 Å-thick oxide layer is chemically dissolved and no current is observed. The current peak observed after chemical dissolution of the oxide is associated with smoothening of the surface [27].

Recent work on etching of silicon in anhydrous HF solutions has shown that silicon is dissolved with a dissolution valence of 4 and with no hydrogen formation [111]. This result also shows that OH^- groups are an essential component of the etching reaction in aqueous solutions.

4.6.2 Surface Chemistry of Porous Silicon

Internal reflection infrared spectra measured in situ during etching of silicon in HF solutions exhibit characteristic Si–H modes, although the Si–H spectrum is broad because of interaction of the surface Si–H groups with the electrolyte. No electrochemical or chemical intermediate species have been detected [112]. Infrared spectra of porous silicon layers after drying reveal characteristic Si–H and $Si-H_2$ peaks similar to the spectra obtained for hydrogen on Si(100) 2×1 surfaces [112].

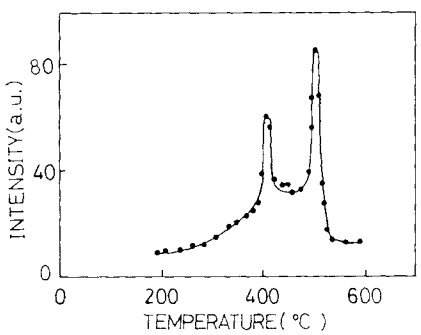

Fig. 27. Hydrogen partial pressure as a function of annealing temperature for a porous layer formed in p-Si(111), 0.01–0.001 Ω cm in HF/C_2H_5OH (1 : 1 by volume) for 3 min at 40 mA cm^{-2} [117].

Thermal annealing of porous silicon in vacuum results in desorption of the surface hydrides [113–116]. As described in Sec. 4.5, Archer [102] performed vacuum annealing measurements on stain etch films on silicon more than 30 years ago and observed that only hydrogen and water were desorbed. Figure 27 shows a plot of the hydrogen partial pressure as a function of annealing temperature for a porous layer formed in p-Si(111) with characteristic desorption peaks at 400 °C and 500 °C. These two peaks are due to dihydride and monohydride, respectively. Infrared spectroscopy has shown that $Si-H_2$ is completely removed from the porous silicon surface at 450 °C and that Si–H is completely desorbed at 550 °C [113]. Figure 28 shows infrared absorbance spectra of the $Si-H_2$ stretch and scissor modes as a function of annealing temperature, illustrating that the dihydride is completely desorbed at 450 °C. The activation energies for desorption of the dihydride and monohydride were found to be 1.86 and 2.82 eV, respectively [2]. Electron microscopy has shown that there is no evidence of significant structural changes in porous silicon after annealing in vacuum up to 800 °C [114]. At temperatures above 1000 °C, surface diffusion is sufficiently fast to induce coarsening of the porous structure.

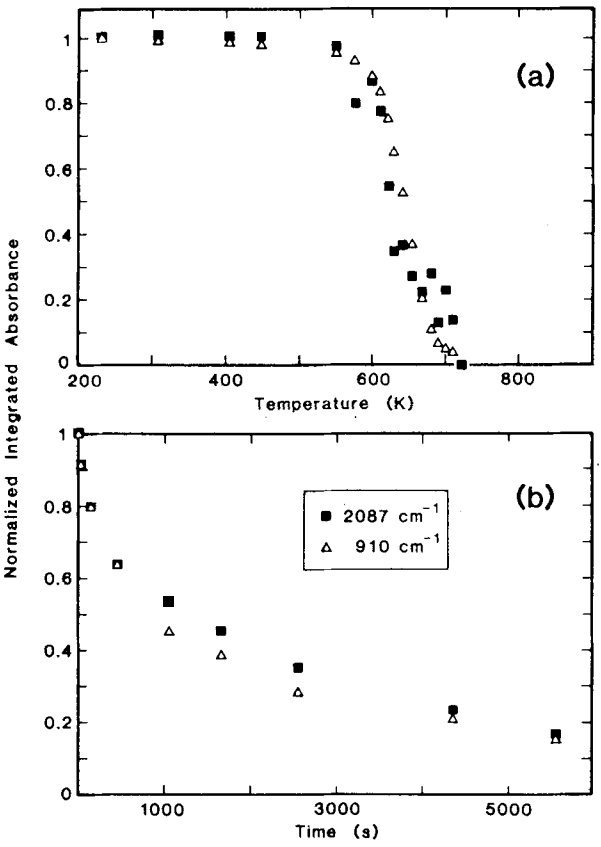

Fig. 28. Integrated infrared absorbance of the $Si-H_2$ stretch and scissor modes as a function of (a) annealing temperature, and (b) time at 580 K [113].

4.6.3 Photoelectrochemical Etching

The effect of illumination on pore formation in n-type silicon has been studied by a number of groups [117, 118]. In general, photogenerated holes appear to make the porous structure similar to the porous layers formed in p-type silicon. The structure of porous layers as a function of depth formed under illumination is strongly dependent on wavelength and whether frontside or backside illumination is used.

The optical properties of porous silicon layers formed in n-type silicon under illumination are dependent on both wavelength and intensity. This effect has been used to record images in the surface on n-type silicon wafers [119]. Photolithographic etching has been used to generate a spatially dependent illumination intensity so that the properties of the porous layer were related to the local illumination. Photoluminescence images of the surface revealed the original image recorded in the surface.

The photoanodic dissolution of n-type silicon in fluoride electrolytes has been of fundamental interest, since electron injection during light-induced dissolution of silicon in ammonium fluoride solutions gives rise to a characteristic photomultiplication effect [82, 120–124]. The initial step in the reaction sequence involves capture of a photogenerated hole. At low light intensities where the surface hole concentration is relatively small, the initial hole capture is followed by three successive electron injection steps, resulting in a quantum efficiency of 4. At higher light intensities, the quantum efficiency is decreased to 2, corresponding to sequential hole capture/electron injection. In the absence of fluoride, an oxide layer is formed through a reaction involving four holes. The morphology of n-type silicon surfaces after photoanodic dissolution in NH_4F is not well characterized and any similarities to porous structures remain to be established.

4.6.4 Luminescence

In addition to the observation of visible photoluminescence from porous silicon structures, visible light emission at liquid junctions has been reported both on open circuit and with an applied potential. Indeed, luminescence during the anodic oxidation of porous layers formed in p-Si(100), (5 Ω cm in 1 M H_2SO_4 at 1.6 mA cm^{-2}) was reported by Gee more than 30 years ago [109]. Kelly and coworkers [125, 126] have observed luminescence at porous silicon layers in aqueous solutions containing certain oxidizing agents under open-circuit conditions. At negative potentials, in the region where hydrogen evolution is observed at n-type silicon, strong visible electroluminescence was reported to occur via hole injection from oxidizing species such as H_2O_2 and $S_2O_8^{2-}$. At positive potentials, oxidation of porous silicon layers formed in n- and p-type silicon in aqueous solutions gives rise to an irreversible visible luminescence [127, 128].

4.7 Reaction Mechanism for Anodic Etching of Silicon in Fluoride Electrolytes

4.7.1 Introduction

Although the overall dissolution reactions for pore formation in HF and photoanodic dissolution of silicon in NH_4F are well charaterized, many details of the reaction sequences remain unresolved. Assuming that pore growth in n-type silicon occurs by propagation of inverted four-sided pyramids defined by (111) planes, the etching reaction is thought to proceed by successive removal of the (111) faces at the pore tip. This process is expected to involve recession of steps along these faces. For this ideal situation, the etching reaction must involve the reaction of $Si-L_2$ groups, where L is a ligand. An additional feature of the pore formation process in aqueous solutions involves the formation of molecular hydrogen. Although the surface of the

porous silicon is terminated by Si–H groups, it is unclear whether pore propagation proceeds through direct etching of the Si–Si backbonds at the Si–H surface or through the formation of other species such as Si–F or Si–OH. In the latter case, the hydrogen passivation reaction must occur by subsequent chemical steps after the pore front has advanced further into the bulk.

As described in Sec. 2.2.2, there is strong evidence to suggest that OH^- is involved in the chemical etching of silicon in HF or NH_4F. In unbuffered HF at low pH, the reaction of steps and kinks is slow and the surface remains atomically rough. In contrast, the reaction in NH_4F is much faster, resulting the formation of large, atomically flat terraces. Further, electrochemical etching of silicon in anhydrous HF results in a change in reaction mechanism characterized by the exchange of four electrons and the absence of molecular hydrogen formation. In addition, electrochemical hydrogen passivation in NH_4F is characterized by a dark current transient and, as described in Sec. 4.6.1, the silicon surface at the peak of the current transient is characterized by Si–OH and $Si-H_2$ species [27]. These results suggest that the reaction proceeds through the formation of Si–OH groups followed by reaction of the Si–Si backbonds with HF.

In general, structural schemes for the dissolution of silicon in fluoride solutions can be summarized by the following models, for which it is assumed that the reaction occurs at surface silicon atoms with two bonds to the silicon lattice and two ligand bonds. Surface sites with three bonds to the bulk lattice are assumed to have large activation energies for dissolution so that any etching processes is expected to occur through step recession, as described in Sec. 2.2.2. The common features of these reaction schemes are steps that involve electrochemical ligand exchange (e.g. Si–H → Si–F or Si–H → Si–OH) and chemical reaction of Si–Si backbonds with HF or H_2O. A wide range of processes, including pore formation in n- and p-type silicon in HF solutions, pore formation in n-type silicon in HF solutions under illumination, and photoanodic dissolution of n-type silicon in NH_4F solutions, can be explained by these models. In addition, they are consistent with the models developed for open-circuit etching of silicon in fluoride solutions, discussed in Sec. 2.2.2.

4.7.2 Two-Electron Processes

In the two-electron model, the reaction sequence involves initial electrochemical steps including ligand exchange followed by the chemical reaction of HF with the remaining Si–Si backbonds. The ligand exchange is typically considered to be oxidation of surface Si–H groups to form Si–F. Weakening of the Si–Si backbonds by polarization of the Si–F group then allows chemical attack of the backbonds, ultimately leading to formation of the reaction product, SiF_6^{2-}. Theoretical calculations for HF insertion into Si–Si bonds have shown that the activation energy for HF insertion is decreased from 1.6 eV for $H_3Si-SiH_3$ to 1.0 eV for $H_2Si-SiH_2F$ (see Table 3). These calculations illustrate the relative stability of the Si–Si bonds to HF insertion at hydrogen-terminated surfaces.

This model is shown schematically in Fig. 29a. Reactions (1) and (2) correspond to the two initial electrochemical steps and reactions (3) and (4) correspond to the

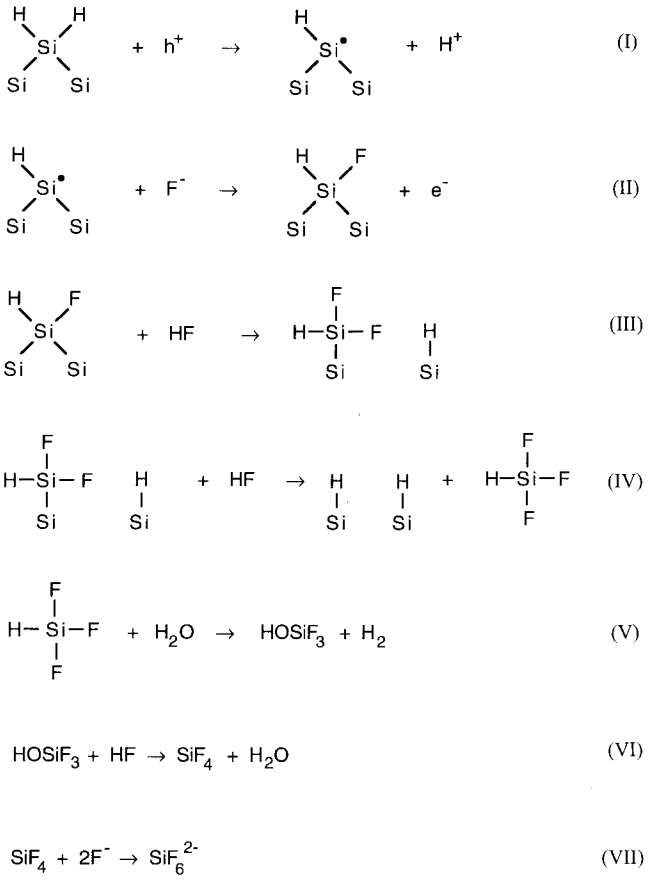

Fig. 29. Structural model for two-electron dissolution of silicon by electrochemical ligand exchange followed by insertion of HF into the Si–Si backbonds. Insertion of H_2O into the backbonds is also possible. Reaction of the unstable products results in the formation of SiF_6^{2-}. The reaction can proceed through the formation of Si–F (a) or Si–OH (b).

insertion of HF into the Si–Si backbonds. The reaction product $HSiF_3$ is unstable and is hydrolyzed resulting in the formation of molecular hydrogen and SiF_6^{2-}, as shown in steps (5)–(7) [123]. Steps (3) and (4) can also occur by insertion of water molecules leading to the reaction product $HFSi(OH)_2$, which can also be hydrolyzed to SiF_6^{2-}. Note that a reaction mechanism involving either HF or H_2O insertion will maintain a hydrogen-passivated surface and result in the formation of molecular hydrogen.

An energy-level model for this mechanism, proposed by Gerischer et al. [123], is shown in Fig. 30. The energy levels associated with $Si-H_2$ groups at kink sites are assumed to be located just above the valence band edge and hence sites for hole capture. A hole trapped at the kink site oxidizes one of the Si–H groups to release a

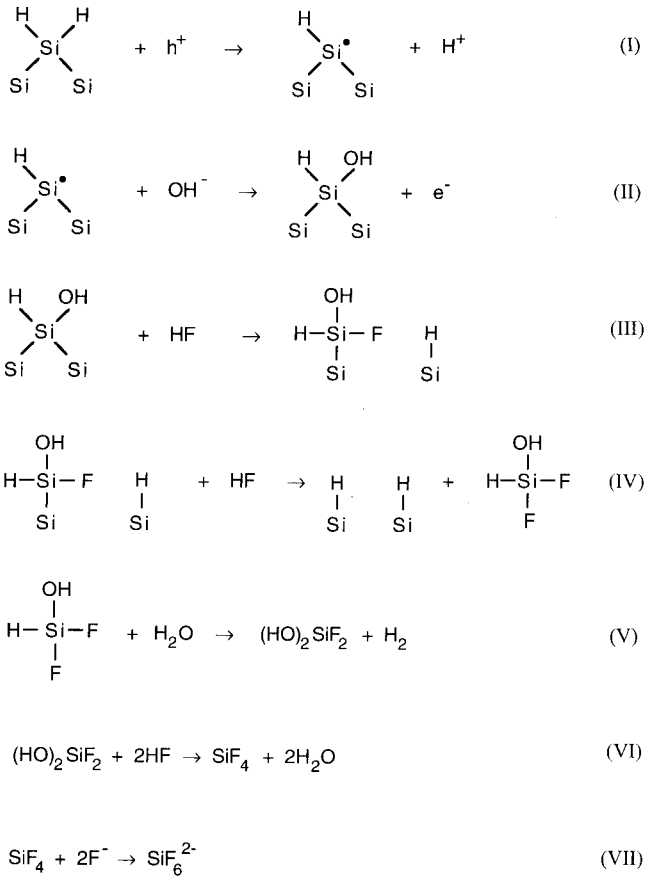

Fig. 29b

proton from the surface. The unpaired electron on the dangling bond is then able to form an Si–F bond by hole capture or by thermally activated electron injection. The highly stable Si–F bond is assumed to be below the valence band edge, and polarization of the silicon atom by the fluoride ion makes the Si–Si backbonds susceptible to attack by HF or H_2O molecules.

Assuming that the single Si–F ligand at the kink site is sufficiently polar to allow successive reaction of the two Si–Si backbonds with HF, then the overall reaction is consistent with pore formation in n- and p-type silicon where two charges are transferred per silicon atom. For the case of photoanodic dissolution of n-type silicon in NH_4F [120–124] the characteristic photomultiplication effect at low light intensities is also consistent with the hole capture/electron injection sequence shown in Fig. 29a.

Figure 29b shows a structural scheme for a reaction sequence where the initial electrochemical steps involve formation of Si–OH groups are the surface. This

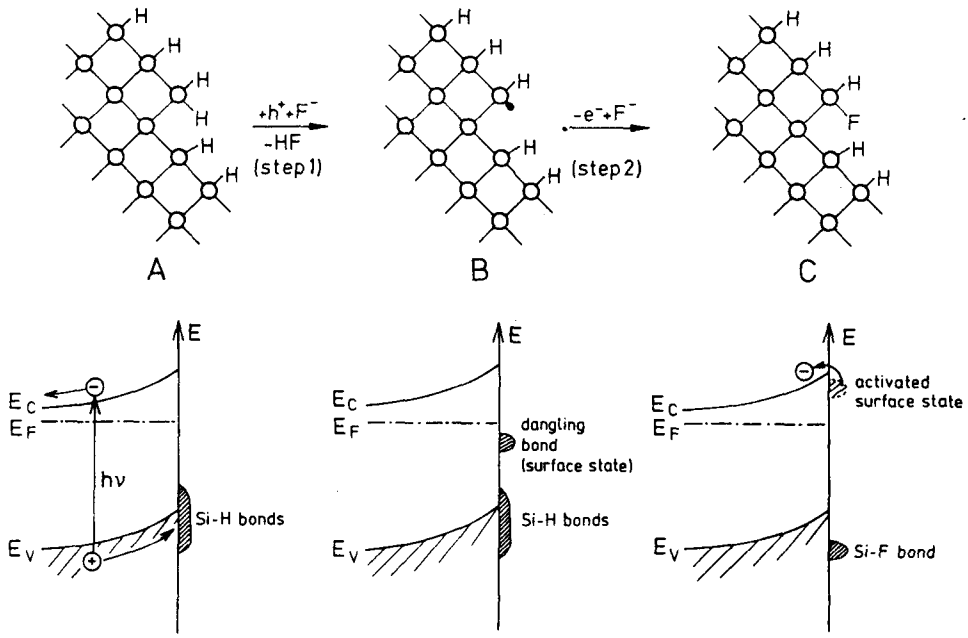

Fig. 30. Energy model for electrochemical oxidation of Si–H and the formation of Si–F by electron injection [123].

scheme is consistent with the etching of silicon in buffered fluoride solutions under open-circuit conditions where the decrease in the atomic-scale roughness is correlated to step recession at high pH.

4.7.3 Four-Electron Processes

Photoanodic dissolution of n-type silicon in NH_4F at high light intensities and pore formation in anhydrous HF–MeCN [111] occurs through a four-electron process. Two possible reaction mechanisms are consistent with these processes. In the first mechanism, shown in Fig. 31, the ligand exchange reactions occur successively, converting both Si–H groups to Si–F, steps (1)–(4), and involving four charges per silicon atom. Both Si–Si backbonds are then broken by reaction with HF molecules as shown in steps (5) and (6). This mechanism implies that the breaking of the Si–Si backbonds may be associated with H_2O in aqueous solutions since a change of mechanism is observed in anhydrous HF [111]. In addition, molecular hydrogen is not generated in this mechanism, which is consistent with experimental observations in anhydrous HF.

In the second four-electron mechanism, electrochemical reaction of the Si–Si backbonds with holes is assumed to be fast in comparison with electrochemical ligand exchange or chemical reaction with HF or H_2O. For the case shown in Fig. 32,

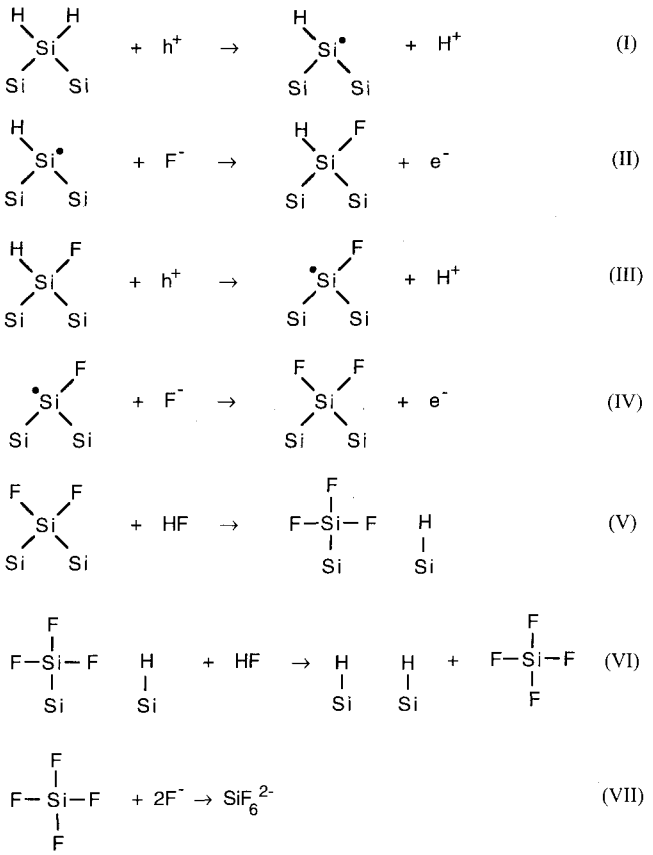

Fig. 31. Structural model for two-electron dissolution of silicon by electrochemical reaction of SiH_2 to SiF_2 and subsequent insertion of HF (or H_2O) into the Si–Si backbonds.

both Si–Si backbonds are oxidized by this mechanism steps (1)–(4). It is also possible that this process can compete with HF or H_2O insertion in the reaction scheme shown in Fig. 29. In both cases, a fluoride-terminated surface is expected during the etching process, although it should be noted that this has not been confirmed experimentally.

Some insight into possible reaction mechanisms can be gained from examination of the Si/KOH system. Chemical etching of silicon in KOH involves reaction with water and is characterized by the formation of two H_2 molecules per silicon atom dissolved [129, 130]. The reaction product is thought to be $Si(OH)_2(O^-)_2$ [130]. Palik et al. [129] have suggested that the reaction mechanism proceeds through attack of Si–Si backbonds at a Si–OH-terminated surface by H_2O:

$$Si-Si+H_2O \leftrightarrow Si-H+Si-OH \tag{27}$$

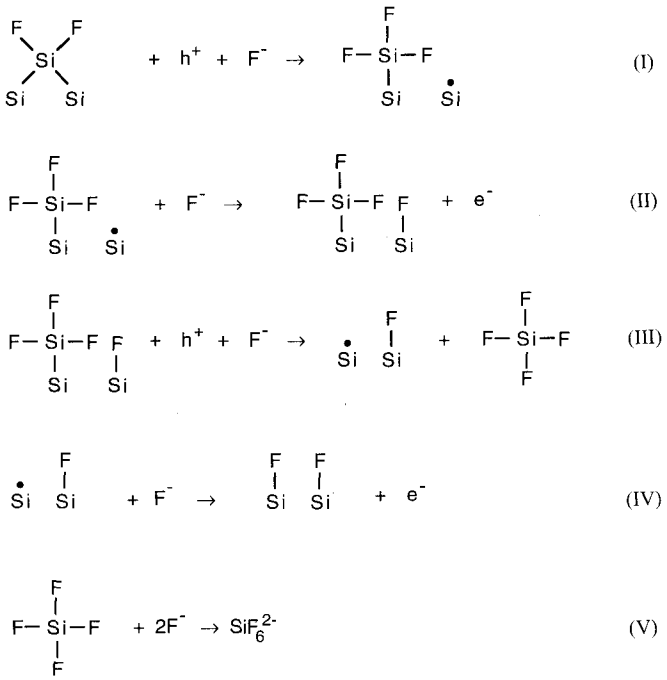

Fig. 32. Structural model for four-electron process involving direct oxidation of Si–Si backbonds by trapped holes. This processes may also compete with HF insertion in the model shown in Fig. 29.

The next step in the sequence is slow attack of the Si–H bond by OH^-:

$$Si-H+Si-OH+OH^- \rightarrow Si-O^- +Si-OH+H_2 \tag{28}$$

For an OH-terminated silicon atom, corresponding to a site on a (100) surface or a kink site on a (111) facet, reactions (27) and (28) are repeated for each backbond, resulting in the formation of the reaction product $Si(OH)_2(O^-)_2$. The overall reaction is given by:

$$Si+2\,H_2O+2\,OH^- \rightarrow 2\,H_2+Si(OH)_2(O^-)_2 \tag{29}$$

The reaction in KOH is consistent with the observation that di- and tri-hydrides are attacked in water under open-circuit conditions [20, 21] resulting in the characteristic smoothening of HF-treated surfaces. However, reaction (28) represents an open-circuit process where charge balance for the oxidation reaction is maintained by proton reduction.

Reactions (27) and (28) are similar to the proposed mechanism for the smoothening process that occurs during open-circuit etching of silicon in buffered HF solutions, given in reactions (2) and (3). In this case, electrochemical ligand exchange involves the transformation of Si–H → Si-OH followed by HF attack of the Si–Si backbonds.

4.8 Pore Formation in Other Semiconductors

The electrochemical formation of etch tunnels have been reported for a number of other semiconductor/electrolyte systems, including n-GaAs in H_2SO_4 [132], KOH [132, 133], and GaP in CH_3OH-Cl_2 [134]. Porous films have also been reported for p-GaAs etched in HF [135] and for the chemical etching of InSb in HCl containing Fe^{3+} [136]. As for the case of pore formation in silicon, it has been verified that the pores are initiated randomly and are not dependent on heterogeneities such as the dopant atoms or dislocations. Since pores can be formed in GaAs in HF, H_2SO_4, and KOH, it can be concluded that the role of HF in porous silicon formation is only to suppress oxide formation. For GaAs, oxides such as As_2O_3 can be dissolved in a variety of solution compositions and hence pore formation should be a more general phenomenon.

The preferred growth direction of pores in n-type gallium arsenide is along the ⟨111⟩ directions from Ga to As. The pore walls appear to be defined by the {110} planes giving rise to hexagonal pore shapes, as shown in Fig. 23. Although attempts have been made to correlated these effects with dangling bond density and surface polarity [137], the underlying mechanism of pore formation in GaAs remains unknown. For the case of n-type silicon, the preferred direction of pore growth in silicon along the ⟨100⟩ directions and the characteristic square cross-sections defined by the {011} planes are consistent with the relative etch rates {100}>{110}>{111} [83, 93].

In summary, it appears that pore formation is a general phenomenon that can occur in any semiconductor if oxide formation is suppressed and there is sufficient selectivity in the etch rates of different crystallographic planes. For the case of silicon, the oxide dissolves only in HF solutions and hence pore formation is limited to this electrolyte. For the case of GaAs and GaP, and probably most other semiconductors, the poor stability of the oxide makes pore formation possible in a wide variety of electrolytes. This approach suggests that it is the orientation-dependent etch rates that control the pore growth direction. Anisotropy in the pore shape is expected to be strongest for the slowest growth rates, where the more slowly dissolving orientations in the plane of the pore will determine the pore shape. While these criteria are consistent with experimental observations, a general model for pore formation should predict the orientation-dependent etch rates and the pore morphologies.

5 Dynamics of Pore Formation

5.1 Introduction

The mechanism of pore formation is controlled by the three-dimensional structure of the potential distribution at the interface between the silicon and the porous layer. For the case of n-type silicon, field enhancements at the pore base, due to the small radius of curvature, result in local regions where the field exeeds the breakdown field

and the current flow is controlled by tunneling into the conduction band in these regions, as shown in Fig. 33 [138]. As a result, the current flow is confined to these regions and stable pore growth is sustained. For the case of p-type silicon, the majority carrier (hole) concentration at the silicon/electrolyte interface is in equilibrium and exclusion of carriers from geometrically small regions where the bandgap is enlarged results in current concentration at the pore base. For both cases, the result is that selective dissolution of the silicon occurs at the pore base and the pores continue to propagate. The characteristic spacing between the primary pores propagating in the ⟨100⟩ directions is related to the the depletion layer width for n-type silicon. For p-type silicon the band gap enlargement gives rise to a minimum feature size on the order of 40 Å.

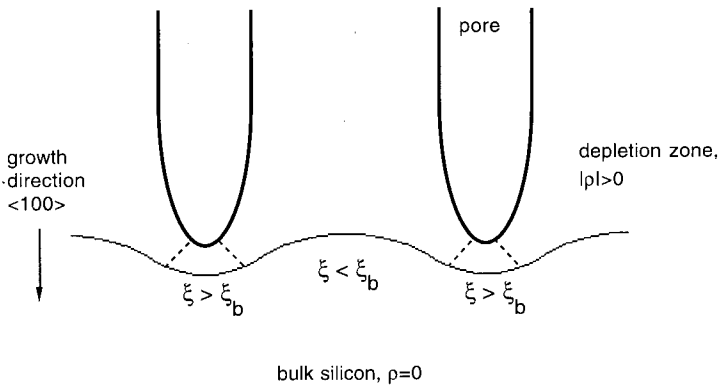

Fig. 33. Illustration of pore growth in n-type silicon in the absence of illumination [138].

5.2 Computer Simulations

Pore formation in silicon can be considered a growth process in which the growing phase (the pores) propagates into a receding phase (bulk silicon). This approach allows the analysis of pore propagation by techniques used to model a wide range of processes, such as physical deposition, aggregation, evaporation/condensation, and solidification [139–141].

Stability analysis shows that for perturbations in the surface to propagate, the rate-limiting step in the growth process must be in the receding phase [142]. For the case of pore growth in silicon, the stability criterion implies that pore growth is controlled by a reaction step in the bulk silicon and not on the electrolyte side of the interface. Based on the overall reaction for silicon dissolution during pore formation and the discussion in the preceding section, it appears that the unique morphologies associated with porous silicon are related to the reaction of holes with surface silicon atoms and hence the surface hole concentration.

Smith and coworkers [143, 144] were the first group to use Monte Carlo simulations as a tool to investigate the pore growth process. They used a model equivalent

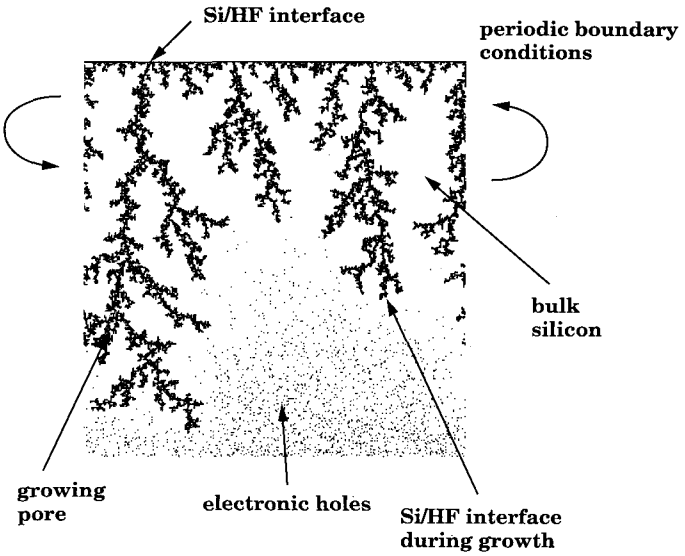

Fig. 34. Model for computer simulations of pore growth in silicon.

to the Witten and Sander model [145, 146] for diffusion-limited aggregation where the particles (holes) follow purely random walks on a two dimensional lattice. The structures formed by this model are highly branched and fractal over a wide range of length scales. The morphologies formed by this model, however, do not reveal the highly directional channels seen in porous silicon structures.

This approach has been modified to incorporate the effects caused by the high-field region ahead of the growth front in n-type silicon [147, 148]. In this model, a two-dimensional lattice is randomly populated by particles representing electronic holes and the particles are allowed to move on the lattice following certain restrictions, as shown in Fig. 34. In the electroneutral region in the bulk of the silicon away from the pore front, transport is controlled by migration and hole motion is considered random because of the very low field. Close to the pore front, holes are swept to the pore tips with trajectories determined by the local field. The distance from the pore front, χ, is analogous to a screening length and follows the contour of the growth front. When a hole reaches the silicon/HF interface, the silicon atom at that site is removed and the pore extends into the lattice, locally moving the interface. Constant carrier concentration is maintained at the base of the lattice far from the interface.

Figure 35 shows results of the simulations at a particle density of 0.01 and as a function of screening length, χ. For $\chi = 0$, hole transport is entirely random and the resultant structures correspond to those obtained by diffusion-limited aggregation. As the screening length is increased, however, the pores become highly directional and the concentration of secondary pores is reduced. In all cases the simulated pore structures attain a steady-state growth mode with a constant porosity, as expected for a constant particle flux. These morphologies exhibit many of the characteristic fea-

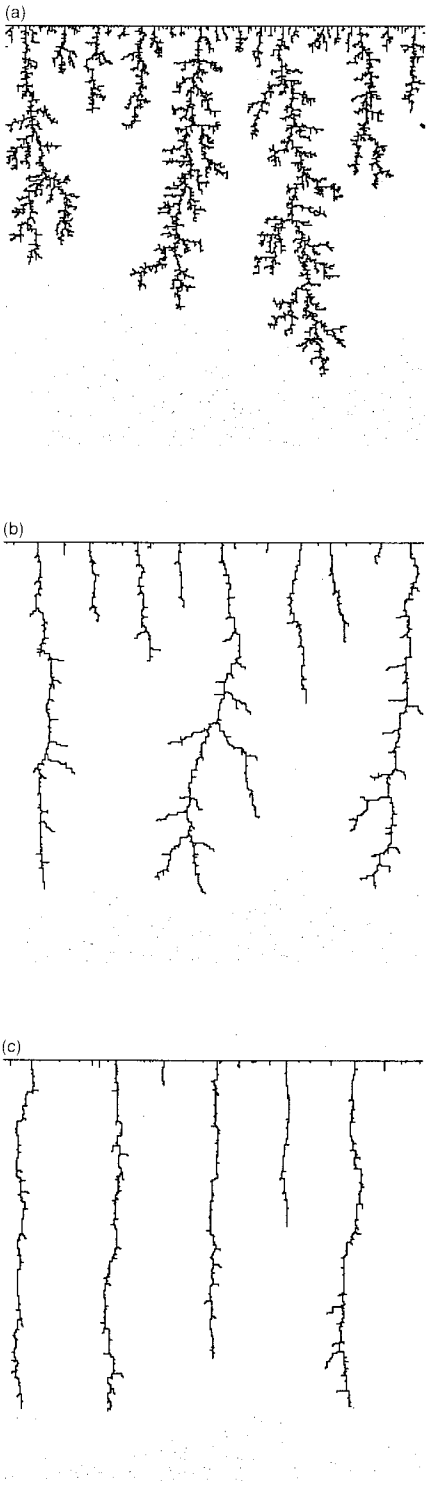

Fig. 35

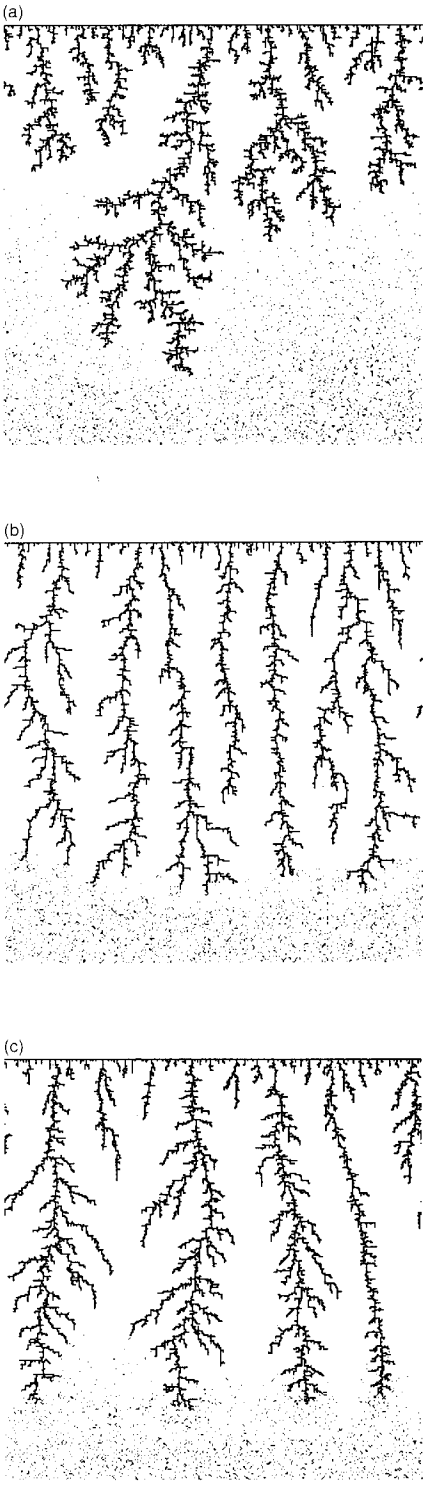

Fig. 36

tures of porous silicon layers formed in n-type silicon, suggesting that the local field plays an important role in pore formation. Figure 36 shows simulated porous layers for a particle concentration of 0.1. Again $\chi = 0$ corresponds to the diffusion-limited aggregation case although the pore density is higher due to the increased particle density. As the screening length is increased the pores become highly directional although the concentration of secondary pores is much larger in comparison with lower particle density. This type of structure is similar to the porous layers formed in highly doped p-type silicon although the pores remain unconnected. Nonetheless, improvements in computer simulations in conjunction with structural characterization may give better insight into the parameters controlling the pore morphology.

6 Electropolishing

At large applied potentials, a transition is observed from pore formation to electropolishing. From Fig. 9 it can be seen that the domain of pore formation is extended to higher potentials and current densities with increasing HF concentration. Pore formation can be contrasted to the electropolishing reaction, which exhibits an effective dissolution valence of 4 [61], as can be seen in Figure 10b. In this case, silicon dissolution proceeds through the formation of an interfacial silicon oxide layer and the etching process results in a uniform thinning of the silicon substrate:

$$Si + 4\,H_2O + 4\,h^+ \rightarrow Si(OH)_4 + 4\,H^+ \tag{30}$$

$$Si(OH)_4 \rightarrow SiO_2 + 2\,H_2O \tag{31}$$

As for the case of pore formation, although kinetics of silicon dissolution in the electropolishing regime have been studied by a number of groups [149–152], the detailed reaction mechanism is not well understood. The properties of electrochemically formed silicon oxides have been reviewed recently [34, 153] and will not be discussed here.

Figure 37 presents a current-potential curve for p-type silicon showing two distinct current peaks. The region below the first current peak corresponds to the pore formation regime. The first current peak corresponds to the critical current for electropolishing and exhibits a linear dependence on fluoride concentration, as shown in Fig. 38. Although the potential onset for electropolishing is dependent on the dopant type and concentration, the critical current density is independent of doping level [64], as can be seen in Fig. 9. This is also seen in the current-voltage curves as

Fig. 35. Structures of simulated porous layers for a particle (hole) density of 0.01 as a function of screening length, χ: (a) $\chi = 0$; (b) $\chi = 10$; (c) $\chi = 20$ [148].

Fig. 36. Structures of simulated porous layers for a particle (hole) density of 0.1 as a function of screening length, χ: (a) $\chi = 0$; (b) $\chi = 10$; (c) $\chi = 20$ [148].

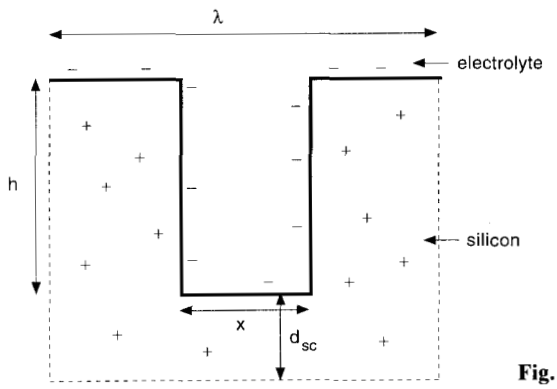

Fig. 37. Cross-section of a porous silicon layer.

a function of acceptor concentration in Fig. 39, showing that the current peaks are shifted to more positive potentials. The first-order dependence on HF concentration indicates that dissolution of the surface oxide layer is rate-controlling [64, 67].

The second current peak exhibits a square-root dependence on HF concentration, as shown in Fig. 38, suggesting that the electropolishing mechanism becomes transport-limited at high potentials. The two regions of electropolishing defined by the two peaks have been ascribed to different forms of the oxide [152]. In the potential

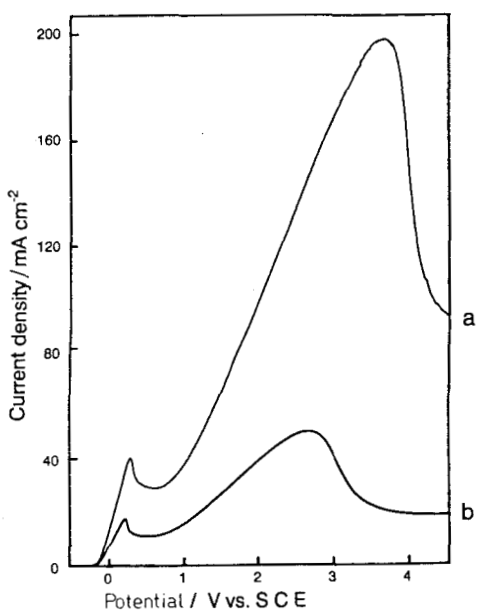

Fig. 38. Current-potential curves for p-Si(100), *0.075–0.125* Ω cm in (a) *0.1%* and (b) *0.05%* solution of 40 wt.% NH_4F+48 wt.% HF (13:2) [67].

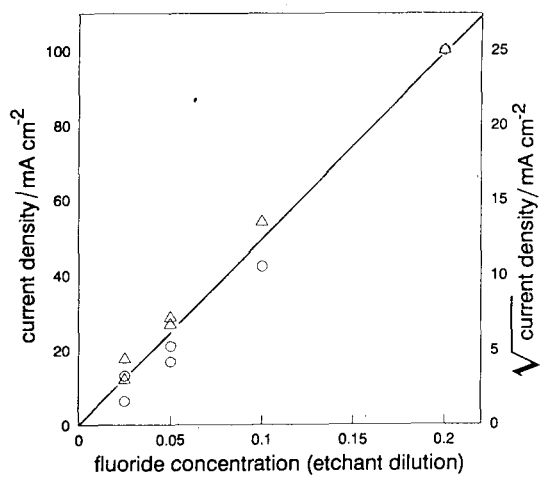

Fig. 39. Dependence of the first (○) and second (△) current peaks on fluoride ion concentration [67].

range beyond the second peak, current oscillations have been reported, although the origin is not known [152, 153].

For n-type silicon under illumination, the current-voltage curves are dependent on illumination intensity, as shown in Fig. 40. At high illumination intensity, the current-voltage curves exhibit two current peaks, as seen for p-type silicon. At lower illumination intensities the photocurrent is limited by the supply of photogenerated holes and exhibits a characteristic plateau.

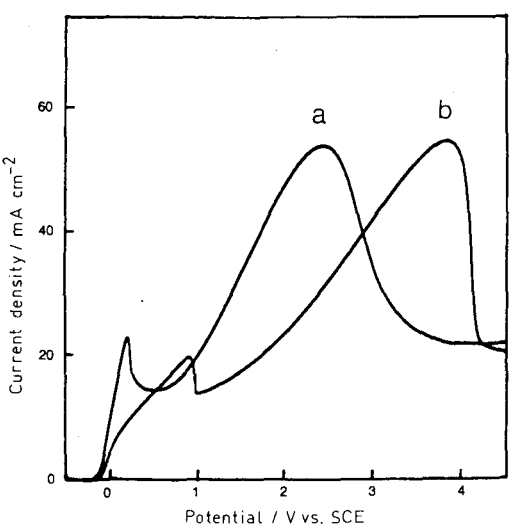

Fig. 40. Current-potential curves for p-Si(100), (a) 0.075–0.125 Ω cm, and (b) 4–6 Ω cm, in 0.05% solution of 40 wt.% NH_4F+48 wt.% HF (13:2) [67].

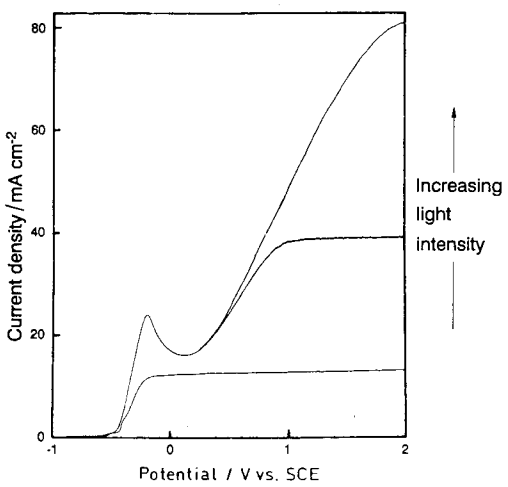

Fig. 41. Current-potential curves for n-Si(100), 14–20 Ω cm under illumination in 0.05% solution of 40 wt.% NH_4F+48 wt.% HF (13:2) [67].

7 Summary

Although surface reactions at the silicon/electrolyte interface have been studied for many years, the nature of the interactions between the silicon surface and fluoride containing electrolytes are only recently becoming understood. Recent characterizations using various spectroscopic and microscopic techniques have resulted in new insight into the properties of silicon surfaces on an atomistic scale. Significant issues remain to be resolved, however, such as the reaction mechanisms, the processes leading to pore formation, and the nature of surface oxides.

Acknowledgements. The author acknowledges numerous discussions with students and colleagues, in particular John Macaulay, Frances Ross, Sharka Prokes, and Gerko Oskam. He thanks G.S. Higashi, who provided Fig. 3. The author is also indebted to the editors for providing helpful comments on the manuscript and for reprints of recent work. This work was supported by the National Science Foundation under grant DMR-9202645.

8 References

1. R.B. Heimann in: Crystals-Growth, Properties and Applications, Vol. 8: Silicon-Chemical Etching, J. Grabmaier (ed.), Springer-Verlag, New York (1982).
2. K.E. Petersen, Proc. IEEE 70, 420 (1982).
3. D.L. Kendall, Annu. Rev. Mater. Sci. 9, 373 (1979).
4. E. Bassous in: Electrochemical Technology in Electronics, L.T. Romankiw, T. Osaka (eds.), The Electrochemical Society, Pennington, NJ (1988) Proceedings Volume 88-23, p. 619
5. W.K. Zwicker, S.K. Kurtz in: Semiconductor Silicon, H.R. Huff, R.R. Burgess (eds.), Electrochemical Society, Pennington, NJ (1973), p. 315.
6. T. Sakurai, H.D. Hagstrum, Phys. Rev. B 14, 1593 (1976).
7. F. Stucki, J.A. Schaefer, J.R. Anderson, G.J. Lapeyre, W. Gopel, Solid State Commun. 47, 795 (1983).
8. Y.J. Chabal, K. Raghavachari, Phys. Rev. Lett. 54, 1055 (1985).
9. H. Ubara, T. Imura, A. Hiraki, Solid State Commun. 50, 673 (1984).
10. E. Yablonovitch, D.L. Allara, C.C. Chang, T. Gmitter, T.B. Bright, Phys. Rev. Lett. 57, 249 (1986).
11. R. Walsh, Acc. Chem. Res. 14, 246 (1981).
12. J.I. Pankove, D.E. Carlson, J.E. Berkeyheiser, R.O. Wance, Phys. Rev. Lett. 51, 224 (1983).
13. N.M. Johnson, F.A. Ponce, R.A. Street, R.J. Nemanich, Phys. Rev. B 35, 4166 (1987).
14. W. Kern, D. Puotinen, RCA Rev. 31, 187 (1970).
15. W. Kern, RCA Rev. 39, 278 (1978).
16. G.S. Higashi, Y.J. Chabal in: Handbook of Semiconductor Wafer Cleaning Technology, W. Kern (ed.), Noyes, Park Ridge, NJ (1994), p. 433.
17. H. Ogawa, N. Terada, K. Sugiyama, K. Moriki, N. Miyata, T. Aoyama, R. Sugino, T. Ito, T. Hattori, Appl. Surf. Sci. 56–58, 836 (1992).
18. K. Sugiyama, T. Igarishi, K. Moriki, Y. Nagasawa, T. Aoyama, R. Sugino, T. Ito, T. Hattori, Jap. J. Appl. Phys. 29, L2401 (1990).
19. T. Takahagi, I. Nagai, A. Ishitani, H. Kuroda, Y. Nagasawa, J. Appl. Phys. 64, 3516 (1988).
20. G.S. Higashi, Y.J. Chabal, G.W. Trucks, K. Raghavachari, Appl. Phys. Lett. 56, 656 (1990).
21. S. Watanabe, N. Nakayama, T. Ito, Appl. Phys. Lett. 59, 1458 (1991).
22. Y.J. Chabal, G.S. Higashi, K. Raghavachari, V.A. Burrows, J. Vac. Sci. Technol. A7, 2104 (1989).
23. P. Dumas, Y.J. Chabal, P. Jakob, Surf. Sci. 269/270, 867 (1992).
24. Y. Morita, K. Miki, H. Tokumoto, App. Phys. Lett. 59, 1347 (1991).
25. E. Tomita, N. Matsuda, K. Itaya, J. Vac. Sci. Technol. A8, 534 (1990).
26. V.A. Burrows, Y.J. Chabal, G.S. Higashi, K. Raghavachari, S.B. Christman, Appl. Phys. Lett. 53, 998 (1988).
27. T. Bitzer, M. Gruyters, H.J. Lewerenz, K. Jacobi, Appl. Phys. Lett. 63, 397 (1993).
28. Y.J. Chabal, G.S. Higashi, S.B. Christman, Phys. Rev. B28, 4472 (1983).
29. G.S. Higashi, R.S. Becker, Y.J. Chabal, A.J. Becker, Appl. Physl. Lett. 58, 1656 (1991).
30. K. Itaya, R. Sugawara, Y. Morita, H. Tokumoto, Appl. Phys. Lett. 60, 2534 (1992).
31. P. Dumas, Y.J. Chabal, Chem. Phys. Lett. 181, 537 (1991).
32. R.S. Becker, G.S. Higashi, Y.J. Chabal, A.J. Becker, Phys. Rev. Lett. 65, 1917 (1990).
33. S.M. Hu, D.R. Kerr, J. Electrochem. Soc. 114, 414 (1967).
34. H.J. Lewerenz, Electrochim. Acta 37, 847 (1992).
35. J.S. Judge, Proc. Symp. Etching and Pattern Definition, The Electrochemical Society, Pennington, NJ (1976), p. 19.
36. P. Jakob, P. Dumas, Y.J. Chabal, Appl. Phys. Lett. 59, 2968 (1991).
37. P. Jakob, Y.J. Chabal, K. Raghavachari, R.S. Becker, A.J. Becker, Surf. Sci. 275, 407 (1992).
38. G.W. Trucks, K. Raghavachari, G.S. Higashi, Y.J. Chabal, Phys. Rev. Lett. 65, 504 (1990).
39. P. Jakob, Y.J. Chabal, J. Chem. Phys. 95, 2897 (1991).

40. D. Graf, M. Grunder, R. Schultz J, Vac. Sci. Technol. A7, 808 (1989).
41. J.W. Corbett, D. Peak, J.J. Pearton, A.G. Sganga in: Hydrogen in Disordered and Amorphous Solids, G. Bambakidis, R.C. Bowman (eds.), Plenum, New York (1986).
42. H.F. Winters, J.W. Coburn, Appl. Phys. Lett. 34, 70 (1979).
43. J.W. Coburn, H.F. Winters, J. Appl. Phys. 50, 3189 (1979).
44. H.F. Winters, D. Haarer, Phys. Rev. B36, 6613 (1987).
45. T.J. Chuang, Phys. Rev. Lett. **42**, 815 (1979).
46. T.J. Chuang, J. Appl. Phys. 51, 2614 (1980).
47. F.R. McFeely, J.F. Morar, F.J. Himpsel, Surf. Sci. 165, 277 (1986).
48. H.F. Winters, J.W. Coburn, T.J. Chuang, J. Vac. Sci. Technol. B1, 469 (1983).
49. C.G. Van De Walle, F.R. McFeely, S.T. Pantelides, MRS Res. Soc., Symp. Proc. 141, 425 (1989).
50. J.W. Coburn, H.F. Winters, J. Appl. Phys. 50, 3189 (1979).
51. A.K. Kuriakose, J.L. Margrave, J. Phys. Chem. 68, 2671 (1964).
52. M. Nishijima, K. Edamoto, Y. Kubota S, Tanaka, M. Ouchi, J. Chem. Phys. 84, 6458 (1986).
53. H. Ibach, H. Wagner, D. Bruchmann, Solid State Commun. 42, 457 (1982).
54. J.A. Schaefer, F. Stucki, D.J. Frankel, W. Gopel, G.J. Lapeyre, J. Vac. Sci. Technol. B2, 359 (1984).
55. P. Gupta, A.C. Dillon, A.S. Bracker, S.M. George, Surf. Sci. 245, 360 (1991).
56. J.S. Judge, J. Electrochem. Soc. 118, 1772 (1971).
57. H.N. Farrer, F.J.C. Rossotti, J. Inorg. Nucl. Chem. 26, 1959 (1964).
58. R.E. Mesmer, C.F. Baes, Inorg. Chem. 8, 618 (1969).
59. A. Uhlir, Bell System Tech. J. 35, 333 (1956).
60. D.R. Turner, J. Electrochem. Soc. 105, 402 (1958).
61. R. Memming, G. Schwandt, Surf. Sci. 4, 109 (1966).
62. M.J.J. Theunissen, J. Electrochem. Soc. 119, 351 (1972).
63. T. Unagami, J. Electrochem. Soc. 127, 476 (1980).
64. X.G. Zhang, S.D. Collins, R.L. Smith, J. Electrochem. Soc. 136, 1561 (1989).
65. F. Gaspard, A. Bsiesy, M. Ligeon, F. Muller, R. Herino, J. Electrochem. Soc. 136, 3043 (1989).
66. I. Ronga, A. Bsiesy, F. Gaspard, R. Herino, M. Ligeon, F. Muller, A. Halimaoui, J. Electrochem. Soc. 138, 1403 (1991).
67. M.J. Eddowes, J. Electroanal. Chem. 280, 297 (1990).
68. V. Lehmann, J. Electrochem. Soc. 140, 2836 (1993).
69. R.L. Meek, J. Electrochem. Soc. 118, 437 (1971).
70. G. Oskam, P.C. Searson, in preparation.
71. H. Gerischer, Electrochim. Acta 35, 1677 (1990).
72. P.C. Searson, X.G. Zhang, J. Electrochem. Soc. 137, 2539 (1990).
73. P.C. Searson, X.G. Zhang, Electrochim. Acta 36, 499 (1991).
74. P.C. Searson, Appl. Phys. Lett. 59, 832 (1991).
75. D. Vanmaekelbergh, P.C. Searson, J. Electrochem. Soc. 141, 697 (1994).
76. S.M. Sze, Physics of Semiconductor Devices, Wiley, New York (1981).
77. H. Gerischer, Physical Chemistry, Academic Press, New York (1970) Vol. 9A, p. 463.
78. V. Lehmann, U. Goesele, Appl. Phys. Lett. 58, 856 (1991).
79. F.M. Ross, A. Natarajan, G. Oskam, P.C. Searson, in preparation.
80. F. Ozanam, J.N. Chazalviel, A. Radi, M. Etman, J. Electrochem. Soc. 139, 2491 (1992).
81. V.A. Myamlin, Y.V. Pleskov, Electrochemistry of Semiconductors, English translation, Plenum, New York (1967).
82. H. Gerischer, M. Lubke, J. Electrochem. Soc. 135, 2782 (1988).
83. P.C. Searson, J.M. Macaulay, F.M. Ross, J. Appl. Phys. 72, 253 (1992).
84. V. Lehmann, H. Foll, J. Electrochem. Soc. 137, 653 (1990).
85. R.C. Anderson, R.S. Muller, C.W. Tobias, J. Electrochem. Soc. 138, 3406 (1991).
86. X.G. Zhang, J. Electrochem. Soc. 138, 3750 (1991).
87. M.I.J. Beale, N.G. Chew, M.J. Uren, A.G. Cullis, J.D. Benjamin, App. Phys. Lett. 46, 86 (1985).

88. M.I.J. Beale, J.D. Benjamin, M.J. Uren, N.G. Chew, A.G. Cullis, J. Cryst. Growth 73, 622 (1985).
89. S.F. Chuang, S.D. Collins, R.L. Smith, Appl. Phys. Lett. 55, 1540 (1989).
90. A.G. Cullis, L.T. Canham, Nature (London) 353, 335 (1991).
91. R.L. Smith, S.D. Collins, J. Appl. Phys. 71, R1 (1992).
92. H. Sugiyama, O. Nittono, Jpn. J. Appl. Phys. 28, L2013 (1989).
93. P.C. Searson, J.M. Macaulay, S.M. Prokes, J. Electrochem. Soc. 139, 3373 (1992).
94. F. Phillip, K. Urban, M. Wilkens, Ultramicroscopy 13, 379 (1984).
95. K. Barla, G. Bomchil, R. Herino, J.C. Pfister, J. Baruchel, J. Cryst. Growth 68, 721 (1984).
96. K. Barla, R. Herino, G. Bomchil, J.C. Pfister, A. Freund, J. Cryst. Grwoth 68, 727 (1984).
97. I.M. Young, M.I.J. Beale, J.D. Benjamin, Appl. Phys. Lett. 46, 1133 (1985).
98. G. Bomchil, R. Herino, K. Barla, J.C. Pfister, J. Electrochem. Soc. 130, 1611 (1983).
99. G. Bomchil, R. Herino, K. Barla in: Proc. 1985 MRS Meeting, Strasbourg, V.T. Nguyen, A.G. Cullis (eds.), (1985) Vol. 4, p. 463.
100. R.C. Anderson, R.S. Muller, C.W. Tobias, J. Micromechan. Systems 3 (1994).
101. C.S. Fuller, J.A. Ditzenberger, J. Appl. Phys. 25, 550 (1957).
102. R.J. Archer, J. Phys. Chem. Solids 14, 104 (1960).
103. H. Robbins, B. Schwartz, J. Electrochem. Soc. 106, 505 (1959); idem, ibid. 107, 108 (1960).
104. B. Schwartz, H. Robbins, J. Electrochem. Soc. 108, 365 (1961); idem, ibid. 123, 1903 (1976).
105. M.I.J. Beale, J.D. Benjamin, M.J. Uren, N.G. Chew, A.G. Cullis, J. Cryst. Growth 75, 408 (1986).
106. R.W. Fauthauer, T. George, A. Ksendzov, R.P. Vasquez, Appl. Phys. Lett. 60, 995 (1992).
107. J. Sarathy, S. Shih, K. Jung, C. Tsai, K.-H. Li, D.-L. Kwong, J.C. Champbell, S.-L. Yau, A.J. Bard, Appl. Phys. Lett. 60, 1532 (1992).
108. Z. Zhang, M.M. Lerner, T. Alekel, D.A. Deszler, J. Electrochem. Soc. 140, L97 (1993).
109. A. Gee, J. Electrochem. Soc. 107, 787 (1960).
110. R.E. Hummel, S.S. Chang, Appl. Phys. Lett. 61, 1965 (1992).
111. E.A. Propst, P.K. Kohl, J. Electrochem. Soc. 141, 1006 (1994).
112. A. Venkateswara Rao, F. Ozanam, J.-N. Chazalviel, J. Electrochem. Soc. 138, 153 (1991).
113. P. Gupta, V.L. Colvin, S.M. George, Phys. Rev. B37, 8234 (1988).
114. T. Ito, T. Yasumatsu, H. Watabe, A. Hiraki, Jpn. J. Appl. Phys. 29, L201 (1990).
115. C. Tsai, K.-H. Li, J. Sarathy, S. Shih, J.C. Campbell, B.K. Hance, J.M. White, App. Phys. Lett. 59, 2814 (1991).
116. S.M. Prokes, O.J. Glembocki, V.M. Bermudez, R. Kaplan, L.E. Friedersdorf, P.C. Searson, Phys. Rev. B45, 13788 (1992).
117. C. Levy-Clement, A. Lagoubi, R. Tenne, M. Neumann-Spallart, Electrochim. Acta 37, 877 (1992).
118. C. Levy-Clement, A. Lagoubi, D. Ballutaud, F. Ozanam, J.-N. Chazalviel, M. Neumann-Spallart, Appl. Surf. Sci. 65/66, 408 (1993).
119. V.V. Doan, M.J. Sailor, Science 256, 1791 (1992).
120. M. Matsumura, S.R. Morrison, J. Electroanal. Chem. 144, 113 (1983).
121. M. Matsumura, S.R. Morrison, J. Electroanal. Chem. 147, 157 (1983).
122. H. Gerischer, M. Lubke, Ber. Bunsenges. Phys. Chem. 91, 394 (1987).
123. H. Gerischer, P. Allongue, V. Costa Kieling, Ber. Bunsenges. Phys. Chem. 97, 753 (1993).
124. L.M. Peter, J. Li, R. Peat, H.J. Lewerenz, J. Stumper, Electrochim. Acta 35, 1657 (1990).
125. E.A. Meulenkamp, P.M.M.C. Bressers, J.J. Kelly, Appl. Surf. Sci. 64, 283 (1993).
126. P.M.M.C. Bressers, J.W.J. Knapen, E.A. Meulenkamp, J.J. Kelly, Appl. Phys. Lett. 61, 108 (1992).
127. A. Halimaoui, C. Oules, G. Bomchil, A. Bsiesy, F. Gaspard, R. Herino, M. Ligeon, F. Muller, Appl. Phys. Lett. 59, 304 (1991).
128. P.C. Searson, S.M. Prokes, O.J. Glembocki, J. Electrochem. Soc. 140, 3327 (1993).
129. E.D. Palik, V.M. Bermudez, O.J. Glembocki, J. Electrochem. Soc. 132, 871 (1985).
130. R.M. Finne, D.L. Klein, J. Electrochem. Soc. **114**, 965 (1967).

131. E. D. Palik, H. F. Gray, P. B. Klein, J. Electrochem. Soc. 130, 956 (1983).
132. J. P. Krume, M. E. Strumanis, Trans. Metall. Soc. AIME 239, 395 (1967).
133. M. M. Faktor, D. G. Fiddyment, M. R. Taylor, J. Electrochem. Soc. 122, 1566 (1975).
134. B. D. Chase, D. B. Holt, J. Electrochem. Soc. 119, 314 (1972).
135. M. I. J. Beale, J. D. Benjamin, M. J. Uren, N. G. Chew, A. G. Cullis, J. Cryst. Growth 73, 622 (1985).
136. H. C. Gatos, M. C. Levine, J. Electrochem. Soc. 107, 433 (1960).
137. D. B. Holt, J. Mater. Sci. 23, 1131 (1988).
138. P. C. Searson, J. M. Macaulay, Nanotechnology 3, 188 (1988).
139. G. H. Gilmer, Science 208, 355 (1980).
140. E. Ben-Jacob, P. Garik, Nature (London) 343, 523 (1990).
141. P. Meakin in: The Fractal Approach to Heterogeneous Chemistry, D. Avnir (ed.), Wiley, New York (1989), p. 131.
142. W. W. Mullins, R. F. Sekerka, J. Appl. Phys. 34, 323 (1963); idem, ibid. 35, 444 (1964).
143. R. L. Smith, S. D. Collins, Phys. Rev. B39, 5409 (1989).
144. R. L. Smith, S. F. Chuang, S. D. Collins, Phys. Rev. B39, 5409 (1989).
145. T. A. Witten, L. M. Sander, Phys. Rev. Lett. 47, 1400 (1981).
146. T. A. Witten, L. M. Sander, Phys. Rev. B 27, 5686 (1983).
147. J. Erlebacher, P. C. Searson, K. Sieradzki, Phys. Rev. Lett. 71, 3311 (1993).
148. J. Erlebacher, K. Sieradzki, P. C. Searson, J. Appl. Phys. 76, 182 (1994).
149. J.-N. Chazalviel, M. Etman, F. Ozanam, J. Electroanal. Chem. 297, 533 (1991).
150. M. Etman, M. Neumann-Spallart, J.-N. Chazalviel, F. Ozanam, J. Electroanal. Chem. 301, 259 (1991).
151. F. Ozanam, J.-N. Chazalviel, A. Radi, M. Etman, Ber. Bunsenges. Phys. Chem. 95, 98 (1991).
152. H. Gerischer, M. Lubke, Ber. Bunsenges. Phys. Chem. 92, 573 (1988).
153. J.-N. Chazalviel, Electrochim. Acta. 37, 865 (1992).
154. H. E. Hessel, A. Feltz, M. Reiter, U. Memmert, R. J. Behm, Chem. Phys. Lett. 186, 275 (1991).

Advances in Electrochemical Science and Engineering
Edited by Heinz Gerischer and Charles W. Tobias

In-Situ Fourier Transform Infrared Spectroscopy: A Tool to Characterize the Metal-Electrolyte Interface at a Molecular Level

T. Iwasita[1] and F.C. Nart[2]

[1] Institute for Physical Chemistry, University of Bonn, Römerstraße 164, D-53179 Bonn, Germany
[2] Institute for Physics and Chemistry of São Carlos, University of São Paulo, Brazil

Contents

List of Symbols

a_{jk}	coefficients in Taylor expansion
c	velocity of light
d	depth, thickness
e	elementary charge
E	electrode potential
E_T	potential of reference electrode
E_0^M	potential of zero charge (pzc)
$\boldsymbol{E}$	electric field
I	intensity of solution loss band
M_x, M_y, M_z	dipole moment components in cartesian axis directions
$M_z(Q)$	dipole moment function
n	refractive index
N	number of IR-active species
k	absorption coefficient
p	linearly polarized light parallel to the reflection plane
$\boldsymbol{P}_0'$	permanent dipole moment
Q	normal coordinate
R	reflectivity
s	linearly polarized light perpendicular to the reflection plane
$T(\delta)$	truncation function
$U(Q)$	potential energy function
α	angle of incidence; polarizability
Γ	surface concentration
δ	moving mirror retardation of Michelson interferometer
δ_{SE}	change in absorption caused by the electric field
Δ	absorption
ε	dielectric function
ε_0	permittivity of free space
θ	angle of incidence; degree of coverage
λ	wavelength of radiation
μ	dipole moment
ν	frequency of radiation
$\bar{\nu}$	wavenumber of radiation
ϕ^M	work function
Ψ_v	eigenfunctions of vibrational states
ω	frequency of radiation
Ω	vibrational frequency of a molecule

Abbreviations

ACN	acetonitrile
ATR	attenuated total reflection
BS	beam splitter
dc	direct current
d.l.	double layer
EELS	electron energy loss spectroscopy
EMIRS	electrochemically modulated infrared spectroscopy
FTIRS	Fourier transform infrared spectroscopy
FT-IRRAS	Fourier transform infrared reflection-absorption sepctroscopy
h.e.r.	hydrogen evolution reaction

IRRAS	infrared reflection-absorption spectroscopy
PA	propargyl alcohol
PMIRRAS	polarization modulation infrared reflection-absorption spectroscopy
p.z.c.	potential of zero charge
SCF	self-consistent field
SERS	surface enhanced Raman spectroscopy
SFG	sum frequency generation
SNIFTIRS	subtractively normalized Fourier transform infrared spectroscopy
TBAP	tetrabutylammonium perchlorate
UHV	ultrahigh vacuum
upd	under potential deposition

1 Introduction

The increasing application of spectroscopic methods in electrochemistry has characterized the last decade and marked the beginning of new developments in electrochemical science [1]. Among these methods, in-situ infrared spectroscopy provides a very useful tool for characterizing the electrode-solution interface at a molecular level. First in-situ infrared (IR) electrochemical measurements were performed in 1966 [2] using the *internal* reflection form [3]. However, problems in obtaining very thin metal layers on the surface of the prisms used as IR windows, delayed the extensive application of in-situ IR spectroscopy until 1980, when the method was applied in the *external* reflection form [4]. The importance of this step does not need to be emphasized today.

The external absorption-reflection method, originally developed for grating spectrometers, required the modulation of the electrode potential (at *c.* 12 Hz) during the measurement of the spectrum [5]. A further development was achieved by modulating the state of polarization of light (s−p modulation) while keeping the electrode at a constant potential [6]. But the most important improvement [7, 8] was achieved by the use for Fourier transform (FT) instruments [9]. The high rate of collection of spectra in this case makes unnecessary the modulation of potential, thus giving the possibility of collecting spectra during the application of any desired potential program. The number of groups using in-situ external reflection FTIR spectroscopy is growing continuously.

A significant improvement in the internal reflection technique for in-situ electrochemical measurements was achieved in 1981 with the use of FT spectrometers [10]. Since then the technique has been used to study a variety of systems such as semiconductor processes [11, 12], metal corrosion [13], and polymerization reactions [14].

The importance gained by IR spectroscopy in electrochemistry was a justified reason for the publication of numerous monographs where the basis of the method as well as examples and applications have been comprehensively covered [15−18]. However, considerable progress has been achieved in the last few years and this makes

it necessary to sample the experience gained in the different groups which are working with the method worldwide. Some details of the method, which has been described extensively in earlier work will be given briefly here when necessary. The analysis of the state-of-the-art is not only important for those who are interested in the application of the method –, it should also be of help to establish further goals in the development of the experimental technique. It is in this sense that we have selected the examples given as applications of the method.

2 The Fourier Transform Infrared Method

2.1 The Working Principle of a Fourier Spectrometer

A Fourier transform infrared spectrometer is based on the use of an interference pattern resulting from the passage of polychromatic radiation from an IR source through a Michelson interferometer. After passing through the interferometer the beam reaches the sample and its interference pattern changes because of the absorption of radiation by the sample. The signal is then detected and finally decoded by means of a Fourier transform calculation. The result of this operation is the ordinary single-beam spectrum.

A schematic diagram of a Fourier transform instrument is given in Fig. 1. The simplest form of the Michelson interferometer consists of two mutually perpendicular mirrors, one of which can move in the direction of the beam. Between both mirrors there is a beam-splitter where the radiation is partially reflected (to the moving mirror) and partially transmitted (to the fixed mirror). Both parts of the beam return to the beam-splitter where, because of the difference in path (δ), they interfere. The resultant beam is again divided into two parts (transmitted and reflected). One of these parts is focused to the sample and then to the detector.

2.2 The Interferogram

The detected signal, known as an interferogram, shows the changes of the beam intensity as a function of the retardation δ of the moving mirror. Though the spectral information is not recognizable in the interferogram, this contains the data of the measurement without any mathematical manipulation. It is therefore worthwhile paying some attention to its characteristics.

For monochromatic radiation of wavenumber $\bar{\nu}\,(= 1/\lambda)$, the interferogram can be described by a cosine function:

$$I(\delta) = 0.5\, I(\bar{\nu}) \cos 2\pi \bar{\nu} \delta \tag{1}$$

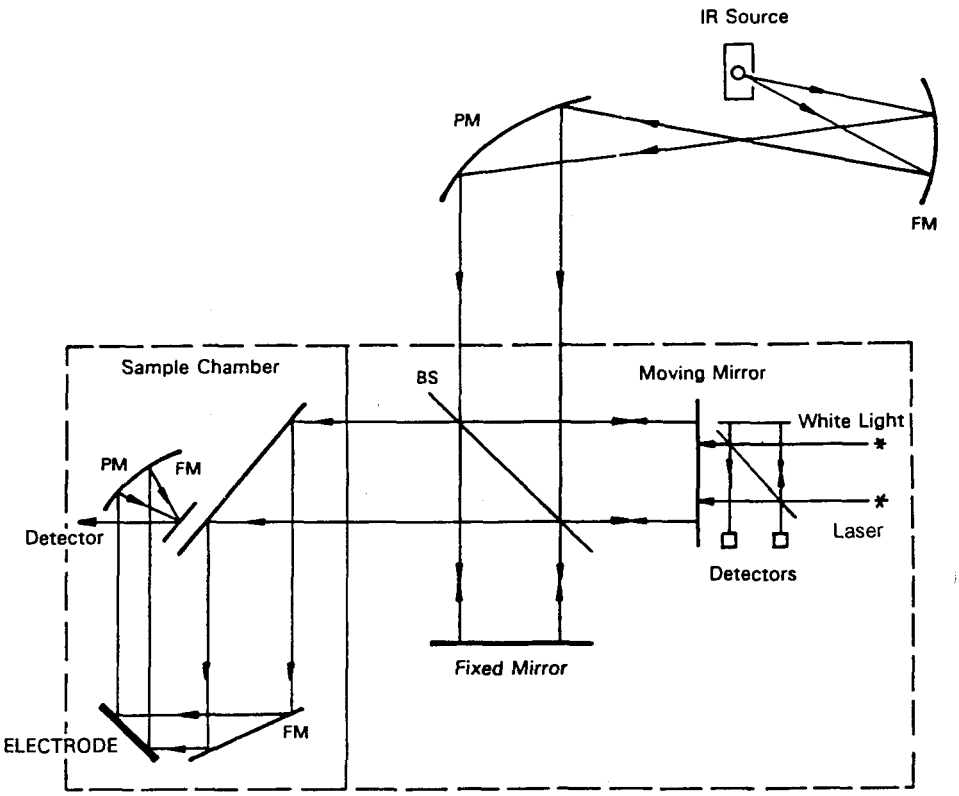

Fig. 1. Scheme of a Fourier transform infrared spectrometer with a Michelson interferometer. BS, beam splitter; FM, focussing mirror; PM, parallelizing mirror. (Adapted from [16]).

Thus the interferogram of a monochromatic source has the form depicted in Fig. 2a. The signal goes through the constant-dc value ($0.5\,I(\bar{\nu})$) at all points where $\delta = n\,\lambda$ (where n is an integer).

The interferogram of a polychromatic source exhibits a maximum at $\delta = 0$, which is called a centerburst (Fig. 2b). At zero retardation both parts of the beam have equal optical path and consequently neither constructive nor destructive interference is produced: all frequencies pass the beam splitter undisturbed and the intensity reaches a maximum.

In an FTIR spectrometer the maximum retardation δ_m determines the resolution of the spectrum. For two spectral lines separated by $\Delta\bar{\nu} = (\bar{\nu}_2 - \bar{\nu}_1)$ the respective cosine waves are out of phase for all values of $\delta \neq (\Delta\bar{\nu})^{-1}$ and become in phase again after a retardation $\delta = (\Delta\bar{\nu})^{-1}$. Therefore, in order to separate both lines, the maximum retardation must be equal to the reciprocal of the resolution:

$$\delta_m = (\Delta\bar{\nu})^{-1}$$

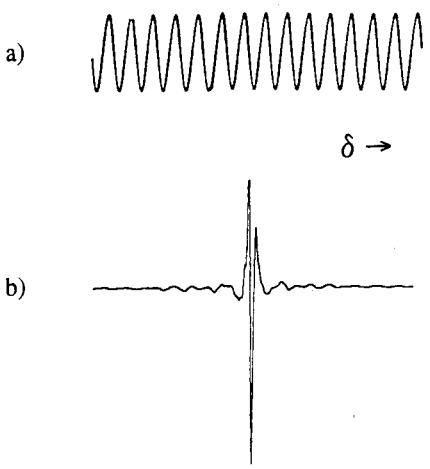

Fig. 2. Interferograms for a monochromatic (a) and a polychromatic source (b).

The height of the centerburst can be taken as a measure for the sensitivity of the measurement. However, since the signals beyond the centerburst contain the spectral information, the big difference in intensities between the centerburst and the rest of the interferogram is one of the factors limiting the quality of a spectrum. Lowering this difference improves the signal-to-noise ratio. This can be accomplished by filtering undesired frequency regions out of the spectrum, so that the only radiation reaching the detector is that containing useful information.

2.3 The Signal-to-Noise Ratio

One of the problems of infrared spectroscopy is the low energy per unit time from usual infrared sources[1] and the relatively high internal noise of infrared detectors. Since these are the basic working conditions, infrared spectrometers must be designed to have a high energy throughput in order to improve the signal-to-noise ratio.

Prisms or grating monochromators allow the observation of a narrow frequency domain during the spectrum recording, which is determined by the width of the exit slit. Thus grating spectrometers have a serious limitation in the energy throughput, particularly at high resolution when very narrow slits are required. Interferometers as used in a Fourier transform spectrometer do not require slits, thus enabling higher throughput of radiation.

The second advantage of Fourier transform instruments is the so-called multiplex advantage. This is related to the fact that in a Fourier transform spectrometer, in con-

[1] The problem is praticularly serious for the very weak metal-adsorbate bonds which are expected in the far-infrared region. Recently the IR radiation from a synchrotron has been used as a source for in-situ measurements at the electrode-solution interface [19]. The far-IR radiation from a synchrotron has an intensity between 100 and 1000 times higher than standard black body sources.

trast to a grating instrument, the detector is viewing all frequencies all the time during the measurement. Consequently, the signal-to-noise ratio of spectra measured on a Fourier transform spectrometer will be greater than that of a spectrum measured in the same time and at the same resolution on a grating instrument. The multiplex advantage is proportional to the number M of frequency elements observed and is given by $(M)^{1/2}$ [9]. Thus for a measurement between 4000 cm^{-1} and 400 cm^{-1} at a resolution of 4 cm^{-1} the multiplex advantage is $\sqrt{900}$, or 30.

The time necessary for one interferometer scan depends on the required resolution. Typically *c.* 0.3 s or less is needed for a resolution of 8 cm^{-1}. However, in order to diminish the electronic noise and make use of the multiplex advantage, several interferograms are scanned, added, and averaged, in a couple of minutes.

2.4 The Single-Beam Spectrum

The encoded spectral information in the interferogram (I (δ)) is stored in a computer and transformed into the more familiar form of a single-beam spectrum (Fig. 3) by means of a fast Fourier transform.

For polychromatic radiation Eq. (1) must be written in the form of an integral covering all the frequencies:

$$I(\delta) = \int_{-\infty}^{+\infty} I(\bar{\nu}) \cos 2\pi\bar{\nu}\delta \, d\bar{\nu} \tag{2}$$

The Fourier transform gives the desired intensity as a function of the wavenumber:

$$I(\bar{\nu}) = \int_{-\infty}^{+\infty} I(\delta) \cos 2\pi\bar{\nu}\delta \, d\bar{\nu} \tag{3}$$

Equation (3) implies an integration between $-\infty$ and $+\infty$ with an infinitely high resolution. But we have a limit for the maximal retardation of the interferogram δ_m and this means that we are multiplying the interferogram by a truncation function $T(\delta)$, which fulfills the conditions:

$$T(\delta) = 1 \quad \text{if} \quad -\delta_m \leq \delta \leq \delta_m$$

$$T(\delta) = 0 \quad \text{if} \quad -\delta_m \geq \delta \geq \delta_m$$

So, the function representing the calculated single-beam spectrum is:

$$I(\bar{\nu}) = \int_{-\infty}^{+\infty} I(\delta)\, T(\delta) \cos 2\pi\bar{\nu}\delta \, d\bar{\nu} \tag{4}$$

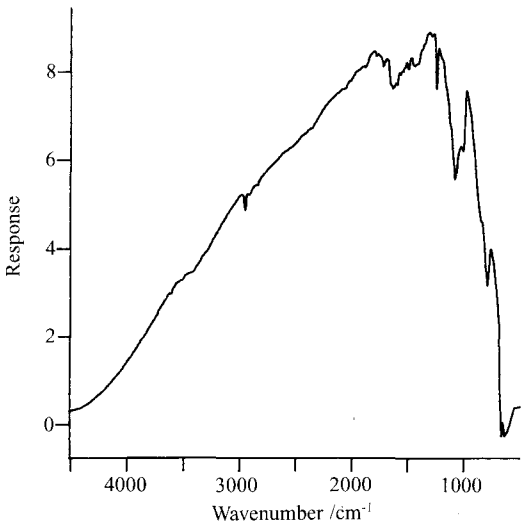

Fig. 3. Single-beam spectrum resulting from the Fourier transformation of the interferogram in Fig. 2b.

The computation of the Fourier transform requires the values of δ to be given very precisely. For this purpose the FTIR spectrometer is provided with two additional interferometers, one for a laser beam and another for a white light source. Both of them are mechanically coupled to the moving mirror of the main interferometer (see Fig. 1). The laser, being a monochromatic source of a very accurately known frequency, gives an output sine wave with an accurately known period. It is therefore used to follow the position of the moving mirror. Each zero crossing of the sine wave is taken to digitize the displacements of the moving mirror in the main interferometer. The centerburst of an interferogram from the white light beam is used to indicate the start position for data collection; in this way repetitive scans begin always at the same position of the moving mirror in the main system.

3 Reflection-Absorption Infrared Spectroscopy

The development of infrared reflection-absorption spectroscopy to study gas-phase/solid interface started as a necessary step to avoid the practical limitations imposed by the use of oxide-supported metals [20]. This improvement opened the possibility of studying adsorbed species on well-defined metal surfaces, from which a considerable knowledge of the vibrational properties at the gas-phase/metal interface has been gained [21]. This information from ultrahigh vacuum (UHV) systems provides the basis for the application of the infrared technique to studying the (more complex) electrochemical interface.

3.1 The Band Intensity

The absorption of infrared radiation by a submonolayer of adsorbed material is the result of the interaction of the electric field of the light with the vibrating molecule and with the electrons of the metal surface. Therefore intensity of absorption is determined to a great extent by the dielectric properties of the metal [20]. The absorption, Δ, is measured as a difference in reflectivity with (R) and without (R_0) absorbing material

$$\Delta = \frac{R_0 - R}{R_0} \tag{5}$$

Searching for the conditions to obtain a maximum value for Δ, Greenler [20] in 1966 developed a theory of reflection-absorption at metal surfaces.

When light is reflected on a metal surface the amplitude of the standing wave at the surface, which results from the sum of the electric vector of incident and reflected beams, depends on both the state of light polarization and the angle of incidence. This is a consequence of the phase shift upon reflection, as illustrated in Fig. 4a and b. The component perpendicular to the plane of incidence (s-polarized field) presents a phase shift of *c.* 180°, for all angles of incidence. On the other hand, the phase change for the parallel component (p-polarized field) remains small until high angles, where it changes rapidly toward 180° at the grazing angle. This phenomenon

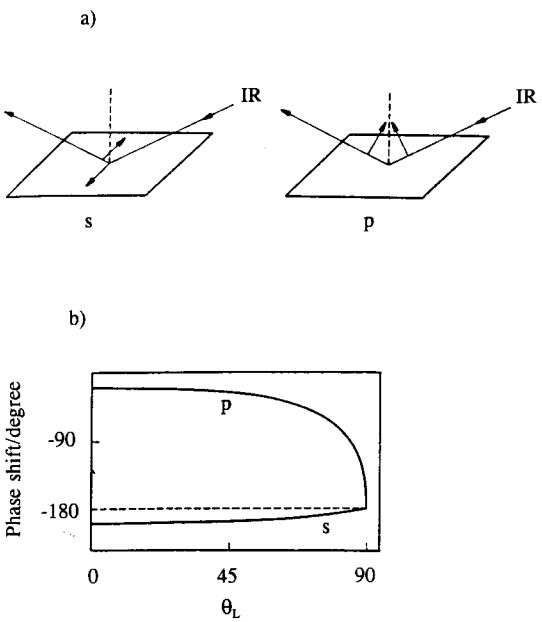

Fig. 4. Phase shifts upon reflection on a metal surface for p- and s-polarized radiation. (a) Incident and reflected field vector; (b) phase shift as a function of the angle of incidence.

has direct consequences on the intensity of light available for absorption, as we shall see by considering the magnitude of the electric field upon reflection.

The intensity of a spectral band is a measure of the dissipation of electromagnetic energy by the absorbing medium. In such a medium the change in the energy flow is proportional to the square of the electric field. Therefore the behavior of the electric field at a metallic surface is important for an understanding of the optical factors governing the intensity of light absorption. The ratio of the electric field at the surface (E) to the electric field of the incident beam (E_0) is plotted as a function of the angle of incidence in Fig. 5 for s- and p-polarized radiation. For s-polarized radiation the electric field of the standing wave has negligible values at all angles of incidence. On the contrary the effective field for p polarization grows with the angle of incidence and is almost doubled at angles close to grazing incidence.

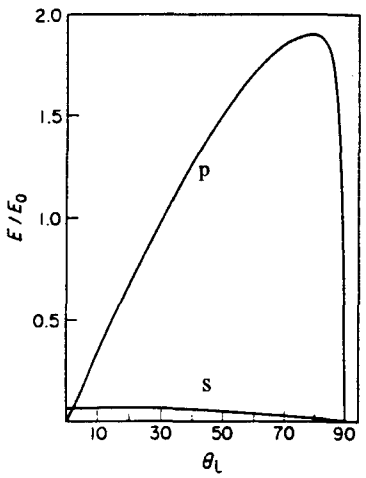

Fig. 5. Normalized electric field at the reflecting surface as a function of the angle of incidence.

Two obvious consequences can be extracted from the plot of Fig. 5. One is that in order to have high values of the electric field at the surface, the incident (p-polarized) light should be reflected almost at grazing angle. The second, which can also be deduced from Fig. 4, is that the metallic substrate imposes a condition for the IR activity of dipolar species on the surface, known as the surface selection rule:

Only modes with a dipole moment perpendicular to the surface are IR-active.

In practice, s- and p-polarized radiation are used to discriminate between spectral features due to absorbates or solution species; we shall return to this subject in Sec. 4.4.

Greenler approached the problem of the calculation of the absorption Δ by describing the absorbing material on the surface as a dielectric with optical constants approaching the values of the adsorbate in the solid or liquid state. The calculation of Δ according to Greenler [20] requires solution of a set of relatively complicated expressions to evaluate the electric field at the surface. More simplified treatments

of the problem were proposed by Ibach (see [22]) and Persson [23]. The latter considers in his model the discrete structure of the monolayer, as follows.

The intensity of energy absorption by an adsorbed molecule is the result of a non-zero transition probability in the direction normal to the surface. Basically, Persson [23] calculates the transition probability using the Hamiltonian:

$$H = -\mu \cdot E(0) \tag{6}$$

for the energy of interaction between one adsorbed molecule and the electric field at the surface ($x = 0$). The electric field on the surface in the presence of an adsorbed layer is considered to be the same as on the bare metal. Moreover the expression for the E-field assumes that this remains unaltered close to the surface where there may be fluctuations in the E-field due to the ion cores of the metal. With these simplications, Persson gives the following expression for the absorption:

$$A(\omega) = \frac{16\pi^2}{\hbar c} \frac{N}{A} \mu^2 \Omega G(\alpha) \delta(\Omega - \omega) \tag{7}$$

N/A represents the surface coverage by species, μ is the magnitude of the dipole moment perpendicular to the surface, Ω is the vibrational frequency, ω is the frequency of the incident radiation and $G(\alpha)$ is a reflectivity factor containing the angle of incidence, α, and the dielectric function of the metal, ε:

$$G(\alpha) = \frac{\sin^2 \alpha}{\cos \alpha} \left| \frac{\sqrt{\varepsilon} \cos \alpha}{\sqrt{\varepsilon} \cos \alpha - 1} \right|^2 \tag{8}$$

As expected, this function goes through a maximum at incident angles close to grazing incidence. A plot of $G(\alpha)$ against α is given in Fig. 6.

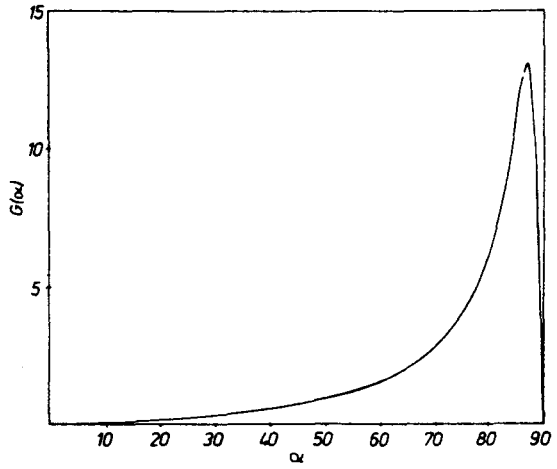

Fig. 6. Change in the reflectivity as a function of the angle of incidence. $G(\alpha)$ is defined through Eq. (8). (After [23]). Reprinted by permission of Pergamon Press.

The validity of Eq. (7) was checked by comparing the calculated dipole moments of CO adsorbed on Cu and Pt with the corresponding values from inelastic electron scattering and from IR spectra in the gas phase [23]. For this purpose, Eq. (7) was written in the form of the integrated band intensity:

$$\int d\omega \, \Delta(\omega) = \frac{16\pi^2}{\hbar c} \frac{N}{A} \mu^2 \Omega \, G(\alpha) \tag{9}$$

This is the mathematical expression for the integrated band intensity obtained from an IR reflection-absorption experiment.

3.2 Vibrational Frequencies and Bandshapes

The analysis of the vibrational frequencies of adsorbed species on electrodes can give information on the structure and orientation at the surface. These properties can be extracted from analysis of the frequencies and the number of bands observed. The latter is a function of the adsorption geometry and requires the application of group theory to adsorbed species (see [22]).

Frequency shifts are usually observed as a consequence of interactions with neighboring species, with the metal substrate, and with the electric field at the interface. These phenomena have often been studied in connection with the adsorption of carbon monoxide (Secs. 6 and 10) and more recently with the adsorption of ions (Secs. 9 and 10).

Another important parameter giving information on the adlayer interactions is the bandshape. The experimental phenomena causing a band broadening have been classified in two groups: homogeneous and inhomogeneous broadening.

A *homogeneous broadening* is caused by interaction of the adsorbate with the metal [21]. Coupling with surface phonons is possible, for instance, when an adsorbate mode frequency lies near some substrate phonon frequency. Another mechanism of homogeneous broadening is electron-hole pair creation. In this case the oscillating molecule can excite electron-hole pairs. The periodic charge fluctuation diminishes the lifetime of the vibrational excited state, thus causing a band broadening, as expected from the uncertainty principle. One interesting example of this lifetime broadening is that of CO adsorbed on metals. It was established that on Cu(100) and Pt(111) the CO stretch has a lifetime of a few picoseconds, in contrast to the radiative lifetime of milliseconds in the gas phase or micro-to nano-seconds on insulators [24].

An *inhomogeneous broadening* refers to the collective motion frequency of the adsorbate and is the consequence of an inhomogeneous distribution of individual molecules either due to heterogeneity of adsorption sites or to nonhomogeneous intermolecular distances. Whilst for a perfect ordered layer a sharp, symmetric band is expected, random occupation, island formation, and repulsive or attractive interactions give rise to a variety of characteristic lineshapes [21].

4 In-situ External Reflectance Infrared Spectroscopy in Electrochemistry

4.1 The Spectroelectrochemical Cell

The cell shown in Fig. 7 has been designed to be placed outside the sample compartment of the spectrometer. It has the advantage of requiring only a small volume of electrolyte (*c.* 5 ml). The solution can be replaced while the working electrode is kept under potential control. This can be very useful in adsorption experiments with organic fuels, as we shall see in the sections devoted to adsorption of alcohols.

Working electrodes consist of well-polished metal disks embedded in a glass tube. To offset the solvent absorption, particularly in aqueous solutions, the electrode must be placed at a distance of 1 – 5 μm from the IR-window. A reasonably flat surface can be obtained after careful mechanical polishing.

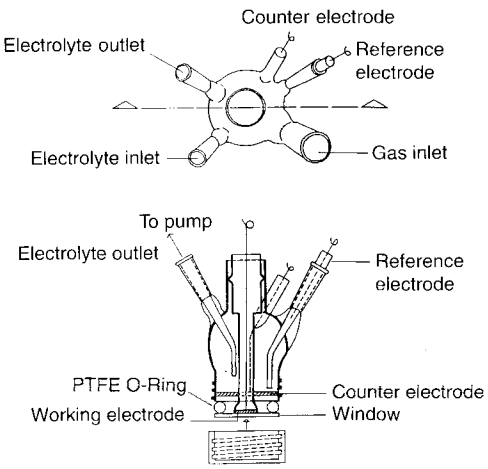

Fig. 7. Electrochemical cell designed for spectroscopic measurements.

4.2 The Form of the Spectra

Relatively weak signals are expected from submonolayers of adsorbed species on the electrode surface and, in addition, these signals have to be extracted from a single-beam spectrum containing strong features from the background. This can be achieved by *subtracting* two spectra taken either (1) using two states (s and p) of light polarization (see, the surface selection rule, or Sec. 4.2.1 (2) applying two different

potentials, where the surface process of interest undergoes some change with the potential while the background remains constant.

Unfortunately the tendency to create expressions just highlighting some particular experimental approach have led to an unnecessary multiplicity of names in the literature for the in-situ IR method. They give the erroneous impression that a large number of different mehtods exist, while in fact these are only different experimental approaches all using the same basic principle: the subtraction of two spectra measured either at two potentials or under two conditions of light polarization.

4.2.1 The Use of Polarization Modulation

The technique of subtracting spectra taken with linearly s- and p-polarized radiation is based on the surface selection rule for reflection-absorption on a metal surface [20]:

> Only vibrational states involving changes in dipole moment components perpendicular to the reflecting surface can interact with the electric field of infrared radiation.

Therefore, only p-polarized radiation which has an electric field vector parallel to the plane of incidence can interact with absorbed species at the surface. On the contrary, s-polarized light, having the electric field vector perpendicular to the plane of incidence, can interact only with species in solution.

The technique using p−s modulation has received different names depending on the kind of IR instrument used. Thus for grating instruments it was called PMIRRAS (polarization modulation infrared reflection-absorption spectroscopy) [6]. For FT spectrometers the name FTIRRAS [8] was suggested. However this name was later used also in connection with Fourier transform spectra applying the potential difference approach.

A p−s modulation is performed by placing a photoelastic modulator (PEM) in the optical path of the spectrometer. Thus the difference spectrum at a given potential calculated as

$$(I_p - I_s)/(I_p + I_s) \tag{10}$$

is expected to contain *only* bands of adsorbed species. We shall see in Sec. 4.4 that this statement can be valid only under particular experimental conditions and for these reasons this technique has serious limitations.

4.2.2 The Use of Spectra Taken at Two Potentials

In the techniques using the potential difference, the ratio

$$(R_0 - R_1)/R_0 \tag{11}$$

is calculated, where R_0 and R_1 are reflectances at the two potentials. Thus positive- and negative-going features are expected, depending on whether $R_0 > R_1$ or $R_0 < R_i$ (i.e., on whether a substance is formed or consumed at the potential of spectrum R_1). However, some authors compute the difference $(R_1 - R_0/R_0$ (or simply the ratio R_1/R_0); then loss and gain features at the potential of the spectrum R_1 are opposite to the former case.

Techniques of taking the sample and reference spectra at two potentials have received different names depending on the kind of spectrometer used or on the applied potential program. Thus EMIRS [5] (electrochemically modulated infrared reflection spectroscopy) takes the spectrum by slowly scanning the frequencies with a grating instrument, while the electrode potential is modulated between two given values at *c.* 12 Hz. The equivalent of this approach using a Fourier transform instrument has received the name SNIFTIRS (substractively normalized Fourier transform infrared spectroscopy) [25]. In this case spectra are measured by repeating many times the collection of a given number of scans at each of the two potentials.

In fact, these procedures (EMIRS or SNIFTIRS) should be used only when the system under study undergo reversible changes with potential [16]. Bipolar bands are obtained in the difference spectrum for species irreversibly adsorbed, if the band-center frequency is shifted with the potential, e.g., CO adsorbed on platinum (Fig. 8a). But the situation is problematic when the frequency shift with potential is negligible. Then *signals cancel out* in the computed spectrum. This question has giv-

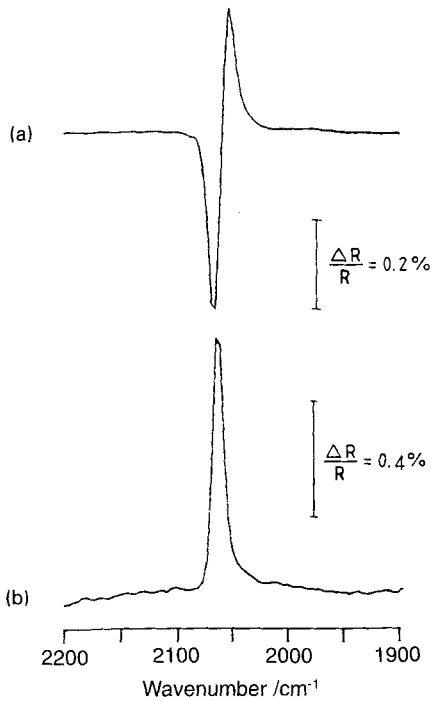

Fig. 8. Comparison of bipolar and absolute bands for adsorbed CO; difference spectrum calculated with two spectra taken in the presence of adsorbed CO at 0.05 V and a spectrum at (a) 0.40 V vs. RHE and (b) 0.8 V vs. RHE (after CO was totally oxidized).

en rise to erroneous conclusions related to the absence of features in the difference spectrum of some irreversibly adsorbed substances. Bipolar bands can only be used qualitatively. They indicate the presence of some species absorbing in the given range of wavenumbers. They do not permit, however, any quantitative interpretation based on the band intensity. In fact, in such cases one cannot measure a band intensity at all. Also, the band centers corresponding to the two potentials cannot be extracted from a bipolar band. Some important parameters, such as the bandshape and halfwidth, which can give important information related to the interactions in the adsorbed layer (see Sec. 3.4), are lost under a bipolar band.

Working with irreversible systems it is necessary to collect spectra using appropriate potential programs in order to obtain *absolute* bands. This can be achieved, for instance, by collecting one spectrum at a potential where the species is adsorbed and a second one after applying a potential at which the adsorbate is totally eliminated from the surface, e.g., through oxidation. In Fig. 8b we present a spectrum for adsorbed carbon monoxide obtained as the difference of two spectra measured at 0.05 V and 0.8 V vs RHE. The positive-going band for the difference spectrum at the two potentials $(R_{0.8}-R_{0.05})/R_{0.05}$ indicates the complete oxidation of CO at 0.8 V. Other examples of this and alternative methods of obtaining absolute bands, will be given in the sections dedicated to electrocatalysis.

4.3 Criteria to Distinguish Between Solution and Adsorbate Bands

Most of the solvents used in electrochemistry, and particularly water, present strong absorption in the mid-IR range. Therefore the use of external reflection IR spectroscopy for the in-situ observation of electrode processes requires a considerable reduction in the solution thickness in the path of the IR beam. Only a very thin layer of electrolyte between electrode and IR window is allowed in order to have enough energy reaching the electrode surface. Typically, the thickness of the solution layer produced by a well-positioned, flat-polished electrode is of the order of $1-5\,\mu m$. Within this cavity, which has been described by Yeager et al. as *diffusionally decoupled,* migration is the predominant form of mass transport [26].

A potential step produces changes in the composition of the solution in the thin layer, which can cause bands in the spectrum [26–30]. A systematic analysis of these effects is necessary in order to discuss the criteria for establishing the origin of spectral signals.

4.3.1 Double Layer Charging Effects

When a potential step is applied, the migration of a number of ions equivalent to the charge involved in the double layer (d.l.) charging is to be expected. Weaver et al. [28] have shown this effect using a gold electrode and $NaClO_4$ as a base electrolyte. A gold electrode, which has a wide double layer region, is the appropriate material to investigate this effect. The intensity of the solution band due to ClO_4^- ions

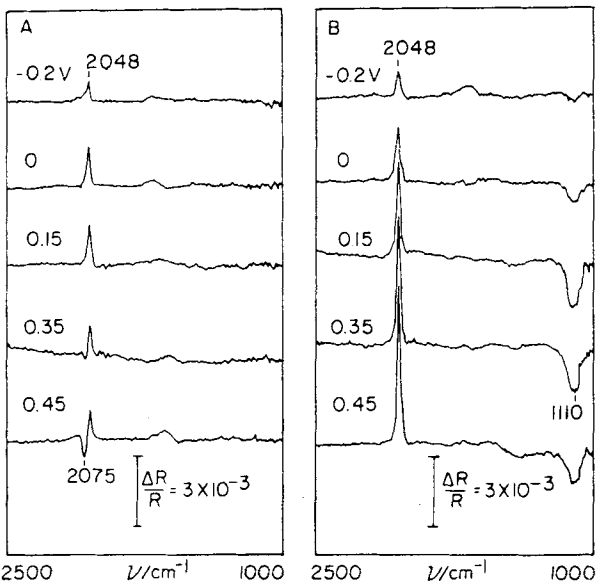

Fig. 9. Comparison of spectra in the 1000–2500 cm^{-1} region for azide adsorption at gold for (A) a single electrolyte (0.05 M NaN_3), and (B) a mixed electrolyte (0.05 M NaN_3 + 0.5 M $HClO_4$). Sample potentials as indicated, reference potential −0.6 V vs. SCE. (Reproduced from [28] by permission of Elsevier Science).

increases linearly with the increase in positive charge at the metal electrode. The spectra of adsorbed azide (N^{3-}) on gold obtained after application of a potential step, strongly depend on whether or not a base electrolyte is present (Fig. 9). The bands for adsorbed azide are considerable larger when ClO_4^- is used to reduce the migration of azide ions as the potential is shifted positively. A larger amount of azide remains avialable in the thin layer.

4.3.2 Faradaic Surface Effects

Working with a Pt electrode in the potential range between 50 and 1500 mV, hydrogen adsorption-desorption and oxide formation cause a change in the concentration of hydrogen ions:

$$Pt-H \rightarrow Pt+H^+ + e^- \tag{12}$$

$$Pt+H_2O \rightarrow PtOH+H^+ + e^- \tag{13}$$

In a thin layer having a volume of 1 $cm^2 \times 1$ μm, containing a 0.1 M solution of a 1:1 electrolyte, 1×10^{-8} gram-equivalent of ions of each sign are present. This quantity is comparable with the amount of protons produced during the desorption

of a monolayer of hydrogen on polycrystalline platinum (2.2×10^{-9} gram-equivalent/cm^2). Thus, the increase in concentration of hydrogen ions during the desorption of a monolayer of hydrogen cannot be neglected.

The migration of ions to recover the equilibrium of charges is a relatively fast process. Under thin layer conditions in 1 M $HClO_4$ the time for the current to drop to the ground level, after applying a potential step of 100 mV within the H-region, lies below 0.1 s. Thus the system recovers a charge equilibrium in a timescale below that of the FTIR experiment (several seconds). Taking the ionic conductivities of H^+ and ClO_4^-, the respective limiting transport numbers of 0.84 and 0.16 can be calculated. This means that, although most of the H^+ ions produced can migrate out of the thin layer, transporting the positive charge required by the electroneutrality condition, about 16% of the charge is neutralized through the migration of ClO_4^- ions from the solution outside. This causes an enrichment of $HClO_4$ in the thin layer. The leveling-out of concentrations with the solution outside has a large timescale. The diffusion of species can take several minutes and, depending on the actual size of the thin layer, it can be completed in hours. Therefore ion concentration changes produced by migration are detected during the FTIR experiment. This is a source of problems in the technique since most of the usual supporting electrolytes are infra-

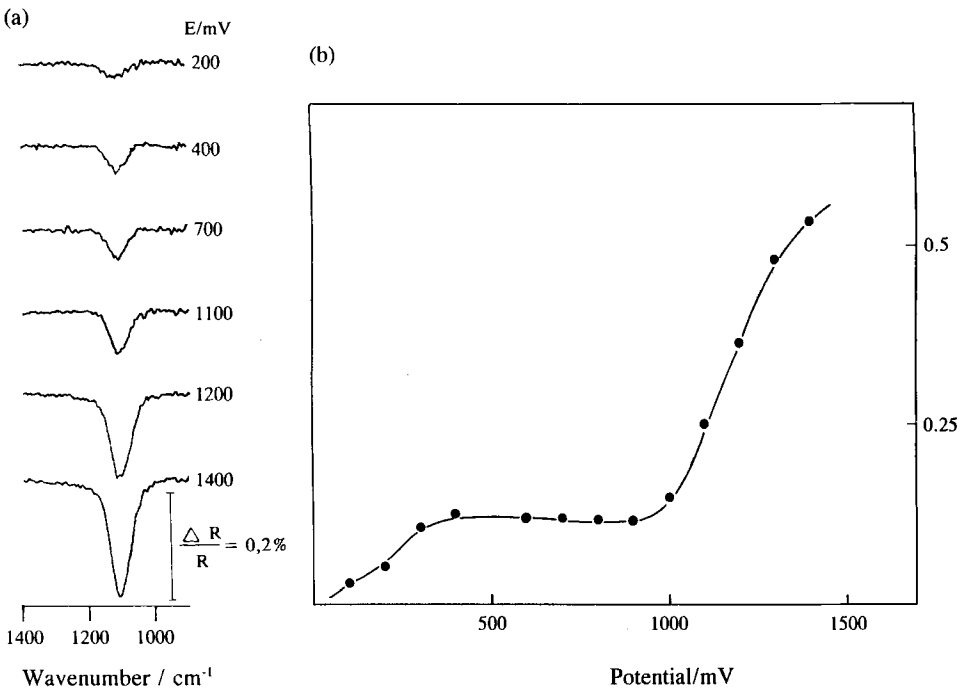

Fig. 10. Typical spectral features for solution species. (a) Band for the asymmetric Cl–O vibration of ClO_4^- ions, measured with s-polarized light. Spectra calculated as the ratio between the single-beam spectrum at the sample potential (as indicated) and a spectrum at 0.05 V. (b) Integrated band intensity for the Cl–O stretching of perchlorate ions in solution as a function of potential.

red-active, thus causing bands in the spectra which sometimes overlap on features of the system under study. At the same time the transport of water, which accompanies the ion migration, produces additional features in important regions of the spectra.

Figure 10a and b shows the effect of applying an increasing positive potential to a plantinum electrode in $HClO_4$ solution. The integrated band intensities were taken from spectra measured with s-polarized radiation. The intensity of the band at 1100 cm^{-1}, which is due to the asymmetric mode of ClO_4^- ions in the solution, follows the changes in H^+ concentration in the thin layer.

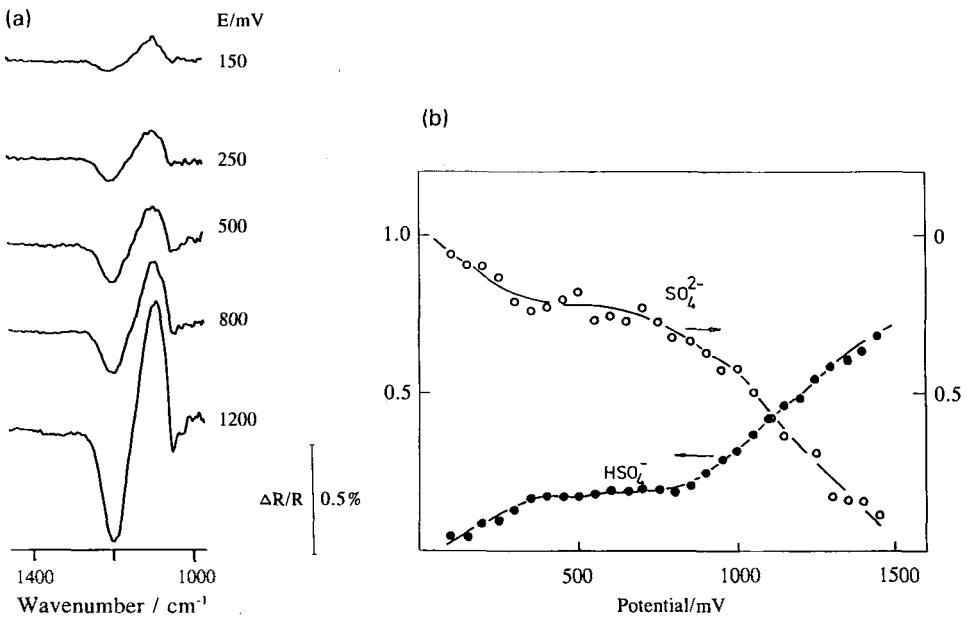

Fig. 11. (a) Spectral features for sulfate species in solution, measured with s-polarized light at the indicated potentials; reference spectrum taken at 0.05 V vs. RHE. Loss band at 1120 cm^{-1}: asymmetric S–O stretch of SO_4^{2-}; gain band at 1190 cm^{-1}: asymmetric stretch of HSO_4^-. Solution: 0.5 M K_2SO_4 + 0.01 M H_2SO_4. (b) Integrated band intensities as a function of potential.

A second aspect of this problem must be considered: the situation in the presence of weak-acid-base systems [26, 27, 29]. Protonation of solution species having IR active modes causes gain and loss of solution features which appear in the spectrum, complicating its interpretation. Figure 11a and b shows an increase in intensity of the gain band for HSO_4^- (1190 cm^{-1}) and loss band for SO_4^{2-} (1120 cm^{-1}) at increasing positive potentials in a solution containing 0.5 M K_2SO_4 and 0.01 M H_2SO_4. The spectra were obtained using s-polarized radiation taking a reference spectrum at 50 mV vs. RHE [27]. The same bands were also detected using p-polarized radiation.

4.3.3 Adsorption

If the potential change causes the adsorption of a species, its concentration in the solution phase will decrease in an equal amount thus causing a loss feature from the solution. In this case, if adsorption causes a sufficient band shift in the adsorbed state, bipolar bands caused by the the loss and gain of species from the solution and surface respectively will be observed. Otherwise, when the band shift is too small, the overlapping of both features can produce an unpredictable result. Roth and Weaver [30] have designed a cell with forced electrolyte flow through the thin layer. Replenishment of the thin layer with fresh solution succeeded in compensating for the loss of solution species. Moreover, it was shown that deconvolution of surface and solution features can be attained by subtracting spectra with an without electrolyte convection [30].

4.4 Reflectance for s- and p-Polarized Radiation

The difference in spectral response for s- and p-polarized light has been used very often to discriminate between adsorbate and solution bands. This criterion has been criticized [27] on the basis that the intensity of the electric field vector for s-polarized light may be very low if the solution layer between electrode and IR window is very thin. This causes the spectrum obtained with s-polarized light to have a very low intensity. In this case the absence of bands with s-polarized light does not necessarily imply the absence of absorbing species in solution.

The intensity of the electric field of light in the thin layer cavity has been studied by different authors [31 – 34]. For a practical analysis of the problem, the reflectance difference $\Delta R/R$ for s- and p-polarized light under typical experimental situations in electrochemisty was calculated by Nart [34], using Fresnel equations. The approach to the problem was to consider an absorbing background and simulate absorption changes in the thin layer cavity between electrode and IR window by changing the imaginary part of the refraction index.

Changes in the composition of the solution in the thin layer cavity can be estimated in the order of 20% for the cases described in Sec. 4.3. For this condition it was assumed that the real part of the refraction index remains constant. $\Delta R/R$ was calculated as a function of the thickness of the thin layer of solution between electrode and IR window. The optical parameters (refractive index n_i and absorption coefficient k_i) used for the simmulation were: $n_{window} = 1.4$; $n_{solution} = 1.29$, $k_{solution} = 0.0348$; $n_{metal} = 8.9$, $k_{metal} = 46$. The results for two different wavelengths and two angles of incidence are shown in Fig. 12.

At 2000 cm^{-1} both s- and p-polarized light present comparable values of the reflectivity, while at 1250 cm^{-1} marked differences are observed particularly *at high angles of incidence.* Such high angles, which are desired to increase the sensitivity for surface species, are achieved by the use of prismatic windows. Flat windows do not allow angles higher than *c.* 40°. The results in Fig. 12 indicate that for wavenumbers close to 1250 cm^{-1} (i.e., in the absorption range of oxyanions), s-polarized light is much less sensitive to solution species than p-polarized light.

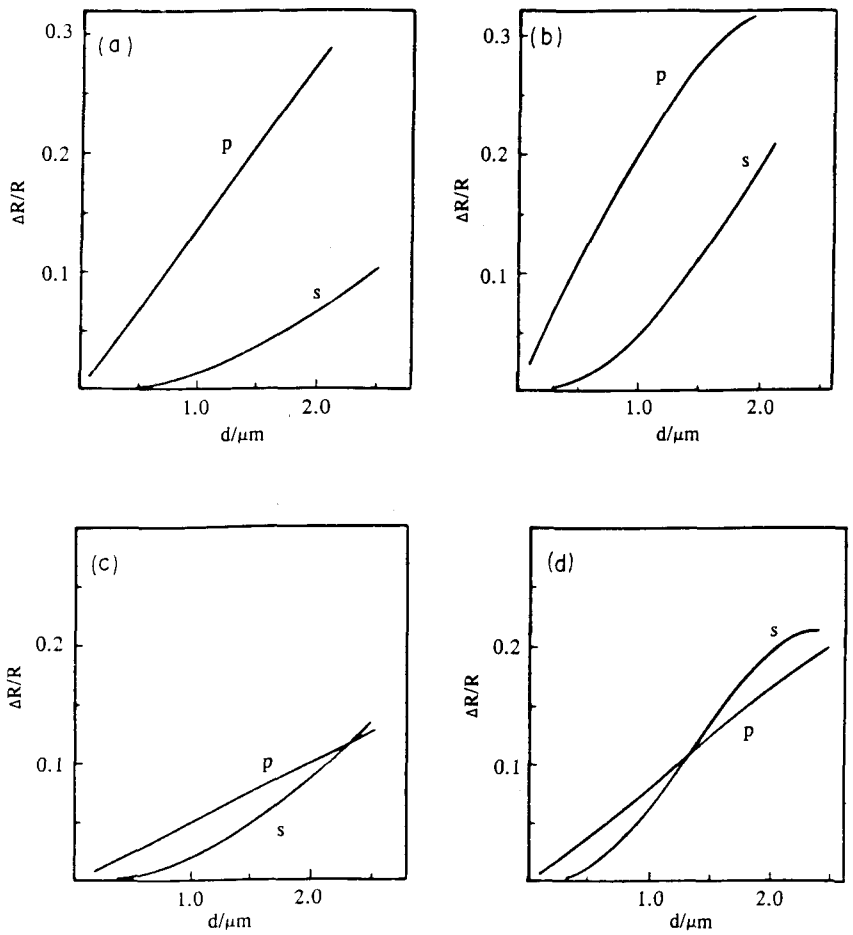

Fig. 12. Calculated reflectance difference $\Delta R/R$ at different wavenumbers (ν) and angles of incidence (α), plotted as a function of the thickness of solution between electrode and IR window. (a) $\nu = 1250\,cm^{-1}$, $\alpha = 60°$; (b) $\nu = 1250\,cm^{-1}$, $\alpha = 38°$; (c) $\nu = 2000\,cm^{-1}$, $\alpha = 60°$; (d) $\nu = 2000\,cm^{-1}$, $\alpha = 38°$. Optical parameters were taken as for a CaF_2 window and a silver electrode/aqueous solution interface (see text).

This result could explain differences in spectral data in the same systems obtained with low incidence angles (flat window) and high incidence angles (prismatic or spherical windows). The latter can furnish almost featureless spectra for solution species with s-polarized light (compare the curves in Fig. 12 at $d = 1$ μm) and induce the wrong conclusion that no solution feature interferes in the spectra measured with p-polarized radiation [35–37]. On the contrary, the use of a flat window leads to comparable intensities for s- and p-polarized radiation spectra [27, 38].

Undoubtedly, use of p-polarized light and a 60° prism gives a very high surface sensitivity. This is reflected by the fact that the center of the superimposed solution

plus surface feature shifts with the applied potential [35–37]. While the band center position can present the correct potential dependence, the band intensities are strongly affected by the solution contribution, i.e., they do not measure the magnitude of adsorption.

The use of s- and p-polarized light to discriminate between solution and adsorbate bands under thin layer conditions, is possible only with careful consideration of the influence of the angle of incidence and the wavenumber on the differential reflectance.

4.5 Selected Applications

In Secs. 5–10 we present a series of selected examples of the use of the external reflectance technique to investigate some electrochemical systems of interest. Results from the electrochemical literature on the adsorption of hydrogen, carbon monoxide and alcohols are discussed and compared with the data from UHV measurements (Secs. 5–7).

Because of the short lifetime of ions in gaseous atmospheres, even at low pressure, gas-phase IR measurements are limited to adsorption of neutral molecules. Electrochemical applications of the IR method offer the interesting possibility of providing data on the adsorption properties of charged particles (Secs. 8 and 9). In the electrochemical environment the applied potential allows ionic adsorbates to be studied under energetically controllable conditions. Otherwise the electrochemical double layer offers exceptional conditions to investigate the Stark effect on vibrational transitions by setting tunable electric fields of the order of $10^6\ V\ cm^{-1}$ at the interface. This phenomenon will be discussed in Sec. 10.

5 Hydrogen Adsorption

Adsorbed hydrogen on metal surfaces is of particular interest from both theoretical and experimental points of view. Vibrational spectroscopy data on hydrogen adsorbed from the gas phase have been obtained from IR reflection-absorption experiments as well as from electron energy loss spectroscopy and inelastic neutron scattering techniques [39–41]. In UHV, absorption bands for the M–H bond have been reported in the mid- and far-infrared regions [41, 42].

In electrochemcial environments hydrogen adsorption has been investigated on polycrystalline Pt, Rh, and Ir as well as on single-crystal Pt(111) [43]. Only one band was observed in the $600–3000\ cm^{-1}$ wavenumber region investigated. The feature, at $2090\ cm^{-1}$, was assigned to hydrogen adsorbed on top of a surface metal atom. This band was observed only at potentials below 100 mV, as shown in Fig. 13a for a polycrystalline platinum electrode. The reflectance spectra in this figure, measured in an H_2SO_4 solution, are referred to a spectrum taken at 443 mV (RHE). A com-

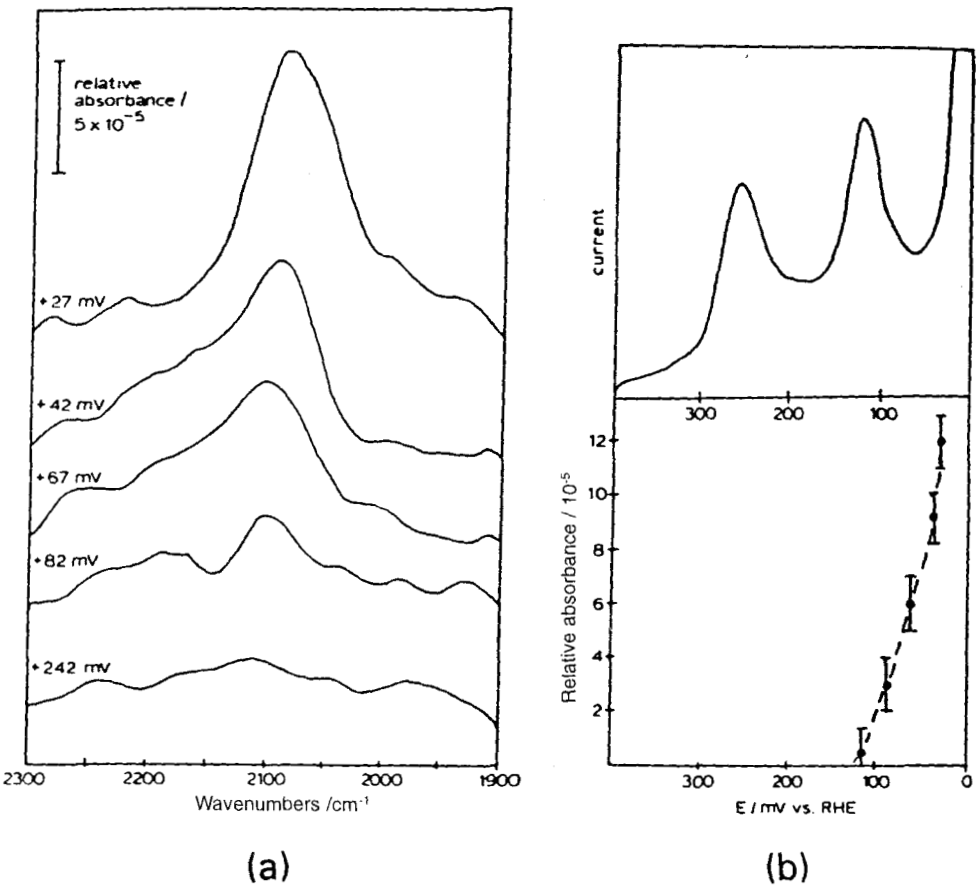

Fig. 13. (a) Reflectance spectra for adsorbed hydrogen on polycrystalline Pt in 1 M H_2SO_4 at different potentials as indicated. Reference potential 442 mV (RHE). (b) Comparison of the linear sweep voltammogram at 0.1 V s^{-1} on the negative scan over the hydrogen adsorption region with the integrated band intensity for the 2090 cm^{-1} absorption band shown in (a). (After [43]). Reprinted by permission of Elsevier Science.

parison of the potential dependence of the band intensity with the potentiodynamic current-potential curve in Fig. 13 b indicates that the band is not related to the peaks in the hydrogen adsorption region of the voltammogram. It has been suggested that the species related to the 2090 cm^{-1} feature is the adsorbed intermediate of the H-evolution reaction (h.e.r). It is interesting to point out that this result could explain kinetic data on the h.e.r.: the experimentally observed E-log i slope of 29 mV at low cathodic potentials on Pt, requires the assumption of a low degree of coverage by hydrogen adatoms [44].

Comparatively more features related to adsorbed hydrogen were observed in UHV experiments; for example, on Al_2O_3-supported Ir, bands in the region

1850–1940 cm^{-1} were reported in addition to others at 2120–2050 cm^{-1} [41]. However, the spectroscopic data are somewhat contradictory with regard to the bands observed and the respective band assignment. Theoretical calculations predict for a threefold (hollow) adsorption on Pt(111) a symmetric mode at 1328 cm^{-1} and an asymmetric one at 912 cm^{-1} [42]. On Pt(111), Electron Energy Loss (EELS) spectra [40] exhibit two bands, at 1230 cm^{-1} and 550 cm^{-1}, attributed to the asymmetric and symmetric stretching respectively, of hydrogen in a hollow position. Other UHV data report the symmetric mode at 1240 cm^{-1} [42]. While the asymmetric mode is surface-forbidden, the symmetric mode should be observable for adsorption in a hollow position in the electrochemical environment. It is unclear why for all electrode materials only one band (at 2090 cm^{-1}) was observed. Also the lack of any signal from adsorbed species in the hydrogen adsorption region of platinum remains unexplained. A systematic investigation using single-crystal metals, (including Pd) should help to understand this interesting system.

6 Carbon Monoxide Adsorption

Adsorbed carbon monoxide is a matter of special interest in ultrahigh vacuum as well as in electrochemical systems. CO has been used as probe molecule in surface vibrational spectroscopy. For important reviews of CO adsorbed from the gas phase, see [21, 42, 45, 46]. The rather large dynamic dipole moment ($\partial\mu/\partial Q$) of adsorbed CO is particulary suited for infrared spectroscopy at electrochemical interfaces, where submonolayer amounts of species must be observed in the presence of IR-active solution compontents.

The interaction of CO with the solid surface produces several physical and chemical effects on the vibrational properties of the adsorbed species. The adsorption of CO can be envisaged as a two-dimensional condensation, leading to lateral coupling between adsorbed molecules. The vibrational properties of adsorbed CO can thus be used to monitor the effects of other interface properties, such as surface defects, two-dimensional phase transitions [45] and co-adsorption. Finally, CO is formed as an intermediate or poison during the oxidation of several organic molecules at electrodes, thus constituting one of the subjects of interest in electrocatalysis.

Chemical shift and lateral coupling are the most striking effects in the adsorption of CO on metal surfaces [45]. Chemical shift applies to the frequency displacements caused by CO-metal interactions, while lateral coupling refers to adsorbate-adsorbate interactions.

In electrochemical environments the vibrational spectra are additionally affected by solvation effects, the electric field in the double layer, and the co-adsorption of water and/or ions in the inner Helmholtz plane.

6.1 Effect of the Metal Electronic Structure

The M-CO bond, according to Blyholder [47, 48], is formed by charge transfer from the 5 σ molecular orbital of CO to the metal and back-donation of electrons from the metal d-orbitals to the 2 π^* orbital of adsorbed CO. Since the 2 π^* is strongly antibonding and the 5 σ only weakly bonding, the C–O bond strength is lowered in the adsorbed state. Consequently the C–O stretching frequency is shifted to lower wavenumbers.

The backbonding mechanism has been evidenced by experiments with species changing the density of d-electrons in the metal; e.g., CO was coadsorbed with strong electron donors [49, 50] or electron acceptors [51]. The frequency shift is proportional to the 2 π^* occupancy, as shown by Baerends and Ros [52] for carbonyl complexes. On this basis, it could be concluded that the site occupancy of CO adsorbed on different metals is determined to a large extent by the electronic properties of the metal surface.

A very detailed comparison of CO adsorption on transition metals in UHV has been given in [21]. The large amount of data on well-ordered metal surfaces enables the comparison of surfaces having identical structures.

The CO stretching frequency at low coverages for on-top adsorption is practically constant for all d-metals. It has been established that the site occupancy is dependent on coverage and varies from one metal to another. Thus, threefold bridge-bonded CO appears first on Pd and Ni; while on-top sites are occupied first on Pt and Rh [21].

Apparently two factors are responsible for the specificity of site occupancy: the d-band width (an electronic factor) and the metal atom spacing (a geometric factor), but no definitive conclusions can be obtained from this comparison.

Compared with the gas phase, the spectroscopic studies of adsorbed CO on electrodes are still just beginning. Data are available for only a few metals. CO has been studied on single-crystal surfaces of Pt [53–58], Pd [59] and Rh(111) [60].

A direct comparison of the results for Rh(111) and Pt(111) (i.e. for the same surface structure) at the same rational potential (referred to the potential of zero charge, pzc) must give directly the effect of the electronic structure. On both metals, on-top and bridge-bonded CO is observed (Figs. 14 and 15). Comparing the band center position of adsorbed CO on these two metals at an estimated potential of zero charge, Leung et al. [60] have found that the wavenumbers for the same adsorption site are very close: namely, 2060 and 1835 cm^{-1} for Rh(111) and 2090 and 1855 cm^{-1} for Pt(111) for on-top and bridged CO, respectively. The coincidence of vibrational frequency was observed in UHV for group VIII metals with equivalent surface geometry ((111) for face-centered and (001) for hexagonal close-packed) [21].

On Pd(100) CO adsorbs only in the two-fold bridged form. The band center shifts to higher frequencies with increasing coverage and potential [61]. On Pd(111) two forms of bridged CO, two- and three-fold coordinated, coexist over a wide range of degree of coverage [59]. For both single-crystal faces the results are similar to those of UHV conditions.

Spectra for CO adsorbed on single-crystal Pt(100) and Pt(110) are given in Fig. 16 [54, 55]. On Pt(110), only on-top bonded CO has been reported [55].

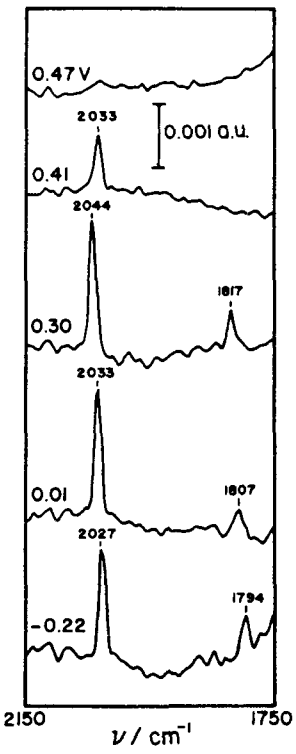

Fig. 14

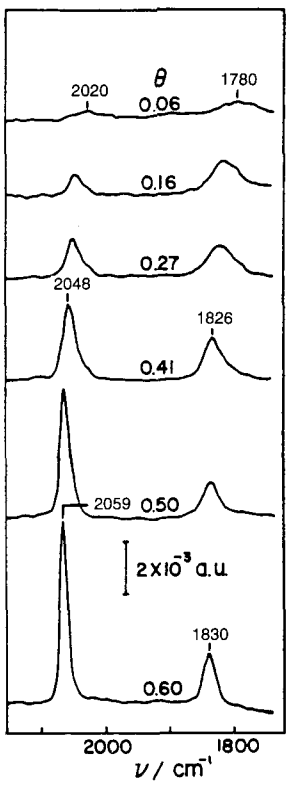

Fig. 15

Fig. 14. Potential-dependent FTIR spectra of adsorbed CO on Rh(111) at −0.25 V vs. SCE in 0.1 M $HClO_4$. Each spectrum was obtained by averaging 40 scans and subtracting a spectrum taken at 0.6 V vs. SCE after complete oxidation of CO. (After [60]). Reprinted by permission of Journal of Chemical Physics AIP.

Fig. 15. FTIR spectra for adsorbed CO at different coverage degrees obtained by dosing different amounts of CO on Pt(111) at −0.25 V vs. SCE in 0.1 M $HClO_4$. Spectra were obtained by means of 30 interferometer scans and subtracting another set taken at 0.5 V after total oxidation of CO. (After [53]). Reprinted by permission of Journal of Chemical Physics AIP.

Pt(100) presents both on-top (at $2015-2048\,cm^{-1}$) and bridge-bonded CO (at $1801-1872\,cm^{-1}$). The site occupancy is not only affected by the coverage, but is strongly sensitive to the double layer environment, as shown by changes in the coordination with potential at constant degree of coverage [54].

On-top/bridge site interconversion has been demonstrated for Pt(100) by Kitamura et al. [57], who made a careful analysis of intensity changes with the applied potential. The bridged CO species moves to the on-top geometry as the potential is made more positive. This result explains why bridge-bonded CO does not present a bipolar band in EMIRS experiments.

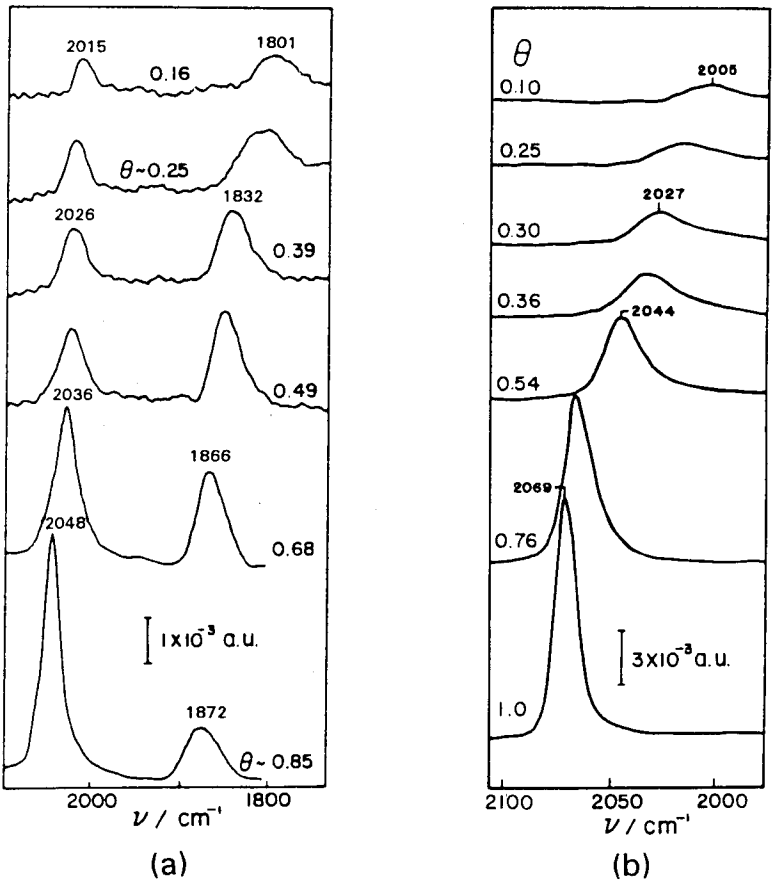

Fig. 16. Spectra of irreversibly adsorbed CO on (a) Pt(100) and (b) Pt(110) at different degrees of coverage obtained by dosing different amounts of CO at −0.25 V vs. SCE in 0.1 M $HClO_4$. Spectra acquisition as in Fig. 15. (After [54, 55]). Reprinted by permission of the American Chemical Society and Elsevier Science.

A very interesting comparison was reported by Ikezawa et al. [61] for polycrystalline Pt, Pd, Au, and Ag at a neutral pH. The results shown in Fig. 17 allow a comparison of CO adsorption at the same applied potential. On Pt electrodes mainly linearly bonded CO is formed, as shown by the strong band at 2072 cm^{-1} and the weak band for bridge-bonded CO around 1870 cm^{-1}. For Pd a strong feature at 1960 cm^{-1} and a weak one at 2070 cm^{-1} indicate the predominance of the bridged form (see also [62]). In contrast to the d-metals, silver and gold electrodes present weak adsorption of CO under the same conditions of potential and pH. At Ag electrodes only a weak band is observed at 2021 cm^{-1}, while gold electrodes show two features at 2027 cm^{-1} and 1863 cm^{-1}. From these data the differences in

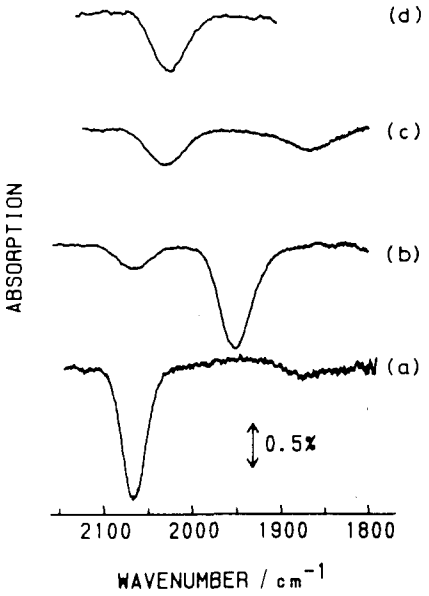

Fig. 17

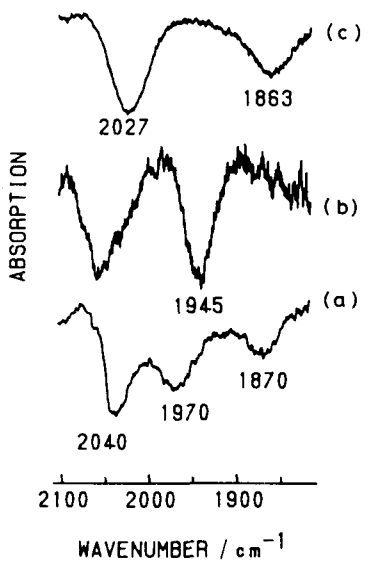

Fig. 18

Fig. 17. PMIRRAS spectra of adsorbed CO on various electrodes in 0.1 M $NaClO_4$ at 0.2 V vs. SCE: (a) Pt, (b) Pd, (c) Au, (d) Ag. (After [61]). Reprinted by permission of Elsevier Science.

Fig. 18. IRRA spectra of CO adsorbed on Au electrodes in 0.1 M $HClO_4$ at (a) 0.1 V at low CO coverage; (b) −0.2 V at low CO coverage; (c) −0.2 V at high CO coverage (all potentials referred to SCE). (After [61]). Reprinted by permission of Elsevier Science.

site occupancy on different metals is very clear. However, the band positions given may be affected by lateral coupling since the comparisons are made at unknown surface coverage. In addition, band frequencies for different electrodes should be compared under the same electrostatic condition at the metal surface. For this purpose the pzc should be used as a reference potential. However the pzc in the presence of adsorbed CO is not known for these systems, and the externally applied potential could be a first approximation for the sake of comparison.

In general, the feature at the highest wavenumber has been assigned to linear-bonded CO and the lower wavenumber mode to the bridge-bonded CO. The differences in wavenumber between bridge-bonded CO on Pt, Au and Pd (1870, 1863 and 1960 cm^{-1} respectively), suggest that different kinds of coordination porbably occur in the bridge-bonded CO.

At low coverage and 0.1 V vs SCE on a gold electrode, adsorbed CO exhibits three bands (2040, 1970 and 1870 cm^{-1}), as can be seen in Fig. 18. The difference in wavenumber is too high to be attribued to adsorption on defect sites. Thus the three bands are related to three types of coordination for CO on polycrystalline gold. Tentatively, the 1870, 1970 and 2040 cm^{-1} bands have been assigned to threefold, twofold and on-top adsorbed CO [61].

6.2 Potential-Dependence of the CO Band Center

In electrochemical systems the energetics of the interface can be controlled very elegantly by changing the electrode potential. In the case of CO adsorption, mechanisms such as backbonding should be very sensitive to potential change, i.e., to the electronic density of the surface. Furthermore, the strong electric field in the inner double layer can produce a band shift known as the Stark effect, as discussed in Sec. 10 in more in detail.

On platinum electrodes (single crystals and polycrystalline) the potential-induced band shift for on-top adsorbed CO presents a linear change which lies between 30 and 40 cm^{-1}/V for a CO-saturated surface in acidic media [63]. The value of $d\bar{\nu}/dE$ depends on the degree of coverage, θ. Particularly on Pt(100), a rather strong dependence of $d\bar{\nu}/dE$ on the degree of coverage has been reported (from 30 cm^{-1}/V for $\theta = 1.0$ to 70 cm^{-1}/V for $\theta = 0.2$). Furthermore, at a low degree of coverage the $\nu - E$ behavior is no longer linear.

The coverage-induced change in $d\bar{\nu}/dE$ could be explained by an increasing competition for d-electrons at increasing coverage or by a change in the effective electric field, due to a shift of the potential of zero charge. The latter shifts in the negative direction in the presence of CO [60]. Probably the most reasonable explanation is that both kinds of effects are operative.

Rh(111) electrodes in acid media present a $d\bar{\nu}/dE$ of 35 and 45 cm^{-1}/V for on-top and bridge-bonded CO, respectively [66]. On Pd electrodes $d\bar{\nu}/dE$ is 48 cm^{-1}/V for on-top adsorbed CO. On Pd, bridge-bonded CO which is the major component, presents nonlinear behavior. Potential-induced band shifts are reported for Au, Ag, Pt and Pd in neutral media also [61], giving 47, 48, 50 and 50 cm^{-1}/V, respectively; i.e. in neutral media $d\bar{\nu}/dE$ is almost independent of the metal. This effect was not studied in detail. A more systematic approach could be of great importance to elucidate the role of the applied potential in the vibrational properties of adsorbates.

6.3 Effect of the Co-adsorption of Hydrogen and Water on the Adsorbed CO Layer

Kunimatsu et al. were the first to report differences in the oxidation mechanism of adsorbed CO on polycrystalline platinum [63–65] and single-crystal Pt(111) [56], depending on the position of the adsorption potential (hdyrogen desorption or double layer region). It was suggested [63–65] that when the CO layer is formed at 0.6 V vs. NHE, i.e., at the double layer of the polycrystalline Pt electrode, the oxidation of CO occurs at the edges of CO islands, while when CO is adsorbed at 0.05 V vs. NHE, i.e., in the presence of upd hydrogen, the oxidation occurs in a random way. The latter is probably caused by formation of bridge-bonded CO, which would be oxidized first, leaving the on-top adsorbed CO either randomly distributed, or in small islands. The same interpretation was proposed for single-crystal Pt(111), although no bridge-bonded CO was observed on this face [56].

The coverage dependencies of vibrational wavenumber and band halfwidth are sensitive to the potential region where CO is adsorbed on single-crystal Pt electrodes [53–55]. When CO is adsorbed in the presence of adsorbed hydrogen, the band center frequency changes monotonically with coverage, while for adsorption in the double layer region a sharp transition at $\theta \simeq 0.2$ on Pt(111) and from $\theta \simeq 0.4$ to 0.6 on Pt(110) can be observed (Figs. 19 and 20).

Experiments in UHV with co-adsorption of hydrogen or water show that, in both cases, the formation of CO aggregates occurs. Wagner et al. [66] sugest that co-adsorbed water molecules cause a repulsive interaction with adsorbed CO generating segregated domains of CO and water. On the other hand, IRRAS studies on co-adsorbed hydrogen or water with CO at Pt(111) [67] show island formation in both cases.

In the electrochemical environment, co-adsorbed hydrogen probably induces smaller CO islands than co-adsorbed water. Based on these arguments, the band splitting at intermediate θ_{CO} on Pt(110) for adsorption in the double layer region could be explained by different dipole-dipole interactions of the molecules inside and at the border of the islands. According to theoretical predictions [68] this kind of configuration should give a band splitting of the order of 8 cm^{-1} while the observed experimental value in Fig. 20 gives 17 cm^{-1}, i.e. well above the predicted value. In UHV experiments [21] such high band separation has been attributed to the coexistence of disordered CO molecules and ordered CO in islands. It cannot be excluded that co-adsorbed water interacts strongly with the CO molecules at the border of the island producing a more pronounced difference between dipole-dipole interactions inside and at the border of the island.

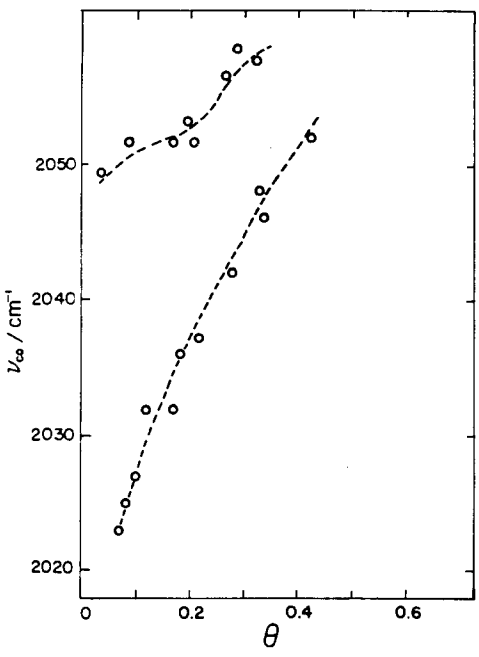

Fig. 19. Plot of the coverage-induced band shift for CO adsorbed on Pt(111) in 0.1 M $HClO_4$ in the double layer region at 0.1 V vs. SCE (upper curve) and in the hydrogen region at −0.25 vs. SCE (lower curve). (Extracted from data of [53]). Reprinted by permission of Journal of Chemical Physics AIP.

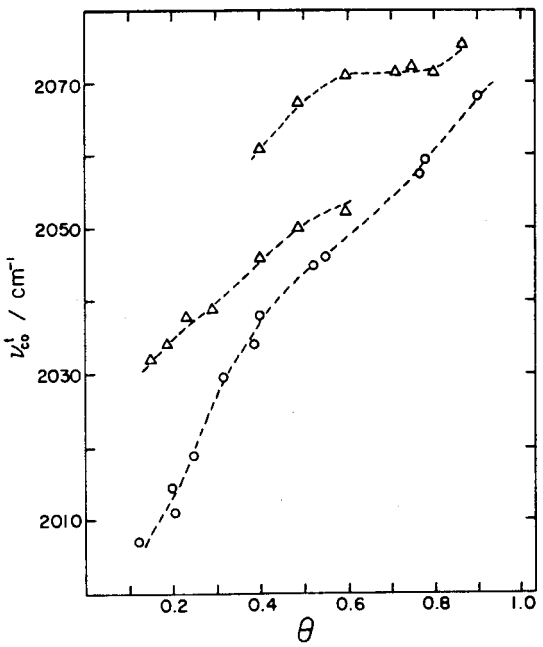

Fig. 20. Plot of the coverage-induced band shift for CO adsorbed on Pt(110) in 0.1 M $HClO_4$ in the double layer region at 0.05 V vs. SCE (△) and in the hydrogen region at −0.25 V vs. SCE (○). Observe the band splitting at intermediate coverage. (Extracted from data of [55]). Reprinted by permission of Elsevier Science.

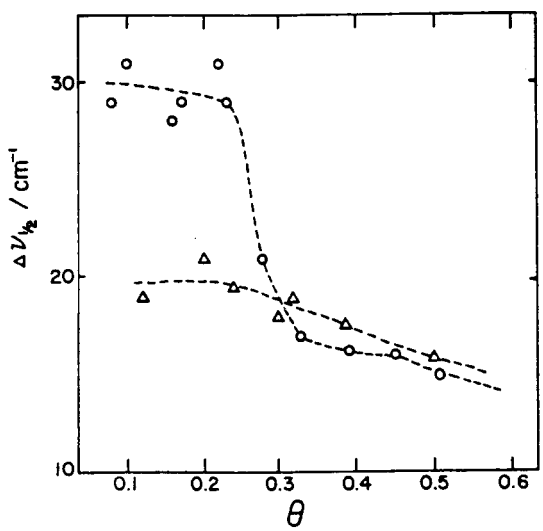

Fig. 21. Dependence of the bandwidth $\Delta\nu_{1/2}$ on the coverage for CO adsorbed on Pt(111) electrodes in 0.1 M $HClO_4$ in the double layer region at 0.1 V (△) and in the hydrogen region at −0.25 V (○) vs. SCE. (Extracted from data of [53]). Reprinted by permission of Journal of Chemical Physics AIP.

Strong band broadening upon adsorption in the hydrogen region is observed for both Pt(111) (Fig. 21) and Pt(110) (Fig. 22) surfaces. On Pt(111) much less band broadening is observed for CO/H_2O than for CO/H co-adsorption. In the case of CO adsorbed on Pt(110) in the double layer region, the band splitting makes it diffi-

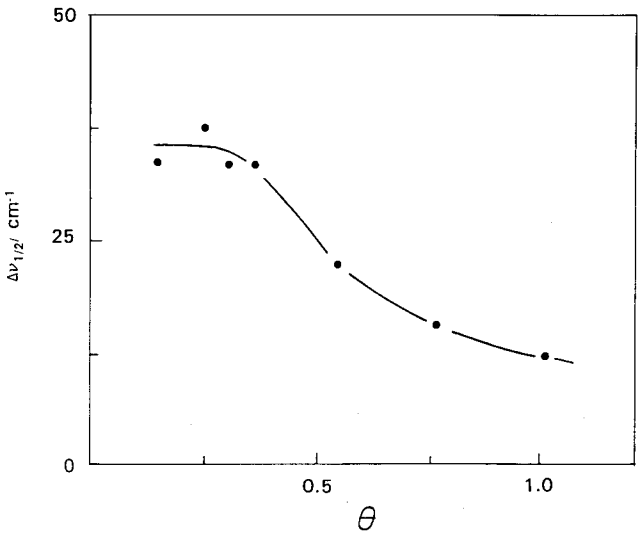

Fig. 22. Dependence of the bandwidth $\Delta r_{1/2}$ on the coverage for CO adsorbed on Pt(110) electrodes in 0.1 M $HClO_4$ in the hydrogen region at -0.25 V vs. SCE. (Data obtained from spectra of [55]). Reprinted by permission of Elsevier Science.

cult to define a bandwidth. The splitting of the band at intermediate coverages suggest that mixture of island and lattice gas with repulsive interactions is present [21], in agreement with the discussion above.

Broadening effects can be caused by several mechanisms, as reviewed recently by Tobin [46] (see Sec. 3.4). The most probable effect is inhomogeneous broadening caused by CO island formation induced by hydrogen or wate co-adsorption. The results of Figs. 19 and 20 indicate a stronger effect of co-adsorbed hydrogen on the size of the CO islands at low and intermediate coverages. In this case, more homogeneous broadening is expected since more boundary domains are formed and the CO molecules close to these domains experience different dipole and static lateral interactions [46]. A very curious feature is the relatively sharp bandwidth transition in the case of co-adsorbed hydrogen on Pt(111) electrodes (Fig. 21), which suggests a rearrangement of the small islands at low coverage to larger domains for $\theta > 0.3$. This conclusion is in good agreement with the observation that when CO is adsorbed in the presence of co-adsorbed hydrogen the oxidation occurs more readily. The small islands or randomly distributed molecules (at low coverage) favor the adsorption of water molecules necessary for the CO oxidation.

6.4 Effect of Solvent Molecules on the Singleton Frequency

Besides the effect of hydrogen and water of inducing different sizes of island formation, it is interesting to establish whether there is an effect of the components of the

double layer on the vibrational frequency of adsorbed CO as compared with the value in UHV, where CO is the only component of the adlayer. Such effects were investigated by Chang and Weaver on Pt single crystals [53–55].

In order to avoid the influence of lateral interactions on the vibrational frequency of adsorbates, it is common to analyze the frequency of a single adsorbed molecule, i.e., the singleton frequency, which is obtained by extrapolating the adsorbate frequency to zero coverage. For the sake of comparison, the electronic backdonation must be the same for both UHV and electrochemical system. Since in UHV the potential is governed by the work function of the metal, an equivalent potential must be found for the electrochemical system.

As discussed by Chang and Weaver [53–55], the equivalent electrochemical potential is the potential of zero charge, E_0^M. No experimental values of the potential of zero charge for Pt single-crystal surfaces are available, however. Based on empirical observations for other systems, E_0^M has been suggested to be [69]:

$$E_0^M = (\phi^M/e) - E_T\,(\text{ref}) \tag{14}$$

where ϕ^M is the metal work function and E_T is the potential of the reference electrode in the vacuum scale [53, 69]. The potential of zero charge obtained from work function values for low-index planes of single-crystal platinum lies above the CO oxidation potential. In pronounced contrast with this, Wagner et al. [66] have suggested a value of 0.2 V for single-crystal Pt(111), based on results of cyclic voltammetry and water adsorption in UHV.

The singleton frequency for adsorbed CO at Pt(111) in an electrochemical interface was reported by Chang and Weaver [53] as 2076 cm^{-1} at an estimated potential of zero charge for Pt(111) of 1.1 V vs. SCE. In UHV the singleton frequency for adsorbed CO has been found to be 2082 cm^{-1} [70] and 2065 cm^{-1} [71]. If the E_0^M value suggested by Wagner et al. is taken [66], a value of 2027 cm^{-1} is obtained, i.e. far below the UHV value.

Actually, the absence of reliable values for the potential of zero charge makes this kind of comparison extremely difficult. On the other hand, for Pt(100), taking the potential of zero charge based on work function measurements ($E_0^M = 1.0$ V vs. SCE), a value 2045 cm^{-1} is found for the singleton frequency, which is well below that of the gas phase. Possibly the increasing formation of bridge-bonded CO at low coverages makes the analysis for the Pt(100) surface difficult.

Although no values for the singleton frequency of CO adsorbed on Pt(110) were given, the extrapolation of the results of Chang and Weaver [55] for $\theta \to 0$, at E_0^M (0.9 V vs. SCE [55]), gives 2080 cm^{-1} for the *single* adsorbed CO molecule. This value coincides with the singleton frequency of CO adsorbed from the gas phase in UHV (2080 cm^{-1} [70]).

If only the potential of zero charge based on the work function is taken, the results show that the electrostatic potential induced by co-adsorbed water molecules or ions in the double layer has a negligible effect on the vibrational properties of the single adsorbed CO molecule on well-ordered Pt surfaces [60], at least for Pt(111) and Pt(110).

Reliable values of the potential of zero charge are needed for a more precise analysis of this phenomenon. Furthermore, the difference in the singleton frequency for

Pt(100) in UHV and at the electrochemical interface remains an interesting point for further studies.

6.5 Dipole-Dipole Coupling

The coverage dependence of the CO stretching frequency has been studied extensively for the metal/UHV interface [21]. The coverage-induced frequency shift is due to increasing dipole-dipole coupling [72] and chemical interactions between adsorbed molecules.

Experimentally, these effects can be distinguished by using isotope mixtures. As shown theoretically by Hammaker et al. [73], only vibrations with identical frequencies couple strongly. Therefore, an isotopic $^{13}CO/^{12}CO$ mixture is appropriate to differentiate experimentally between dipole-dipole coupling and other effects. The experimental method has been reviewed by Hoffmann and the effects upon CO adsorbed on Pd(100) have been analyzed in detail [21].

The use of isotope mixtures to study lateral interaction between adsorbed CO molecules in electrochemical interfaces was first reported for CO adsorbed on-top at polycryalline platinum where only one band for the isotopic mixture was observed [74]. The existence of only one band indicates a strong energy transfer, suggesting a strong dipole-dipole coupling of the adsorbed molecules. Using a theoretical model, an effective coupling force constant of 1.1 mdyn Å was found for an adsorption potential of 0 V vs. SCE at saturation coverage [74]. This value is about twice as large as that of CO adsorbed on Pt(111) in UHV, which is 0.54 mdyn Å [74]. Similar results were reported from EMIRS measurements on polycrystalline platinum at high coverages [75]. For low coverage, the EMIRS spectra indicate a decrease in the dipole-dipole coupling, as shown by the separation of the two bipolar bands.

On Pt(111)/ and Pt(100)/aqueous solution interfaces, $^{13}CO/^{12}CO$ isotope mixtures present relatively well-separated bands [53, 54]. In this case dipole-dipole coupling can be analyzed in detail. Results for CO adsorbed on these two single-crystal faces are shown in Fig. 23. Different coverages are attained both by either dosing[2] different quantities of CO in solution or by stripping from higher CO coverages [53–55]. A typical result of the decoupling mechanism for $^{13}CO/^{12}CO$ isotopic mixtures is shown in Fig. 24.

When the amount of ^{12}CO decreases to vanishing values, the frequency of ^{12}CO is practically decoupled and this value can be used to calculate the contribution of the dynamic dipole coupling $\Delta\nu_D(\theta)$ as follows [53]:

$$\Delta\nu_D(\theta) = \nu_{CO}(\theta) - \nu_{CO}(\theta, \text{dl}) \tag{15}$$

[2] There are some differences in results when the different degrees of coverage are obtained by dosing from a dilute ($\simeq 10^{-5}$ M) CO solution or by oxidative stripping from higher CO coverages [56]. We discuss here mainly the results of dosing experiments.

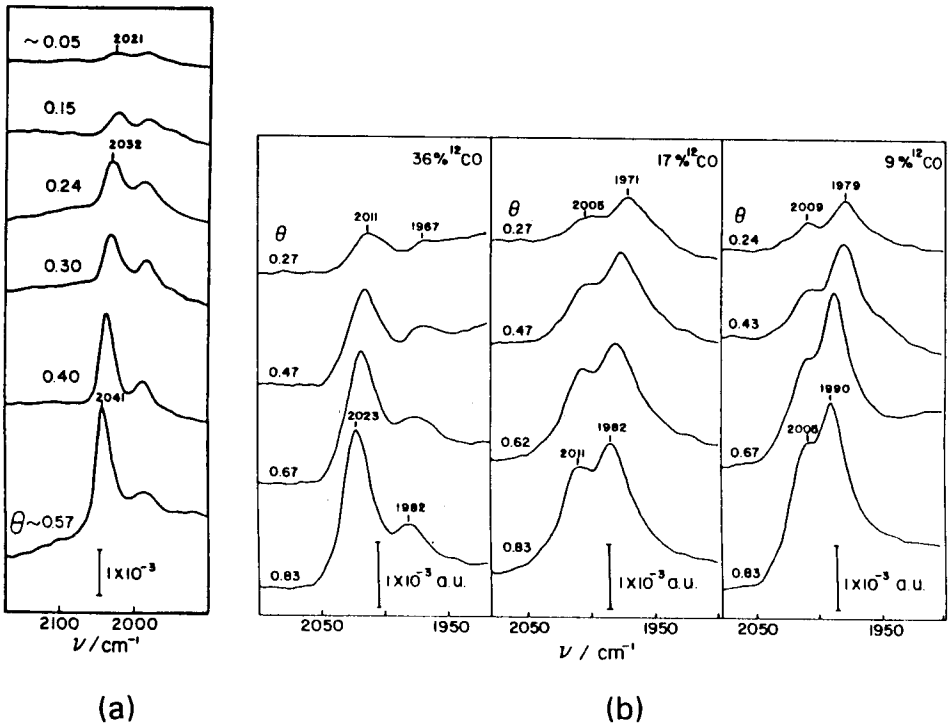

Fig. 23. Spectra for isotopic mixtures of $^{13}CO/^{12}CO$ in 0.1 M $HClO_4$ at −0.25 V vs. SCE. (a) Pt(111), 46% ^{12}CO. Coverage obtained by dosing; (b) Pt(100), percentage of ^{12}CO as indicated. Coverage obtained by stripping. (Reproduced from [53, 54]). Reprinted by permission of Journal of Chemical Physics AIP and the American Chemical Society.

where $\nu_{CO}(\theta, \text{dl})$ is the frequency value of the ^{12}CO extrapolated to the dilution limit of the isotopic mixture (e.g., from plots like Fig. 24). Under this condition the dynamic dipole coupling is virtually eliminated. The chemical coupling contribution to the lateral interaction ($\Delta\nu_C(\theta)$) is given by the difference between $\nu_{CO}(\theta, \text{dl})$ and the singleton frequency for ^{12}CO (i.e., the frequency for $\theta \to 0$, obtained from pure ^{12}CO coverages) [53]:

$$\Delta\nu_C(\theta) = \nu_{CO}(\theta, \text{dl}) - \nu_{CO}(\theta \to 0) \tag{16}$$

The results for Pt(111) are summarized in Fig. 25 where $\Delta\nu_D$ (solid lines) and $\Delta\nu_C$ (broken lines) are plotted against θ for adsorption at −0.25 V (A) and +0.1 V vs. SCE (B). Under dosing conditions (lines without arrows) the frequency shift is mainly produced by dynamic dipole-dipole coupling for both adsorption potentials. Under electrooxidative stripping (lines with arrows) chemical contributions survive at least down to $\theta \simeq 0.1$. The dipole-dipole coupling decreases with coverage for different dosed coverages ($\Delta\nu_D < 10\ \text{cm}^{-1}$ for $\theta < 0.1$), while a strong dipole-dipole coupl-

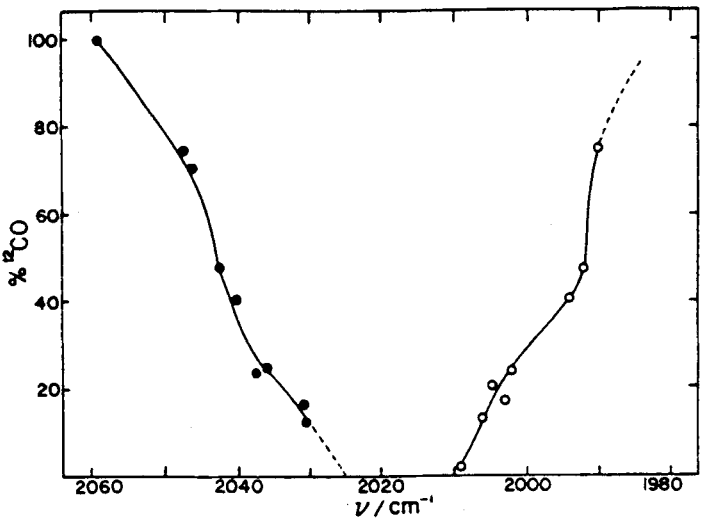

Fig. 24. Band center wavenumber for ^{12}CO (fully symbols) and ^{13}CO (open symbols) for $^{13}CO/^{12}CO$ isotopic mixtures adsorbed on Pt(111) electrode at -0.25 V, at $\theta = 0.6$. (Reproduced from [53]). Reprinted by permission of Journal of Chemical Physics AIP.

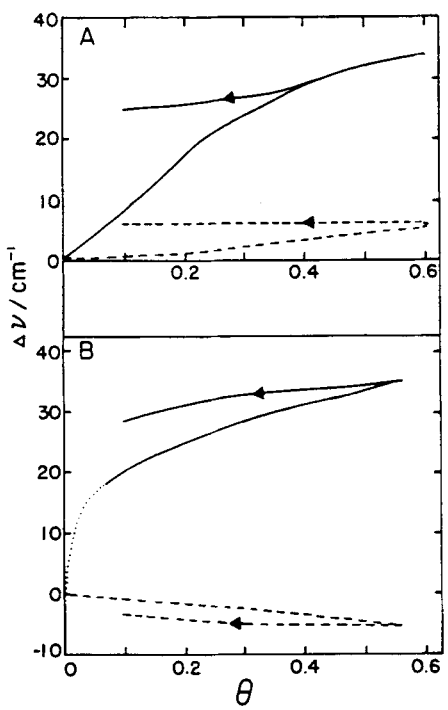

Fig. 25. Coverage-induced frequency shift for CO adsorbed on Pt(111) in 0.1 M $HClO_4$. Dipole-diple coupling is indicated by the solid traces and the chemical shift by the broken traces. A: $E_{ads} = -0.25$; B: $E_{ads} = 0.1$ V vs. SCE. Traces with arrows are for electrooxidative stripping, and without arrows for dosing conditions. (Reproduced from [53]). Reprinted by permission of Journal of Chemical Physics AIP.

ing ($\Delta\nu_D$ around 30 cm^{-1}) is maintained even for very low coverages when part of the CO layer is removed by electrooxidative stripping (see Fig. 25). For further details see [53].

There are two points in these analysis that must be taken with care. The first is that on Pt(111) and Pt(100) both on-top and bridge-adsorbed CO are present. This could induce some coupling between ^{13}CO and bridge-bonded ^{12}CO frequencies in the high ^{12}CO coverage limit, as pointed out already by Chang and Weaver [53]. Second, instead of using the limiting coverage frequency of the ^{12}CO isotope (which may be affected by coupling to the ^{13}CO) to evaluate $\Delta\nu_D$ and $\Delta\nu_C$, the limiting dilution frequency for ^{13}CO is more convenient. The latter lies well separated from the ^{12}CO frequency (see Fig. 24).

7 Adsorption of Alcohols

7.1 Methanol

The adsorbed species formed when alcohols interact with sp- and d-metals has been the subject of a number of investigations at the metalgas interface in UHV. Methoxy (CH_3O) surface intermediates have been observed, particularly on oxide catalysts [76, 77]. Using high-resolution electron loss spectroscopy, methoxide species were observed on Ni [78] at low temperature (up to 200 K) and on Cu(111) [79] up to 370 K. On Pd(111) Davis and Barteau [80] have reported the simultaneous adsorption of molecular methanol and methoxide at 170 K. On a clean Pt(111) surface multilayers of methanol formed at 155 K decompose on heating, forming adsorbed CO and hydrogen [81]. If the Pt surface is previously covered with oxygen, multilayers of adsorbed methanol at 100 K convert to adsorbed methoxide on heating to 170 K. However, these species are not stable at higher temperatures [81]. On all metals the final conversion products are adsorbed CO and hydrogen.

The adsorption of methanol on Pt has been the subject of one of the first investigations using external reflectance infrared spectroscopy in an electrochemical environment [82]. Using the EMIRS technique it was demonstrated that two forms of adsorbed carbon monoxide giving bands near 2050 cm^{-1} and 1850 cm^{-1} are present when the potential of a platinum electrode is modulated between 400 mV and 50 mV in an acidic solution containing methanol. The bands were assigned to linear- and bridge-bonded CO respectively [82]. These two forms of adsorbed CO as components of methanol adsorbate were later observed in other EMIRS [83, 84] and SNIFTIRS [85, 86] experiments. Beden et al. [84] report results obtained by varying the time for spectra accumulation and conclude that some spectral features disappear due to rearrangement among adsorbed species. Using FTIR spectroscopy Corrigan and Weaver have reported the formation of linearly bonded CO as adsorbed species from formic acid and methanol on platinum [86]. The absorption band for linearly bonded CO has been used to monitor the activity of bimetallic catalysts toward methanol oxidation [87, 88].

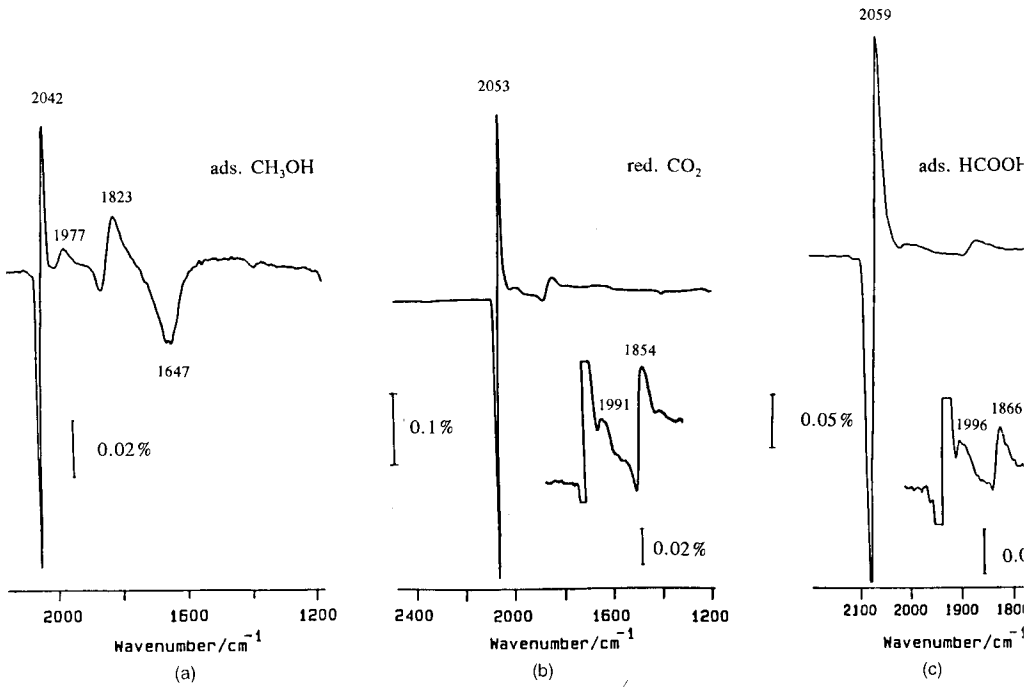

Fig. 26. Fourier transform reflection-absorption spectra from a platinum electrode for (a) adsorbed methanol, (b) reduced carbon dioxide, (c) adsorbed formic acid. Ratio spectra calculated from single-beam spectra collected alternately at 0.05 V and 0.35 V vs. RHE (see text for band assignment).

More recently, another band at 1970 cm^{-1} was reported for methanol, formic acid, reduced carbon dioxide and carbon monoxide [89]. According to the position of the bands for adsorbed CO on different metals in UHV experiments (see Sec. 6.1), the new band was assigned to double-coordinated carbon monoxide, while the feature at 1850 cm^{-1} was assigned to the triply bonded species.

Figure 26 shows a spectrum of adsorbed CO from (a) adsorbed methanol (b) reduced carbon dioxide and (c) adsorbed formic on platinum. The spectra were obtained using th SNIFTIRS procedure (alternate collection of interferometer scans at two potentials). No other features in the 950–4000 cm^{-1} region were observed using the procedure. However, species other than carbon monoxide are expected for adsorbed methanol, as the results from other techniques indicate [90]. Besides CO, species with different degrees of dehydrogenation are formed. As explained in Sec. 4.2, when a substance is irreversibly adsorbed, bands having a small frequency shift with potential can cancel out in the difference (or ratio) spectrum if the single spectra are alternately collected at two potentials (as in an EMIRS or SNIFTIRS experiment).

In the case of methanol, the fact that methanol is practically not adsorbed when the hydrogen coverage is high (e.g., at 0.05 V vs. RHE), can be used to obtain a difference spectrum containing only absolute bands for adsorbed methanol [91]. This ap-

proach requires that methanol enters in contact with the Pt electrode at 0.05 V vs. RHE. For this purpose a flow cell procedure must be used in order to keep the working electrode under potential control. The reference spectrum must then be taken at this potential, i.e., in the absence of adsorbed methanol. Then, after applying a potential step to 0.35 V, where methanol is adsorbed, the sample spectrum can be measured. Sample spectra taken at different times show the development of absolute bands for the adsorbate (Fig. 27). The intensity of the band for linear-bonded CO grows for *c.* 20 min after application of the potential step (under thin layer conditions). In the 1200–1300 cm^{-1} region other bands are developed whose intensity grows during *c.* 40 min.

According to results of theoretical ab-initio calculations, the C–O stretching frequency of an unperturbed particle having the composition C–O–H is expected at 1370 cm^{-1} [92]. Taking a frequency shift of *c.* 100 cm^{-1} to lower wavenumbers in the adsorbed state, the 1270 cm^{-1} mode can be assigned to COH. This adsorbed particle was postulated largely from results of mass spectrometry [90]. Comparative measurements of the CO band intensities for methanol, formic acid, and carbon monoxide adsorbates applying PMIRRAS [93] indicate that in the case of methanol other adsorbates must be present.

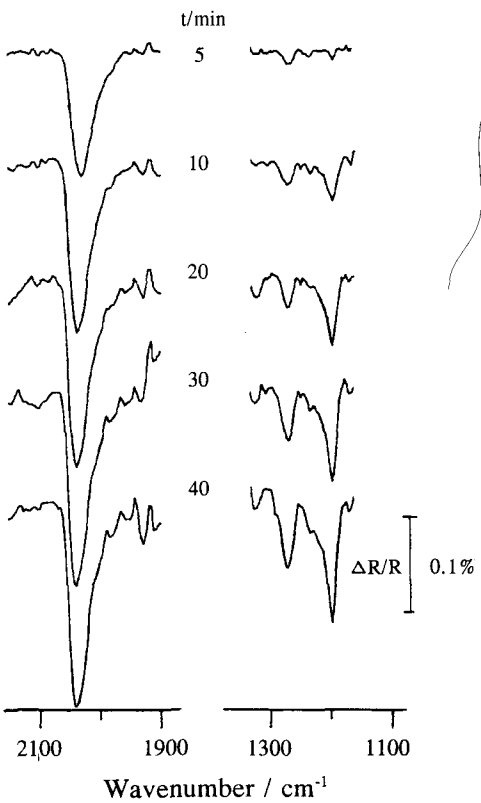

Fig. 27. FTIR spectra during the adsorption of methanol on polycrystalline Pt at 0.35 V vs. RHE (1 M CH_3OH, 0.5 M $HClO_4$). A reference spectrum was taken at 0.05 V (at this potential methanol adsorption is negligible). Then the potential was set to 0.35 V and sample spectra were collected at the indicated times.

The second band observed in this region, at 1200 cm^{-1}, is more difficult to assign. Using isotope-labelled methanol (CD_3OH) the band at 1200 cm^{-1} disappears. This fact led to a tentative assignment of the band to a C–H (C–D) deformation. However, recent experiments on D/H exchange in adsorbed alcohols give evidence that C–H groups undergo D/H exchange at the Pt surface [94], thus invalidating the use of isotope band shifts as a diagnostic criterion for a C–H vibration.

A feature at 1200–1230 cm^{-1} was observed in EELS spectra of methanol adsorbed on Pt(111) [81]. Sexton suggested that this band could be due to adsorbed hydrogen (compare with Sec. 5) which is stabilized in the presence of co-adsorbed CO [81]. However, as discussed in Sec. 7.1, there is no agreemnt over the assignment of the H–Pt band at 1200 cm^{-1} to an asymmetric or a symmetric mode. While EELS experiments, due to the impact scattering mechanism, can show modes parallel and perpendicular to the surface [22, 40], this is not the general case for surface IR spectroscopy.

Applying the EMIRS technique (with methanol in the solution) [84] features near 3000 cm^{-1} and 1700 cm^{-1} decrease after a long period of spectra accumulation. These features were not observed in FTIR experiments measured in the absence of bulk methanol [91]. The question of the nature of the methanol adsorbate deserves further attention.

One of the problems in identifying reaction intermediates at potentials above 0.5 V vs. RHE is the depletion of reactants in the thin layer cavity. This concentration change disturbs the electrochemical reaction and causes bands in the spectra due to uncompensated solution species. An electrochemical flow cell was designed which allows a continuous flow of fresh solution in the thin layer during spectra acquisition [95]. The experiment in Fig. 28 was performed using this cell with a 0.01 M CH_3OH, 0.5 M $HClO_4$ solution flowing through the thin layer [95]. The continuous supply of reactant can keep its concentration at a level high enough to maintain a

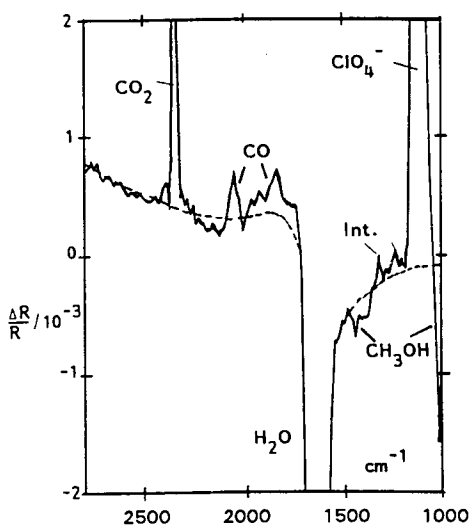

Fig. 28. Difference spectrum in a 0.01 M methanol solution in 0.5 M $HClO_4$ obtained using a continuous flow of electrolyte. Working electrode: polycrystalline Pt. Sample and reference potentials: 500 and 0 mV vs. SCE. (After [95]). Reprinted by permission of Pergamon Press.

stationary current flow. But, as long as a faradaic reaction is taking place, the compensation of solution features cannot be attained. This is attested by the presence of bands for the consumption of methanol and production of CO_2 in the spectrum of Fig. 28. In view of this, it is difficult to say whether the bands indicated as features for intermediates in that Figure are due to adsorbed or soluble species.

The interest in the use of methanol in fuel cell has re-activated fundamental and applied research in the last decade. Approaching the conditions for practical systems, Hamnett and coworkers have obtained FTIR spectra during the adsorption of methanol on finely divided Pt catalysts deposited on graphite [96]. These authors suggest that the activity of the fine-particle catalyst toward the dehydrogenation of methanol is enhanced. Correspondingly, spectra obtained using this catalyst show the formation of adsorbed carbon monoxide at potentials as low as 50 mV vs. RHE.

7.2 Ethanol

7.2.1 Soluble Products

In-situ FTIR studies on the electrooxidation of ethanol on polycrystalline Pt [97–99] as well as on single-crystal Pt electrodes [100, 101] have shown the formation of acetaldehyde and acetic acid in addition to carbon dioxide as soluble products. Figure 29 shows the typical features for these products, which were assigned according to Table 1.

Table 1. Assignment of some of the fundamental bands in the spectra of Fig. 29 corresponding to oxidation products of ethanol at polycrystalline platinum in acid solution.

Wavenumber (cm^{-1})	Species	Functional group	Comments	Ref.
2500–3000	Acetic acid	COOH	OH str. (broad)	[102]
2342	CO_2		O–C–O asym. str.	[103]
2050	$CO_{ads.}$		C–O str.	[15]
1717	Acetaldehyde	CHO	C–O str. (carbonyl)	[102]
1724	Acetic acid	COOH	C–O str. (carbonyl)	[102]
1395/1281	Acetic acid	COOH	Coupled C–O str./OH def.	[104]
1353	Acetaldehyde	CH_3	CH_3 def.	[105]

The band intensities have been used for a quantitative determination of the soluble products during ethanol oxidation [99–101]. However, soluble substances formed in the thin layer slowly diffuse to the surrounding solution, introducing a time-dependent uncertainty in the measurements.

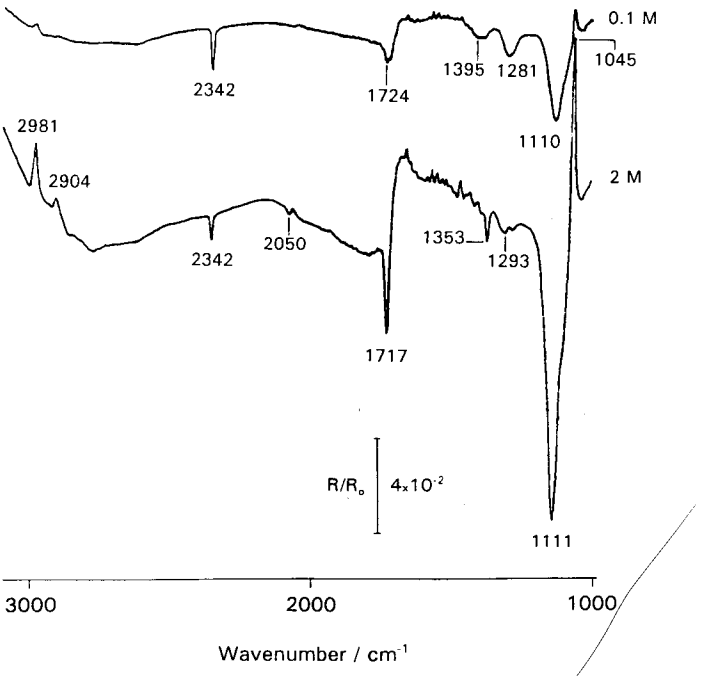

Fig. 29. FTIR spectra, taken with p-polarized light, during the electrooxidation of ethanol on a platinum electrode at 1.4 V vs. RHE (see Table 1 for band assignment).

7.2.2 Adsorbed Intermediates

The adsorption of ethanol on Pd(111) in UHV was examined by Davis and Barteau [80]. At 170 K, surface ethoxide (CH_3CH_2O) was observed. Annealing to 200 K transforms the ethoxide into acetyl, which degrades above 300 K to CO.

EMIRS studies of ethanol on platinum electrodes have demonstrated the presence of linearly bonded carbon monoxide on the surface [106]. An important problem in the use of EMIRS to study alcohol adsorption is the choice of a potential window where the modulation is appropriate without producing faradaic reactions involving soluble products. Ethanol is reduced to ethane and methane at potentials below 0.2 V [98, 107] and it is oxidized to acetaldehyde at *c* 0.35 V. Accordingly, a potential modulation would be possible only within these two limits. Outside these potential region, soluble products and their own adsorbed species complicate the interpretation of the spectra. The problem is more serious when the adsorbate band frequencies are almost independent of potential. In this case, the potential window (0.2 – 0.35 V) is too narrow to obtain an appropriate band shift and spectral features can be lost in the difference spectrum.

As explained in Sec. 4.2, the FTIR technique does not constrain the operator to modulate the potential. Thus the experimental conditions for collecting spectra can be chosen according to the physicochemical properties of the system under study. In

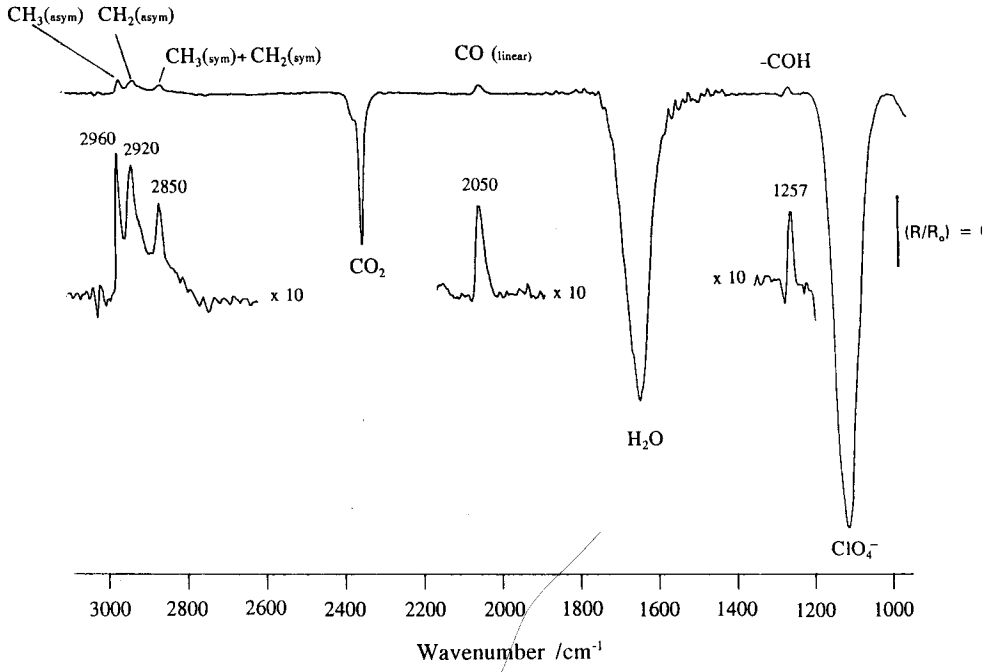

Fig. 30. Spectrum for adsorbed ethanol on a platinum electrode. Ethanol adsorbed from 0.1 M C_2H_5OH+0.5 M $HClO_4$ at 0.35 V vs. RHE. After electrolyte replacement by base solution, a reference spectrum was taken at 0.35 V vs. RHE in the presence of ethanol adsorbate. After oxidative stripping at 1.5 V, the potential was re-set to 0.35 V and the sample spectrum was collected.

a recent study on the adsorption of ethanol at platinum electrodes in acids [107], the following experimental procedure was applied.

After adsorption of ethanol at 0.35 V electrolyte was replaced by the base solution (0.5 M $HClO_4$). Then two groups of interferograms were collected, one in the presence of adsorbed ethanol at 0.35 V and the second one after oxidizing the adsorbate by applying a potential step to 1.50 V, and resetting the potential to 0.35 V.[3]

The difference spectrum of Fig. 30 shows the *loss* bands (positive-going) for all *adsorbed* species which have been oxidized at 1.5 V. The negative-going bands are due to the increase in concentration of solution species during the electrochemical processes in the cavity of the thin layer between the working electrode and the IR window. These are the negative-going band at 2343 cm^{-1} form the CO_2 produced at 1.50 V (which slowly diffuses out of the thin layer), and the bands at 1642 and 1100 cm^{-1} due to water and ClO_4^- ions, respectively.

Besides the band for linearly bonded CO at 2055 cm^{-1} one observes the asymmetric CH_3 and CH_2 group frequencies at 2960 cm^{-1} and 2940 cm^{-1} respectively

[3] Taking sample and reference spectra at the same potential diminishes spectral distortion due to changes in the thin layer.

[106]. The corresponding symmetric modes overlap under the band observed at 2850 cm^{-1}. At 1257 cm^{-1} a feature is observed which can be assigned to the C–O stretch of a species containing a COH group (e.g., a tertiary alcohol group) [102].

The CH group frequencies mentioned above could suggest the presence of species of the from $-CH_2CH_3$ (ethyl) or $-OCH_2CH_3$ (ethoxide). However, taking into account an sp^3 hybridization of the carbon atoms, the asymmetric CH_2 vibration of an ethyl group directly bound to the metal surface would have a transition moment vector parallel to the surface, i.e. forbidden by the surface selection rule. It was therefore suggested [107] that the bands in the 2900 cm^{-1} region are due to an ethoxide species:

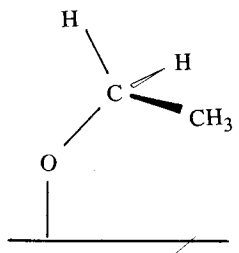

In this species the C–O bond is tilted away from the surface normal and the CH_2 group becomes a favorable position for the excitation of both symmetric and asymmetric vibrations. Both vibrations would also be active for the methyl group. This species can therefore explain the spectrum of ethanol adsorbate. The dipole moment of the C–O bond in the ethoxide may have a negligible component perpendicular to the surface, a situation which is unfavorable to observation of the corresponding mode (expected at *c.* 1000–1050 cm^{-1}).

The band at 1257 cm^{-1} in the spectrum of Fig. 30 has been assigned to the C–OH stretch of a tertiary carbon atom [107]. Accordingly, a species of the form $=COH-CH_3$, has been suggested. Tertiary alcohols absorb in the range 1205–1125 cm^{-1} [102]. In the adsorbed state, a band shift to higher frequencies could be expected in view of the towfold coordination to the metal surface.

A species of the form $-CO-CH_3$ was also suggested as one of the constituents of ethanol adsorbate [107]. For an sp^2 hybridization the C–O stretching could have a negligible component perpendicular to the electrode surface. The spectrum in Fig. 30 does not allow a $-CO-CH_3$ species to be either confirmed or discarded.

7.3 Other Alcohols

Bands in the C–H stretching region were observed by similar procedures to those used in the case of ethanol, during the adsorption of propanol ($CH_3CH_2CH_2OH$), allyl alcohol ($CH_2=CHCH_2OH$) and propargyl alcohol ($CH\equiv CCH_2OH$) [108]. The spectrum in Fig. 31, taken after absorption of propargyl alcohol, exhibits the stretching bands of CH_3 and CH_2 groups. Particularly interesting is the presence of the

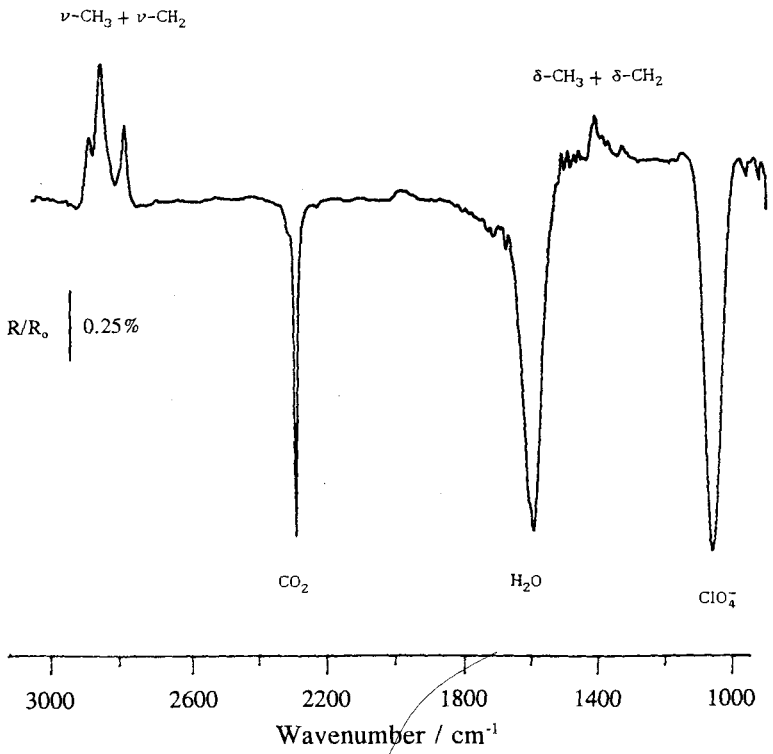

Fig. 31. Spectrum for adsorbed propargyl alcohol (PA) on a platinum electrode. PA was adsorbed from 5×10^{-3} M PA + 0.5 M $HClO_4$ at 0.4 V. Experimental procedure as in Fig. 30, but with reference potential = 0.4 V.

C–H bending modes in the 1400–1330 cm^{-1} region. Propargyl alcohol presented the highest intensity for the C–H stretching. The presence of methyl groups in the adsorbates of allyl and propargyl alcohols indicates a hydrogenation during the adsorption process. Since adsorbed carbon monoxide is observed at the same time, a disproportionation process has been suggested to occur during the adsorption [108].

8 Adsorption of Pseudohalide Ions

The adsorbed ions so far studied using in-situ infrared spectroscopy can be divided into two classes: the pseudohalides and the oxyanions (sulfates and phosphate species). Other ions, such as chloride, have been the subject of investigations using in-situ far-infrared spectroscopy, but the results are not conclusive.

Pseudohalide ions (CN^-, SCN^-, OCN^-, N_3^- generally present a strong and irreversible adsorption which parallels their great capacity to form complexes.

8.1 Cyanide

The cyanide ion is the most studied adsorbed ion of the pseudohalides group. Cyanide, being a charged species isoelectronic with carbon monoxide, is an important reference point for understanding the role of charge in adsorption as well as the vibrational properties of charged adsorbates in relation to neutral molecules. Surface Enhanced Raman Spectroscopy (SERS), measurements [109] have shown that several surface species are formed on silver electrode surfaces interacting with CN^-. This property reflects its ability to form complexes with silver. In-situ infrared spectroscopy has the advantage of not being limited to the group of metals presenting a SERS effect, although the first studies using in-situ infrared spectroscopy were made on silver and gold [110–114].

8.1.1 Cyanide Adsorbed on Ag, Au and Cu

Spectra taken using polarization modulation in CN^- solutions are shown for Ag(111) and Au(111) in Fig. 32a and b (see p. 170), respectively [111]. The spectra exhibit not only adsorbate but also solution features assigned to metal complexes as summarized in Table 2. The band at 2080 cm^{-1} observed in the spectra of CN^- on silver, which was also observed using s-polarized radiation, corresponds to the stretching vibration of free CN^- ions in solution [115]. Likewise the bands at 2136 cm^{-1} for silver and 2146 cm^{-1} for gold are assigned to the $Ag(CN)_2^-$ and $Au(CN)_2^-$ complex ions respectively [111, 114]. They appear at potentials where the electrode metals begin to be oxidized in the presence of CN^-.

The band at 2167 cm^{-1} appearing at potentials above than 0.3 V vs. NHE on the silver electrode, was assigned to an AgCN solid film deposited on the metal [111]. In both series of spectra a potential-dependent band situated around 2097 cm^{-1} on Au and 2100 cm^{-1} on Ag has been attributed to the linearly adsorbed CN^- ion (in

Table 2. Vibrational frequencies for metal cyanide complexes and solid cyanide films with metal electrodes.

Metal	Frequency (cm^{-1})	Approximate assignment
Cu	2077	$Cu(CN)_4^{3-}$
	2093	$Cu(CN)_3^{2-}$
	2126	$Cu(CN)_2^-$
	2170	CuCN film
Ag	2136	$Ag(CN)_2^-$
	2167	AgCN film
Au	2146	$Au(CN)_2^-$
Pd	2135	$Pd(CN)_4^{2-}$
	2170	$Pd(CN)_6^{2-}$

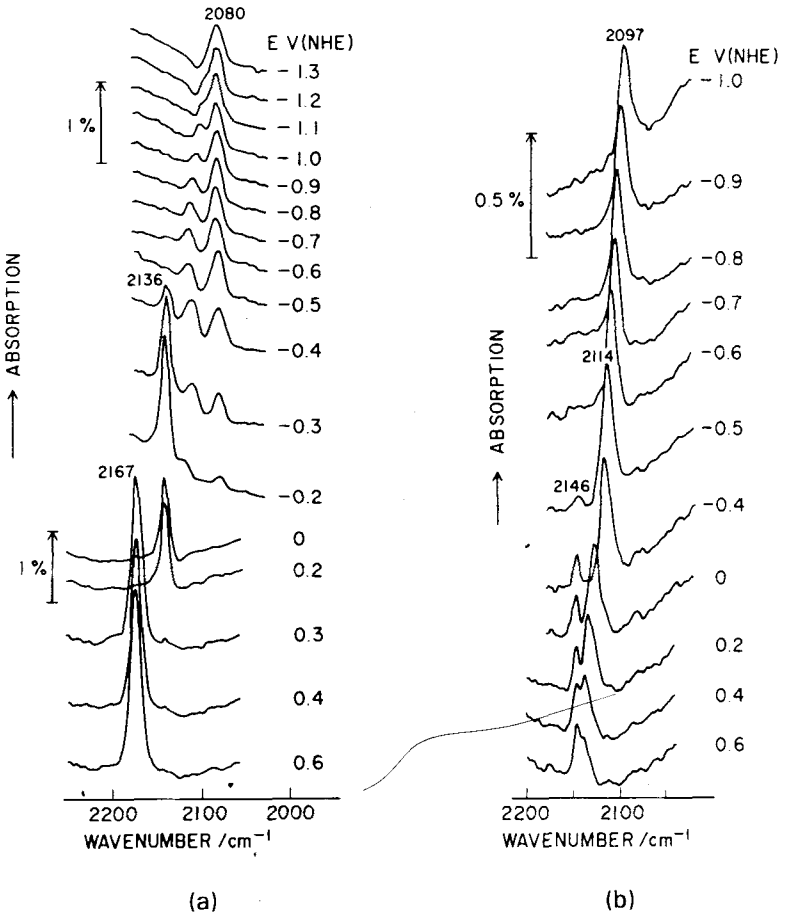

Fig. 32. FT-IRRAS spectra for adsorbed CN^- on polycrystalline Ag (a) and Au (b) electrodes in 0.1 M KCN + 0.5 M K_2SO_4. Adsorption potentials as indicated. (Taken from [111]). Reprinted by permission of Elsevier Science.

the spectra for silver this feature is very weak). This band was observed only with p-polarized radiation and presents the characteristic potential shift of adsorbed species. On both metals this mode shows a positive shift with respect to the free solution ion.

Adsorption of CN^- on a silver metal film was reported by Hatta et al. [112], using multiple internal reflection in an ATR (attenuated total reflection) prism configuration. Basically the same features were observed by Hatta et al. as in the external reflection approach, namely a potential-dependent band located between 2100 and 2118 cm^{-1} assigned to the adsorbed CN^- ion and another band located at 2143 cm^{-1}, assigned to the $Ag(CN)_2^-$ complex. The feature at 2167 cm^{-1} was not observed, because of the limited potential range used in this experiment to avoid the dissolution of the silver film [112].

The adsorption of CN^- on a polycrystalline copper electrode has been studied experimentally by Lee et al. [116]. Since copper oxidizes more readily than gold and silver, the results depend strongly on the cyanide concentration. At low cyanide concentration in solution (2×10^{-3} M), a potential dependent band between 2084 and 2120 cm^{-1} was assigned to the linearly adsorbed CN^- ion (Fig. 33, p. 172).

In concentrated cyanide solutions the copper electrode presents three bands in the 2077–2126 cm^{-1} range assigned to Cu–CN complexes. These bands make the identification of adsorbed species very difficult. At the highest potential observed, −0.2 V vs. Ag/Ag^+ a CuCN film was identified through a band centered at 2172 cm^{-1} [116].

A common feature of the adsorbate band for these metals is the shift of the C–N mode to higher wavenumbers in the adsorbed state in relation to the free ion in solution. This positive shift is also observed for cyanide complexes, and has been attributed to the fact that CN^- is a better σ-donor than it is a π-acceptor. Due to the weak antibonding character of the 5 σ orbital, σ-donation produces a bond strengthening effect [115]. These facts were the subject of theoretical calculations [117, 118].

Anderson et al. [117] have shown that the σ_p-donation upon bond formation is dominant, while the shifts for π and π* are very small. Accordingly, the frequency shift to higher wavenumbers should be due to the strengthening effect of σ donation, since the σ_p-orbital is antibonding, as stated above. Recent calculations of Nelin et al. [118] show, however, that CuCN molecules are highly ionic. It has been found that the ionicity of the Cu–CN bonding is even higher in a $Cu_{10}CN$ cluster [119], indicating that for metal surfaces CN^- should preferentially form an ionic bond. It is expected, however, that ionic bonds produce a less pronounced charge transfer than proposed above for σ_p-donation. Consequently the results of [118] cannot explain the band shift to higher wavenumbers.

Besides this theoretical controversy, it is interesting to observe that the band intensity for silver (see Fig. 32a) and copper (Fig. 33) is potential-dependent. This suggests that the interaction of CN^- with the metal surface presents some electrostatic contribution, as expected for ionic bonding. Contrary to this, a nearly constant intensity of the CN^- adsorbate band is observed on gold [114] (Fig. 32b) and a bipolar band was observed in SNIFTIRS experiments [113]. These facts suggest a more irreversible adsorption of CN^- on gold than on Ag and Cu. Irreversible adsorption is expected for bonds with a higher covalent than ionic character.

8.1.2 Cyanide Adsorbed on Transition Metals

The adsorption of CN^- on transition metals electrodes has been studied on Pt [120–123] and Pd [124]. In contrast to Ag, Au, and Cu, bands below 2080 cm^{-1}, which is the frequency for the C–N stretching in solution, appear for adsorbed species on these metals. On a Pt electrode Kawashima et al. [120] have observed that the number of bands of adsorbed CN^- depends on the CN^- concentration in solution. As observed in Fig. 34, a feature between 2060 and 2090 cm^{-1} is present at all concentrations and has been assigned to linearly adsorbed CN^- ions [120]. For a CN^- concentration of 0.4 mM or lower, an additional feature appears at about

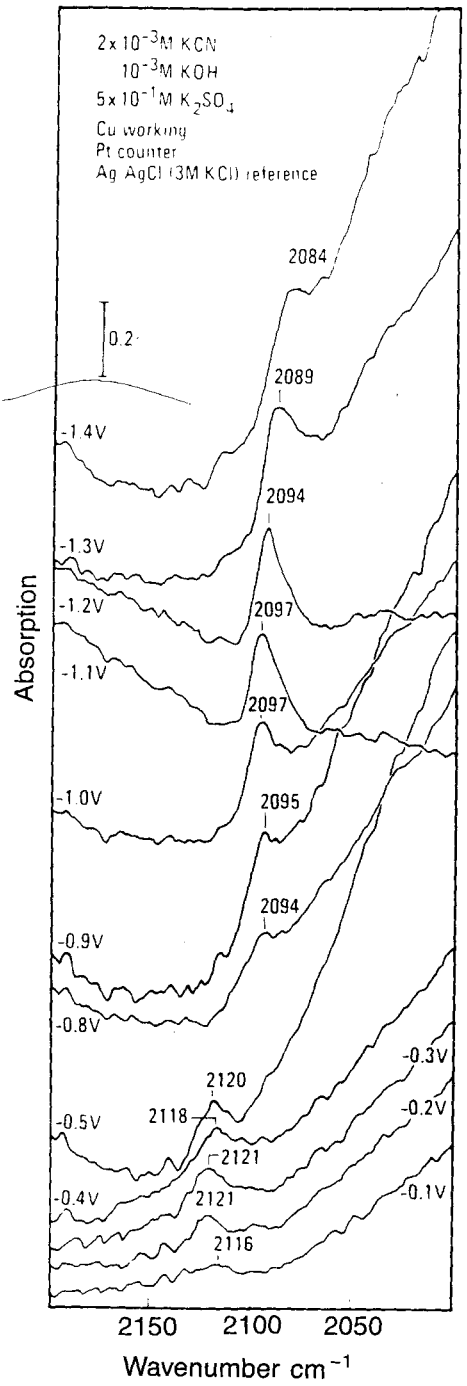

Fig. 33. FT-IRRAS spectra of the adsorbed CN^- on a polycrystalline Cu electrode at different adsorption potentials. Experimental conditions as indicated in the figure. (After [116]). Reprinted by permission of the Electrochemical Society.

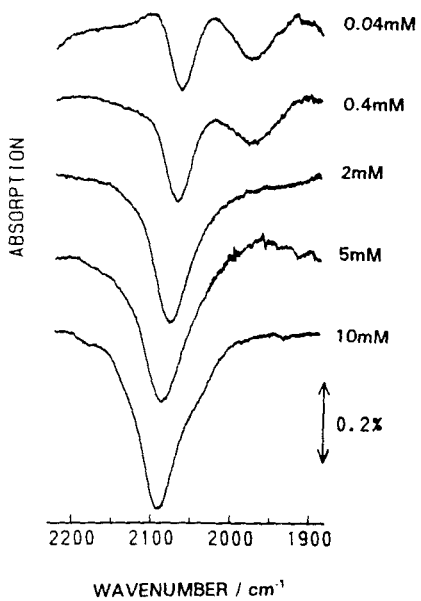

Fig. 34. PM-IRRAS spectra of adsorbed CN^- on a polycrystalline Pt electrode in KCN +1 M $NaClO_4$ solutions at −0.5 V vs. SHE. The CN^- concentrations are indicated. Note the formation of bridge-bonded CN^- at low CN^- concentrations. (After [120]). Reprinted by permission of Elsevier Science.

1980 cm^{-1} which was assigned to bridge-bonded CN^-. It must be emphasized that the band for linearly adsorbed CN^- obtained at low concentrations is slightly shifted to lower wavenumbers as compared with that of the free CN^- ion. The red shift observed for the platinum electrode contrasts with the blue shift discussed above for Au, Ag, and Cu. This could be an indication of a higher covalent character of the cyanide bond to platinum.

The adsorption of CN^- on Pt was also reported by Ashley et al. [121], using SNIFTIRS experiments. The interpretation of these results is complicated by the high potential used to measure the reference spectrum (+0.5 V vs. Ag/AgCl). At this potential CN^- can be oxidized to OCN^-. A bipolar band showing a negative-going part at 2171 cm^{-1} and a positive-going one at 2147 cm^{-1} was attributed to the adsorbate centered about 2155 cm^{-1}. However, an alternative explanation of the bipolar band could be given. The 2170 cm^{-1} peak can be due to the formation of OCN^- and the peak at 2147 cm^{-1} could be due to an adsorbate. Further experiments are necessary to clarify this question.

More recently, Ashley et al. [123], using a model of Korzeniewski et al. [125], suggested that the 2147 cm^{-1} band is due to the C-down adsorbed CN^-. This model, however, has several adjustable parameters that were obtained by the best fit to experimental data, i.e., presuming that the 2147 cm^{-1} band is due to the C-down adsorbed CN^-. Besides this, the formation of bridge-adsorbed CN^- observed by Kawashima et al. [120] was not taken into account.

Possible evidence of both forms of coordination was suggested by Tadjeddine and Guyot-Sionest [126, 127], using measurements of sum frequency generation (SFG). SFG is a nonlinear spectroscopic technique based on the incidence of an infrared tunable laser beam plus a visible pulsed laser beam. Upon reflection both frequencies are summed and detected in the visible region of the spectrum. The fact that the frequency mixing occurs only at the surface, i.e., in a noncentrosymmetric medium [128, 129], makes this technique highly surface-sensitive.

The SFG spectra for adsorbed CN^- on a Pt electrode can be seen in Fig. 35. At the most negative potential (−1 V vs. SCE) the adsorbed CN^- ion presents a very broad band centered at 2070 cm^{-1} (the same wavenumber was observed in the work of Kawashima et al. [120]), whose frequency changes rapidly with the applied potential ($d\bar{\nu}/dE$ = 60 cm^{-1}/V). A second band centered at 2150 cm^{-1} with a tuning rate of 10 cm^{-1}/V appears at more positive potentials. The band at 2070 cm^{-1} in the SFG measurement was attributed to a N-bound adsorbate, and the 2150 cm^{-1} band was attributed to a second layer of adsorbate. According to the authors, the best fitting of the experimental results is obtained when two layers of adsorbate with antiparallel dipoles are assumed, suggesting an adsorbate bilayer with the first layer bonded to the metal through the N atom and the second one bonded through the C atom. The difference in the tuning rate between the two bands was attributed to the closer proximity of the N-bound layer to the metal, where it experiences the highest potential drop [127]. An alternative explanation of the SFG results can be suggested. Thus the two peaks observed could be due to an interconversion of N-bonded and C-bonded adsorbates, with the coexistence of both at intermediate potentials.

Summarizing, the adsorption of CN^- on Pt presents some unclear features. The arguments used for band assignments are not convincing. It is not clear why

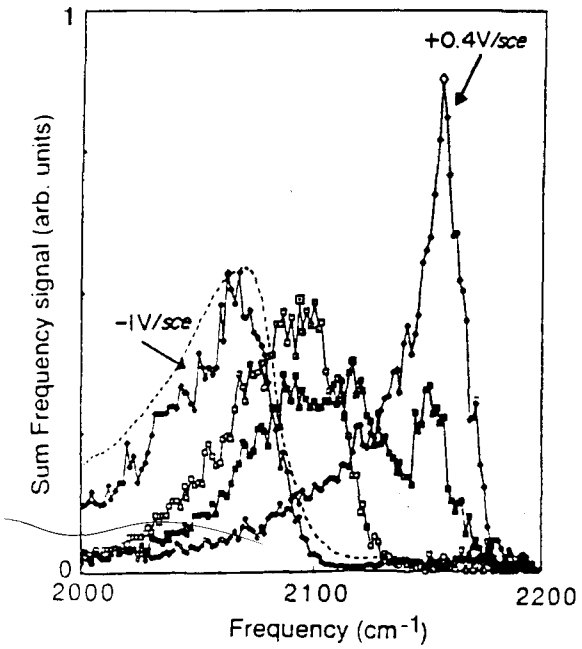

Fig. 35. SFG spectra of adsorbed CN^- on a polycrystalline Pt electrode in 0.1 M $NaClO_4$ + 0.025 M KCN. Potentials: −1 V, −0.6 V, −0.2 V and +0.4 V vs. SCE. Dotted line indicates adsorbed SCN^- at −1 V vs. SCE under the same conditions. (After [127]). Reprinted by permission of Pergamon Press.

Kawashima et al. [120] (see Fig. 34) have not observed the high-frequency mode. The small difference in CN^- concentration between the different studies (10 mM [120] and 25 mM [126]) is not sufficient to account for the different results. The observation of the M−CN vibration could clarify the situation, but his mode lies in the far-infrared region where the experimental difficulties are still not overcome.

The adsorption of cyanide on Pd electrodes was studied by using a combination of polarization and potential modulation (FT-IRRAS and SNIFTIRS) [124]. The reason for this combination is to enhance the surface signal, since two FT-IRRAS spectra taken at two different potentials were ratioed to obtain the SNIFTIRS spectrum. Despite this effort, a solution band at 2135 cm^{-1} (also observed with s-polarized light) persists in the spectrum (Fig. 36). The spectrum in this Figure taken with p-polarized radiation presents, however, a strong band at 1980 cm^{-1}, which was attributed to a bridged-bonded cyanide ion, and a weak band at 2065 cm^{-1} assigned to linearly adsorbed C-down CN^-.

The band for bridge-bonded CN^- at 1980 cm^{-1} has a higher intensity on Pd than on Pt. Also, higher amounts of bridge-bonded CO have been observed on Pd than on Pt in electrochemical and UHV environments (see Sec. 7.2.1). The reason was discussed in terms of a higher backdonation mechanism at Pd. As stressed by Ashley et al. [124], the work function and the 4d-band for Pd lie around 1 eV above the work function and the 5d-band for Pt. This difference favors the $d-\pi$ backdonation on palladium. This could be the reason for the lower wavenumbers observed for the adsorbate in comparison with the free ion in solution. Therefore, the bonding

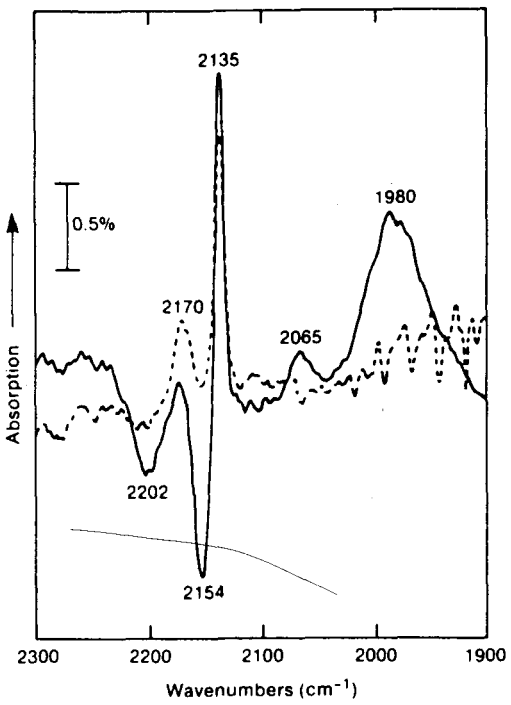

Fig. 36. Spectra for polycrystalline Pd electrode in 0.1 M $NaClO_4$ + 25 mM NaCN. The solid line is a combination of SNIFTIRS and IRRAS spectra. Two SNIFTIRS spectra at −0.9 V (reference potential) and +0.7 V vs. Ag/AgCl are ratioed to obtain the spectrum shown. The dotted spectrum was obtained by a SNIFTIRS with s-polarized radiation. (After [124]). Reprinted by permission of Journal of Chemical Physics AIP.

of CN^- to the Pd surface should have a stronger covalent character than the bonding to the other metals.

The bands at 2135 and 2170 cm^{-1} were assigned to soluble $Pd(CN)_4^{2-}$ and $Pd(CN)_6^{2-}$, respectively, based on values for palladium complexes in solution. The bands at 2202 and 2154 cm^{-1} were assigned to a PdCN film.

8.1.3 Vibrational Perturbations on the Cyanide-Adsorbed Layer

Potential Effects

The reason for the band shifts with potential for adsorbed CN^- is controversial. Either chemical effects (e.g., backdonation) or purely electrostatic effects (e.g., the Stark effect) are invoked to explain the dependence of frequency on the applied potential.

On Pd, the tuning rates for adsorbed CN^- are 12 cm^{-1}/V and 20 cm^{-1}/V for the linear CN^- and bridge-bonded CN^- respectively. The difference cannot be explained on the basis of a pure Stark effect but on the differences in backdonation between linear and bridged adsorbed CN^- [124]. The tuning rates and the band center frequencies on different metals are summarized in Table 3.

Table 3. Compilation of the frequency range of the band center frequency and tuning rate for adsorbed CN^- on different metals.

Metal	ν_{ads} (cm^{-1})	$(d\nu/dE)$ ($cm^{-1}\,V^{-1}$)	Ref.
Cu	2084 – 2120	45	[116]
Ag	2093 – 2115	40	[111]
Au	2097 – 2117	33	[114, 111]
Pd	2065	12	[124]
	1980[a]	20	
Pt	2060 – 2090	30	[120]
	1980[a]	–	
	2070	60	[127]
	2150	–	

[a] Bridge-bonded CN^-.

Lateral Interactions

The dependence of the C – N stretching frequency on the CN^- concentration in solution has been studied at gold [114] (Fig. 37). Since the band intensity increases with the CN^- concentration in solution, it is reasonable to conclude that the shift in the band position is associated with increasing lateral interactions. No band broadening is observed with increasing coverage by CN^-, indicating that possibly the free charge causes electrostatic repulsion and avoids an inhomogeneous broadening (see Sec. 3.4) or the formation of ordered islands.

Using the method suggested by Crossley and King [130], lateral interactions of adsorbed CN^- ions on gold electrodes were studied using isotopic mixtures of $^{12}CN^-$ and $^{13}CN^-$ [114], as shown in Fig. 38. The principle of the method was described in Sec. 6.5 for adsorbed CO, and consists in separating the dynamic dipole-dipole coupling from the chemical shift.

The decrease in wavenumber when diluting $^{12}CN^-$ in $^{13}CN^-$ (or vice versa) in the adsorbed layer can be seen in Fig. 38. This is clear evidence that a dynamic dipole-dipole coupling is operative at increasing concentrations. Although it was concluded that practically all the shift observed in Fig. 37 is produced by dipole-dipole coupling [114], a static (or chemical) shift could contribute to the overall band shift. In order to separate the two effects it is necessary to know the singleton frequency of the adsorbed CN^- (i.e., the frequency under conditions of no lateral coupling). In principle, this frequency can be obtained by extrapolating the band center frequency to vanishing coverages. Although the actual CN^- degree of coverage is not known, we observe in Fig. 37 that the band center frequency at the lowest CN^- concentration is 2096 cm^{-1}. Thus the singleton frequency must be even lower. The extrapolated frequency for $^{12}CN^-$ from Fig. 38 is 2101 cm^{-1}, i.e., the shift observed in Fig. 37 cannot be attributed only to dipole-dipole coupling. A chemical shift of comparable magnitude must also be operative.

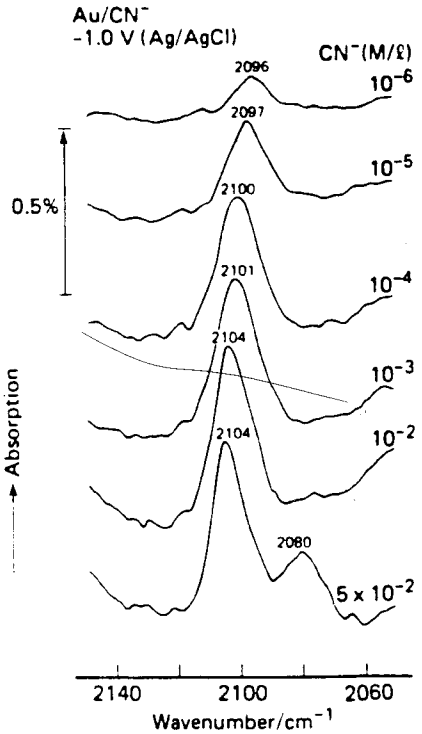

Fig. 37. FT-IRRAS of the adsorbed CN^- on polycrystalline gold electrode in KCN with 0.5 M K_2SO_4 at different CN^- concentrations as indicated. (Taken from [114]). Reprinted by permission of the American Chemical Society.

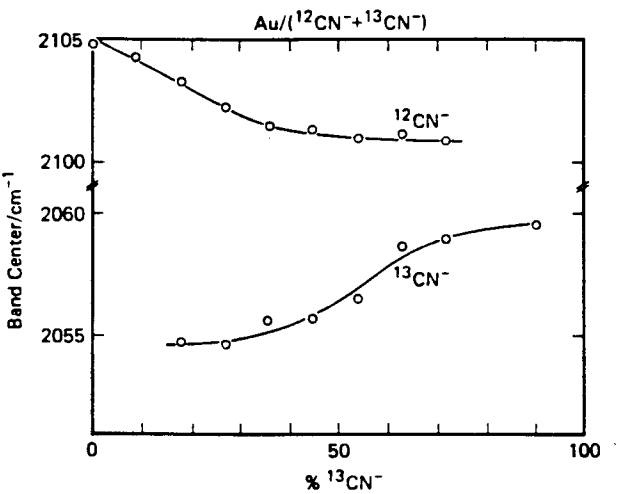

Fig. 38. Dependence of the C–N stretching frequency of adsorbed $^{12}CN^-/^{13}CN^-$ isotopic mixtures on a gold electrode in 0.5 M $K_2SO_4+CN^-$ solution. The relative concentration $^{12}CN^-/^{13}CN^-$ in solution was changed in a solution of constant concentration (10^{-2} M) of cyanide. (After [114]). Reprinted by permission of the American Chemical Society.

The dynamic dipole-dipole coupling for CN^- is relatively small compared with that of adsorbed CO. For CO on Pt(111) a shift of *c.* 30 cm^{-1} is observed for half coverage [55] and for polycrystalline platinum the coupling is so strong that the two bands collapse at intermediate coverages [131]. The chemical shift for CN^- is of the same order as that for CO adsorbed on a Pt(111) electrode [55] (see Sec. 6.2).

The relatively low dynamic dipole-dipole coupling in the case of adsorbed CN^- could be indicative of a relatively high electrostatic repulsion between adsorbed charged species, generating a large distance between neighboring ions.

8.2 Adsorption of Thiocyanate

8.2.1 Chemical Properties and Electrooxidation Reactions

Thiocyanate forms metal complexes [115] coordinating through both S and N atoms. Likewise, both kinds of coordination are expected when SCN^- is adsorbed on metal electrodes.

For the free SCN^- ion in solution the C–N and C–S stretching vibrations are observed at 2065 and 750 cm^{-1}, respectively [115]. In solid KSCN these bands are located at 2053 and 746 cm^{-1}, respectively, i.e., very close to those of SCN^- in solution. However, when SCN^- coordinates to Ag^+ a strong band shift is observed. Thus the S–C and C–N stretching vibrations are located at 2140 and 718 cm^{-1}, respectively, indicating a strong chemical effect produced by the formation of the silver complex. It is worth noting here that both modes are shifted in opposite directions compared with the free SCN^- ion. It is also interesting to point out that the coordination through the N atom produces a lower C–N stretching vibration (by 40 cm^{-1}) than coordination through the S atom.

The oxidation of SCN^- on platinum and silver electrodes was studied in aqueous solution as well as in acetonitrile solutions [132]. In water, the primary oxidation product of SCN^- on a platinum electrode is rapidly hydrolyzed producing CO_2, NO_2^- and SO_4^{2-}, as shown by the characteristic features of these species at 2345, 1215, and 1111 cm^{-1}, respectively (Fig. 39). On silver electrodes an AgSCN film is formed at potentials above 0.5 V vs. SCE.

8.2.2 Adsorption of SCN^- on Silver Electrodes

The coordination of SCN^- to silver has been investigated by Samant et al. [133] from both experimental and theoretical points of view. The spectra in Fig. 40 were obtained using polarization modulation at 0.0 V vs. Ag/AgCl in solutions containing different concentrations of SCN^-.

Two remarkable characteristics are observed in these spectra: (a) there is practically no frequency change with the concentration of SCN^- in solution, suggesting that lateral interactions are very weak; and (b) in the spectrum for 10 mM SCN^- two bands, centered at 2114 and 2098 cm^{-1}, are observed. For other concentrations the

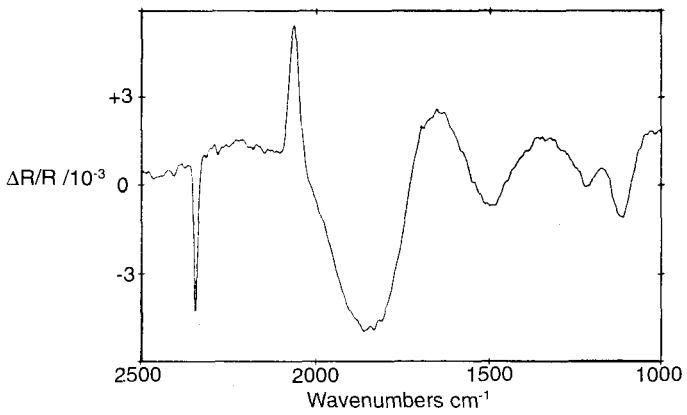

Fig. 39. Difference spectrum for oxidation of 10 mM SCN^- at polycrystalline Pt in 1 M KF. Potential modulation 0.0 to 1.0 V vs. SCE. (After [132]). Reprinted by permission of the American Chemical Society.

low-frequency mode appears as a shoulder. These bands have been assigned to SCN^- ions adsorbed through the S and N atom, respectively, based on the fact that the C–N stretching frequency is lower for coordination through the N atom than through the S atom.

The 2098 cm^{-1} band was not observed using internal reflection spectroscopy [112, 134]. In these experiments, the electrode was a very thin Ag film deposited on an IR-transparent substrate. It is likely, as pointed out by Samant et al. [133], that N-bonded SCN^- coordinates only in a very well defined low-index plane which may be not present in the thin Ag films.

From Fig. 40 it is possible to conclude that the S-bonded SCN^- adsorbate must be the predominant species. Self-consistent field (SCF) calculations [133] show, however, that to obtain comparable energies for the S- and the N-bonded SCN^- adsorbate, the S-down adsorbate must be almost flat-adsorbed (about 100° compared with the perpendicular adsorption for N-down adsorbate), otherwise the N-bonded adsorbed SCN^- is energetically more favorable. According to Parry et al. [134], the six polarizable lone-pair electrons on the S atom should induce a relatively flat orientation for S-bound adsorbate, while the single lone-pair electron on the N atom would induce a perpendicular adsorption for the N-bound adsorbate.

Evidence of a relatively flat orientation for adsorbed SCN^- is also given by the studies by Weaver and coworkers [113, 135] (Fig. 41), using SNIFTIRS, where the loss of thiocyanate from solution (positive band) can be observed simultaneously with the gain of adsorbed thiocyanate (negative band). Since both quantities must be equal, the smaller intensity of the adsorbate band indicates that the absorptivity for adsorbed SCN^- is smaller than for the solution species. This could account for the proposed flat orientation. The S-coordination of the SCN^- ion leads to a considerable decrease in the dynamic dipole moment [135].

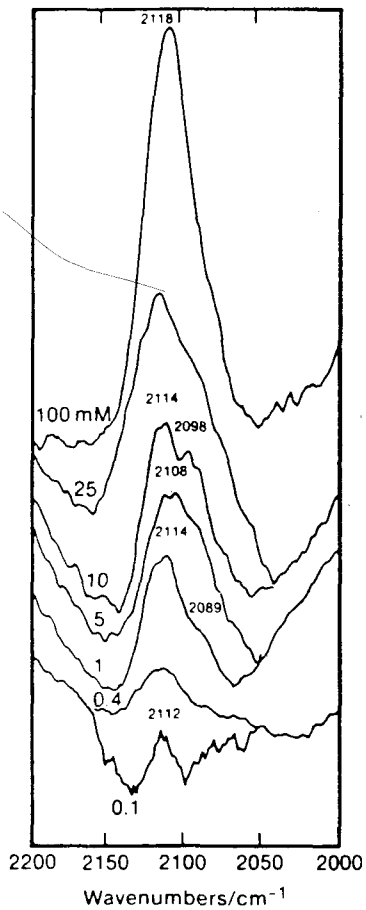

Fig. 40

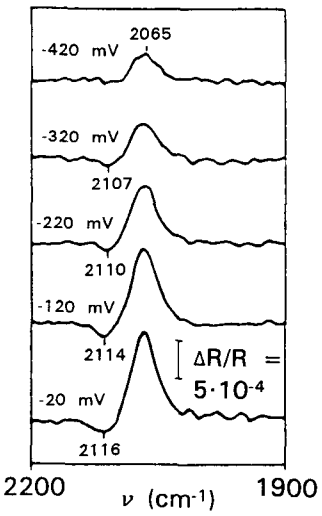

Fig. 41

Fig. 40. FT-IRRAS of adsorbed thiocyanate ions on Ag at 0.0 V vs. Ag/Ag^+ in solutions of various concentrations as indicated. (Taken from [133]). Reprinted by permission of the American Chemical Society.

Fig. 41. Spectra for adsorbed thiocyanate at silver. Reference potential −920 mV vs. SCE; sample potentials as indicated; 5 mM NaNCS+0.1 M $NaClO_4$. (Reproduced from [135]). Reprinted by permission of the American Chemical Society.

8.2.3 Adsorption of SCN^- on Gold Electrodes

The presence of N-bonded adsorbed SCN^- on gold electrodes has been suggested by Parry et al. [134], based on the spectra shown in Fig. 42. The features shown in these spectra have been interpreted as two superimposed bands: one very broad band gaining intensity at more positive potentials, which was assigned to the C−N stretch of S-bound adsorbed SCN^-, and another narrow band pointing in the opposite

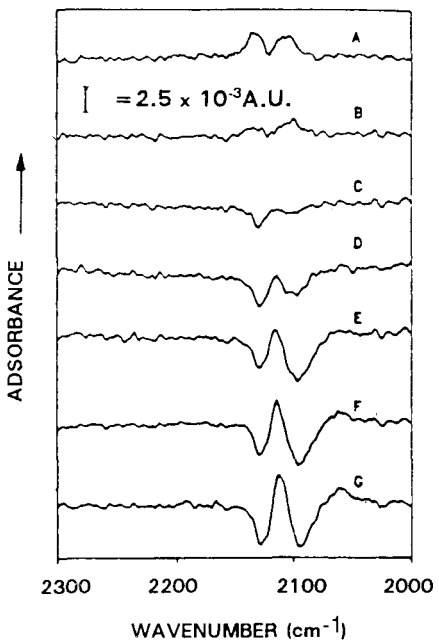

Fig. 42. Difference spectra for the oxidation of 25 mM NaSCN in 0.15 M $NaClO_4$ on Au. Reference spectrum taken at 0.0 V vs. SCE; sample spectra from (A) to (G)+0.2, +0.1, −0.1, −0,2, −0.3, −0.4, −0.5 V. (After [134]). Reprinted by permission of the American Chemical Society.

direction and peaking between 2112 and 2122 cm^{-1}, assigned to N-bound adsorbed SCN^-. As the potential is scanned, an interconversion of the adsorbate seems to occur, as suggested by the opposite direction of these two bands.

The S-down adsorbate, being non-perpendicular to the surface, presents a variable adsorption angle, which leads to different interactions of the C−N stretching vibration with the electric field. A strong inhomogeneous broadening is thus expected for the S-bonded SCN^- ions, justified by the inhomogeneity of the polycrystalline electrode surface.

8.2.4 Adsorption of SCN^- on Platinum Electrodes

The potential-induced interconversion of S- to N-down adsorbed SCN^- ion was suggested by Ashley et al. [136] for the adsorption on a platinum electrode, based on the existence of a bipolar band in the spectrum (Fig. 43). A complication in these spectra, however, is that the same bands are observed with p- and s-polarized light, indicating the interference of solution species. The stronger intensity of the spectrum with p-polarized light was taken as a criterion to assign the observed bands to adsorbed SCN^-. In Sec. 4.3 we have discussed the invalidity of this criterion. Moreover, platinum complexes present strong bands between 2100 and 2130 cm^{-1}, i.e., in the region shown in Fig. 43.

In spite of these difficulties, the features at 2106 and 2137 cm^{-1} seem to be correctly assigned by Ashley et al. The former band was observed by Pons [137] as a

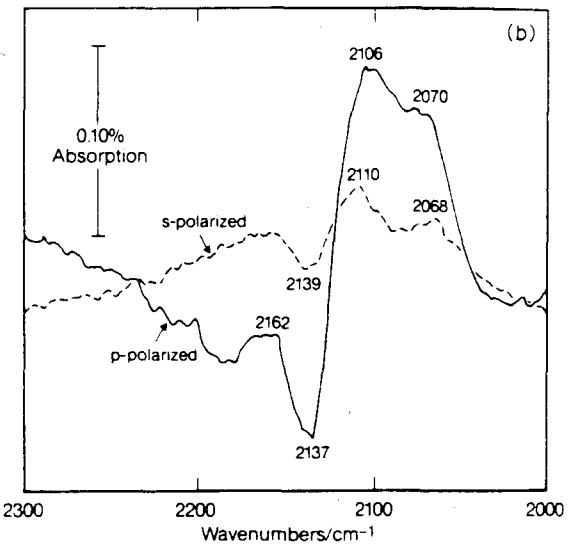

Fig. 43. SNIFTIR spectra from a Pt electrode in 25 mM NaSCN+0.1 M $KClO_4$. Applied step, 0.4 V to −0.95 V vs. Ag/AgCl. The latter was taken as the reference potential. (Taken from [136]). Reprinted by permission of Elsevier Science.

unique adsorbate feature at 2100 cm^{-1} mounted on a broad C−N solution band (located at 2075 cm^{-1}) due to SCN^- loss in the thin layer upon adsorption. The band located at 2137 cm^{-1} was observed in SFG experiments which, as discussed above, are only surface-sensitive. Based on these results, the data from Ashley et al. could be understood as a mixture of solution and adsorbate features.

Several aspects of this system are not clear; for example, what causes a bipolar band in the spectrum with s-polarized light and why has Pons [137] not observed the 2137 cm^{-1} feature? A comprehensive survey of the spectroscopic features observed for thiocyanate at electrochemical interfaces was given by Corrigan et al. [113] for gold and silver and by Ashley et al. for gold, silver and platinum [123].

8.3 Adsorption of Other Pseudohalide Ions

Results on the adsorption of azide (N_3^-) and cyanate (CNO^-) ions have been reported by Corrigan et al. [113, 135]. For adsorbed azide ion on a silver electrode only one potential-dependent band has been reported between 2074 and 2083 cm^{-1}. As discussed by Corrigan and Weaver [135], at low potentials a loss of azide ions in solution is observed (band at 2048 cm^{-1} in Fig. 44) without a corresponding adsorbate gain. As the potential is made more positive a weak adsorbate band is developed (2074 cm^{-1}). The most probable interpretation, according to Corrigan and Weaver, is that at low potentials the linear N_3^- ion is flat-adsorbed. As the degree of

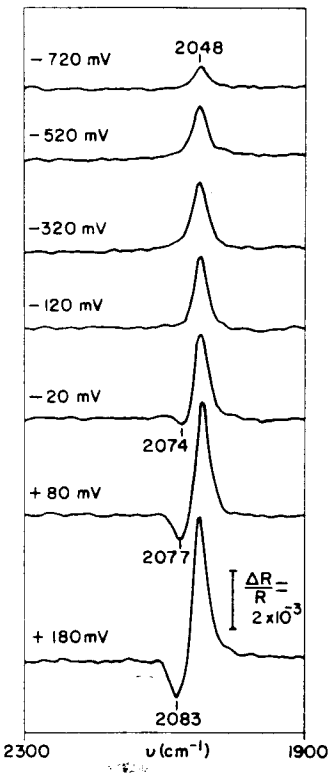

Fig. 44

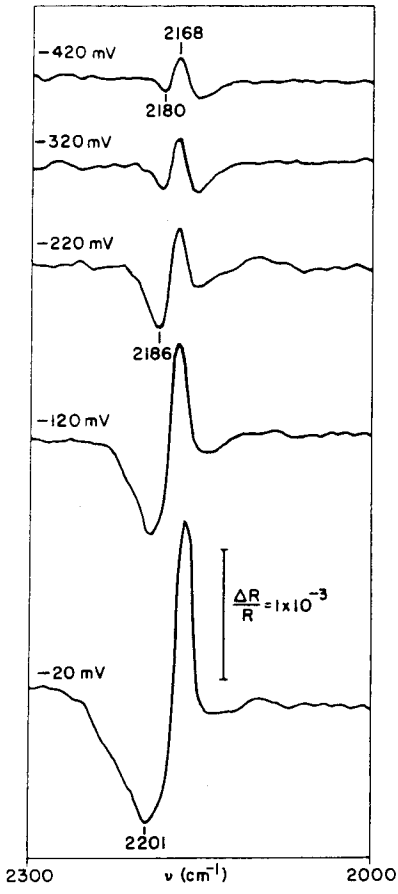

Fig. 45

Fig. 44. Difference spectra for adsorbed azide on Ag obtained in 0.01 M NaN_3 + 0.49 M $NaClO_4$. Reference spectrum taken at −970 mV vs. SCE; sample potentials as indicated. (From [135]). Reprinted by permission of the American Chemical Society.

Fig. 45. Difference spectra for adsorbed cyanate on Ag obtained in 0.01 M NaOCN + 0.1 M $NaClO_4$. Reference spectrum taken at −920 mV vs. SCE; sample potentials as indicated. (From [135]). Reprinted by permission of the American Chemical Society.

coverage increases, at more anodic potentials, the ions become perpendicularly adsorbed. Other possibilities such as chemical effects are ruled out, since no significant chemical effects are observed for azide complexes [135].

The adsorption of cyanate ions was studied on silver [113, 135] and gold electrodes. A bipolar band can be observed for adsorption on a silver electrode [135] (Fig. 45). Corrigan and Weaver [135] have attempted a deconvolution of this band after observing that the intensity of the positive-going part was lower than expected

from differential capacity measurements. Based on this, they suggested that the two negative-going parts in the spectra of cyanate on silver (Fig. 45) are the "wings" of a single broad surface band centered at 2170 cm^{-1}, close to the frequency of the positive band at 2168 cm^{-1}, which is due to the loss of cyanate from the thin layer. The negative band at 2170 cm^{-1} has been assigned to N-bound OCN^- in a bridged position (two- or three-fold coordinated) at low coverage, and the shoulder located at *c.* 2210 cm^{-1} at high coverage has been assigned to N-terminally bonded adsorbed OCN^-.

9 Oxyanions

The adsorption of oxyanions is important in electrochemistry because of the wide application of these ions in electrochemical systems of practical and fundamental interest.

Among the oxyanions, sulfate and phosphate are two systems of very great interest from both fundamental and applied points of view. First reports on FTIR investigations of phosphoric acid adsorbed on platinum electrodes appeared in 1985 [138]. Some years later a series of papers were published dealing with the spectroscopic investigation of sulfate species adsorbed on polycrystalline platinum [35, 36, 139, 140] and on single-crystal platinum(111) [141]. The common characteristic in the experimental approach used in these works is the use of solutions of single electrolytes, either sulfuric acid or an alkaline sulfate salt. The complexity of these multianion systems, involving different acid-base equilibria in solution and possibly also at the electrode surface, requires a careful consideration of the experimental conditions for their study. The ions under investigation must be kept at a low concentration and a supporting electrolyte must be chosen which fulfills the following conditions.

1. It must be infrared-inactive in the range of interest.
2. It should not be adsorbed.
3. If weak acids or bases are involved in the system under study, it must act as a buffer to compensate pH changes which can be caused by a potential change.

Mixtures of hydrofluoric acid and potassium fluoride were found to fulfill these conditions at a pH around the pK value for HF ($K = 6.74 \times 10^{-4}$). The buffer capacity of HF/KF mixtures diminishes at pH values higher and lower than the pK.

Results on the adsorption of sulfate and phosphate using this experimental approach were published recently [38, 142–147] and are summarized in the next sections.

9.1 Adsorption of Ions and Splitting of Degenerate States

Very important information on the physicochemical properties of the adsorbed ions can be gained through the analysis of the vibrational spectra. The interpretation of the spectral features is, however, in no way straightforward. Due to the interaction

with the metal surface, ions or molecules change their symmetry properties in the adsorbed state. This leads to the splitting of degenerate modes.

Whether a band splitting occurs in the case of sulfate adsorption at platinum was questioned recently [148]. It has been argued that, because of the weak interaction with the metal, attested by the reversibility of the adsorption, the degenerate mode of sulfate ions cannot split upon adsorption. Adsorbing ions have to replace water molecules, which have an adsorption energy of the order of 40–65 kJ/mol [149]. For the ions to become adsorbed, the bond energy should exceed this value. For bisulfate ions on polycrystalline Pt electrodes, the bond energy per oxygen atom has been estimated as 71 kJ/mol [148]. This value is of the order of a weak chemisorption, but considering the possibility of multicoordination, the strength of the bond per ion can reach the order of a true chemisorption.

The direct comparison of adsorbate modes with the modes for the *free* ions in solution, without considering symmetry changes in the adsorbed state, is not the correct procedure for band assignment. One must use the elements of group theory with the aid of the surface selection rule in order to make a proper spectral analysis.

9.2 Factors Determining the Symmetry of Adsorbed Sulfate Species: General Considerations

Pt(111), being the most closely packed of the three basal planes, presents almost ideal geometric dimensions for studying the symmetry properties of the adsorbed tetrahedral sulfate ion.

Free sulfate ions in solution, having the symmetry of a regular tetrahedron, belong to the T_d symmetry group. At frequencies above 900 cm^{-1} only one mode, the asymmetric S–O stretching vibration (1104 cm^{-1}) is infrared-active (Table 4). This high symmetry is broken upon adsorption. Oxygen atoms in direct contact with the surface become distinguishable from those directed toward the solution. In general a change to a group of lower symmetry (e.g. C_{3v} or C_{2v}) causes the splitting of degenerate bands (F or E) (Table 5). Consequently a larger number of modes become infrared-active.

Table 4. Fundamental modes for SO_4^{2-} and HSO_4^- [150, 151].

Species	Mode[a] (cm^{-1})			
	ν_1	ν_2	ν_3	ν_4
SO_4^{2-}	981(A)	451(E)	1104(F)	613(F)
HSO_4^-	1050(A)	417(E)	1230(E) 1341(A)	593(E) 885(A)

[a] (A) symmetric mode; (E) doubly degenerated mode; (F) triply degenerated mode.

Table 5. Correlation of the fundamental vibrations ν_1 and ν_3 of the T_d point group with C_{3v}, C_{2v}, and C_s point groups [103, 115].

Point group	ν_1 [a]	ν_3 [a]
T_d	$A_1(M_z)$: R	F_2 (M_x, M_y, M_z): IR, R
C_{3v}	$A_1(M_z)$: IR, R	$A_1(M_z)$: IR, R $E(M_x, M_y)$: IR, R
C_{2v}	$A_1(M_z)$: IR, R	$A_1(M_z)$: IR, R $B_1(M_x)$: IR, R $B_2(M_y)$: IR, R
C_s	$A'(M_z)$: IR, R	$A'(M_z)$: IR, R $A'(M_y)$: IR, R $A''(M_x)$: IR, R

[a] R, Raman-active mode; IR, infrared-active mode.
The direction of the dipole moment vector for the ions in solution is given in parentheses.

The main considerations for assignment of a band can be summarized as follows:

1. The possible symmetries for adsorbed sulfate are C_{3v} (for adsorption through one or three oxygen atoms) and C_{2v} (for adsorption through two oxygen atoms).

   When sulfate ions form complexes in solution having a C_{3v} symmetry, the triply degenerate (F) mode at 1100 cm^{-1} (ν_3 in Table 5) splits into two bands. Under C_{2v} the same mode splits into three bands [103, 115]. Besides this, in both cases a totally symmetric mode centered at about 980 cm^{-1} (ν_1 in Table 5), which is only Raman-active under the T_d symmetry, becomes infrared-active. Consequently, in the spectral range above 900 cm^{-1} "free" sulfate should present three modes under a C_{3v} symmetry and four modes under a C_{2v} symmetry. Whether the IR-active modes for the free ions under a given symmetry are also active for the adsorbed species depends on the orientation of the dynamic dipole moment with respect to the surface.
2. Bisulfate ions in solution belong to the C_{3v} symmetry group. Adsorption through three oxygen atoms does not change the symmetry. But if the ion is one- or two-fold coordinated upon adsorption, a change to a symmetry C_s should be observed. Table 5 indicates four IR-active bands for this symmetry of sulfate ions in solution.
3. The IR-active components of the dipole moments, indicated in Table 5 as M_x, M_y and M_z for the free ions, are restricted for adsorption on a metal surface to those allowed by the surface selection rule, i.e., to symmetric bands (A) having a component parallel to the z-axis (perpendicular to the surface). Modes having the allowed transitions in the y and x directions are forbidden by the surface selection rule. This is the case for all asymmetric bands. Thus, only symmetric bands should be infrared-active for reflection on a metal surface. This statement, however, requires a more careful analysis. In an electrochemical interface, where very

strong electric fields are operative, dipole moment components can be induced in the direction of the electric field: thus asymmetric bands can become IR-active.

4. Studies on sulfate complexes with transition metals indicate that coordination causes an enlargement of the S–O bond length of the oxygen atoms coordinated to the metal. This causes a decrease in the bond strength with a subsequent shift of the corresponding S–O stretch to lower wavenumbers [152]. At the same time the S–O bond involving non-coordinated O atoms is shortened.

9.3 Adsorption of Sulfate Ions on Single-Crystal Pt(111) Electrodes

As already shown by the early work of Clavilier et al. [153], the voltammetric response of Pt(111) depends strongly on the nature of the ions in solution. The adsorption states observed in the potential region between 0.4 and 0.9 V of a voltammogram measured in a fluoride solution (Fig. 46a) characterize the absence of specifically adsorbed ions. In the presence of sulfate species these states are shifted cathodically, as observed in the voltammogram taken in the fluoride base electrolyte after addition of 2.5×10^{-2} M H_2SO_4 (Fig. 46b).

Figures 47 and 48 show spectra taken at different potentials in sulfate solutions containing a fluoride base electrolyte at pH 2.8 (0.5 M KF+0.69 M HF) and 0.23 (7.3 M HF) respectively. Positive-going bands represent the solution loss of species being adsorbed. Negative-going bands are due to the adsorbate.

Adsorption begins at about 0.4 V, coinciding with the onset of the wave caused by specific adsorption in the voltammogram. Thus adsorption must be related to the processes causing the current under this wave, as indicated by Orts et al. [154]. However, it is noteworthy that the adsorption of sulfate increases beyond the limits of the voltammetric wave. At pH 2.8 the latter starts at 0.42 V and goes through a maximum at *c.* 0.55 V (Fig. 46b), while the band intensity for adsorbed sulfate grows continuously from the onset potential of the wave up to a maximum at *c.* 0.8 V (Fig. 47).

The solution loss band which is very pronounced at pH 2.8 indicates that no replenishment of these ions occurs in the thin layer within the time necessary to collect 1000 interferometer scans (*c.* 30 s) and to execute some software work (*c.* 8 s). The potential-dependent negative band located between 1230 and 1260 cm^{-1} and the shoulder near 1190 cm^{-1} are adsorbate features.

Only one adsorption band is observed at pH 0.23 (Fig. 48). Considering first the solution modes, according to Table 4 we expect two loss bands for bisulfate, which is the main solution species at this pH, at 1043 and 1195 cm^{-1}. The first is very weak and the second is missing in the spectra of Fig. 48. Only one strong band is observed between 1220 and 1280 cm^{-1}. A possible explanation for the missing *solution* feature at 1200 cm^{-1} could be that it is superimposed on an *adsorbate* feature, and both cancel out.

Adsorbed HSO_4^- ions should present the S–OH stretching vibration just above 900 cm^{-1}. This band, which is surface-allowed for bisulfate adsorbed either through

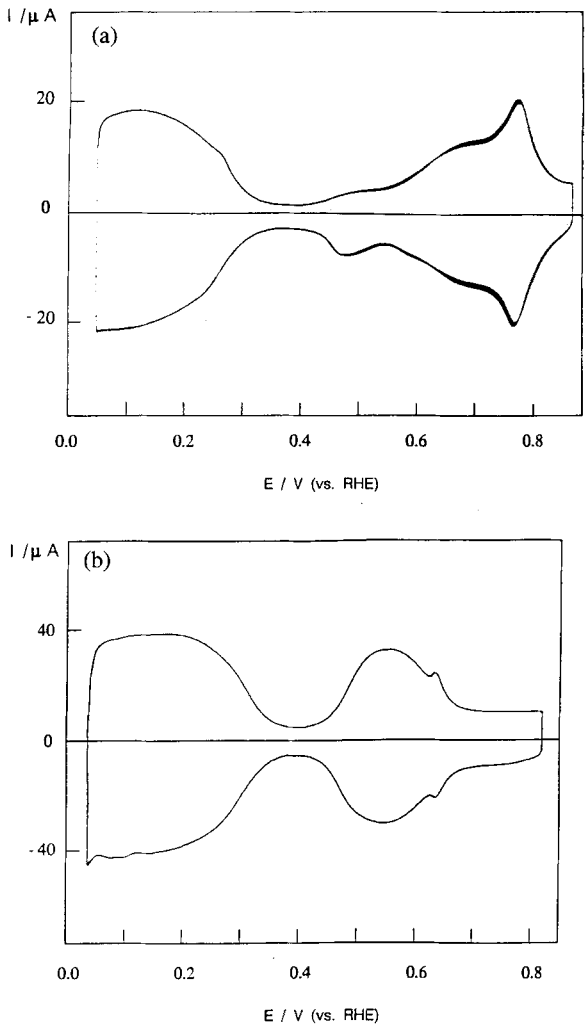

Fig. 46. Cyclic voltammograms for a Pt(111) electrode in (a) 0.5 M HF+0.69 M HF; $v = 50\,\text{mV s}^{-1}$; (b) 0.5 M KF+0.69 M KF+2.5×1^{-2} M K_2SO_4; sweep rate = 100 mV s^{-1}.

one, two or three oxygen atoms, is observed on polycrystalline platinum at 950 cm^{-1} (see Fig. 57). The absence of the S–OH stretching vibration could be a strong indication that bisulfate dissociates on the surface, i.e. at pH 0.23, as at pH 2.8, the species present on the surface is SO_4^{2-}. This possibility is further reinforced by other experimental facts, as follows.

In Fig. 49 the band center frequency is plotted against the potential for the 1220–1280 cm^{-1} mode at both pH values. Potentials in this plot are referred to the normal hydrogen electrode. The wavenumbers for the band centers coincide at both pHs, giving a common slope of 112 $cm^{-1}\,V^{-1}$. Other parameters, such as the halfwidths measured at the potential of maximum adsorption, are also similar (36.5 and 37.5 cm^{-1} at pH 2.8 and 0.23, respectively). These properties, which are a

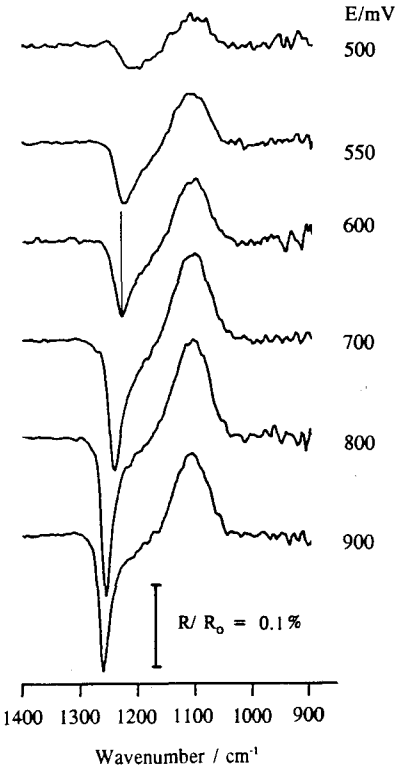

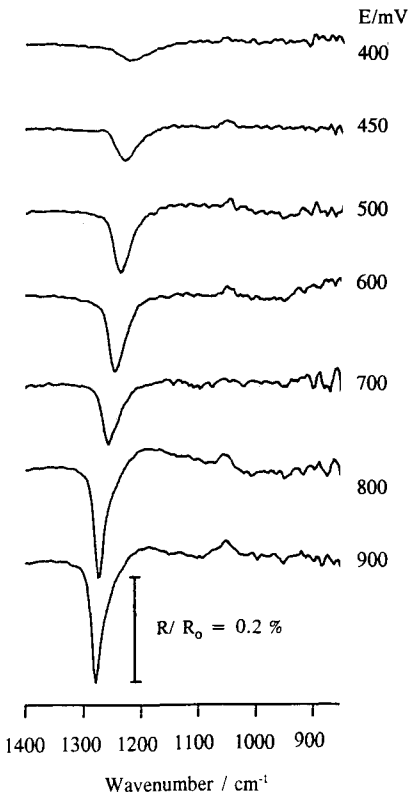

Fig. 47

Fig. 48

Fig. 47. FTIR spectra for adsorbed sulfate at Pt(111) in 2.5×10^{-2} M K_2SO_4 + 0.5 M KF + 0.69 M HF (pH = 2.8). Reference spectrum taken at 0.03 V vs. Pd/H_2. Sample potentials as indicated.

Fig. 48. FTIR spectra for adsorbed sulfate at Pt(111) in 2.5×10^{-2} M K_2SO_4 + 7.3 M HF (pH 0.23). Reference spectrum taken at 0.03 V vs. Pd/H_2. Sample potentials as indicated.

measure for the interaction with the applied electric field (see Sec. 10) and for the lateral interactions [21], are extremely sensitive to the mode involved and to the direction of the dipole moment. This supports the view that the $1220-1280\,cm^{-1}$ feature observed at both pH values belongs to the same vibrational mode, i.e. to the same species, namely SO_4^{2-}.

SO_4^{2-} is also the predominant species in solution at pH 2.8 (SO_4^{2-}/HSO_4^- concentration ratio = 6.7). The conversion of sulfate into bisulfate at the surface would require an enhancement of the base character of SO_4^{2-} ions in the adsorbed state, e.g. through a partial charge transfer from the metal to the adsorbed ion. Theoretical calculations [148] and recent experimental results [154] indicate a charge transfer in the opposite direction, i.e., from the adsorbed ion to the Pt substrate. Therefore no conversion of sulfate into bisulfate occurs on the surface.

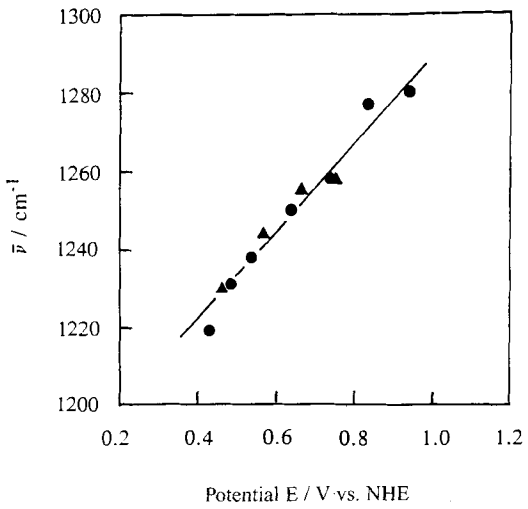

Fig. 49. Potential dependence of the band center frequency for the 1220–1280 cm^{-1} mode of adsorbed SO_4^{2-} on Pt(111). ● Data at pH 0.23, ▲ data at pH 2.8. Solution compositions as in Figs. 47 and 48. Note that the potentials are given against the normal hydrogen electrode.

The dissociation of HSO_4^- during the adsorption causes an increase of the H^+ concentration in the thin layer, which is additional to that produced by the desorption of hydrogen. There must be a competition for H^+ among the ions in solution (F^- and SO_4^{2-}), which could explain the low intensity for the solution loss band at 1050 cm^{-1}.

In conclusion, the possibility of HSO_4^- adsorption to a large extent at the Pt(111) electrode surface can be ruled out. This interpretation contrasts with that in the literature, where the adsorbed species at Pt(111) are considered to be bisulfate ions [141].

9.3.1 Symmetry of Adsorbed Sulfate

According to Table 5 for sulfate ions under C_{3v} symmetry three stretching modes are IR-active (two symmetric (A_1) and one doubly degenerate (E)). From these, only the symmetric modes are surface-allowed, i.e., they have a dipole moment component perpendicular to the surface (M_z in Table 5). Identical considerations for a C_{2v} symmetry leads to the conclusion that, in this case also, adsorbed species should present two bands.

The distance between two adjacent Pt atoms, 2.77 Å, fits well with the distance between two oxygen atoms in the sulfate ion, *c.* 2.5 Å (value given for bisulfate in [36]). So, from geometric considerations, a C_{3v} symmetry is very probable. A C_{2v} symmetry has been proposed for the adsorption of sulfate on well-ordered Pt(100) electrodes (see below) where the threefold coordination is not possible due to mismatch between surface structure and threefold coordination. Two well-separated strong bands (1200 and 1100 cm^{-1}) are observed, which account for the C_{2v} symmetry. There is definitely a difference in the behavior of the adsorbate on both single

crystal faces which allows us to assign a C_{3v} symmetry (threefold coordination) to adsorbed sulfate on Pt(111).

For the reasons given in Sec. 9.2, an enlargement of the S–O bond length involving coordinated oxygens is expected. Thus we expect that the group frequency characterizing the symmetric stretching vibration of the coordinated SO_3 group be that observed at the lower wavenumbers (shoulder at 1190 cm^{-1}).

Summarizing, it is likely that the characteristic group frequencies for the S–O stretching vibrations of SO_3^* and SO are represented by the shoulder around 1190 cm^{-1} and the strong band located between 1220 and 1280 cm^{-1} respectively.

9.4 Adsorption of Sulfate on Pt(100)

In Fig. 50 we present spectra obtained with a Pt(100) electrode prepared by flame annealing and cooling in an H_2/Ar atmosphere. Spectra were collected in the 0.03 – 0.80 V potential range, that at the lowest potential being used as the reference spectrum. The negative-going bands in the frequency regions near 1200 and 1100 cm^{-1} are the IR-active modes for the adsorbed sulfate species. As in the case of Pt(111), the loss of solution species is observed as a positive band at 1100 cm^{-1}. Adsorption starts at *c.* 0.2 V and goes through a maximum at potentials between 0.4 and 0.5 V vs. Pd/H_2.

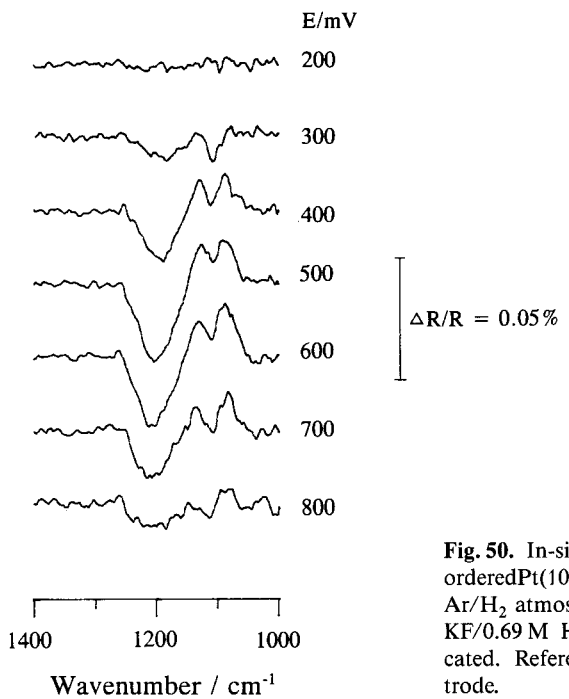

Fig. 50. In-situ FTIR reflectance spectra from a well-orderedPt(100) electrode (flame-annealed and cooled in Ar/H_2 atmosphere), in 10^{-2} M K_2SO_4 + 0.5 M KF/0.69 M HF (pH = 2.8). Sample potentials as indicated. Reference potential 0.030 V vs. a Pd/H_2 electrode.

9.4.1 Symmetry of Adsorbed Sulfate

A two fold coordination has been suggested for sulfate ions on the Pt(100) surface, i.e., a C_{2v} symmetry [144]. As for Pt(111), the atomic distances of adsorbate and substrate match very well.

Both modes observed are symmetric stretching vibrations according to the restrictions imposed by the surface selection rule. The coordinated (SO_2^*) group causes the low-frequency mode (1100 cm^{-1}) and the noncoordinated (SO_2) group the high-frequency mode (1200 cm^{-1}).

If after annealing the electrode is cooled in air, the spectrum presents additionally a weak band at 1050 cm^{-1} (Fig. 51). Electrodes treated in this way present steps with smaller (100) terraces. In view of this the additional band at 1050 cm^{-1} could be assigned to onefold coordinated SO_4^{2-} ions adsorbed on defect sites.

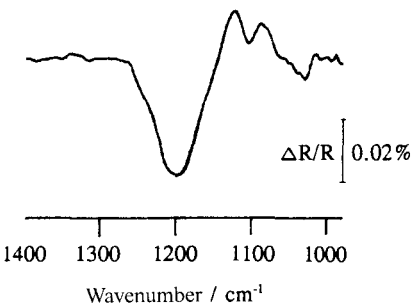

Fig. 51. In-situ FTIR reflectance spectrum for adsorbed sulfate at 0.6 V vs. Pd/H_2 on a Pt(100) electrode flame-annealed and cooled in air. Other conditions as in Fig. 50.

9.4.2 Potential Dependence of the Band Center at Pt(100)

The potential behavior of the band centers is given in Fig. 52. The 1100 cm^{-1} mode is less sensitive to the potential than the 1200 cm^{-1} one. The band shift is *c.* 12.5 cm^{-1}/V for the 1100 cm^{-1} mode and 60 cm^{-1}/V for the 1200 cm^{-1} mode.

In the noncoordinated (SO_2) group, the negative part of the dipole is oriented towards the solution. Thus the S–O stretching vibration is constrained by the positively charged surface and a blue frequency shift occurs with positively growing electric field. This effect is reinforced by the increase in coverage with potential (lateral coupling), thus causing the pronounced band center shift of the 1200 cm^{-1} mode. On the other hand, in the coordinated (SO_2^*) group the dipole charges does not oppose the electric field. In this case, lateral interactions and electric field have opposite effects on the band frequency (i.e., they shift the band centers in opposite directions). The result is that the 1100 cm^{-1} mode is apparently less sensitive to the potential. This behavior of the high- and low-frequency modes agrees with the assignment of the group frequencies given above.

Multicoordination to the surface produces a mechanical hindrance which may be responsible, at least in part, for a blue shift of the band center [155]. The results on

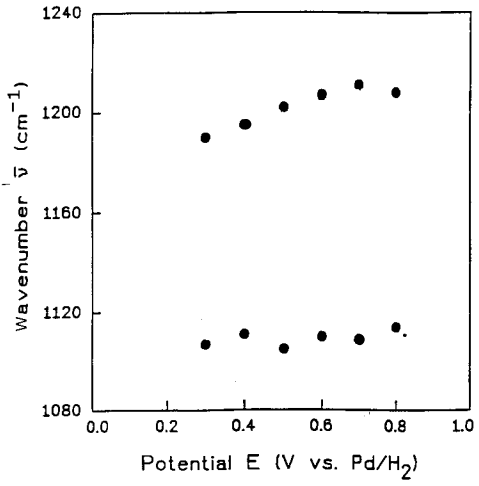

Fig. 52. Potential dependence of the band center frequencies for adsorbed SO_4^{2-} on Pt(100); 10^{-2} M K_2SO_4 + 0.5 M KF + 0.69 M HF (pH = 2.8).

Pt(100) and Pt(111) suggest that coordination shifts the frequencies of the S–O stretching of the coordinated groups as follows

$$\nu_{SO_3^*)} > \nu_{SO_2^*)} > \nu_{SO^*)}$$

However, the shifts are probably too large to be explained on the basis of mechanical hindrance alone. More experimental as well as theoretical work should clarify to what extent the character of the intramolecular bonds is altered when the species go from the "free" state in solution to the adsorbed state. In other words, it is necessary to establish whether changes in the vibrational frequency can be addressed to changes in the force constants of intramolecular bonds.

9.5 Coverage-Dependent Band Shift and Lateral Coupling for Sulfate Adsorbed on Pt(111)

The effects of lateral interactions in adsorbed layers can be studied through the coverage dependence of the band center frequencies. Using reported results on sulfate adsorption at Pt(111) obtained with the radiochemical method [156, 157], an operative absorption coefficient can be calculated which allows the estimation of the surface concentrations for adsorbed species. The change in band center frequency with coverage is shown in Fig. 53 for different applied potentials. A linear upward shift with an average change of *c.* 12 cm^{-1} for a $\Delta\Gamma$ of 1×10^{14} ions cm^{-2} indicates that lateral coupling effects are operating.

The estimated surface concentration in a 2.5×10^{-2} M K_2SO_4 solution is 2.7×10^{14} ions cm^{-2}. Taking into account the number of Pt atoms per cm^2 (1.5×10^{15} for Pt(111)) and a threefold coordination for the adsorbate, a high degree

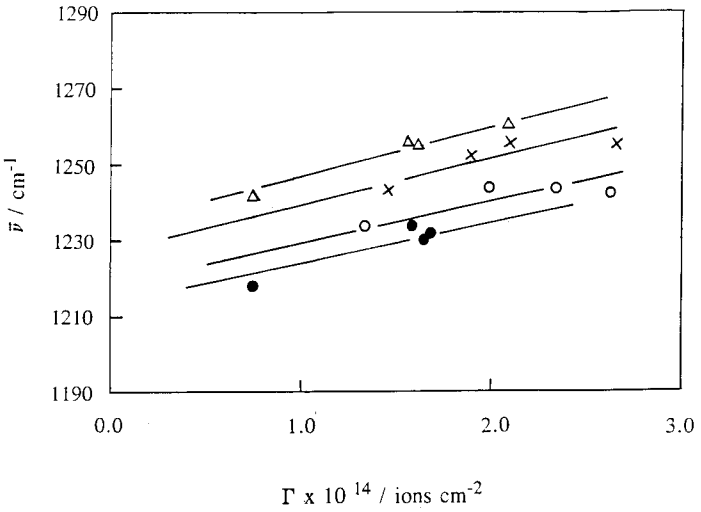

Fig. 53. Dependence of the band center frequency for adsorbed sulfate on Pt(111) on the coverage. ● 0.60 V, ○ 0.70 V; x 0.80 V, △ 0.90 V vs. Pd/H_2. Solution concentration range of K_2SO_4: $4\times10^{-4}-2.5\times10^{-2}$ M (pH = 2.8).

of coverage can be estimated. This is one of the most striking aspects of sulfate adsorption on Pt(111). If SO_4^{2-} ions retain their charge in the adsorbed state, strong repulsing effects would make the ionic layer energetically unstable. These effects could be attenuated by co-adsorption of positive ions (e.g., K^+). Alternatively a partial charge transfer from the adsorbed anions to the metal could contribute to stabilize the adsorbed layer. In a recent study of sulfate adsorption, a charge transfer of 0.2 was estimated [148]. Orts et al. [154] have presented convincing experimental results demonstrating that the adsorption of sulfate on Pt(111) at 0.5 V vs. RHE from a 0.5 M H_2SO_4 solution is accompanied by a transfer of 92 μC cm^{-2} of negative charge to the electrode. No data for the surface concentration under these conditions are available and consequently the degree of discharge cannot be calculated.

9.6 Bandshape Analysis and Adlayer Ordering

To avoid the distortion produced by the shoulder, the bandwidth at Pt(111) was analyzed at two-thirds of the peak height ($\Delta\nu_{2/3}$). The results are plotted in Fig. 54 as a function of potential. The band narrows as the potential increases, going through a minimum at 0.8 V. The dependence of the coverage on the electrode potential is presented in Fig. 55. This Figure shows a maximum adsorption at 0.8 V. Thus the band narrowing can be related to an increase of homogeneous lateral interactions as the adsorbate layer becomes more compact. The band asymmetry (see Fig. 47) indicates a random distribution of the adsorbed ions with low surface mobility [21].

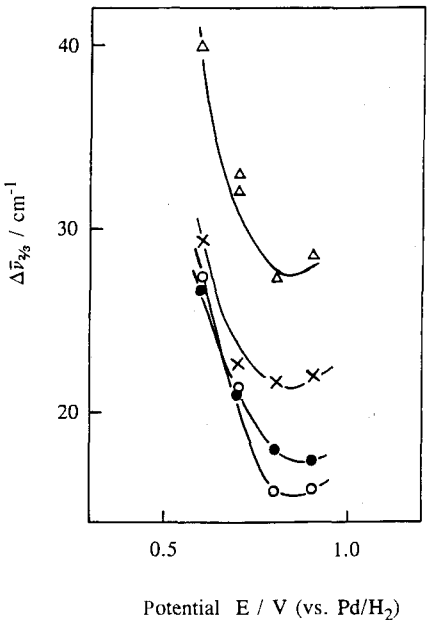

Fig. 54

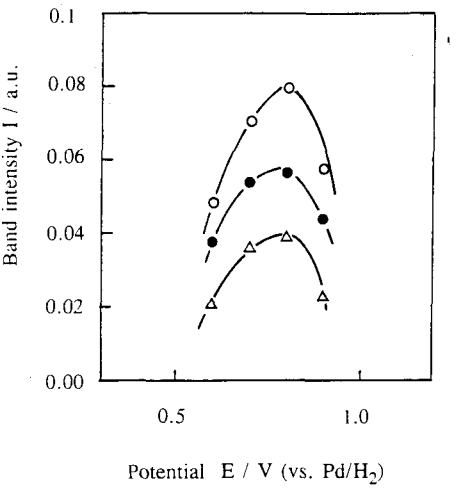

Fig. 55

Fig. 54. Potential dependence of the bandwidth at two-thirds of the band height for adsorbed sulfate on Pt(111). ○ $2.5\times10.^{-2}$ M; ● 10^{-2} M; x 5×10^{-3}; △ 5×10^{-4} M.

Fig. 55. Potential dependence of the surface coverage by sulfate ions for a Pt(111) electrode. ○ 2.5×10^{-2} M; ● 10^{-2} M; △ 5×10^{-4} M.

9.7 Interaction with Double-Layer Components

Extrapolating the results on the bandwidth to zero sulfate coverage (singleton), one can analyze the interaction of the ion with other components in the double layer. The singleton bandwidth is plotted in Fig. 56 as a function of potential. There is a sharp narrowing near 0.70 V vs. Pd/H_2, i.e., at the beginning of the sharp peak in the voltammogram taken in the fluoride base electrolyte (see Fig. 46a). Whatever the origin of the wave between 0.45 and 0.90 V in HF/KF solutions, this behavior of the singleton bandwidth for sulfate indicates a sudden increase in order at the surface at potentials under the sharp peak observed at 0.78 V in the cyclic voltammogram.

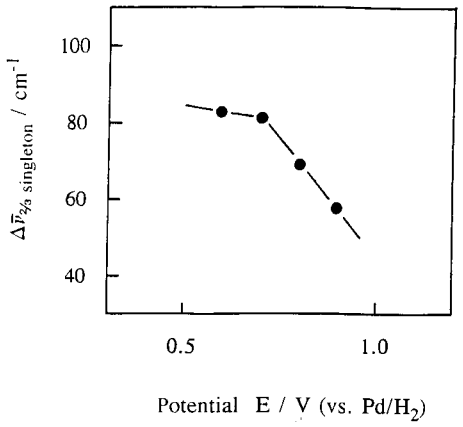

Fig. 56. Values of the bandwidth at two-thirds of the band height for adsorbed SO_4^{2-} ions on Pt(111), obtained by extrapolation to $\theta = 0$ (singleton bandwidth).

9.8 Adsorption of Sulfate and Phosphate on Polycrystalline Pt

9.8.1 Sulfate

The adsorption of sulfate on polycrystalline Pt electrodes has been studied many times [35, 36, 38, 139, 140, 142]. Spectra taken in the presence of a fluoride supporting electrolyte at different pH values are given in Fig. 57. The knowledge gained from the studies on single crystals makes necessary a revision of the interpretation of the data in [38] and [142]. It was assumed [142] that the static electric field activates asymmetric modes, a fact that seems to be less probable according to the results at Pt single crystals.

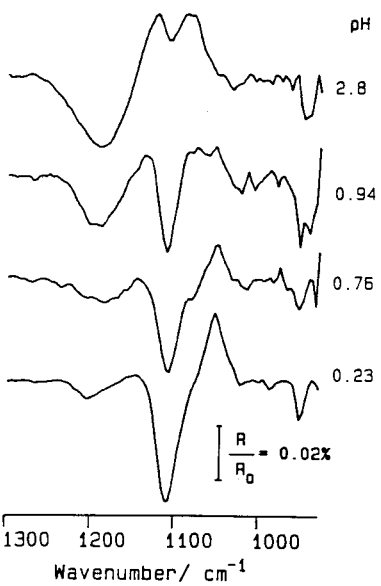

Fig. 57. In-situ FTIR reflectance spectra of adsorbed sulfate species on polycrystalline Pt in solutions of various pH values, as indicated.

At pH 2.8, SO_4^{2-} is the predominant species in solution and at the electrode surface. The evolution of the bands (Fig. 57) indicates a change in the nature of the adsorbate as the pH is made more acidic. The co-adsorption of both SO_4^{2-} and HSO_4^{2-} occurs at intermediate pH values [142]. Finally, at pH 0.23, HSO_4^- is adsorbed.

For SO_4^{2-} a twofold coordination on polycrystalline platinum was suggested and the 1200 cm^{-1} mode was interpreted in terms of the group frequency of noncoordinated SO_2. This interpretation coincides with that given in Sec. 9.4 for the same symmetry on Pt(100). However, the earlier assignment of the 1100 cm^{-1} feature must be corrected. This band was suggested to be the asymmetric SO_2 mode [142]. In view of the results for Pt(100) this band is caused by the symmetric stretching of the coordinated SO_2^* group.

It has been proposed that adsorbed bisulfate ions present a C_{3v} symmetry on polycrystalline platinum, i.e., these ions were suggested to be threefold coordinated. For polycrystalline Pt the geometric arrangement of atoms required by a threefold coordination must have a lower probability than that for a twofold coordination. Thus most adsorbed bisulfate ions are probably twofold coordinated, presenting the group frequencies for the SO, SO_2^* and SOH groups near 1200 cm^{-1}, 1100 cm^{-1} and 950 cm^{-1}. The persistence of the latter band at pH 2.8 could be due to some co-adsorption of bisulfate. The band intensity in this region is meaningless because of the proximity of the cutoff of the CaF_2 window.

9.8.2 Phosphate

First in-situ infrared investigations of phosphoric acid adsorption on platinum and gold were performed in $HClO_4$ as base electrolyte [138]. More recently, spectroscopic data in alkaline solutions were reported [37, 158]. However, not enough attention was paid in these studies to the problem of acid-base equilibrium displacements in solution and to the overlapping of solution and surface features which make the interpretation of spectra very difficult. Results on the adsorption of phosphate species on polycrystalline platinum at pH 2.8 (79% $H_2PO_4^-$ and 21% H_3PO_4) are shown in Fig. 58a [146].

The loss bands at 1077 cm^{-1} and 1153 cm^{-1} are due to solution $H_2PO_4^{2-}$ ions [159]. Below 900 mV two features due to adsorbed $H_2PO_4^-$ (1125 and 1000 cm^{-1}) are observed. As the potential shifts positively the intensity of the band centered at 1000 cm^{-1} decreases and a third (weak) band centered at 1185 cm^{-1} appears.

At pH 0.23 only one strong negative band at 1055 cm^{-1} is observed at low potentials. A second band centered at 1110 cm^{-1} is developed at more anodic potentials (Fig. 58b). The data from Habib and Bockris [138] also show a small band at 1074 cm^{-1}, for adsorbed phosphoric acid. The potential dependence of the band intensities fits very well to radiotracer results on the adsorption of phosphoric acid in strongly acidic medium [160].

The changes in the spectra indicate that either the nature of the adsorbed species or the coordination to the surface (or both) are potential-dependent. The observed modes have been assigned and the geometry of adsorbed phosphoric acid established [146]. The main problem for band assignment is that some modes have frequencies

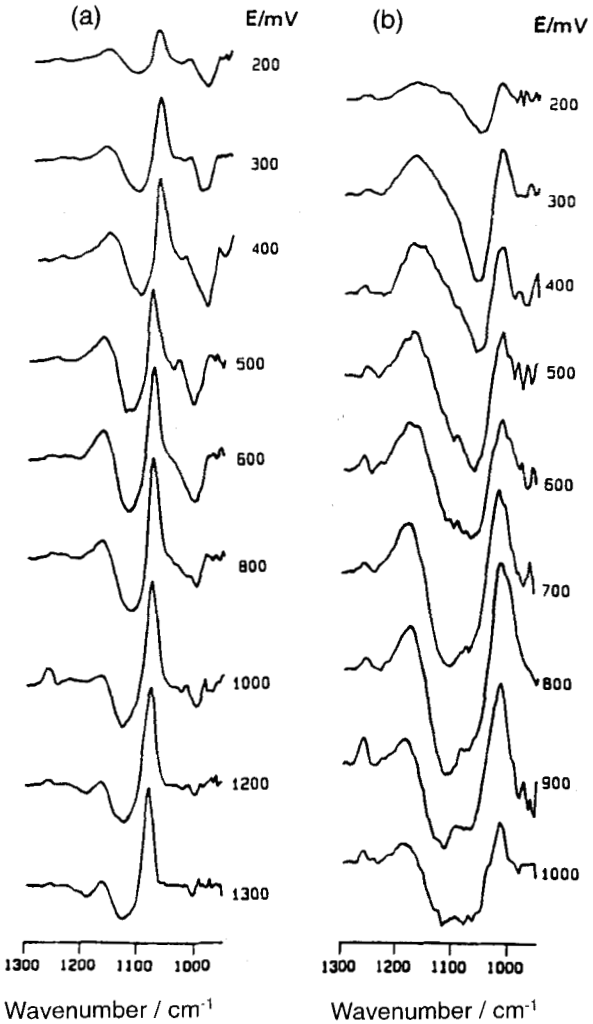

Fig. 58. (a) In-situ reflectance spectra for adsorbed phosphate species on polycrystalline Pt. Solution: 1.5×10^{-2} M KH_2PO_4 at pH 2.8. Base electrolyte 0.69 M HF/0.5 M KF. Reference potential 30 mV vs. Pd/H_2. (b) Spectra as in (a) but for a solution of pH 0.23, base electrolyte 7.3 M HF.

below the range accessible with the CaF_2 window used in the experiments. Therefore, only a tentative band assignment can be considered.

At pH 2.8 the $H_2PO_4^-$ ions are adsorbed through two oxygen atoms (C_{2v} symmetry). The 1120 cm^{-1} and 1000 cm^{-1} modes were assigned to the PO_2 and $P(OH)_2$ group frequencies respectively. Above 0.9 V a change in geometry was suggested [146]. At pH 0.23 the band observed at 1055 cm^{-1} is due to the PO group of onefold coordinated PO_4H_3.

9.9 Concluding Remarks on the Adsorption of Oxyanions

The adsorption of anions of weak oxyacids indicates a Lewis acid character of the Pt surface. The tendency of the metal to attract electrons, in particular in the case of Pt(111), is reflected in several facts. Thus anions of weak acids tend to dissociate on the surface, indicating that the strength of the adsorbed acids is enhanced by the metal. Furthermore, the anions seem to transfer their charge to a great extent, at least in the case of adsorption at Pt(111), as demonstrated by the experiment of Orts et al. [154] and indirectly confirmed by the high degrees of coverage reached by adsorbed sulfate ions on this surface.

As demonstrated for the adsorption of sulfate on Pt(111), vibrational spectroscopy offers the possibility of investigating the nature of the adsorbed ions on the surface, its site occupancy and the interactions with other ions or molecules at the interface and with the metal substrate. Further spectroscopic data on these systems may contribute greatly to the interpretation of double-layer phenomena.

10 The Stark Effect at the Electrochemical Interface

Changes in rotational and vibrational transitions of molecules under the influence of strong electric fields are known as the Stark effect. The effect of strong electric fields was found first on atomic spectra and extended by Condon to vibrational transitions in molecules in 1932 [161].

The Stark effect requires the application of electric fields of the order of $10^4\ V\ cm^{-1}$ or higher. The electrochemical interface, where molecules and ions are subjected to fields in the order of $10^6\ V\ cm^{-1}$, seems to be the ideal place to study this phenomenon.

Potential-dependent frequencies in spectra of adsorbates in electrochemical interfaces are commonly observed. Thus so-called Stark tuning rates, $\partial\bar{\nu}/\partial E$, of $30\ cm^{-1}\ V^{-1}$ have been reported for adsorbed CO on platinum [65, 111] (Fig. 59) and adsorbed CN^- on silver [109, 111, 162]. Even higher values were found for sulfate species adsorbed on polycrystalline platinum ($100\ cm^{-1}\ V^{-1}$ [36, 38]) or on single crystal Pt(111) [141, 143] ($120\ cm^{-1}V^{-1}$). In some cases, as for adsorbed tetracyanoethylene [163] and anthracene [164], vibrational features which are forbidden by the surface selection rule become active under the influence of the electric field at the interface.

However, the electrochemical interface is in many respects more complicated than simply a very high electric field. Adsorbed species there, can suffer different degrees of charge transfer, interacting not only electrostatically but also chemically with the metal surface, with neighboring species of their own type, with co-adsorbed ions and solvent molecules. These interactions can affect the vibrational energies to an extent similar to that of the electric field, making necessary a separation of effects by an appropriate control of the experimental parameters.

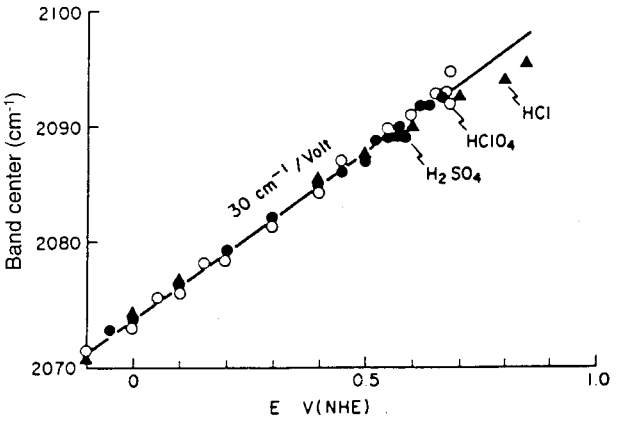

Fig. 59. Potential dependence of the band center frequency for adsorbed carbon monoxide on a platinum electrode. (After [111]). Reprinted by permission of Elsevier Science.

The large frequency shift ($\simeq 100\,cm^{-1}\,V^{-1}$) observed for the $1200\,cm^{-1}$ band of adsorbed sulfate was attributed to a Stark effect by Kunimatsu et al. [36] and to a backbonding mechanism by Faguy et al. [141]. The potential-induced band shift in the case of sulfate ions must be analyzed in more detail. It was observed that the band center for the $1200\,cm^{-1}$ feature of adsorbed sulfate presents, additionally, a dependence on the degree of coverage [142, 165]. Since the latter is also a function of the potential, it is clear that a part of the frequency change can be due to lateral interactions, as discussed in Sec. 9.5 for sulfate ions adsorbed on Pt(111).

In the next sections we discuss the available data on the electrochemical Stark effect on the vibrational spectrum of adsorbed carbon monoxide and adsorbed sulfate ions at platinum.

10.1 Adsorbed Carbon Monoxide

Whether the potential-induced frequency shift of adsorbed CO is due to a Stark effect or to a change in the backbonding mechanism has been the subject of controversy [119, 166–169]. Holloway and Worskov [168] have discussed the potential-induced red shift of adsorbed CO in terms of a backbonding mechanism. The applied electrode potential changes the occupancy of the $2\pi^*$ electrons in the adsorbed CO molecule due to a change in resonance position and width of the $2\pi^*$ orbitals. This gives rise to a modified intramolecular bond, changing the CO stretching vibrational frequency. Using a semiempirical calculation, the experimentally observed shift of $30\,cm^{-1}\,V^{-1}$ (Fig. 59) was reproduced. However, Kunimatsu et al. [111] have reported calculations for a cluster model of CO adsorbed on Cu(111) showing that the occupancy change of the $2\pi^*$ orbital is very low at fields below $10^7\,V\,cm^{-1}$.

Bagus et al. [119] have proposed that the largest contribution to the field-induced band shift of carbon monoxide is due to a Stark effect, represented by a first-order perturbation of the energy. A first-order Stark effect has been also proposed by Lambert [170, 171], who has derived an expression based on the effect of the potential upon the dipole moment. The theoretical treatment proposed by Lambert is based on a perturbation of the electric field on the potential energy function, which is written as a double Taylor expansion [171]:

$$U(Q, E) = \sum_{jk} a_{jk} Q^j E^k \tag{17}$$

where Q and E are the normal coordinate and the electric field, respectively.

To a good approximation the Stark tuning rate is given by

$$\mathrm{d}\nu/\mathrm{d}E = \nu_0 \left(\frac{2\, a_{20}\, a_{21} - 3\, a_{30}\, a_{11}}{4\, a_{20}^2} \right) \tag{18}$$

where ν_0 is the vibrational frequency of the harmonic oscillator and the a_{jk} are the coefficients of the double Taylor expansion, which can be divided into a potential energy function,

$$U(Q) = a_{00} + a_{20} Q^2 + a_{30} Q^3 + \ldots \tag{19}$$

and the dipole moment function,

$$M_z(Q) = -(a_{01} + a_{11} Q^2 + a_{21} Q^2 + \ldots) \tag{20}$$

The perturbation caused by the applied electric field results in a change of the curvature of the potential energy function, thus causing a change in the transition frequency.

Applying the model to adsorbed CO, Lambert has evaluated the coefficients a from experimental data. Thus a_{20} was taken from the unperturbed frequency (ν_0), a_{30} from gas-phase values of a Morse potential, a_{11} from the IR cross-section of adsorbed CO and a_{21} from the first overtone observed by EELS. Equation (18) has been applied successfully to CO/Ni(111) and CO/Pt, both in the gas phase and at electrodes, reproducing the observed Stark tuning rate with a good accuracy.

On the other hand, the dependence of the potential-induced frequency change on the nature of the metal surface ($\mathrm{d}\bar{\nu}/\mathrm{d}E$ of about $30\ \mathrm{cm^{-1}\ V^{-1}}$ and $48\ \mathrm{cm^{-1}\ V^{-1}}$ for Pt and Pd electrodes, respectively) has been used to support the suggestion that changes in backdonation are the major causes for the potential-induced band shift. Recent calculations of Bagus and Pacchioni [169] show that a Stark effect of the Pd_2CO cluster model gives a tuning rate of $45\ \mathrm{cm^{-1}\ V^{-1}}$, a value which is very close to that observed experimentally.

It is very interesting that the Stark tuning rate is coverage-dependent for adsorbed CO, in electrochemical media [55–57] as well as in vacuum [172]. It is found that at lower degrees of coverage the Stark tuning rate increases significantly. This depen-

dence has been explained by Lambert [171] in terms of a static field screening caused by the conduction electrons.

It can thus be concluded that CO is too ambiguous a system for use to study the effect of an applied electric field on the band position.

10.2 Adsorbed Sulfate Ions

A Stark effect for adsorbed sulfate on Pt electrodes has been reported for the 1200 cm^{-1} symmetric stretching mode of the adsorbed ion [165]. A quadratic dependence of the band center on the applied electric field is observed (Fig. 60). But this field dependence changes with the degree of coverage. The frequency values extrapolated to zero coverage (singleton frequency) present a linear dependence on the applied electric field (Fig. 61). So we conclude that the second-order Stark effect is induced when the ions are close together on the surface.

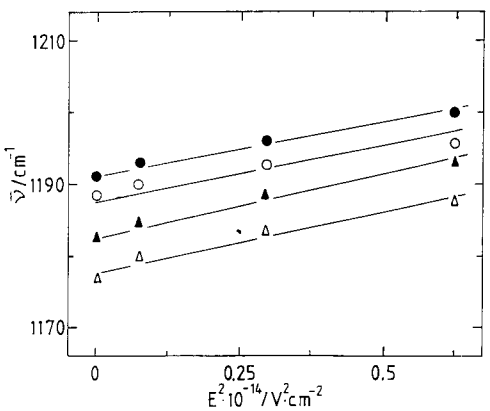

Fig. 60. Quadratic dependence of the band center frequency for the 1200 cm^{-1} mode of adsorbed sulfate on polycrystalline platinum: △ $I_s = 0.8$; ▲ $I_s = 2.25$; ○ $I_s = 4$; ● $I_s = 6.25$. I_s is the intensity of the solution loss band of sulfate obtained with s-polarized light and is proportional to the degree of coverage with sulfate ions [165].

On a Pt(111) single-crystal surface the effect of the potential on the band position has been evaluated for different coverages [143]. No linear dependence is found for any surface coverage, not even for the singleton frequency. This shows that on Pt(111) a correction of higher order is necessary and, in this case, the effect is not induced by the presence of neighboring ions alone.

Differences in the $\nu - E$ relation for adsorbed sulfate on polycrystalline Pt and on Pt(111) single crystals are not surprising, since there is a specificity in the behavior of sulfate at each surface. Thus the site coordination is twofold for both polycrystalline Pt and single-crystal Pt(100), while it is threefold for single-crystal Pt(111). Furthermore, there is evidence, at least for Pt(111), that during adsorption a considerable charge transfer to the metal occurs [154]. At polycrystalline Pt a possibility of island formation was suggested [165]. On Pt(111) single crystals the effects of lateral coupling can be negligibly small.

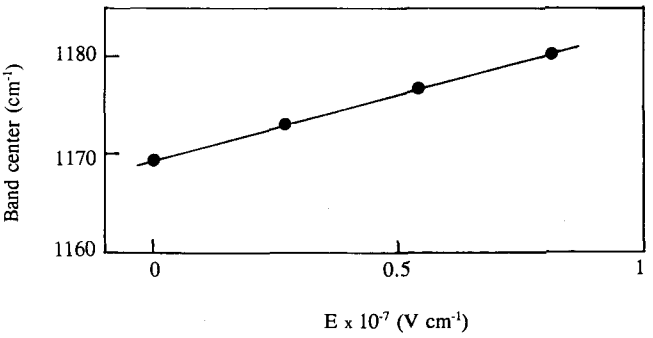

Fig. 61. Plot of the singleton frequency for the 1200 cm^{-1} mode of adsorbed sulfate on polycrystalline platinum as a function of the applied electric field at the interface.

10.3 The Effect of Field on Band Intensity

In contrast to the Stark effect on the vibrational frequency, the changes of the transition probability with the electric field have been investigated less. For electrochemical systems an expression for the integrated absorption coefficient, B, was proposed by Korzeniewski et al. [164] as follows:

$$B = \frac{2\pi^2 \nu N}{\varepsilon_0 hc} |\langle \Psi_{vf} | P_0' | \Psi_{vi} \rangle| + E\langle \Psi_{vf} | \alpha' | \Psi_{vi} \rangle|^2 \tag{21}$$

where P_0' and α' are the permanent dipole moment and the polarizability, respectively. The functions Ψ_v are the eigenfunctions of the final (f) and initial (i) vibrational states, ν is the frequency of the infrared transition, N is the number of absorbed particles, ε_0 is the permittivity of free space, h is Planck's constant, and c is the velocity of light.

Semiempirical calculations of B are reported [164] for the A_g mode dependence on the applied static electric field for adsorbed CO, ethylene, naphthalene, anthracene and $TCNQ^-$. It was observed that for systems with high polarizability such as $TCNQ^-$ and anthracene, a good fit between B and the square of the electric field is obtained, while for CO a linearity is observed only at very high electric fields ($>2\times10^9$ V cm^{-1}). These results are used to explain the breakdown of the surface selection rule for the C = C symmetric stretch of flat adsorbed molecules like ethylene, anthracene and naphthalene at platinum electrodes.

An equivalent treatment was proposed by Lambert [176] to account for the field-induced intensity changes in adsorbed CO in UHV and at electrodes. The proposed semiclassical equation is based on the fact that the integrated intensity is proportional to the dynamic dipole moment $|\partial\mu/\partial Q|^2$ (or $(dM_z/dQ)^2$) for the component in the direction of the applied field. The deduced expression for the change in intensity with the applied field is:

$$\delta_{SE} = 2\left(\frac{\alpha_1}{M_1} + \frac{M_2}{U_2}\right) \tag{22}$$

where α_1 is $d\alpha/dQ$, M_1 is dM_z/dQ, M_2 is d^2M_z/dQ^2 and U_2 is d^2U/dQ^2. These are the expansion coeffients of the polarizability $\alpha(Q)$, the dipole moment $M_z(Q)$ and the potential energy function $U(Q)$, respectively.

The agreement of δ_{SE} with experimental data for adsorbed CO on Pd(100) and Pt(110) is very poor [176]. However, the values agree with ab-initio data for the effect of the static electric field on the band intensity [169]. The problem stresses once again the complex behavior of adsorbed CO at electrochemical interfaces.

The integrated band intensity for adsorbed sulfate ions on polycrystalline platinum shows a nonlinear dependence on the applied static electric field [165]. To account for this kind of behavior, an expression was derived [173] based on the fact that the integrated intensity is proportional to the transition moment $|\langle \Psi_{1k}|\mu|\Psi_{0k}\rangle|^2$ (see Sec. 3.1) [23, 174]:

Assuming both mechanical and electrical harmonicity, the transition moment can be written in terms of the normal coordinates [175]:

$$|\langle \varphi_{1k}|\mu|\varphi_{0k}\rangle|^2 = \frac{h}{c\bar{\nu}_k 8\pi^2}\left|\frac{\partial\mu}{\partial Q_k}\right|^2 \tag{23}$$

If the kth mode is polarizable, the electric field gives rise to an induced dipole moment:

$$\mu = \mu^0 \pm \alpha E \tag{24}$$

which leads to the following result for the integrated band intensity in the presence of an electric field effect (compare with Eq. (9) in Sec. 2.1):

$$\int d\bar{\nu}_k \Delta(\bar{\nu}_k) = \frac{N}{c^2\varepsilon_0 A} G(\theta)\left|\frac{\partial\mu}{\partial Q_k} \pm \frac{\partial\alpha}{\partial Q_k}E\right|^2 \tag{25}$$

where $\Delta(\bar{\nu})$ stands for the absorption $(R^0 - R)/R_0$, N is the number of IR-active species, A is the area, c is the velocity of light, $G(\theta)$ is a function of the angle of incidence (θ), and $\partial\mu/\partial Q_k$ and $\partial\alpha/\partial Q_k$ are the dynamic dipole moment and the dynamic polarizability, respectively.

It must be stressed that the polarizability gradient $\partial\alpha/\partial Q_k$ also appears in the equation for Raman intensities [175], as indicated also by Lambert [176]. Thus, in view of Eq. (25), we can extend the consequences of the static electric field to vibrations which are forbidden by the surface selection rule: the high electric field in the double layer can induce a dipole moment component in the direction of the field on permanent dipoles which are parallel to the surface. Thus the effect of orientation due to the electric field is just a manifestation of the Stark effect.

A plot of the integrated band intensities for the 1200 cm^{-1} mode of sulfate adsorbed on Pt according to Eq. (25) is given in Fig. 62. From the slopes and the extrap-

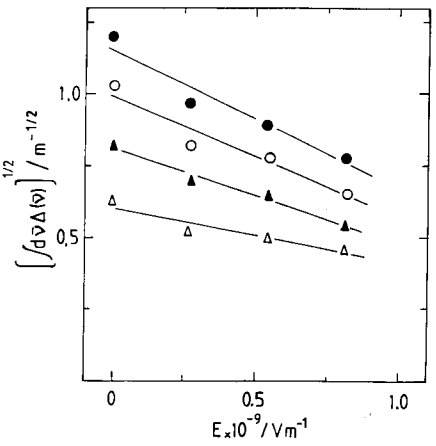

Fig. 62. Square root of the integrated band intensity for the 1200 cm^{-1} mode of adsorbed sulfate ions as a function of the applied electric field for: △, $I_s = 2$; ▲, $I_s = 3$; ○, $I_s = 4$; ●, $I_s = 5$. I_s is the intensity of the solution loss band of sulfate obtained with s-polarized light and is proportional to the degree of coverage with surface ions [165].

olated values at zero electric field (potential of zero charge) the dipole moment gradients and the dynamic dipole moments are obtained. These parameters depend on the degree of coverage. Values for the dynamic dipole moment range between 104 and 127 esu $g^{-1/2}$. This is the order of magnitude for a band of medium intensity in the liquid phase [177]. The specific intensity for gaseous SO_2 molecules gives a value of about 163 esu $g^{-1/2}$ [178].

Increasing coverage produces an enhancement of both dipole moment gradient and polarizability gradient. These effects of the lateral interactions are in good agreement with the possibility of island formation as suggested previously [165]. The lateral coupling of the adsorbed anions requires a more detailed study.

10.4 Concluding Remarks on the Electrochemical Stark Effect

The electrochemical double layer offers the exceptional possibility of investigating the Stark effect at very high electric fields. Some important progress has been made in the theoretical treatment of the problem. Experimental data of potential effects upon the frequency and/or the intensity of vibrational modes must discriminate between the pure electric field effect and the secondary effect of potential on the coverage and, consequently, on the lateral interactions.

Infrared investigations of the Stark effect can afford data on the molecular properties of adsorbates (polarizability, dipole moment gradients, and polarizability gradients). However such studies are at their very beginning and require to know the actual value of the electric field at the interface. Data on the potentials of zero charge for solid electrode materials would be welcome.

At present it is difficult to establish whether the band shift for CO is caused by a Stark effect or by an electronic backbonding. Probably both effects are operative and cannot be properly separated.

11 Attenuated Total Reflection (Internal Reflection Infrared Spectroscopy)

In internal reflection infrared spectroscopy, the IR beam reaches the electrode/electrolyte interface not from the solution side (as is the case in external reflection spectroscopy) but from the window side, as shown in Fig. 63 for an arrangement with multiple internal reflections. The IR beam strikes the electrode-solution interface at an angle greater than the critical angle, so total reflection occurs. At this interface the beam partially penetrates the medium with a lower refractive index in the form of an evanescent wave which interacts with the species in the thinner medium. When the refractive index is changed by an IR-absorbing substance located at the electrode or in a solution layer of *c.* 1 μm, a change in the internal reflection occurs. Since the imaginary part of the refractive index is frequency-dependent, the change in reflectivity generates a spectrum of the substance. Because of the loss of energy due to the interaction with an absorbing substance the technique is called attenuated total reflection (ATR). The physics of the phenomenon of partial reflection at the interface is described by the Fresnel formulas. An extensive treatment of the optical problem has been given by Hansen [3] and Harrick [179].

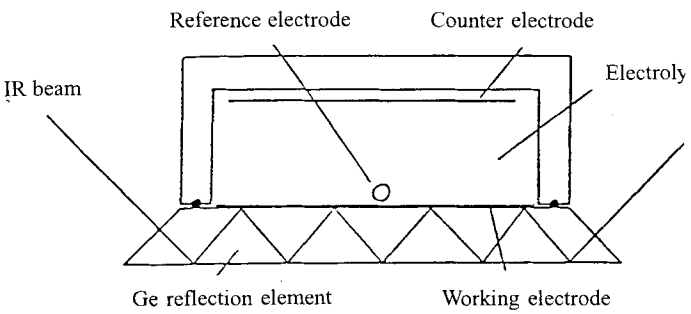

Fig. 63. Scheme of a cell for ATR infrared spectroscopy. (After [182]).

The electrode can be set directly over the reflection element. For the study of electrochemical reactions under current flow, this arrangement has the advantage that the electrode is in direct contact with the whole solution, i.e., no thin-layer configuration is used, thus avoiding its inherent problems. However, the preparation of thin layers of metals on the surface of reflection elements such as Ge or ZnSe may present some problems. The metal deposits must be thin enough (*c.* 10 nm) to allow the beam to reach the metal/solution interface. On the other hand, it is difficult to avoid island formation in such thin metal deposits and when this happens the film can have very poor conductivity.

An important parameter for the use of ATR in electrochemistry is the penetration depth of the evanescent wave. This is defined as the distance where the amplitude

of the electric field decays to e^{-1} of its value at the interface. The penetration depth changes according to Eq. (26) [179]:

$$d_p = \frac{\lambda_1}{2\pi (\sin^2 \theta - n_{21}^2)^{1/2}} \tag{26}$$

where $\lambda_1 = \lambda/n_1$ is the wavelength in the denser medium, $n_{21} = n_2/n_1$, n_2 and n_1 being the refractive indices of the thinner and denser medium respectively, and θ is the angle of incidence.

For bulk materials the strength of coupling between the evanescent wave and the absorbing material is given by the so-called effective thickness [33], which is a function of the amplitude of the electric field E_0, the refractive indices and the angle θ:

$$d_e = \frac{n_{21} E_0^2 d_p}{2 \cos \theta} \tag{27}$$

It can be stressed, therefore, that not only is the ATR method surface-sensitive, but it is also sensitive to species located inside d_e. The penetration of p-polarized light is slightly greater than that of s-polarized light and both depend on the incidence angle. Using the ATR method, surface substances as well as those in solution can be detected.

Contrary to external reflection, where the field amplitude for s-polarized radiation is zero upon reflection, in the case of internal reflection the amplitude of the field at the reflecting surface is not zero for any direction of the field. The magnitude of the amplitude depends on the angle of incidence and on the difference of the refractive indices [33].

The amplitude of the the electric field vectors in the different directions can be used to study the orientations of adsorbed molecules at the interface of the internal reflection element [33].

The ATR geometry offers another interesting advantage for the study of adsorbed species. Since multiple internal reflections are possible and, in addition, relatively large electrode surfaces are used, the signal-to-noise ratio can be greatly improved. This is particularly useful for detecting very small amounts of adsorbed species.

In the next sections we discuss some selected examples of the use of ATR spectroscopy to study semiconductors, polymers, and corrosion processes.

11.1 Semiconductors

One very promising application of IR-ATR spectroscopy is the study of the semiconductor/electrolyte interface. This is a surprisingly unexplored field.

In order to study the surface of a silicon electrode, Ozanam and Chazalviel [180] have suggested the use of the ATR technique, applying to the electrode a potential

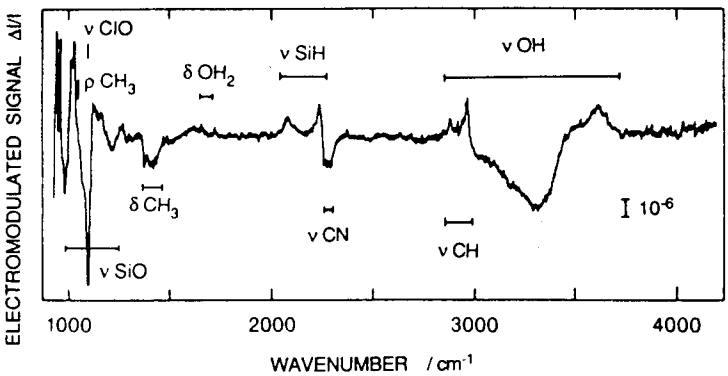

Fig. 64. Typical electromodulated spectrum of a silicon/acetonitrile+0.1 M TBAP interface. Electromodulation potentials −0.3 V, +0.3 V vs. Ag/AgCl. Modulated charge: 5×10^{-7} C cm^{-2}. (After [180]). Reprinted by permission of Elsevier Science.

modulation as in EMIRS but using a Fourier transform spectrometer. With this arrangement the advantages of both FT spectroscopy and lock-in detection are operative. Using nonaqueous solvents and after a complicated cleaning procedure including an etching treatment with HF, they obtained spectra (Fig. 64) showing the presence of Si−H bonds (identified by a band at 2100 cm^{-1}. This spectrum shows that the ATR technique detects not only surface species but also species accumulated on the solution side of the interface as a consequence of the potential difference (C−H and C−N bands of acetonitrile (ACN). Physisorption of residual water is suggested by the bending mode of water observed at *c.* 1650 cm^{-1} (Fig. 65). The hydrogenated silicon surface in contact with the electrolyte is quite stable, but after several hours a band at 1075 cm^{-1} indicates the formation of SiO during anodic polarization.

The band for SiO was observed by Boonekamp et a l. [12]. These authors pointed out that silicon bulk absorption below 1500 cm^{-1} increases the noise in the spectra.

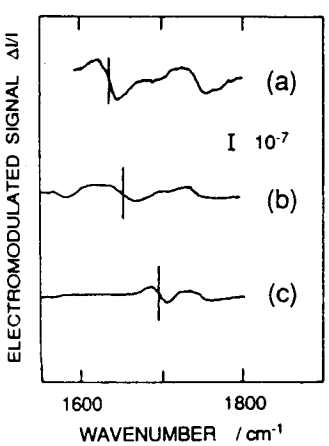

Fig. 65. Spectrum of water (bending mode) at various silicon/electrolyte interfaces: (a) nitromethane; (b) acetonitrile; (c) dimethyl sulphoxide. Note the progressive shift of the frequency upon increasing basicity of the solvent. (After [180]). Reprinted by permission of Elsevier Science.

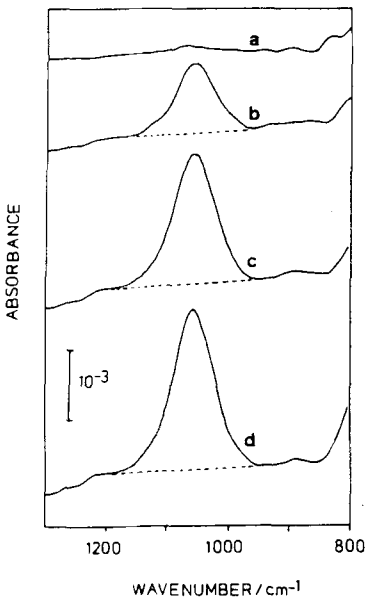

Fig. 66. Absorbance spectra of the Si–ACN interface after anodic polarization: (a) 0 mC, (b) 0.20 mC, (c) 0.41 mC, (d) 0.51 mC. (After [12]). Reprinted by permission of Elsevier Science.

They suggested the use of a very thin wafer of low-doped silicon mounted on a germanium reflection element. In this way FT spectra could be measured after applying different doping charges without potential modulation. Figure 66 shows the development of the oxide layer with increasing anodic doping in ACN.

A very strong Si–H band was observed by Peter et al. [11] during photocorrosion measurements of Si in NH_4F. The band at 2100 cm^{-1} appeared during illumination and persisted over several minutes in the dark spectrum. It was thus concluded that the band is not related to intermediates of the photocurrent but to relatively stable, long-lived species.

Recently, Gerischer and coworkers [181], using the ATR technique, have shown that the Si–H bond is preserved during the etching process of Si in alkaline solution. During cathodic polarization at $-200\ \mu A\ cm^{-2}$ in 0.5 M NaOH, a band assigned to the Si–H stretching is observed at 2070 cm^{-1} (Fig. 67, spectrum b). At pH 4.0 in NaF/HF, the band is shifted toward higher wavenumbers (spectrum a), due to a larger contribution from SiH_2, thus demonstrating the influence of the OH concentration on the surface preparation [181].

11.2 Conducting Polymers

One important application of internal reflection FTIR is the study of conducting polymers. In the thin-layer configuration (for external reflection) large changes in electrolyte composition can seriously disturb the doping processes and create ghost

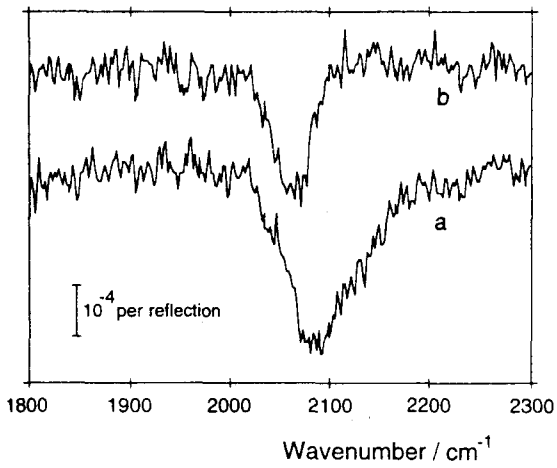

Fig. 67. Bands for the Si–H stretching vibration in FTIR spectra of an n-Si(111) surface at cathodic bias (200 $\mu A\ cm^{-2}$). The oxidized surface, where the Si–H band is absent, was taken as a reference. (a) Spectra in 0.1 M NaF, pH 4.0 adjusted with HF, (b) after exchange of this solution by 0.5 M NaOH. (After [181]). Reprinted by permission of the Electrochemical Society.

bands complicating the interpretation of the spectra. Therefore the most appropriate geometry for the study of polymer processes is that of the internal reflection method.

The use of a Ge reflection element to study polymers has the disadvantage of the instability of germanium to positive polarizations. Nonconducting elements such as ZnSe prisms require the deposition of a metal layer as electrode substrate. However, the transmitivity of this arrangement is poor and results in a low signal-to-noise ratio [182]. Recently Moser et al. [14] have suggested the use of a metal grid arrangement on the surface of a ZnSe element, prepared by evaporation platinum using a grid mask with line distances of about 0.1 mm (Fig. 68). Spectral changes during the oxidation of polyaniline as obtained using this technique are shown in Fig. 69. At pH 1 the bands in the 1450–1600 cm^{-1} region have been interpreted as due to aromatic-ing transformations from a benzoid to a semiquinoid structure, and the broad band with a maximum at *c.* 4000 cm^{-1} was assigned to the metallic form of polyaniline. With increasing pH the intensity of the broad absorption band decreases and shifts to higher wavenumbers. No metallic semiquinoid form of polyaniline is stable at pH 5 [14].

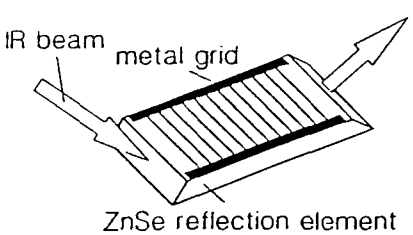

Fig. 68. Metal grid electrode for in-situ ATR spectroscopy. (After [14]). Reprinted by permission of Springer Verlag.

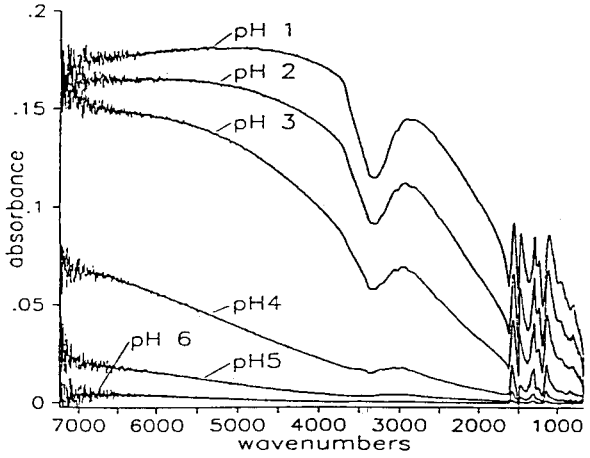

Fig. 69. Maximum spectral changes during the doping of polyaniline in solutions of different pH. Spectra were obtained with the metal grid electrode of Fig. 68. (After [14]). Reprinted by permission of Springer Verlag.

11.3 Corrosion Processes

Spectroscopic studies on the corrosion of iron have been performed using the ATR technique [13]. The working electrode was prepared by depositing a thin layer of iron, produced through evaporation in vacuum. Spectra were taken during a potential cycle. The spectra shown in Fig. 70 exhibit a sharp peak at 3632 cm^{-1} assigned to the O–H stretching vibration of $Fe(OH)_2$ formed during an anodic potential scan. At higher anodic potentials (above −823 mV vs. $Hg/HgO/OH^-$ the loss for $Fe(OH)_2$ increases due to its oxidation to δ-FeOOH. The latter causes absorption bands at 1130 cm^{-1} and 915 cm^{-1}.

12 Issues and Prospects

The in-situ infrared method has been applied to a number of systems and a considerable volume of data are now available. These show that the electrochemical interface can be monitored by means of the vibrational spectrum of the species at the surface. Criteria to discriminate between features for adsorbates and solution species are now better defined and should help to establish the experimental conditions needed for obtaining reliable spectra. A very important step in the application of the technique is the use of well-defined single-crystal surfaces. The vibrational properties of adsorbed species can now be studied in detail. Thus the IR method is not only an important analytical tool to establish the nature of adsorbates, it can also afford data on the interaction of adsorbates with the electric field, with the substrate surface and with neighboring molecules.

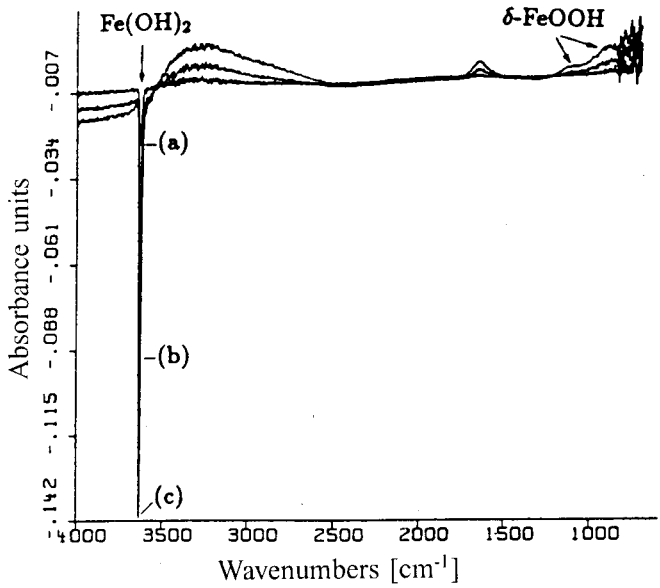

Fig. 70. ATR spectra during the oxidation of iron. Potential scanned at 1 mV s^{-1}. Reference spectrum −823 to −746 mV; (a) −746 to −669 mV; (b) −669 to −592 mV: (c) −592 to −550 mV. (After [13]). Reprinted by permission of the Electrochemical Society.

From the point of view of the instrumentation, the combination of high baseline stability and rapid scan interferometers should afford the use of time-resolved techniques. Much of important information on the vibrational spectrum of adsorbates lies in the far infrared region. Access to frequencies near 100 cm^{-1} or lower would allow the observation of adsorbate-metal vibrations and furnish straightforward information on the strength of the bond to the surface. Instrumentation for the far-infrared region is still limited by the low energy of standard IR sources. The use of synchrotron radiation could be an alternative way of overcoming this problem. No less important is the development of new materials to be used as windows. The stability of the window to aggressive chemical solutions is a factor at present limiting the reasonable use of the 1000–600 cm^{-1} IR region in many electrochemical systems.

13 References

1. H. Gerischer, Ber. Bunsenges. Phys. Chem. 92, 1436 (1988).
2. H.B. Mark, B.S. Pons, Anal. Chem. 38, 119 (1966).
3. W.N. Hansen in: Advances in Electrochemistry and Electrochemical Engineering. P. Delahay, C.W. Tobias (eds.), Wiley, New York (1973), Vol. 9, p. 1.
4. A. Bewick, K. Kunimatsu, S. Pons, Electrochim. Acta 25, 465 (1980).
5. Bewick, K. Kunimatsu, B.S. Pons, J.W. Russell, J. Electroanal. Chem. 160, 47 (1984).

6. J.W. Russell, J. Overend, K. Scanlon, M.W. Severson, A. Bewick, J. Phys. Chem. 86, 3066 (1982).
7. S. Pons, T. Davidson, A. Bewick, J. Am. Chem. Soc. 105, 1802 (1983).
8. W. Golden, K. Kunimatsu, H. Seki, J. Phys. Chem. 88, 1275 (1984).
9. P.R. Griffiths, J.A. de Haseth, Fourier Transform infrared spectrometry, in Chemical Analysis, P.J. Elving, J.D. Winefordner (eds), Wiley-Interscience, New York (1986), Vol. 83.
10. N. Brinda-Konopik, H., Neugebauer, G. Gidaly, G. Nauer, Mikrochim. Acta (Suppl. 9) 329 (1981).
11. L.M. Peter, D.J. Blackwood, S. Pons, J. Electroanal. Chem. 294, 111 (1990).
12. E.P. Boonekamp, J. Kelly, J. van der Ven, A.H.M. Sondag, J. Electroanal. Chem. 344, 187 (1993).
13. H. Neugebauer, A. Moser, P. Strecha, A. Neckel, J. Electrochem. Soc. 137, 1472 (1990).
14. A. Moser, H. Neugebauer, K. Maurer, J. Theiner, A. Neckel in: Springer Series in Solid State Science, H. Kuzmany, M. Mehring, S. Roth (eds.), Springer-Verlag, Berlin 1992, Vol. 107, p. 276.
15. A. Bewick, S. Pons in: Advances in Infrared and Raman Spectroscopy, R.J.H. Clark, R.E. Hester (eds.), Wiley-Heyden, London (1985), Vol. 12, p. 1.
16. M.A. Habib, J. O'M. Brockris, J. Electroanal. Chem. 180, 287 (1984).
17. J.K. Foley, K. Korzeniewski, J.L. Daschbach, S. Pons in: Electroanalytical Chemistry, a Series of Advances, A.J. Bard (ed.), Marcel Dekker, New York (1986), Vol. 14, p. 310.
18. P. Christesen, A. Hamnett in: Comprehensive Chemical Kinetics, C.H. Bamford, R.G. Compton (eds.), Elsevier, Amsterdam (1989), Vol. 29, p. 1.
19. A.G. Russell, G.P. Williams, A.S. Lin, W. O'Grady, J. Electroanal. Chem. 356, 309 (1993).
20. R.G. Greenler, J. Chem. Phys. 44, 310 (1966).
21. F.M. Hoffmann, Surf. Sci. Rep. 3, 107 (1983).
22. H. Ibach, D.L. Mills, Electron Energy Loss Spectroscopy and Surface Vibrations, Academic Press, New York (1982).
23. B.N.J. Persson, Solid State Commun., 30, 163 (1979).
24. J.C. Tully, Y.C. Chabal, K. Raghavarchari, J.M. Bowman, R.R. Luchese, Phys. Rev. B31, 1144 (1985).
25. J.K. Foley, S. Pons, Anal. Chem. 57, 945A (1985).
26. T. Bae, D.A. Scherson, E. Yeager, Anal. Chem. 62, 45 (1990).
27. T. Iwasita, F.C. Nart, J. Electroanal. Chem. 295, 215 (1990).
28. D.S. Corrigan, M. Weaver, J. Electroanal. Chem. 239, 55 (1988).
29. T. Iwasita, F.C. Nart, H. Polligkeit, Ber. Bunsenges. Phys. Chem. 95, 638 (1991).
30. J.D. Roth, M. Weaver, Anal. Chem. 63 (1991) 1603.
31. H. Seki, K. Kunimatsu, W.G. Golden, Appl. Spectrosc. 39, 437 (1985).
32. D.S. Bethune, A.C. Luntz, J.K. Sass, D.K. Roe, Surf. Sci 197, 44 (1988).
33. W.N. Hansen, J. Opt. Soc. Am. 58, 380 (1968).
34. F.C. Nart, PhD Thesis, University of São Paulo, Brazil.
35. K. Kunimatsu, M. Samant, H. Seki, M.R. Philpott, J. Electroanal. Chem. 243, 203 (1988).
36. K. Kunimatsu, M. Samant, H. Seki, J. Electroanal. Chem. 258, 163 (1989).
37. V.B. Paulissen, C. Korzeniewski, J. Electroanal. Chem. 290, 181 (1990).
38. F.C. Nart, T. Iwasita, J. Electroanal. Chem. 308, 277 (1991).
39. I. Ratajezykova, Surf. Sci. 48, 549 (1975).
40. A.M. Baró, H. Ibach, H.D. Bruchmann, Surf. Sci. 88, 384 (1979).
41. U.A. Jayasooriya, M.A. Chesters, M.W. Howard, S.F.A. Kettle, D.B. Powell, N.S. Sheppard, Surf. Sci. 93, 526 (1980).
42. Y.J. Chabal, Surf. Sci. Rep. 8, 211 (1988).
43. R.J. Nichols, A. Bewick, J. Electroanal. Chem. 243, 445 (1988).
44. K. Vetter, Eletrochemische Kinetik, Springer Verlag, Berlin (1961).
45. P. Hollins, Surf. Sci. Rep. 16, 51 (1992).
46. R.G. Tobin, Surf. Sci. 183, 266 (1987).

47. G. Blyholder, J. Phys. Chem. 68, 2773 (1964).
48. G. Blyholder, J. Phys. Chem. 79, 756 (1975).
49. J.C. Bertolini, G. Dalmai-Imelik, J. Rousseau, Surf. Sci. 68, 539 (1977).
50. H. Ibach, G. Somorjai, Appl. Surf. Sci. 3, 293 (1979).
51. E.L. Garfunkel, J.E. Cromwell, G.A. Somorjai, J. Phys. Chem. 86, 310 (1982).
52. E.J. Baerends, P. Ros, Int. J. Quantum Chem. 12, 169 (1978).
53. Si-Chung Chang, M.J. Weaver, J. Chem. Phys. 92, 4582 (1990).
54. Si-Chug Chang, M.J. Weaver, J. Phys. Chem. 94, 5095 (1990).
55. Si-Chung Chang, M.J. Weaver, Surf. Sci. 230, 222 (1990).
56. N. Furuya, S. Motoo, K. Kunimatsu, J. Electroanal. Chem. 239, 347 (1988).
57. F. Kitamura, M. Takeda, M. Takahashi, M. Ito, Chem. Phys. Lett. 142, 318 (1987).
58. F. Kitamura, M. Takahash, M. Ito, J. Phys. Chem. 92, 3320 (1988).
59. K. Yoshioka, F. Kitamura, M. Mitsuaki, M. Takahashi, M. Ito, Surf. Sci. 227, 90 (1990).
60. L.W.H. Leung, Si-Chung Chang, M.J. Weaver, J. Chem. Phys. 90, 7426 (1989).
61. Y. Ikezawa, H. Saito, H. Matsubayashi, G. Toda, J. Electroanal. Chem. 252, 395 (1988).
62. K. Kunimatsu, J. Phys. Chem. 88, 2195 (1984).
63. K. Kunimatsu, W.G. Golden, H. Seki, M.R. Philpott, Langmuir 1, 245 (1985).
64. K. Kunimatsu, K. Shimazu, H. Kita, J. Electroanal. Chem. 256, 371 (1988).
65. K. Kunimatsu, H. Seki, W.G. Golden, M.R. Philpott, J.G. Gordon II, Langmuir 2, 464 (1986).
66. F.T. Wagner, T.E. Moylan, S.J. Schmieg, Surf. Sci. 195, 403 (1988).
67. D. Hoge, M. Tüshaus, A.M. Bradshaw, Surf. Sci. 207, L935 (1988).
68. H. Pfnür, D. Menzel, F.M. Hoffmann, A. Ortega, A.M. Bradschaw, Surf. Sci. 93, 431 (1980).
69. S. Trasatti, J. Electroanal. Chem. 150, 1 (1983).
70. C.W. Olsen, R.I. Masel, Surf. Sci. 201, 444 (1988).
71. S.R. Bare, P. Hoffmann, D.A. King, Surface Sci. 144, 347 (1984).
72. G.D. Mahan, A.A. Lucas, J. Chem. Phys. 68, 1344 (1978).
73. R.M. Hammaker, S.A. Francis, R.P. Eischens, Spectrochim. Acta 21, 1295 (1965).
74. M.W. Severson, W.J. Tornquist, J. Overend, J. Phys. Chem. 88, 469 (1984).
75. A. Bewick, M. Razaq, J.W. Russell, J. Electroanal. Chem. 256, 165 (1988).
76. R.G. Greenler, J. Chem. Phys. 37, 2094 (1962).
77. N. Takezawa, H. Kobayashi, J. Catal. 25, 179 (1972).
78. B.A. Sexton, Surf. Sci. 88, 299 (1979).
79. J.E. Demuth, H. Ibach, Chem. Phys. Lett. 60, 395 (1979).
80. J.L. Davis, M.A. Barteau, Surf. Sci. 235, 235 (1990).
81. B.A. Sexton, Surf. Sci. 102, 271 (1988).
82. B. Beden, C. Lamy, A. Bewick, K. Kunimatsu, J. Electroanal. Chem. 121, 343 (1981).
83. B. Beden, S. Juanto, J.M. Leger, C. Lamy, J. Electroanal. Chem. 238, 323 (1987).
84. B. Beden, F. Hahn, J.M. Leger, C. Lamy, M. Lopes, J. Electroanal. Chem. 258, 463 (1989).
85. T. Iwasita, W. Vielstich, J. Electroanal. Chem. 250, 451 (1988).
86. D.S. Corrigan, M.J. Weaver, J. Electroanal. Chem. 241, 143 (1988).
87. T. Iwasita, F.C. Nart, V. Vielstich, Ber. Bunsenges. Phys. Chem. 94, 1030 (1990).
88. S. Chung Chang, Y. Ho, M.J. Weaver, Surf. Sci. 295, 81 (1992).
89. T. Iwasita, F.C. Nart, B. López, W. Vielstich, Electrochim. Acta 37, 2361 (1992).
90. T. Iwasita in: Advances in Electrochemical Science and Engineering, H. Gerischer, C. Tobias (eds.), Verlag Chemie, Weinheim (1990) Vol. 1, p. 127.
91. F.C. Nart, T. Iwasita, J. Electroanal. Chem. 317, 291 (1991).
92. J.M. Bowman, J.S. Bittman, L.B. Harding, J. Chem. Phys. 85, 911 (1986).
93. K. Kunimatsu, J. Electroanal. Chem. 213, 149 (1986).
94. E. Pastor, T. Iwasita, Electrochim. Acta 39, 547 (1994).
95. R.J. Nichols, A. Bewick, Electrochim. Acta, Electrochim. Acta 33, 1691 (1987).
96. P.A. Christensen, A. Hamnett, J. Munk, G.L. Throughton, J. Electroanal. Chem. 370, 251 (1993).
97. T. Iwasita, B. Rasch, E. Cattaneo, W. Vielstich, Electrochim. Acta 34, 1073 (1989).

98. B. Bittins Cattaneo, S. Wilhelm, E. Cattaneo, H. W. Buschmann, W. Vielstich, Ber. Bunsenges. Phys. Chem. 92, 1210 (1988).
99. P. Gao, S. Chang, Z. Zhou, M. Weaver, J. Electroanal. Chem. 272, 161 (1989).
100. L. H. Leung, S. Chang, M. Weaver, J. Electroanal. Chem. 266, 317 (1989).
101. S. Chang, L. W. H. Leung, M. Weaver, J. Phys. Chem. 94, 6014 (1990).
102. G. Socrates, Infrared Characteristic Group Frequencies, Wiley, New York (1980).
103. G. Herzberg, Molecular Spectra and Molecular Structure II: Infrared and Raman Spectra of Polyatomic Molecuels, Van Nostrand Reinhold, New York (1945).
104. D. Hadzi, N. Sheppard, Proc. R. Soc. London, Ser. A 216, 247 (1953).
105. J. Carrell Morris, J. Chem. Phys. 11, 230 (1943).
106. J. M. Perez, B. Beden, F. Hahn, A. Aldaz, C. Lamy, J. Electroanal. Chem. 262, 251 (1989).
107. T. Iwasita, E. Pastor, Electrochim. Acta 39, 531 (1994).
108. E. Pastor, S. Wasmus, T. Iwasita, C. Arévalo, S. González, A. J. Arvía, J. Electroanal. Chem. 350, 97 (1993); idem. ibid. 353, 81 (1993).
109. M. Fleischmann, I. R. Hill, M. E. Pemble, J. Electroanal. Chem. 136, 361 (1982).
110. K. Kunimatsu, H. Seki, W. G. Golden, Chem. Phys. Lett. 108, 195 (1985).
111. K. Kunimatsu, H. Seki, W. G. Golden, J. G. Gordon II, M. R. Philpott, Surf. Sci. 158, 596 (1985).
112. A. Hatta, Y. Sasaki, W. Suëtaka, J. Electroanal. Chem. 215, 93 (1986).
113. D. S. Corrigan, P. Gao, L. W. H. Leung, M. J. Weaver, Langmuir 2, 744 (1986).
114. K. Kunimatsu, H. Seki, W. G. Golden, J. G. Gordon II, M. R. Philpott, Langmuir 4, 337 (1988).
115. K. Nakamoto, Infrared and Raman Spectra of Inorganic and Coordination Compounds, Wiley, New York (1978).
116. K. A. B. Lee, K. Kunimatsu, J. G. Gordon, W. G. Golden, H. Seki, J. Electrochem. Soc. 134, 1676 (1987).
117. A. B. Anderson, R. Kötz, E. Yeager, Chem. Phys. Lett. 82, 130 (1981).
118. C. J. Nelin, P. S. Bagus, M. R. Philpott, J. Chem. Phys. 87, 2170 (1987).
119. P. S. Bagus, C. J. Nelin, W. Müller, M. R. Philpott, H. Seki, Phys Rev. Lett. 58, 559 (1987).
120. H. Kawashima, Y. Ikezawa, T. Takamura, J. Electroanal. Chem. 317, 257 (1991).
121. K. Ashley, M. Lazaga, M. G. Samant, H. Seki, M. R. Philpott, Surf. Sci. 219, L590 (1989).
122. F. Kitamura, M. Takahashi, M. Ito, Chem. Phys. Lett. 130, 181 (1986).
123. K. Ashley, F. Weinert, D. L. Feldheim, Electrochim. Acta 36, 1863 (1991).
124. K. Ashley, F. Weinert, M. G. Samant, H. Seki, M. R. Philpott, J. Phys. Chem. 95, 7409 (1991).
125. C. Korzeniewski, S. Pons, P. P. Schmidt, M. W. Severson, J. Chem. Phys. 85, 4153 (1986).
126. P. Guyot-Sionnest, A. Tadjeddine, Chem. Phys. Lett. 172, 341 (1990).
127. A. Tadjeddine, P. Guyot-Sionnest, Electrochim. Acta 36, 1849 (1991).
128. J. H. Hunt, P. Guyot-Sionnest, Y. R. Shen, Chem. Phys. Lett. 133, 189 (1987).
129. P. Guyot-Sionnest, R. Superfine, J. H. Hunt, Y. R. Shen, Chem. Phys. Lett. 144, 1 (1988).
130. A. Crossley, A. King, Surf. Sci. 95, 528 (1977).
131. M. W. Severson, A. Russel, D. Campbell, J. Russell, Langmuir 3, 202 (1987).
132. J. K. Foley, S. Pons, Langmuir 1, 697 (1985).
133. M. G. Samant, K. Kunimatsu, R. Viswanathan, H. Seki, G. Pacchioni, P. S. Bagus, M. R. Philpott. Langmuir 7, 1261 (1991).
134. D. B. Parry, J. M. Harris, K. Ashley, Langmuir 6, 209 (1990).
135. D. S. Corrigan, M. J. Weaver, J. Phys. Chem. 90, 5300 (1986).
136. K. Ashley, M. G. Samant, H. Seki, M. R. Philpott, J. Electroanal. Chem. 270, 349 (1989).
137. S. Pons, J. Electroanl. Chem. 150, 495 (1983).
138. M. A. Habib, J. O'M. Bockis, J. Electrochem. Soc. 132, 108 (1985).
139. K. Kunimatsu, M. G. Samant, H. Seki, J. Electroanal. Chem. 272, 185 (1989).
140. M. G. Samant, K. Kunimatsu, H. Seki, M. R. Philpott, J. Electroanal. Chem. 280, 391 (1990).
141. P. E. Faguy, N. Markovic, R. R. Adzic, C. A. Fierro, E. B. Yeager, J. Electroanal. Chem. 289, 245 (1990).

142. F.C. Nart, T. Iwasita, J. Electroanal. Chem. 322, 289 (1992).
143. F.C. Nart, T. Iwasita, M. Weber, Electrochim. Acta, 39, 961 (1994).
144. F.C. Nart, T. Iwasita, M. Weber, Electrochim. Acta, 39, 2093 (1994).
145. T. Iwasita, F.C. Nart, A. Rodes, E. Pastor, M. Weber, Electrochim. Acta, in press.
146. F.C. Nart, T. Iwasita, Electrochim. Acta 37, 385 (1992).
147. F.C. Nart, T. Iwasita, M. Weber, Ber. Bunsenges. Phys. Chem. 97, 737 (1993).
148. J. O'M. Bockris, M. Gamboa-Aldeco, M. Szklarczyk, J. Electroanal. Chem. 339, 355 (1992).
149. P.A. Thiel, T.E. Madey, Surf. Sci Rep. 7, 211 (1987).
150. B.S. Dawson, D. Irish, G.E. Toogood, J. Phys. Chem. 90, 334 (1986).
151. G.E. Walrafen, D.M. Dodd, Trans. Faraday Soc. 57, 1286 (1961).
152. A. Cotton, L.R. Falvello, S. Hahn, Inorg. Chem. 21, 2889 (1982).
153. J. Clavilier, J. Electroanal. Chem. 107, 211 (1980); J. Clavilier, R. Faure, D. Guinet, R. Durand, ibid. 107, 205 (1980).
154. J.M. Orts, R. Gómez, J.M. Feliú, A. Aldaz, J. Clavilier, International Conference on Progress in Electrocatalysis Theory and Practice, Ferrara (1993), Extended Abstract A8.
155. B. Hess, private communication, May 1993.
156. M.E. Gamboa-Aldeco, E.H. Herrero, P. Zelenay, A. Wieckowski, J. Electroanal. Chem. 348, 451 (1993).
157. A. Wieckowski, P. Zelenay, K. Varga, J. Chim. Phys. 88, 1247 (1991).
158. S. Ye, H. Kita, A. Aramata, J. Electroanal. Chem. 333, 299 (1992).
159. A.C. Chapman, L.E. Thirlwell, Spectrochim. Acta 20, 937 (1964).
160. G. Horanyi, E.M. Rizmayer, G. Inzelt, J. Electroanal. Chem. 93, 183 (1978).
161. E.U. Condon, Phys. Rev. 41, 759 (1932).
162. R. Kötz, E. Yeager, J. Electroanal. Chem. 123, 335 (1981).
163. S. Pons, S.B. Khoo, A. Bewick, M. Datta, J.J. Smith, A.S. Hinman, G. Zachmann, J. Phys. Chem. 88, 3575 (1984).
164. C. Korzeniewski, R.B. Shirts, S. Pons, J. Phys. Chem. 89, 2297 (1985).
165. F.C. Nart, T. Iwasita, Electrochim. Acta 37, 2179 (1992).
166. N.K. Ray, A.B. Anderson, J. Phys. Chem. 86, 4851 (1982).
167. S.P. Mehandru, A.B. Anderson, J. Phys. Chem. 93, 2044 (1989).
168. S. Holloway, J.K. Worskov, J. Electroanal. Chem. 101, 193 (1984).
169. P.S. Bagus, G. Paccioni, Surf. Sci. 236, 233 (1990).
170. D.K. Lambert, Solid State Comm. 51, 297 (1984).
171. D.K. Lambert, J. Chem. Phys. 89, 3847 (1988).
172. L.S. Luo, R.G. Tobin, D.K. Lambert, Chem. Phys. Lett. 204, 445 (1993).
173. F.C. Nart, T. Iwasita, in preparation.
174. B.N.J. Persson, R. Ryberg, Phys. Rev. B, 24, 6954 (1981).
175. G. Zerbi in: Vibrational Intensities in Infrared and Raman Sepctroscopy, W.B. Person, G. Zerbi (eds.), Elsevier, Amsterdam (1982), p. 67.
176. D.K. Lambert, J. Chem. Phys. 94, 6237 (1991).
177. G. Riley in: Vibrational Intensities in Infrared and Raman Spectroscopy, W.B. Person, G. Zerb (eds.), Elsevier, Amsterdam (1982), p. 159.
178. J. Overend in: Vibrational Intensities in Infrared and Raman Sepctroscopy, W.B. Person and G. Zerbi (eds.), Elsevier, Amsterdam (1982), p. 190.
179. N.J. Harrick, Internal Reflection Spectroscopy, Harrick Scientific, New York (1987).
180. F. Ozanam, J.N. Chazalviel, J. Electroanal. Chem. 269, 251 (1989).
181. J. Rappich, H.J. Lewerenz, H. Gerischer, J. Electrochem. Soc. 140, L187 (1993).
182. H. Neugebauer, A. Neckel, H.S. Sariciftci, H. Kuzmany, Synthetic Metals, 29, E185 (1989).

Advances in Electrochemical Science and Engineering
Edited by Heinz Gerischer and Charles W. Tobias

Electrochemical Reactions in Nonaqueous and Mixed Solvents

Zbigniew Galus

Department of Chemistry, The University of Warsaw, ul. L. Pasteura 1, 02-093 Warsaw, Poland

Contents

List of Symbols

$a = \gamma^{\neq}$	number of water molecules (associates) removed from the electrode surface to make place for one activated complex
a_s (a_{H_2O})	activity of solvent s (water) in the solvents mixture
A	pre-exponential factor
ACN	acceptor number
c	reactant concentration (c^s and c^b denote concentrations on the electrode surface and in the solution bulk respectively)
d	electrode-reactant distance in the charge-transfer reaction
D	diffusion coefficient of reactant
DN	donor number
e	charge of electron
E_e	electron energy
E^{of}	formal potential of the electrode reaction
$E^{\gamma}_{1/2}$	half-wave potential of the electrode reaction
E_{Lj}	liquid junction potential
E_{SIRE}	potential of the solvent-independent electrode
E_τ	Lewis acidity parameter
f_1, f_2	fractional amplitudes
F	Faraday constant
g	second factor in Marcus expression for electrode kinetics (defined in Eq. (42))
ΔG^o	free energy of electrode reaction
ΔG^*	free energy of activation of the charge-transfer reaction at the equilibrium potential
ΔG^*_i	free energy of activation corresponding to the reorganization of the reactant itself or/and its first coordination (solvation) sphere
ΔG^*_o	free energy of activation corresponding to the reorganization of solvent molecules around reactant
$\Delta G^{\neq}$	free energy of activation of the deposition-type reaction and electrode reactions in mixed solvents
ΔG_s	electrostatic part of the free energy of ion solvation
ΔG_{tr}	free energy of transfer of reactant from one solvent to another
ΔG^o_{ipf}	free energy of the ion-pair formation reaction
h	Planck's constant
k	electrode rate constant at the formal potential in mixed solvents
k_{bh}	rate constant of the anodic reaction at a given potential
k_{fh}	rate constant of the cathodic reaction at a given potential
k_s	standard rate constant of the electrode reaction
k_s^{ap}	apparent standard rate constant of the electrode reaction
k_{sol}	rate constant in organic solvent
k_w	rate constant in water
K_{ipf}	equilibrium constant of the ion-pair formation reaction
K_p	formation constant of the precursor state of the electrode reaction
L	average distance which reactant traverses between two nearest lattice positions in the solvent structure
M	molecular mass
n	number of moles of electrons transferred in the electrode reaction
N_A	Avogadro constant
P	partition coefficient of reactant between surface and bulk phases
r	reactant radius
R	gas constant
T	absolute temperature
w_p	average free energy required to transport reactant from the bulk to the reaction zone

x_S	mole fraction of solvent S
z	charge number of the ion
α	transfer coefficient of the cathodic reaction
α_B	Brönsted coefficient as described by Eq. (59)
β	transfer coefficient of the anodic reaction
β_{KT}	Kamlet-Taft coefficient of Lewis basicity
β_i	stability constant of solvates
γ	Pekar factor
Γ	surface excess
Γ_n	nuclear tunneling factor
δr	thickness of the charge transfer reaction zone
ε_s	static dielectric permittivity
ε_{op}	optical dielectric permittivity
ε_∞	high-frequency dielectric permittivity of the solvent in the near-infrared region
η	solvent viscosity
θ	electrode surface coverage
κ	transmission coefficient
λ	energy of reorganization
μ	chemical potential of the reactant
ν_n	nuclear frequency factor
ν_o	frequency of solvent reorganization
ν_i	inner shell bond vibration
τ_D	Debye relaxation time
τ_L	longitudinal relaxation time
τ_{rot}	rotation time of solvent molecules
τ_1	time corresponding to hydrogen bond rupture in structured solvents
τ_2	diffusional rotation time of monomers
$\tau_{L\infty}$	relaxation time as described by Eq. (51)
φ_2	potential of the outer Helmholtz layer

Abbreviations

AC	acetone
AcAc	acetylacetone; acetylacetonate
AN	acetonitrile
BCr	bis(biphenyl)chromium(0)
BN	benzonitrile
Coc	cobaltocene
Cp	cyclopentadienyl
DE	1,2-dichloroethane
DMA	*N,N*-dimethylacetamide
DMF	*N,N*-dimethylformamide
dmg	double deprotonated dimethylglyoxime
DMPU	1,3-dimethyl-3,4,5,6-tetrahydro-2/1*H*-pyrimidinone
DMSO	dimethyl sulfoxide
En	ethylenediamine
Foc	ferrocene
hfac	hexafluoroacetylacetonate
HMPA	hexamethylphosphortriamide
L	neutral ligand
MeOH	methanol
MSA	mean spherical approximation

NB	nitrobenzene
NE	nitroethane
NM	nitromethane
NMF	*N*-methylformamide
Ox	oxidized species
PC	propylene carbonate
PN	propionitrile
1-PrOH	1-propanol
Py	pyridine
Red	reduced species
salen	*N,N*-bis(salicylidene)ethylenediamine
SIRE	solvent-independent reference electrode
THF	tetrahydrofuran
TMS	sulfolane
TMU	tetramethylurea

1 Introduction

Although water is used preferentially as a medium for electrode reactions, there is growing interest in the use of nonaqueous solvents. This is for several reasons: first, there are compounds which exhibit very limited solubility in water. Second, some species may not be stable in aqueous media. Third, the range of available potentials, relatively narrow in water, may be wider on both the cathodic and the anodic side in an aptly chosen solvent. Also, some processes of industrial or technical importance are sometimes carried out in nonaqueous or mixed solvents. For instance, in recent years different types of batteries, especially those with lithium electrodes, have been developed and further improved. They are based on the application of nonaqueous solvents. These applications frequently result from the fact that thermodynamic and kinetic parameters of various electrode reactions are greatly affected by the reaction medium.

This effect has been studied quite intensively in recent years in order to understand better the course and nature of electrode reactions. In particular, simple charge-transfer reactions have been used as models to check predictions of modern theories of the effect of solvents on reaction rates.

In the case of deposition-type reactions, where no appropriate theory exists, the studies carried out in various solvents may be helpful for a better understanding of such reactions.

Sections 2 and 3 are concerned mainly with electrochemical reactions in single solvents, and electrode reactions occurring in mixed solvents are covered in Secs. 5–7. The chapter concludes with suggestions for future work.

The change of the solvent (or, in the case of mixed solvents, the change of its composition) affects various parameters of the electrode reaction

$$\mathrm{Ox} + ne \Leftrightarrow \mathrm{Red} \tag{1}$$

where Ox and Red represent the oxidized and reduced species, respectively.

Therefore, knowledge of the solvent properties and ion solvation in such media is essential. Although an exact determination of the solvation energy of individual ions is not possible, extrathermodynamic assumptions have been introduced in order to estimate this parameter. These ideas will be presented before the influence of solvents on equilibrium and kinetic parameters of electrode reactions is discussed. As a basis for this discussion, a brief presentation of the properties of solvents frequently used in electrochemical experiments will be given.

2 Equilibrium at Electrodes and Comparison of Electrode Potentials in Pure Nonaqueous Solvents

2.1 The Characteristics of Solvents Used in Electrochemical Studies

Various solvents have been used as a reaction medium in electrochemical studies (Table 1).

Although these solvents should be electrochemically inactive over a wide potential range, this is not always the case since some solvents may be relatively easily reduced (e.g., nitrobenzene) or oxidized (e.g., amines). However, acetonitrile, which is frequently used in such studies, exhibits a very wide potential window from +3.4 to −2.9 V vs. SCE [5] when tetrabutylammonium salts are used as background electrolytes. In acetonitrile and liquid SO_2 as solvents, alkali metal cations could be oxidized [6] at an ultramicroelectrode, even to the divalent state.

In order to exploit the wide range of available potentials an appropriate background electrolyte must be used. These are very frequently tetraalkylammonium salts, because the cations of such salts are reduced at quite negative potentials; e.g., Me_4N^+ at −2.65 V, and the cations containing larger alkyl fragments require even more negative potentials. Gritzner [7] documented useful potential ranges using the dropping mercury electrode and the stationary platinum electrode in nonaqueous solvents.

At very positive potentials the oxidation of anions of the background electrolyte may also limit the range of available potentials. Therefore, MBF_4 or MPF_6 should be used in work at such potentials [5]. These electrolytes are generally preferred to perchlorates, as the preparation of water-free perchlorates can be dangerous because of their oxidative properties. Another advantage is that they are relatively soluble in various solvents and it is quite easy to prepare these salts in pure form.

The solvents used in electrochemical experiments should exhibit fairly high static dielectric permittivity, exceeding 10, in order to decrease the formation of ion-pairs, and consequently to guarantee good conductivity. The dielectric permittivity is also important in the calculation of the rate constant of the charge-transfer processes on

Table 1. Selected parameters of solvents frequently used in electrochemical experiments.

Solvent	Donor number, DN	Acceptor number, ACN	ε_{op}	ε_s	ε_∞	τ_D (ps)	τ_L (ps)	$\varepsilon_{op}^{-1} - \varepsilon_s^{-1}$
Acetonitrile (AN)	14.1	18.9	1.80	37.5	2	3.3	0.,2	0.528
Acetone (AC)	17.0	12.5	1.84	21	2	3.3	0.3	0.495
Benzonitrile (B)	11.9	15.5	2.33	25.6	3.9	38	5.8	0.390
Formamide (F)	24.0	39.8	2.09	110	7.0	37	2.35	0.469
N-Methylformamide (NMF)	27.0	32.1	2.04	182	5.4	123	3.7	0.485
N,N-Dimethylformamide (DMF)	26.6	16.0	2.04	36.7	4.5	11.0	1.3	0.472
N,N-Dimethylacetamide (DMA)	27.8	13.6	2.06	37.8	4.5	12.8	1.5	0.459
Dimethyl sulfoxide (DMSO)	29.8	19.3	2.18	46.7	5.7	19.5	2.4	0.438
Nitrobenzene (NB)	4.4	14.8	2.40	35.7	4.1	45.6	5.2	0.389
Hexamethylphosphoric triamide (HMPA)	38.8	10.6	2.12	29.6	3.3	80	8.9	0.438
Propylene carbonate (PC)	15.1	18.3	2.02	65	4.1	43	2.7	0.480
Methanol (MeOH)	19	41.3	1.76	32.7	5.6	48	8.2	0.628
Ethanol (EtOH)			1.85	24.5	4.2	1.30	22	0.499
1-Propanol (1-PrOH)			1.92	20.4	2.2	390	42	0.472
Pyridine (Py)	33.1	14.2	2.27	13.3	2.3	6.9	1.2	0.365
Nitromethane (NM)	2.7	20.5	1.90	36	2	3.9	0.2	0.498
1,2-Dichloroethane (DE)	0	16.7	2.08	10.4	2.4	6.9		0.385
Tetramethylurea (TMU)	29.6		2.10	23.1	4.5	31	6.0	0.433
Tetrahydrofuran (THF)	20.0	8	1.97	7.58	2.3	3.3	1.0	0.376
Water (H_2O)	18.1	54.8	1.78	80.3		8.5		0.550

τ_D, τ_L, ε_{op}, ε_s, and ε_∞ were taken from the [1 – 4], which include references to original literature. Different properties of many solvents were collected recently by Y. Marcus [Chem. Soc. Rev. 22, 409 (1993)].

the basis of the Marcus theory [8]. Therefore, a brief discussion concerning the behavior of solvents which influence these parameters is important for a better understanding of the phenomena which occur in liquid polar media. The discussion which follows is based on the Dogonadze [9] presentation.

In a polar medium, three types of polarization are observed. The first type results from the deformation of the electron coulds in solvent molecules. The frequency of fluctuation of this polarization, ν_e, is given by

$$\nu_e = E_e/h \tag{2}$$

where E_e is the energy of the electrons; ν_e is of the order of $10^{16}\,s^{-1}$ and occurs in the visible and ultraviolet range of the spectrum.

The second type of atomic polarization is attributable to intramolecular vibrations of the bonds between atoms and the change of bond length. It occurs in the near-infrared region with the frequency ν_i of the order of $10^{12} - 10^{13}\,s^{-1}$.

The third type of polarization is observed over a wide frequency range of the electromagnetic spectrum, ν_o, in the far-infrared region from 10^9 to $10^{12}\,s^{-1}$, and corresponds to the orientational rotation of polar solvent molecules.

The wide range of frequency of this polarization is due to the fact that not only simple molecules, but also more complex associates, may participate in the process.

When the frequency of the field, ν, is higher than ν_e, the average polarization should be equal to zero. Under such circumstances even electrons cannot follow very quick changes of the external field, and the real part of the dielectric permittivity should be approximately equal to one, while the imaginary part should be approximately equal to zero.

If $\nu \ll \nu_o$, all three types of polarization should be observed. For water, the dielectric permittivity in vacuum will then be equal to 80. This is the so-called static permittivity. The permittivity of the vaccum is $0.855 \times 10^{-12}\,C^{-1}\,m^{-1}$. The static dielectric permittivity ε_s near the ion or the surface of the charged electrodes, however, will exhibit smaller values. For instance, in the case of water ε_s at the electrode surface is assumed to approach 6. When applying the Marcus theory [8] both static and optical permittivities are used in calculations. These parameters therefore are listed in Table 1. In other calculations and correlations of the rate constants of electrode reactions and the dynamic relaxation properties of the solvents, the relaxation time of the solvents is used (Table 1).

Some solvents may be characterized by one Debye relaxation time, τ_D, corresponding to the rotational diffusion; in the case of alcohols and solvents, where hydrogen bonds are formed, more than one relaxation process is observed [10].

Some parameters of electrode reactions have been related to the donor and acceptor properties of the solvents. The solvent is considered here as a Lewis base and/or acid. These acid-base properties of solvents are usually represented by the Gutmann donor number (DN) [11, 12] and acceptor number (ACN) [13], which are also reported in Table 1. The donor number is defined as the molar enthalpy value for the 1 : 1 reaction of the donor-solvent with $SbCl_5$ as an acceptor in dichloroethane. The acceptor number is a dimensionless number from 0 to 100, given by the relative chemical shift of ^{31}P in Et_3PO in the solvent under consideration, with hexane as a reference solvent, related to the shift of the $Et_3PO \cdot SbCl_5$ adduct in 1,2-dichloroethane, to which the acceptor number 100 has been assigned. Although other empirical solvent donor and acceptor parameters have been proposed, in electrochemical studies the use of DN and ACN is most frequently used.

Information on solvent purification, purity tests and properties can be found in several reviews [14–20].

2.2 Electrochemical Studies of Ion Solvation

Since in electrochemical reactions either the reactants or the products, or both, are in an ionic state, the influence of ion solvation on electrochemical reactions is important.

The solvation of ions significantly affects their properties and reactivities. Ion solvation is studied quite extensively by electrochemical methods.

Prior to the presentation of such electrochemical studies, theoretical predictions on the influence of solvents on ion solvation will be discussed briefly.

2.2.1 Models of Ion Solvation

The energy of interaction of an ion with a solvent may be represented by three parts: its electrostatic interaction, a solvophobic component, and a specific interaction due to the donor-acceptor interactions. In recent considerations of the electrostatic interaction energy, the basic ideas of the Born model [21] are accepted, though its shortcomings and limitations are evident and the original equation has been modified. The ion, M^{n+}, in this model is represented by a nonpolarizable metallic sphere with a radius r.

The charge is assumed to be uniformly distributed on the surface of the sphere. Such an ion is transferred from vacuum, with a relative dielectric permittivity equal to 1, to the solvent, which is considered to be a structureless dielectric continuum characterized by the static dielectric permittivity, ε_s. This transfer may be divided into two processes: the transfer of a noncharged sphere from vacuum to continuum and the charging (to ne) of the transferred sphere.

It is assumed that the work of the first process is equal to zero, under the condition that the cohesion of the medium is zero. The work related to the second process is equal to the electrostatic part of the free energy of solvation of the ion, ΔG_s, given by the equation

$$\Delta G_s = -\frac{N_A z^2 e^2}{2r}\left(1-\frac{1}{\varepsilon_s}\right) \tag{3}$$

which is known as the Born equation. N_A is the Avogadro number and ze the charge of the ion.

It was assumed in the derivation of Eq. (3) that the charging process was so slow that all types of polarization could be changed during the charging of the sphere. However, if the charging process were so fast that only electronic or atomic polarization could be changed, in Eq. (3) either ε_{op} or ε_a should be substituted instead of ε_s.

Following Krishtalik [22], Eq. (3) can be rearranged to show approximately the role of the different types of polarization in the interaction of the ion with the medium.

$$\Delta G_s = -\frac{N_A z^2 e^2}{2r}\left[\left(1-\frac{1}{\varepsilon_{op}}\right)+\left(\frac{1}{\varepsilon_{op}}-\frac{1}{\varepsilon_a}\right)+\left(\frac{1}{\varepsilon_a}-\frac{1}{\varepsilon_s}\right)\right] \tag{4}$$

Assuming that the ion is situated in water, one has $\varepsilon_{op} = 1.8$, $\varepsilon_a = 5$, and $\varepsilon_s = 80$. Using these values and Eq. (4), one may conclude that the largest role in such an interaction is played by the electronic polarization corresponding to the first term in parentheses in Eq. (4), which is equal to 0.44. The second term, corresponding to atomic polarization, is equal to 0.36. The role of the orientational polarization is the smallest (0.19).

The nature of the solvent is represented in the Born equation only by the static dielectric permittivity ε_s, which includes all types of polarization. The Born assumption on the structureless nature of the solvent may be only approximately fulfilled in the case when the ion is considerably larger than the solvent molecules. The problem of ion size and the applicability of the dielectric model has been discussed by Evans et al. [23].

Also, as we discussed earlier, the assumption that the dielectric permittivity is independent of the distance from the ion is not correct. The strong electric field around the ion greatly affects the dielectric properties of the solvent. In consequence, the static dielectric permittivity in the solvent layer which surrounds the ion is lower than the bulk value, making the energy of solvation of the ions less negative. These changes are larger for small, highly charged ions.

The so-called mean spherical approximation (MSA) treatment of the solvation energy should also be mentioned. Within the frame work of that model the electrostatic energy of ions is given by a Born-like expression [25], where the effective radius of the ion is considered to be the sum of the ionic radius and a correction term which depends not only on the solvent molecule diameter but also on the dielectric permittivity. Thus, the effective radius is a function of the frequency of the electromagnetic field.

The MSA corrections to the continuum model depend on the relative sizes of the ion and the solvent. Only when the solvent molecule is small compared with the ion the continuum model gives a relatively good description of solvation [26].

Extended and more precise elaborations of the MSA model have been published [27].

In order to compare the solvation energy of a given species in two solvents, very frequently its free energy of transfer is used, which gives the difference in the free energy of solvation in both solvents. However, such parameters may be strictly determined only for noncharged molecules or for electrolytes transferred across the phase boundary between two solvents.

In order to separate such strictly determined values for electrolytes into ionic parts, some extrathermodynamic assumptions are necessary. In the literature many different types of such assumptions are described which may be divided into three main groups. One of the approaches used in such studies is the measurement of the potential difference, ΔE, of the following cell:

$$\mathrm{M}\,|\,\mathrm{M}^{n+}\,\mathrm{A}^{n-}\,(\mathrm{S}_1)\,|\,\mathrm{M}^{n+}\,\mathrm{A}^{n-}\,(S_2)\,|\,\mathrm{M} \tag{5}$$

where the common electrolyte MA is dissolved, and in both solvents S_1 and S_2 we have the same electrode M/M^{n+}.

The electromotive force of cell (Eq. 5), corrected for the liquid junction potential, E_{Lj}, is simply related to the free energy of transfer, ΔG_{tr}, of ion M^{n+} from solvent S_1 to S_2:

$$\Delta G_{tr}\,(\mathrm{M}^{n+}) = nF\,(\Delta E - E_{Lj}) \tag{6}$$

In order to obtain reliable results, there should be identical concentrations of M^{n+} in both solvents, no complexes or ion pairs should be formed by M^{n+} ions, and the M/M^{n+} electrodes in both solvents should behave reversibly.

In the second approach to the electrochemical determination of the ion solvation energy, a cell without a liquid junction is used. Such a cell consists of an electrode formed by the ions to be studied, and as a reference a solvent-independent reference electrode (SIRE):

$$\text{SIRE}\,|\,\text{M}^{n+},\ \text{A}^{n-}\ |\ \text{(different solvents)}\,|\,\text{M} \tag{7}$$

is used. The potential difference of this cell with solvent S_1 is

$$\Delta E_1 = E_{\text{SIRE}}(S_1) - E_{\text{M}^{n+}/\text{M}}(S_1) \tag{8}$$

In the second solvent S_2 we have

$$\Delta E_2 = E_{\text{SIRE}}(S_2) - E_{\text{M}^{n+}/\text{M}}(S_2) \tag{9}$$

and because we make the extrathermodynamic assumption

$$E_{\text{SIRE}}(S_1) \equiv E_{\text{SIRE}}(S_2) \tag{10}$$

the difference between the electromotive forces ΔE_1 and ΔE_2 should give directly the free energy of transfer of the ion M^{n+},

$$\Delta E_2^1 = E_{\text{M}^{n+}/\text{M}}(S_1) - E_{\text{M}^{n+}/\text{M}}(S_2) = -\frac{\Delta G_{\text{tr}}(\text{M}^{n+})}{nF} \tag{11}$$

Equation (11) is valid under the condition that the electrode M^{n+}/M exhibits reversible behavior in all solvents used.

Since this approach and measurements based on this concept are very common in electrochemical practice, they will be discussed more extensively in Sec. 2.2.3.

The third approach may be called the reference electrolyte assumption. It is based on the assumption that the thermodynamic parameters of the electrolyte composed of a large and symmetrical anion and a similarly shaped cation of a 1:1 type can be divided into two equal components. This approach is due to Born [21] but was further developed by other workers who, as a reference electrolyte, suggested tetraphenylphosphonium tetraphenylborate [28], tris(isoamyl)butylammonium tetraphenylborate [29] and tetraphenylarsonium tetraphenylborate [30–33].

2.2.2 Liquid Junction Potential Between Two Different Solvents

The determination of the liquid junction potential between two solvents (Fig. 1) was considered by a number of authors [32, 34–36]. More recently this problem has been investigated by Izutsu and coworkers. The brief presentation given below follows the summary of their work [37].

Three sources of the formation of the liquid junction potential E_{Lj} may be distinguished:

$$E_{\text{Lj}} = E_{\text{Lj}}(\text{a}) + E_{\text{Lj}}(\text{s}) + E_{\text{Lj}}(\text{ss}) \tag{12}$$

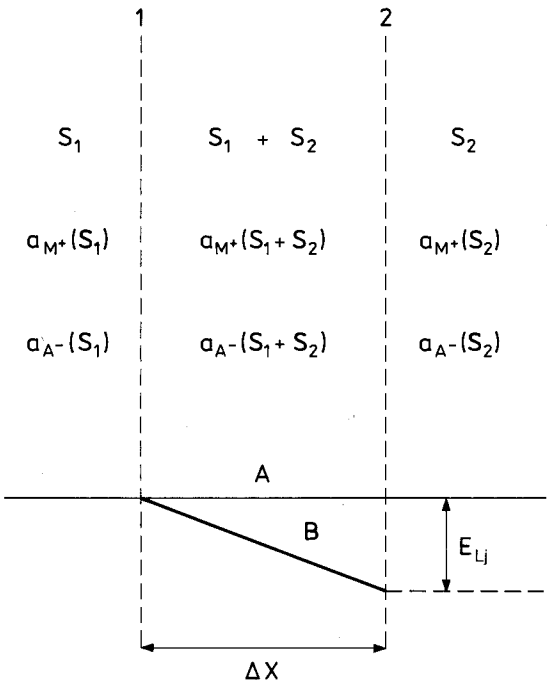

Fig. 1. Schematic representation of the liquid junction between two solvents S_1 and S_2 containing electrolyte MA. Between lines 1 and 2 there is the intermediate layer, thickness ΔX, where the liquid junction potential arises due to the difference in activities and mobilities of ions M^+ and A^- in the two solvents and due to the interaction of molecules of both solvents. Line A represents the situation when there is no liquid junction, while line 2 represents the change in the potential in the layer. Its linear change with distance was assumed arbitrarily.

$E_{Lj}(a)$ is due to different salt concentrations and different mobilities of cations and anions on both sides of the junction. This component alone determines the liquid junction potential if solutions of electrolyte in the same solvent on both sides of the junction are moderately concentrated.

The second source, $E_{Lj}(s)$, has its origin in the difference of ion solvation when there are different solvents on either side of the junction. The last component, $E_{Lj}(ss)$, arises from the interaction of the molecules of both solvents at the junction.

The strict separation of the components of Eq. (12) is rather difficult, but Izutsu [37] claims that under appropriate conditions, using the free diffusion junction, the separation of these components may be possible.

Component $E_{Lj}(a)$ may be estimated in a way similar to that used for the calculation of the liquid junction potential in aqueous solutions. It may be added that the KCl saturated calomel electrode which minimizes the liquid junction potential in aqueous solutions produces rather large E_{Lj} values when used for boundaries with aprotic solvents [38–40].

When there is the same electrolyte MA with different concentrations on the two sides of the interface, $E_{Lj}(a)$ may be described by a relatively simple equation [41–43] and is dependent on ionic transference numbers and the electrolyte concentration in both solvents. Obviously, if the activity of the electrolyte in both solvents is identical, then $E_{Lj}(a)$ drops to zero.

In order to minimize liquid junction potentials, Parker and coworkers [32, 38, 39, 44, 45] advocated the use of 0.1 M tetraethylammonium picrate in acetonitrile for the construction of a salt bridge. This approach, confirmed by Izutsu [37], is based on the finding that both of the ions Et_4N^+ and picrate have similar mobilities in many solvents, but not in other solvents such as methanol. Also, in the case of mixed solvents formed by water and a solvent of high acidity this bridge does not work properly [46].

The second component, $E_{Lj}(s)$, is independent of the electrolyte concentration, but it depends on the ionic transport numbers in both solvents and on the difference between the standard chemical potentials of ions in both solvents. In this case also, an equation which describes $E_{Lj}(s)$ was given [47]; however, it has only a qualitative significance.

Izutsu [37] compared the calculated $E_{Lj}(s)$ components with those found experimentally for junctions of aqueous solutions of MA-type salts with their solutions in dimethyl sulfoxide (DMSO), acetonitrile (AN), dimethylformamide (DMF), methanol (MeOH), propylene carbonate (PC), and benzonitrile (BN). Different MA salts were used, where $M = Et_4N^+$, Me_4N^+, Pr_4N^+ and Bu_4N^+ and A = picrate, Cl^-, Br^-, I^-, and ClO_4^-. The relations between the two measured and calculated components were linear, but the slope $\Delta E_{meas}/\Delta E_{calc}$ was only equal to unity in the case of the immiscible H_2O-nitrobenzene junction. In the case of junctions with other solvents it was about 0.5. Even lower slopes were obtained for junctions of methanol and other organic solvents. The origin of the difference between calculated and determined $E_{Lj}(s)$ values is not known, but it should be kept in mind that the $E_{Lj}(s)$ estimates are only qualitative in nature.

In some cases the $E_{Lj}(s)$ value may even exceed 150 mV. However, when tetraethylammonium picrate is used as a salt its value is usually quite small.

The electrolyte concentration usually has a limited influence on the third component, $E_{Lj}(ss)$. Though the exact mechanism of its formation is not well known, it is possible to estimate its sign and magnitude, on the basis of the potential difference which should arise due to the interaction and orientation of molecules of both solvents at the interface.

The problems related to this component have been discussed in several papers [48–51]. In the case of solvents which fairly strongly interact with each other, such as H_2O-DMF or H_2O-DMSO, the $E_{Lj}(ss)$ value is quite high, equal to about 100 mV. The charge of the aqueous side is more negative compared with the organic side, since both DMF and DMSO exhibit stronger donor properties than water.

For solvents with weak interaction, such as H_2O-AN or H_2O-PC, $E_{Lj}(ss)$ is considerably lower, being equal to 30 mV or less.

If the junction is formed by a single and a mixed solvent, it has been found [50] that $E_{Lj}(ss)$ varies practically linearly with the volume fraction of one component of the mixed solvent.

The stability and reproducibility of the liquid junction potential should also be briefly discussed. When the free-diffusion junction is used with an MA electrolyte on both sides, this potential settles within a few seconds and is later stable to ± 2 mV h^{-} and reproducible to ± 2 mV [52], although due to mutual diffusion the interface region does expand in time. However, such good reproducibility is observed only when there is the same electrolyte, MA, on both sides of the interface, even at different concentrations. When two different electrolytes AM (C_1) and MB (C_2) are used in both solvents, relatively stable potentials are observed only when $C_1 \gg C_2$ or $C_2 \gg C_1$.

2.2.3 Solvent-Independent Reference Electrodes

In order to use Eq. (6) in electrochemical studies of ion solvation, the problems related to the liquid junction potential have been presented in Sec. 2.2.2. Equation (11) may also be used in such studies, but the measured potentials should be expressed versus the same solvent-independent reference electrode. Such electrodes, which give a basis for the formation of a uniform scale of electrode potentials in different solvents, are available. A scale of this kind is also needed for a correlation of equilibrium potentials (E^{of}, $E^{\gamma}_{1/2}$) of electrode systems in various solvents.

One can determine exactly ΔG^{o}_{tr} for noncharged species or for salts, in the latter case using a galvanic cell without transference. However, as shown by Guggenheim [53], this value cannot be precisely divided among ionic components, on the basis of thermodynamics. Therefore the introduction of a uniform potential scale valid for various solvents, related to the properties of individual ions, must be based on an extrathermodynamic assumption. Such a scale was already proposed in 1947 by Pleskov [54]. It is based on the assumption that the rubidium electrode should have a potential independent of the solvent: therefore $\Delta G^{o}_{tr}(Rb^{+}) = 0$. This assumption follows from the Born equation which shows that the electrostatic part of the free energy of ion solvation, for large ions with a small charge, should not be significant. The cesium electrode would be better for that purpose, but at that time there were more data related to rubidium than to cesium.

This idea was later applied to redox systems formed by large complex ions with a small charge where the solvation energy varies little with the state of oxidation. Three such electrodes are now in frequent use. One is formed by ferrocene (Foc) and its oxidation product – ferricinium ion (Foc^{+}). Another also proposed by Strehlow and coworkers [55] is formed by its cobalt analogue: cobaltocene (Coc) and cobalticinium ion (Coc^{+}). The third electrode system, formed by neutral bis(biphenyl)chromium(0) (BCr) and its first oxidation product (BCr^{+}), was proposed by Schroer and Vlcek [56].

The BCr molecule is larger than that of ferrocene or cobaltocene, but all these complexes have a rather compact structure which diminishes the interaction of solvent molecules with the metal ion screened from two sides by ligands (sandwich structure). They have also a very delocalized multielectron system and, in consequence, when one electron is removed, the change in polarizability of these species is rather small.

Their electrode reactions in all simple solvents are fast and they thus exhibit reversible behavior. Such behavior was also found in mixed solvents, especially for the Foc^+/Foc electrode.

The BCr^+/BCr electrode was used preferentially by Gutmann and his school [57–60] and by Gritzner [61], because BCr is larger than Foc (Coc) and in consequence its interaction with the medium should be smaller. However, the solubility of BCr in aqueous and water-rich water-organic mixed solvents is very low.

The solubility of ferrocene in water is greater, equal to 5.01×10^{-5} mol l^{-1} [62]. Therefore, for investigations with mixed solvents of this kind, where water is one of the components, the Foc^+/Foc and Coc^+/Coc electrodes may be preferred. However, there is no evident preference for one of these three electrodes in experimental work with single nonaqueous solvents.

Gritzner and Kuta [63], who conducted a comparative study of the Foc^+/Foc and BCr^+/BCr systems, found that the difference of potentials between these two electrodes in various solvents is practically constant. In Table 2 we give the differences for selected solvents taken from their paper [63]. ΔE_1 values are taken from the paper by Krishtalik et al. [64]. Since the ΔE_2 values for 22 various solvents were similar (as illustrated in Table 2) Gritzner and Kuta recommended that both redox couples Foc^+/Foc and BCr^+/BCr may be used as reference systems.

Perhaps the most effective approach to that problem was proposed by Senda and Takahashi [65]. It is based on the assumption that the energy of transfer from one solvent to another of anion A^- and cation A^+ formed from the neutral species A,

$$A^- - e \Leftrightarrow A \Leftrightarrow A^+ + e \tag{13}$$

should be equal. Speaking in terms of potentials, this means that the formal potential of the A^+/A^- system with a two-step electrode reaction should be independent of the solvent. Madec and Courtot-Coupez [66] have measured formal potentials of monocyclic and polycyclic aromatic hydrocarbons ($E^{of}_{Ar^+/Ar}$ and E^{of}_{Ar/Ar^-}) and found that the difference between these potentials is constant in various solvents for a given hydrocarbon.

Table 2. Difference between $E^{\gamma}_{1/2}$ or E^{of} potentials for the Foc^+/Foc and BCr^+/BCr (ΔE_1) as well as for the Foc^+/Foc and Co_c^+/Coc (ΔE_2) systems.

Solvent	ΔE_1 (V)	ΔE_2 (V)	$E^{of}_{Coc^+/Coc}$(corr) (V)
1,2-Dichloroethane	1.13_1		
Acetone	1.13_0	1.31_0	−0.665
Hexamethylphosphoric triamide	1.12_4	1.31_0	
Water		1.34_6	−0.946
Dimethyl sulfoxide	1.12_3	1.30_9	
Acetonitrile	1.11_8	1.30_8	−0.675
Acetonitrile + H_2O (50 vol.%)		1.31_1	
Butyrolactone	1.11_2	1.30_8	−0.680
Butyrolactone + H_2O (20 vol.%)		1.31_4	
N,N-Dimethylformamide	1.12_7		−0.649

This concept was further developed by Krishtalik and coworkers [64], who used the $Coc^+/Coc/Coc^-$ system in their work. They have shown [64] that the solvation of Coc^+ and Coc^- is described by the simple Born equation, which in turn suggests that this solvation is only of an electrostatic nature.

They recommended and used the scale of potentials based on the Coc^+/Coc system corrected for the transfer energy of the Coc^+ cation, calculated from the Born equation. This scale is almost identical with that based on the average potential of Coc^+/Coc and Coc/Coc^- couples.

Potentials $E^{of}_{Coc^+/Coc}$(corr) given versus NHE are also reported in Table 2. Assuming that a liquid junction is formed between water and another solvent for which $E^{of}_{Coc^+/Coc}$(corr) is known, the potential difference between $E_{Coc^+/Coc}$(corr) in water and this solvent gives directly the liquid junction potential. For instance, for H_2O and acetone (AC) it amounts to -0.28 V (Table 2).

Krishtalik et al. [64] also arrived at a conclusion that cobaltocene and ferrocene electrodes are equivalent as the reference electrodes. The difference of potentials between these two electrodes is practically independent of the nature of the solvent and is given in Table 2.

The data collected in Table 2 show that the three electrodes based on the Foc^+/Foc, Coc^+/Coc and BCr^+/BCr systems are equivalent. When the experiments are carried out in different solvents, including those which exhibit low dielectric permittivity, one should take into account the possibility of ion-pair formation by cations of the reference system Foc^+, Coc^+ or BCr^+ with anions of the background electrolyte. Therefore, when the behavior of one system is analyzed in several solvents the potentials should be corrected for the ion-pairing process, using (if known) the stability constant of such species or making a theoretical estimate.

Recommendations for measuring electrode potentials in nonaqueous solvents are given by Gritzner and Kuta [63].

It is not our purpose in this chapter to discuss these problems more extensively. We are not presenting any results based on the so-called tetraphenylarsonium tetraphenylborate assumption [30–33, 67]. In this approach, it was assumed that the free energy of transfer of such species may be divided into equal parts due the fact that the anions and cations are large and have similar size. Also, this extrathermodynamic assumption has limitations [64, 68].

We only list some other redox systems which have been proposed for the construction of solvent-independent reference electrodes. In the collection of such systems, one finds tris(2,2-bipyridine)iron(I)/(0) [69], tris(phenantroline)iron(III)/(II) [72], redox systems composed of polynuclear aromatic hydrocarbons [66, 71], I_3^-/I_2 [72], and cryptate complexes [73, 74]. The use of these systems in practice is quite limited.

The free energies of transfer of various ions related to different solvent systems obtained on the basis of various assumptions were collected and discussed by Y. Marcus [75, 76].

It should be kept in mind, however, that the values determined are not always accurate and comparison of data reported for selected systems, especially those obtained under different assumptions, sometimes reveals striking differences.

2.3 Influence of Solvents on Potentials of Reversible Electrode Reactions

The effect of the solvent on the standard potential of electrode reactions can be derived from a thermodynamic cycle. In the case of the ion-transfer type of reaction, where the reduced form is the metal deposited on the solid electrode, we have

$$E^{\circ} = \frac{\Delta G_{s,Ox} - A}{nF} \tag{14}$$

where A is the sum of the free energy of atomization of the metal and the ionization potential necessary to form the M^{n+} ion from a metal atom M in the gas phase. It also contains the electron affinity of the metal.

In this case the difference between the standard potentials in two solvents, ΔE°, is dependent only on the difference between the free energy of solvation of the M^{n+} ion in the two solvents,

$$\Delta E^{\circ} = \frac{\Delta\Delta G^{\circ}_{s,Ox}}{nF} \tag{15}$$

The difference between the standard potential of an electron-transfer electrode reaction in two solvents, ΔE°, is accordingly

$$\Delta E^{\circ} = \frac{\Delta\Delta G^{\circ}_{s,Ox} - \Delta\Delta G^{\circ}_{s,R}}{F} \tag{16}$$

It is seen that this parameter depends only on the solvation energy difference of Ox and Red in the two solvents. In practice, however, the standard potentials are rarely determined. Instead, one determines either the formal potential, E^{of}, or the half-wave potential $E^{\gamma}_{1/2}$, of the reversible process.

The well-known dependence between the standard potential and $E^{\gamma}_{1/2}$ is

$$E^{\gamma}_{1/2} = E^{\circ} + \frac{RT}{nF} \ln \frac{f_{Ox} D_R^{1/2}}{f_R D_{Ox}^{1/2}} \tag{17}$$

The half-wave potential is equal to the standard potential, E° (for which $f_{Ox} = f_R = 1$), corrected by the term

$$\frac{RT}{nF} \ln \frac{f_{Ox} D_R^{1/2}}{f_R D_{Ox}^{1/2}}$$

In principle, both diffusion coefficients D_{Ox} and D_R may be precisely determined from independent measurements.

The activity coefficients f_{Ox} and f_R in a given solution differing from the standard state may be estimated, but these data are sometimes not sufficiently precise. Therefore, very frequently the formal potential, E^{of}, is used instead of the standard potential; it is described by the following relation:

$$E^{of} = E^{o} + \frac{RT}{nF} \ln \frac{f_{Ox}}{f_R} \tag{18}$$

E^{of} is related to the given background electrolyte concentration and concentrations of reactants, which influence the activity coefficients.

From Eqs. (17) and (18),

$$E^{of} = E^{\gamma}_{1/2} + \frac{RT}{nF} \ln \frac{D_{Ox}^{1/2}}{D_R^{1/2}} \tag{19}$$

Since usually D_{Ox} is not much different from D_R, it is frequently assumed that

$$E^{of} \cong E^{\gamma}_{1/2} \tag{19a}$$

Neither the formal potential nor the $E^{\gamma}_{1/2}$ potential should be very dependent on the logarithmic activity term in solutions with moderate concentrations of background electrolyte, since the activity coefficients f_{Ox} and f_R should be similar for the oxidized and reduced forms.

Under such conditions in noncomplexing solutions these potentials should be close to the E^{o} potential.

In consequence, the dependence of the standard potential E^{o} on the difference of the free energy of solvation in different solvents, given by Eqs. (15) and (16), should be satisfactorily reflected in the change of E^{of} or $E^{\gamma}_{1/2}$.

Although various workers have contributed to these data, the most extensive work on determination of $E^{\gamma}_{1/2}$ in various solvents was done by Gutmann and his school (see, for instance, [77]). In order to arrange the collected data so that they form a logical system it was necessary to find a correlation between $E^{\gamma}_{1/2}$ (E^{of}) potentials of the system being studied and parameters of the solvents used which characterize their solvating properties. The systematic studies of Gutmann and associates [77] were oriented toward the correlation of the half-wave potentials of reversible reactions with the Gutmann donor number. Especially carefully and critically prepared is the collection of $E^{\gamma}_{1/2}$ potentials by Gritzner [7] (see also [78]).

Gritzner [79] reported $E^{\gamma}_{1/2}$ of electroreduction of alkali metal cations and Tl(I), Cu(I), Ag(I), Zn(II), Cd(II), Cu(II) and Pb(II) in 22 different solvents. Some of the analyzed data were determined by this author [79], while others were taken from the literature. In addition to the above-mentioned cations, the potentials of the 0.01 mol l^{-1} Ag(I)/Ag electrode were considered. The author took care to check the reversibility of the systems analyzed. He found the linear dependence of $E^{\gamma}_{1/2}(K^{+})$ on the potential of the silver electrode mentioned in hard donor solvents. However, analysis of the dependence of the potentials of the same process $E^{\gamma}_{1/2}(K^{+})$ on the re-

ciprocal of the relative dielectric permittivity, which is based on the Born equation, showed no correlation, since the correlation coefficient was below 0.26. Most important are Gritzner's [79] linear (Eq. (20)) and multiple linear regression analyses (Eq. (21)) of the dependence of the half-wave potentials of a number of cation electroreduction on the donor (DN) and acceptor (ACN) numbers of hard donor solvents according to the relations

$$E^{\gamma}_{1/2} = a_1 + a_2\mathrm{DN} \tag{20}$$

and

$$E^{\gamma}_{1/2} = a'_1 + a'_2\mathrm{DN} + a'_3\mathrm{ACN} \tag{21}$$

The analysis of $E^{\gamma}_{1/2}$ according to Eq. (21) follows from a more general proposal of Krygowski and Fawcett [80, 81] to analyse solvent effects on thermodynamic parameters, taking into account both Lewis base and acid properties of the solvents.

The results of Gritzner's [79] analysis according to Eq. (20) are given in Table 3, while those according to Eq. (21) are given in Table 4. Potentials used for the analysis presented in Tables 3 and 4 are expressed versus BCr^+/BCr as a reference electrode. It can be observed that a linear correlation according to Eq. (20) represents well the dependence of $E^{\gamma}_{1/2}$ on the donor number of the solvents. The correlation coefficient, excepting Rb^+ and Cs^+, significantly exceeds 0.9.

A multiple linear analysis in which the influence of donor and acceptor properties of solvents on $E^{\gamma}_{1/2}$ potentials was taken into account (Eq. (21)) did not significantly improve the correlation and the standard error remained almost unchanged.

Both analysis give logical results. As expected, the coefficient a_2 (a'_2) in both analyses decreases significantly when going from Li^+ to Cs^+. However, even in the case of cesium, they still have a significant value, which indicates that such a system would not serve properly as a reference electrode in various nonaqueous solvents. The a_1 values in Table 3 represent the half-wave potentials at DN = 0, i.e. in

Table 3. Analysis, according to Eq. (20), of $E^{\gamma}_{1/2}$ potentials of electroreduction of various cations [79].

Cation	No. of solvents	a_1 (V)	$10^3\, a_2$	Standard error of estimate	Correlation coefficient
Li^+	16	−0.836	−30.1	0.085	0.935
Na^+	16	−0.903	−16.2	0.055	0.925
K^+	16	−1.080	−9.93	0.037	0.912
Rb^+	16	−1.133	−7.36	0.031	0.888
Cs^+	15	−1.124	−6.96	0.030	0.886
Tl^+	17	0.622	−12.6	0.041	0.953
Zn^{2+}	13	0.627	−30.1	0.090	0.959
Cd^{2+}	17	0.857	−24.3	0.092	0.938
Cu^{2+}	10	1.624	−30.0	0.076	0.952
Pb^{2+}	16	1.016	−25.4	0.071	0.945

Table 4. Analysis, according to Eq. (21), of $E^{\gamma}_{1/2}$ potentials of electroreduction of various cations.

Cation	No. of solvents	a'_1 (V)	$10^3\, a'_2$	$10^3\, a'_3$	Standard error of estimate	Correlation coefficient
Li^+	11	−0.717	−35.8	−1.07	0.076	0.956
Na^+	13	−0.903	−17.7	1.14	0.054	0.941
K^+	13	−1.095	−10.4	1.10	0.038	0.923
Rb^+	13	−1.152	−7.78	1.29	0.032	0.911
Cs^+	13	−1.165	−6.92	2.00	0.028	0.921
Tl^+	13	0.646	−15.1	1.73	0.038	0.960
Zn^{2+}	11	0.745	−36.5	−1.17	0.062	0.984
Cd^{2+}	13	0.981	−26.4	−4.88	0.094	0.925
Cu^{2+}	9	1.724	−32.1	−3.07	0.078	0.963
Pb^{2+}	13	1.085	−26.7	−2.45	0.075	0.950

1,2-dichloroethane. The change of these values from less negative to more negative ones when going from Li to Cs is monotonic, as opposed to the change of standard potentials, E°, of these metals in aqueous solutions. The differences ΔE between a_1 and E° values are equal to 1.811 V (Na), 1.84 V (K), 1.787 V (Rb) and 1.80 V (Cs). However, in the case of lithium this difference amounts to 2.209 V. Also these data are logical because the more negative potential of the Li^+/Li couple results from the more negative value of $\Delta G^{\circ}_{s,Li^+}$ (see Eq. (14)), since parameter A in that equation is highest for lithium in this group of metals and becomes less positive going down the group. An analogous trend of the formal potentials should also be observed in a solvent which interacts weakly with alkali metal cations.

All the analyses of potentials discussed above were carried out for hard donor solvents. Gutmann donor numbers for soft donors are not available. These numbers were not expected [82] to account for soft-soft interactions.

The data collected by Gritzner [79] and his analysis led him to the conclusion that different interactions of hard and soft cations with donors cannot be accounted for by using only one parameter. Gritzner [79] also tried other correlations. No correlation was found with the acceptor number and the other Lewis acidity parameter, E_T, introduced by Dimroth and Reichardt [19, 83]. Only those parameters which represent donor properties of solvents are correlated with the change of $E^{\gamma}_{1/2}$ potentials for the electroreduction of cations.

There is also, as expected, a correlation between the formal potentials of various systems with DN or the Kamlet-Taft, β_{KT}, Lewis basicity parameter [84] shown in other papers (see for instance [85]). Also, in this case, with increasing donor properties of the solvents, the formal potential is moving to more negative values expressed versus a solvent-independent reference electrode, the Foc^+/Foc system.

In conclusion, all systems analysed which belong to the ion-transfer (deposition) type of electrode reactions change their E^{of} ($E^{\gamma}_{1/2}$) potentials to more negative values versus a solvent-independent electrode when the DN of the solvent increases. This conclusion seems to be valid also for electron-transfer type reactions, if both the oxidized and the reduced form are cations. Sahami and Weaver [86] have stud-

ied the charge-transfer process in the systems $Ru(NH_3)_6^{3+/2+}$, $Ru(En)_3^{3+/2+}$ and $Co(En)_3^{3+/2+}$ (En = ethylenediamine) in eight solvents. They found that ΔG_{tr}^{o} and consequently also E^{of} change in approximate agreement with the DN of the solvents. A more negative potential was observed for a given system in solvents of high Lewis basicity.

A similar trend in the change of the formal or $E_{1/2}^{\gamma}$ potentials was observed for solvated cations, for instance for the Eu^{3+}/Eu^{2+} couple in different solvents [87, 88]. The analysis of Gibbs energies, entropies and enthalpies of single ion transfer led Gritzner [89] to search for general trends in the interaction of different ions with solvent molecules. The interactions of cations with different solvents were considered, in terms of the Lewis concept, i.e., as a reaction of the acid (cation) with the base (solvent).

If the electrode reaction proceeds with the participation of anions in the electrode system A/A^{n-}, A^{n-}/A, or A^{n-}/A^{m-}, the interaction of these anions with the solvent can now be understood as the reaction between the base (anion) and the acid (solvent). Now the formal potential should be dependent on the acceptor number of the solvent,

$$E^{of} = b_1 + b_2 ACN \tag{22}$$

where b_1 represents the formal potential of the analysed system in a solvent with the acceptor number equal to zero and b_2 reflects the sensitivity of the studied system to the influence of solvents. Such a correlation was observed for several A/A^- electrode systems.

In Table 5 we give the results of Kalinowski and coworkers [90] on the electroreduction of several quinones. The first reversible step was considered in several solvents. Potentials in this analysis were expressed versus the Foc^+/Foc electrode. With an increase of the acceptor number the electroreduction potential shifted to less negative values.

A very good linear correlation of the Eq. (22) type was observed by Paduszek and Kalinowski [91] for the electroreduction of phenazine at mercury electrodes in several solvents. It is shown in Fig. 2.

Jaworski [92] has found that E^{of} of perylene and fluoren-9-one are independent of the acceptor number, as opposed to formal potentials of anthracene and benzoquinone, which exhibit a linear dependence on the ACN of the used solvents. The

Table 5. Analysis of E^{of} potentials of several quinones according to Eq. (22) [90].

Quinone	b_2 (V)	r	No. of solvents used
1,4-Benzoquinone	0.040 ± 0.002	0.997	7
1,4-Naphthoquinone	0.026 ± 0.001	0.997	7
9,10-Phenanthrenequinone	0.022 ± 0.002	0.974	8
9,10-Anthraquinone	0.021 ± 0.002	0.981	8

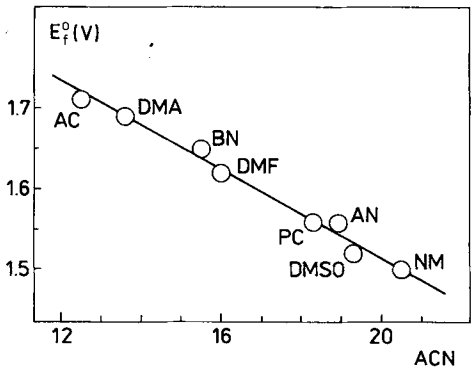

Fig. 2. The change in the formal potential of the phenazine/phenazine radical anion system (against the Foc^+/Foc electrode) with the acceptor number of the solvent [91]. Abbreviations are defined in Table 1.

explanation is based on a highly delocalized charge in the anions which are produced during electroreduction of perylene and fluoren-9-one. Delocalization is much weaker in the case of anions produced from two other compounds. Recently the effect of several aprotic solvents on multielectron electroreduction of buckminsterfullerene (C_{60}) was examined [93]. The authors found that $E_{1/2}^{\gamma}$ of the first reduction wave depends linearly on the donor number with a positive slope, and exhibits also a linear correlation with the acceptor number with a negative slope. $E_{1/2}^{\gamma}$ of the first three reversible reduction waves correlate with the normalized Dimroth-Reichardt parameter.

The solvatochromic method developed by Taft and coworkers [94] has also been used to explain the solvent effect on redox potentials. Lay [95] considered specific hydrogen bonding contributions to the thermodynamics and kinetics of electron transfer.

These correlations, especially with the donor number, mostly reflect the enthalpic effect. There was no correlation of the entropic effect with DN in the case of metal cations [86], since this term reflects more the extent of solvent orientation by the component of the redox system and disordering of the original solvent structure, than the strength of the complex-solvent interactions. Also, Svaan and Parker [96] did not find any correlation between the entropy of formation of different ion radicals and the empirical solvent parameter.

However, the study of the entropy of formation of anion radicals formed by electroreduction of selected organic species such that the charge is localized at an unshielded heteroatom (e.g., *p*-dicyanobenzene [97]) shows that this parameter is linearly dependent on the acceptor number of solvents.

These problems have been discussed at greater length by Jaworski and Kalinowski [98].

All these correlations may be influenced by the ion-pair formation process, more advanced in solvents of lower static dielectric permittivity. This process, with free energy, ΔG_{ipf}^{o}, given by

$$\Delta G_{ipf}^{o} = -nF(E^{of} - E^{oipf}) = RT \ln (1 + K_{ipf}) \tag{23}$$

is reflected both in the change of the free energy of transfer and the formal potential of the system.

E^{oipf} in Eq. (23) denotes the formal potential of the redox system with ions involved in ion-pairing, and K_{ipf} is the ion-pair stability constant. Since there is no correlation of the donor and the acceptor number with the static dielectric permittivity (see Table 1), ion-pair formation may lead to deviations from the dependences suggested by Eqs. (20) and (22).

Ion-pair formation in nonaqueous media was frequently observed in electrochemical studies (see [98]). There is no space here to discuss these problems. For illustration we mention only the study carried out in the present author's laboratory, on ion-pairing in the electroreduction of nitrobenzene and related compounds [99, 100]. Ion-pairing of intermediates may in some cases change the mechanism of electrode reactions.

3 Kinetics of Electrode Reactions in Pure Nonaqueous Solvents

3.1 Electron-Transfer Reactions

3.1.1 Influence of Solvents on the Energy of Activation

Theories of simple charge-transfer electrode reactions developed since the late 1950s (for review see [8, 101–105]) gave a rather simplified view of solvent effects on the rate of electrode reactions.

Let us consider again reaction (1), assuming now that both Ox and Red are dissolved in the solution. The electron-transfer reaction (1) may be considered as the outer-sphere process in which original bonds are not broken or formed and it is assumed that neither Ox nor Red is adsorbed on the electrode. A reaction occurring in the system $Fe(CN)_6^{3-/4-}$ or $Cr(H_2O)_6^{3+/2+}$ may serve as an example of such a process. Such a reaction was analyzed in detail by Marcus [8, 101].

The rate constant at the standard (formal) potential is

$$k_s = \kappa A \exp\left(\frac{-\Delta G^*}{RT}\right) \tag{24}$$

where A is the pre-exponential factor, being in the Marcus model equal to the heterogeneous collision frequency and practically independent of the solvent, and κ is the transmission coefficient (near to 1), though it was assumed that the energy barrier forms a cusp (Fig. 3) and the barrier is not decreased by the donor-acceptor interactions.

Here and further on, it is assumed that the rate constant (or energy of activation) is independent of the influence of the double-layer structure. It should be noted that

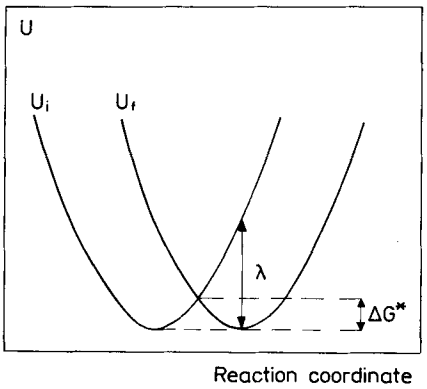

Fig. 3. The dependence of the potential energy (u) of substrate and product on an one-dimensional reaction coordinate. Abbreviations are defined in Table 1.

not always in experimental studies have the necessary corrections been made to account for this influence. This problem will be further discussed in Sec. 3.1.5.

In this model the main influence of the solvent on the rate of electrode reactions is exerted by the activation barrier. The free energy of activation is simply related to the reorganization energy λ by

$$\Delta G^* = \frac{\lambda}{4} \tag{25}$$

where ΔG^* is the intrinsic barrier when the free energy of reaction is equal to zero. The reactant and surrounding solvent molecules must be reorganized, before the charge-transfer step can occur, in order to reach the coordinates of the transition state. The explanation of λ is given in Fig. 3. The expression for the energy of activation at potentials other than E^0 (E^{of}) is more complex; additional terms which then appear in Eq. (25) are dependent on the overpotential.

Marcus divided the energy of activation (reorganization energy) into two parts [8, 101]:

$$\Delta G^* = \Delta G_i^* + \Delta G_o^* \tag{26}$$

where ΔG_i^* is due to reorganization of the reactant itself (e.g., an organic molecule) and its first coordination sphere (solvated or complex ion), while ΔG_o^* is due to reorganization of the solvent around reactant, as a result of the change in its charge. Both parts may be calculated from the following relations. The component of inner reorganization is

$$\Delta G_i^* = 0.5 \sum f_i (\Delta r/2)^2 \tag{27}$$

where the reactants are represented by a system of independent harmonic oscillators [101, 106], with f_i the reduced force constant of the ith bond and Δr the difference

in the length and angle of this bond in Ox and Red forms respectively. The outer part contribution [8, 101],

$$\Delta G_o^* = \frac{N_A e^2}{8}\left(\frac{1}{r}-\frac{1}{2d}\right)\left(\frac{1}{\varepsilon_{op}}-\frac{1}{\varepsilon_s}\right) \tag{28}$$

may be derived using the Born solvation model.

In Eq. (28) e is the charge of the electron, r the radius of the reactant, N_A Avogadro's number, and d the reactant–electrode distance. The solvent was considered here as a continuous medium with a fast electronic polarization characterized by the optical dielectric permittivity ε_{op} and a slower oscillatory plus orientational polarization characterized by the static dielectric permittivity ε_s.

Since Eq. (28) was obtained under assumptions similar to those used by Born, the calculation of ΔG_o^* suffers from the same limitations as the Born solvation model. The dielectric continuum model is valid for electron transfer in a structureless dielectric medium with a reactant approximated by a hard conducting sphere. It is obeyed when the specific solute–solvent interactions are negligible.

The assumption that the medium is structureless between the reacting species is certainly not fulfilled, since the solvent molecules around a reactant will be to some extent oriented due to short-range interactions. Therefore a bulk solvent property, such as the dielectric permittivity, may not describe correctly the medium around the reacting species. To account for that behavior, an average dielectric permittivity was used [107] in the calculation of ΔG_o^*.

There were efforts to modify Eq. (28) slightly, based on the assumption that a reactant has a nonspherical shape [108, 109]. A short-range reactant–solvent interaction was also taken into account [110]. Some authors questioned the importance of the $1/2\,d$ term in Eq. (28). This term accounts for the effect of image forces on reorganization of a solvent. In the Marcus theory d should be close to r, though in some calculations the $1/2\,d$ term was neglected, based on the assumption that the reaction plane is at a distance from electrode surface significantly exceeding r (for discussion of this problem, see [111]). Another reason for neglecting this term was sought in the screening of reactant–image interaction by the presence of ions of the background electrolyte [112].

In the Marcus model the solvent influence on the rate of electrode reactions is expressed by the change of ΔG_o^* and ΔG_i^* in the activation energy. In order to separate the influences of ΔG_o^* and ΔG_i^* it is desirable to study model reactions in which the inner-sphere reorganization energy is not significant ($\Delta G_o^* \gg \Delta G_i^*$). Therefore, complexes with a fixed first coordination sphere in the oxidized and the reduced form, and redox reactions of some large organic molecules producing free radicals in the electrode reaction, were studied.

For such model reactions, according to Eqs. (26) and (28), the changes of the rate constant should be simply related to the properties of the solvent by their dielectric permittivities:

$$\ln k_s = \text{const} + \text{const}'\left(\frac{1}{\varepsilon_{op}}-\frac{1}{\varepsilon_s}\right) \tag{29}$$

Therefore, if the Marcus theory describes properly the effect of solvents of k_s, a linear correlation between $\ln k_s$ and $(\varepsilon_{op}^{-1} - \varepsilon_s^{-1})$ should be observed in the experimental results. Before turning to the experimental studies, the $(\varepsilon_{op}^{-1} - \varepsilon_s^{-1})$ parameter for various solvents used in electrochemical work is presented in Table 1. Inspection of these data reveals that the largest difference of the $(\varepsilon_{op}^{-1} - \varepsilon_s^{-1})$ parameter for the listed solvents amounts to 0.263. Thus, on the basis of the Marcus theory for the outer-sphere electrode reactions, the largest change of the reaction rate for different solvents should amount to exp (const' 0.263). In this estimation any double-layer effect on the rate constant was neglected.

In general, the rate constants determined experimentally are not in accordance with this prediction [113, 114].

Although some rare results are roughly in line with this theory [115], the observed changes are usually larger than those theoretically predicted (see, for instance, [106]). These discrepancies were explained, especially in papers which appeared up to the early 1980s, by the change of distance of the reaction site from the electrode [116, 117]. Also, the influence of short-range specific reactant–solvent interactions was claimed to be responsible for these differences [106, 118]. It was even more difficult to explain the results obtained for solvated ions where the change of solvent not only influenced ΔG_o^*, but could also change ΔG_i^*, when in the first solvation sphere molecules of one solvent were substituted by molecules of another solvent. Such a situation exists in the system Eu^{3+}/Eu^{2+} which we had studied earlier [88] in several solvents. In this case also it was not easy to suggest a simple explanation of the kinetic results obtained.

Some difficulties in comparing the experimental kinetic data with the outer-sphere reorganization energy calculated from the Marcus formula (28) result from several assumptions made in this theory. The reactant was assumed to have a spherical shape with a symmetric charge distribution. No field penetration into the metal was considered. Also, the spatial dispersion of the dielectric permittivity of the medium was not taken into account. In fact, the positions and orientations of dipoles around a given ion are correlated with each other; therefore the reorientation of one dipole, under the influence of the external field, changes to some extent the reorientation of other dipoles within the distance defined by the correlation length.

Various improvements have been introduced into the Marcus description. Fawcett and Kharkats [119], Kharkats [108, 120, 121], Grampp et al. [122] and Fawcett and Fedurco [123] considered changes in the volume and shape of the reactants. The effects of a thin structureless dielectric layer between the metal electrode and a surrounding solution on the electrostatic works terms and solvent reorganization energy were also studied [124]. Such a layer is formed in mixed aqueous–organic solvents. Beyond the interlayer, the outer reorganization energy rises within the approach of the ion to the electrode, but after its penetration into this layer the reorganization energy decreases due to the low dielectric permittivity of this region.

One should also mention the so-called mean spherical approximation (MSA) treatment of solvent reorganization [25]. McManis and Weaver [125] considered how the solvent radius and dielectric parameters affect the electron transfer within the frame of this theory. The frequency dependence of the effective radius should cause significant deviations from the Marcus expression for the activation energy of

charge-transfer reactions, giving lower values of ΔG_0^*. An MSA estimation of the ΔG_0^* parameter using a different approach was given also by Fawcett and Blum [126] for homogeneous reactions. MSA estimations are in very good agreement with experimental values of the activation enthalpy determined for the Coc^+/Coc couple.

Another model, in which the reactant is represented by a dielectric cavity with point charge in its center, has been forwarded by German und Kuznetsov [127]. It is beyond the scope of the present review to discuss all the above-mentioned improvements in detail.

We would like to present somewhat more extensively the results of the work of Dzhavakhidze et al. [111], who studied the role of the spatial dispersion of the solvent dielectric permittivity and field penetration into a metal in determining the kinetics of electrode reactions. Considering the particular case of the field penetration effect on the reorganization energy, they found [111] that the ΔG_0^* value obtained is greater than predicted by the Marcus theory. Moreover, under some conditions the dependence of ΔG_0^* on the reactant–electrode distance (d) exhibits an "anti-Marcusian" behavior.

Close to the electrode surface, under some conditions, ΔG_0^* rises with a decrease of d, contrary to the prediction of Eq. (28). This „anti-Marcusian" behavior arises from a consideration of field penetration into the metal together with solvent spatial dispersion.

The authors [111] claim that the discrepancy between experimental kinetic data and those obtained from the Marcus theory is not sufficient to conclude that a violation of the equilibrium distribution polarization occurs. A more involved description of solvent reorganization leads to corrections which have the proper sign and order of magnitude. However, in view of the very approximate parametrization, the results obtained do not give the basis for quantitative agreement.

These problems were further developed by Phelps et al. [128]. In order to estimate the barrier height from electrochemical data and to compare it with the theoretical prediction, independent information on the pre-exponential factor is necessary. For analysis of experimental kinetics they selected a series of metallocenes, and specifically the Coc^+/Coc system in seven solvents. Without going into the details of the calculations, one finds that for model reactions the calculated ΔG_0^* values, based on the more advanced model presented, are significantly larger than those based on the Marcus equation.

These theoretical considerations also gave a basis for the consideration of the optimal distance of discharge, which is a result of competition between the activation energy ΔG^* and the overlap of electronic wave functions of the initial and final states. The reaction site for outer-sphere electrochemical reactions is presumed to be separated from the electrode surface by a layer of solvent molecules (see, for instance, [129]). In consequence, the influence of imaging interactions on ΔG_0^* predicted by the Marcus equation is small, which explains why such interactions are neglected in many calculations. However, considerations of metal field penetration show that the reaction sites close to the electrode are not favored [128], though contributions to k_s from more distant reaction sites will be diminished by a smaller transmission coefficient. If the reaction is strongly nonadiabatic, then the closest approach to the electrode is favorable.

Different solvents may exert different effects on the optimal distance of adiabatic electron-transfer reactions, due to a very strong influence on the ΔG_o^* versus d dependence. Therefore, the closest approach is not always optimal for the reaction rate and the effective distance may be strongly influenced by the structure of the solvent.

Such corrections of the original Marcus theory may still be insufficient to describe adequately the activation energy of electron-transfer reactions. However, the discrepancies between the experimental and calculated rate constant using Eq. (24) may also result from the assumption that the frequency factor developed for the collision in the gas phase should also be valid in condensed media.

Marcus [8, 101] expressed A in equation (24) by

$$A = \left(\frac{RT}{2\pi M}\right)^{1/2} \tag{30}$$

where M is the molecular mass of the reactant. Equation (30) was taken from the collision model for collisions in a gas phase.

For the condensed phase, another expression was proposed [130]:

$$A = 3D/2L \tag{31}$$

where D is the diffusion coefficient of the reactant and L is the average distance which the reactant traverses between two nearest lattice positions in the solvent structure.

Since L may be around 3×10^{-8} cm and D is about 10^{-5} cm^2 s^{-1}, A values calculated from Eq. (31) are close to 5×10^2 cm s^{-1} and are about one order of magnitude lower than those obtained using Eq. (30).

The use of Eqs. (30) and (31) was criticized by Hupp and Weaver [131], because these equations imply that the activation occurs only by the transfer of translational energy. However, in the condensed phase the activation may occur through solvent polaron fluctuations and the transfer of oscillation energy of solvent molecules in the bulk to solvent molecules in the immediate vicinity of the reactant or even to electronic levels of the reactant [105, 132].

Such an energy transfer is taken into account in the encounter pre-equilibrium model [131, 133], which considers the outer-sphere electrode reaction to be a two-step process. In the first step the reactant diffuses to the reaction zone with a thickness δr at the electrode surface, where the probability of the charge transfer process between reactant and electrode is significant [133]. Here the electrode and reactant in the reaction zone are similar to a pair of reactants which exchange the electrons in a homogeneous reaction.

The effective pre-equilibrium constant K_p for the formation of the precursor state, expressed in nm or Å, describes the statistical probability of the formation of an electrode–reactant configuration appropriate for the electrode reaction [131, 134]:

$$K_p = \delta r \exp\left(-W_p/RT\right) \tag{32}$$

where W_p is the average free energy required to transport the reactant from the bulk solution to the reaction zone.

The rate-determining step, the second step of the process, involves activation within an encounter complex formed in a solvent cage.

For such a model, the electrochemical frequency factor A is [131]:

$$A = K_p \Gamma_n \nu_n \tag{33}$$

where Γ_n is a nuclear tunneling factor and ν_n is a nuclear frequency factor, which gives the effective nuclear barrier-crossing frequency from the precursor state. It is expressed as a weighted mean [135, 136] of characteristic frequencies of solvent reorganization ν_o, and inner-shell bond vibrations ν_i:

$$\nu_n^2 = (\nu_o^2 \Delta G_o^* + \nu_i^2 \Delta G_i^*)/(\Delta G_o^* + \Delta G_i^*) \tag{34}$$

where ΔG_o^* and ΔG_i^* are free energies of activation from the precursor state of the outer and inner shell, respectively.

For a typical metal–ligand bond ν_i is of the order of $10^{13}\,s^{-1}$, while ν_o in water is about $10^{11}\,s^{-1}$ [135, 137]. For some organic compounds ν_i may even be as high as $10^{14}\,s^{-1}$. Therefore for typical values of ΔG_i^* and ΔG_o^*, ν_n may be close to ν_i.

Γ_n in Eq. (33) takes into account the fact that the electron transfer can also occur for reactant molecules without fully overcoming the energy barrier. At normal temperatures for electrode reactions Γ_n approaches 1 [131]. Therefore Eq. (33) is often used without the Γ_n term. K_p in this equation was estimated to have a value of the order of 60 pm [138]. However, the quantitative estimation of K_p depends on the adiabaticity factor κ (see Eq. (24)), which varies with the reactant–electrode separation distance. It was suggested [139] that the electrode reactions should be more adiabatic than the corresponding homogeneous redox reactions. But as the reaction site, for outer-sphere systems, is probably separated from the electrode surface by a layer of solvent molecules [129], κ may drop below 1 since the reaction may become less adiabatic. These problems were more extensively discussed in [131].

In conclusion, returning to the frequency factor (Eq. (33)) and assuming that, at 25 °C, $K_p = 60$ pm, $\nu_n = 10^{13}\,s^{-1}$ and $\Gamma_n = 1$, one obtains $A = 6 \times 10^4\,cm\,s^{-1}$, approximately one order of magnitude higher than the value obtained using Eq. (30) with $M = 100$.

3.1.2 The Role of Solvent Dynamics

Though combination of Eqs. (33) and (34) gives more realistic values of the frequency factor, it shows that this parameter should not be very dependent on the solvent reorganization. This conclusion was challenged in recent years, when the role of the dynamics of solvent reorganization in charge-transfer reactions was taken into account in theoretical work [140–146] and also experimentally by Kapturkiewicz and Behr [147] and later by Weaver and coworkers [1, 3, 148] and Opallo and Kapturkiewicz [2, 149, 150].

In the theoretical studies it was shown that in the course of collective solvent motion along the reaction coordinate, the effective frequency of that process is significantly diminished. The reason is the so-called solvent friction which, by irreversible energy dissipation from the reactant solvent molecule to the other solvent molecules, decreases the rate of the passage over the energy barrier significantly in comparison with the rate expected in the frame work of the transition state theory.

Expecially when ΔG_i^* is very small, such overdamped solvent relaxation due to dielectric friction may contribute significantly to ν_n, so that in some cases

$$\nu_n \cong \nu_o \tag{35}$$

Based on theoretical works which take into account the dynamics of solvent molecules [140, 142, 144, 145], ν_o may be expressed [1] in the following way:

$$\nu_o = \tau_L^{-1} \left(\frac{\Delta G_o^*}{4\pi RT} \right)^{1/2} \tag{36}$$

where τ_L is the longitudinal relaxation time of solvent molecule which is related to the experimental Debye relaxation time τ_D by the formula [151]

$$\tau_L = \tau_D \varepsilon_\infty / \varepsilon_s \tag{37}$$

in which ε_∞ is the high-frequency dielectric permittivity of the solvent in the near-infrared region, which is two to five times higher for polar solvents than the optical dielectric permittivity [137]. Equation (36) is valid under the assumption [144] that the solvent relaxation dynamics are overdamped.

The effective time of such a relaxation is much higher than the rotation time of solvent dipoles. In the frame work of the transition state theory, when the inner-sphere reorganization can be neglected, ν_n is related to the rotation time of solvent molecules in the dielectric medium, τ_{rot}, by

$$\nu_n = (2\pi\tau_{rot})^{-1} \tag{38}$$

Most of the solvents usually used in electrochemical studies [152] are within the overdamped region; however, for those with τ_L below 0.5 ps, such as acetonitrile or acetone, the friction by surrounding molecules is small and ν_o will be determined partly by the individual solvent dipole rotational frequency approaching the solvent inertial limit.

Experimental τ_D values of different solvents are given in Table 1. The frequency of crossing the transition state for a given reaction may be controlled in solvents of short relaxation time by ν_i, but in solvents which have longer relaxation times Eq. (36) will be obeyed.

The barrier crossing frequency described by Eq. (36) is dependent not only on the barrier height, but also on its shape. Equation (36) was derived under the assumption that there is no donor–acceptor overlap and the barrier has a cusp-like shape.

In the presence of solvent friction ν_n should decrease monotonically as the barrier-top becomes more rounded [144].

One should add that solvent friction also influences the rate of reactions proceeding with significant inner-sphere changes, since it limits the rate of the formation of the solvent configurations characteristic of the top of the barrier, which in turn impedes the crossing of the barrier by inner-shell motion. In the model discussed above, the main contribution to the solvent polarization results from the reorientation of the solvent dipoles. However, another mechanism of relaxation of solvent polarization may also operate [153–157], consisting in a translation of the solvent molecules. Such a mechanism may be very important in solvents with slow reorientation. Zusman [158] presented a theory of electron-transfer reactions which takes into account this mode of relaxation. It was shown that when the solvent dynamics control the rate constant of the reaction, the solvent molecule self-diffusion contributes to the pre-exponential factor in addition to the reorientation. In solvents which exhibit a large self-diffusion coefficient and Debye relaxation time, this diffusion relaxation may be dominating.

By combining Eqs. (23), (33), and (36), one obtains

$$k_s = \kappa K_p \tau_L^{-1} \left(\frac{\Delta G_o^*}{4\pi RT} \right)^{1/2} \exp\left(\frac{-\Delta G^*}{RT} \right) \tag{39}$$

where ΔG^* is described by Eq. (26). The analysis of Eq. (39) reveals that, in contrast to the Marcus theory, the influence of solvent on the standard rate constant corrected for the double layer influence not only changes the energy of activation, but may also modify significantly the pre-exponential factor. However, based on work by Marcus and coworkers [159, 160], it may be shown [161] that when intramolecular contributions are appreciable in comparison with ΔG_o^* the rate constant may be described by the dependence

$$k_s = \kappa K_p \tau_L^{-a} \left(\frac{\Delta G_o^*}{4\pi RT} \right)^{1/2} \exp\left(-\frac{\Delta G^*}{RT} \right) \tag{40}$$

where a is within the limits $0 < a < 1$.

Equation (39) should be valid when $\Delta G_o^* \gg \Delta G_i^*$ and the reaction is strongly adiabatic. For the reverse situation, a approaches 0.

3.1.3 Methods of Analysis of Experimental Results

Several methods of analysis of kinetic results obtained for a given charge-transfer reaction have been proposed. These analyses were oriented toward the separation of the roles of solvent dynamics and energy of activation in the kinetics of such a reaction in order to learn more about their mechanisms.

This separation may not be possible if there is a dependence of τ_L on ΔG_o^*. Problems related to such analyses were considered critically by Weaver [162], who

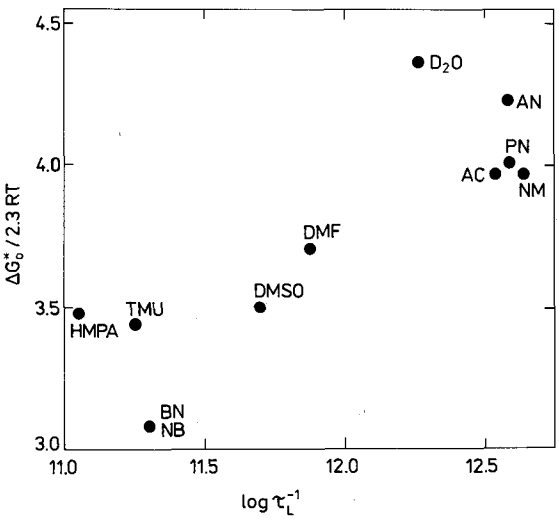

Fig. 4. Plot of $\Delta G_0^*/2.3\,RT$ (25 °C) for metallocene electron self-exchange measurements [162] analyzed by means of the dielectric-continuum formula versus log τ_L^{-1} for polar Debye solvents. PN, propionitrile; for definition of the other solvents, see Table 1.

has shown that for electron self-exchange of metallocenes in 11 Debye polar solvents there exists a rough increase of ΔG_0^* with an increase of log τ_L^{-1} (Fig. 4), probably related to the size of the solvent molecules. Therefore, for the Debye solvents in the case of the reaction studied, the separation of dynamic and energetic contributions is difficult, though it may be easier in the case of nonpolar solvents.

In equations used in the analysis there appear the Pekar factor, γ, and the second factor of the Marcus expression for the electrode kinetics, which we denote by g:

$$\gamma = (\varepsilon_{op}^{-1} - \varepsilon_s^{-1}) \tag{41}$$

$$g = \frac{Ne^2}{8RT}\left(\frac{1}{r} - \frac{1}{2d}\right) \tag{42}$$

From Eqs. (24), (33), (41) and (42), one arrives at the dependence [1, 2, 163]:

$$\ln k_s = \ln \kappa K_p \nu_n - g\gamma \tag{43}$$

assuming that ΔG_i^* may be neglected.

When one uses Eq. (43) the analysis may not be straightforward because, as shown above, τ_L^{-1} is dependent on γ in polar solvents; therefore when $\kappa\nu_n$ depends on τ_L^{-1} the plot of ln k_s against γ may increase with an increase of the Pekar factor, contrary to the prediction of Eq. (43). Such positive slopes of the ln k_s versus γ dependence point to the significant influence of solvent friction in the reaction dynamics [1, 157].

Another method of analysis was proposed by Weaver and coworkers [146, 159]. It is based on the rearranged Eq. (43),

$$(\kappa\nu_n)_{obs} = k_s\{K_p \exp[-(\Delta G_o^* + \Delta G_i^*)/RT]\}^{-1} \tag{44}$$

which relates the observed pre-exponential factor $(\kappa\nu_n)_{obs}$ to ΔG_o^* and ΔG_i^* terms.

The plot of $(\kappa\nu_n)_{obs}$, which may be calculated if the rate constant and the ΔG_o^* and ΔG_i^* terms are known, versus $\log \tau_L^{-1}$ may in some cases give information on the role of solvent dynamics of the reaction being studied. If these dynamics control the rate, the slope of such a dependence should be close to 1.

The equation

$$\ln(k_s\tau_L/\gamma^{1/2}) = \ln \kappa K_p (g/4\pi)^{1/2} - \frac{\Delta G_i^*}{RT} - g\gamma \tag{45}$$

has also been used [165–168]. It follows from Eq. (45) that the plot of $\ln(k_s\tau_L/\gamma^{1/2})$ against γ should be linear with a slope equal to g, assuming that other terms in this equation are not dependent on the solvent. This method may be useful in the analysis, but it may also lead to incorrect results [162] when the process is nonadiabatic or inner-shell controlled and also when non-Debye solvent dynamic effects play an important role.

Fawcett and Foss [161, 169] have proposed the use in the analysis of the dependence expressed in Eq. (46), which follows from Eq. (40):

$$\ln k_s = \ln Y - a \ln \tau_L - g\gamma \tag{46}$$

where Y collects terms which should be only slightly dependent on the solvent. On the basis of Eq. (46), in addition to the plot of $\ln k_s$ versus $\ln \tau_L$, when parameter a is known one may use the plot of $(\ln k_s + a \ln \tau_L)$ versus γ [170]. These equations were used by Fawcett and Foss [4, 166, 169, 170] for the analysis of published data. Although this multiparametric analysis may give deeper insight into the mechanism of charge-transfer electrode reactions, its results should be considered with care. One should remember that the mutual dependence of energetic and dynamic terms found for polar solvents [162] may lead to difficulties in such an analysis. Therefore, multiparametric analysis of solvent effects for weakly adiabatic processes is not advised by Weaver [162].

From this presentation, it follows that there may be difficulties with the unequivocal separation of the dynamic and energetic influences.

3.1.4 Influence of Solvents on Model Electron-Transfer Reactions

Two groups of reactants have been used preferentially in the study of the influence of solvents on the rate of electrode reactions for a correlation of the obtained data with the existing theories. One of these groups comprises metal ions in complexes and organometallic compounds where the first coordination sphere remains un-

changed in the course of the electrode reaction, while the other contains organic compounds which are either oxidized or reduced in a one-electron process.

In this brief review we present only results where these species were studied in several solvents in one laboratory. We believe that such data, usually obtained with the same method and sufficient precision, are more useful for an analysis of this kind than the collection of data obtained for a single compound in different laboratories.

Reactions of Metal Ion Complexes

In order to study the influence of solvents on model reactions, their mechanism should not be changed with the solvent. Therefore, electrode reactions involving the transfer of one electron are the best candidates.

Since in some cases the influence of solvents on the rate constant is not significant, the effect of the double layer on the constants to be determined can become relatively important. In order to diminish this influence and to decrease the ion-pair formation effects, complexes with low charge are preferred. The ideal situation offer couples like:

$$Ox^+ + e \Leftrightarrow Red \tag{47}$$

or

$$Ox + e \Leftrightarrow Red^- \tag{48}$$

Electroreduction and electrooxidation of salene (*N,N'*-bis(salicylidene)-ethylediamine) complexes of cobalt and copper studied by Kapturkiewicz and Behr [147] in eight aprotic solvents obey these conditions. These authors were the first to demonstrate experimentally the significant influence of the dielectric relaxation time of solvents on the electrode kinetics. They found earlier [171] that the mechanism of electrode reactions of salene complexes is independent of the solvents applied. No correlation with the prediction of the Marcus theory was found, but the kinetic data correlated well with the viscosity of the solvents and their dielectric relaxation time. However, because the ohmic drop was not well compensated, their rate constants are likely to be too low, as was shown in DMSO by Lasia and coworkers [172].

Good models for such studies are also metallocenes (M = Mn, Fe, Co) and $Cr(C_6H_6)_2^{+/o}$, which were studied by Weaver and Gennett [148] in seven solvents. The authors compared the experimental data with two sets of calculated results. In the calculations of the first set of data, ν_n was identified with the inner-shell vibration frequency ν_i and it was assumed that the reaction is adiabatic ($\kappa \cong 1$). In the second set the authors assumed that the frequency of surmounting the free energy barrier is controlled entirely by the dynamics of solvent reorganization. It was found that the second set of calculated data was much closer to the experimental results.

Weaver and coworkers [1, 3] have also studied the kinetics of the cyclooctatetraen-iron (0/−) and Coc^+/Coc system [3] in 12 solvents at mercury electrodes. They found that most solvents yield relative rate constants in agreement with the solvent relaxation model, but the rate constants for both these reactions in methanol,

ethanol, and 1-propanol were about 50 times larger than the expected values on the basis of this model.

Similar anomalous kinetic behavior in alcohols was observed for other systems as well [148, 173]. Weaver and coworkers [3] discussed this behavior, considering the influence of high-frequency dielectric relaxation associated with rotation of solvent monomers and with translational motion of solvent dipoles.

Fawcett and Foss [169, 170] analyzed these systems using Eq. (46) and estimated coefficient *a*. For the Coc^+/Coc system they found this coefficient to be approximately equal to 0.7. An even higher value was reported for cyclooctatetraene-iron.

Khan [174] studied the electrooxidation of ferrocene at a Pt electrode in polar solvents ranging from methanol to heptan-1-ol. Experimental data concorded well with the calculated results when solvent influence on the pre-exponential coefficient was considered. In calculations $\nu_n = \tau_D^{-1}$ was used. Khan [174] points out that ν_n expressed by Eq. (36) exhibits a temperature dependence different from that predicted by the classical expression $\nu_n = k_B T/h$. Another conclusion which may follow from the same paper is that the transmission coefficient for the electrochemical outer-sphere electron-transfer reactions in polar alcoholic solvents may not be equal to unity.

A linear dependence of $\log k_s$ on $\log \tau_L^{-1}$ was found [175] in the case of a one-electron reduction of cobalt(III) complexes with acetylacetone (AcAc) in several aprotic solvents, but the behavior in protolytic solvents was different.

Mu and Schulz [176] have shown that chloro(tetraphenylporphinato)manganese(III) complex, in one electron reduction in six aprotic solvents exhibits a dynamic solvent effect, though its inner reorganization energy is larger than the outer one. The plot of $\left[\log k_s + \frac{\Delta G_0^*}{2.3\,RT}\right]$ versus $\log \tau^{-1}$ exhibited a slope equal to 1.03.

Fawcett and Opallo [177] have studied the kinetics of electroreduction of Mn(III) and Fe(III) complexes with acetylacetone, $Mn(AcAc)_3^{0/-}$ and $Fe(AcAc)_3^{0/-}$ in seven aprotic solvents.

The analysis of rate constants not corrected for the double-layer influence in terms of Eq. (46) gave for the parameter *a* the values of 0.6 and 1.0 for $Mn(AcAc)_3^{0/-}$ and $Fe(AcAc)_3^{0/-}$, respectively (Fig. 5).

Weaver and coworkers [163] have reported the rate constants for electrochemical reaction in the $Ru(hfac)_3^{0/-}$ system (hfac = hexafluoroacetylacetonate) in six solvents at a gold electrode and compared these data with the self-exchange rate constant and earlier data for metallocene and related organometallic redox systems. The rate constants obtained were relatively small and insensitive to solvent dynamics, correlating instead with the expected solvent-dependent energetics. Nielson and Weaver [164] have also studied the electrode behaviour of $Co(dmg)_3(BF)_2^{+/0}$ and $Co(dmg)_3(BC_4H_9)_2^{+/0}$ complexes (dmg = double deprotonated dimethylgloxime) at gold and mercury electrodes. The solvents were chosen in such a way as to provide large variations in the frequency of barrier passage from overdamped solvent relaxation.

It was found that in the overall energy of reorganization, there is a significant contribution from the inner-shell component, roughly comparable with the outer-shell reorganization.

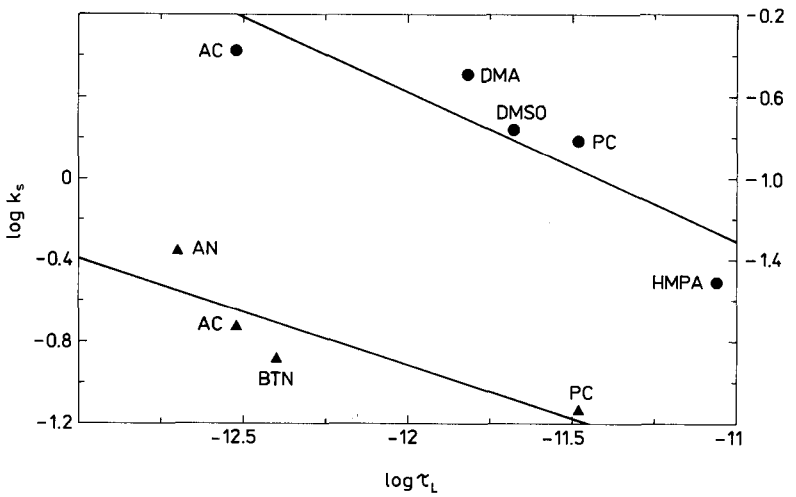

Fig. 5. Plot of the logarithm of the standard rate constant for electroreduction of $Mn(AcAc)_3$ (▲) and $Fe(AcAc)_3$ (●) in a given solvent against the logarithm of the longitudinal relaxation time of the solvent [177]. The left-hand ordinate scale applies of the Mn system and the right-hand scale of the Fe system. BTN, butyronitrile; for definition of the other solvents see Table 1.

Another group of reactions have been investigated which should be presented in this section. These are systems of the form $ML_n^{3+/2+}$ (where L stands for neutral ligand). Their electrode behavior can also be interpreted in terms of the theories presented above. The main difference between these and the above-listed reactants is that the latter complexes have a higher charge (3+ and 2+) than the previous ones, and in consequence the influence of the double layer on their kinetics may be large. Even corrected kinetic data may not be precise enough for comparison with theory. Therefore, in recent years reactions of the types (47) and (48) were preferentially studied.

Nonetheless, $ML_n^{3+/2+}$ systems should also be studied, because their interaction not only with the double layer but also with the reaction medium is stronger, and such studies may supply further information about the role of the inner- and outer-sphere reactant in the electrode kinetics.

From earlier investigations, one should mention the work of Sahami and Weaver [113] on the electroreduction of $CoEn_3^{3+}$ (En = ethylenediamine), $Co(NH_3)_6^{3+}$ and $Co(NH_3)_5F^{2+}$. They found that solvent effects do not agree with predictions of the Marcus theory. The discrepancies between theory and experiment (experimentally observed changes were higher than those theoretically predicted) were ascribed to contributions to the energy of activation from extensive reorientation of solvent molecules.

The $Ru(NH_3)_6^{3+/2+}$ system was also studied [106]. Again, considerable changes of experimental rate constants corrected for double-layer effects were observed in several solvents, which contrasted with small changes expected from the dielectric continuum treatment. Elzanowska et al. [88] studied the electrode reaction of

solvated europium(III) and europium (II) ions. In this case the change of solvent significantly affects the inner-sphere composition also. Therefore the explanation of the experimental results, even corrected for the double layer, is more complex.

Bard and coworkers [178] studied the electrode reactions of $Fe(CN)_6^{3-/4-}$ and Foc^+/Foc systems in water and DMSO, respectively. They found that the rate of charge transfer in these systems decreases with an increase in the viscosity of the medium, which was changed by addition of sugar.

The Debye relaxation time is dependent on viscosity,

$$\tau_D = 4\pi\eta r_s^3/RT \tag{49}$$

and τ_D is related to τ_L by Eq. (37), where r_s is the radius of the spherical particle. The finding of Bard and associates points also to the influence of solvent dynamics on the electrode kinetics.

Reactions of Organic Compounds

Cathodic or anodic reactions of the type described by Eqs. (47) and (48) will be discussed.

Opallo and Kapturkiewicz [149] studied the one-electron oxidation of phenothiazine to the radical cation. They explained the experimental kinetic data in terms of dynamic properties of the solvents. A linear relationship between k_s and τ_L^{-1} of the solvents has been found in aprotic and also in hydrogen-bonded solvents, as the two sets of data shown in Fig. 6 demonstrate. The rate constant in hydrogen-bonded alcohols used as solvents was above one order of magnitude higher, as seen in Fig. 6.

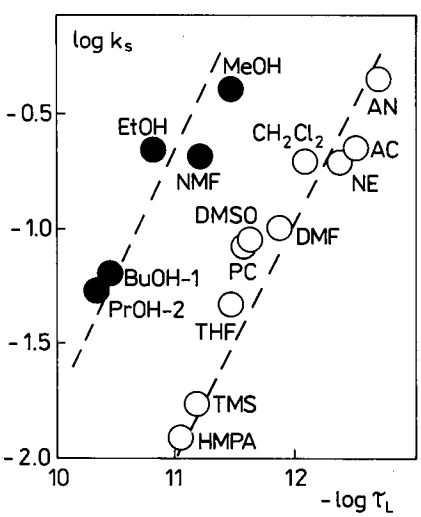

Fig. 6. Dependence of the logarithm of the standard rate constant of phenothiazine oxidation on a Pt electrode on the logarithm of the solvent's longitudinal relaxation time. NE, nitroethane; TMS, sulfolane. For other abbreviations see Table 1.

The electrooxidation of 1,4-diaminobenzene [2] exhibits the linear dependence of k_s on τ_L^{-1}. In this case also, the reaction in alcohols was faster than in solvents without hydrogen bonding. The one-electron electroreduction of 2,4,6-trimethylnitrobenzene to the corresponding radical anion was studied in five organic solvents [150]: k_s was found to depend on the cation of the supporting electrolyte and on the solvent. It was shown that the rate constants corrected both for the double-layer effects and ion-pair formation exhibit the dependence on τ_L^{-1} predicted by Eq. (39).

Fawcett and Jaworski [118] have studied the electroreduction of *p*-dicyanobenzene and anthracene in five nonaqueous solvents using 0.1 M tetrabutylammonium perchlorate as background electrolyte. The authors tried to explain the rate constants corrected for the double-layer influence in terms of the Marcus theory, since in 1983 the importance of solvent dynamics on the rate of charge transfer was not clearly understood. No correlation was found between $\log k_s$ and the γ parameter, pointing to a more complex behavior of these systems.

Russell and Jaenicke [115] investigated the electroreduction of *p*-benzoquinone to the radical, in several solvents. They tried to explain their kinetic results, after correction for the double-layer influence, by the Marcus theory. Only in some of the applied solvents was an agreement with that theory observed. Earlier, Sharp [179] had studied several quinonoidic compounds at Pt and Au electrodes. Measurements were carried out in AN, DMF, DMSO and PC. Discrepancies between experimental data and the Marcus and Levich-Dogonadze theory were discussed qualitatively in terms of reactant and solvent structures.

Phelps et al. [180] have studied the influence of seven solvents on the rate constants for three sesquibicyclic hydrazine-radical cation redox systems. The authors have found that the electrode kinetics of these systems depends on the overdamped solvent dynamics, though the activation barrier due to reactant vibrational rearrangements is substantial.

Fernandez and Zon [181], when studying the heterogeneous electron exchange between *N,N,N′,N′*-tetramethyl-*p*-phenylendiamine and its mono-cation radical in 12 aprotic and hydrogen-bonded solvents, using a platinum electrode, have found that Eq. (40) is approximately fulfilled with $a = 0.53$.

One should also mention the work on electroreduction of *t*-nitrobutane in AN, DMF, DMSO and pyridine by Corrigan and Evans [182]. The results obtained were not in agreement with the dielectric continuum theory. They explained their results by ion-pairing between the anion radical product and cations of the background electrolyte.

Finally we cite the work of Grzeszczuk and Smith [117, 183] on the influence of solvents on the rate of electroreduction of several diphenyls in a limited number of solvents. In this case, disagreement of the kinetic data with the Marcus theory, but concordance with the dynamic model of the solvents, were observed.

Some of the data presented above on the influence of the solvent on the electrode kinetic behavior or organic compounds were analyzed by Fawcett and Foss [4, 169, 170]. Although the results of these analyses were criticized [162], they may be useful since, in some cases, they give a systematic view on the problem.

Table 6 gives the value of the coefficient *a* from Eq. (40) which was obtained [169, 170] from such an analysis for several organic compounds. Other types of analysis

Table 6. Analysis of kinetic data using Eq. (40) [169, 170].

System	Longitudinal relaxation time coefficient, a	No. of solvents	Regression coefficient
1. Phenothiazine (0/+) [149]	0.7 ± 0.1	7	0.972
2. 1,4-Diaminobenzene (0/+) [2]	0.6 ± 0.1	7	0.965
3. *t*-Nitrobutane (0/−) [182]	0.3 ± 0.3	4	0.853
4. 2,4,6-Trimethylnitrobenzene (0/−) [150]	0.3 ± 0.1	5	0.992
5. Tetrathiafulvalene (0/+)	1.0 ± 0.5	7	0.924

of experimental data were also reported. A very good linear dependence between $\log k_s$ and the acceptor number of solvents for *p*-dicyanobenzene was found [118]. The rate was found to be slower in solvents of higher acceptor numbers. Weaver and coworkers [184], in their studies of solvent effects on intervalence electron-transfer energies for biferrocene cations, analyzed deviations of the observed optical energy transfer energies from the corresponding dielectric continuum predictions on solvent acceptor numbers. Electron transfer kinetics were found to be dependent [185] on the so-called „solvatochromic" shift, which is a measure of the polarizability of solvents. Earlier, this shift was related to thermodynamic and other kinetic properties [93].

Jaworski et al. [186] found that the reaction constants from the Hammett equation, in the case of the irreversible electroreduction of substituted chloro- and bromo-benzenes in a number of organic solvents, are linearly dependent on the logarithms of the solvent longitudinal relaxation times.

3.1.5 Possible Reasons for Discrepancies Between Experimental and Theoretical Results

Research upon the influence of solvents on simple electron-transfer electrode reactions, carried out in recent years, has been oriented toward the elucidation of their mechanism and agreement with predictions of the charge-transfer theories. Before going into a more detailed discussion, one should mention that not all published results may be very precise. The rates of many of the reactions examined were high or very high, since both inner- and outer-sphere reorganization energies were small. Frequently in their kinetic studies the authors used cyclic voltammetry, which for such fast reactions may not supply exact data in solutions which do not have high conductivity when the electrodes are not very small. Total compensation of the solution resistance, even applying modern potentiostats, was not possible, especially at high scan rates. The application of ultramicroelectrodes by decreasing the total current makes the ohmic drop, and in consequence the distortion of the voltammograms, smaller. Wightman and coworkers [187], who used ultramicroelectrodes when studying several systems, including ferrocene in acetonitrile, demonstrated that some earlier kinetic results with larger electrodes gave rate constants that were too low.

Baranski et al. [188] also applied ultramicroelectrodes in the study of the kinetics of oxidation of ferrocene in nine aprotic solvents and in three alcohols as a function of temperature. The data obtained in acetonitrile were concordant with those given by Wightman and coworkers [187].

The comparative and careful study of Lasia and coworkers [172] on electroreduction of *N,N'*-bis(salicylidene)-ethylenediaminocobalt(II) (Co(salen)), with the use of ultramicroelectrodes has also shown that earlier kinetic results on Co(salen) in DMSO [147, 171] are too low.

Systematic errors could furthermore change the results in such a way that they could simulate an influence of solvent dynamics [162]. But even assuming that all kinetic data are precise, there are other factors which may affect either experimental or theoretical results in an insufficiently described way and may thus cause discrepancies between experiment and theory.

Double-Layer Influence on the Rate Constant

In order to draw a good comparison between experimental and theoretical results, it is necessary that the kinetic data should not be influenced by the double layer. Therefore, the experimental data should be corrected for the double-layer influence. This was not always done in the literature. But even when such correction was carried out, it was sometimes done with insufficient precision. Particularly in the case when solid electrodes are used, it often happens that not only the adsorption of ions used as background electrolytes in various solvents but even the zero-charge potentials of such electrodes are not known with sufficient accuracy. Therefore, as we indicated earlier, the reactions of neutral or low-charge reactants have been preferred in recent experimental studies, since then, as follows from the simple relation for the double-layer correction:

$$k_s^{ap} = k_s \exp\left[\frac{(\alpha n - z)F\varphi_2}{RT}\right] \tag{50}$$

the influence of the double-layer structure on the rate constant, expressed by the potential of the outer Helmholtz plane φ_2, should be low. In Eq. (50) k_s is the corrected (true) and k_s^{ap} the experimental rate constant, αn is the Tafel slope coefficient and z the reactant charge number. One should remember, however, that the potential at the reaction site is not necessarily equal [189] to the φ_2 potential.

Although Eq. (50) works well in aqueous solutions (see for instance [190]) as shown by the dependence of k_s^{ap} on the φ_2 potential calculated from the concentration of the background electrolyte, in nonaqueous solvents such a dependence has not always been observed. For instance, in the study of the electrooxidation of phenothiazine [149] and the cathodic reduction of Coc^+ [3] no influence of the concentration of background electrolyte on k_s^{ap} was found.

Also, Ahlberg and Parker [191], when studying the electroreduction of benzonitrile in DMF in the presence of tetraalkylammonium salts as background elec-

trolytes, found that the k_s^{ap} is only slightly dependent on the nature and concentration of the background electrolyte. They found that the simple Frumkin correction given by Eq. (50) works for processes which occur at potentials close to zero charge.

Gennett and Weaver [192] have found, when studying double-layer effects on electrochemical kinetics in nonaqueous media, that the rate constants of metallocenes $M(Cp)_2^{+/0}$, where M = Fe, Mn and Co, were virtually independent of the double-layer structure. However, the structurally similar anionic couple $Co(Cp)_2^{0/-}$ and some other metallocenes have exhibited the expected sensitivity upon changes of the double layer. These differences in behavior of cationic and anionic metallocenes were explained in terms of charge distribution between the cyclopentadienyl (Cp) ring and the metal.

Mayrhofer et al. [193] studied the electrode reaction of the BCr(I)/BCR system in two organic solvents; they found that the dependence of $\ln k_s^{ap}$ on φ_2 plotted according to Eq. (50) yields strange values of the slope.

All these findings may point to limitations of the classical Frumkin model for correction of the double-layer influence on electrode kinetics in nonaqueous solvents, although it works well in aqueous solution. In the present author's opinion these rather surprising results may follow from some kind of compensation effects. For instance, ion-pair formation in these solutions by decreasing the effective charge of the reactant could reduce the double-layer effect.

In addition to this influence, the change of τ_L with the background salt concentration and ε_s may slightly change ΔG_o^*. The influence of the double layer on the τ_L and ε_s parameters should also be considered.

As is well known, the change in k_s by the double-layer effect is large at potentials which are either quite negative or very positive in respect to the zero-charge potential, since then the value of the $|\varphi_2|$ potential is high. However, the influence of the double layer at zero charge potential may also be significant, since the variation of the φ_2 potential with the electrode potential is greatest there.

The usual procedure, i.e., to diminish the φ_2 potential by increasing the background electrolyte concentration, does not always work well in nonaqueous solvents, because in some solvents the typical salts used as background electrolytes have a limited solubility.

Table 7. Potential of zero charge of the Hg/solution interface in several solvents and φ_2 potential at an electrode charge density of $-10\,\mu C\,cm^{-2}$ and electrolyte concentration of 0.10 M [4].

Solvent	Static dielectric permittivity, ε_s	Outer Helmholtz plane potential, φ_2 (V)	Potential of the zero charge vs. potential of the Foc^+/Foc electrode (V)
Acetone	20.7	−0.121	−0.670
Acetonitrile	37.5	−0.106	−0.622
Dimethyl sulfoxide	46.7	−0.101	−0.717
Formamide	110	−0.080	−0.729
Propylene carbonate	64.9	−0.093	−0.601

Also, when increasing the salt concentration one should be certain that the ions of the background electrolyte are not specifically adsorbed. Table 7 gives as an illustration, following Fawcett [4], the double-layer parameters in several solvents. Different φ_2 potentials and potentials of zero charge as shown in Table 7 may change very significantly the experimental rate constant k_s^{ap} for a particular electrode reaction in different solvents.

Time of Dielectric Relaxation

In the calculation of the rate constants for comparison with experimental results one uses, in addition to other parameters, the longitudinal relaxation time τ_L (see Eqs. (39) and (40)). This parameter, discussed by Friedman [194], is related to the Debye relaxation time by Eq. (37).

In this equation ε_∞ is the dielectric permittivity measured at infrared or microwave frequencies, which is up to five times higher than ε_{op}. This dielectric permittivity has a very significant influence on the final values of τ_L (see Eq. (37)).

Because of measurements of dielectric relaxation made at frequencies that were too low, and a long extrapolation to high frequencies, this parameter is frequently not determined precisely, and in the literature there are discrepancies between data reported for a given solvent. For instance, for DMF one may find the following ε_∞ values: 2.51 [195], 3 [196], 4.5 [197] and 5.0 [198]; ε_{op} for DMF is 2.040. For other solvents also, the reported data of ε_∞ vary considerably.

Some differences, though usually small, are observed in the τ_D data for a given solvent. Another problem is the dependence of the parameters used in the calculation of τ_L on salt concentration. Such a dependence is observed not only for ε_s but also for τ_D, while ε_∞ is rather insensitive to salt concentration (see, for instance, [198]).

In the correlations the data reported for pure solvents were used. Solvents of low dielectric permittivity which contain salt may exhibit multiple relaxations due to ion-pair formation [199]. The above information relates to aprotic solvents which do not form hydrogen bonds and have one relaxation time.

The situation is more complex in the case of the so-called non-Debye liquids – the protic solvents. Due to their internal structure, these liquids exhibit a complicated dielectric relaxation behavior. This group of solvents comprises alcohols, formamide, propylene carbonate, and some other liquids. One should remember that in the $\ln k_s$ vs. $\ln \tau_L$ analysis (Sec. 3.1.3), the rate constants measured in these solvents deviated from the values measured in aprotic solvents.

For the aliphatic alcohols methanol, ethanol, and propanol, three relaxation times were observed. Then there is the question of which relaxation process most determines ν_0 (see. Eq. (36)). In the analysis of the rate constant dependence on the longitudinal relaxation time, the longest time, τ_1, corresponding to hydrogen bond rupture in clusters caused by hydrogen bond formation was used earlier.

The problem of a proper calculation of the barrier-crossing frequency, in such cases, was described by Hynes [200]; τ_1 may be used in ν_0 calculations of a strongly adiabatic reactions. For weakly adiabatic reactions, the effective longitudinal relax-

ation time for a solvent with two relaxations is a function of frequency and is determined by a high-frequency value $\tau_{L\infty}$,

$$\tau_{L\infty} = \frac{\varepsilon_\infty}{\varepsilon_s}\left(\frac{f_1}{\tau_1} + \frac{f_2}{\tau_2}\right)^{-1} \tag{51}$$

where τ_2 corresponds to the diffusional rotation of the monomers and f_1 and f_2 are the fractional amplitudes related to the corresponding relaxations.

McManis and Weaver [201] considered the consequences of non-Debye solvent relaxation upon the barrier-crossing dynamics of adiabatic electron-transfer processes using a formulation due to Hynes [200].

The use of $\tau_{L\infty}$ calculated from τ_1 according to Eq. (37), instead of τ_L, in the correlation of $\ln k_s$ with the time of relaxation led to a single linear dependence valid for Debye and non-Debye solvents. Such behavior is illustrated by the plot prepared [169, 170] for the Coc_0^+/Coc system in 12 solvents, including methanol, ethanol, propanol, and propylene carbonate, which also exhibits a non-Debye behavior [202]. This plot is shown in Fig. 7.

An extended discussion of the behavior of redox system in non-Debye solvents has been given recently [169]. These problems were further discussed by Baranski et al. [188] in their work on the oxidation of ferrocene at a Pt microelectrode in several alcohols in the temperature range 190–295 K. One should remember that the structure of such non-Debye solvents, which is related to the large-amplitude τ_1 relaxations, may be changed considerably [3] under the influence of ions, and also at the charged electrode surface.

The role of dipole-dipole interactions in relaxation processes in polar solvents has been discussed by Fawcett [203].

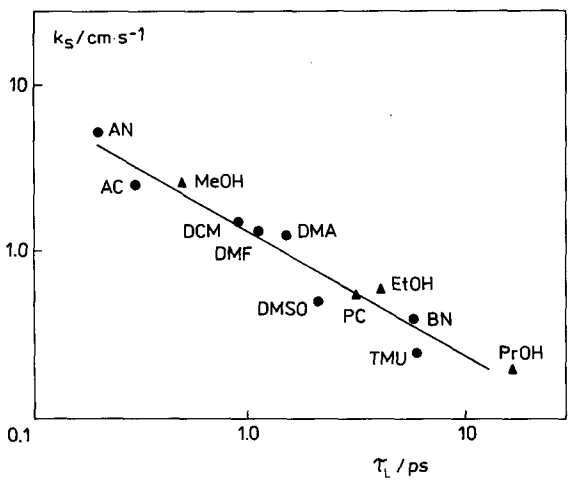

Fig. 7. Plot of the logarithm of the standard rate constant for the electroreduction of Coc^+ at an Hg electrode versus the logarithm of the solvent's longitudinal relaxation time [169, 170].

Also, when considering the systems in non-Debye solvents, the γ parameter (Eq. (41)) should be changed [169] to

$$\gamma' = \left(\frac{1}{\varepsilon_{op}} - \frac{1}{\varepsilon_{mw}}\right) \tag{52}$$

where ε_{mv} is the limiting dielectric permittivity defining the end of the first relaxation process. The use of the γ' parameter in correlations based on Eq. (46) improves the linearity of $(\ln k_s + a \ln \tau_L)$ versus γ dependences [169].

Such behavior may be due to solvation of the reactant by monomers in non-Debye solvents and to the lower local dielectric permittivity with respect to the bulk value.

This short discussion shows that in the case of the non-Debye solvents further work is necessary on both the electrode kinetics and the dielectric relaxation behavior of the solvents in the presence of various electrolytes. There are also significant discrepancies between the results on the relaxation dynamics of these solvents reported by various authors (see [169]).

Influence of Solvents on the Parameters κ and K_p

K_p is given by Eq. (32), where δr is the reaction zone thickness beyond the plane of closest approach, in which the reactant must be present in order to participate effectively in the electrode reaction. K_p is expected to be dependent to some extent on solvent dynamics.

The κ parameter, the electronic transmission coefficient, is related to the extent of overlap between the donor and acceptor orbitals. When this overlap is very small, electron tunneling frequency determines the pre-exponential factor, the reaction is nonadiabatic and $\kappa \ll 1$. Such overlap may be diminished if the electrode-reactant distance, in the course of the charge transfer, is increased due, for instance, to the presence of a blocking film on the electrode. On the other hand, when the overlap is relatively large, κ is close to 1. Only when the reactant is near the electrode surface does significant overlap of donor and acceptor orbitals occur.

This close distance determines also the δr value. Therefore, the product $\kappa^o \delta r$ may be considered as an effective reaction zone thickness [139], where κ^o is the electronic transmission coefficient at a distance of closest approach of the reactant to the electrode surface. For adiabatic reactions the value of κ^o should approach 1.

For nonadiabatic reactions, when one moves from the plane of closest approach away from the electrode, it is assumed [204] that the transmission coefficient decreases according to the equation

$$\kappa(r) = \kappa^o \exp\left[-b(r - r_o)\right] \tag{53}$$

where r_o is the distance between the electrode and the site of closest approach, and b is a constant estimated [205] to be in the range of $1-2\ \text{Å}^{-1}$.

Using Eq. (53) it can be seen that $\kappa(r)$ decreases to κ^{o}/e for $(r - r_o) = \delta r = b^{-1}$. Therefore, the effective value of the reaction zone thickness will be equal to b^{-1}. Assuming for b an approximate value of 1.6 $Å^{-1}$ one obtains $\delta r = 0.6$ Å [1, 139]. This result is to some extent arbitrary.

When the distance of the reactant from the surface increases beyond r_o, the electronic coupling will decrease, leading consequently to nonadiabaticity. For such nonadiabatic reactions, with a small overlap of orbitals, the net pre-exponential factor $\kappa\nu$ should not be influenced by solvent dynamics [206, 207], because κ is inversely proportional to ν_n.

Since κ depends on the distance of the reaction site from the electrode, for outer-sphere electrode reactions where the reactant is separated from the electrode by a layer of solvent molecules [128], the adiabaticity of such reactions may also be dependent on the nature of the solvent.

Fawcett and Foss [161, 166], using experimental kinetic data for nonaqueous solvents, have tried to determine the parameter κK_p for several heterogeneous outer-sphere reactions from the corresponding plot; however, this was done under the assumption that κ is constant. They found the values of this parameter to be much lower than the 0.6 Å expected [139] for adiabatic reactions as shown above, which was criticized by Phelps et al. [128].

Such data, especially when obtained from the analysis of rate constants that have not been corrected for the double-layer influence, should be considered with care. The validity of such determinations is limited by the fact that several parameters in the applied equation (for instance, Eq. (39)) may be influenced by the nature of the solvents.

One should add here that since parameter a may change with solvent, the analysis based on Eq. (46) may give an averaged value of that parameter. The problem of adiabatic and nonadiabatic charge-transfer reactions calls for further study.

Estimation of ΔG_o^*

The separation of the dynamic and energetic effects on the rate of simple electrode reactions may be easier if the activation energy of such reactions could be calculated precisely.

However, even assuming that for some reactions the inner part (ΔG_i^*) is very small, the calculation of the outer part of the energy of activation (ΔG_o^*) is still not very precise.

In Sec. 3.1.1 we have discussed the improvements on the original expression for ΔG_o^* made by Marcus, which give more realistic values. This kind of description in the case of spherical reactants is carried out in the framework of the MSA approach and also assuming a nonspherical shape for the reactants. The theory of such charge-transfer reactions has been reviewed [208, 209].

Is appears that the description of ΔG_o^* is still not satisfactory. Further work should simulate the shape of natural reactants with proper localization of the charge. It seems that ion-pair formation may also affect the ΔG_o^* values. Since the stability constant of an ion-pair reaction for a given reactant should depend on the static

dielectric permittivity of the solvents used, the ion-pairing process may influence the rate constant by changing the Pekar factor or the longitudinal relaxation time of the solvents.

3.2 Electrode Kinetics of Ion-Transfer (Deposition-Type) Reactions

In Sec. 3.1 we discussed the effect of solvents on simple electrode reactions in which the reactant preserves its first coordination sphere in the course of the electrode process. Now we are going to consider the influence of solvents on reactions which proceed with total breaking of bonds between the central metal ion and the ligands.

Assuming that such a process is represented by the cathodic reaction of a solvate ion MS_p^{n+}:

$$MS_p^{n+} + ne \rightarrow M + pS \tag{54}$$

one can see the complexity of the process, where p solvent molecules are released from the primary solvation sphere. In addition to that process, other solvent molecules in the second and further solvation spheres may also influence the rate of such reactions.

It is not possible in this case, as it was for the charge-transfer reactions, to find a proper model for these reactions.

Since there exists no general theory of such reactions, only the changes of the rate constant can be correlated either with the solvent parameters or with thermodynamic parameters of the solvation of the reactants.

In the case of some ion-transfer reactions the chemical desolvation step controls the rate of the overall process and the currents observed are lower than those expected for the process limited solely by the mass transport rate. The formation of such less-hydrated species was attributed [210] in the case of the electroreduction of nickel(II) in water to a slow exchange of water molecules from the first solvation sphere of Ni(II) under the influence of the crystal field stabilization. A similar mechanism was found for Ni(II) and Co(II) in methanol [211].

The dependence of the rate constant logarithm on the free energy of solvation was reported by Parker and coworkers [212] for lithium and by Baranski and Fawcett [213] for the $Na^+/Na(Hg)$ system in several solvents.

In our earlier work [85] the literature data were analyzed under the assumption that the influence of solvents on the standard rate constant of the electrode reaction may be expressed by the Brönsted-type relation

$$\Delta G^{\neq} = \Delta G_{\infty}^{\neq} + \alpha_B(\Delta G^{\circ} - \Delta G_0^{\circ}) \tag{55}$$

where $\Delta G_{\infty}^{\neq}$ and ΔG_0° stand for the free energy of activation and free energy of reaction, respectively, in the reference solvent, $\Delta G^{\neq}$ and ΔG° determine the same parameters of the reaction studied in another solvent and α_B is the Brömsted coefficient.

The difference $(\Delta G^{\circ} - \Delta G_{o}^{\circ})$ in Eq. (55) may be expressed by the difference of formal potentials measured versus an electrode with a solvent-independent potential. Then one obtains

$$\Delta G^{\neq} = \Delta G_{\infty}^{\neq} - \alpha_B nF(E_f^{of} - E_o^{of}) \tag{56}$$

or

$$\Delta G^{\neq} = \Delta G_{\infty}^{\neq} - \alpha_B \Delta G_{tr} \tag{56a}$$

In this approach the cation is considered as a reaction center, with the solvent molecules in the first coordination sphere as substituents. Combination of Eq. (24) with Eq. (56) suggests a linear dependence between the logarithm of the standard rate constant of a given system and its formal potential.

Such a dependence is given for several $M^{n+}/M(Hg)$ in Fig. 8 [85]. In the literature there are a limited number of data useful for such an analysis.

A more extensive analysis was carried out using the dependence of $\Delta G^{\neq}(\log k_s)$ on the free energy of transfer of a cationic reactant from the reference solvent to other solvents using Eq. (56a) and results obtained in an identical or similar background electrolyte: these data are given in Table 8.

A negative sign before α_B in Eqs. (56) and (56a) means that an increase in the energy of activation was observed when moving from a solvent of lower Lewis basicity to more basic solvents. This is a quite logical result, which demonstrates that ions more strongly solvated in basic solvents exhibit slower rates in electrode reactions and that the activated complex should be less strongly solvated. All the systems analyzed, and probably all those that have been studied, show such a dependence, though the coefficient α_B varies widely, from -0.57 for potassium to practically 0

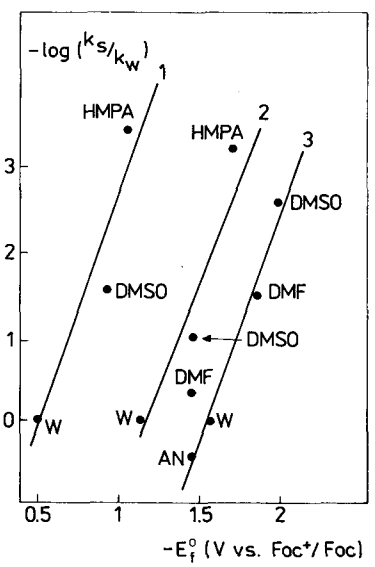

Fig. 8. Dependence of the logarithm of the standard rate constant in mixed solvents related to the rate in aqueous solution (w) on the formal potential for the following systems: (1) Pb(II)/Pb(Hg); (2) Zn(II)/Zn(Hg); and (3) Mn(II)/Mn(Hg).

Table 8. Results of analysis of ion-transfer electrode reactions at mercury electrodes.

Cation	Equation (56a)					Equations (57) and (58)						
	α_B	$\Delta G^{\ddagger}_{\infty}$	r	n	Ref.	*Sc*	r	n	*Sa*	r	n	Ref.
Li^+	0.44	+38.0	0.97	5	214, 215	1.1	0.99	5				214, 216
Na^+	0.14	+24.6	0.98	5	214	0.75	1.0	4				213, 214
K^+	0.57	+21.8	0.80	3	214	0.6		2				214
Ca^{2+}						0.77	1.0	3	−0.05		3	217, 218
Sr^{2+}						0.8		2	0		2	218
Ba^{2+}	0.12	+42.9	0.992	3	215, 218	0.86	0.99	4	−0.01		3	215, 218, 219
Zn^{2+}	0.10		0.89	8	221, 222, 224, 232	0.38	0.99	8				216, 220 – 224
Pb^{2+}	0.16	+17.9	0.95	3	215, 225	0.6		2				225
Cd^{2+}	0.006	+24.4	0.66	3	221, 227, 234	0.48	0.92	4				221, 226, 227
Mn^{2+}	0.16		0.994	4	228 – 230	0.99	1.0	3	0.05	0.93	4	228 – 230
Eu^{2+}						0.9		2	0.1		2	231
Ni^{2+}	0.13		0.98	4	233							

r is the correlation coefficient and n is the number of solvents considered in analysis.

for cadmium, with a very poor correlation coefficient in the latter case. However, the cadmium reaction does not violate this rule, and $\alpha_B \cong 0$ points to a complicated mechanisms for the electrode reaction, as was already observed for this system by Randles [234] in aqueous media.

There is practically no correlation between α_B and the nature of the cations studied, which is illustrated by a deep minimum of the α_B value for Na^+ when moving from Li^+ to K^+.

The literature cited in Table 8 refers to kinetic data, but not to free energies of transfer.

Since the values of ΔG_{tr} obtained in various solvents for the ions under consideration sometimes differ, one can also obtain slightly different α_B values. We also tried [235] to analyze the kinetic data related to anodic and to cathodic processes separately, by considering the changes of the cathodic rate constant (k_{fh}) or anodic rate constant (k_{bh}) at constant potential on a solvent-independent scale. Such an analysis is based of the following equations for cathodic (Eq. (57)) and anodic (Eq. (58)) reactions:

$$RT(\ln k_{fh}^{s} - \ln k_{fh}^{w}) = (\bar{\alpha} + \alpha)\,\Delta G_{tr} = \mathrm{Sc}\,\Delta G_{tr} \tag{57}$$

$$RT(\ln k_{bh}^{s} - \ln k_{bh}^{w}) = (\bar{\alpha} - \beta)\,\Delta G_{tr} = \mathrm{Sa}\,\Delta G_{tr} \tag{58}$$

where superscripts s and w relate to organic solvent and water, respectively, while α and β denote cathodic and anodic transfer coefficients, respectively, and $\bar{\alpha}$ is defined by the following equation,

$$RT(\ln k_{s}^{s} - \ln k_{s}^{w}) = \bar{\alpha}\,\Delta G_{tr} \tag{59}$$

$\mathrm{Sc} = \bar{\alpha} + \alpha$ and $\mathrm{Sa} = \bar{\alpha} - \beta$.

The rate constants k_{fh} and k_{bh} at some selected potentials were calculated from literature data using the equation for cathodic reactions,

$$\ln k_{fh}^{s} = \ln k_{s}^{s} - \frac{\alpha nF}{RT}(E^{of,w} - E^{of,s}) \tag{60}$$

and a similar equation for anodic processes.

The analysis has shown that the plots of $\ln k_{fh}$ (k_{bh}) vs. ΔG_{tr} were linear. In agreement with Eqs. (57) and (58) a much higher slope of such plots was observed for the cathodic process ($\bar{\alpha} + \alpha$), while for anodic reactions in some cases the observed slopes, now equal to ($\bar{\alpha} - \beta$), where very close to zero.

The results of such an analysis are also given in Table 8. Similarly to the previously obtained results, they too show that the less solvated intermediates are formed in the course of the electrode reaction. Relatively good correlation coefficients may suggest that the mechanisms of a given reaction in various solvents are similar. However, in view of the complexicity of such reactions and the influence of the double-layer structure on their rate, this suggestion should be considered with caution.

The rate of these reactions may be significantly influenced by the double-layer structure. Particularly large effects were observed during electroreduction of alkali metal ions [214, 236, 237] and alkaline earth metal ions [218]. In the case of these reactions not only has the concentration of the background electrolyte influenced the observed rate constant in different solvents, but also a significant change of the rate constant was observed, when the cation of the background electrolyte was changed, maintaining the electrolyte concentration constant. This behavior was explained [238] by the assumption that the rate-controlling step is located in the inner Helmholtz double layer.

In addition to the correlations given in Table 8, the kinetic data were also correlated with donor properties of the solvents. The following dependences were used:

$$\log k_s = a + b\,\mathrm{DN} \qquad [85] \tag{61}$$

$$\log k_s = c + d\beta_{KT} \qquad [85] \tag{62}$$

$$\ln (k_s \tau_L) = e + f\,\mathrm{DN} \qquad [4] \tag{63}$$

$$\ln k_s = g - h \ln \tau_L + i\,\mathrm{DN} \qquad [239] \tag{64}$$

The results obtained with the help of Eqs. (61) and (62) are given in Table 9 [85]. For the process of the $Cd^{2+}/Cd(Hg)$ system a poor correlation was found again when using Eq. (61). Therefore this process, and also the kinetic parameters of the lithium reaction were analyzed using Eq. (63) [4, 239]. For lithium it was found that $e = -29.3$ and $f = -0.40$ with the correlation coefficient $r = 0.97$ and $n = 6$, while for cadmium $e = -30$ and $f = -0.11$, but with a worse correlation coefficient, $r = 0.864$ (for $n = 6$), were reported.

Table 9. Results of analysis according to Eqs. (61) and (62) of ion-transfer reactions at mercury electrodes.

Cation	Equation used in analysis								Ref.
	Equation (61)				Equation (62)				
	a	*b*	*r*	*n*	*c*	*d*	*r*	*n*	
Li^+	1.9	−0.21	0.97	5	2.0	−8.3	0.97	5	208, 216
Na^+	0.63	−0.61	0.99	5	0.75	−2.4	0.94	5	214
K^+	2.5	−0.13	0.93	3	2.5	−4.9	0.90	3	214
Ba^{2+}	1.2	−0.12	0.96	3	1.1	−4.7	0.99	3	215, 218
Pb^{2+}	3.4	−0.17	0.997	3	1.2	−4.2	0.98	3	215, 222, 225
Zn^{2+}	2.7	−0.14	0.90	7	1.6	−3.5	0.70	8	221, 222, 224, 232
Ni^{2+}	2.9	−0.15	0.993	4	0.68	−2.5	0.72	4	233
Mn^{2+}	0.011	−0.20	0.99	4	−2.0	−4.7	0.88	4	228–230
	−0.019[a]	−0.22[a]	0.96[a]	4[a]					

[a] The second line for Mn^{2+} gives analysis for double-layer corrected kinetic data.

Equation (63) was applied to the analysis of the dependence of the rate of cadmium, lithium and sodium deposition on the solvent parameters [4, 239]. These correlations with solvent basicity parameters show, in agreement with the preceding analysis, that all these reactions decrease in rate when the Lewis basicity of the solvent increases. This behavior is common for all the systems analyzed.

Again, the reaction of the $Cd^{2+}/Cd(Hg)$ system, which was sometimes used as a model reaction in electroanalysis, exhibited a rather complicated behavior. It was studied extensively by Lasia and coworkers [239–241]. Their study of this reaction in seven solvents with different donor numbers [239] is especially interesting.

The foregoing discussion reveals that in order to understand better the influence of solvents on the ion-transfer type of reactions, further progress is needed both in the theory of such processes and also in experimental studies of their mechanism in solvents with different donor properties.

4 Electrochemical Reactions in Mixed Solvents

Mixtures of two solvents have frequently been used as a reaction medium. Such mixed solvents have also been applied in electrochemical analysis. Very often, water was one of the components of such binary mixtures. One should add here that even in experiments carried out in single solvents, especially with a relatively low donor number, water that has not been carefully removed could cause changes in thermodynamic and kinetic parameters of the electrochemical reaction under study.

There are two important differences, when we compare the behavior of a selected electrode system in (1) two single solvents S_1 and S_2 and (2) two mixed solvents of different composition formed from these two solvents. In pure solvents, both the electrode surface and the first and further coordination spheres of the reactant are populated by the same molecules, while in mixed solvents there is no *a priori* answer concerning their solvation. Usually preferential solvation occurs, and the compositions of the electrode surface layer and the solvation sphere of the reactants are different from the composition of the bulk phase.

In general, three main cases may be distinguished:

1. both the reactant and the electrode are not specifically solvated;
2. the electrode and the reactant are preferentially solvated by the same component of the mixture (either S_1 or S_2); and
3. the electrode and the reactant are preferentially solvated by different solvent molecules.

Therefore, in order to explain the influence of mixed solvents on the course of electrochemical reactions, information about the reactant solvation and the composition of the electrode surface layer should be available.

Presentation of experimental data on adsorption of nonaqueous solvents from their binary mixtures with water is beyond the scope of this review. However, we will discuss ion solvation briefly, insofar as it is related to the potentials of redox systems and thus to the nature of their electrochemical reactions.

5 Electrode Potentials in Mixed Solvents

5.1 The Electrode Potential Scale for Mixed Solvents

In the first part of this review we have briefly presented several redox systems which have both Ox and Red components only weakly interacting with the solvents, while their free energy of transfer between various solvents was assumed to be equal to zero.

From two such electrodes, Foc^+/Foc and BCr^+/BCr, suggested by Gritzner and Kuta [63] as equally good reference electrodes in nonaqueous electrochemistry, the Foc^+/Foc electrode is preferred in the use of mixed solvents, particularly with water as one of the components of the mixture, since the solubility of BCr in water is very low (see, however, [242]). Also the behavior of the Foc^+/Foc electrode in water is not ideal, because of poor solubility of Foc [62] in this solvent. Since the product of electroreduction, Foc, is to some extent accumulated on the electrode surface, cyclic voltammetric curves starting with the electroreduction of ferricinium ions exhibit an anodic current which is greater than the diffusion-limited one. Nevertheless, the error which results from the Foc adsorption should not be significant, especially in mixtures where the water content is not very high.

The other system, Coc^+/Coc, with a structure and performance very similar to the Foc^+/Foc electrode (though the formal potential of the former system is more negative, by 1.31 V), exhibits similar limitations both in aqueous and water-rich mixtures.

The assumption about equal solvation energies of a large cation and a large anion which form salts like Ph_4AsBPh_4 is frequently used in practice (see, for instance, [30–33, 243] and should work better in mixtures of solvents which exhibit amphoteric properties.

The decrease in liquid junction potential at the boundary of two solvents by the use of tetraethylammonium picrate [38, 39, 44, 45] as discussed in Sec. 2.2.2, should be more effective for mixtures of solvents with similar dielectric permittivities, while it works less well when water is one of the components of the mixture.

In conclusion, there is no fully satisfactory system for the construction of a unified potential scale which could be used for mixed solvents of different compositions. In fact, the scales used are the same as those applied for pure solvents, but in the case of mixed solvents the extrathermodynamic assumption may be even less strictly obeyed, especially if there are even small preferential interactions of the reference electrode components with one of the solvents of the mixture. In our work we used the Foc^+/Foc system as a solvent-independent reference electrode. The consequent use of one reference electrode in a series of experiments with mixed solvents of different composition should diminish the error.

5.2 The Change in Reactant Solvation and the Potential of Redox Systems Caused by Mixed Solvent Composition

Mixed solvents prepared from two single solvents S_1 and S_2 are attractive, because the properties of such mixtures may be varied in a programmed fashion by changing their composition. One should remember, however, that the change in such properties from those characteristic of S_1 to those typical of S_2 is not always represented by a monotonic function since molecules of both solvents interact with one another and the solvation sphere of ionic reactants can be quite different from the bulk composition.

This behavior may be simply described by the equation

$$x^{M}_{S_1}/x^{M}_{S_2} = K\,(x_{S_1}/x_{S_2}) \tag{65}$$

derived from thermodynamic considerations [244] similar to those used in the case of preferential adsorption of molecules from the mixture $S_1 + S_2$ on a surface-active solid: $x^{M}_{S_{1(2)}}$ and $x_{S_{1(2)}}$ describe the mole fraction of solvent $S_1(S_2)$ in the first coordination sphere of ion and bulk phase, respectively.

In the case of regular solutions, the dependence of $x^{M}_{S_1}/x^{M}_{S_2}$ on x_{S_1}/x_{S_2} is linear [244] and the slope of this function depends on the extent of preferential solvation. However, the change of the free energy of solvation, represented by the free energy of transfer, when the solvent composition changes from S_1 to S_2 is not always monotonic, as shown in Fig. 9.

Various methods were used to obtain such information. For instance, chemically inert, differently solvated chromium(III) species $Cr(H_2O)_{6-p}(DMSO)_p^{3+}$ formed in

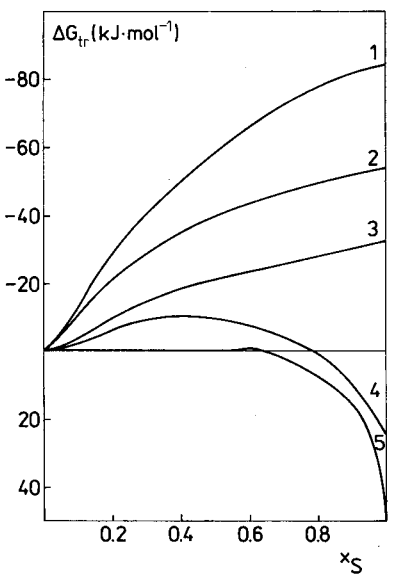

Fig. 9. Free energy of transfer of several cations versus the mole fraction (x_s) of the organic solvent. Curve 1, Pb(II) in H_2O-DMSO [225]; curve 2, Mn(II) in H_2O-DMF [228]; curve 3, Tl(I) in H_2O-DMSO [225]; curve 4, Mn(II) in H_2O-AN [230]; curve 5, Zn(II) in H_2O-AC [220].

mixed solvents H_2O+DMSO of various compositions were isolated by King and coworkers [245] using ion-exchange chromatography. It was shown that different solvates with the number of DMSO molecules p ranging from 0 to 6 in the first solvation sphere of chromium(III) are formed, depending on the mixed solvent composition.

For more labile ions which exchange solvent molecules fast from the first solvation sphere, spectrometric methods (such as NMR) which monitor the change in the immediate neighborhood of the ion are especially useful for the study of ion solvation in mixed solvents.

An example of NMR application, the magnetic resonance of ^{27}Al in the study of the solvation of Al(III) in mixtures of DMF with DMSO [246], is shown in Fig. 10. This example is spectacular, because Al solvates of different composition ex-

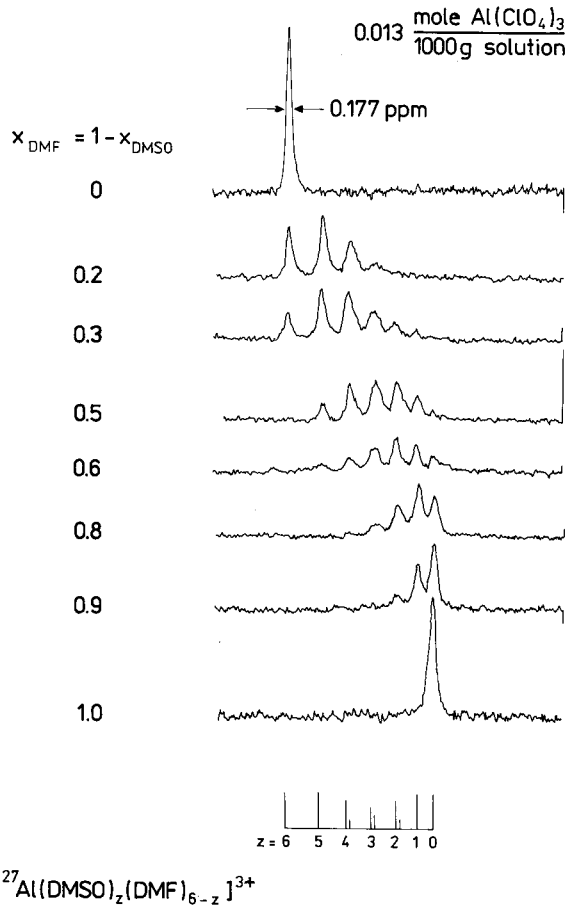

Fig. 10. ^{27}Al-NMR spectra of $Al(ClO_4)_3$ solutions in mixtures of DMSO and DMF in nitromethane [246].

hibit separate signals. Such separated signals as those observed in the NMR studies of the Al(III)-DMF-DMSO system can only be observed if the average lifetime of solvent molecules in the first solvation sphere is sufficiently long (see [247]).

NMR spectroscopy has been used in the study of the preferential solvation of ions in two-component mixtures by Frankel et al. [248]. They assumed that the midpoint of the chemical shift between two pure solvents, when studying the resonance frequency of the ion in question, points to the isosolvation point at which the inner solvation shell of the studied ion is equally populated by molecules of both solvents. If at this point the mole fraction of one of the two solvents in the bulk is low, its solvating properties are high, and conversely.

However, this model is only valid [249] under the assumptions that the total solvation number does not change with the solvent composition, and that the ion-ion interactions may be neglected. If these conditions are fulfilled, the above-described approach gives important information on the solvating ability of various solvents in their binary mixtures.

Table 10. Isosolvation points of Na(I) in binary solvent mixtures [250].

Solvent added of NMF	Mole fraction to NMF at isosolvation point, x_i	Donor number of solvent added to NMF	$\frac{38.8\,x_i}{0.74}$
HMPA	0.74	38.8	38.8
Pyridine	0.33	33.1	17.3
Water	0.59	33	30.9
Ethanol	0.40	31.5	21.0
DMSO	0.54	29.5	28.3
DMF	0.50	26.6	26.2
Methanol	0.48	25.7	25.2
FA	0.50	24.7	12.4
THF	0.19	20	9.96
Acetone	0.12	17	6.29
Acetonitrile	0.12	14	6.29
NM	0.02	2.7	1.05

Abbreviations: HMPA, hexamethylphosphoric triamide; DMSO, dimethyl sulfoxide; DMF, dimethylformamide; FA, formamide; THF, tetrahydrofuran; NM, nitromethane.

In Table 10 we give, as an illustration, such isosolvation points for sodium(I) in the binary mixtures of *N*-methylformamide (NMF) with various solvents determined by Popov and coworkers [250]. The last column shows the normalized values of the parameter which, in the ideal case, should be close to the donor numbers of the applied solvents. By comparing pairs of values from the last two columns of Table 10, we can see that although these values are not identical, the trend of the change of the $(38.8\,x_i/0.74)$ parameter for the applied solvents is similar (with the exception of pyridine (Py) and ethanol) to that of the donor numbers. This order of solvating power, found for Na(I), may differ to some extent for other cations. This study [250] also shows that the earlier proposed DN value of 18.1 for water is too low.

The possibilities of NMR techniques are also well illustrated by the use of ^{31}P-NMR [251] in the study of the resolvation of Be(II) ions (which are not very labile either) when the composition of the H_2O-HMPA mixed solvent was changed. This study led to the determination of consecutive stability constants of the Be(II)-HMPA species.

The above presentation shows that the detailed analysis of the dependence of ΔG_{tr} on the mixed solvent composition and on the stability and concentration of various solvated reactant species may be quite complicated, especially in the case of labile ions. The free energy of ions is dependent not only on their interaction with the solvent and with other components of the mixture [252] (for instance, ions of background electrolyte), but also on the change in solution structure [252] and on the change in hydrogen bond formation [253].

In the literature there are studies dealing with the relationship between changes of the free energy of transfer and the concentration of different solvated species. For the transfer of a cation from a single solvent S_1 to the mixture S_1+S_2, one has [254]

$$\Delta G_{tr} = -RT \ln \left[1 + \sum_{1}^{s} \beta_i (a_{S_2}/a_{S_1})^i \right] - n_s RT \ln a_{S_1} + \Delta G_{el} \tag{66}$$

where β_i is the stability constant of solvates, a_{S_1} and a_{S_2} denote the activity of both solvents in the mixture, n_s is the solvation number of cation, and ΔG_{el} the difference between the energy of the electrostatic interaction of the solvated cation with the mixed solvent and with the solvent S_1.

When molecules of both solvents only weakly interact specifically, the last term of Eq. (66) can be neglected for isodielectric mixtures. Such a simplified equation was used [255] for the calculation of the ΔG_{tr} of Ag(I) and Cu(I) from AN or DMSO to their mixtures with other solvents. A good agreement was found between the calculated and the experimental data.

Cogley et al. [256] were the first to determine stability constants of the solvated species from the NMR chemical shift, while Covington and coworkers [249] related the chemical shift to ΔG_{tr}.

Potentiometric measurements have also been used in such studies. As an example we mention only the work of Larson and Iwamoto [257] on Cu(II) hydration in nitromethane, that of Luehrs coworkers [258, 259] on stability constants of silver(I) with DMF, DMSO, and HMPA, and the studies of interaction of sodium(I) with different protic and aprotic solvents and acetonitrile media carried out by Izutsu and coworkers [260].

Although several other methods have been used in such solvation studies, NMR spectroscopy seems to be the most useful.

The influence of the interaction in binary solvents on ΔG_{tr} ions was analyzed by Y. Marcus [261], who assumed a quasi-lattice model for the electrolyte in such solutions. Free energies of transfer of various ions were collected and discussed [75, 76]. Ion solvation including mixed solvent media has been reviewed by several authors [45, 76, 262–265].

In the case of the study of electrode reactions in several single solvents, it was useful to have a simple dependence between the measured E^{of} ($E^{\gamma}_{1/2}$) potentials and

the donor or acceptor properties of pure solvents (Sec. 2.3). There have also been attempts to obtain similar solvent parameters for mixed solvents.

The change in the Lewis acidity parameter, E_T with the mixed solvent composition is either monotonic or exhibits a maximum with an E_T value higher than those found for the pure solvents [266].

The Kamlet-Taft [84] parameter of the Lewis basicity β_{KT} (see Sec. 2.3) was also determined for 14 mixtures of solvents with methanol [267] and 12 mixtures of organic solvents with water [268]. The change of β_{KT} with the mixed solvent composition is determined by changes occurring in the structure of methanol and water after addition of the second solvent. However, the use of these parameters for a systematic analysis of electrochemical potentials is rather limited.

As an example we mention the dependence of the free energy of transfer of manganese(II) ions from water to water–acetonitrile mixtures on the parameter β_{KT} [85]. It is a complicated nonlinear dependence, which suggests that the interaction of *p*-nitroaniline (used in determination of β_{KT}) and manganese(II) with aqueous solutions of acetonitrile is totally different. One may expect that complicated dependences of ΔG_{tr} or E^{of} ($E^{\gamma}_{1/2}$) potentials on parameters of the Lewis basicity or acidity of mixed solvents will be observed for other ions also. Such relationships of the solvation abilities of water–organic solvent mixtures in respect to different cations are determined by several factors:

1. the Lewis basicity of the organic solvent;
2. structural changes which occur when water or another structured solvent with hydrogen bonds is mixed with the organic component; and
3. the dual role of organic molecules which are donors in the interaction with metal ions and acceptors of the hydrogen bond.

Since in many cases these influences may act in opposite directions, the changes of formal potentials, E^{of}, with the solvent composition cannot be described by simple correlations.

Nonetheless, knowledge of the donor number of the solvents which form the binary mixture is useful in the qualitative prediction of the change of the formal potential of the system being studied. As we have shown in Sec. 2.3, E^{of} ($E^{\gamma}_{1/2}$) expressed versus the potential of the solvent-independent electrode always moves to more negative values when a single, less basic, solvent is substituted by a solvent characterized by a higher DN. Therefore, when the mole fraction of this second, more basic, solvent increases in the binary mixture, the potential should change toward more negative values. However, this change in the intermediate composition range may sometimes be more complicated, as exemplified in Fig. 9.

The use of chemical probes for the characterization of solvent mixtures with water as one of the components and completely nonaqueous mixtures was recently analysed and discussed by Y. Marcus [269].

6 The Kinetics of Electrode Reactions in Mixed Solvents

The presentation of the influence of binary mixed solvents on the rate of electrode reactions will be limited to inorganic ions solvated by both solvents, with water as one of the components.

This presentation deals with ion-transfer and electron-transfer types of reactions. The electrode reactions in mixtures of water with solvents of lower Lewis basicity will be discussed first, followed by the presentation of such reactions in mixtures of water with solvents of higher donor properties.

This organization of the experimental studies is based on the observations that, as a rule, the organic component of the mixed solvent is preferentially adsorbed on the electrode and the electrode surface may be largely covered by adsorbed organic molecules, even at relatively small concentrations of the organic solvent in the bulk. Therefore, the electrode behavior of the reactants studied depends also on the extent of their solvation with organic molecules.

If the donor number of the organic component is lower than that of water, then the electrode surface layer will be preferentially populated by molecules of the organic solvent while the reactant remains hydrated (the heterosolvation case). Its resolvation may usually occur in organic-rich mixtures of solvents. On the other hand, when the donor number of the organic solvent is higher than that of water, the reactant may exchange its water molecules for molecules of the second solvent, even at low concentrations of the organic component in the mixture. Since there should again be preferential adsorption or organic molecules on the electrode surface, if the electrode potential is not too negative or positive, one has the homosolvation case – the electrode surface layer and the inner sphere of reactant are populated by the organic solvent. In consequence the electrode behavior, as a function of solvent composition, should differ for these two cases of hetero- and homo-solvation.

6.1 Experimental Studies of Ion-Transfer Reactions

Jaenicke and Schweitzer [224], who studied the kinetics of the electrode reaction of the Zn(II)/Zn(Hg) system in mixtures of water with dioxane, ethanol, acetonitrile, tetrahydrofuran, and acetone, initiated and gave impetus to the practical study of electrode kinetics in mixed solvents. Their kinetic results are given in Fig. 11, where one may observe a decrease in the exchange current when the concentration of organic component increases in the mixture. This decrease is not large in the case of dioxane, but it amounts to 2.5 orders of magnitude when acetone is added to water.

The authors [224] explained these kinetic changes qualitatively by considering the energy of activation at different mole fractions of the organic component in the mixture. The minimum on the rate constant (exchange current) – mixed solvent composition dependence occurs at the largest difference in composition between the surface layer and the first solvation sphere of zinc(II).

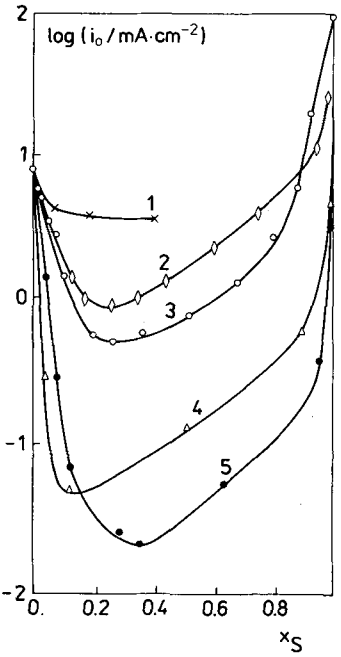

Fig. 11. Dependence of the exchange current of the Zn(II)/Zn(Hg) system on the mole fraction (x_s) of organic solvents in their mixtures with water. Curve 1, water-dioxane; curve 2, water-ethanol; curve 3, water-acetonitrile; curve 4, water-tetrahydrofuran; curve 5, water-acetone.

Miles and Gerischer [270] have also studied the electrode reaction of the Zn(II)/Zn(Hg) system but in water-propanol mixtures. After passing a minimum, the increase in exchange current corrected for the double layer effect in propanol-rich mixtures was explained by desolvation of solvated Zn(II) ions being easier than their dehydration in water-rich mixtures.

Lipkowski and Galus [271, 272] have investigated the electrode reactions of $HPbO_2^-$, Mn(II), and Cd(II) in mixtures of water with propanol and *t*-butanol. In these cases also, minima in the rate constant-solvent composition dependence were observed.

Parsons and coworkers [227] have studied the Cd(II)/Cd(Hg) electrode reaction in the water-acetonitrile system and in mixtures of organic solvents.

In addition to the above-listed systems, a minimum of the rate constant was observed for the Zn(II)/Zn(Hg) systems in water-methanol [232] and for the Mn(II)/Mn(Hg) systems in water-acetonitrile mixtures [230]. Electroreduction of Tl(I), Zn(II) and maleic acid was also studied in water-acetone [273] and water-ethanol [274] mixtures.

The investigations carried out on the rate of ion-transfer electrode reactions in mixtures of water with solvents with a higher donor number than water, such as HMPA, DMF, or DMSO, revealed that the rate constant was decreased when the concentration of the organic solvent in the mixture increased [221–223, 225, 226, 228, 229, 231, 233, 275], but no minimum was found. The shape of this decrease depends on the mixed solvent and to some extent also on the nature of the reaction under study.

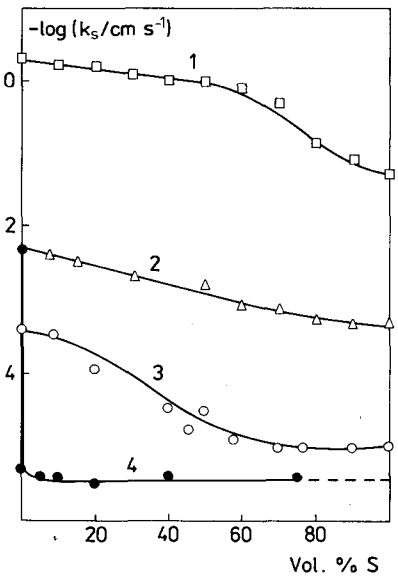

Fig. 12. Dependence of the logarithm of the standard rate constant on mixed solvent composition.
Curve 1, Pb(II)/Pb(Hg) in H_2O-DMSO [225]
Curve 2, Zn(II)/Zn(Hg) in H_2O-DMSO [221]
Curve 3, Mn(II)/Mn(Hg) in H_2O-DMF [228]
Curve 4, Zn(II)/Zn(Hg) in H_2O-HMPA [222]

Examples of such behavior are shown in Fig. 12 and the systems studied are listed in Table 11 (p. 276).

Sometimes, even a small maximum was observed in water-rich mixtures [221, 223].

6.2 Electron-Transfer Reactions in Mixed Solvents

The inorganic systems studied are limited in practice to solvated Eu(III)/Eu(II) and V(III)/V(II) couples. In mixtures of water with less basic solvents, both the europium [276–278] and the vanadium couples [272, 279–281] exhibited a minimum similar to that observed for ion-transfer systems.

A minimum was also observed [282] for complexes of Cr(III/II) with *trans*-1,2-cyclohexanediaminotetraacetate in mixtures of water with alcohols. The work of Parsons and Bockris [283] on the hydrogen evolution reaction in water-methanol mixtures should also be mentioned.

In the case when mixtures of water with more basic solvents were used, a monotonic increase of the rate constant was observed for the Eu(III)/Eu(II) system in DMF [276] and DMSO [278] and V(III)/V(II) in DMF [284] and DMPU (1,3-dimethyl-3,4,5,6-tetrahydro-2/1*H*-pyrimidinone) [285], as opposed to the behavior of the ion-transfer systems. However, in H_2O-HMPA mixtures both the Eu(III)/Eu(II) [286] and the V(III)/V(II) [285] systems exhibited a minimum. In the case of the Cu(II)/Cu(I) system in H_2O-DMSO mixtures at Pt electrodes [287], only a small decrease of the rate constant was observed.

Table 11. The ion-transfer reactions studied in binary solvent mixtures.

Electrode system	Solvent system	Ref.
Cd^{2+}/Cd(Hg)	H_2O-HMPA	226
	H_2O-PrOH	271, 272
	H_2O-*t*-BuOH	271, 272
	H_2O-AN	227
	H_2O-DMSO	221
Eu^{2+}/Eu(Hg)	H_2O-DMF	231
Mn^{2+}/Mn(Hg)	H_2O-DMF	228
	H_2O-DMSO	229
	H_2O-AN	230
Ni^{2+}/Ni(Hg)	H_2O-DMF	275
	H_2O-DMSO	233
	H_2O-MeOH	211
Pb^{2+}/Pb(Hg)	H_2O-HMPA	222
	H_2O-DMSO	225
	H_2O-PrOH	271, 272
	H_2O-*t*-BuOH	271, 272
Zn^{2+}/Zn(Hg)	H_2O-DMSO	221
	H_2O-MeOH	232
	H_2O-DMF	223
	H_2O-HMPA	222
	H_2O-AC	220, 224, 273
	H_2O-THF	224
	H_2O-dioxane	224
	H_2O-EtOH	274
	H_2O-PrOH	270

6.3 The Influence of Surface Layer Composition on the Reaction Rate

Early experiments carried out on the electrode kinetics in mixed solvents already showed the important role played by adsorption of the organic component on the electrode. In order to demonstrate this role more clearly we studied the Mn(II)/Mn(Hg) system [271], which has a quite negative standard potential. Voltammetric cathodic curves of Mn(II) electroreduction in the presence of *n*-propanol, isopropanol and *t*-butanol were observed at such negative potentials that the molecules of alcohols were almost desorbed from the electrode surface. On the other hand, the manganese amalgam was oxidized in the potential range -0.4 to -0.6 V (depending on the alcohol concentration), while the electrode was covered by adsorbed alcohol, as illustrated in Fig. 13 by the differential capacity curves for the water-*t*-butanol system. In order to move the potential of the cathodic reaction to even more negative values and to desorb the alcohol molecules totally, the experiments were carried out in an ammonia buffer.

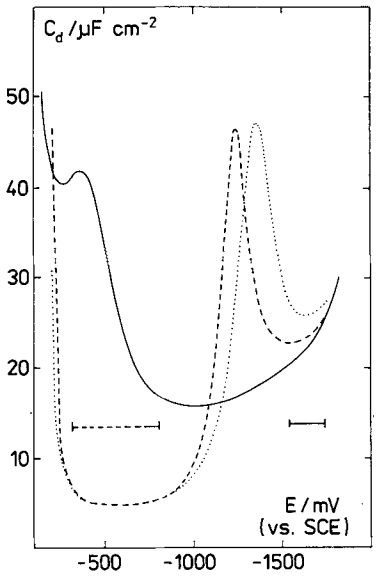

Fig. 13

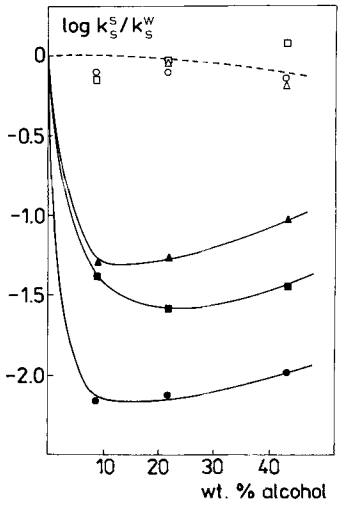

Fig. 14

Fig. 13. The differential capacity (C_d) of a mercury electrode in solutions of 0.4 M NH_4Cl and 0.8 M NH_3 in pure water (−), 8.1% *t*-butanol (---) and 43.5% *t*-butanol (. . .) versus potential (see text).

Fig. 14. The logarithm of the ratio of the standard rate constants of the Mn(II)/Mn(Hg) system in mixtures of water with *n*-propanol (▲, △), isopropanol (■, □) and *t*-butanol (●, ○). Black and open symbols refer to anodic and cathodic processes respectively.

The main results obtained are given in Fig. 14. One sees that the relative rate constants calculated at the formal potentials separately from cathodic and anodic current-potential dependences are different. While the rate constants calculated from cathodic curves are virtually independent of alcohol concentration, the constants calculated from anodic dependences exhibit a deep minimum when the concentration of alcohols in the solution is increased.

The formal potential was measured with the use of the saturated manganese amalgam electrode in a mixture containing 10^{-2} M Mn(II). This was also used for the rate constant calculations.

The main cause of the decrease of the anodic rate constant, observed when the second solvent is added to water, consists in the preferential adsorption of the organic solvent molecules (which play the role of an inhibitor) on the electrode surface. When there is no such adsorption (at very negative potentials) the cathodic reaction of manganese(II) is independent of the mixed solvent composition.

Additional experiments related to the influence of the composition of the surface layer in mixed solvents on electrode kinetics were carried out [281] with the V(III)/V(II) system. The electrode kinetics of this system in water-*t*-butanol mixtures were studied in parallel with the kinetics of the homogeneous electron exchange

$V^{3+} + e^- \Leftrightarrow V^{2+}$. These studies revealed that in this case also a large decrease of the heterogeneous rate constant was observed at low concentrations of *t*-butanol in the solution, which corresponded to the rising part of the adsorption isotherm of this compound on the mercury electrode. However, no change was observed in the homogeneous rate constant in this concentration range of *t*-butanol. All these experiments show that a significant drop of the rate constant occurs due to preferential adsorption of the organic component on the electrode surface.

A parallel change of the rate constants of homogeneous and heterogeneous processes in solutions containing more than 10 mol% of *t*-butanol may indicate that the image forces in the electrode kinetics are negligible.

The decrease of the rate constant under the influence of organic solvent was described by the equation [228]

$$k = k_w (1-\theta) + k_{sol}\,\theta \tag{67}$$

where k_w and k_{sol} stand for the rate constant in water and organic solvent, respectively, and θ is the electrode surface coverage. However, it appeared later when studying the Pb(II)/Pb(Hg), Zn(II)/Zn(Hg) [222], and Cd(II)/Cd(Hg) systems [226] in mixtures of water with HMPA that the equation

$$k = k_w (1-\theta)^a + k_{sol}\theta^b \tag{68}$$

describes better the observed experimental data. Exponents a and b are positive numbers of the order of 1 to 4.

Equation (68) is similar to that derived by Parsons [288, 289] for inhibition of electrode reactions

$$k = k_{\theta=0} (1-\theta)^{r^*} \exp(A\theta) \tag{69}$$

$k_{\theta=0}$ is the rate constant in the absence of inhibitor, and $r^{\ddagger}$ is the number of water molecules (associates) removed from the surface in order to make place for one molecule of the activated complex. If one assumes that $k_w \gg k_{sol}$ and the interaction of the activated complex with the inhibitor, represented by coefficient A, may be neglected one then obtains

$$k = k_w (1-\theta)^a \tag{68a}$$

and from Eq. (69)

$$k = k_{\theta=0} (1-\theta)^{r^*} \tag{69a}$$

In Eq. (68a) the exponent a should be understood either

1. the number of water molecules from the surface which interact with the reactant which penetrates the surface phase, or
2. the number of water molecules which should be removed to make place on the electrode for the reactant.

It is not easy to choose one of these two mechanisms on the basis of experimental data.

Irrespectively of how it is understood, parameter a for a given reactant should not be influenced by the nature of the solvent, provided that in the concentration range studied no interaction of the activated complex with the adsorbed molecules of the organic solvent occurs. However, there should be a dependence of a on the size of the reactant.

Equations (68a) and (69a) are not only formally similar. In the case of heterosolvation, when an organic solvent is added to water in small quantities, it is adsorbed on the electrode but does not change the solvation sphere of a reactant. Such a solvent behaves like an inhibitor. In fact, under such conditions $k_w = k_{\theta=0}$ and $a = r^{\neq}$.

Table 12. Typical a values from Eq. (68) for several reactants and solvent systems.

Electrode reaction	Solvent system	a
Zn(II)/Zn(Hg)	H_2O-HMPA	2.5
	H_2O-acetone	2
Cd(II)/Cd(Hg)	H_2O-HMPA	3.7
Mn(II)/Mn(Hg)	H_2O-DMF	1.2
	H_2O-DMSO	1.5
Eu(III)/Eu(II)	H_2O-acetone	2
	H_2O-acetonitrile	1.9

In Table 12 we give the values of a for several reactions. Inspection of those values reveals that they are similar for different solvents (see Zn and Mn in Table 12). They are also similar to the $r^{\neq}$ values found [290, 291] for several electrode reactions in the presence of inhibitors analyzed by means of Eq. (69) or (69a).

Therefore, it may be concluded that for many systems, at low concentrations of the organic solvent added to water, this solvent behaves like an inhibitor. One should mention that the determination of b is usually not precise.

6.4 The Increase of the Rate Constant with Organic Solvent Concentration

In general, an increase of the rate constant for ion-transfer reactions should be observed in mixtures rich in organic solvent, when the organic component has a lower DN than water.

This supposition is based on the discussion presented in Sec. 3.2, where it was shown that in pure solvents the rate constant of ion-transfer reactions should increase in solvents of lower donor numbers.

In cases such as those discussed in Sec. 6.1 a minimum is observed in the dependence of k_s upon the mixed solvent composition. The results given in Fig. 15 show that the position and depth of such a minimum depend on the surface coverage by molecules of the organic solvent on the one hand, and on the change in the free energy of transfer with solvent composition on the other hand. In this case the increase of the rate constant begins at practically full coverage of the electrode surface by acetonitrile. Since this important factor is not changed when a change of the rate constant occurs, the changes of kinetics should result from the resolvation of a reactant. In fact, the rise of the rate constant is accompanied by a simultaneous increase of ΔG_{tr} from 0 to a value characteristic of pure acetonitrile solutions.

The dependence of the increase of k_s on the resolvation process was studied by Gorski and the present author [285]. As a model, the V(III)/V(II) system was used. In this system one could follow in a more direct way the resolvation of vanadium ions in several mixed solvents by using spectrophotometry. The results obtained are given in Fig. 16, the upper panel of which shows the change in the rate constant with $\log(1-\theta)$ for the vanadium reaction in mixtures of water with DMF, DMPU,

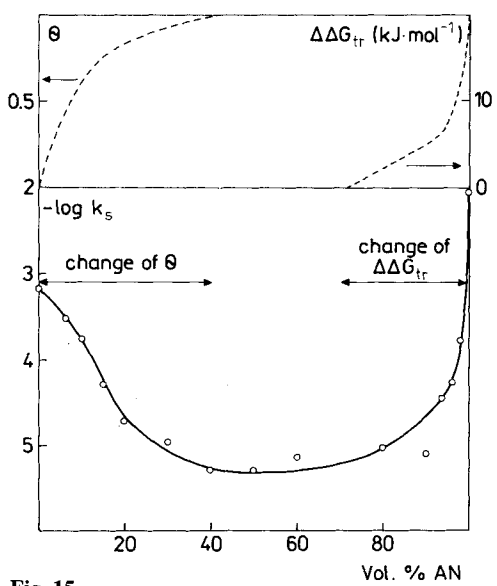

Fig. 15

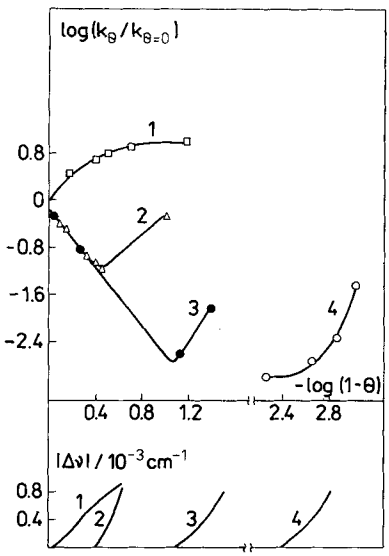

Fig. 16

Fig. 15. The dependence of the logarithm of the standard rate constant of the Eu(III)/Eu(II) system on acetonitrile concentration in its mixtures with water. The upper panel shows the surface coverage and the change in the free energy of transfer for the system studied. $\Delta\Delta G_{tr} = \Delta G_{tr,Eu(III)} - \Delta G_{tr,Eu(II)}$.

Fig. 16. Variation of the standard rate constant of the V(III)/V(II) system (upper panel) and the absorption spectra of V(III) (lower panel) with mixed solvent composition in terms the surface coverage of the electrode by the organic component. Solvent system: curve 1, H_2O-DMF; curve 2, H_2O-DMPU; curve 3, H_2O-HMPA; curve 4, H_2O-AN.

AN and HMPA. The lower panel shows the difference $\Delta\nu_{V(III)}$ as a function of $\log(1-\theta)$. $\Delta\nu_{V(III)} = \nu_{V(III)}(H_2O) - \nu_{V(III)}(H_2O+S)$ gives the difference between the position of the absorption band maximum in water at 16900 cm^{-1} and in mixtures of water with the same four solvents. The increase of $\Delta\nu_{V(III)}$ from 0 points to the beginning of substitution of water molecules in the first coordination sphere of vanadium ions by molecules of the added solvent.

Comparison of both parts of Fig. 16 shows that as long as V(III) ions are hydrated ($\Delta\nu_{V(III)} = 0$), the rate constant decreases with the decrease of the free surface of the electrode $(1-\theta)$. In these water-rich mixtures the change of the electrode kinetics is very well described by a simplified form of Eq. (69) (with $A = 0$), with the $\log k/k_w$ versus $\log(1-\theta)$ dependence having an identical slope for the three different mixtures.

The change from inhibition to acceleration of the rate of electrode reaction occurs exactly at the mixed solvent composition at which the process of reactant resolvation begins in the bulk of the solution. It appears that even partial resolvation of vanadium(III) ions ($\Delta\nu_{V(III)} > 0$) initiates the increase of the rate of reaction in the surface phase, when the concentration of the organic solvent is considerably higher there than in the bulk. Such behavior is observed in mixtures of water with solvents of Lewis basicity lower (AN) and also higher (HMPA) than water.

In the case when resolvation already occurs at a very low concentration of the added second solvent, in which the reaction being studied is faster than in water, an increase of the rate constant is observed instead of a minimum (H_2O-DMF mixtures in Fig. 16). The composition of the mixed solvent at which the change from inhibition to acceleration is observed does not follow the order of Lewis basicity of the solvents involved, but is a function of the affinity of the added solvent for the electrode surface and for the reactant.

Although in the experiments presented in Fig. 16, HMPA has the largest donor number of all solvents used, its adsorption on the electrode surface already occurs at concentrations that are not sufficient for resolvation of vanadium ions. Therefore, in this case in the intermediate concentration range of the mixture an inhibition of the electrode reaction is observed.

6.5 The Models of Electrode Reactions in Mixed Solvents

A quantitative model of electrode reactions in mixed solvents was proposed by Behr and coworkers in 1975 [220, 292]. It is based on the assumption that the electrode reaction occurs in two steps:

1. The transfer of reactant from the bulk to the electrode surface and penetration of the surface phase. The partition of the reactant between the surface and bulk phases is in equilibrium.
2. A slow charge transfer process which is the rate-determining step.

It was first assumed that the energy of activation changes linearly from the value found in solvent S_1 to that found in S_2. Later [276], a nonlinear change of the energy of activation with the solvent composition was also considered.

In this model the change of the rate of the electrode reaction, following the change of the ratio of concentrations of the two solvents in the mixture, is due to the alteration of the reactant concentration in the surface phase, c^s.

This concentration is

$$c^s = c^b \exp\left[\frac{\mu_i^b - \mu_i^s}{RT}\right] \tag{70}$$

where μ stands for the chemical potential of the reactant. Superscripts s and b refer to surface and bulk phases, respectively.

Equation (70) may be written in an equivalent form as

$$c^s = c^b \exp\left[\frac{-\Delta\bar{G}_{tr}}{RT}\right] = c^b P \tag{70a}$$

where P is the partition coefficient of the reactant between the surface and bulk phases, related to the free energy of transfer $\Delta\bar{G}_{tr}$ of the reactant between these phases. In the model it was in fact assumed that the surface layer is slightly thicker than the monolayer, as a result of which the reactant located in this layer is not exposed to interactions with the second layer of mixed solvent molecules, whose composition should be similar to that of the bulk phase.

$\Delta\bar{G}_{tr}$, and in consequence P, may be calculated from the Born equation, using information about the composition of the surface layer supplied by the adsorption studies. The following equation may be used in such calculations

$$\Delta\bar{G}_{tr} = \frac{Nz^2e^2}{2r}\left[\frac{1}{\varepsilon_s(x^s)} - \frac{1}{\varepsilon_s(x^b)}\right] \tag{71}$$

where $\varepsilon_s(x^s)$ and $\varepsilon_s(x^b)$ denote dielectric permittivity for the solvent having the composition of the surface and bulk phases, respectively.

In Fig. 17 we show [292] a partition of Zn^{2+} between the surface and bulk phase in binary mixtures of H_2O with methanol (curve 1) and H_2O with acetone (curve 2). Both curves exhibit a deeper minimum for acetone which is more strongly adsorbed on the surface of a mercury electrode than methanol and whose dielectric permittivity is more different from that of water.

For both pure solvents $P = 1$, since there is no difference between the composition of the surface phase and bulk phase.

A total change of the rate constant in this model is dependent on the change in the P coefficient and the energy of activation. Assuming that the energy of activation is due to partial desolvation of the ionic reactant and that the reaction site is in the surface layer, then, at least for certain reactions, one may expect that the energy of activation will change monotonically from the value characteristic of the reaction carried out in one pure solvent to that typical of the reaction proceeding in the second pure solvent.

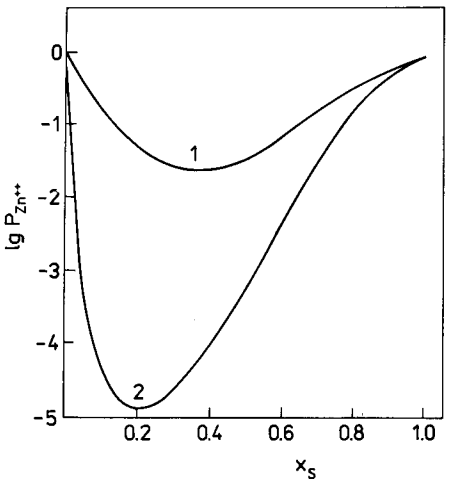

Fig. 17. The variation of the partition coefficient P of Zn^{2+} between the surface phase and the bulk solution; curve (1) H_2O-MeOH and curve (2) H_2O-AC [292].

Therefore, the dependence of the rate constant on solvent composition results from superposition of the monotonic change in the energy of activation and the change in P.

Such an approach could explain, though in a semiquantitative way, the behavior of the systems studied earlier, when a minimum was observed on the k_s^{ap} versus solvent composition dependence. Analysis of the change in the rate of reaction, expressed as a product of the electrode reaction rate constant and the reactant concentration in the surface phase, c^s, in mixtures of water with acetone reveals a deep minimum, which corresponds to the greatest difference in composition of the surface and bulk phases.

However, the model proposed by Behr and coworkers [220, 292] cannot explain the change in the rate of electrode reactions occurring in binary mixtures of water with solvents more basic than water. Instead of a decrease of the rate with an increase of the organic component, an increase of the rate is expected for ion-transfer reactions. Experimentally such a maximum has never been observed [293]. One should also add that basic properties of solvent molecules adsorbed on the electrode surface may be quite different from those of bulk molecules.

In order to describe the changes in the rate constant with the composition of such mixtures, we have proposed [228] another model, which takes into account only the change of coverage of the electrode surface by organic molecules.

Equation (67), which describes the change in the experimental rate constant k [228] in this model, is formally very similar to the equation which was used earlier to describe the inhibition [294, 295] of electrode reactions. Such an equation was used by Kisova [296]. Later it was found that Eq. (68) better describes the rate constant-solvent composition dependence. However, it fails to describe this dependence at high concentrations of an organic solvent which has a donor number lower than that of water. In general, it fails when the rate constant-solvent composition dependence exhibits a minimum.

To overcome these difficulties we have proposed [297] a model of the reaction based on resolvation of the reactant in the surface phase. The direct electrode reaction occurs with this type of resolvated complex.

The resolvation reaction is

$$M^{n+}_{i(b)} + a\,S_{1(s)} + b\,S_{2(s)} \Leftrightarrow M^{n+}_{j(s)} + p\,S_1 + q\,S_2 \tag{72}$$

where $M^{n+}_{i(b)}$ and $M^{n+}_{j(s)}$ denote solvated forms of reactant in the bulk and in the surface phases, respectively. S_1 and S_2 stand for molecules of water and organic solvent, respectively, and a, b, p and q are stoichiometric coefficients of the surface reaction. Assuming that the equilibrium constant, K_{ij}, of reaction (72) may be described by the Frumkin-type isotherm, the rate constant of the electrode reaction at a given solvent composition may be described [297]. This rate constant is dependent on K_{ij} and on the rate constant of differently solvated ions.

The resulting equation is too complex, because it contains parameters which cannot be easily obtained by experiment. However, using several approximations one may obtain [297] simplified versions of this equation.

For mixtures of water with a less basic solvent, assuming that one solvated form predominates in the mixtures, we arrive at the expression

$$k = k_w \frac{(1-\theta)^a}{a^p_{H_2O}} + k'_2 \frac{\theta^b}{a^q_{H_2O}} \tag{73}$$

where k'_2 denotes the product of the rate constant corresponding to the minimum of the rate constant-solvent composition dependence k_{min} and the water activity in such mixture.

Another simplified form, also valid for mixtures of water with less basic solvents, is [297]:

$$k_s = k_w (1-\theta)^a \exp(-Q\theta) + k_{min}\theta \tag{74}$$

where Q is the coefficient which expresses a difference in interaction of the surface complex with surface molecules of water and organic solvent.

Both Eqs. (73) and (74) predict a decrease of k_s with an increase in the organic component in the mixture with water. These equations were used for the analysis of electrode reactions of the Zn(II)/Zn(Hg) and Eu(III)/Eu(II) systems in water-acetone mixtures. The best fit for both ractants was found for $a = 2$ and $Q = 0$.

This result may indicate that the ionic depolarizer reacts with two molecules (trimers) of water from the surface phase. This conclusion may not be strictly valid since the shape of the k versus mixed solvent composition dependence, calculated for the Eu(III)/Eu(II) system by means of Eq. (73), is only very slightly dependent on the b, p and q parameters.

One should emphasize again that these simple equations do not describe the change of the rate constant in the whole concentration range, because it was assumed in their derivation that the reactant exists only in one hydrated form. If one assumes

[277] that a second form also exists in the solution, with a fraction of water molecules in the first coordination sphere substituted by the organic solvent, then one obtains an equation similar to Eq. (73) but with an additional term.

The description of electrode processes in mixtures of water with more basic solvents seems to be even more complicated than in the previous case. Now the organic solvent resolvates the cationic reactant more easily and may cover the electrode surface extensively even at low concentration in the solution.

Another method of analyzing experimental data has been proposed [298]. It is based on Eqs. (57) and (58) with parameters Y_{fh} and Y_{bh}, which for the mixed solvents take the form

$$Y_{fh}^{m} = RT(\ln k_{fh}^{m} - \ln k_{fh}^{w}) = \delta_c \Delta G_{tr} \tag{75}$$

$$Y_{bh}^{m} = RT(\ln k_{bh}^{m} - \ln k_{bh}^{w}) = \delta_a \Delta G_{tr} \tag{76}$$

Superscripts m and w relate to mixed solvent and water, respectively, and the rate constants k_{fh} (k_{bh}) are calculated at constant potential, on the solvent-independent scale. Such formal adoption of Eqs. (57) and (58) gives equations which can be valid only when there is no difference between the composition of the bulk and the surface phases, as in pure solvents where the validity of Eqs. (57) and (58) was proved.

The application of Eq. (75) to the analysis of the Zn(II)/Zn(Hg) electrode reaction in several mixed solvents, shown in Fig. 18, illustrates a good way of determining the mixed solvent composition range, where the organic solvent acts as an inhibitor of the electrode reaction (see Eq. (68)).

In H_2O-HMPA and H_2O-AC mixtures at $\Delta G_{tr}^{m} = 0$ a significant decrease of the rate constant is observed (Y_{fh} assumes negative values). This behavior corresponds to the process of inhibition and covers a significant solvent composition range for the H_2O-AC system. One should note that inhibition is observed after adding a solvent less basic than water (acetone) to water, and also after adding HMPA, which

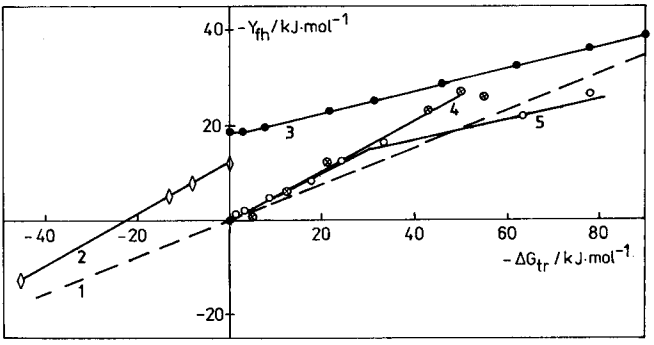

Fig. 18. Dependence of Y_{fh} on ΔG_{tr} for electroreduction of Zn(II) in mixed solvents; curve 2 (◇), H_2O-AC; curve 3 (●), H_2O-HMPA; curve 4 (⊗). H_2O-DMF; curve 5 (○), H_2O-DMSO. Curve 1 (---) gives the dependence in pure solvents.

exhibits a significantly higher Lewis basicity than water. As soon as the interaction of the reactant with the second solvent begins ($\Delta G_{tr} > 0$) there is a change of the rate of the Zn(II)/Zn(Hg) reactions. A significant increase of the rate in mixtures of H_2O+AC (curve 2 in Fig. 18) and a rather small decrease in H_2O+HMPA mixtures (curve 3) is observed. This difference results from the fact that the free energy of transfer of Zn(II) to AC and HMPA has a different sign in the two cases, and in agreement with Eq. (57) the rate constant in pure AC should be larger than in pure HMPA. When the concentration of the nonaqueous solvent in either mixtures increases the rate constant should approach line 1, which gives the expected dependence for single solvents. Such plots as that shown in Fig. 18 also indicate the extent of resolvation of the reactant when the concentration of the nonaqueous component in the mixture increases.

The difference between Y_{fh}^{m} for the different solvent compositions at a given ΔG_{tr} and the broken line in Fig. 18 may be used as an approximate measure of such resolvation. Inspection of Fig. 18 reveals that the behavior of the Zn(II)/Zn(Hg) system in H_2O-DMF and H_2O-DMSO mixtures is different from that described above. In this case there is no pure inhibition of the electrode reaction, since the decrease of the rate constant (Y_{fh}) is accompanied by the change in ΔG_{tr}. There occur progressive adsorption of the organic solvent (e.g., DMSO) on the electrode and in parallel the resolvation of Zn(II) ions.

A practicaly linear dependence between Y_{fh}^{m} and ΔG_{tr} for lead(II) was observed in mixtures of water with DMSO [225]. A linear dependence between $\log k_s$ and ΔG_{tr} was also found for the Zn(II)/Zn(Hg) and Li(I)/Li(Hg) systems in mixtures of PC with DMSO [216], and the electroreduction of Mn(II) in H_2O-DMF mixtures [228]. These linear dependences may be explained by the occurrence of the studied reactions at quite negative potentials, where the organic component of the mixture should be desorbed and the composition of the surface phase may be similar to the bulk composition over a large range of mixed solvent compositions.

This explanation may be extended to other systems where electrode reactions occur either at negative or positive potentials outside the adsorption range of the organic component of the mixture.

Dependences like the one shown in Fig. 18 for the Zn(II)/Zn(Hg) couple in H_2O-HMPA and H_2O-AC mixtures have also been more extensively analysed [298]. Practically straight lines, observed in the analysis, exhibit a slope differing from Sc (Sa) (see Eqs. (57) and (58)) in pure solvents.

The fact that Y_{fh}^{m} is a linear function of ΔG_{tr} for some of the mixed solvent composition range may suggest that the adsorption energy of the activated complex, ΔG_{ads}, is also a linear function of ΔG_{tr} of the reactant.

In order to describe the change in the rate constant over the entire composition range of the mixed solvent, one may modify Eq. (57) to account for the composition difference of the bulk and surface phases. This difference may be expressed by the relative surface excess. The general from of this modified equation is

$$k_{fh}^{m} = k_{fh}^{w} \exp(Sc\, \Delta G_{tr}/RT)\, P(\Gamma) \tag{77}$$

where $P(\Gamma)$ is a function of surface excess.

The relation between $P(\Gamma)$ and Γ may be established by dividing the electrode reaction into three steps. The first step is partial desolvation of the reactant in the bulk phase. The next step consists in removal of solvent molecules (associates) from the electrode surface, and the final step is the formation of the activated complex. Considering also a parallel reaction route with selective resolvation with b organic molecules, one obtains [298]

$$k_{\mathrm{fh}}^{\mathrm{m}} = \{k_{\mathrm{fh}}^{\mathrm{w}} (1 - \Gamma/\Gamma_\infty)^a + k_{\mathrm{fh},i} K_i \Gamma^b / \Gamma_\infty^b\} \exp [\mathrm{Sc}\, \Delta G_{\mathrm{tr}} / RT] \tag{78}$$

where K_i is the resolvation equilibrium constant and $k_{\mathrm{fh},i}$ is the charge transfer rate constant of the resolvation product.

For a low concentration of the organic solvent in the mixture the ratio of surface excesses Γ/Γ_∞ may be identified with the degree of surface coverage θ.

The exponential term in Eq. (78) accounts for the bulk resolvation of the reactant and the formation of the activated complex in the surface phase.

Equation (78) applied to the analysis of kinetic data of the Eu(III)/Eu(II) system was found to work satisfactorily at a lower concentration of the organic component. However, the description of experimental dependences at a high concentration of the organic component was worse.

Afanasev and Skobochkina [299] obtained other equations which may describe under some approximations the rates of reactions in mixed solvents. They also considered the increase in the rate constant with organic solvent concentration in organic solvent-rich mixtures.

It follows from the foregoing discussion that the change of surface coverage on the one hand, and the resolvation which changes the energy of activation on the other, are responsible for major changes in the electrode kinetics in mixed solvents. However, the change in the energy of activation may also occur in mixtures of organic solvents with water as a result of hydrogen bond formation or breaking. Lipkowski and coworkers [300], who studied the V(III)/V(II) system in H_2O-DMF mixtures, arrived at a conclusion that the changes in hydrogen bonding in the outer solvation shell contribute to the activation energy of electron exchange. The difference between the values of the Walden product was assumed as a measure of the difference in the number of hydrogen bonds in solvated V(III) and V(II) ions.

The important role of hydrogen bonds in changes of electrode kinetics in mixed water-dipolar aprotic solvents, when the electrode is covered by organic molecules, has also been found recently [301]. The substitution of water in the first coordination sphere of vanadium(III) and vanadium(II) ions by organic molecules should decrease the number of hydrogen bonds between the inner and outer shell and make the outer sphere more susceptible to reorganization. These experiments [301] have shown that the introduction of an aprotic molecule into the first coordination shell exerts larger kinetic effects than the exchange in the outer shell.

The role of the outer solvation shell in mixed solvents was also studied using the $CoEn_3^{3+/2+}$ system as a model [302] (En = ethylenediamine). In this system the inner sphere of the substrate ($CoEn_3^{3+}$) and the product ($CoEn_3^{2+}$) was not changed in the course of the one-electron electrode reaction. Therefore, the changes in the rate constant (determined by chronocoulometric method), observed when the composi-

tion of the mixed solvent was varied, could be explained by the changes occurring in the outer solvation sphere of both complex ions.

Recently Jaworski and coworkers [303] have analyzed mixed solvent influence on surface intramolecular reactions. The authors tried to explain the change in the rate constant with the H_2O-DMF mixed solvent composition in terms of the change in the estimated longitudinal relaxation time. A linear correlation was found between k for various H_2O-DMF compositions and τ_L^{-1}.

The results of investigations on electrode kinetics of various solvated metal ions in mixed solvents were obtained mostly with the use of the mercury electrode. Although explanations of kinetic data obtained with such electrodes are simpler than with solid electrodes, the understanding and detailed description of the observed changes is still not satisfactory. A reasonable explanation was only given for the results obtained in water-rich solutions for the case when a decrease in the rate of the electrode reaction occurs.

7 Future Work

Though much research on the influence of the solvent on the rate of electrode reactions has been done in recent years the problem is still far from a profound understanding. The basic question is the role of the dynamic and energetic terms in the control of the kinetics of simple electron-transfer electrode reactions. To answer this question it is essential to have reliable kinetic data for analysis. Unfortunately some kinetic data are too low and should be redetermined, preferably using submicroelectrodes.

Such data, both in single and mixed solvents, should be carefully corrected for the double layer influence. The ion-pairing processes of reactant ions in the solvents should be studied more widely and carefully, because they may significantly influence both thermodynamic and kinetic parameters of electrode reactions.

In the analysis of experimental kinetic data, more attention should be paid to a careful determination of the longitudinal relaxation times. In the literature there are discrepancies between permittivities used for calculation of that parameter from the Debye relaxation time. Static dielectric permittivities and, to some extent, the Debye relaxation times exhibit a dependence on the electrolyte concentration. Therefore, in any analysis of the kinetic data, carefully measured and selected values fo the above parameters should be used.

In future work it would be advisable to study to a greater extent the kinetics of selected organic compounds as model reactants. Though one-electron transfer reactions of such compounds are frequently very fast, the application of submicroelectrodes in the measurement of the kinetic data of such processes should provide good results. Fullerenes are other good subjects for study (for a review see [304]).

Also, more attention should be paid to the study and analysis of electron-transfer reactions in non-Debye solvents which exhibit several relaxation times. Wider use of mixtures composed to two nonaqueous solvents of different Lewis basicity is advised. So far, such studies are rather limited (see, for instance, [227, 305]).

More extensive research should be carried out on complexes which have fixed coordination sphere in the oxidized and reduced forms. Then the role of the primary and further solvation spheres in the kinetics in mixed solvents could be more clearly elucidated. In such studies one should consider, particularly in the case of protic solvents, the interaction between solvent molecules from the first and further solvation shells.

8 References

1. T. Gennett, D.F. Milner, M.J. Weaver, J. Phys. Chem. 89, 2787 (1985).
2. M. Opallo, J. Chem. Soc. Faraday Trans. 1 82, 339 (1986).
3. G.E. McManis, M.N. Golovin, M.J. Weaver, J. Phys. Chem. 90, 6563 (1986).
4. W.R. Fawcett, Langmuir 5, 661 (1989).
5. M. Fleischmann, D. Pletcher, Tetrahedron Lett. 6255 (1968).
6. C. Jehoulet, A.J. Bard, Angew. Chem. 103, 882 (1991).
7. G. Gritzner, Pure Appl. Chem. 62, 1893 (1990).
8. R.A. Marcus, J. Chem. Phys. 43, 679 (1965).
9. R.R. Dogonadze, Quantum Theory of Chemical Reactions in Polar Liquids (in Russian), Znane, Moscow (1973).
10. S.K. Garg, C.P. Smyth, J. Phys. Chem. 69, 1294 (1965).
11. V. Gutmann, E. Wychera, Inorg. Nucl. Chem. Lett. 2, 257 (1966).
12. V. Gutmann, Coordination Chemistry in Non-Aqueous Solutions, Springer, Wien (1969).
13. U. Mayer, V. Gutmann, Monatsh. Chem. 101, 912 (1970).
14. C.K. Mann in: Electroanalytical Chemistry, A.J. Bard (ed.), Dekker, New York (1969), Vol. 3, p. 57.
15. H. Lund, P. Iversen in: Organic Electrochemistry, M. Baizer (ed.), Dekker, New York (1973), p. 208.
16. J.A. Riddick, W.B. Bunger, Organic Solvents, 3rd ed., Wiley, New York (1970).
17. J.F. Coetzee, C.D. Ritchie, Recommended Purification Methods for Selected Solvents, Dekker, New York (1969).
18. J.A. Riddick, W.B. Bunger, T.K. Sakano, Organic Solvents-Physical Properties and Methods of Purification, 4th ed., Wiley, New York (1986).
19. C. Reichardt, Solvents and Solvent Effects in Organic Chemistry, Verlag Chemie, Weinheim (1988).
20. A.J. Fry, W.E. Britton in: Laboratory Techniques in Electroanalytical Chemistry, P.T. Kissinger, W.R. Heineman (eds), Dekker, New York (1984), p. 367.
21. M. Born, Z. Phys. 1, 45 (1920).
22. L.I. Krishtalik, Charge Transfer Reactions in Electrochemical and Chemical Processes, Consultants Bureau, New York (1986).
23. D.F. Evans, T. Tominaga, J.B. Hubbard, P.G. Wolynes, J. Phys. Chem. 20, 2669 (1979).
24. R.R. Dogonadze, A.A. Kornyshev, J. Chem. Soc. Faraday Trans. 1, 70, 1121 (1974).
25. P.G. Wolynes, J. Chem. Phys. 86, 5133 (1987).
26. I. Rips, J. Klafter, J. Jortner, J. Chem. Phys. 88, 3246 (1988).
27. I. Rips, J. Klafter, J. Jortner, J. Chem. Phys. 89, 4188 (1988).
28. E. Grunwald, G. Baughman, G. Kohnstam, J. Am. Chem. Soc. 82, 580 (1960).
29. O. Popovych, A.J. Dill, Anal. Chem. 41, 456 (1969).
30. A.J. Parker, R. Alexander, J. Am. Chem. Soc. 90, 3313 (1968).
31. E.M. Arnett, D.R. McKelvey, J. Am. Chem. Soc. 88, 2598 (1966).

32. B.G. Cox, A.J. Parker, W.E. Waghorne, J. Am. Chem. Soc. 95, 1010 (1973).
33. J. Rais, Coll. Czechoslov. Chem. Commun. 36, 3253 (1971).
34. M. Alfenaar, C.L. de Ligny, A.G. Remijnse, Rec. Trav. Chim. Pays-Bas 86, 986 (1967).
35. R.C. Murray Jr., D.A. Aikens, Electrochim. Acta 21, 1045 (1976).
36. G. Senanayake, D.M. Muir, J. Electroanal. Chem. 237, 149 (1987).
37. K. Izutsu, Anal. Sci. 7, 1 (1991).
38. J.W. Diggle, A.J. Parker, Electrochim. Acta 18, 97 (1973).
39. J.W. Diggle, A.J. Parker, Austr. J. Chem. 27, 1617 (1974).
40. J. Datta, S. Bhattacharya, K.K. Kundu, Aust. J. Chem. 36, 1779 (1983).
41. K. Izutsu, T. Nakamura, M. Muramatsu, J. Electroanal. Chem. 283, 435 (1990).
42. K. Izutsu, T. Nakamura, M. Muramatsu, Y. Aoki, J. Electroanal. Chem. 297, 49 (1991).
43. K. Izutsu, T. Nakamura, T. Kitano, C. Hirasawa, Bull. Chem. Soc. Jpn. 51, 783 (1978).
44. R. Alexander, A.J. Parker, J.H. Sharp, W.E. Waghorne, J. Am. Chem. Soc. 94, 1148 (1972).
45. A.J. Parker, Chem. Rev. 69, 1 (1969).
46. A.J. Parker, Electrochim. Acta 21, 671 (1976).
47. K. Izutsu, T. Nakamura in: Ion-Selective Electrodes. E. Pungor (ed.), Pergamon, Oxford (1989), Vol. 5, p. 425.
48. K. Izutsu, T. Nakamura, I. Takeuchi, N. Karasawa, J. Electroanal. Chem. 144, 391 (1983).
49. K. Izutsu, N. Gozawa, J. Electroanal. Chem. 171, 373 (1984).
50. K. Izutsu, T. Nakamura, N. Gozawa, J. Electroanal. Chem. 178, 165 (1984); idem, ibid., 178, 171 (1984).
51. K. Izutsu, T. Nakamura, M. Muramatsu, J. Electroanal. Chem. 283, 435 (1990).
52. K. Izutsu, T. Nakamura, T. Yamashita, J. Electroanal. Chem. 225, 255 (1987).
53. E.A. Guggenheim, J. Phys. Chem. 33, 842 (1929).
54. V.A. Pleskov, Usp. Khim. 16, 254 (1947).
55. H.M. Koepp, H. Wendt, H. Strehlow, Z. Elektrochem. Ber. Bunsenges. Physik. Chem. 64, 483 (1960).
56. H.P. Schroer, A.A. Vlcek, Z. Anorg. Allg. Chem. 334, 205 (1964).
57. V. Gutmann, Coordination Chemistry in Non-aqueous Solutions, Springer, Vienna (1969).
58. V. Gutmann, R. Schmidt, Monatsh. Chem. 100, 2113 (1969).
59. O. Duscheck, V. Gutmann, Monatsh. Chem. 104, 990 (1973).
60. V. Gutmann, Chemische Funktionslehre, Springer, Vienna (1971).
61. G. Gritzner, P. Rechberger, J. Electroanal. Chem. 109, 333 (1980), G. Gritzner, J. Electroanal. Chem. 144, 259 (1983).
62. A.A. Pendin, Dokl. Akad. Nauk SSSR 241, 404 (1978); A.A. Pendin, S.O. Karabaev, O.M. Susareva, Zh. Fiz. Khim. 61, 972 (1987).
63. G. Gritzner, J. Kuta, Pure Appl. Chem. 56, 461 (1984).
64. L.I. Krishtalik, N.M. Alpatova, E.V. Ovsyannikova, Electrochim. Acta 36, 435 (1991).
65. M. Senda, R. Takahashi, Rev. Polarogr. (Jpn) 20, 56 (1974).
66. C. Madec, J. Courtot-Coupez, J. Electroanal. Chem. 84, 177 (1977).
67. R. Alexander, A.J. Parker, J. Am. Chem. Soc. 89, 5549 (1967).
68. J.F. Coetzee, W.R. Sharp, J. Phys. Chem. 75, 3141 (1971).
69. N. Tanaka, T. Ogata, Inorg. Nucl. Chem. Lett. 10, 511 (1974).
70. T. Kakutani, Y. Morihiro, M. Senda, T. Takahashi, K. Matsumoto, Bull. Chem. Soc. Jpn. 51, 2847 (1978).
71. D. Bauer, J.P. Beck, Bull. Soc. Chim. Fr. 1252 (1973).
72. E. Grunwald, G. Baughmann, G. Kohristan, J. Am. Chem. Soc. 82, 5081 (1960).
73. S. Villermaux, J.-J. Delpuech, J. Chem. Soc. Chem. Commun. 478 (1975).
74. J. Gutknecht, H. Schneider, J. Stroka, Inorg. Chem. 17, 3326 (1978).
75. Y. Marcus, Pure Appl. Chem. 55, 977 (1983).
76. Y. Marcus, Ion Solvation, Wiley, New York (1985).
77. V. Gutmann, The Donor-Acceptor Approach to Molecular Interactions, Plenum, New York (1978).

78. L. Meites, P. Zuman, A. Narayanan, Handbook in Inorganic Electrochemistry, CRC Press, Boca Raton, FL USA (1978).
79. G. Gritzner, J. Phys. Chem. 90, 5478 (1986).
80. T.M. Krygowski, W.R. Fawcett, J. Am. Chem. Soc. 97, 2143 (1975).
81. W.R. Fawcett, T.M. Krygowski, Can. J. Chem. 54, 3283 (1976).
82. V. Gutmann, Top. Curr. Chem. 27, 59 (1972).
83. K. Dimroth, C. Reichardt, T. Siepmann, F. Bohlmann, Liebigs Ann. Chem. 661, 1 (1963).
84. M.J. Kamlet, R.W. Taft, J. Am. Chem. Soc. 98, 377 (1976).
85. J. Broda, Z. Galus, J. Electroanal. Chem. 198, 233 (1986).
86. S. Sahami, M.J. Weaver, J. Electroanal. Chem. 122, 171 (1981).
87. V. Gutmann, G. Peychal-Heiling, Monatsh. Chem. 100, 1423 (1969).
88. H. Elzanowska, Z. Galus, Z. Borkowska, J. Electroanal. Chem. 157, 251 (1983).
89. G. Gritzner, Pure Appl. Chem. 60, 1743 (1988).
90. J. Jaworski, E. Lesniewska, M.K. Kalinowski, J. Electroanal. Chem. 105, 329 (1979).
91. B. Paduszek, M.K. Kalinowski, Electrochim. Acta 28, 639 (1983).
92. J. Jaworski, Electrochim. Acta 31, 85 (1986).
93. D. Dubois, G. Moninot, W. Kutner, M.T. Jones, K.M. Kadish, J. Phys. Chem. 96, 7137 (1992).
94. M.J. Kamlet, J.L.M. Abboud, M.H. Abraham, R.W. Taft, J. Org. Chem. 48, 2877 (1983).
95. P. Lay, J. Phys. Chem. 90, 878 (1986).
96. M. Svaan, V.D. Parker, Acta Chem. Scand. 1338, 759 (1984).
97. J.S. Jaworski, J. Electroanal. Chem. 219, 209 (1987).
98. J.S. Jaworski, M.K. Kalinowski, in: Studies in Organic Chemistry, R.I. Zalewski, T.M. Krygowski, J. Shorter (eds.), Elsevier, Amsterdam (1991), Vol. 42.
99. T.M. Krygowski, M. Lipsztajn, Z. Galus, J. Electroanal. Chem. 42, 261 (1973); M. Lipsztajn, T.M. Krygowski, E. Laren, Z. Galus, idem, ibid 54, 313 (1974).
100. M. Lipsztajn, K. Buchalik, Z. Galus, J. Electroanal. Chem. 105, 341 (1979).
101. R.A. Marcus, Annu. Rev. Phys. Chem. 15, 155 (1964).
102. V.G. Levich, Advances in Electrochemistry and Electrochemical Engineering, P. Delahay (ed.), Interscience, New York (1966), Vol. 4, p. 249.
103. R.R. Dogonadze, A.M. Kuznetsov, Itogi Nauki. Elektrokhimiya, M.M. Mielnikova (ed.), VINITI, Moscow (1969).
104. R.R. Dogonadze, A.M. Kuznetsov, Prog. Surf. Sci. 6, 1 (1975).
105. J. Ulstrup, Charge Transfer Processes in Condensed Media, Springer, Berlin (1979).
106. J.T. Hupp, H.Y. Liu, J.K. Farmer, T. Gennett, M.J. Weaver, J. Electroanal. Chem. 168, 313 (1984).
107. M. Sharp, M. Petersson, K. Endstrom, J. Electroanal. Chem. 109, 271 (1980).
108. Yu.I. Kharkats, Elektrokhimiya 10, 612 (1974).
109. A. Yamagishi, J. Phys. Chem. 80, 1271 (1976); M.E. Peover, J.S. Powell, J. Electroanal. Chem. 20, 427 (1969).
110. J.T. Hupp, M.J. Weaver, J. Phys. Chem. 89, 1601 (1985).
111. P.G. Dzhavakhidze, A.A. Korynshev, L.I. Krishtalik, J. Electroanal. Chem. 228, 329 (1987).
112. J.M. Hale, Reactions of Molecules at Electrodes, N.S. Hush (ed.), Wiley, London (1971), p. 244.
113. S. Sahami, M.J. Weaver, J. Electroanal. Chem. 124, 35 (1981).
114. J.K. Farmer, T. Gennett, M.J. Weaver, J. Electroanal. Chem. 191, 357 (1985).
115. C. Russel, W. Jaenicke, J. Electroanal. Chem. 180, 205 (1984); idem, ibid. 200, 249 (1986).
116. W.R. Fawcett, A. Lasia, J. Phys. Chem. 82, 1114 (1978).
117. M. Grzeszczuk, D.E. Smith, J. Electroanal. Chem. 157, 205 (1983).
118. W.R. Fawcett, J. Jaworski, J. Phys. Chem. 87, 2972 (1983).
119. W.R. Fawcett, Y.I. Kharkats, J. Electroanal. Chem. 47, 413 (1973).
120. Yu.I. Kharkats, Elektrokhimiya 12, 592 (1976).
121. Yu.I. Kharkats, Elektrokhimiya 12, 1284 (1976); ibid. 12, 1866 (1976).

122. G. Grampp, W. Jaenicke, Ber. Bunsenges. Phys. Chem. 88, 325 (1984); idem, ibid. 88, 335 (1984); G. Grampp, W. Jaenicke, Ber. Bunsenges. Phys. Chem. 95, 904 (1991).
123. W. R. Fawcett, M. Fedurco, J. Phys. Chem. 97, 7075 (1993).
124. Yu. I. Kharkats, H. Nielsen, J. Ulstrup, J. Electroanal. Chem. 169, 47 (1984).
125. G. E. McManis, M. J. Weaver, J. Chem. Phys. 90, 1720 (1989).
126. W. R. Fawcett, L. Blum, Chem. Phys. Lett. 187, 173 (1991).
127. E. D. German, A. M. Kuznetsov, Elektrokhimiya 26, 931 (1990); idem, Electrochim. Acta 26, 1595 (1981).
128. D. K. Phelps, A. A. Kornyshev, M. J. Weaver, J. Phys. Chem. 96, 1454 (1990).
129. M. J. Weaver, T. L. Satterberg, J. Phys. Chem. 81, 1772 (1977).
130. H. Reiss, J. Chem. Phys. 18, 996 (1950).
131. J. T. Hupp, M. J. Weaver, J. Electroanal. Chem. 152, 1 (1983).
132. B. S. Brunschwig, C. Creutz, D. H. Macartney, T. K. Sham, S. Sutin, Faraday Discuss. Chem. Soc. 74, 113 (1982).
133. R. A. Marcus, Int. J. Chem. Kin. 13, 865 (1981).
134. M. J. Weaver, Inorg. Chem. 18, 402 (1979).
135. B. S. Brunschwig, J. Logan, M. D. Newton, N. Sutin, J. Am. Chem. Soc. 102, 5798 (1980).
136. B. L. Tembe, H. L. Newton, M. D. Newton, J. Chem. Phys. 76, 1490 (1982).
137. M. J. Weaver, in: Comprehensive Chemical Kinetics, R. D. Compton (ed.), Elsevier, New York (1987), Vol. 27.
138. J. T. Hupp, M. J. Weaver, J. Phys. Chem. 88, 1463 (1984).
139. J. M. Hale, J. Electroanal. Chem. 19, 315 (1968).
140. L. D. Zusman, Chem. Phys. 49, 295 (1980).
141. L. D. Zusman, Chem. Phys. 80, 29 (1983).
142. I. V. Aleksandrov, Chem. Phys. 51, 449 (1980).
143. M. Ya. Ovchinnikova, Theor. Exp. Khim. 17, 651 (1981).
144. D. F. Calef, P. G. Wolynes, J. Phys. Chem. 87, 3387 (1983).
145. D. F. Calef, P. G. Wolynes, J. Chem. Phys. 78, 470 (1983).
146. L. D. Zusman, Elektrokhimiya, 21, 621 (1985).
147. A. Kapturkiewicz, B. Behr, J. Electroanal. Chem. 179, 187 (1984).
148. M. J. Weaver, T. Gennett, Chem. Phys. Lett. 113, 213 (1985).
149. M. Opallo, A. Kapturkiewicz, Electrochim. Acta 30, 1301 (1985).
150. A. Kapturkiewicz, M. Opallo, J. Electroanal. Chem. 185, 15 (1985).
151. H. Fröhlich, Theory of Dielectrics, Oxford University Press, London (1949).
152. R. M. Nielson, G. E. McManis, M. N. Golovin, M. J. Weaver, J. Phys. Chem. 92, 3441 (1988).
153. P. G. Wolynes, J. Chem. Phys. 68, 473 (1978).
154. P. Colonomos, P. G. Wolynes, J. Chem. Phys. 71, 2644 (1979).
155. J. H. Chen, S. A. Adelman, J. Chem. Phys. 72, 2819 (1980).
156. J. B. Hubbard, P. J. Stiles, Chem. Phys. Lett. 114, 121 (1985).
157. B. Bagchi, A. Chandra, G. R. Fleming, J. Phys. Chem. 94, 5197 (1990).
158. L. D. Zusman, Electrochim. Acta 36, 395 (1991).
159. H. Sumi, R. A. Marcus, J. Chem. Phys. 84, 4894 (1986).
160. A. Nadler, R. A. Marcus, J. Chem. Phys. 86, 3906 (1987).
161. W. R. Fawcett, C. A. Foss Jr., J. Electroanal. Chem. 270, 103 (1989).
162. M. J. Weaver, Chem. Rev. 92, 463 (1992).
163. M. J. Weaver, D. K. Phelps, R. M. Nielson, M. N. Golovin, G. E. McManis, J. Phys. Chem. 94, 2949 (1990).
164. R. M. Nielson, M. J. Weaver, J. Electroanal. Chem. 260, 15 (1989).
165. W. Harrer, G. Grampp, W. Jaenicke, J. Electroanal. Chem. 209, 223 (1986).
166. W. R. Fawcett, C. A. Foss Jr., J. Electroanal. Chem. 252, 221 (1988).
167. G. Grampp, W. Harrer, W. Jaenicke, J. Chem. Soc. Faraday Trans. 1, 83, 161 (1987); idem, ibid. 84, 366 (1988).
168. G. Grampp, A. Kapturkiewicz, W. Jaenicke, Ber. Bunsenges. Phys. Chem. 94, 439 (1990).

169. W. R. Fawcett, C. A. Foss Jr., J. Electroanal. Chem. 306, 71 (1991).
170. W. R. Fawcett, C. A. Foss Jr., Electrochim. Acta 36, 1767 (1991).
171. A. Kapturkiewicz, B. Behr, Inorg. Chim. Acta 69, 247 (1983).
172. G. M. Brisard, M. Manzini, A. Lasia, J. Electroanal. Chem. 326, 317 (1992).
173. K. M. Kadish, J. Q. Ding, T. Malinski, Anal. Chem. 56, 1741 (1984).
174. S. U. M. Khan, J. Chem. Soc. Faraday Trans. 1, 85, 2001 (1989).
175. A. Urbanczyk, K. Wrzesinska, M. K. Kalinowski, Pol. J. Chem. 61, 247 (1987).
176. X. H. Mu, F. A. Shultz, J. Electroanal. Chem. 353, 349 (1993).
A. Urbanczyk, Ph. D. Thesis, University of Warsaw (1990).
177. W. R. Fawcett, M. Opallo, J. Electroanal. Chem. 331, 815 (1992).
178. X. Zhang, J. Leddy, A. J. Bard, J. Am. Chem. Soc. 107, 3719 (1985).
179. M. Sharp, J. Electroanal. Chem. 88, 193 (1978).
180. D. K. Phelps, M. T. Ramm, Y. Wang, S. F. Nelsen, M. J. Weaver, J. Phys. Chem. 97, 181 (1993).
181. H. Fernandez, M. A. Zon, J. Electroanal. Chem. 332, 237 (1992).
182. D. A. Corrigan, D. H. Evans, J. Electroanal. Chem. 233, 161 (1987).
183. M. Grzeszczuk, D. E. Smith, J. Electroanal. Chem. 198, 245 (1986).
184. G. E. McManis, A. Gochev, R. M. Nielson, J. M. Weaver, J. Phys. Chem. 93, 7733 (1989).
185. A. P. Abbott, J. F. Rusling, J. Phys. Chem. 94, 8910 (1990).
186. J. S. Jaworski, P. Leszczynski, M. K. Kalinowski, J. Electroanal. Chem. 358, 203 (1993).
187. D. O. Wipf, E. W. Kristensen, M. R. Deakin, R. M. Wightman, Anal. Chem. 60, 306 (1988).
188. A. Baranski, K. Winkler, W. R. Fawcett, J. Electroanal. Chem. 313, 367 (1991).
189. A. Baranski, W. R. Fawcett, J. Electroanal. Chem. 100, 185 (1979).
190. P. Delahay, Double Layer and Electrode Kinetics. Interscience, New York (1965).
191. E. Ahlberg, V. D. Parker, Acta Chem. Scand. 837, 723 (1983).
192. T. Gennet, M. J. Weaver, J. Electroanal. Chem. 186, 179 (1985).
193. W. Mayrhofer, A. Lasia, G. Gritzner, J. Electroanal. Chem. 317, 219 (1991).
194. H. L. Friedman, J. Chem. Soc., Faraday Trans. 2, 79, 1465 (1982).
195. S. J. Bass, W. I. Nathan, R. M. Meighan, R. H. Cole, J. Phys. Chem. 68, 509 (1964).
196. Ju. Ja. Karapetyants, V. I. Eychis, Fiziko-Khimicheskiye Svoistva Elektrolitnykh Nevodnykh Rastvorov, Khimiya, Moscow (1989).
197. H. Behret, F. Schmithals, J. Barthel, Z. Phys. Chem. N.F. 96, 73 (1975).
198. P. Winsor IV, R. H. Cole, J. Phys. Chem. 86, 2486 (1982).
199. J. Barthel, R. Buchner, Pure Appl. Chem. 58, 1077 (1986).
200. J. T. Hynes, J. Phys. Chem. 90, 3701 (1986).
201. G. E. McManis, M. J. Weaver, J. Chem. Phys. 90, 912 (1989).
202. J. Barthel, F. Feuerlein, J. Solution Chem. 13, 393 (1984).
203. W. R. Fawcett, Chem. Phys. Lett. 174, 167 (1990).
204. M. D. Newton, Int. J. Quantum Chem., Symp. 14, 363 (1980); idem ACS Symposium Ser. No. 198, American Chemical Society, Washington DC (1982), p. 255.
205. J. Logan, M. D. Newton, J. Chem. Phys. 78, 4086 (1983).
206. G. E. McManis, A. K. Mishra, M. J. Weaver, J. Chem. Phys. 86, 5550 (1987).
207. A. Gochev, G. E. McManis, M. J. Weaver, J. Chem. Phys. 91, 906 (1989).
208. B. Bagchi, Annu. Rev. Phys. Chem. 40, 115 (1989).
209. M. Newton, Chem. Rev. 91, 767 (1991).
210. L. Dandoy, L. Gierst, J. Electroanal. Chem. 2, 116 (1961).
211. W. Gorski, J. Lipkowski, J. Electroanal. Chem. 123, 157 (1981).
212. J. W. Diggle, A. J. Parker, D. A. Owensby, Aust. J. Chem. 28, 237 (1975).
213. A. Baranski, W. R. Fawcett, J. Electroanal. Chem. 94, 237 (1978).
214. A. S. Baranski, W. R. Fawcett, J. Chem. Soc. Faraday Trans. 1, 76, 1962 (1980).
215. G. J. Hills, L. M. Peter, J. Electroanal. Chem. 50, 175 (1974).
216. C. Cronnolly, K. Chandrasekara Pillai, W. E. Waghorne, J. Electroanal. Chem. 207, 177 (1986).
217. J. Chlistunoff, Z. Galus, J. Electroanal. Chem. 267, 171 (1989).

218. W.R. Fawcett, J. Jaworski, J. Chem. Soc. Faraday Trans. 1, 78, 1971 (1982).
219. J. Chlistunoff, T. Jedral, Z. Galus, J. Electroanal. Chem. 236, 177 (1987).
220. B. Behr, J. Taraszewska, J. Stroka, J. Electroanal. Chem. 58, 71 (1975).
221. J. Taraszewska, A. Walega, J. Electroanal. Chem. 171, 243 (1978).
222. J. Stroka, K. Maksymiuk, Z. Galus, J. Electroanal. Chem. 167, 211 (1984).
223. J. Taraszewska, A. Walega, J. Electroanal. Chem. 200, 261 (1986).
224. W. Jaenicke, P.H. Schweitzer, Z. Phys. Chem. N. F. 52, 104 (1967).
225. A. Broda, J. Stroka, Z. Galus, Electrochim. Acta 28, 817 (1983).
226. J. Stroka, K. Maksymiuk, A. Mital, J. Electroanal. Chem. 272, 145 (1989).
227. T. Biegler, E.R. Gonzales, R. Parsons, Collect. Czech. Chem. Commun. 36, 853 (1971).
228. J. Broda, Z. Galus, J. Electroanal. Chem. 130, 229 (1981).
229. J. Broda, Z. Galus, Electrochim. Acta 28, 1523 (1983).
230. J. Broda, Z. Galus, J. Electroanal. Chem. 145, 147 (1983).
231. J. Chlistunoff, Z. Galus, J. Electroanal. Chem. 193, 175 (1985).
232. J. Taraszewska, A. Broda, J. Electroanal. Chem. 153, 243 (1983).
233. L. Janiszewska, Z. Galus, Electrochim. Acta. 29, 1419 (1984).
234. J.E.B. Randles, Transaction of Symposium on Electrode Processes, E. Yeager (ed), Wiley, New York (1961), p 209.
235. K. Maksymiuk, Z. Galus, J. Electroanal. Chem. 234, 361 (1987).
236. A.S. Baranski, W.R. Fawcett, J. Chem. Soc. Faraday Trans. 1, 78, 1279 (1982).
237. A.S. Baranski, M.A. Drogowska, W.R. Fawcett, J. Electroanal. Chem. 215, 237 (1986).
238. W.R. Fawcett, J. Phys. Chem. 93, 2675 (1989).
239. G.M. Brisard, A. Lasia, J. Electroanal. Chem. 314, 103 (1991).
240. G.M. Brisard, A. Lasia, J. Electroanal. Chem. 221, 129 (1987).
241. A. Lasia, G. Brisard, J. Electroanal. Chem. 266, 69 (1989).
242. G. Gritzner, F. Horzenberger, J. Chem. Soc. Faraday Trans. 88, 3013 (1992).
243. G.T. Hefter, J.P. McLay, J. Solution Chem. 17, 535 (1988).
244. L.S. Frankel, C.H. Langford, T.R. Stengle, J. Phys. Chem. 74, 1376 (1970).
245. L.P. Scott, T.J. Weeks Jr., D.E. Bracken, E.L. King, J. Am. Chem. Soc. 91, 5219 (1969).
246. H. Schneider, Electrochim. Acta 21, 711 (1976).
247. J.J. Delpuech, A. Peguy. M.R. Khaddar, J. Magn. Reson. 6, 325 (1972).
248. L.S. Frankel, T.R. Stengle, C.H. Langford, J. Chem. Soc. Chem. Commun. 393 (1965).
249. A.K. Covington, T.H. Lilley, K.E. Newman, G.A. Porthouse, J. Chem. Soc. Faraday Trans. 1, 69, 963 (1973); A.K. Covington, K.E. Newman, T.H. Lilley, ibid 69, 973 (1973).
250. H.-J. Chuang, L.-L. Soong, G.E. Leroi, A.I. Popov, J. Solution Chem. 18, 759 (1989).
251. H.-H. Fuldner, H. Strehlow, Ber. Bunsenges. Phys. Chem. 86, 68 (1982).
252. C.F. Wells, in: Thermodynamic Behavior of Electrolytes in Mixed Solvents – II, W.F. Further (ed), American Chemical Society, Washington DC (1979).
253. V.S. Goncharov, P.S. Yastremskii, J.M. Kessler, R.Kh. Bratishko, A.I. Mishustin, V.P. Yemelin, Zhurn. Fiz. Khim. 51, 789 (1977).
254. A.K. Covington, K.E. Newman, Pure Appl. Chem. 51, 2041 (1979).
255. B.G. Cox, A.J. Parker, W.E. Waghorne, J. Phys. Chem. 78, 1731 (1974).
256. D.R. Cogley, J.N. Butler, E. Grunwald, J. Phys. Chem. 75, 1477 (1971).
257. R.C. Larson, R.T. Iwamoto, Inorg. Chem. 1, 316 (1962).
258. D.C. Luehrs, J. Inorg. Nucl. Chem. 33, 2701 (1971).
259. D.C. Luehrs, R.W. Nichols, D.A. Hamm, J. Electroanal. Chem. 29, 417 (1971).
260. K. Izutsu, T. Nomura, T. Nakamura, H. Kazama, S. Nakaijma, Bull. Chem. Soc. Jpn. 47, 1657 (1974).
261. Y. Marcus, Aust. J. Chem. 36, 1719 (1983).
262. H. Strehlow, H. Schneider, Pure Appl. Chem. 25, 327 (1971).
263. O. Popovych, Crit. Rev. Anal. Chem. 1, 73 (1970).
264. H. Schneider, Top. Curr. Chem. 68, 105 (1976).
265. J. Taraszewska, Wiad. Chem. 42, 481 (1988).

266. K. Dimroth, C. Reichardt, Z. Anal. Chem. 215, 344 (1966); Z.B. Maksimovic, C. Reichardt, A. Spiric, Z. Anal. Chem. 270, 100 (1974).
267. T.M. Krygowski, C. Reichardt, P.K. Wrona, C. Wyszomirska, U. Zielkowska, J. Chem. Res. (S) 116 (1983).
268. P.K. Wrona, T.M. Krygowski, U. Zielkowska, Z. Naturforsch. 44, 673 (1989).
269. Y. Marcus, J. Chem. Soc. Perkin Trans. 2, 1015 (1994); idem, ibid., 1751 (1994).
270. M.H. Miles, H. Gerischer, J. Electrochem. Soc. 118, 837 (1971)
271. J. Lipkowski, Z. Galus, J. Electroanal. Chem. 48, 337 (1973).
272. J. Lipkowski, Z. Galus, J. Electroanal. Chem. 58, 51 (1975).
273. B.N. Afanasev, G.G. Serdjukova, Elektrokhimiya 22, 1141 (1986).
274. G.G. Serdjukova, A.V. Lizogub, B.N. Afanasev, Elektrokhimiya 22, 840 (1986).
275. L. Janiszewska, Z. Galus, Electrochim. Acta 27, 1781 (1982).
276. B. Behr, Z. Borkowska, H. Elzanowska, J. Electroanal. Chem. 100, 853 (1979).
277. L. Kisova, L. Reichstadter, J. Komenda, J. Electroanal. Chem. 230, 155 (1987).
278. M. Cetnarska, K. Maksymiuk, J. Stroka, Electrochim. Acta 33, 11 (1988).
279. W. Gorski, Z. Galus, J. Electroanal. Chem. 237, 209 (1987).
280. L. Kisova, J. Langpaul, J. Komenda, Electrochim. Acta 33, 439 (1988).
281. J. Lipkowski, A. Czerwinski, E. Cieszynska, Z. Galus, J. Sobkowski, J. Electroanal. Chem. 119, 261 (1981).
282. N. Tanaka, K.-I. Kanno, A. Yamada, J. Electroanal. Chem. 65, 703 (1975).
283. R. Parsons, J. O'M. Bockris, Trans. Faraday Soc. 45, 916 (1949).
284. W. Gorski, Z. Galus, J. Electroanal. Chem. 201, 283 (1986).
285. W. Gorski, Z. Galus, Electrochim. Acta 33, 1397 (1988).
286. M. Cetnarska, J. Stroka, J. Electroanal. Chem. 234, 263 (1987).
287. J. Malyszko, M. Scendo, J. Electroanal. Chem. 250, 61 (1989).
288. R. Parsons, Ann. Univ. Ferrara, Ser. V, Suppl. 5/3 (1970).
289. R. Parsons, J. Electroanal. Chem. 21, 35 (1969).
290. J. Lipkowski, Z. Galus, J. Electroanal. Chem. 61, 11 (1975).
291. M. Goledzinowski, L. Kisova, J. Lipkowski, Z. Galus, J. Electroanal. Chem. 95, 43 (1979).
292. B. Behr, Adsorption on Mercury Electrodes from Water-Organic Mixed Solvents (in Polish), Panstwowe Wydawnictwo Naukowe, Warsaw (1976).
293. K. Maksymiuk, J. Stroka, Z. Galus, Pol. J. Chem. 61, 529 (1987).
294. J. Heyrovsky, J. Kuta, Principles of Polarography, Academic Press, New York (1966).
295. A. Aramata, P. Delahay, J. Phys. Chem. 68, 880 (1964).
296. L. Kisova, Scr. Fac. Sci. Nat. UJEP Brun. Chemia 5, 41 (1975).
297. K. Maksymiuk, J. Stroka, Z. Galus, J. Electroanal. Chem. 181, 51 (1984).
298. K. Maksymiuk, J. Stroka, Z. Galus, J. Electroanal. Chem. 248, 35 (1988).
299. B.N. Afanasev, Ju.P. Skobochkina, Elektrokhimiya 25, 1357 (1989).
300. J. Wilson, O. Hwa Kai Ting, J. Lipkowski, A. Czerwinski, J. Electroanal. Chem. 247, 85 (1988).
301. W. Gorski, Z. Galus, J. Electroanal. Chem. 312, 27 (1991).
302. K. Maksymiuk, Z. Galus, Electrochim. Acta 34, 415 (1989).
303. J.S. Jaworski, Z. Kebede, M. Malik, J. Electroanal. Chem. 333, 371 (1992).
304. M. Opallo, Pol. J. Chem. 67, 2093 (1993).
305. L. Kisova, J. Jurik, J. Komenda, J. Electroanal. Chem. 366, 93 (1994).

Advances in Electrochemical Science and Engineering
Edited by Heinz Gerischer and Charles W. Tobias

Charge Transfer Kinetics at Water-Organic Solvent Phase Boundaries

Z. Samec[1] and T. Kakiuchi[2]

[1] The J. Heyrovský Institute of Physical Chemistry, Dolejškova 3, 18223 Prague 8, Czech Republic
[2] Department of Physical Chemistry, Yokohama National University, Tokiwadai 156, Hodogaya-ku, Yokohama 240, Japan

Contents

List of Symbols

a	activity
A	interfacial area (m^2)
c^x	particle concentration in the bulk solution (W, O) or at a specified position x ($mol\,m^{-3}$)
d	thickness of Helmholtz inner layer (m)
D_i^x	diffusion coefficient of a particle i in the bulk solution (W, O) or at a specified position x ($m^2\,s^{-1}$)
e	electronic charge (C)
E	electrical potential differences across a galvanic cell (V)
E^0	standard potential difference across a galvanic cell; standard potential of a charge transfer reaction (V)
$E_{1/2}^{rev}$	reversible half-wave potential of a charge transfer reaction (V)
$E_{O/R}^0$	standard redox potential of a redox couple O/R on the hydrogen scale (V)
F	Faraday constant, $9.648456\times10^4\,C\,mol^{-1}$
$\bar{G}_i^0$	standard electrochemical Gibbs energy of a particle i ($kJ\,mol^{-1}$)
G_i^0	standard chemical Gibbs energy of a particle i ($kJ\,mol^{-1}$)
h	Planck constant, $6.626176\times10^{-34}\,J\,s$
I	electrical current (A)
J	material flux in the direction from the phase W to the phase O ($mol\,m^{-2}\,s^{-1}$)
$\bar{k}\,(\vec{k}_t)$	apparent (true, corrected) forward rate constant of a charge transfer reaction ($m\,s^{-1}$, $m^4\,mol^{-1}\,s^{-1}$)
k_0^s	apparent rate constant at the standard potential E^0 of a charge transfer reaction; apparent standard rate constant ($m\,s^{-1}$, $m^4\,mol^{-1}\,s^{-1}$)
k_B	Boltzmann constant, $1.380662\times10^{-23}\,J\,K^{-1}$
$K=\bar{k}/\vec{k}$	equilibrium constant: ratio of the backward and forward rate constants
L	distance between locations of two neighboring potential barriers or equilibrium positions in ion diffusion jumps (m)
m	particle mass (kg); convolution integral ($A\,s^{1/2}$)
M	molar particle mass ($kg\,mol^{-1}$)
n	number of electrons transferred in an electron transfer reaction
N_A	Avogadro's number, $6.022045\times10^{23}\,mol^{-1}$
$p(x,t)$	probability of a particle having the coordinate x at time t
r	critical radius of pore (m)
R	molar gas constant, $8.31441\,J\,mol^{-1}\,K^{-1}$
t	time (s); transference number
T	temperature (K)
$v(t)$	translational velocity of ion motion ($m\,s^{-1}$)
x	coordinate perpendicular to the interface (m)
z	ion charge number; partition function
Z	pre-exponential or frequency factor

$\vec{\alpha}(\vec{\alpha}_0)$	apparent charge transfer coefficient (at the standard potential) for the forward charge transfer
β	Brønsted coefficient
γ	activity coefficient
Γ	surface excess (mol m^{-2})
$\Delta_x^y\phi$	electrical potential difference between two locations or phases y and x (V)
$\Delta_x^y\bar{G}_i^0$	standard electrochemical Gibbs energy change for transfer of a particle i from the location or phase x to y (kJ mol^{-1}) (transition state is denoted by asterisk)
$\Delta_x^y G_i^0$	standard chemical Gibbs energy change for transfer of a particle i from the location or phase x to y (kJ mol^{-1})
$\Delta_x^y H_i^0$	standard enthalpy change for transfer of a particle i from the location or phase x to y (kJ mol^{-1})
$\Delta_x^y S_i^0$	standard entropy change for transfer of a particle i from the location or phase x to y (J mol^{-1} K^{-1})
$\Delta\bar{G}_i^*$	standard electrochemical Gibbs energy of activation at $\Delta_a^b\bar{G}_i^0 = 0$
ε	dielectric constant
η	viscosity (N s m^{-2})
κ	transport parameter
λ	reorganization energy (kJ mol^{-1})
ζ	friction coefficient (kg s^{-1} mol^{-1})
Π	surface pressure (J m^{-2})
ϕ	electrical potential (V)
Φ (1,2)	two-particle distribution function
ω	angular frequency (s^{-1})

Abbreviations

A	electron acceptor
ac	alternating current
BLM	bilayer lipid membrane
Bu	butyl
D	electron donor
DAPC	diarichidoylphosphatidylcholine
DBPC	dibehenoylphosphatidylcholine
dc	direct current
DCC^-	dicarbollylcobaltate
DLPC	dilauroylphosphatidylcholine
DLPE	dilauroylphosphatidylethanolamine
DMPC	dimyristoylphosphatidylcholine
DPPC	dipalmitoylphosphatidylcholine
DSPC	distearoylphosphatidylcholine
Et	ethyl
Fc	ferrocene
$HTMA^+$	hexadecyltrimethylamonium ion
Hx	hexyl
ITIES	interface between two immiscible electrolyte solutions
Me	methyl
O	organic phase
Pi^-	picrate
Ph	phenyl
Pn	pentyl
Pr	propyl
V	viologene
W	aqueous phase

1 Introduction

Electrochemistry at the interface between two immiscible electrolyte solutions (ITIES) has a long history dating back to the end of the 19th century [1], shortly after Lippmann's electrocapillarity studies [2]. However, more than 80 years elapsed before its fully fledged development, which came after the establishment of two pillars in this field: one an experimental method for realizing a polarizable ITIES, by Gavach [3], and the other the concept of polarizability of ITIES based on the standard free energy of ion transfer, by Koryta [4]. After these two key contributions, electrochemistry dealing with structure and charge transfer at ITIES has rapidly grown to become a new branch of electrochemistry. In the earlier stage of the development, the analogy in methodology between the study of electrochemical processes at ITIES and that at electrode-solution interfaces played a vital role. The arsenal of key concepts in electrochemistry has been utilized effectively in analyzing what is occurring at ITIES, e.g., reversibility of charge transfer, significance of half-wave potential, and properties of current-potential characteristics for various modes of controlling potential or current.

It has become increasingly clear, however, that the properties intrinsic to ITIES should be studied beyond this simple analogy. Whereas electrochemistry of the reversible charge transfer is influenced only by bulk properties of matter, e.g., the standard potential of charge transfer and diffusion coefficient, the interfacial structure and the charge transfer mechanism at ITIES are primarily revealed in the kinetics of charge transfer processes. Since the ion transfer across ITIES is the process of the transport of charged particles in anisotropic media, with respect to both solvent orientation and ion distribution, detailed analysis of the ion transfer will reveal the dynamics of ion-solvent and ion-ion interactions which are not observed in homogeneous media. The same is true in electron transfer processes at ITIES.

Recent fundamental improvements in experimental methods for studying the structure and kinetics at ITIES, on the one hand, and theoretical developments in describing the double layer structure and charge transfer kinetics – the contributions mainly from the field of statistical mechanics – on the other hand, have provided us with factual and conceptual means of elucidating dynamic aspects at ITIES.

The primary purpose of this review is to summarize comprehensively advances in the study of this kinetic aspect of charge transfer across ITIES since 1981, when Koryta and Vanysek gave a timely review at that early stage of the development of electrochemistry at ITIES. Reviews [5–14] and monographs [15, 16] are available of other aspects of the electrochemistry at ITIES, e.g., ion transfer facilitated by ionophores, applications to analytical purposes or to liquid extraction, and instrumentation. In a recent review on charge transfer across ITIES, Girault [14] addressed key issues regarding the mechanism of ion transfer: the dependence of the rate constant of ion transfer on the applied potential, the presence of an activation barrier, the double layer correction, the effect of solvent viscosity, theoretical treatments, etc. Since the author's [14] opinions differ in several respects from ours, we have tried to review this subject as systematically and critically as possible.

In Sec. 2, we will briefly summarize current understanding of equilibrium properties of ion partition and of double layer structure at ITIES, insomuch as the present review of the kinetics of charge transfer is concerned. Considerable progress has been made in the last decade in the study of adsorption phenomena at ITIES, which has significant relevance to charge transfer kinetics and will also be discussed in Sec. 2. Section 3 deals with ion transfer kinetics, of which our understanding has been deepened in the past ten years. Various models for the mechanism of ion transfer across ITIES have been proposed since 1981. We first summarize their features and physical meanings. Comparison with experimentally obtained kinetic parameters will then be described. Most of the studies of facilitated ion transfer at ITIES so far reported are concerned with reversible processes. We briefly touch upon contributions to the kinetics of facilitated ion transfer. Electron transfer at ITIES, another field in which we have seen a significant progress since 1981, will be dealt with in Sec. 4, including the subject of photo-assisted electron transfer.

2 Equilibrium Properties

2.1 Distribution Potential

Distribution potential established when ionic species are partitioned in equilibrium between the aqueous and organic phases, W and O, is a fundamental quantity in electrochemistry at liquid-liquid interfaces, through which the equilibrium properties of the system are determined. In any system composed of two immiscible electrolyte solutions in contact with each other, the equilibrium is characterized by the equality of the electrochemical or chemical potentials for each ionic or neutral species, respectively, commonly distributed in the two phases [4]. It follows from the former equality that the distribution potential $\Delta_O^W \phi$, which is the inner electrical potential of the aqueous phase, ϕ^W, with respect to the inner potential of the organic phase, ϕ^O, is given by the Nernst equation [17, 18],

$$\Delta_O^W \phi = \Delta_O^W \phi_i^0 + \frac{RT}{z_i F} \ln \frac{a_i^O}{a_i^W} \tag{1}$$

where R is the gas constant, T the absolute temperature, F the Faraday constant, z_i the ion charge number and a_i^α (α = O or W) is the activity of i in α. The standard ion transfer potential, $\Delta_O^W \phi_i^0$, is defined in terms of the difference of the standard chemical potentials for the ionic species i, which is the standard Gibbs energy of transfer of the ion i from the organic phase to the aqueous phase, $\Delta_W^O G_i^0$,

$$\Delta_O^W \phi_i^0 = -\frac{1}{z_i F} \Delta_W^O G_i^0 \tag{2}$$

$\Delta_W^O G_i^0$ and $\Delta_O^W \phi_i^0$ are not experimentally accessible quantities, e.g., the standard ion transfer potential can be measured with respect to the potential difference between the two terminals of an electrochemical cell using two appropriate reference electrodes. The values of these quantities have been compiled for several organic solvent-water systems on the basis of a nonthermodynamic assumption [4, 11]. In general, the values of the Gibbs energy of transfer of an ion in Eq. (2) differ from those for the transfer from one pure solvent to another pure solvent.

Hung derived a general expression for calculating the distribution potential from the initial concentrations of ionic species, their standard ion transfer potentials, and the volumes of the two phases [19]. When all ionic species in W and O are completely dissociated, and the condition of electroneutrality holds in both phases, the combination of Nernst equations for all ionic species with the conservation of mass leads to

$$\sum_i \frac{z_i c_i^{0,W}}{1+r(\gamma_i^W/\gamma_i^O)e_i} + \sum_i \frac{rz_i c_i^{0,O}}{1+r(\gamma_i^W/\gamma_i^O)e_i} = 0 \tag{3}$$

where $c_i^{0,\alpha}$ (α = W or O) is the initial concentration of ion i in the phase α, r is the ratio of the volume of O to that of W, γ_i^O and γ_i^W are activity coefficients of i in O and W, and

$$e_i = \exp\left[\frac{z_i F}{RT}(\Delta_O^W\phi - \Delta_O^W\phi_i^0)\right] \tag{4}$$

In Eq. (3), summations are taken for all ionic species. The only unknown in Eq. (3) is $\Delta_O^W\phi$. By knowing initial concentrations of ionic species and their standard ion transfer potentials, together with the volumes of W and O phases, the distribution potential can be calculated by solving Eq. (3). The concentration of each ionic component at a distribution equilibrium can then be obtained through $\Delta_O^W\phi$ using the relation

$$c_i^W = c_i^{0,W}[r(\gamma_i^W/\gamma_i^O)e_i + 1]^{-1} \tag{5}$$

and the Nernst equation.

The classification of ITIES based on the $\Delta_O^W\phi_i^0$ values of ions dissolved in the two phases was first introduced by Koryta [4].

When all ions initially reside in W phase, Eq. (3) reduces to

$$\sum_k z_k(\gamma_k^W/\gamma_k^O)c_k^{0,W}\prod_{j\neq k}[1+r(\gamma_j^W/\gamma_j^O)e_j] = 0 \tag{6}$$

where $j \neq k$ under the product II means that the product is taken over all ionic species except k. An interesting limiting case of the distribution equilibrium is obtained from Eq. (6). When $r \to 0$, i.e., the volume of the organic phase is very small compared with that of the aqueous phase [20],

$$\sum_k z_k(\gamma_k^{\mathrm{W}}/\gamma_k^{\mathrm{O}})c_k^{0,\mathrm{W}}\left[\sum_{j\neq k}(\gamma_k^{\mathrm{W}}/\gamma_k^{\mathrm{O}})e_j\right]=0 \tag{7}$$

In this limiting case, the distribution potential, and hence the equilibrium concentrations of ionic species, do not depend on the volumes of W and O. Equation (7) is useful in calculating the distribution equilibria in systems involving small particles, e.g., emulsions and thin membranes.

The treatment of partition equilibrium was further generalized to the cases in the presence of ion-pair formation [19] and ion-ionophore complex formation [21]. An important corollary of this theory of partition equilibrium based on standard ion transfer potentials of single ions is to give a new interpretation to liquid extraction processes. Kakutani et al. analyzed the extraction of anions with tris(1,10-phenanthroline) iron(II) cation from the aqueous phase to nitrobenzene [22], which demonstrated the effectiveness of the theory and gave a theoretical backbone for ion-pair extraction from an electrochemical point of view.

When each of the aqueous and organic phases contains one redox couple, O1/R1 in W and O2/R2 in O, and no appreciable partition of ionic components including these redox couples takes place, the reaction at the inferface

$$\mathrm{O1\,(W)+R2\,(O)=R1\,(W)+O2\,(O)} \tag{8}$$

ensures a contact equilibrium [23] and $\Delta_{\mathrm{O}}^{\mathrm{W}}\varphi$ is given by [24]

$$\Delta_{\mathrm{O}}^{\mathrm{W}}\phi=E_{\mathrm{O2/R2}}^{\mathrm{O},0}-E_{\mathrm{O1/R1}}^{\mathrm{W},0}+\Delta_{\mathrm{O}}^{\mathrm{W}}\phi_{\mathrm{H^+}}^{0}+\frac{RT}{nF}\ln\frac{a_{\mathrm{O2}}^{\mathrm{O}}a_{\mathrm{R1}}^{\mathrm{W}}}{a_{\mathrm{R2}}^{\mathrm{O}}a_{\mathrm{O1}}^{\mathrm{W}}} \tag{9}$$

where $E_{\mathrm{O1/R1}}^{\mathrm{W},0}$ and $E_{\mathrm{O2/R2}}^{\mathrm{O},0}$ are the standard redox potentials of O1/R1 in O and O2/R2 in W related to the standard $\mathrm{H^+/H_2}$ reference electrode in the respective phases, $\Delta_{\mathrm{O}}^{\mathrm{W}}\varphi_{\mathrm{H^+}}^{0}$ is the standard proton transfer potential (cf. Eq. (2)), n is the number of electrons transferred in reaction (8) and a_j^{α} ($j=$ O1, R1, O2, or R2; α is O or W) is the activity of j in α. The potential drop across the interface is thus determined by the activity ratios of the two redox couples. Since Eq. (9) may be rewritten as

$$\Delta_{\mathrm{O}}^{\mathrm{W}}\phi-\Delta_{\mathrm{O}}^{\mathrm{W}}\phi_{\mathrm{H^+}}^{0}=\left[E_{\mathrm{O2/R2}}^{\mathrm{O},0}+\frac{RT}{nF}\ln\frac{a_{\mathrm{O2}}^{\mathrm{O}}}{a_{\mathrm{R2}}^{\mathrm{O}}}\right]-\left[E_{\mathrm{O1/R1}}^{\mathrm{W},0}+\frac{RT}{nF}\ln\frac{a_{\mathrm{O1}}^{\mathrm{W}}}{a_{\mathrm{R1}}^{\mathrm{W}}}\right] \tag{9a}$$

$\Delta_{\mathrm{O}}^{\mathrm{W}}\varphi$ is thus related to the standard proton transfer potential, which can be controlled or measured in an electrochemical experiment, and is formally the difference between the two redox potentials on the $\mathrm{H^+/H_2}$ reference scale in each phase.

When the partition of certain ionic species is appreciable, the potential becomes a mixed potential with which both the redox reaction and ion partition are involved [25]; addition of ionic components transferrable across the interface causes the shift of the contact potential originally dictated by Eq. (9) [26, 27].

2.2 Polarizability

The establishment of the polarized liquid-liquid interface [3] was a pivotal achievement in electrochemical studies of liquid-liquid interfaces, in that it is the polarizability that enables us to control the electrical state of the interface externally.

Although the thermodynamic definition of an ideally polarized interface is unequivocal [28], the polarizability of an actual interface is understood differently, depending on what is to be measured at the interface. Gavach et al. [3] obtained the polarized range of *c.* 150 mV at the interface between an aqueous 10^{-3} M KCl solution and a nitrobenzene solution of 5×10^{-4} M dodecyltrimethylammonium dodecylsulfate. By choosing appropriate supporting electrolytes in aqueous and organic phases, e.g., 0.02 M $MgSO_4$ in water and 0.02 M tetrahexylammonium tetrakis[3,5-bis(trifluoromethyl)phenyl]borate in nitrobenzene, one can now achieve the potential window of 0.5 V for a conventional electrochemical measurement, e.g., detection of 1 mM acetylcholine in the aqueous phase by cyclic voltammetry with a scan rate of 100 mV s^{-1}.

In general, however, the quality of polarizability of liquid-liquid interfaces is far behind the polarizability of electrode-solution interfaces, e.g., a mercury-solution interface, in view of both the magnitude of residual current density and the width of the potential window.

The nonideality of both polarized ITIES and nonpolarized ITIES, the latter of which is usually employed as a reference ITIES to define the potential of the organic phase, often poses experimental difficulty in obtaining reliable kinetic parameters of charge transfer and double layer capacitance. It is worth considering in depth the degree of ideality of both ITIES before dealing with the kinetics of charge transfer at ITIES.

2.2.1 Polarized ITIES

The range of polarized potential (the potential window) is limited by the transfer of ions constituting supporting electrolytes. Let us consider an ITIES formed by the contact of an organic phase containing a supporting electrolyte KA and of an aqueous phase containing an electrolyte K′A′,

$$\left|\begin{array}{c|c|}\mathrm{KA} & \mathrm{K'A'} \\ (\mathrm{O}) & (\mathrm{W})\end{array}\right|$$

where K and K′ are cations and A and A′ are anions. When K and A are more easily transferable than A′ and K′ at each end of the potential window, the current-potential curve in the case of semi-infinite linear diffusion and reversible ion transfers of K and A has the form [29, 39]:

$$\frac{\mathrm{I}}{FA} = -\frac{c_{\mathrm{s}}^{\mathrm{O}}\sqrt{D_{\mathrm{s}}^{\mathrm{O}}}}{(\pi t)^{1/2}}\left[\frac{z_{\mathrm{K}}q + z_{\mathrm{A}}p}{pq + (1-t_{\mathrm{K}}^{\mathrm{O}})q + t_{\mathrm{K}}^{\mathrm{O}}p}\right] \tag{10}$$

where

$$p = \left(\frac{D_s^O}{D_K^W}\right)^{1/2} \exp\left[\frac{z_K F}{RT}(\Delta_O^W \phi - \Delta_O^W \phi_K^O)\right] \tag{11}$$

and

$$q = \left(\frac{D_s^O}{D_A^W}\right)^{1/2} \exp\left[\frac{z_A F}{RT}(\Delta_O^W \phi - \Delta_O^W \phi_A^0)\right] \tag{12}$$

The current I is taken to be positive when it passes from the aqueous phase to the organic phase. In Eqs. (10–12), A is the area of the interface, c_s^O is the concentration of KA in the organic phase, z_K and z_A are the charges on K and A with signed units, D_K^W and D_A^W are the diffusion coefficient of K and A in the aqueous phase, and D_s^O is the composite diffusion coefficient defined by $D_s^O = 2D_K^O D_A^O/(D_K^O + D_A^O)$, where D_K^O and D_A^O are the diffusion coefficients of K and A, respectively, in the organic phase; t_K is the transference number of K in the organic phase. A dc current-potential curve recorded at the interface between 0.1 M LiCl in water and 0.1 M tetrabutylammonium tetraphenylborate (Bu_4NPh_4B) in nitrobenzene was well represented by Eq. (10) [29]. This current is measured by using a four-electrode cell (Sec. 3.2.1), in which (for example) the ion-selective type of reference electrode reversible to cation K or K′ is connected to the phase O or W, respectively.

The interfacial potential difference at $I = 0$ is a kind of a mixed potential and is given by

$$\Delta_O^W \phi = -\frac{1}{z_K + |z_A|}\frac{RT}{F}\ln\left[\frac{z_K}{|z_A|}\left(\frac{D_s^O}{D_A^W}\right)^{1/2}\right] - \frac{1}{z_K + |z_A|}(z_K \Delta_O^W \phi_K^0 - |z_A|\,\Delta_O^W \phi_A^0) \tag{13}$$

In the case of a metal-electrolyte interface, e.g., in studies with the dropping mercury electrode, the faradaic current due to redeox reactions of impurities can be made much smaller than the double layer charging current by carefully preparing the solution, e.g. by deoxygenation. The potential at which the measured current becomes zero then corresponds to the point of zero charge [31]. In contrast, in the case of polarized ITIES, the faradaic current due to the transfer of supporting electrolyte ions can exceed the charging current when the concentrations of supporting electrolytes are high and the potential window is narrower. The zero current potential may then be determined by Eq. (13) rather than by the zero charging current. Therefore, care must be exercised in applying a streaming method to determine accurately the point of zero charge [32–34].

In ac impedance measurement at ITIES, admittance due to the transfer of supporting electrolyte ions is significant even in the middle of the potential window, as was first suggested and treated quantitatively by Samec et al. [35]. This imposes a difficulty in accessing double layer capacitance from the admittance, particularly when the transfer of supporting electrolyte ions is not reversible. There is no straightforward way to deconvolute the admittance ascribable to double layer capacitance and that ascribable to ion transfer admittance [30]. A nonlinear least-squares

fitting of the total admittance at different frequencies to a certain model equivalent circuit [36, 37] is a promising approach. However, a reliable estimate of capacitance values at the edge of the potential window is very difficult, owing to the increase in ion transfer currents of supporting electrolyte ions.

Polarizability of ITIES has given us a thermodynamic degree of freedom for controlling the potential drop across the interface. The nonideal polarizability at an actual ITIES does not, however, necessarily imply ambiguity in controlling the potential drop across the interface. From an experimental point of view, the potential control in the presence of a residual current is primarily determined by the capability of the potentiostat, in particular its fast response and *IR* compensation. Appropriate design of a potentiostat [38–41] and of a measuring cell [42, 43] assures the precise control of the potential drops across the ITIES, even in the presence of appreciable flow of current across the interface.

2.2.2 Potential of Nonpolarized ITIES

A reference electrode which can directly be dipped in the organic phase is not available, except the $AgPh_4B/Ag$ electrode [44]. It is customary to use a nonpolarized liquid-liquid interface, i.e., a reference ITIES. The potential drop across this interface is primarily determined by an ionic species distributed commonly in both aqueous and organic phases. There are two points to be taken into account in using this reference ITIES: the deviation from nernstian behavior and limited reversibility.

First, when only one ionic species can be distributed between the phases, there is a contact equilibrium [23] at the interface and the potential difference is completely determined by the standard ion transfer potential of this potential-determining ion. In actual cases, however, this contact equilibrium is seldom achieved at the ITIES, since the transfer of counter ions of the potential-determining ion across the interface is not always negligible. If a distribution equilibrium is established at the reference ITIES, the degree of interference can be estimated using Eq. (3). However, the distribution equilibrium is not usually realized in an actual reference ITIES. Rather, the final equilibrium, if achieved, would nullify the potential difference between the two aqueous phases. Consider the following example:

I	II	III
0.1 M	0.1 M	0.1 M
Bu_4NCl	Bu_4NPh_4B	LiCl
(water)	(nitrobenzene)	(water)

where Bu_4NCl is tetrabutylammonium chloride. Since all ionic components are more or less soluble in both water and nitrobenzene, Bu_4N^+ ion gradually dissolves into phase III and Li^+ ion dissolves into phases I through phase II. At the final distribution equilibrium, the composition of phases I would be the same as that of phase III and the eventual potential difference between phase I and III would disappear, provided that the volume of phase I and III are the same. The reference interface made of a nonpolarized ITIES should, therefore, be intrinsically of nonequilib-

rium character, unlike reference electrodes commonly used in electrochemistry, e.g., a silver-silver chloride and a calomel electrode.

The potential built at the interface in the presence of the transfer of more than one ionic species is a kind of mixed potential, as pointed out by Koryta in the context of ion-selective electrodes [45]. The theory of the mixed potential at the ITIES was presented for the case in the presence of supporting electrolyte [46] and then extended to the case in the absence of supporting electrolyte [47]. Consider the cell

$$\left| \begin{array}{c|c} K_1A_2 & K_1A_1 \\ (O) & (W) \end{array} \right|$$

where a monovalent cation K_1 is the primary ion and a monovalent anion A_1 is the interfering ion, while monovalent anion A_2 does not cross the interface. When the approximation $D^O_{K1}\,c^O_{K1}+D^O_{A2}\,c^O_{A2} \gg D^O_{A1}\,c^O_{A1}$ is valid, the mixed potential is given by [47]

$$\Delta^W_O\phi_{mix} = \Delta^W_O\phi^0_{K1}+\frac{RT}{F}\ln\left\{\frac{1}{2}\left[\frac{c^O_{K1A2}}{c^W_{K1A1}}+\left\{\left(\frac{c^O_{K1A2}}{c^W_{K1A1}}\right)^2+4\alpha\xi\right\}^{1/2}\right]\right\} \tag{14}$$

where

$$\alpha = \left(\frac{D^O_{A1}}{D^W}\right)^{1/2}\frac{c^O_{K1A2}}{c^W_{K1A1}}+\frac{1}{2}\left(\frac{D^O_1}{D^O_{A1}}\right)^{1/2}\left(1+\frac{D^O_{A1}}{D^O_{K1}}\right)+\frac{D^O_2}{D^O_{A1}+(D^O_{A1}D^O_1)^{1/2}} \tag{15}$$

and

$$\xi = \exp\left[\frac{F}{RT}(\Delta^W_O\phi^0_{A1}-\Delta^W_O\phi^0_{K1})\right] \tag{16}$$

D^O_1, D^O_2 and D^W are defined by $D^O_2 = 2D^O_{K1}D^O_{A2}/(D^O_{K1}+D^O_{A2})$, $D^W = D^O_{K1}(D^O_{A1}-D^O_{A2})/(D^O_{K1}+D^O_{A2})$, and $D^O_1 = 2D^W_{K1}D^W_{A1}/(D^W_{K1}+D^W_{A1})$. D^j_i (i is K1, A1, or A2 and j is O or W) is the diffusion coefficient of ion i in the phase j and c^W_{K1A1} and c^O_{K1A2} are the bulk concentration of K_1A_1 in W and of K_1A_2 in O, respectively.

When the condition

$$\left(\frac{c^O_{K1A2}}{c^W_{K1A1}}\right)^2 \gg 4\alpha\xi \tag{17}$$

is fulfilled, Eq. (14) reduces to

$$\Delta^W_O\phi_{mix} = \Delta^W_O\phi^0_{K1}+\frac{RT}{F}\ln\frac{c^O_{K1A2}}{c^W_{K1A1}} \tag{18}$$

Thus, as long as c^W_{K1A1} is sufficiently small, the ITIES shows the nernstian response with respect to the ion K_1, even when A_1 is moderately lipophilic.

Figure 1 shows the experimentally obtained response of a nonpolarized ITIES of the type of cell (II), when A_1 is Cl^-, A_2 is Ph_4B^-, and K_1 is tetrapropylam-

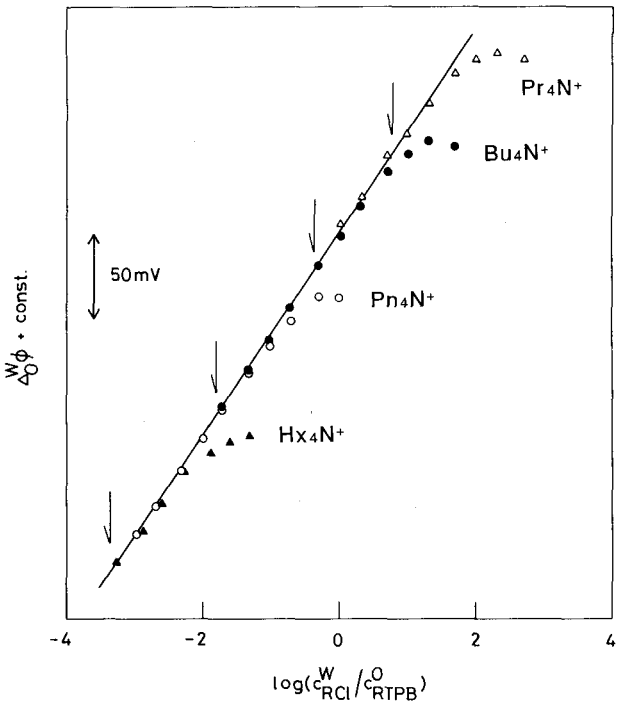

Fig. 1. Change in the potential at a nonpolarized ITIES with the concentration ratio, c^W_{RCl}/c^O_{RTPB}, at 25 °C for the system: RPh_4B (*nitrobenzene*)/RCl(*water*), where R = tetrapropylammonium (Pr_4N^+), tetrabutylammonium (Bu_4N^+), tetrapentylammonium (Pn_4N^+), or tetrahexylammonium (Hx_4N^+) ion and Ph_4B = tetraphenylborate. (Reprinted from [47] with permission. Copyright The Chemical Society of Japan).

monium (Pr_4N^+), Bu_4N^+, tetrapentylammonium (Pn_4N^+), or tetrahexylammonium (Hx_4N^+) ion, for the water-nitrobenzene interface [47]. The solid line shows the nernstian response and each arrow in Fig. 1 indicates the concentration, calculated from Eq. (14), at which the curve deviates by 1 mV from the nernstian slope. With increasing lipophilicity of K_1, the range of nernstian response narrows to a smaller range of c^W_{K1A1}/c^O_{K1A2}. The similar trend of the deviation from the nernstian slope was observed when $K_1 = Bu_4N^+$ and $A_1 = Cl^-$, Br^-, or I^-. Thus, the more lipophilic are K_1 and A_1, the wider the potential window at the polarized ITIES, but the lower the concentration of K_1A_1 required for the nernstian response at the reference ITIES. A low concentration of K_1A_1, in turn, gives rise to less reversibility of the reference ITIES. The nonideality of the nonpolarized interface should be taken into account, particularly when a two-electrode configuration is used in impedance measurements [30].

2.3 Structure of Electrical Double Layers

Although the structure of electrical double layers at an ITIES has been a primary concern of the electrochemical study of the ITIES ever since its dawning, the most fruitful advances were made in the 1980s after the establishment of the polarized ITIES. A recent review by Samec [12] covers the main body of progress up to 1988. The sharpness of the interfacial region, behavior of the diffuse double layer, presence of the inner layer, and the potential profile across the interface, have been the main points to be clarified in recent double layer studies of the ITIES. In the following, we will briefly summarize the salient features of the double layer structure inferred from the studies in the 1980s and early 1990s. The emerging picture differs from that presented in the review [14].

2.3.1 Diffuse Part of the Double Layer and Specific Adsorption of Ions

Elegant studies of electrocapillarity of a nonpolarized ITIES by Gavach et al. [48] showed that the tetraethyl-, tetrapropyl- and tetrabutylammonium ions are not adsorbed within the compact layer and suggested that the interface is made of two space charge layers, described by the Gouy-Chapman theory, on either side of a central compact layer [49–51]. In a nonpolarized ITIES, the potential drop across the interface cannot be altered independently of the chemical potential of a salt of ionic constituents in either of the phases. The degree of specific adsorption cannot therefore be quantitatively estimated at a nonpolarized interface [28].

In contrast, at an ideally polarized ITIES, the chemical potential of a salt can be varied while keeping the potential drop across the interface constant. This degree of freedom enables us to quantify the amount of specifically adsorbed ions, assuming a theoretical model for the diffuse part of the double layer [52, 53]. The electrocapillarity of the polarized ITIES was first studied by Kakiuchi and Senda for the interface between an aqueous solution of LiCl and a nitrobenzene solution of Bu_4NPh_4B, varying the concentrations of LiCl and Bu_4NPh_4B [52]. The dependence of measured surface excesses of all the ionic components on the excess surface charge density was found to be well described by the Gouy-Chapman theory, provided that the presence of an inner layer of about 1 nm thickness was allowed for. This indicates the absence of specific adsorption of these ionic species and the presence of an ion-free inner layer, at least within the concentration range studied: 0.01 – 1.00 M LiCl and 0.01 – 0.17 M Bu_4NPh_4B.

In general, the phenomenological definition of specific adsorption depends on the model of the diffuse part of the double layer. However, at the potential of zero charge, the contribution of the nonspecific adsorption in the diffuse part of the double layer should be absent. According to the phenomenological definition of specific adsorption [53], at the point of zero charge it is said that there is specific adsorption if the measured surface excess of any ionic species is positive.

The increase in interfacial tension with the activity of LiCl (Fig. 2) unambiguously evidences the negative adsorption of Li^+ and Cl^- ions. The solid line was calcu-

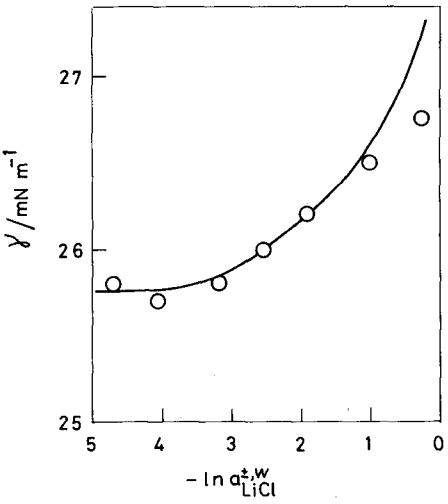

Fig. 2. Variation of interfacial tension at the point of zero charge with activity of lithium chloride. The solid line is calculated assuming the exclusion of lithium and chloride ions from the inner layer. (Reprinted from [52] with permission. Copyright The Chemical Society of Japan).

lated by assuming a monomolecular thickness of ion-free water. The agreement with the experimental points is excellent when $\ln a^{\pm,W}_{LiCl} \leq -1$. The deviation at a higher value of $\ln a^{\pm,W}_{LiCl}$ may correspond to the negative adsorption of water at the interface between an aqueous electrolyte solution of LiCl, NaCl, KCl, or $MgSO_4$, and *n*-heptane, 1,2-dichloroethane, or nitrobenzene, found by Girault and Schiffrin [54]. The latter results obtained at relatively high concentrations of electrolytes led them to the idea of mixed solvation and interfacial mixing [54, 55]. However, at least at the concentrations of the electrolyte below 0.1 M, there is no evidence of specific adsorption of alkali and alkaline-earth metal ions, symmetric tetraalkylammonium ions, and tetraphenylborate ions at the nitrobenzene-water interface. The possibility of specific adsorption at higher concentrations cannot be excluded, although at such concentrations reliable values of interfacial tension are difficult to obtain, particularly when using a quiescent interface, e.g., a pendant drop. A similar increase in interfacial tension with the concentration of tetrabutylammonium tetraphenylborate was observed at the point of zero charge, indicating the absence of specific adsorption of Bu_4N^+ and Ph_4B^- ions.

While electrocapillary data amenable to thermodynamic analysis of ion adsorption are available only at the nitrobenzene-water interface, a considerable number of double layer capacitance data have been compiled at both nitrobenzene-water and 1,2-dichloroethane-water interfaces. From a thermodynamic point of view the analysis of capacitance data is less straightforward, since to be equivalent to capillary data, the capacitance data must be supplemented by an independently determined integration constant. The presence of ion-pair formation between ions in the aqueous phase and the ions in the organic phase, a recently proposed concept based on capacitance measurements [56], should be able to be substantiated thermodynamically from electrocapillarity measurements. A detailed discussion of capacitance data has been given in the review by Samec [12].

2.3.2 Inner Layer and Potential Profile Across the ITIES

The inner potential drop across the ITIES, $\Delta_{O2}^{W2}\phi$, is related to the rational potential [57], $\Delta_O^W\phi_r = E - E_{pzc}$, and the two diffuse layer potentials, each in the aqueous phase and in the organic phase, $\phi^W - \phi_2^W$ and $\phi_2^O - \phi^O$, through

$$\Delta_{O2}^{W2}\phi = \Delta_O^W\phi_r - (\phi^W - \phi_2^W) - (\phi_2^O - \phi^O) + \Delta_O^W\phi_{pzc} \tag{19}$$

in which E and E_{pzc} are the potential drop across the interface and the point of zero charge referred to two appropriate reference electrodes, one in the aqueous phase and the other in the organic phase, and $\Delta_O^W\varphi_{pzc}$ is the inner potential difference between the two phases at the point of zero charge. An extrathermodynamic assumption is required to evaluate $\Delta_O^W\phi_{pzc}$. The potential of the electrocapillary maximum or the differential capacity minimum in combination with the (Ph_4AsPh_4B) assumption led to values of $\Delta_O^W\phi_{pzc}$ ranging from 20 mV to −30 mV both at nitrobenzene-water and 1,2-dichloroethane-water interfaces [58]. The often-employed assumption that $\Delta_O^W\phi_{pzc} \simeq 0$ as a first approximation would not very much oversimplify the reality.

The evaluation of $\Delta_{O2}^{W2}\phi$ thus depends on a particular diffuse layer model which gives the values of $\phi^W - \phi_2^W$ and $\phi_2^O - \phi^O$, apart from $\Delta_O^W\phi_{pzc}$. On the basis of the Gouy-Chapman model, Kakiuchi and Senda showed that $\Delta_{O2}^{W2}\phi$, which was once supposed to be insignificant [59, 60], has in fact a sizable value and varies with the total applied potential drop across the interface [61]. Figure 3 shows the potential profile of the interface between 0.1 M Pn_4NPh_4B in nitrobenzene and 0.05 M LiCl in water when $\Delta_O^W\phi = 0.2$ V. The Gouy-Chapman theory gives $\phi^W - \phi_2^W = 54$ mV

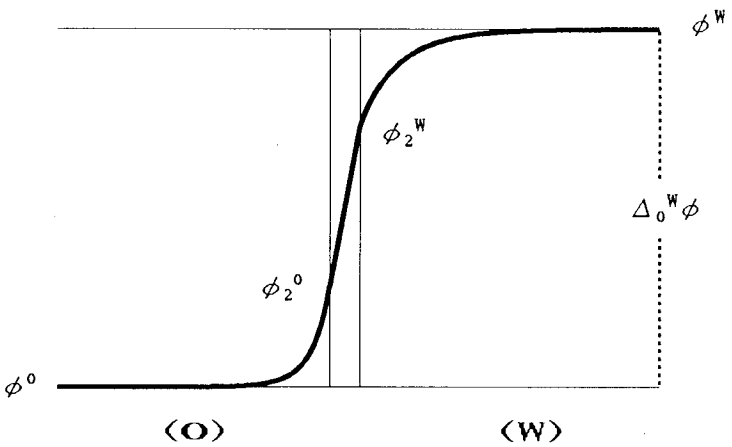

Fig. 3. Schematic representation of the double layer structure at the nitrobenzene-water interface at 25 °C. The full curve illustrates the potential distribution at $\Delta_O^W\phi = 0.2$ V for the interface between a 0.1 M solution of Pn_4NPh_4B in nitrobenzene and a 0.05 M aqueous solution of LiCl at 25 °C. The thickness of the inner layer is assumed to be 1 nm and the potential distribution is calculated using the Gouy-Chapman theory. (Reprinted from [61]. Copyright Elsevier Science Publishers, Amsterdam).

and $\phi_2^O - \phi^O = 56$ mV, predicting 90 mV for $\Delta_{O2}^{W2}\phi$; 45% of the total potential drop resides within the inner layer [61].

Recent statistical-mechanical theories [62] and Monte Carlo simulations of the diffuse double layer [63, 64] predict that the potential of the outer Helmholtz plane is generally overestimated in the Gouy-Chapman theory. If this is the case, the potential drop across the inner layer can be even greater, e.g., by *c.* 15% if a hypernetted-chain approximation is applied to the primitive model of the diffuse layer [12].

The inner layer is a concept within the framework of the classical Gouy-Chapman-Stern model of the double layer [57]. Recent statistical-mechanical treatments of electrical double layers taking account of solvent dipoles has revealed a microscopic structure of „inner layer" and other intriguing features, including pronounced oscillation of the mean electrostatic potential in the vicinity of the interface and its insensitivity at the interface to changes in the salt concentration [65–69].

2.3.3 Sharpness of the ITIES

Monte Carlo and molecular dynamics calculations of the density profile of model system of benzene-water [70], 1,2-dichloroethane-water [71], and decane-water [72] interfaces show that the thickness of the transition region at the interface is molecularly sharp, typically within 0.5 nm, rather than diffuse (Fig. 4). A similar sharp density profile has been reported also at several liquid-vapor interfaces [73, 74]. The sharpness of interfaces thus seems to be a general characteristic of the boundary between two stable phases and it is likely that the presence of supporting electrolytes would not significantly alter the thickness of the transition region at an ITIES. The interfacial mixed solvent layer [54, 55], if any, would probably have a thickness comparable with this thin inner layer.

Benjamin recently found for a 1,2-dichloroethane-water model system that, although the interface was molecularly sharp on time-average over hundreds of picoseconds, thermal fluctuations superimposed capillary waves as long as 0.8 nm on the sharp interface and generated a rough surface on the timescale of tens of

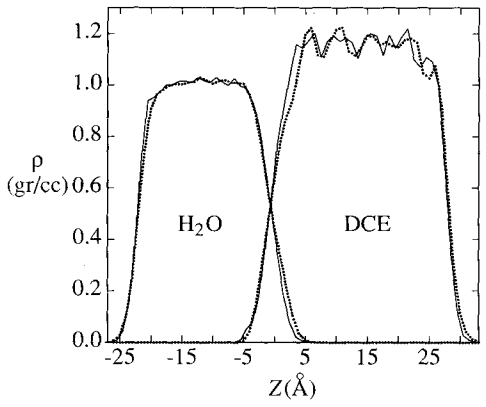

Fig. 4. Average density of water and 1,2-dichloroethane (DCE) at 300 K. Solid lines, density calculated relative to the system's center of mass; dotted lines, densities calculated relative to the location of the interface. (Reprinted from [71] with permission. Copyright American Institute of Physics).

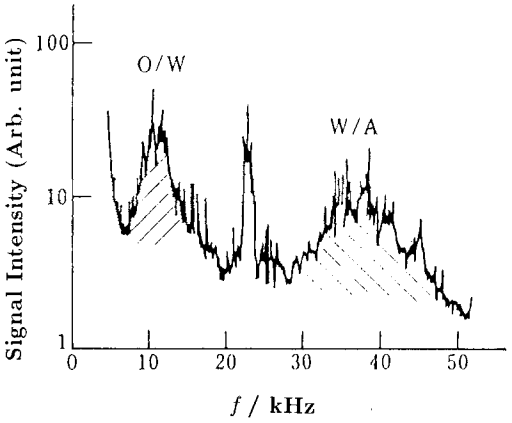

Fig. 5. Typical power spectrum of the optically mixed light intensity. O/W, ripplon (capillary wave) frequency at nitrobenzene-water interface; W/A, ripplon frequency at water-air interface. (Reprinted from [76] with permission. Copyright The Japan Society of Analytical Chemistry).

picoseconds [75]. On the other hand, from quasielastic laser scattering measurements, Takahashi et al. [76] determined the frequency of the capillary wave at the nitrobenzene-water interface at 26 °C to be 13.5 kHz (Fig. 5), which decreased to 11.1 kHz in the presence of a dipalmitoylphosphatidylcholine (DPPC) monolayer with the area occupied by a DPPC molecule being 0.825 nm^2. The estimation of the interfacial tension from capillary wave measurements agreed well with the values from the du Noiiy ring method. These thermal fluctuations, which do not appear in the aforementioned thermodynamic analysis of the structure of the ITIES, probably play an important role in the dynamics of ion transfer, as has been shown by Benjamin [75]. A zigzagged ITIES [77], a model introduced to interpret high values of inner layer capacitance, would be given a microscopic rationale from this surface fluctuation approach in the presence of ionic components.

2.4 Adsorption Phenomena

2.4.1 Adsorption of Surfactants

Introduction of the polarized ITIES opened a new stage in the study of adsorption of ionic surfactants, which had been used from the early studies of the ITIES onward [78–81].

Electrocapillary studies of an ionic surfactant at the polarized nitrobenzene-water interface showed a remarkable dependence of adsorption of hexadecyltrimethylammonium ion ($HTMA^+$) on the potential drop across the interface; $HTMA^+$ adsorbs only when $\Delta_O^W\phi$ is negative [82]. By using the mixed electrolyte method [83], the double layer structure was analyzed quantitatively. The change in potential profile due to the adsorption of the $HTMA^+$ ion and, in particular, the inversion of the potential at the outer Helmholtz plane in the nitrobenzene phase (Fig. 6), have significant implications in studying the kinetics of ion transfer. The degree of

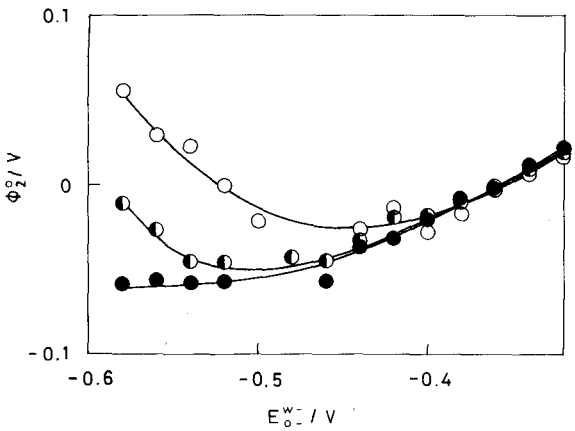

Fig. 6. Change in the potential at the outer Helmholtz plane in the nitrobenzene phase, ϕ_2^o, with potential difference across the cell at 25 °C. The concentration of hexadecyltrimethylammonium ion in nitrobenzene is (●) 0.01, (◐) 0.02, and (○) 0.05 M. (Reprinted from [82] with permission. Copyright The Chemical Society of Japan).

$HTMA^+$ adsorption is enhanced by counter ions on the aqueous side of the interface – F^-, Cl^-, and Br^-, in this order [84]. Wiles et al. found similar potential-dependent adsorption of a triazine dye, a derivative of Cibacron Blue F3GA, at the 1,2-dichloroethane-water interface by electrocapillary and capacitance measurements [85]. A pronounced potential dependence of the adsorption of ionic dyes at the ITIES has recently been confirmed for the adsorption of 2-(*n*-octadecylamino)naphthalene-6-sulfonate at the 1,2-dichloroethane-water interface by using the optical second harmonic generation technique (Fig. 7) [86].

Kakiuchi et al. studied the adsorption of tetra-, hexa- and octaethylene glycol monododecyl ethers at the nitrobenzene-water interface by determining electrocapillary curves [87, 88]. Unlike ionic surfactants, these nonionic surfactants adsorb in the entire range of the polarized potential. However, the fact that the oxyethylene group can form a complex with various ions on the aqueous side of the interface explains the strong dependence of adsorption of these surfactants on the potential drop across the interface. The dependence of the adsorption Gibbs energy on applied potential shown in Fig. 8 can be well explained assuming complex formation of the surfactant adsorbed from the nitrobenzene side of the interface with the ions on the aqueous side of the interface, and also assuming that the surface concentration of ions on the aqueous side follows the Gouy-Chapman theory [87]. The adsorption properties of these surfactants have been successfully utilized to interpret quantitatively the behavior of cyclic voltammograms of ion transfer facilitated by these surfactants [89]. Chen et al. reported the double layer capacitance at the nitrobenzene-water interface in the presence of the same surfactant [90].

Sorbitan fatty acid esters, whose hydrophilic head group does not show discernible complexation with ions, cause the lowering of interfacial tension in the entire

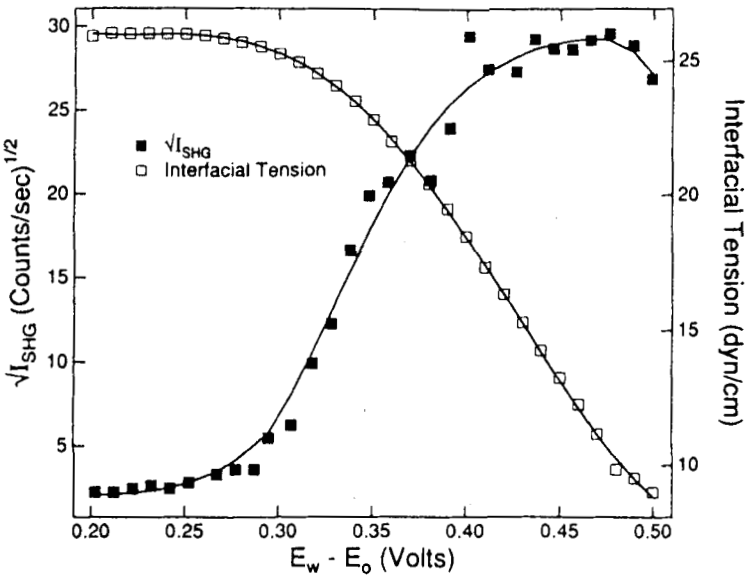

Fig. 7. Interfacial tension (open squares) and the square root of the SHG intensity (filled squares) as a function of the applied potential for 20 μM 2-(*n*-octadecylamino)naphthalene-6-sulfonate, 50 mM KCl, and 25 mM Na_2HPO_4 in water (pH = 9) and 1 mM Bu_4NPh_4B in 1,2-dichloroethane. (Reprinted from [86] with permission. Copyright American Chemical Society).

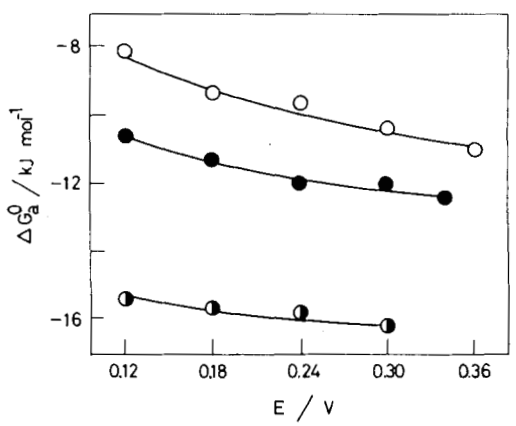

Fig. 8. Dependence of standard adsorption free energy, ΔG_a^0, on applied potential for (○) tetra-, (●) hexa-, and (◑) octa-oxyethylene glycol monododecyl ethers at nitrobenzene-water interface at 25 °C. (Reprinted from [88] with permission. Copyright The Chemical Society of Japan).

range of the potential window [91]. Sorbitan monooleate has been used to minimize the convective motion of the solutions in the vicinity of the ITIES [92]. No detectable change was observed on the rate of ion transfer upon the adsorption of this surfactant [93].

2.4.2 Adsorption of Compounds of Biological Significance

Koryta first pointed out the importance of adsorbed phospholipid monolayers at the ITIES in elucidating the mechanism of complex formation at the ITIES and its general relevance to biological membranes [94]. A first attempt to characterize quantitatively the phosphatidylcholine and phosphatidylethanolamine monolayers at the ITIES of the 1,2-dichloroethane-water interface with electrocapillary measurements by Girault and Schiffrin suggested the importance of surface pH in the ionization of the amino group of phosphatidylethanolamine [95]. The effect of pH on the state of a dilauroylphosphatidylethanolamine monolayer at the nitrobenzene-water interface and its significance to ion transfer across the ITIES were analyzed in detail with an ac impedance technique [96]. From capacitance measurements, dilauroylphosphatidylcholine (DLPC) was found to form a liquid-expanded monolayer with an occupied area of one DLPC molecule being 0.73 nm^2 at the nitrobenzene-water interface at 25 °C [97].

The liquid-expanded state of the saturated DLPC monolayer was confirmed by thermodynamic analysis of electrocapillary curves [98]. A DLPC monolayer is stable when $\Delta_O^W\phi$ is negative [98]. A schematic representation of the double layer structure in the presence of a saturated DLPC monolayer at the point of zero charge is shown in Fig. 9 [98]. The dipole of the zwitterionic head group was predicted to lie in paral-

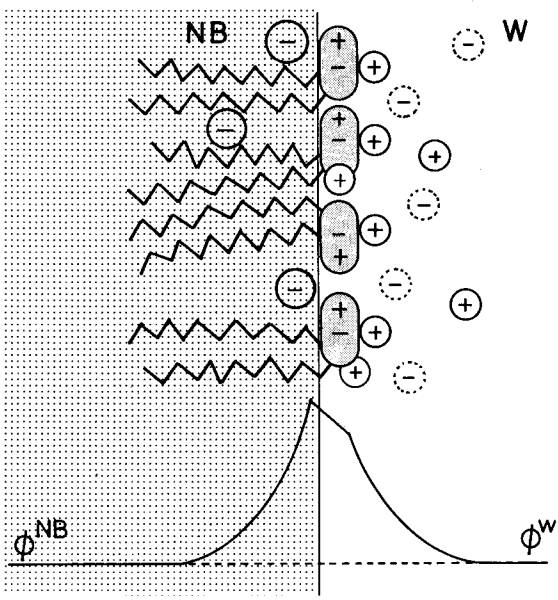

Fig. 9. Schematic representation of double layer structure and potential profiles of the interface between a nitrobenzene (NB) solution of 0.1 M Pn_4Ph_4B and an aqueous (w) solution of 0.05 M LiCl in the presence (solid line) and absence (broken line) of a saturated DLPC monolayer at the potential of zero charge, where the surface potential was assumed to be negligible. (Reprinted from [98] with permission. Copyright The Chemical Society of Japan).

lel with the interface, making no significant contribution to the surface potential. The elongation of alkyl side chains of phosphatidylcholine increases the surface activity [99, 100] and eventually leads to the phase transition of the monolayer from the liquid-expanded state to the liquid-condensed state [100].

The phase transition was induced by Ca^{2+} and Mg^{2+} in the case of dipalmitoylphosphatidylserine to form a condensed monolayer at the nitrobenzene-water interface, which was stable throughout the potential window. The capacitance in the presence of the condensed monolayer was as low as 1.5 $\mu F\,cm^{-2}$ [101]. The phase transitions from the expanded to the condensed monolayer accompanied the concomitant decrease in the rate of ion transfer but even the condensed monolayers were unable to block it completely [100, 101].

At the nitrobenzene-water interface a dipalmitoylphosphatidylcholine monolayer undergoes the phase transition at 13 °C, while at the air-water interface the phase transition temperature is 43 °C. This difference demonstrates weaker lateral interaction between phospholipid side chains at the nitrobenzene-water interface and suggests the penetration of nitrobenzene molecules in the hydrocarbon chain part of the monolayer (Fig. 9) [99, 100].

Adsorption of proteins at an ITIES has also been reported for cytochrome *c* at the 1,2-dichloroethane-water interface [102], and for ovalbumin [103] and bovine serum albumin [104] at the nitrobenzene-water interface.

3 Ion Transfer Reactions

3.1 Theoretical Studies

Theoretical studies have focused mainly on the simple ion transfer,

$$X^z(W) \rightleftarrows X^z(O) \tag{20}$$

where X^z as an ion with the charge number z, and W or O denote the aqueous or the organic solvent phase, respectively. Before summarizing the results of these studies, we introduce the apparent kinetic parameters that are accessible experimentally (Sec. 3.1.1). Then we proceed with the analysis based on the multibarrier (Sec. 3.1.2) or stochastic (Sec. 3.1.3) models, which refer to the activation or diffusion path mechanism, respectively. Although often no distinction is made between these two mechanisms, theories have originated from different grounds, and are worth considering separately. We end this section with a summary of ion trajectory calculations in a molecular dynamics model of the liquid-liquid interface (Sec. 3.1.4).

3.1.1 Apparent Kinetic Parameters

Heterogeneous reaction (21) is currently supposed to follow the first-order rate law

$$J = \vec{k} c^{W} - \overleftarrow{k} c^{O} \tag{21}$$

where J is the interfacial ion flux, c^W or c^O are the ion concentrations on its aqueous or organic solvent side, and $\vec{k}$ or $\overleftarrow{k}$ are the heterogeneous rate constants (e.g., in cm s^{-1}) for the forward or the backward ion transfer, respectively. There is no obvious relation between these two rate constants, except for the equilibrium state where $J = 0$, $\overleftarrow{k}/\vec{k} = c^W/c^O$. However, a link can be established on assuming that the Gibbs distribution is applicable also to slightly nonequilibrium systems [105]. By taking into account the principle of microscopic balancing, the forward and the backward rate constants are then related to each other by [24]

$$\vec{k}/\overleftarrow{k} = \exp(-\Delta_W^O \bar{G}_i^0/RT) = \exp[zF(E-E^0)/RT] \tag{22}$$

where $\Delta_W^O \bar{G}_i^0 = \Delta_W^O G_i^0 - zF\Delta_O^W \phi = -zF(\Delta_O^W \phi - \Delta_O^W \phi_i^0)$ is the standard electrochemical Gibbs energy change for the ion transfer (20). A similar relationship is used in the semiphenomenological theory of electrode reactions [105]. Equation (22) holds, irrespective of the actual dependence of the two rate constants on the potential E. For the sake of comparison, two apparent kinetic parameters are usually introduced: first, the standard rate constant k_0^s at the equilibrium potential $E = E^0$,

$$k_s^0 = \vec{k}(E = E^0) = \overleftarrow{k}(E = E^0) \tag{23}$$

The second parameter is the apparent charge transfer coefficient $\vec{\alpha}$ (sometimes denoted as α_{app}), which characterizes the potential dependence of the forward rate constant,

$$\vec{\alpha} = (RT/zF)(\partial \ln \vec{k}/\partial E) \tag{24}$$

Its value at $E = E^0$ will be denoted at $\vec{\alpha}_0$.

3.1.2 Multidimensional Energy Barrier Models

The existence of a multidimensional energy barrier, which the ion must overcome in crossing the liquid-liquid interface, has been widely anticipated. However, its origin, shape, height, and the location have been a matter for ongoing discussions. A reference has been usually made either to Marcus's nonequilibrium thermodynamic [106] or Levich's quantum-mechanical [107] theories of charge transfer in polar media, or to Eyring's transition state theory of multistep ion transfer in liquids [108]. The former two theories are more explicit in regard to the role of various subsystems (ions, intramolecular degrees of freedom, solvent molecules), but their application to a specific ion transfer system would require exact definition of the reaction system and detailed knowledge of the wave functions of the subsystems. On the other hand, Eyring's theory of transport processes is easier to extend to interfacial ion transfer. This theory has provided a simple way of introducing the effects of the electrical field on the ion transfer rate, though with little justification. An explicit assumption about the mechanism of the ion transfer is common to all these approaches.

Three-Step Mechanism

Due to the existence of the electrical double layer, the concentration of an ion near the interface varies, which should influence the ion transfer rate. Typically, the double layer effect is accounted for by assuming an equilibrium ion distribution up to a point located close to the interface, from which the ion becomes driven by the local potential gradient to cross the interface. The assumption of a three-step (four-position) mechanism has been introduced by Gavach and coworkers [109], but the idea can be traced back to a review by Buck [110]. Following this assumption, Eq. (20) can be expanded into

$$X^z(W) \rightleftarrows X^z(a) \rightleftarrows X^z(b) \rightleftarrows X^z(O) \tag{25}$$

where the positions a and b are located in the interfacial region. Gavach et al. [109] suggested that the positions a and b are those of the outer Helmholtz planes x_2^W and x_2^O in the two phases in contact, and that the ion transfer from a to b is the rate-determining step. This suggestion was adopted by Samec [24], by Koryta [6] and by Melroy and Buck [111], while Girault and Schiffrin [60] have left the exact locations of a and b open to further discussion. Unless we refer to the latter model, we shall assume that $a = x_2^W$ and $b = x_2^O$.

The apparent rate constant $\vec{k}$ was expressed [60] by an equation which is equivalent to the classical Frumkin correction:

$$\vec{k} = \vec{k}_t (c^a/c^W) = \vec{k}_t \exp\left[-(\Delta_W^a G_i^0 + zF\,\Delta_W^a\phi)/RT\right] \tag{26}$$

where $\vec{k}_t$ is the rate constant for the rate-determining step (i.e., the true or corrected rate constant), c^a is the concentration of the transferred ion at the location a, $\Delta_W^a G_i^0$ is the standard Gibbs energy for the ion transfer from the bulk aqueous phase to the position a, and $\Delta_W^a\phi$ is the corresponding difference in the electrostatic potential. This approach is consistent with the idea of the mixed solvent layer introduced earlier [54], which would imply a partial resolvation of the ion prior to the rate-determining step, and would give substance to the Gibbs energy term in Eq. (26). However, as discussed in Sec. 2.3.3, molecular dynamics studies point to a molecularly sharp boundary of two immiscible liquids. Consequently, the solvation structure of the ion near the boundary is probably the same as in the bulk of the solution, and the term $\Delta_W^a G_i^0$ should equal zero. Actually, in order to illustrate ideas behind their theory, the authors [60] also made use of Gavach's assumption that $a = x_2^W$ and $b = x_2^O$.

Quantum-Mechanical Approach

Attempts to extend the theory of charge transfer in polar media [106, 107] to ion transfer across a liquid-liquid interface were reviewed by Kunetsov and Kharkats [112]. The complexity of interfacial ion transfer follows from the fact that this is essentially a many-body problem, comprising motions of various components of the system interacting with each other which are difficult to separate. In particular, the

analysis must account for the transferred ion and for solvent molecules in the first solvation shell, as well as for solvent molecules in the surrounding medium and in disrupted solvent structures at the liquid-liquid interface. Components of the system having frequency ω_s which is less than the frequency of the ion motion ω_i form a quasistatic potential barrier, and those having frequency ω_f higher than ω_i form a fluctuating part of the ion potential, giving rise to the field of stochastic forces [113]. Computer simulations of ion-solvent systems [114] shows that the characteristic frequencies of ion motion in water ($10^{12}-10^{13}\,s^{-1}$) are lower by one order of magnitude than those of solvent librational motions and intramolecular (e.g., ion-solvent) vibrations ($10^{13}-10^{14}\,s^{-1}$). Hence, in contrast to electron transfer reactions, the contribution of this part of the solvent subsystem to the activation energy of the ion transfer is likely to be small [115].

An attempt to rationalize the kinetics of the rate-determining step in Eq. (25) with the help of the quantum-mechanical approach was made by Samec [24], who assumed that a molecularly sharp liquid-liquid boundary formed by the oriented molecules of both solvents (the compact layer) introduces a barrier, through which the ion can penetrate after some thermally populated reorganization in the surrounding medium. An analogy was drawn with the atom transfer reactions in polar liquids [105] and, hence, the classification [60] of the treatment as the direct transposition of electron transfer theories can be misleading. The model was criticized by Girault and Schiffrin [60] (cf. also the review [14]), who questioned the existence of a compact solvent layer at the ITIES and the reliability of the quantum transition path for a heavy ion. However, evidence in favor of the classical concept of the inner layer (Sec. 2.3.2) and the molecularly sharp ITIES (Sec. 2.3.3) implies that a compact solvent layer is likely to be formed at the ITIES. On the other hand, the latter objection [60] is sound, inasmuch the character of the ionic motion is probably classical. Nevertheless, in the classical limit, the formalism of the quantum-mechanical treatment has been shown [116] to evolve into the activated-complex theory, as formulated by Marcus [106]; this is applicable to transfer of atoms, ions or molecular groups in liquids [116]. Thus, the temperature dependence of the ion transfer rate constant $\vec{k}_t$ for the rate-determining step can be expected to have the form of the Arrhenius equation,

$$\vec{k}_t = Z \exp\left(-\Delta_a^* \bar{G}_i^0 / RT\right) \tag{27}$$

where $\Delta_a^* \bar{G}_i^0$ is the standard activation Gibbs energy. The existence of a relationship between $\Delta_a^* \bar{G}_i^0$ and the standard electrochemical Gibbs energy change $\Delta_a^b \bar{G}_i^0$ between locations a and b has been demonstrated by using the harmonic approximation for the atom-atom interactions [112, 116]. Such a relationship has been anticipated [24] by assuming that the standard Gibbs energy of activation is proportional to $\Delta_a^b \bar{G}_i^0$,

$$\Delta_a^* \bar{G}_i^0 = \Delta \bar{G}_i^* + \alpha \Delta_a^b \bar{G}_i^0 \tag{28}$$

The effect of the electrical potential difference can then be recovered upon expressing the Gibbs energy change $\Delta_a^b \bar{G}_i^0$ as the sum of the standard Gibbs ener-

gy of transfer $\Delta_O^W G_i^0$ from W to O and the electrostatic energy change between a and b:

$$\Delta_a^b \bar{G}_i^0 = \Delta_W^O G_i^0 - zF\Delta_b^a \phi \tag{29}$$

where $\Delta_b^a \phi$ is a part of the interfacial potential difference $\Delta_O^W \phi$,

$$\Delta_O^W \phi = \Delta_b^a \phi + \Delta_O^b \phi - \Delta_W^a \phi \tag{30}$$

By using Eqs. (26), (27), and (28), the following equation was derived for $\vec{k}$ [24]:

$$\vec{k} = k^s \exp\left[\alpha zF\left(\Delta_O^W \phi - \Delta_O^W \phi_i^0\right)/RT\right] \tag{31}$$

where

$$k^s = k_0 \exp\left\{-zF\left[(1-\alpha)\,\Delta_W^a \phi + \alpha \Delta_O^b \phi\right]/RT\right\} \tag{32}$$

and

$$k_0 = k_0^0 \exp\left(-\Delta \bar{G}_i^*/RT\right) \tag{33}$$

Note than the parameters k^s and α are not identical with the apparent rate constant k_0^s and the apparent charge transfer coefficient $\vec{\alpha}$ defined by Eqs. (23) and (24), respectively. Since k^s can depend on the potential E indirectly through the exponential term with the potential differences across the space charge regions in Eq. (32), $k_0^s = k^s(E = E^0)$. The relationship between $\vec{\alpha}$ and α can be derived from Eqs. (31) and (32),

$$\vec{\alpha} = \alpha\left(\partial \Delta_b^a \phi / \partial E\right) + \left(\partial \alpha / \partial E\right)\left(\Delta_b^a \phi - \Delta_O^W \phi_i^0\right) - \left(\partial \Delta_W^a \phi / \partial E\right) \tag{34}$$

The existence of the relationship described by Eq. (28) can be anticipated for any kinetic process which proceeds from an initial to a final state through a single transition state [105]. A more general form of Eq. (28) is the Brønsted relationship [117],

$$\Delta_a^* \bar{G}_i^0 = \Delta \bar{G}_i^* + \beta_0\, \Delta_a^b \bar{G}_i^0 + \frac{1}{2}\left(\partial \beta / \partial \Delta_a^b \bar{G}_i^0\right)_0 \left(\Delta_a^b \bar{G}_i^0\right)^2 + \ldots \tag{35}$$

where $\beta = \partial \Delta_a^* \bar{G}_i^0 / \partial \Delta_a^b \bar{G}_i^0$ is the microscopic Brønsted coefficient. Obviously, the Brønsted coefficient β differs in value from the parameter α, except for the case when the former coefficient is independent of the Gibbs energy change $\Delta_a^b \bar{G}_i^0$. It has been concluded [117, 118] that the physical significance of the parameters $\vec{\alpha}$ and α is rather obscure, and that the analysis of the molecular mechanism of the rate-determining step should rely rather on the Brønsted coefficient β, which characterizes the symmetry of the energy barrier [105, 119]. The introduction of the Brønsted coefficient by Eq. (35) has been a matter of some misunderstanding [151].

Koryta [6] was the first who realized that when the potential difference across the inner layer $\Delta_b^a \phi = \Delta_{O2}^{W2} \phi$ is negligible, and the parameter α is a constant, the apparent charge transfer coefficient $\vec{\alpha}$ is controlled only by the potential difference

across the space charge region, $\vec{\alpha} \approx -\partial(\phi_2^{\mathrm{W}} - \phi^{\mathrm{W}})/\partial E$; cf. Eq. (34). According to the Gouy-Chapman theory, this potential difference can be expressed as a function of $\Delta_{\mathrm{O}}^{\mathrm{W}}\phi$ [49]:

$$\phi_2^{\mathrm{W}} - \phi^{\mathrm{W}} = \frac{RT}{z_{\mathrm{b}}F} \ln \left\{ \frac{1 + p \exp\left[-z_{\mathrm{b}}F(\Delta_{\mathrm{O}}^{\mathrm{W}}\phi - \Delta_{\mathrm{O}2}^{\mathrm{W}2}\phi)/2RT\right]}{1 + p \exp\left[z_{\mathrm{b}}F(\Delta_{\mathrm{O}}^{\mathrm{W}}\phi - \Delta_{\mathrm{O}2}^{\mathrm{W}2}\phi)/2RT\right]} \right\}$$

where

$$p = (\varepsilon^{\mathrm{O}} c^{\mathrm{O}}/\varepsilon^{\mathrm{W}} c^{\mathrm{W}})^{1/2} \tag{37}$$

in which ε^{O} and ε^{W} are the dielectric permittivities of the organic solvent and water, and c^{O} and c^{W} the concentrations of a $z_{\mathrm{b}}:z_{\mathrm{b}}$ supporting electrolyte in the organic and the aqueous phase, respectively. For a large value of the interfacial potential difference $\Delta_{\mathrm{O}}^{\mathrm{W}}\phi$, Eq. (36) simplifies to [6]

$$\phi_2^{\mathrm{W}} - \phi^{\mathrm{W}} \approx -\frac{1}{2}(\Delta_{\mathrm{O}}^{\mathrm{W}}\phi - \Delta_{\mathrm{O}2}^{\mathrm{W}2}\phi) \mp (RT/z_{\mathrm{b}}F) \ln p \tag{38}$$

and, hence $\vec{\alpha} \approx 0.5$. Therefore, the ion transfer kinetics could exhibit Butler-Volmer behavior, which bears no relation to the properties of the energy barrier, but rather to the double layer structure. However, more recent studies of the electrical double layer have indicated that neither of the two assumptions above is of general validity. In fact, the potential difference across the inner layer represents an appreciable part of the interfacial potential difference $\Delta_{\mathrm{O}}^{\mathrm{W}}\phi$ (Sec. 2.3.2), and the parameter α can depend on the potential E (Sec. 3.2.1 and 3.2.2).

Eyring's Model

Eyring's activation model was adopted by Gavach and coworkers [109], by Melroy and Buck [111] and by Girault and Schiffrin [60]. In the first two contributions, the effect of the potential on the ion transfer rate was analyzed by assuming that the forward rate constant for the rate-determining step is given by Eq. (27), with the pre-exponential factor $Z = k_{\mathrm{B}}T/h$, where k_{B} and h are the Boltzmann and Planck constant, respectively. The next steps were similar to those described above, i.e., the parameter α was introduced through Eq. (28), with a reference to Delahay's phenomenological treatment of electrode kinetics [120]. Apart from introducing a pre-exponential factor of the wrong dimension, the authors [111] dropped the term $\alpha \Delta_{\mathrm{W}}^{\mathrm{O}} G_i^0$, which arises upon the substitution of Eq. (29) into Eq. (28). Although the electrical potential difference $\Delta_{\mathrm{b}}^{\mathrm{a}}\phi$ was not supposed to be negligible as in Koryta's treatment [6], the predictions of the electrical potential [6, 111] and the salt [6, 121, 122] effects on the ion transfer rates in these two models are almost indistinguishable.

Girault and Schiffrin [60] pointed out the multistep character of the ion transport across the liquid-liquid interface, and hence they referred to Eyring's multistep model [108]. The ion was considered to diffuse toward the interface over a sequence

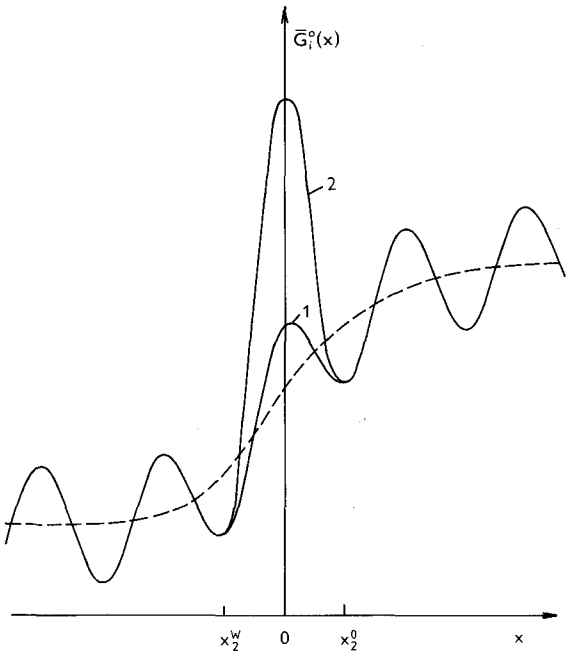

Fig. 10. Standard Gibbs energy profile along the axis of an ion transfer across the liquid-liquid interface in the absence (1) and presence (2) of an additional potential barrier at the interface. The broken line represents the contribution of the long-range electrostatic forces; the solid line corresponds to the sum of the long- and short-range contributions; x_2^W and x_2^O denote the outer Helmholtz planes in the aqueous and the organic solvent phases.

of barriers of various heights (Fig. 10). Then, the steady-state ionic flux J can be described by an equation derived for multistep ion transport in liquids [108],

$$J = \frac{\vec{k}_0 \left(c^0 - c^n \prod_{r=1}^{n} K_r^{-1} \right)}{1 + (\vec{k}_1/\vec{k}_1) + \ldots + \prod_{r=1}^{n-1} (\vec{k}_r/\vec{k}_r)} \tag{39}$$

where n is the number of jumps, $\vec{k}_r$ or $\overleftarrow{k}_r$ is the first-order heterogeneous rate constant for an ion at the rth minimum to jump forward to $(r+1)$ or backward to $(r-1)$ locations, respectively and $K_r = \overleftarrow{k}_{r+1}/\vec{k}_r$. Provided that the barrier for the interfacial jump is much higher than that for the solution jump [60], Eq. (39) simplifies to Eq. [21]. The rate constant $\vec{k}_t$ for the rate-determining step was also given by Eq. (27), but with $Z = (k_B T/h)L^a$, where L^a is the distance between the location of two neighboring equilibrium positions, presumably on opposite sides of the interface (the equivalent jump length). In contrast to previous approaches [6, 24, 111], the

authors have introduced two charge transfer coefficients, so that the standard Gibbs energy of activation in the rate-determining step becomes

$$\Delta_a^* \bar{G}_i^0 = \Delta \bar{G}_i^* + \alpha_n \Delta_W^O G_i^0 - zF\alpha_e \Delta_b^a \phi \tag{40}$$

where α_n and α_e are the chemical and electrical charge transfer coefficient, respectively. From the point of view of the transition state theory, this procedure seems to have little justification for the step with a single transition state, i.e., a single Brønsted coefficient. Further, the overall chemical and electrical charge transfer coefficients for the ion transfer (Eq. 20) were defined with an aim to simplify the analysis, but the presence of four transfer coefficients in the final expression for the electrical current makes it practically useless. Girault [123] extended the discussion of this point, but his procedure represents rather a regrouping of the terms which contribute to $\Delta_a^* \bar{G}_i^0$, leading to the introduction of the poorly defined electrical potential in the transition state ϕ^*.

In an attempt to establish a link between the parameters of ion transport in the bulk solution and across a liquid-liquid interface, Shao and Girault [124] introduced the diffusion coefficient D^a of the interfacial jump as

$$D^a = L^a \vec{k}_t \tag{41}$$

which was assumed to be comparable with the solution diffusion coefficient D, an experimentally accessible quantity. This assumption virtually opened the way to a comparison of the standard activation entropy or Gibbs energy of diffusion between the bulk and the interface [124]. However, the concept of the rate-determining step may not be applicable to bulk ion transport and, hence, a distribution of both the equivalent jump lengths and the standard Gibbs energies of activation for individual diffusion jumps in Eq. (39) should be considered [115].

Note that speculations about the magnitude of the equivalent jump length [60, 124] could be avoided. Following the transition state theory of a monomolecular process [125], the activation entropy term in Eq. (27) can be represented as the ratio of the partition functions of the transition state $z^{*\prime}$, from which the critical translational contributing along the ion reaction coordinate (here the x-axes) has been extracted, and of the initial ground state z, i.e., $\exp(\Delta_a^* \bar{S}_i^0/R) = z^{*\prime}/z$. After separating the x-translation partition function of the initial state, $z = z'(2\pi MRT)^{1/2} L^a/h$ (M is the particle molar mass), Eq. (27) with $Z = (k_B T/h) L^a$ can be written as

$$\vec{k}_t = (RT/2\pi M)^{1/2} \exp(-\Delta_a^* \bar{G}_i^{0\prime}/RT) \tag{42}$$

where the activation entropy does not involve a contribution from the translation of the ion motion along the x-axes. The pre-exponential factor in Eq. (27) would then have the meaning of the heterogeneous collision number.

3.1.3 Stochastic Model

The stochastic model of ion transport in liquids emphasizes the role of fast-fluctuating forces arising from short (compared to the ion transition time), random interactions with many neighboring particles. Langevin's analysis of this model was reviewed by Buck [126] with a focus on aspects important for macroscopic transport theories, namely those based on the Nernst-Planck equation. However, from a microscopic point of view, application of the Fokker-Planck equation is more fruitful [127]. In particular, only the latter equation can account for local friction anisotropy in the interfacial region, and thereby provide a better understanding of the difference between the solution and interfacial ion transport.

The difference between the Nernst-Planck and Fokker-Planck equations can be illustrated by considering the simple model, in which the fluctuating forces are represented by the δ-correlated white noise and the particle velocity follows adiabatically the fluctuating force. In this case, the Fokker-Planck equation can be written as [127]

$$\partial p/\partial t = -\partial J/\partial x \tag{43}$$

with

$$J = -\zeta^{-1}(\partial V/\partial x)\, p - k_B T \partial(\zeta^{-1} p)/\partial x \tag{44}$$

where $p(x,t)$ is the probability of the particle having the coordinate x at time t, $\zeta(x)$ is the local friction coefficient, and $V(x)$ is the static potential of the regular forces. Equation (43), which is also known as the Smoluchowski equation [127], was rederived by Benjamin using a different procedure [128].

Obviously, when the local friction coefficient $\zeta = \zeta^0$ is a constant, Eq. (44) takes the form of the Nernst-Planck equation,

$$J = -(k_B T/\zeta^0)[\partial p/\partial x + (p/k_B T)\partial V/\partial x] \tag{45}$$

Although the latter equation has been often used in microscopic transport analyses [126, 129, 130], the validity of such an approach is restricted either to homogeneous media, or to long-time limits when the friction coefficient reaches a constant value ζ^0,

$$D = k_B T/\zeta^0 = \lim_{t\to\infty} (1/2) \int_0^t \langle v(0)\, v(t')\rangle \mathrm{d}t' \tag{46}$$

where $v = \mathrm{d}x/\mathrm{d}t$ is the velocity and D is the diffusion coefficient. In three-dimensional space, scalar velocities in Eq. (46) must be replaced by vectors, and the denominator 2 by 3 (Green-Kubo equation). The autocorrelation function can be obtained by a molecular dynamics method for a specific molecular model of the system [114].

Gurevich, Kharkats and Samec [113, 131] based their stochastic analysis of the interfacial ion transfer on Eqs. (43) and (44). Provided that this is a stationary process, i.e., $\partial p/\partial t = -\partial J/\partial x = 0$, an integration of Eq. (44) yields

$$J = \frac{(k_B T/\zeta^a)c^a - (k_B T/\zeta^b)c^b \exp(\Delta_a^b \overline{G_i^0}/k_B T)}{\int_a^b \exp(\Delta_a^x \overline{G_i^0}/k_B T)\,dx} = \text{const}(x) \tag{47}$$

where indexes a, b and x refer to the initial, final and intermediate positions in the rate-determining step, respectively. However, this is not exactly the equation used by the authors [113, 131], who rather assumed that the friction coefficient $\zeta = \zeta^*$ is a constant, having a value different from the bulk solution. The problem with calculating the integral in Eq. (47) was overcome [113] by applying the method of steepest descent, which is a minimizing procedure equivalent to the assumption that there is a minimum on the top of the potential barrier (transition state) [125]. The Gibbs energy of the ion was supposed to be a superposition of the potential energy barrier arising from the short-range repulsive interactions between ion and solvent molecules in the inner layer, and the linear potential connected with the long-range electrostatic interactions, comprising the contribution of the polar solvent around the ion (see Fig. 10) [131]. Although the constant field treatment of long-range interactions might be an oversimplification [132], recent estimates of the electrostatic Gibbs energy of finite-size ions near a planar boundary between two dielectric media [133] confirmed the absence of a discontinuity on the energy profile, which then can be linearized in a narrow-range of the coordinate x. It has been argued [113, 131] that, owing to the short-range interactions, the top of the barrier is not sharp but smooth and parabolic in shape, which has led to the introduction of the angular frequency ω^* of the ion motion in the transition state (harmonic approximation). Integration of Eq. (47) yields an expression for the rate constant $\vec{k}_t$ which has the form of Eq. (27), but the pre-exponential factor Z is different:

$$\vec{k}_t = (RT/2\pi M)^{1/2}(M\omega^*/\zeta^a)\exp(-\Delta_a^* \tilde{G}_i^0/RT) \tag{48}$$

The standard Gibbs energy of activation $\Delta_a^* \tilde{G}_i^0$ is given by Eq. (28), with the charge transfer coefficient being a linear function of $\Delta_a^b \tilde{G}_i^0$,

$$\alpha = L^*/L^a + \Delta_a^b \tilde{G}_i^0/2M(\omega^* L^a)^2 \tag{49}$$

where L^* is the distance between the initial (a) and transition locations of the ion. Thus, the equivalent jump length L^a presents only a second-order effect on the charge transfer coefficient, Eq. (49). Unlike treatments that are based on the Nernst-Planck equation [126, 129, 130], the stochastic approach accounts for the local friction anisotropy or variation of the diffusion coefficient in the interfacial region [128]. Besides, the latter approach suggests that the ion transfer rate dynamics depend on both the local friction and the local ion mobility; cf. the hydrodynamic factor $(M\omega^*/\zeta^a)$ in Eq. (48).

Kakiuchi [130] integrated the Nernst-Planck equation by assuming a constant gradient of the electrochemical potential in the inner layer at the ITIES. This layer was not supposed to be necessarily the same entity as the ion-free inner layer at the interface (Sec. 2.3.2). In the absence of an activation barrier at the interface, the

equation for the rate constant $\vec{k}_t$ in Eq. (26) can be written in the present notation as [130]

$$\vec{k}_t = k_0 y e^y / \sinh y \tag{50}$$

with

$$y = (zF/2RT)(\Delta_b^a \phi - \Delta_O^W \phi_i^0) \tag{51}$$

$$k_0 = D/L^a \tag{52}$$

The nonlinear character of Eq. (50) is essentially the same as the Goldman-type rectification [134] known to membrane physiologists, and can also be responsible for various rectification phenomena, e.g., the Fournier effect [135], i.e., the distortion of dc current-potential curves due to the ac noise [130]. Besides the prediction of the curved Tafel plots, the charge transfer coefficient at the standard potential difference should always equal 0.5. Thus, the model provides a simple, yet phenomenological, interpretation of the rate constant of ion transfer. Equation (50) can be derived even without assuming that the process is activationless. Thus, when the ion should overcome a rectangular barrier of the height $\Delta \bar{G}_i^*$, only Eq. (52) is to be modified by introducing the factor $\exp(-\Delta \bar{G}_i^*/RT)$.

3.1.4 Molecular Dynamics

Although all theoretical approaches discussed in previous sections do refer to a particular molecular model, rather they represent attempts to rationalize experimental kinetic data in terms of mean values of electrical field or ion distribution, energy barrier height, energy change, ion mobility and viscosity of medium, which are all supposed to be closely related to the molecular properties of the ions and solvent molecules involved. However, no direct link to molecular properties has been established within the framework of the models discussed above.

Recently, detailed molecular pictures of the interfacial structure on the time and distance scales of the ion-crossing event, as well as of ion transfer dynamics, have been provided by Benjamin's molecular dynamics computer simulations [71, 75, 128, 136]. The system studied [71, 75, 136] included 343 water molecules and 108 1,2-dichloroethane molecules, which were separately equilibrated in two liquid slabs, and then brought into contact to form a box about 4 nm long and of cross-section 2.17 nm × 2.17 nm. In a previous study [128], the dynamics of ion transfer were studied in a system including 256 polar and 256 nonpolar diatomic molecules. Solvent-solvent and ion-solvent interactions were described with standard potential functions, comprising coulombic and Lennard-Jones 6–12 pairwise potentials for electrostatic and nonbonded interactions, respectively. While in the first study [128] the intramolecular bond vibration of both polar and nonpolar solvent molecules was modeled as a harmonic oscillator, the next studies [71, 75, 136] used a more advanced model [137] for water and a four-atom model, with a united atom for each of two

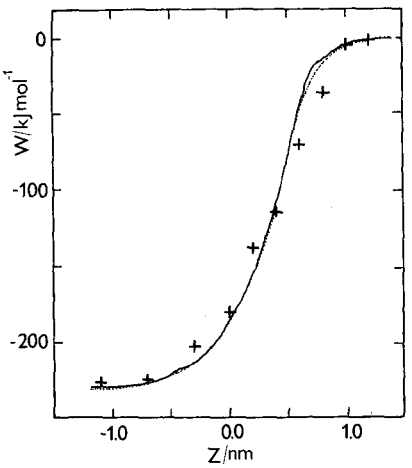

Fig. 11. Standard Gibbs energy profile (solid line) for an ion transfer across the sharp interface calculated through a non-Boltzmann sampling using a total of 1.6 ns molecular dynamics trajectories. The crosses denote half of the average ion-solvent electrostatic energy. (After [128]).

CH_2 groups, including all bond stretches. bending and torsion around the C–C bond for 1,2-dichloroethane. The chosen ions included Cl^- [75, 136], F^-, Na^+, K^+, and $(CH_3)_4N^+$ [136].

Several fundamental questions have been answered in these few studies. Firstly, on the long time-scale (hundreds of pico-seconds), the water-1,2-dichloroethane interface has been shown to be molecularly sharp [71, 128]. The density profile for each solvent varies abruptly over the distance of 0.5 – 1.0 nm, which is roughly the sum of the solvent molecule diameters. In this limit also the profile of the Gibbs energy of the ion is a smooth function of the distance (Fig. 11), indicating the absence of an activated process, which resembles the result reported by Kharkats and Ulstrup [133]. Such behavior indicates that ion diffusion in the bulk solution is not an activated process, i.e., attempts [60, 124, 126] to interpret the diffusion coefficient in terms of transition state theories are rather misleading. The local diffusion (or friction) coefficient is also a smooth function of the coordinate perpendicular to the interface [128], showing a considerable drop on going from nonpolar to polar solvent. While this result is understandable from a physical point of view [128], it is at variance with an experimentally observed change in the apparent diffusion coefficient, which is just the opposite.

Secondly, on a shorter timescale (tens of picoseconds), which is actually the timescale of ions crossing the interface [75, 128], thermal fluctuations superimpose capillary waves as long as about 0.8 nm on the sharp interface and generate a rather rough interface [71]. Benjamin [75] has shown that these waves are moving "fingers" of water that protrude into the other liquid, and that the reactive ion trajectory is that in which a water "finger" happens to "find" the ion. Thus, capillary waves play a dynamic role in the ion transfer process. In the opposite direction, i.e., from water to organic phase, the ion carries at least part of its hydration shell to the organic phase. During this process, the interfacial region becomes highly disordered and broadened, and capillary waves are longer.

Thirdly, it has been concluded [75, 136] that ion transfer is an activated rather than a simple diffusion process. However, the existence of an activation barrier of several tens of kilojoules per mole is predicted only in the model, which accounts for the change in the liquid structure near the ion. When the system is treated as two homogeneous dielectric media with the ion as a charged sphere, the Gibbs energy profile is smooth even on the short timescale (cf. Fig. 2). In any case, the presence of the electrical field leads to an acceleration of the ion transfer, so that at a field strength of $2\times10^9\ V^{-1}$ 75% of the ion trajectories are completed within 15 ps. A comparison or correlation of computer and real kinetic data might be prevented by the lack of reliable experimental data for the water-1,2-dichloroethane system. Kinetic parameters for three of the five ions mentioned above, namely for Cl^-, F^-, and Na^+, are quite difficult to acquire.

3.2 Experimental Results of Simple Ion Transfer Reactions

Four particular problems have been addressed in experimental kinetic studies of ion transfer kinetics across liquid-liquid interfaces. The effect of the electrical potential difference on the ion transfer rate has been always in the limelight [38, 42, 61, 96, 100, 101, 109, 115, 117, 118, 121, 124, 132, 138–151]. Second, there have been attempts to clarify the role of the nature of the ion in terms of ion mobility and solvation energy. In order to reach this goal, kinetic data for series of homologous ions were gathered and analyzed [42, 109, 115, 117, 118, 132, 138, 144]. Third, because the rate of both bulk and interfacial ion transport should depend on properties of the medium, effects of the temperature [115], the viscosity [124] and the dielectric constant [139] were examined. Finally, a monolayer of amphiphilic molecules formed at polarized liquid-liquid interfaces has been proposed as a suitable model of the biological membrane-solution interface [94]. Phase behavior and ion permeability of monolayers were investigated by several authors [94, 96, 100, 101, 140, 141]. Most of the experimental work was done on the water-nitrobenzene system; kinetic studies of the water-1,2-dichloroethane interface are few [124]. Highlights of these efforts are now summarized, with a comment on experimental techniques.

3.2.1 Experimental Techniques

Basically, experimental approaches to ion transfer kinetics rely on classical galvanostatic [152] or potentiostatic [146] techniques, such as chronopotentiometry [118, 138], chronocoulometry [124], cyclic voltammetry [146], convolution potential sweep voltammetry [147], phase selective ac voltammetry [142], or equilibrium impedance measurements [148]. These techniques were applied mostly to liquid-liquid interfaces with a macroscopic area (typically around 0.1 cm^2). However, microelectrode methodology has been successfully introduced into liquid-liquid electrochemistry as a novel electroanalytical tool by Senda and coworkers [153] and

Taylor and Girault [154], and has been further developed by Girault and coworkers [155], Vanýsek and Hernandez [156] and Mareček et al. [149]. The use of a microscopic interface is an essential requirement for a fluctuation analysis of ion transfer system under thermodynamic equilibrium which was attempted first by Mareček et al. [149]. No kinetic data have been reported from voltammetric or noise measurement at microliquid interfaces, though a new insight into the interfacial dynamics comprising ion transfer has been thought possible [149].

Experimental difficulties in obtaining reliable kinetic parameters can arise from high solution resistance (typically of order $10^2 - 10^3\ \Omega$) compared with kinetic resistance (typically less than $10\ \Omega$), as well as from nonhomogeneous polarization due to the curved interface and/or an improper electrode configuration, or from electromechanical phenomena induced by the potential-dependent surface tension [42, 148]. Artifacts in the ac impedance measurements of liquid-liquid interfaces, which can originate from an improper design of the electrolytic cell, were discussed by Schiffrin and coworkers [43]. It was concluded that the main origin of the observed high-frequency dispersion is the high value of the resistance of the potential probe for the organic phase. Electrochemical cells allowing formation of an ideally flat liquid-liquid interface have been recognized as an essential requirement, together with the symmetric configuration of electrodes [42, 157, 158] and low-impedance potential probes [43]. A first attempt to construct such a cell was made by Buck and coworkers [157], but the improper use of Pt wires as reference electrodes probably prevented the authors from obtaining meaningful kinetic data. Two approaches to the cell design are illustrated in Fig. 12, showing a two- [42] or four-electrode [158] galvanic cell. In either case, it is necessary to measure precisely the solution resistance, which is subtracted from the total impedance either numerically under zero dc conditions, or instrumentally under nonzero dc conditions, e.g., by using positive feedback [146]. VanderNoot and Schiffrin [36] suggested that, in order to extract kinetic information from impedance data, a nonlinear regression technique must be used. Convenient software for performing a nonlinear least-squares fitting of impedance data is available [159].

Kinetic data that have been obtained so far fall into three groups. The first comprises data measured without the proper ohmic drop compensation or subtraction and/or the ideal polarization of the liquid-liquid interface being considered. Thus, from kinetic measurements made by Gavach et al. [138] Buck and coworkers [121, 122], or Samec et al. [38], rather low values of the standard rate constant k_0^s were obtained ($10^{-3} - 10^{-4}$ cm s^{-1}).

In the more advanced kinetic measurements, which were carried out by using chronopotentiometry [118], chronocoulometry [124, 139], linear [146] and convolution [18, 147] potential sweep voltammetry, or phase-sensitive ac polarography [142, 143], the ohmic drop was either numerically subtracted [118], or compensated [124, 139, 142, 143, 146, 147] with the help of the positive feedback. The feedback adjustment was based either on the assumption that the separation of the current peaks measured by the slow potential sweep voltammetry should reach the value of $(59/z)$ mV [124, 139, 146, 147], or on the value of the solution resistance obtained by an ac bridge technique [142, 143]. However, the former adjustment is not very sensitive, whereas the estimated accuracy of $10\ \Omega$ [142] in the latter case may not be

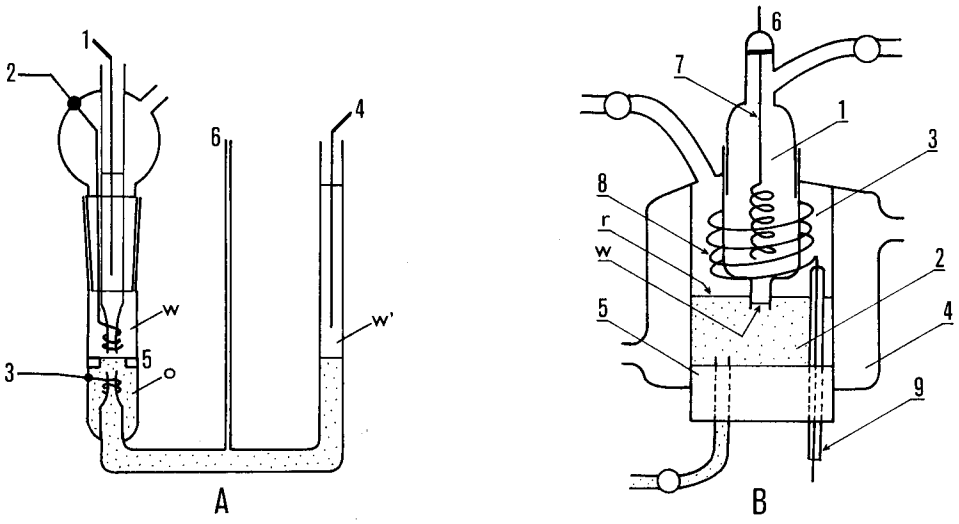

Fig. 12. Design of the galvanic cell with a flat liquid-liquid interface. (A) The four-electrode type of cell with the aqueous (w, w') and the organic solvent (o) phases, silver/silver chloride reference electrodes (1, 4), platinum counter electrodes (2, 3), a glass barrier with a round hole for the liquid-liquid interface (5) and a tube connected to a syringe for adjustment of the interface. (After [158]). (B) The two-electrode type of cell with the aqueous (1, 3) and organic solvent (2) phases, water jacket (4), PTFE silicone rubber (5), silicone rubber cap, silver/silver chloride reference electrodes (7, 8), glass tube (9) and polarized working (w) or nonpolarized reference (r) interface. (After [42]).

sufficient, inasmuch as the kinetic resistance are of a comparable magnitude. Hence, the values of the standard rate constant ($10^{-2}-5\times10^{-1}$ cm s^{-1}) reported in these studies can also be underestimated, though probably to a lesser degree.

It has been shown [42] that the phase angle measurements by ac polarography can provide a very sensitive test for the correct adjustment of the positive feedback. Kinetic analysis based on this technique [42, 61, 144, 145], or on the equilibrium impedance measurements [115, 132, 148], yielded k_0^s around 0.1 cm s^{-1}. Owing to very good agreement between kinetic data inferred for the same ion transfer reactions [42, 115, 132, 148], we propose to use these results as the most reliable reference, until other techniques provide a more reliable basis for consideration. In this respect, fluctuation analysis [149] or faradaic rectification [160] appear to be promising. Recently, ion transfer fluorometry has been introduced by Kakiuchi and coworkers [161, 162] as a very specific means of minimizing problems with double layer charging and ohmic drop compensation.

Obviously, a comparison of kinetic data without critically analyzing their reliability can eventually be misleading. Girault [14] has made a dubious conclusion that the flow of the direct current can alter the solution composition in the vicinity of the interface, which makes the rate constant measured by a dc technique significantly lower, as compared with data obtained by an ac technique. However, the highest rate constants have been reported from ac impedance studies irrespective of whether the direct current flows through the interface [42], or not [132]. Analogous-

ly, an evaluation [14] of the standard activation Gibbs energies from Gavach's data [109, 138], which are only of historical value, can hardly provide actual information about the standard Gibbs energy profile at the ITIES.

3.2.2 Electrical Potential Difference

There is ample evidence that the plots of the logarithm of the apparent rate constant $\bar{k}$ against the potential difference (Tafel plots) for univalent ions have reciprocal slopes of about 118 mV per decade [42, 61, 124, 132, 142–144, 146]. This behavior is illustrated for several cations and anions in Fig. 13, which displays data obtained from equilibrium impedance measurements [132]. Tafel plots derived from dc or ac voltammetric measurements in a sufficiently broad potential range are usually curved [144, 145, 163]. Chronocoulometry has been claimed [124] to provide independently the rate constants for the forward and the backward ion transfer in Eq. (21); cf. also Girault's review [14]. However, this is impossible in principle, because these rate constants should always be related to each other by Eq. (22). The origin of the value of the apparent charge transfer coefficient and its variation with the potential has been always the key issue.

Initially, the potential difference across the liquid-liquid interface has appeared to be concentrated in the diffuse double layer (Sec. 2.3). On this basis Koryta [6] concluded that the apparent charge transfer coefficient $\bar{\alpha}$ is not related to the activation barrier and should have a value close to 0.5, as explained in Sec. 3.1.2. A numerical analysis based on Eq. (36) revealed however that, depending on the value of the parameter p (Eq. (37)), $\bar{\alpha}$ can vary with the potential difference $\Delta_{\mathrm{O}}^{\mathrm{W}}\phi$, i.e., Tafel plots should not be linear curves [60].

In order to account for the effect of the electrical double layer on the apparent charge transfer coefficient, the Frumkin-type correction was applied to kinetic data in the earliest kinetic analyses [109, 147]. As a result, the corrected rate constant $\bar{k}_{\mathrm{t}}$ was found to be practically independent of the potential E [117, 118, 147], in agreement with the almost constant value of the inner-layer potential difference, $\Delta_{\mathrm{O2}}^{\mathrm{W2}}\phi \approx 0$. Further systematic studies of the electrical double layer (Sec. 2.3.2) have shown that the inner-layer potential difference $\Delta_{\mathrm{O2}}^{\mathrm{W2}}\phi$ is negligible only near the potential of zero charge. A significant correlation between the corrected rate constant $\bar{k}_{\mathrm{t}}$ and $\Delta_{\mathrm{O2}}^{\mathrm{W2}}\phi$ was disclosed for picrate (Pi^-) ion transfer [143, 148]. Corrected Tafel plots at various concentrations of the aqueous base electrolyte (LiCl) are displayed in Fig. 14. Owing to some doubts about the applicability of the Gouy-Chapman theory in solutions of low electrolyte concentration [163], we ignored kinetic data for 0.02 M LiCl. The electrolyte effect was re-examined for Cs^+ ion transfer [163], with a similar result (Fig. 15). As follows from theoretical studies (Sec. 3.1), the slope of these plots can vary with the potential difference across the inner layer as predicted either for the constant-field model [130] (cf. Eq. (50)) or for the activated-step model [109, 126] (cf. Eq. (49)). Indeed, the denominator $2M(\omega^* L^{\mathrm{a}})^2$ in Eq. (49) can be comparable with $\Delta_{\mathrm{a}}^{\mathrm{b}}\bar{G}_i^0$. For $M \approx 100$ and a characteristic transition time and length of 10 ps (i.e, $\omega^* \approx 10^{11}\ \mathrm{s}^{-1}$) and 1 nm [71, 128], respectively, the former term would

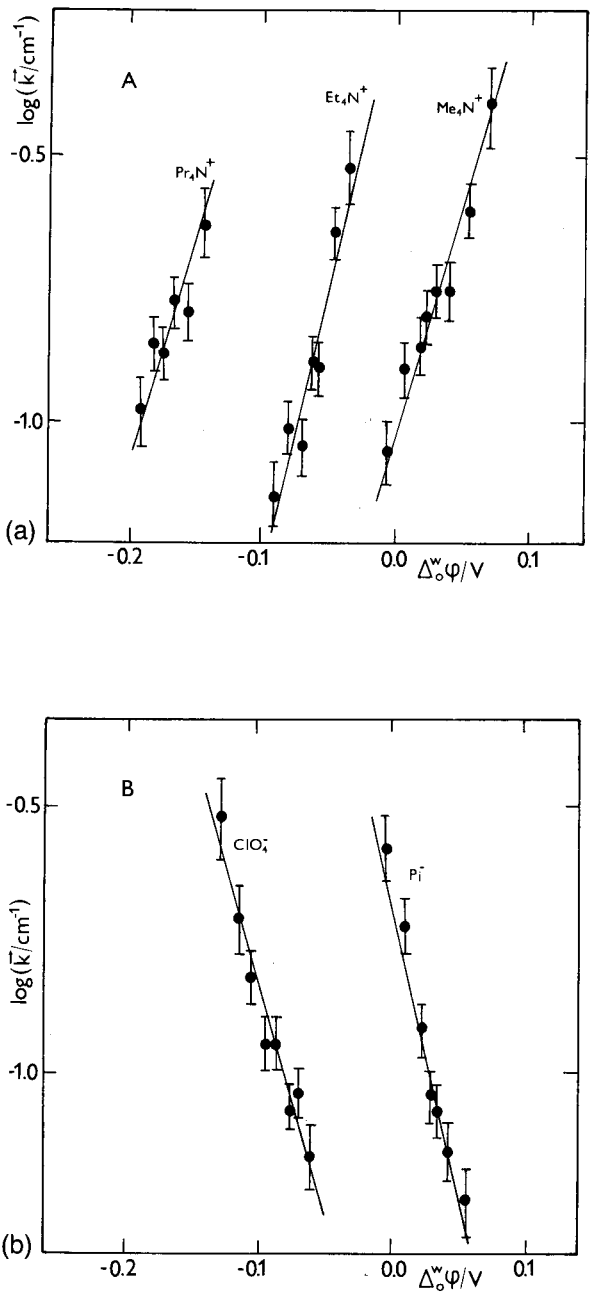

Fig. 13. Logarithm of the apparent forward rate constant $\vec{k}$ vs. the equilibrium potential difference $\Delta_O^W\phi$ (Tafel plot) derived from equilibrium impedance measurements for (A) monovalent cation and (B) anion transfer from a solution of 0.05 M LiCl in water to a solution of 0.05 M Bu_4NPh_4B or (Ph_4AsDCC) in nitrobenzene at 293 K. (After [132]).

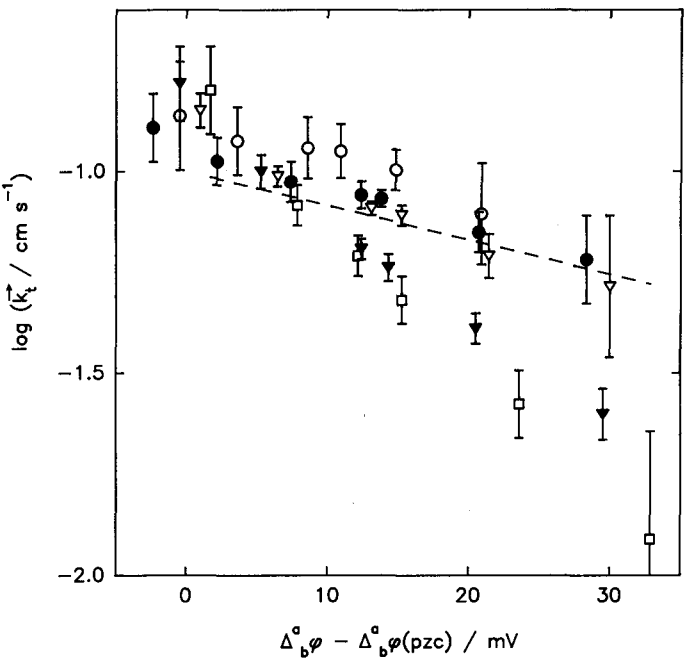

Fig. 14. Logarithm of the true forward rate constant $\vec{k}_t$ vs. the inner layer potential difference $\Delta^a_b\phi$ relative to the potential of zero charge (corrected Tafel plots) for picrate ion transfer between nitrobenzene solution of 0.1 M Bu_4NPh_4B and an aqueous solution of (○) 0.05, (●) 0.1, (▽) 0.2, (▼) 0.5, and (□) 1.0 M LiCl at 298 K. Vertical bars indicate the standard deviation; the broken line corresponds to $\alpha = 0.5$. (After [143]).

have a value around 2 kJ mol^{-1}. Although this is a very rough estimate, it can explain the curvature of corrected Tafel plots (cf. Fig. 15).

On the other hand, the influence of the base electrolyte concentration on the ion transfer rate casts some doubts on the validity of the classical Frumkin correction [143, 145]. First, the corrected rate constant $\vec{k}_t$ should not vary with the base electrolyte concentration. Although this effect is much less pronounced when kinetic data at concentrations lower than 0.05 mol dm^{-3} are disregarded, the tendency to vary exceeds the range of experimental error, in particular for picrate ion transfer (cf. Fig. 14). Second, by using Eq. (33), Kakiuchi [145] has shown that the apparent standard rate constant k^s_0 should vary with the base electrolyte concentration in a way that is opposite for cations and anions, as well as opposite for ions of the same sign but with the standard potential difference on the positive and negative side relative to the potential of zero charge. At the same time, the apparent charge transfer coefficient $\vec{\alpha}_0$ should decrease with increasing base electrolyte concentration. In contrast, experimental rate constants for various ions show a tendency to increase slightly, while $\vec{\alpha}_0$ does not vary at all (Fig. 16, p. 336). However, predicted plots were calculated on the assumption that the parameter α in Eq. (31) is a constant [145]. When

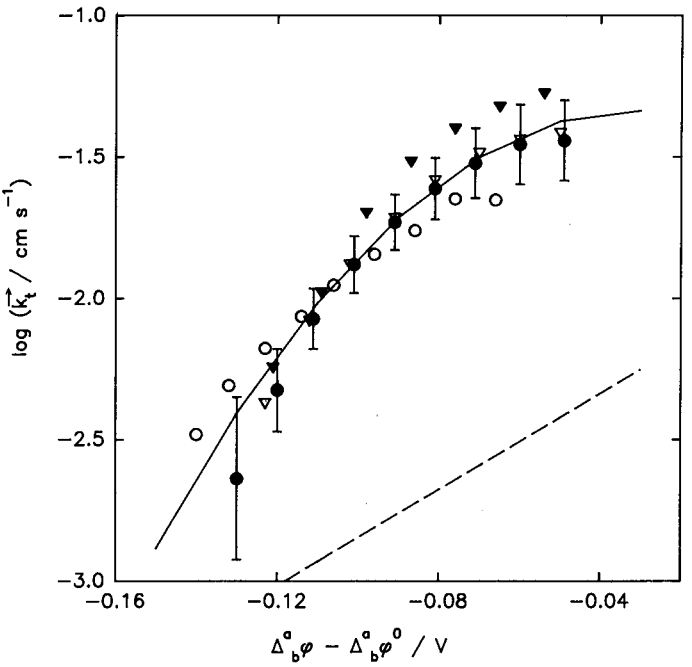

Fig. 15. Logarithm of the true forward rate constant $\vec{k}_t$ vs. the inner layer potential difference $\Delta^a_b\phi$ relative to the standard potential difference (corrected Tafel plots) for Cs^+ ion transfer between nitrobenzene solution of 0.05 M $Pn_4N[(CF_3)_3Ph]_4B$ and an aqueous solution of (○) 0.05, (●) 0.1, (▽) 0.2, and (▼) 0.5 M LiCl at 298 K. Vertical bars indicate the standard deviation in 0.1 M LiCl; the broken line corresponds to $\alpha = 0.5$. (After [163]).

this condition is relaxed, and the validity of Eq. (49) is anticipated, the change in the inner-layer potential difference results in a change in α, which in turn weakens the effect of potential differences across the space charge regions in Eq. (31). These mutual compensations are seen, for example, in Cs^+ ion transfer kinetics, for which both apparent kinetic parameters are practically independent of the base electrolyte concentration, yet the corrected Tafel plots coincide (cf. Fig. 15) [163].

We conclude that, in view of the unequivocal existence of the diffuse double layer at the ITIES, the Frumkin-type correction appears to be a plausible working hypothesis, though its unambiguous proof has not been provided yet. A more advanced approach, which relies on solving the Nernst-Planck equation in the space charge region, has been developed by Matsuda and Delahay [164].

3.2.3 Influence of the Nature of the Ion

One of the characteristic features of ion transfer kinetics is the minor effect of the ionic structure or size (diameter). Table 1 (p. 337) summarizes the apparent kinetic

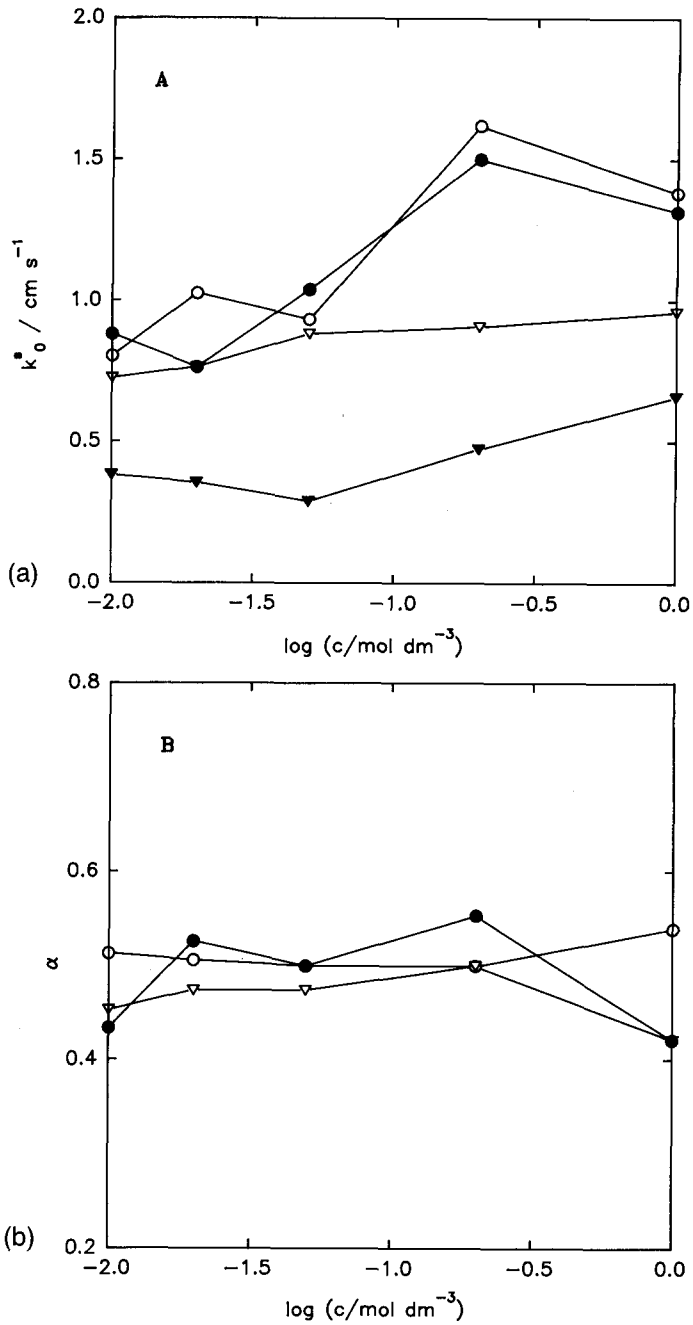

Fig. 16. Observed changes in (A) the apparent standard rate constant k_0^s, and (B) the apparent charge transfer coefficient $\vec{\alpha}_0$ with the concentration of the aqueous base electrolyte (LiCl) for the transfer of (▽) Me_4N^+, (●) Et_4N^+, (▼) Pr_4N^+, and (○) PF_6^- across the water-nitrobenzene interface at 298 K. Composition of the nitrobenzene phase: 0.1 M Pn_4NPh_4B. (After [145]).

Table 1. Standard potential differences $\Delta_O^W\phi_i^0$, diffusion coefficients D^W or D^O (in parentheses), and apparent kinetic parameters k_0^s and $\vec{\alpha}_0$ for the transfer of cations and anions across the water-nitrobenzene interface[a].

Ion	$\Delta_O^W\phi_i^0$ (V)	$10^6 \times D$ ($cm^2\,s^{-1}$)	$10 \times k_0^s$ ($cm\,s^{-1}$)	$\vec{\alpha}_0$	Ref.
Me_3NH^+	0.092	11.1	0.86	0.44	42
Choline	0.079	9.4	0.83	0.47	42
Me_4N^+	0.030	10.6	0.90	0.50	42
		9.5 (3.7)	1.36	0.58	132
		9.5 (4.8)	1.20	–	115
$EtMe_3N^+$	0.003	10.2	0.78	0.50	42
$Et_2Me_2N^+$	−0.022	10.1	0.83	0.43	42
Me_3PrN^+	−0.027	7.4	0.91	0.54	42
Et_3MeN^+	−0.042	8.9	1.12	0.52	42
Me_3BuN^+	−0.063	9.7	1.03	0.54	42
Et_4N^+	−0.067	7.8	1.5	0.55	42
		9.3 (4.0)	0.9	0.64	132
		9.3 (4.5)	1.1	–	115
Et_3PrN^+	−0.093	8.2	0.88	0.50	42
$EtPr_3N^+$	−0.143	– (1.63)	0.80	0.42	42
Pr_4N^+	−0.170	– (1.21)	0.47	0.44	42
		8.5 (3.4)	1.36	0.60	132
Me_4P^+	0.009	8.8 (3.7)	1.48	0.55	132
Me_3EtP^+	−0.020	8.1 (3.6)	1.26	0.51	132
		7.9 (3.6)	1.14	–	115
Me_3PrP^+	−0.050	6.7 (3.1)	1.26	0.58	132
		6.4	1.05	–	115
Me_3BuP^+	−0.084	5.8 (2.9)	0.89	0.57	132
Me_2V^{2+}	−0.015	5.6 (2.3)	0.48	0.50	132
Et_2V^{2+}	−0.043	4.1 (1.5)	0.53	0.49	132
Pr_2V^{2+}	−0.058	3.3 (0.9)	0.68	0.55	132
Pi^-	0.039	6.1 (2.7)	0.83	0.56	148
		8.8	0.37	0.45	143
PF_6^-	−0.007	12.9	1.63	0.50	144
ClO_4^-	−0.083	15.3 (6.7)	0.9	0.57	132
	−0.110	14.9	1.08	0.53	144
BF_4^-	−0.153	15.7	1.73	0.44	144
SCN^-	−0.189	13.7	0.91	0.45	144

[a] Experimental conditions: temperature 293 K [115, 132, 148] or 298 K [42, 143, 144]; base electrolyte concentrations in both phases 0.05 M [115, 132, 148] or 0.1 M [42, 143, 144].

parameters for several homologous series of univalent or divalent ions. Typically, the apparent standard rate constant k_0^s is of the order of 0.1 $cm\,s^{-1}$ and the apparent charge transfer coefficient at the standard potential difference, $\vec{\alpha}_0$, equals 0.5 ± 0.1. While the ion transport rate in the bulk of the solution reflects clearly a change in these ion parameters, no straightforward effect on the interfacial ion transport is

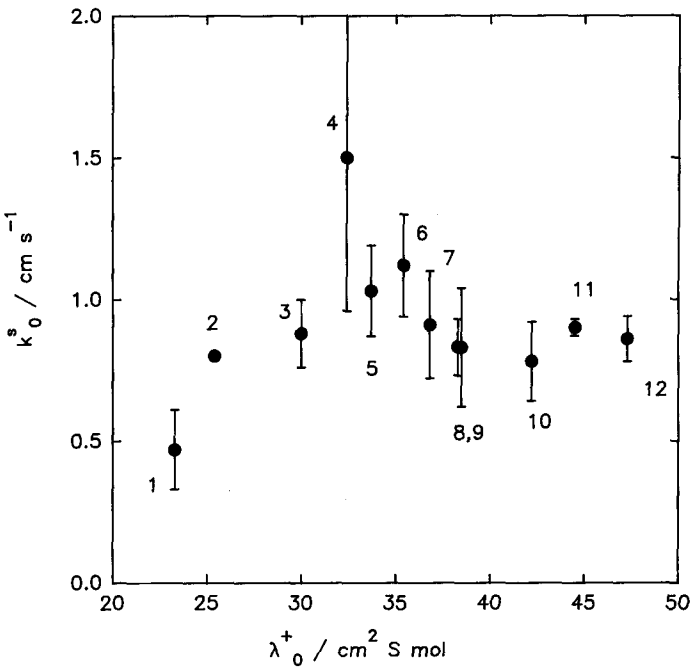

Fig. 17. Apparent standard rate constant k_0^s vs. the limiting ionic conductance λ_0^+ in water for the transfer of (1) Pr_4N^+, (2) $EtPr_3N^+$, (3) Et_3PrN^+, (4) Et_4N_+, (5) Me_3BuN^+, (6) Et_3MeN^+, (7) Me_3PrN^+, (8) choline, (9) $Et_2Me_2N^+$, (10) $EtMe_3N^+$, (11) Me_4N^+, and (12) Me_3NH^+ across the water-nitrobenzene interface. Vertical bars indicate the 95% confidence intervals. (After [42]).

seen. Figure 17 displays the plot of the apparent standard rate constant against the ion mobility [42]. If the ion transfer across the interface were essentially similar to the ion transport in the bulk of the solution, as suggested by Shao and Girault [124], a linear relationship would be observed between k_0^s and the ion mobility. Contrary to this expectation, the plot in Fig. 17 exhibits a maximum for Et_4N^+, and k_0^s decreases with either an increase or a decrease in the ion mobility [42]. A conclusion was drawn that the hydrodynamic friction due to the solvent-ion interactions dynamics, and the viscous momentum transport exerted on the transferring ion by the solvent layers at the interface, play a significant role in the ion transfer dynamics [42].

According to the stochastic theory (Sec. 3.1.3), the hydrodynamic friction should influence mainly the pre-exponential factor of the rate constant. However, ions studied differ considerably in the standard potential difference $\Delta_O^W\phi^0$, which contributes to the standard Gibbs energy change $\Delta_a^b\bar{G}_i^0$ for ion transfer between the locations a and b (Eq. 29), and thereby controls the magnitude of the exponential factor in the expression for the true rate constant (Eqs. 48 and 50). Indeed, when the Frumkin-type correction is applied to apparent kinetic data, the corrected rate constant $\vec{k}_t$ exhibits a significant correlation with $\Delta_a^b\bar{G}_i^0$ for ions which differ in size, structure, and sign of charge [115, 117, 118, 132]. Such a Brønsted-type correlation

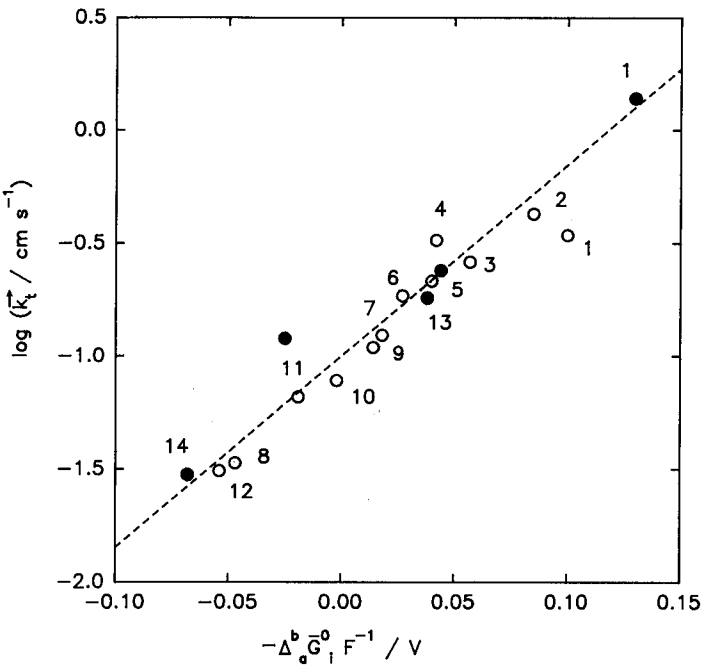

Fig. 18. Logarithm of the true forward rate constant $\vec{k}_t$ vs. the corrected standard Gibbs energy of transfer $\Delta^b_a \bar{G}^0_i$ (Brønsted correlation) for a series of homologous ions: (1) Pr_4N^+, (2) $EtPr_3N^+$, (3) Et_3PrN^+, (4) Et_4N^+, (5) Me_3BuN^+, (6) Et_3MeN^+, (7) Me_3PrN^+, (8) choline, (9) $Et_2Me_2N^+$, (10) $EtMe_3N^+$, (11) Me_4N^+, (12) Me_3NH^+ (13) Pi^- and (14) ClO_4^-. The broken line corresponds to $\alpha = 0.5$. (After [115] from data [42], empty circles and [132], full circles).

is displayed in Fig. 18. Apart from an excellent agreement between data from different kinetic studies [42, 132], the slope of the plot corresponds to $\alpha \approx 0.5$, as predicted by Eq. (50) for a constant-field model, or by Eq. (49) for the activated-step model with a barrier which is located in the middle between the locations a and b. This conclusion is corroborated by the analysis of the corrected Tafel plots (Sec. 3.2.2).

3.2.4 Medium Effects

The effect of temperature on ion transfer across the water-nitrobenzene interface was studied for a series of six quaternary ammonium and phosphonium cations and two anions using cyclic voltammetry and equilibrium impedance measurements [115]. Standard entropies ($\Delta^O_W S^0_i$) and enthalpies ($\Delta^O_W H^0_i$) of ion transfer have been evaluated from the experimentally accessible reversible half-wave potential ($E^{rev}_{1/2}$ and standard Gibbs energy of transfer ($\Delta^O_W G^0_i$),

$$-zF(\mathrm{d}E^{rev}_{1/2}/\mathrm{d}T) = \Delta^O_W S^0_i - \Delta^O_W S^0_{ref} \tag{53}$$

Table 2. Thermodynamic functions, apparent activation energies and parameters of the stochastic theory for various ion transfer reactions at the water-nitrobenzene interface at 293 K [115].

Ion	$\Delta_W^o G_i^0$ (kJ mol^{-1})	$\Delta_W^o H_i^0$ (kJ mol^{-1})	$\Delta_W^o S_i^0$ (J mol^{-1} K^{-1})	E_{tr}^a (kJ mol^{-1})	E_d^a (kJ mol^{-1})	$\Delta\bar{G}_i^*$ (kJ mol^{-1})	$M\omega^*/\zeta^a$ $\times 10^4$
Me_4N^+	2.9	−5.3	−27.4	19.3	18.8	4.7	1.4
Et_4N^+	−6.4	−3.9	−3.9	19.8	16.8	5.4	2.1
Bu_4N^+	−26.5	0.6	–	–	–	–	–
Me_4P^+	0.9	−11.6	−41.8	–	–	–	–
Me_3EtP^+	−1.9	−7.8	−19.6	13.6	16.9	1.5	0.3
Me_3PrP^+	−4.8	−6.4	−5.2	20.1	19.5	4.4	0.9
Me_3BuP^+	−8.1	−3.0	17.0	–	–	–	–
Pi^-	−4.1	−4.6	−1.6	19.2	19.0	3.2	0.6
ClO_4^-	7.9	−12.6	−68.8	–	–	–	–

$$\Delta_W^o G_i^0 = \Delta_W^o H_i^0 - T\Delta_W^o S_i^0 \tag{54}$$

Thermodynamic data are summarized in Table 2. Since, unlike nitrobenzene, water is a highly structured solvent, structure-breaking properties of small ions and enhancement of water structure in the presence of large cations are manifested in both entropic and enthalpic contributions, which both increase with the ion size.

The temperature dependence of the rate constant $\vec{k}_t$ is illustrated in Fig. 19. Table 2 summarizes the apparent activation energies of the ion transfer $E_{tr}^a = -R\,\partial \ln \vec{k}_t/\partial(1/T)$, and of diffusion $E_d^a = -R\,\partial \ln D/\partial(1/T)$. Ion diffusion coefficients at various temperatures were evaluated from voltammetric data [115]. Provided that the temperature dependencies of the friction coefficient in the bulk of the solution, and at the location a, have equal slopes, a relationship can be derived from Eq. (48) [115]:

$$E_{tr}^a - E_d^a \approx \Delta\bar{G}_i^* - (RT/2) + \alpha\,(\Delta_W^o H_i^0 + zF\Delta_b^a\phi) \tag{55}$$

As can be seen from Table 2, the apparent activation energies of the ion transfer and diffusion are almost equal. Nevertheless, the standard Gibbs energy of activation $\Delta\bar{G}_i^*$, which was derived by using Eq. (55), has a positive value for all ions studied, though the potential barrier appears to be rather low [115]. Actually, the potential barrier can be effectively lowered when the potential of the ion has a fluctuating contribution, because the particle has more opportunities to escape at times when the barrier is relatively low and need not wait for thermal excitation [165]. After inserting known values of all parameters of the stochastic theory into Eq. (48), the values of the hydrodynamic factor $M\omega^*/\zeta^a$ are found to be of the order of 10^{-4} (Table 2). In contrast, an estimate based on the frequency of ion vibration $\omega^* \approx 10^{11}\ s^{-1}$ and the friction coefficient $\zeta = RT/D \approx 2.4\times10^{15}\ g\ s^{-1}\ mol^{-1}$ in the bulk solution and M = 100 g mol^{-1} yields $M\omega^*/\zeta^a \approx 40\times10^{-4}$, a value almost two orders of magnitude greater. Since the estimate of the frequency is corroborated by molecular dy-

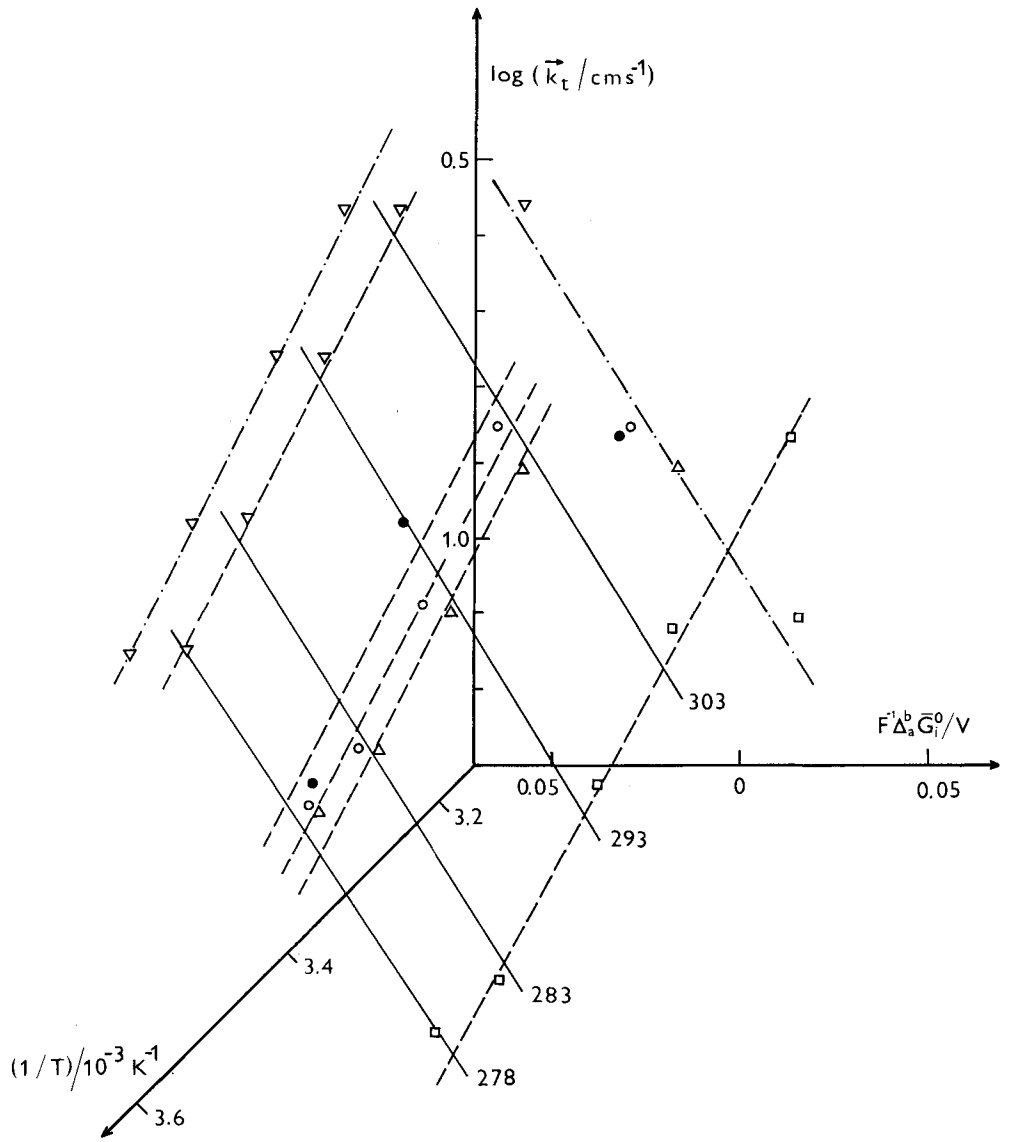

Fig. 19. Logarithm of the true forward rate constant $\vec{k}_t$ vs. the reciprocal temperature T and the corrected standard Gibbs energy of transfer $\Delta_a^b\bar{G}_i^0$ (Brønsted correlation projected on the plane of the page) for (○) Pi^-, (●) Me_3PrP^+, (△)Me_3EtP^+, (▽) Et_4N^+, and (□) Me_4N^+ ion transfer from the solution of 0.05 M LiCl in water to the solution of 0.05 M Bu_4NPh_4B in nitrobenzene. The numbers on the lines indicate the temperature (K). (After [115]).

namics calculations [71, 128], it appears that the reduction in the hydrodynamic factor is the frictional effect. In a previous communication [132], the standard Gibbs energy of activation $\Delta\bar{G}_i^*$ was necessarily overestimated by using the bulk value of the friction coefficient.

Other remarkable effects of the medium which are worth considering are those of viscosity and dielectric constant. In particular, the transfer of acetylcholine across the water-1,2-dichloroethane interface has been studied as a function of the viscosity of the aqueous phase varied by adding sucrose (0–48 wt. %) [124]. Both the ion diffusion coefficient and the apparent standard rate constant k_0^s were found to be inversely proportional to the viscosity and their variation with temperature provided almost equal apparent activation energies (enthalpies) of about 21 kJ mol^{-1}. Plots of $\log k_0^s$ or $\log D$ against the change in the standard Gibbs energy of ion transfer $\delta\Delta_W^O G_i^0$ due to the presence of sucrose were found to have similar slopes. Since the apparent rate constant of diffusion estimated from Eq. (41) was several orders of magnitude higher than $k_0^s \approx 10^{-2}$ cm s^{-1}, the conclusion was made that the main difference between ion transfer and ion transport is the consequence of an entropy effect. The weak point of the argument is the use of Eq. (41), into which a proper value of the effective jump length L^a must be inserted.

Analogously, the transfer of acetylcholine from water to nitrobenzene was studied as a function of composition of the organic solvent, which was varied by adding nonpolar tetrachloromethane [139]. With increasing concentrations of CCl_4 (0–86 wt.%) both the dielectric constant and viscosity of the organic phase decrease, which has an effect on the apparent standard rate constant k_0^s, the ion diffusion coefficient in the organic phase D^O, and the standard Gibbs energy of ion transfer $\Delta_W^O G_i^0$. In order to explain the observed effects of sucrose in the aqueous phase [124] and of CCl_4 in the organic phase [139], an empirical equation was proposed [139]:

$$k_0^s = k_0 \exp\left[-(l^W \Delta G_s^W + l^O \Delta G_s^O)/RT\right] \tag{56}$$

where the standard activation energy for the ion transfer is given as the linear combination (l^W and l^O are constants) of the Gibbs solvation energies ΔG_s^W and ΔG_s^O of the transferring ion in the two adjacent phases. Since, however, no solvation data were available for the solvent systems studied, a test of Eq. (56) could not be performed.

It has been shown [151] that both effects appear to be a direct consequence of the stochastic theory [113, 131] (Eqs. (48) and (49)). From this point of view, the correlation of the apparent standard rate constant with the standard potential difference (or standard Gibbs energy change) may not have a straightforward physical meaning when the solution viscosity can vary. In particular, the parameter to be tested is not k_0^s, but the product of the rate constant and the viscosity η, $k_0^s \eta$. In order to illustrate this point, we have used thermodynamic, kinetic and viscosity data from both of the original communications [124, 139]. Since the standard potential difference is close to the potential of zero charge, no correction for ion distribution was attempted. Figure 20 shows the variation of $\log(k_0^s \eta)$ with the standard potential difference, both related to the state of the system in the absence of sucrose or CCl_4.

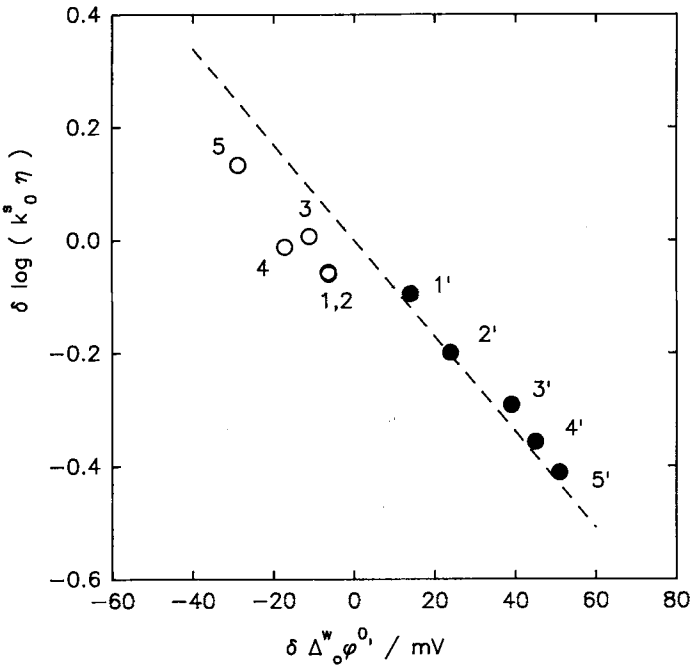

Fig. 20. Variation of the product of the apparent standard rate constant k_0^s and the viscosity η of (○) the aqueous or (●) the organic solvent phase with the formal potential difference $\Delta_O^W \phi_i^0$ for the transfer of acetylcholine across the (○) (water+sucrose)-1,2-dichloroethane or (●) water-(nitrobenzene+tetrachloromethane) interface. Concentration of sucrose (wt.%): (1) 4, (2) 10, (3) 20, (4) 30, and (5) (40); data taken from [124]. Concentration of tetrachloromethane (wt.%): (1') 10, (2') 23, (3') 47, (4') 57 and (5') 71; data taken from [139]. The broken line corresponds to $\alpha = 0.5$.

The slope of this correlation corresponding to $\alpha = 0.5$ is consistent with the model involving a symmetric potential barrier.

3.2.5 Monolayers

Ion transfer across phospholipid monolayers at liquid-liquid interfaces has been studied with the aim of elucidating the mechanism and kinetics of ion transport across a bilayer lipid membrane (BLM). The main advantage of using these systems is in the possibility of controlling the interfacial potential difference, which in the case of the BLM has to be inferred indirectly [141].

In the pioneering study, Koryta et al. [94] found that the rate of the facilitated Na^+ ion transfer across the water-nitrobenzene interface in the presence of dibenzo-18-crown-6 is decelerated by adsorbed egg lecithin molecules, but only when the temperature is lower than 5 °C. Since the change in the ion transfer rate has been thought to be due to the phase transition of phospholipid, which normally occurs at a higher

temperature, a conclusion was made that the transition is influenced by the adjacent nitrobenzene phase. Girault and Schiffrin [140] reported an analogous inhibition of Et_4N^+ ion transfer across the water-1,2-dichloroethane interface in the presence of egg lecithin.

In the first quantitative study, Schiffrin and coworkers [141] have shown that the surface pressure can be the decisive factor in determining the barrier height for Et_4N^+ ion transfer across a lecithin monolayer. The authors have proposed a simple model, in which the rate-determining step is the formation of a pore in the phospholipid layer with the critical radius r equal at least to the radius of the transferrable ion. The work required to open the pore against the surface pressure Π of the adsorbed monolayer was expressed by the term $\pi r^2 \Pi$. When the surface excess of the phospholipid reaches the limiting value, Γ_s, the surface pressure is proportional to the logarithm of the phospholipid concentration c, $\Pi = \text{constant} + RT\Gamma_s \ln c$, and the expression for the apparent standard rate constant can be written as [141]

$$k_0^s = k' \exp(-\pi r^2 \Gamma_s N_A \ln c) \tag{57}$$

where N_A is Avogadro's constant. The experimentally observed slope of $\ln k_0^s$ vs. $\ln c$ yields the critical pore radius which corresponds to the partly hydrated Et_4N^+ ion [141].

These studies have indicated the importance of the phase behavior of the monolayer, as well as the necessity for its characterization from the chemical and structural points of view [96, 100, 101]. With this aim, monolayer characteristics and the ion permeability of saturated monolayers of six L-α-phosphatidylcholines – dilauroyl- (DLPC), dimyristoyl- (DMPC), dipalmitoyl- (DPPC), distearoyl- (DSPC), diarachidoyl- (DAPC), and dibehenoylphosphatidylcholine (DBPC) – have been studied by measuring the ac impedance at the polarized water-nitrobenzene interface [100]. The DLPC and DMPC monolayers are in a liquid-expanded state between 5 and 30 °C, whereas the DSPC, DAPC, and DBPC are in a liquid-condensed state in the same temperature range. The DPPC monolayer exhibits a temperature-induced phase transition at 13 °C. The monolayers in the liquid-condensed state reduce the rate of transfer of both Me_4N^+ and Et_4N^+. This result indicates that a phosphatidylcholine monolayer exerts a hydrodynamic friction on transferring ions. In contrast, the monolayers in the liquid-expanded state accelerate the transfer of both ions, for which an explanation was seen in the change of ion distribution or the solvent structure-related friction [100]. The role of these two factors has been studied in detail by using the same method for the transfer of a cation (Et_4N^+) and anion (ClO_4^-) across a dilauroylphosphatidylethanolamine (DLPE) monolayer [96]. The advantage in using DLPE is that it forms a denser monolayer than phosphatidylcholine, and that the presence of an amino group in the hydrophilic head of DLPE makes it possible to change the surface charge density by changing the pH in the aqueous phase. The ion permeability was found to depend on the packing density of the monolayer, the surface charge density, and the charge and size of transferring ions. When the condensed monolayer was present, the decrease in the ion transfer rate was detectable for Et_4N^+, but not for ClO_4^-, which has a smaller radius

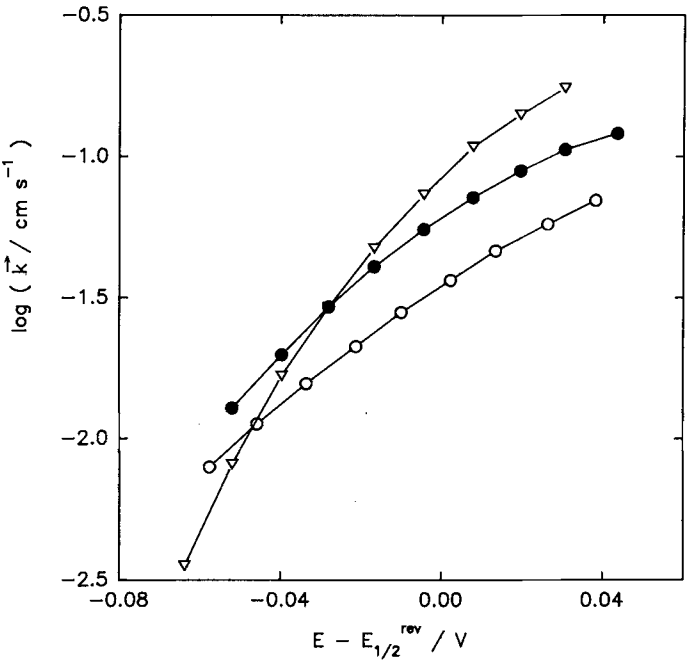

Fig. 21. Logarithm of the apparent rate constant $\vec{k}$ vs the potential E relative to the reversible half-wave potential (Tafel plot) derived from ac impedance measurements of Et_4N^+ ion transfer in the absence (●) and in the presence (▽, ○) of a DLPE monolayer formed at the interface between an aqueous solution of 0.1 M LiCl and a nitrobenzene solution of 0.1 M Pn_4NPh_4B+50 μM DLPE (○), and at the interface between an aqueous solution of 0.09 M LiCl+0.01 M LiOH and a nitrobenzene solution of 0.1 M Pn_4NPh_4B+20 μM DLPE (▽). (After [96]).

(Fig. 21). The negatively charged DLPE monolayer accelerates the transfer of the former ion and reduces appreciably the transfer of the latter ion. The effect is reversed in the case of a positively charged DLPE monolayer. The authors concluded that the ion permeability is primarily determined by the hydrodynamic friction and the double layer effect arising from the sign and density of the surface charge of adsorbed phospholipid molecules.

3.3 Kinetics of Assisted Ion Transfer Reactions

Simple ion transfer, Eq. (20), is often coupled to another process. A more general scheme involves the ion association or the formation of a complex at the liquid-liquid interface, e.g.,

$$X^z(W)+Y^s(O) \rightleftharpoons XY^{z+s}(O) \tag{58}$$

where Y^s is a counter ion or a ligand with the charge number s. Although a large number of ion transfer processes of this type were studied [14], only a few kinetic data have been reported, concerning mainly the transfer of alkali [166–168] or alkaline earth [169] metal cations facilitated by polyether macrocyclic or acyclic ligands.

A most advanced kinetic study was carried out by Senda and coworkers [166], who investigated the transfer of Na^+ across the water-nitrobenzene interface in the presence of dibenzo-18-crown-6. This ligand is known to form a stable 1 : 1 complex with the transferred ion. It was shown that the ac impedance technique makes it possible to distinguish between three basic mechanisms, which can be described as (1) transfer of the ion followed by its complexation in the organic phase (the EC mechanism); (2) complexation of the ion in the aqueous phase followed by transfer of the complex ion (the CE mechanism); or (3) complexation of the ion at the interface with simultaneous transfer of the ion from the aqueous to the organic phase (the E mechanism). For the system studied, the E mechanism described by Eq. (58) has turned out to be most probable. The apparent rate constant of the assisted ion transfer ($\approx 10^{-2}-10^{-1}$ cm s^{-1}) depends on the potential in a way that resembles Butler-Volmer behavior. The rate constant decreases with increasing aqueous electrolyte concentration, in qualitative agreement with the expected double layer effect for a cation transferred at positive potential relative to the potential of zero charge. However, at this potential the rate constant should be independent of the electrolyte concentration, which is not the case.

Another assistance to simple ion transfer can be provided by a photochemical reaction generating the electroactive ion X^z from a precursor P, e.g.,

$$P(w)+h\nu \rightarrow X^z(W) \rightleftharpoons X^z(O) \tag{59}$$

Systematic study of such systems was pioneered by Kuzmin and coworkers [170–172], who measured ionic current after the photochemical reaction of 1,3-dinitrobenzene and 2,4-dinitrotoluene, or after electron transfer between photoexcited protoporphyrin and a series of quinones. In the former case, the electroactive ion was a quinone radical anion. However, in either cases, the ionic product responsible for a change in the interfacial potential (photopotential) [170] or the electrical current flow (photocurrent) [171–173] was supposed to be either a product of photoisomerization or a radical anion arising from the reaction with tetraphenylborate present. In the latter case, the ion transfer was found to be diffusion-controlled, and no kinetic data for the interfacial ion transfer could have been inferred. The photopotential [174] or photocurrent [175, 176] was measured in the presence of some tetraaryl ions, such as Ph_4As^+ or Ph_4B^-. The photopotential was supposed to result from a photothermal effect [174], but photodecomposition of tetraaryl ions according to Eq. (59) appears to be a more plausible explanation [175, 176]. The photocurrent for Ph_4As^+ or Ph_4B^- exhibits Butler-Volmer behavior in a limited potential range, with the apparent rate constant of the order of 10^{-3} cm s^{-1} at $\Delta_O^W\phi = 0$ [176]. The origin of the potential-dependent quenching of the photoeffect at highly positive and negative potentials [174, 176], or in the presence of another electroactive ion [174], is unclear.

4 Electron Transfer Reactions

4.1 Theoretical Studies

Electron transfer between a redox couple O1/R1 in the W phase and a redox couple O2/R2 in the O phase, Eq. (8), represents the second basic type of charge transfer across a liquid-liquid interface. Although this is a second-order process, its mechanism is better understood than the mechanism of ion transfer.

4.1.1 Apparent Kinetic Parameters

Obviously, reaction (8) can be expected to follow the second-order rate law

$$J = \vec{k}\, c_{R1}^{W}\, c_{O2}^{O} - \bar{k}\, c_{O1}^{W}\, c_{R2}^{O} \tag{60}$$

The units of the forward and reverse heterogeneous rate constants, $\vec{k}$ and $\bar{k}$, are seen to be, e.g., $m^4\,mol^{-1}\,s^{-1}$; note that the forward reaction corresponds to electron transfer from the water to the organic phase. The relationship between $\vec{k}$ and $\bar{k}$ is analogous to Eq. (22) [24]:

$$\vec{k}/\bar{k} = \exp\left(-\Delta_W^O \bar{G}_e^0/RT\right) = \exp\left[-nF\left(E-E_e^0\right)/RT\right] \tag{61}$$

where $\Delta_W^O \bar{G}_e^0 = \Delta_W^O G_e^0 + nF\,\Delta_O^W \phi = nF\left(\Delta_O^W \phi - \Delta_O^W \phi_e^0\right) = nF\left(E-E_e^0\right)$ is the standard electrochemical Gibbs energy of electron transfer from W to O, and n is the number of electrons transferred in reaction (8). The standard potential difference of electron transfer $\Delta_O^W \phi_e^0$ is determined by the difference in the standard redox potentials of O1/R1 and O2/R2 related to the same reference electrode, Eq. (9).

Two apparent kinetic parameters are usually introduced, namely the apparent standard rate constant k_0^s at the equilibrium potential $E = E_e^0$ defined by Eq. (23) and the apparent charge transfer coefficient $\vec{\alpha}$ (cf. Eq. (24)):

$$\vec{\alpha} = -(RT/nF)\left(\partial \ln \vec{k}/\partial E\right) \tag{62}$$

4.1.2 Application of the Marcus-Levich Theory

The mechanism of electron transfer across a liquid-liquid interface is probably quite similar to that of a homogeneous electron transfer [106, 107]. In either case, the role of changes in the oxidation state of both reactants, in their molecular structure (including valence bond deformation, breaking or formation), and in the polarization state of the solvent have to be considered. Owing to electrostatic interactions of charged reactants with polar solvent molecules, the electron energy levels of the reac-

tant are displaced with respect to their position in vacuum and, particularly, they differ in general from those in products. However, the energy conservation law requires that electron energy levels in the initial and final states must coincide within the uncertainty limit, before radiationless electron transfer may occur. In accordance with the Franck-Condon principle, electron transfer occurs at a fixed configuration of heavy particles, and its probability can depend on the overlap of electronic wave functions in the initial and final states, which decreases exponentially with increasing distance between reactants. Consequently, the reactants must first approach each other as closely as possible. Then, thermal fluctuations in orientational vibrations (librations) of solvent molecules and intramolecular vibrations of reactants bring the system to an activated state, in which radiationless electron transfer can occur. Reorganization of solvent and of intramolecular degrees of freedom represents the main contribution to the Franck-Condon barrier of the process. The electron transfer probability was calculated by Kharkats [177], who used Levich's quantum theoretical model [107]; compare also an extension of this approach by Kharkats and Volkov [178], and the review by Kuznetsov and Kharakats [112]. Recently, the problem has been addressed by Marcus [179], from the point of view of his nonequilibrium thermodynamic theory [106]. Samec [24] implemented the result [177] into his semiphenomenological theory of electron transfer. Hence, the forward rate constant $\vec{k}$ in Eq. (60) was expressed by

$$\vec{k} = \vec{k}_t \, \Phi(1,2) = Z \, \Phi(1,2) \exp(-\Delta_a^* \bar{G}_e^0/RT) \tag{63}$$

where $\vec{k}_t$ is the corrected rate constant, $\Phi(1,2)$ is the two-particle distribution function and $\Delta_a^* \bar{G}_e^0$ is the standard Gibbs energy of activation. The distribution function $\Phi(1,2)$ was approximated by the product of the single-particle distribution functions, by denoting optimum locations for reactants in each phase as a and b:

$$\Phi(1,2) = \exp[-F(z_{R1}\Delta_W^a\phi + z_{O2}\Delta_O^b\phi)/RT] \tag{64}$$

The pre-exponential factor Z in Eq. (63) is proportional to the volume of molecular dimensions V_m (e.g., the mean molar volume of reactants) and to the thickness of the inner layer, d:

$$Z = B \, V_m \, d \tag{65}$$

where the constant B involves the overlap integral of the electronic wave functions in the initial and final states. When the harmonic approximation is used for the classical subsystem, $\Delta_a^* \bar{G}_e^0$ can be related to the standard electrochemical Gibbs energy of electron transfer from a to b, $\Delta_a^b \bar{G}_e^0$, through a quadratic function [106, 107],

$$\Delta_a^* \bar{G}_e^0 = (\lambda + \Delta_a^b \bar{G}_e^0)^2/4\lambda = \lambda/4 + \alpha \, \Delta_a^b \bar{G}_e^0 \tag{66}$$

where λ is sum of contributions from the reorganization of solvent λ_o and reactant λ_i,

$$\lambda = \lambda_o + \lambda_i \tag{67}$$

Later, Girault and Schiffrin [180] made a similar analysis. The only point which they discussed in more detail concerned the optimum locations a and b for the two reactants, but no explicit relationship was derived.

The solvent reorganization energy λ_o was calculated by Kharkats [177] (cf. also [112, 178]) by taking into account electrostatic contributions from both ions and their images. Here we reproduce the expression derived by Marcus [179], which differs from Kharkats's result [177, 178] in some respects:

$$\lambda_o = \frac{N_A (ne)^2}{8\pi\varepsilon^0}\left[\frac{1}{a}\left(\frac{1}{\varepsilon_{op}^W}-\frac{1}{\varepsilon_s^W}\right)+\frac{1}{b}\left(\frac{1}{\varepsilon_{op}^O}-\frac{1}{\varepsilon_s^O}\right)-\frac{1}{2h^W}\left(\frac{\varepsilon_{op}^O-\varepsilon_{op}^W}{\varepsilon_{op}^W(\varepsilon_{op}^W+\varepsilon_{op}^O)}\right.\right.$$
$$\left.-\frac{\varepsilon_s^O-\varepsilon_s^W}{\varepsilon_s^W(\varepsilon_s^W+\varepsilon_s^O)}\right)-\frac{1}{2h^O}\left(\frac{\varepsilon_{op}^W-\varepsilon_{op}^O}{\varepsilon_{op}^O(\varepsilon_{op}^W+\varepsilon_{op}^O)}-\frac{\varepsilon_s^W-\varepsilon_s^O}{\varepsilon_s^O(\varepsilon_s^W+\varepsilon_s^O)}\right)$$
$$\left.-\frac{4}{R}\left(\frac{1}{\varepsilon_{op}^W+\varepsilon_{op}^O}-\frac{1}{\varepsilon_s^W+\varepsilon_s^O}\right)\right] \tag{68}$$

where e is the electronic charge, ε^0, ε_{op} and ε_s refer to the permittivity of vacuum, optical, and static dielectric constants, respectively, a and b are the radii of the two reactants, h^W and h^O are the perpendicular distances from the center of the reactants to the interfacial boundary in the aqueous and organic phase, respectively, and R is the center-to-center separation distance between the two reactants. Equation (68) can be compared with the expression for the solvent reorganization energy in the homogeneous electron transfer reaction [106, 107],

$$\lambda_o^{hom} = \frac{N_A (ne)^2}{4\pi\varepsilon^0}\left(\frac{1}{2a}+\frac{1}{2b}-\frac{1}{R}\right)\left(\frac{1}{\varepsilon_{op}}-\frac{1}{\varepsilon_s}\right) \tag{69}$$

Since typically $\varepsilon_{op} \approx 2 \ll \varepsilon_s$, both λ_o and λ_o^{hom} are not very sensitive to the nature of the solvent, and a simple relationship between these two reorganization energies can be derived. Thus, when the reactants are approximately the same size, and can approach each other to the contact distance in both situations, i.e. $a \approx b \approx h^W \approx h^O \approx R/2$, then

$$\lambda_o \approx \lambda_o^{hom} \approx \frac{N_A (ne)^2}{8\pi\varepsilon^0 a}\cdot\frac{1}{\varepsilon_{op}} \tag{70}$$

A similar relation holds when the reactants are of different sizes, but the image forces are practically screened by the supporting electrolyte present in an excess, which is equivalent to an assumption that h^W, h^O and $R \to \infty$,

$$\lambda_o \approx \lambda_o^{hom} \approx \frac{N_A (ne)^2}{8\pi\varepsilon^0}\frac{1}{\varepsilon_{op}}\left(\frac{1}{a}+\frac{1}{b}\right) \tag{71}$$

Since the reorganization term of the reactant λ_i in Eq. (67) is also probably not very sensitive to the nature of the solvent, the total reorganization energy for interfacial and homogeneous electron transfer are approximately equal. The same conclusion can be inferred from Kharkat's treatment [177, 178].

Hence, the main difference between these two electron transfer reactions would be in the pre-exponential factor Z (Eq. 65). Following the treatment [24], they differ by a factor equal to the thickness of the inner layer d, i.e., $Z/Z^{hom} \approx d$. By using a rigorous procedure, Marcus [179] derived the expression for Z, which in the case of the sharp liquid-liquid boundary reads

$$Z = 2\pi\gamma\nu(a+b)(\Delta R)^3 \tag{72}$$

where γ is the Landau-Zener nonadiabaticity factor, ν is some relevant frequency for the molecular motion, and $\Delta R \approx 0.1$ nm appears in an exponent for the dependence of the electron transfer rate on separation distance R ($\propto \exp(-R/\Delta R)$) [179]. When each reactant could penetrate the other phase, Z was obtained as larger by a factor $(a+b)^2/2(\Delta R)^2$ [179]. However, in this case the expression for λ_o would be more complicated, and was not derived. By using the same approach to homogeneous electron transfer, we obtain

$$Z^{hom} = 8\pi\gamma\nu(\Delta R)^3 \tag{73}$$

Hence, $Z/Z^{hom} = (a+b)/4$, a result not very different from the approximate one above.

4.2 Experimental Results of Simple Electron Transfer Reactions

4.2.1 Experimental Techniques

Various experimental techniques developed for kinetic measurements of ion transfer (Sec. 3.2.1) are applicable also in the electron transfer case. However, in order to make the kinetic analysis feasible, it is necessary to solve the transport problem with the boundary condition given by Eq. (60). Alternatively, experimental conditions are to be chosen so that the electron transfer occurs as a first-order reaction, for which use can be made of results inferred for an ion transfer reaction.

Solution of the transport problem when the process is controlled by both the interfacial electron transfer and the steady-state or linear diffusion of reactants was derived by Samec [181, 182]. These results represent the basis for the kinetic analysis, e.g., in dc polarography or convolution and potential sweep voltammetry. Under the conditions of steady-state diffusion, Eq. (60) can be transformed into a dimensionless form [181],

$$u\,YP^{-(1-\alpha)} = (1-Y)(r-Y) - P^{-1}(s+Y)(t+Y) \tag{74}$$

where $Y = I/I_{O1}^{d}$ is the dimensionless current ($I_i^d = \kappa_i c_i$ is the limiting current; κ_i is the transport parameter for the reactant i), $P = (\kappa_{R1}\kappa_{O2}/\kappa_{O1}\kappa_{R2}) \exp[nF(E-E_e^0]$ is the potential function, $u = (\kappa_{R1}\kappa_{O2})^{1-\alpha}(\kappa_{O1}\kappa_{R2})^{\alpha}/nFAk_s^0 I_{O1}^d$ is the kinetic function, and the parameters $r = I_{R2}^d/I_{O1}^d$, $s = I_{R1}^d/I_{O1}^d$ and $t = I_{O2}^d/I_{O1}^d$. Four interesting features can be deduced from Eq. (74) [181]. First, on going toward positive or negative potentials, the function Y reaches a limit which is controlled by the limiting current of the reactant (product) with the lower transport rate. Second, under zero current conditions, $P = st/r$ and the equilibrium Nernst equation for the potential difference is recovered. Third, depending on the value of the rate constant k_s^0, i.e., the parameter u, the reversible or irreversible limit in the reaction is reached, with the corresponding reversible or irreversible current-potential curve. It is noteworthy that either limit can be reached by changing not only the rate constant, but also the reactant concentrations. Fourth, the apparent kinetic parameters can be obtained from experimental current-potential curves by plotting the right-hand side of Eq. (74) divided by Y against the potential E.

When the transport of reactants is controlled by linear diffusion, the kinetic analysis can be performed using convolution potential sweep voltammetry [182]. Here it is more convenient to choose one of the reactant concentrations to be equal to zero, i.e., the initial conditions are recovered at sufficiently negative or positive potentials as in linear potential sweep voltammetry. By using the Laplace transform and the convolution theorem in solving the second Fick equation for each reactant, the convolution current m,

$$m = \pi^{-1/2} \int_0^t I(\tau)\,(t-\tau)^{-1/2}\,\mathrm{d}\tau \tag{75}$$

satisfies the equation,

$$(m_{O1}^d - m)\,(m_{R2}^d - m)/(m_{R1}^d + m)\,m = P^{-1} + [I\kappa_{O1}\kappa_{R2}/nFA\vec{k}\,(m_{R1}^d + m)m] \tag{76}$$

where the concentration of O2 is set to zero, P has the same meaning as in Eq. (74), and the limiting convolution integral m_i^d is given by

$$m_i^d = \kappa_i c_i^0 = nFAD_i^{1/2} c_i^0 \tag{77}$$

Upon evaluating the convolution integral from the experimental current-potential (time) curve and its limiting values (Eq. 77), kinetic analysis can be performed with the help of Eq. (76). Conversely, Eq. (76) or similar equations can be used to calculate the theoretical current-potential curve, e.g., for the linear potential sweep voltammogram, provided that the values of all the parameters are known. Some illustrative examples were provided by Girault and coworkers [183].

4.2.2 Electron Transfer Systems

In the work by Samec et al. [147, 184, 185], the electron transfer reaction between ferrocene (Fc) in nitrobenzene and $Fe(CN)_6^{3-}$ in water was demonstrated for the first time. Since then, a number of redox reactions taking place at a water-organic solvent interface have been reported [26, 186–190], though kinetic data are few.

The former reaction proceeds according to the overall mechanism

$$Fe(CN)_6^{3-}(W) + Fc(O) = Fe(CN)_6^{4-}(W) + Fc^+(O) \tag{78}$$

which was corroborated [185] by the predicted [181] dependence of the reversible half-wave potential on the concentrations of the reactants, and by excellent agreement between the measured value of the standard potential difference $\Delta_O^W \phi_c^0$, and that calculated with the help of Eq. (9) [147]. However, the use of ferrocene presents some problems due to the possible transfer of the ferricenium ion (i.e., coupling of electron and ion transfer may occur in this case), and due to the limited solubility of ferrocene in water (1.7×10^{-5} mol dm^{-3} [191], owing to which the reaction plane may be displaced toward the aqueous phase. Although the transfer of ferricenium ion was found to be well separated from electron transfer, the question of the mechanism has been left open to evidence based on kinetic analysis [192].

Electron transfer (78) has been shown to be rather slow [185]. Kinetic parameters were evaluated [147] by means of convolution potential sweep voltammetry [182]. The apparent rate constant $\bar{k}$ was found to be almost independent of the potential and equal to $\bar{k} \approx 4 \times 10^{-7}$ m^4 s^{-1} mol^{-1} (units to Figs. 5 and 6 in [147] should correctly be read as μm s^{-1} M^{-1}). Some features of the apparent kinetic behavior have been confirmed by ac impedance measurements reported by Seno and coworkers [190]. In a further study [193], the effect of the nature and concentration of the cation present in the aqueous phase was examined (Fig. 22). It is well known that both homogeneous and electrode redox reactions involving the $Fe(CN)_6^{3-}/Fe(CN)_6^{4-}$ redox couple depend on the nature and concentration of cation [194–196]. Hence, the quite negligible effect observed in reaction (78) is strong evidence that a mechanism comprising homogeneous electron transfer is unlikely. Moreover, the role of the *electrical double layer seems to be less significant than one would expect for highly* charged ions. This behavior was interpreted as a consequence of ion association, ion size, and the potential of the reaction (78), which is positive relative to the potential of zero charge. Actually, the ion diameter (0.96 nm) is comparable with the thickness of the space charge region, and because anions are repelled from the electrical double layer, the optimum location $x = a$ was supposed to be displaced from the outer Helmholtz plane toward the bulk solution by the Debye screening length (e.g., 1.36 nm at an ionic strength of 0.05 mol dm^{-3}). The corrected Tafel plots evaluated from data in Fig. 22 by Eqs. (63) and (64), for $z_{O1} = -2$, are almost independent of the electrolyte concentration and their slopes roughly correspond to $\alpha = 0.5$, with $\bar{k}_t = 6.6 \times 10^{-6}$ m^4 mol^{-1} s^{-1} at $\Delta_a^b \bar{G}_e^0 = 0$ (Fig. 23). Kinetic data for the interfacial reaction (78) were then correlated with homogeneous kinetic data by using the theoretical relationships derived from the Marcus-Levich theory (Sec. 4.1.2). Since for the homogeneous cross-electron transfer reaction (78) no experimental data are avail-

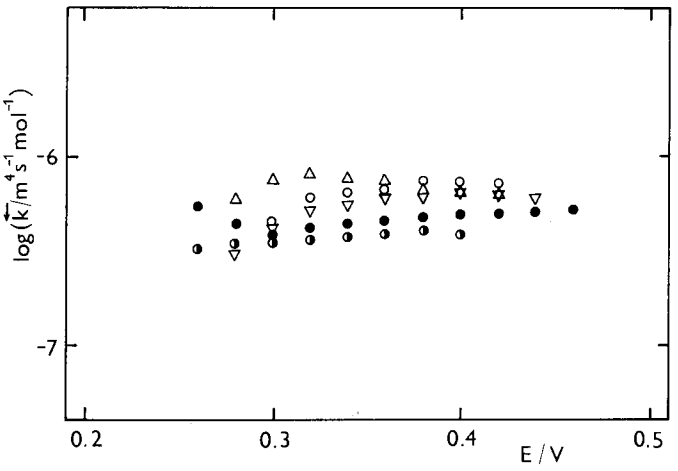

Fig. 22. Logarithm of the apparent backward rate constant $\vec{k}$ vs. the potential E (Tafel plot) of electron transfer between ferrocene in nitrobenzene and hexacyanoferrate(III) in water derived from convolution potential sweep voltammetry. Composition of the aqueous phase: 1 mM $K_3[Fe(CN)_6]$+LiCl (○, △, ▽) or NaCl (●) or KCl (◑). Nitrobenzene phase: 0.01 M ferrocene and Bu_4NPh_4B. Concentration of both base electrolytes: 0.01 M (○, ●, ◑), 0.05 M (△) or 0.1 M (▽). (After [193]).

able, the authors [193] used experimental rate constants 26 $dm^3\,mol^{-1}\,s^{-1}$ at zero ionic strength in water [195] and 5.7×10^6 $dm^3\,mol^{-1}\,s^{-1}$ in acetonitrile [197] for the $Fe(CN)_6^{3-}/Fe(CN)_6^{4-}$ and Fc^+/Fc homogeneous exchange-electron transfer reactions. After a correction for the work term [198], the former rate constant is comparable with the latter one, 1×10^6 $dm^3\,mol^{-1}\,s^{-1}$. Therefore, the homogeneous rate constant at zero corrected standard Gibbs energy can be estimated by the square root of the product of exchange rate constants, i.e., 2.3×10^6 $dm^3\,mol^{-1}\,s^{-1}$. The value of this constant estimated from the heterogeneous corrected rate constant given above, i.e., $\bar{k}_t/d \approx 6.6\times10^6$ $dm^3\,mol^{-1}\,s^{-1}$ for $d \approx 1$ nm, is in very good agreement with the measured one.

By using cyclic voltammetry, Schiffrin and coworkers [26, 186, 187, 189] studied electron transfer across the water-1,2-dichloroethane interface between the redox couple $Fe(CN)_6^{3-}/Fe(CN)_6^{4-}$ in water, and lutetium(III) [186] and tin(IV) [26, 187] diphthalocyanines and bis(pyridine)-*meso*-tetraphenylporphyrinato-iron(II) or ruthenium(III) [189] in the organic solvent. An essential advantage of these systems is that none of the reactants or products can cross the interface and interfere with the electron transfer reaction, which could be clearly demonstrated. Owing to a much higher concentration of the aqueous redox couple, the pseudo-first order electron transfer reactions could be analyzed with the help of the Nicholson-Shain theory. However, though they have all appeared to be quasireversible, kinetic analysis was restricted to an evaluation of the apparent standard rate constant k_0^s, which was found to be of the order of 10^{-3} cm s^{-1} [186, 189]. Marcus [199] has derived a relationship between the pseudo-first-order rate constant for the reaction (8) and the rate

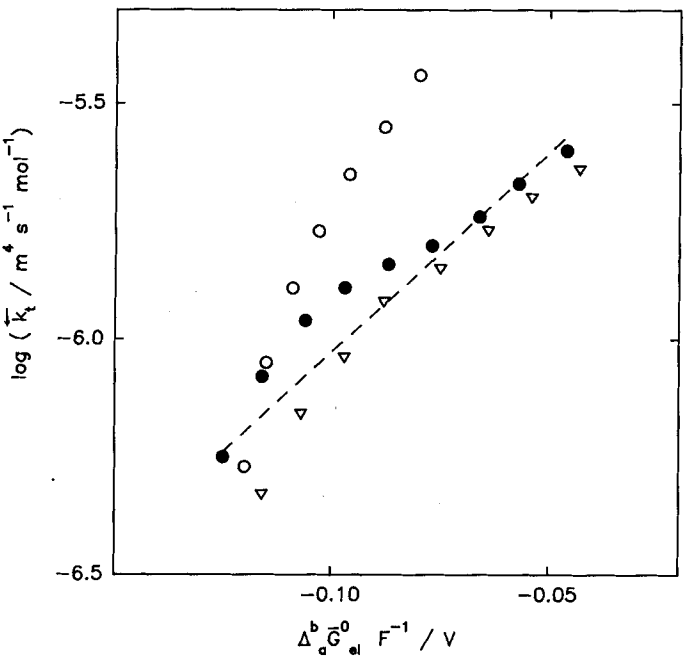

Fig. 23. Logarithm of the true backward rate constant $\vec{k}_t$ vs. the corrected standard Gibbs energy of electron transfer $\Delta_a^b \bar{G}_i^0$ (corrected Tafel plot) between ferrocene in nitrobenzene and hexacyanoferrate(III) in water. Composition of the aqueous phase: 1 mM $K_3[Fe(CN)_6]$ + LiCl. Nitrobenzene phase: 0.01 M ferrocene and Bu_4NPh_4B. Concentration of both base electrolytes: 0.01 M (○), 0.05 M (●) or 0.1 M (▽). (After [193]).

constants of the electrode reactions of the redox couples involved, and has concluded that the values of the rate constant measured [186] and calculated from electrode kinetic parameters are in a reasonable agreement.

Kihara et al. [188] have introduced a series of redox reactions suitable for studying the electron transfer (8). These systems involved ferrocene or tetrathiafulvalene as electron donor or tetracyanoquinodimethane as electron acceptor in the organic solvent phase, and $Fe(CN)_6^{3-}$, Ce^{4+}, Fe^{3+}, or $Cr_2O_7^{2-}$ as electron acceptor, or $Fe(CN)_6^{4-}$ or hydroquinone as electron donor, in the aqueous phase. Since all these systems showed reversible behavior under the conditions of current-scan polarography, no kinetic data have been reported.

4.3 Kinetics of Photoassisted Electron Transfer Reactions

Attention has been paid to the kinetics of photoassisted electron transfer across a liquid-liquid interface [200–203], e.g.,

$$D(W)+A(O)+h\nu \rightarrow D^*(W)+A(O) \rightarrow D^+(W)+A^-(O) \quad (79)$$

where D and A denote the electron donor and acceptor, respectively. The use of the ITIES has been proposed [200, 201] to be a suitable strategy for preventing back-electron transfer, which is one of the key problems in effective photochemical charge separation as the basis for light energy conversion. Electrochemical measurements of photocurrent at the water-1,2-dichloroethane interface have been achieved using Ru(2,2′-bipyridine)$_2^{3+}$ [200–202] or Ru(2,2′-bipyrazine)$_3^{2+}$ [203] as a photosensitizer, and 1,1′-diheptyl-4,4′-bipyridinium [200], 1,1′-dimethyl-4,4′-bipyridinium [201–203], oxygen [202, 203], iodine [202], Fe^{2+} and Fe^{3+} [202], *N,N′*-diphenyl-1,4-phenylenediamine [203], or ferrocene [203] as a quencher. Evidence has been provided that the quenching reaction is an interfacial electron transfer [200–203]. Impedance measurements on the irradiated interface enabled an estimation of its pseudo-first-order apparent rate constant ($\approx 10\,\mathrm{cm\,s^{-1}}$), which points to a rather fast process.

5 Conclusions

Progress in experimental and theoretical studies of the mechanistic and dynamic aspects of charge transfer at the ITIES is developing swiftly. The present reviews is therefore deemed to be a status report concerning the charge transfer kinetics at the ITIES, rather than a systematic presentation of the subject.

On the one hand, the thermodynamic realities of the ITIES, e.g., electrocapillarity and standard ion transfer potential, have been well established. On the other hand, our knowledge of charge transfer kinetics is less solid. Although traditional macroscopic concepts appear to be applicable at least as a first approximation, there is still a rift between macroscopic views and microscopic understanding.

In the course of developing experimental techniques in the past 15 years, we have seen an exponential increase in literature values for apparent rate constants of ion transfer. The mechanism has, however, often been discussed on the basis of scarce data. In order to stimulate further theoretical consideration of charge transfer and double layer structure from a molecular point of view, the compilation of reliable kinetic parameters is of decisive importance.

Besides improving classical electrochemical methods, newly employed techniques such as second harmonic-generation and time-resolved fluorometry, with either control of the potential drop across the interface or fluctuation analysis, are promising in this respect. Also indispensable are further advances in molecular dynamics and statistical-mechanical treatments of structure and charge transfer at the ITIES.

6 References

1. M.M. Krouchkoll, Ann. Chim. Phys. [6], 17, 9 (1989).
2. M.G. Lippmann, Ann. Chim. Phys. [5], 12, 265 (1877).
3. C. Gavach, T. Mlodnicka, J. Guastalla, C.R. Acad. Sci. C 266, 1196 (1968).
4. J. Koryta, P. Vanysek, M. Brezina, J. Electroanal. Chem., Interfacial Electrochem. 75, 211 (1977).
5. J. Koryta, Electrochim. Acta 24, 293 (1979).
6. J. Koryta, Ion-Select. Electrode Rev. 5, 131 (1983).
7. J. Koryta, Electrochim. Acta 29, 445 (1984).
8. J. Koryta, Electrochim. Acta 32, 383 (1987).
9. J. Koryta, Electrochim. Acta 33, 189 (1988).
10. H.H. Girault, Electrochim. Acta 32, 383 (1987).
11. H.H. Girault, D.J. Schiffrin, in: Electroanalytical Chemistry, A.J. Bard (ed.). Marcel Dekker, New York (1989), Vol. 15, p. 1.
12. Z. Samec, Chem. Rev. 88, 617 (1988).
13. M. Senda, T. Kakiuchi, T. Osakai, Electrochim, Acta 36, 253 (1991).
14. H.H. Girault, Modern Aspects of Electrochemistry, R.E. White, B.E. Conway, J. O'M. Bockris (eds.), Plenum, New York (1993), Vol. 25.
15. P. Vanysek, Electrochemistry at Liquid-Liquid Interfaces, Springer, Berlin (1985).
16. V.E. Kazarinov (ed.), The Interface Structure and Electrochemical Processes at the Boundary Between Two Immiscible Liquids, Springer, Berlin (1987).
17. W. Nernst, Z. Phys. Chem. 9, 137 (1892).
18. E.H. Riesenfeld, Ann. Physik, 8, 616 (1902).
19. L.Q. Hung, J. Electroanal. Chem., Interfacial Electrochem. 115, 159 (1980).
20. T. Kakiuchi.
21. L.Q. Hung, J. Electroanal. Chem., Interfacial Electrochem. 149, 1 (1983).
22. T. Kakutani, Y. Nishiwaki, M. Senda, Bunseki Kagaku 33, E175 (1984).
23. E.A. Guggenheim, Thermodynamics, 6th, ed., North-Holland, Amsterdam (1977), Chapter 8.
24. Z. Samec, J. Electroanal. Chem., Interfacial Electrochem. 99, 197 (1979).
25. T. Kakiuchi Electrochim. Acta, submitted.
26. V.J. Cunnane, D.J. Schiffrin, C. Beltran, G. Geblewicz, T. Solomon, J. Electroanal. Chem., Interfacial Electrochem. 247, 203 (1988).
27. K. Maeda, S. Kihara, M. Suzuki, M. Matsui, J. Electroanal. Chem. Interfacial Electrochem. 303, 171 (1991).
28. T. Kakiuchi, M. Senda, Bull. Chem. Soc. Jpn. 56, 2912 (1983).
29. T. Kakiuchi, M. Senda, Bull. Chem. Soc. Jpn. 56, 1322 (1983).
30. T. Kakiuchi, M. Senda, Collect. Czech. Chem. Commun. 56, 112 (1991).
31. J. Heyrovský, J. Kůta, Principles of Polarography, Academic Press, New York (1966), Chapter 3.
32. D.C. Grahame, R.P. Larsen, M.A. Poth, J. Am. Chem. Soc. 71, 2978 (1949).
33. H.H.J. Girault, D.J. Schiffrin, J. Electroanal. Chem., Interfacial Electrochem. 161, 415 (1984).
34. Z. Koczorowski, I. Paleska, J. Kotowski, J. Electroanal. Chem., Interfacial Electrochem. 235, 287 (1987).
35. Z. Samec, V. Marecek, D. Homolka, J. Electroanal. Chem., Interfacial Electrochem. 126, 121 (1981).
36. T.J. VanderNoot, D.J. Schiffrin, Electrochim. Acta 35, 1359 (1990).
37. T.J. VanderNoot, J. Electroanal. Chem., Interfacial Electrochem. 300, 199 (1991).
38. Z. Samec, V. Marecek, J. Koryta, M.W. Khalil, J. Electroanal. Chem., Interfacial Electrochem. 83, 393 (1977).
39. Z. Figaszewski, Z. Koczorowski, G. Geblewicz, J. Electroanal. Chem., Interfacial Electrochem. 139, 317 (1982).

40. T. J. VanderNoot, D. J. Schiffrin, R. S. Whiteside, J. Electroanal. Chem., Interfacial Electrochem. 278, 137 (1990).
41. R. D. G. Olphert, A. J. Strike, D. R. Whitehouse, J. Electroanal. Chem., Interfacial Electrochem. 318, 255 (1991).
42. T. Kakiuchi, J. Noguchi, M. Kotani, M. Senda, J. Electroanal. Chem., Interfacial Electrochem. 296, 517 (1990).
43. M. C. Wiles, D. J. Schiffrin, T. J. VanderNoot, A. F. Silva, J. Electrocanal. Chem., Interfacial Electrochem. 278, 151 (1990).
44. D. J. Clarke, D. J. Schiffrin, M. C. Wiles, Electrochim. Acta 34, 767 (1989).
45. J. Koryta, Anal. Chim. Acta 111, 1 (1979).
46. T. Kakiuchi, M. Senda, Bull. Chem. Soc. Jpn. 57, 1801 (1984).
47. T. Kakiuchi, M. Senda, Bull. Chem. Soc. Jpn. 60, 3099 (1987).
48. C. Gavach, P. Seta, B. Seta, J. Electroanal. Cem., Interfacial Electrochem. 83, 225 (1977).
49. M. Gros, S. Gromb, C. Gavach, J. Electroanal. Cem., Interfacial Electrochem. 89, 29 (1978).
50. P. Seta, B. d'Epenoux, C. Gavach, J. Electroanal. Cem., Interfacial Electrochem. 95, 191 (1979).
51. J. D. Reid, O. R. Melroy, R. P. Buck, J. Electroanal. Chem., Interfacial Electrochem. 147, 71 (1983).
52. T. Kakiuchi, M. Senda, Bull. Chem. Soc. Jpn. 56, 1753 (1983).
53. D. M. Mohilner in: Electroanalytical Chemistry, A. J. Bard (ed.), Marcel Dekker, New York (1966), Vol. 1, p. 331.
54. H. H. Girault, D. J. Schiffrin, J. Electroanal. Cem., Interfacial Electrochem. 150, 43 (1983).
55. H. H. J. Girault, D. J. Schiffrin, J. Electroanal. Cem., Interfacial Electrochem. 170, 127 (1984).
56. C. Yufei, V. J. Cunnane, D. Schiffrin, L. Mutomäki, K. Kontturi, J. Chem. Soc., Faraday Trans. 87, 107 (1991).
57. D. C. Grahame, Chem. Rev. 41, 441 (1947).
58. I. Paleska, Z. Koczorowski, W. Wawryzynczak, J. Electroanal. Chem., Interfacial Electrochem. 280, 439 (1990).
59. E. J. W. Verwey, K. F. Niessen, Philos. Mag. 28, 435 (1935).
60. H. H. J. Girault, D. J. Schiffrin, J. Electroanal. Chem., Interfacial Electrochem. 195, 213 (1985).
61. T. Kakiuchi, J. Noguchi, M. Senda, J. Electroanal. Chem., Interfacial Electrochem. 336, 137 (1992).
62. S. C. Carnie, D. Y. C. Chan, D. J. Mitchell, B. W. Ninham, J. Chem. Phys. 74, 1472 (1981).
63. G. M. Torrie, J. P. Valleau, J. Chem. Phys. 73, 5807 (1980).
64. G. M. Torrie, J. P. Valleau, J. Electroanal. Cem., Interfacial Electrochem. 206, 69 (1986).
65. S. L. Carnie, D. Y. C. Chan, J. Chem. Phys. 73, 2949 (1980).
66. G. M. Torrie, G. N. Patey, Electrochim. Acta 36, 1677 (1991).
67. G. M. Torrie, P. G. Kusalik, G. N. Patey, J. Chem. Phys. 88, 7826 (1988).
68. G. M. Torrie, P. G. Kusalik, G. N. Patey, J. Chem. Phys. 90, 4513 (1989).
69. D. Wei, G. M. Torrie, G. N. Patey, J. Phys. Chem. 94, 4260 (1990).
70. P. Linse, J. Chem. Phys. 86, 4177 (1987).
71. I. Benjamin, J. Chem. Phys. 97, 1432 (1992).
72. A. R. van Buuren, S.-J. Marrink, H. J. C. Berendsen, J. Phys. Chem. 97, 9206 (1993).
73. A. Pohorille, I. Benjamin, J. Chem. Phys. 94, 5599 (1991).
74. M. Matsumoto, Y. Takaoka, Y. Kataoka, J. Chem. Phys. 98, 1464 (1993).
75. I. Benjamin, Science 261, 1558 (1993).
76. S. Takahashi, A. Harata, T. Kitamori, T. Sawada, Bunseki Kagaku 40, 761 (1991).
77. A. Indenbom, Dokl. Phys. Chem. (Eng.-Transl.) 282, 425 (1985).
78. J. Guastalla, Proc. Second International Congress on Surface Activity III, Butterworths, London (1957), p. 112.
79. A. Watanabe, M. Matsumoto, H. Tamai, R. Gotoh, Kolloid Z. Z. Polym. 220, 152 (1967).
80. M. Dupeyrat, J. Michel, J. Colloid Interface Sci. 29, 605 (1969).
81. P. Joos, M. van Bockstacle, J. Phys. Chem. 80, 1573 (1976).

82. T. Kakiuchi, T. Kobayashi, M. Senda, Bull. Chem. Soc. Jpn. 60, 3109 (1987).
83. E. Dutkiewicz, R. Parsons, J. Electroanal. Chem., Interfacial Electrochem. 11, 100 (1966).
84. T. Kakiuchi, M. Kobayashi, M. Senda, Bull. Chem. Soc. Jpn. 61, 1545 (1987).
85. M.C. Wiles, T. VanderNoot, D.J. Schiffrin, J. Electroanal. Chem., Interfacial Electrochem. 281, 231 (1990).
86. D.A. Higgins, R.M. Corn, J. Phys. Chem. 97, 489 (1993).
87. T. Kakiuchi, T. Usui, M. Senda, Bull. Chem. Soc. Jpn. 63, 2044 (1990).
88. T. Kakiuchi, T. Usui, M. Senda, Bull. Chem. Soc. Jpn. 63, 3264 (1990).
89. T. Kakiuchi, J. Colloid Interface Sci. 156, 406 (1993).
90. Q.-Z. Chen, K. Iwamoto, M. Seno, Electrochim. Acta 36, 1437 (1991).
91. T. Kakiuchi, unpublished result.
92. T. Kakiuchi, Y. Takasu, J. Electroanal. Chem., Interfacial Electrochem. in press.
93. T. Kakiuchi, Y. Teranishi, K. Niki, Electrochim. Acta, submitted.
94. J. Koryta, L.Q. Hung, A. Hofmanova, Studia Biophys. 90, 25 (1982).
95. H.H.J. Girault, D.J. Schiffrin, J. Electroanal. Chem., Interfacial Electrochem. 179, 277 (1984).
96. T. Kakiuchi, T. Kondo, M. Kotani, M. Senda, Langmuir 8, 169 (1992).
97. T. Kakiuchi, M. Yamane, T. Osakai, M. Senda, Bull. Chem. Soc. Jpn. 60, 4223 (1987).
98. T. Kakiuchi, M. Nakanishi, M. Senda, Bull. Chem. Soc. Jpn. 62, 403 (1989).
99. T. Wandlowski, V. Marecek, Z. Samec, J. Electroanal. Chem., Interfacial Electrochem. 242, 277 (1988).
100. T. Kakiuchi, M. Kotani, J. Noguchi, M. Nakanishi, M. Senda, J. Colloid Interface Sci. 149, 279 (1992).
101. T. Kakiuchi, T. Kondo, M. Senda, Bull. Chem. Soc. Jpn. 63, 3270 (1990).
102. H.H.J. Girault, D.J. Schiffrin, B.D.V. Schmith, J. Colloid Interface Sci. 101, 257 (1984).
103. P. Vanysek, J.D. Reid, M.A. Craven, R.P. Buck, J. Electrochem. Soc. 131, 1788 (1984).
104. P. Vanysek, Z. Sun, Bioelectrochem. Bioenerg. 23, 177 (1990).
105. R.R. Dogonadze, A.M. Kuznetsov, in: Progress in Surface Science, S.G. Davison (ed.), Pergamon, Oxford (1975), Wiley Interscience, Vol. 6, pp. 3–41.
106. R.A. Marcus, J. Chem. Phys. 43, 679 (1965).
107. V.G. Levich in: Advances in Electrochemistry and Electrochemical Engineering, P. Delahay (ed.), New York (1966), Wiley Interscience, Vol. 4, p. 249.
108. H. Eyring, E.M. Eyring, Modern Chemical Kinetics, Selected Topics in Modern Chemistry, Reinhold, New York (1963), pp. 51–66.
109. B. d'Epenoux, P. Seta, G. Amblard, C. Gavach, J. Electroanal. Chem., Interfacial Electrochem. 99, 77 (1979).
110. R.P. Buck, Crit. Rev. Anal. Chem. 5, 323 (1975).
111. O.R. Melroy, R.P. Buck, J. Electroanal. Chem., Interfacial Electrochem. 136, 19 (1982).
112. A.M. Kuznetsov, Ju. I. Kharkats, in: The Interface Structure and Electrochemical Processes at the Boundary Between Two Immiscible Liquids, V.E. Kazarinov (ed.), Springer, Berlin (1987), pp. 11–46.
113. Yu.Ya. Gurevich, Yu.I. Kharkats, J. Electroanal. Chem., Interfacial Electrochem. 200, 3 (1986).
114. K. Heinzinger, G. Palinkas, in: Chemical Physics of Solvation, R.R. Dogonadze, E. Kalman, A.I. Kornyshev, J. Ulstrup (eds.), Elsevier, Amsterdam (1985), Part A, p. 313.
115. T. Wandlowski, V. Mareček, Z. Samec, R. Fuoco, J. Electroanal. Chem., Interfacial Electrochem. 331, 765 (1992).
116. P.P. Schmidt, J. Chem. Soc., Faraday Trans. 2, 80, 157 (1984); idem, ibid. 80, 181 (1984).
117. Z. Samec, V. Mareček, D. Homolka, J. Electroanal. Chem., Interfacial Electrochem. 158, 25 (1983).
118. Z. Samec, V. Marecek, J. Electroanal. Chem., Interfacial Electrochem. 200, 17 (1986).
119. R.R. Dogonadze, Z.D. Urushadze, J. Electroanal. Chem., Interfacial Electrochem. 32, 235 (1971).

120. P. Delahay, Double Layer and Electrode Kinetics, Wiley – Interscience, New York (1965), Chapter 7.
121. R.P. Buck, W.E. Bronner, J. Electroanal. Chem., Interfacial Electrochem. 197, 179 (1986).
122. W.E. Bronner, O.R. Melroy, R.P. Buck, J. Electroanal. Chem., Interfacial Electrochem. 162, 263 (1984).
123. H.H. Girault, J. Electroanal. Chem., Interfacial Electrochem. 257, 47 (1988).
124. Y. Shao, H.H. Girault, J. Electroanal. Chem., Interfacial Electrochem. 282, 59 (1990).
125. S. Glasstone, K.J. Laidler, H. Eyring, The Theory of Rate Processes, McGraw-Hill, New York (1941).
126. R.P. Buck, J. Membrane Sci. 17, 1 (1984).
127. C.W. Gardiner in: Handbook of Stochastic Methods for Physics, Chemistry and Natural Sciences, H. Haken (ed.), Springer, Berlin (1985), Vol. 13.
128. I. Benjamin, J. Chem. Phys. 96, 577 (1992).
129. W.E. Morf, The Principles of Ion Selective Electrodes and Membrane Transport, Akademiai Kiado, Budapest (1981), pp. 87–161.
130. T. Kakiuchi, J. Electroanal. Chem., Interfacial Electrochem. 322, 55 (1992).
131. Z. Samec, Yu.I. Kharkats, Yu.Ya. Gurevich, J. Electroanal. Chem., Interfacial Electrochem. 204, 257 (1986).
132. T. Wandlowski, V. Mareček, K. Holub, Z. Samec, J. Phsy. Chem. 93, 8204 (1989).
133. Yu.I. Kharkats, J. Ulstrup, J. Electroanal. Chem., Interfacial Electrochem. 308, 17 (1991).
134. D.E. Goldman, J. Gen. Physiol. 27, 37 (1943).
135. M. Fournier, J. Chim. Phys. 49, C183 (1952).
136. K.J. Schweighofer, I. Benjamin, in preparation.
137. H.J.C. Berendsen, J.P.M. Postma, W.F. van Gunsteren, J. Hermans, in: Intermolecular Forces, B. Pullman (ed.), Reidel, Dordrecht (1981), p. 331.
138. C. Gavach, B. d'Epenoux, F. Henry, J. Electroanal. Chem., Interfacial Electrochem. 64, 107 (1975).
139. Y. Shao, J.A. Campbell, H.H. Girault, J. Electroanal. Chem., Interfacial Electrochem. 300, 415 (1991).
140. H.H.J. Girault, D.J. Schiffrin, in: Charge and Field Effects in Biosystems, M.J. Allen, P.N.R. Usherwood (eds.), Abacus, Tunbridge Wells, UK (1984), p. 171.
141. V.J. Cunnane, D.J. Schiffrin, M. Fleischmann, G. Geblewicz, D. Williams, J. Electroanal. Chem., Interfacial Electrochem. 243, 455 (1988).
142. T. Osakai, T. Kakutani, M. Senda, Bull. Chem. Soc. Jpn. 57, 370 (1984).
143. T. Osakai, T. Kakutani, M. Senda, Bull. Chem. Soc. Jpn. 58, 2626 (1985).
144. T. Kakiuchi, J. Noguchi, M. Senda, J. Electroanal. Chem., Interfacial Electrochem. 327, 63 (1992).
145. T. Kakiuchi, Denki Kagaku 61, 132 (1993).
146. Z. Samec, V. Mareček, J. Weber, J. Electroanal. Chem., Interfacial Electrochem. 100, 841 (1979).
147. Z. Samec, V. Mareček, J. Weber, D. Homolka, J. Electroanal. Chem., Interfacial Electrochem. 126, 105 (1981).
148. T. Wandlowski, V. Mareček, Z. Samec, J. Electroanal. Chem., Interfacial Electrochem. 242, 291 (1988).
149. V. Mareček, M. Gratzl, A. Pungor, J. Janata, J. Electroanal. Chem., Interfacial Electrochem. 266, 239 (1989).
150. O. Dvořák, V. Mareček, Z. Samec, J. Electroanal. Chem., Interfacial Electrochem. 284, 205 (1990).
151. Z. Samec, V. Mareček, J. Electroanal. Chem., Interfacial Electrochem. 333, 319 (1992).
152. C. Gavach, F. Henry, J. Electroanal. Chem., Interfacial Electrochem. 54, 361 (1974).
153. T. Ohkouchi, T. Kakutani, T. Osakai, M. Senda, Rev. Polarogr. 31, 179 (1986).
154. G. Taylor, H.H. Girault, J. Electroanal. Chem., Interfacial Electrochem. 208, 179 (1986).

155. J. A. Campbell, H. H. Girault, J. Electroanal. Chem., Interfacial Electrochem. 266, 465 (1989).
156. Vanýsek, C. Hernandez, J. Electrochem. Soc. 137, 2763 (1990).
157. O. R. Melroy, W. E. Bronner, R. P. Buck, J. Electrochem. Soc. 130, 373 (1983).
158. V. Mareček, Z. Samec, J. Electroanal. Chem., Interfacial Electrochem. 185, 263 (1985).
159. B. A. Boukamp, Equivalent Circuit (EQUIVCRT. PAS) Users' Manual, University of Twente, The Netherlands (1988/89).
160. T. Kakiuchi, J. Electroanal. Chem., Interfacial Electrochem. 344, 1 (1993).
161. T. Kakiuchi, Y. Takasu, M. Senda, Anal. Chem. 64, 3096 (1992).
162. T. Kakiuchi, Y. Takasu, Anal. Chem. 66, 1853 (1994).
163. Z. Samec, T. Kakiuchi, M. Senda, Electrochim. Acta, submitted.
164. H. Matsuda, P. Delahay, J. Phys. Chem. 64, 332 (1960).
165. D. L. Stein, C. R. Doering, R. G. Palmer, J. R. van Hemmen, R. M. McLaughlin, J. Phys. A 23, L203 (1990).
166. T. Kakutani, Y. Nishiwaki, T. Osakai, M. Senda, Bull. Chem. Soc. Jpn. 59, 781 (1986).
167. J. A. Campbell, A. A. Stewart, H. H. Girault, J. Chem. Soc., Faraday Trans. 1 85, 843 (1988).
168. M. Seno, K. Iwamoto, Q. Chen, Electrochim. Acta 35, 127 (1990).
169. Z. Samec, D. Homolka, V. Mareček, J. Electroanal. Chem., Interfacial Electrochem. 135, 265 (1982).
170. N. K. Zaitsev, N. I. Kulakov, M. G. Kuzmin, Elektrokhimiya 21, 1293 (1985).
171. N. K. Zaitsev, O. F. Gorelik, N. A. Kotov, V. L. Shapovalov, M. G. Kuzmin, Elektrokhimiya 24, 1346 (1988).
172. N. A. Kotov, M. G. Kuzmin, J. Electroanal. Chem., Interfacial Electrochem. 285, 223 (1990).
173. N. A. Kotov, M. G. Kuzmin, J. Electroanal. Chem., Interfacial Electrochem. 327, 47 (1992).
174. V. Mareček, A. H. De Armond, M. K. De Armond, J. Electroanal. Chem., Interfacial Electrochem. 261, 287 (1989).
175. Z. Samec, A. R. Brown, L. Y. Yellowlees, H. H. Girault, K. Base, J. Electroanal. Chem., Interfacial Electrochem. 259, 309 (1989).
176. Z. Samec, A. R. Brown, L. Y. Yellowlees, H. H. Girault, J. Electroanal. Chem., Interfacial Electrochem. 288, 245 (1990).
177. Yu. I. Kharkats, Sov. Electrochem. (Engl. Transl.) 12, 1257 (1976).
178. Yu. I. Kharkats, A. G. Volkov, J. Electroanal. Chem., Interfacial Electrochem. 184, 435 (1985).
179. R. A. Marcus, J. Phys. Chem. 94, 1050 (1990).
180. H. H. J. Girault, D. J. Schiffrin, J. Electroanal. Chem., Interfacial Electrochem. 244, 15 (1988).
181. Z. Samec, J. Electroanal. Chem., Interfacial Electrochem. 103, 1 (1979).
182. Z. Samec, J. Electroanal. Chem., Interfacial Electrochem. 111, 211 (1980).
183. A. A. Stewart, J. A. Campbell, H. H. Girault, M. Eddowes, Ber. Bunsenges. Phys. Chem. 94, 83 (1990).
184. Z. Samec, V. Mareček, J. Weber, J. Electroanal. Chem., Interfacial Electrochem. 96, 245 (1979).
185. Z. Samec, V. Mareček, J. Weber, J. Electroanal. Chem., Interfacial Electrochem. 103, 11 (1979).
186. G. Geblewicz, D. J. Schiffrin, J. Electroanal. Chem., Interfacial Electrochem. 244, 27 (1988).
187. V. J. Cunnane, D. J. Schiffrin, Ext. Abstr., 39th ISE Meeting, Glasgow (1988), p. 246.
188. S. Kihara, M. Suzuki, K. Maeda, K. Ogura, M. Matsui, Z. Yoshida, J. Electroanal. Chem., Interfacial Electrochem. 271, 107 (1989).
189. Y. Cheng, D. J. Schiffrin, J. Electroanal. Chem., Interfacial Electrochem. 314, 153 (1991).
190. Q. Z. Chen, K. Iwamoto, M. Seno, Electrochim. Acta 36, 291 (1991).
191. I. M. Kolthoff, F. G. Thomas, J. Phys. Chem. 69, 3049 (1965).
192. J. Hanzlík, Z. Samec, J. Hovorka, J. Electroanal. Chem., Interfacial Electrochem. 216, 303 (1987).
193. J. Hanzlík, V. Mareček, Z. Samec, in preparation.
194. M. Shporer, G. Ron, A. Loewenstein, G. Navon, Inorg. Chem. 4, 361 (1965).

195. A.C. Wahl, Z. Elektrochem. 64, 90 (1960).
196. L.M. Peter, W. Durr, P. Bindra, H. Gerischer, J. Electroanal. Chem., Interfacial Electrochem. 71, 31 (1976).
197. E.S. Yang, M.S. Chan, A.C. Wahl, J. Phys. Chem. 79, 2049 (1975).
198. K.W. Frese Jr., J. Phys. Chem. 85, 3911 (1981).
199. R.A. Marcus, J. Phys. Chem. 94, 4152 (1990).
200. F.L. Thompson, L.J. Yellowlees, H.H. Girault, J. Chem. Soc., Chem. Commun. 1547 (1988).
201. V. Mareček, A.H. DeArmond, M.K. DeArmond, J. Am. Chem. Soc. 111, 2561 (1989).
202. O. Dvořák, A.H. DeArmond, M.K. DeArmond, Langmuir 8, 508 (1992).
203. O. Dvořák, A.H. DeArmond, M.K. DeArmond, Langmuir 8, 956 (1992).

Advances in Electrochemical Science and Engineering
Edited by Heinz Gerischer and Charles W. Tobias

Electrolytic Processes for Pollution Treatment and Pollution Prevention

Pallav Tatapudi* and James M. Fenton

Department of Chemical Engineering and Pollution Prevention Research and Development Center, University of Connecticut, Storrs, CT 06269-3222, USA

* Present address: Los Alamos National Laboratory, Los Alamos, New Mexico, USA

Contents

List of Symbols

A_e	electrode area per unit volume
k_i	mass transfer coefficient

Abbreviations

COD	chemical oxygen demand
DSA	dimensionally stable anode
EDP	electrochemical deionization process
EDR	electrodialysis reversal
EDTA	ethylenediaminetetraacetic acid
EIX	electrochemical ion exchange
EOD	electrochemical oxygen demand
EOI	electrochemical oxidizability index
FBE	fluidized bed electrode
PEM	proton exchange membrane
ppi	pores per inch
RVC	reticulated vitreous carbon
RCA	rotating-cylinder anode
SPE	solid polymer electrolyte
TOC	total organic carbon
VMPB	vertically moving particle bed
VPR	voltage polarity relay

1 Introduction

The treatment of industrial discharges to reduce toxicity and recover valuable chemicals/metals has gained impetus since the mid-1970s. A variety of treatment processes have been proposed, the more conventional being either physicochemical or biological in nature. Physicochemical processes tend either to shift pollutants (landfilling), concentrate pollutants (carbon adsorption), transfer pollutants to a different medium (air stripping), or cause secondary pollution (chemical precipitation leading to metal hydroxide sludges). Biological processes tend to have an extremely narrow range of operating conditions.

Electrolytic treatment technologies have definite advantages over these more common treatment processes. The primary benefit is that chemical change in an electrochemical process is brought about by the ability to add or remove electrons from species to be treated. This eliminates the use of redox agents to treat wastes and also removes the need to treat spent redox streams. Other, equally important, benefits of electrochemical processes include: close control of reactions through control of the applied potential or current; lower operating temperatures and hence lower costs; increased possibility of *on-site* treatment, especially in small-scale use; possible simultaneous use of the anode and cathode for waste minimization; and the ability to

recover and recycle valuable chemicals and/or metals from waste streams, thereby preventing pollution.

Recent developments in material science, electrochemical reactor design, and electrocatalysis have led to an increasing number of electrolytic applications in the area of effluent treatment. These developments have allowed electrochemical treatment processes to become competitive with physicochemical and biological processes, in terms of both capital and operating costs. Some cost-competitive cases of electrochemical pollution control have appeared in the literature over the past several years [1–6].

2 Analysis of Specific Applications

An overview of currently practiced electrolytic treatment technologies which have been, or promise to be successful is presented. Processes under the headings of cathodic processes, anodic processes, electrodialysis, electromembrane processes, electrochemical effluent gas treatment, electrochemical soil treatment, electroflotation, and electrochemical ion exchange are discussed in terms of their applicability to a given waste effluent. The anodic processes section has been subdivided into direct electrochemical oxidation and indirect oxidation by *in-situ* electrochemical oxidant generation; electrochemical synthesis of oxidizing agents is covered in another section. Emphasis has been placed on novel reactor designs, new electrode materials, and unique electrocatalytic techniques. This review should serve to augment and update the earlier reviews by Kuhn [7, 8].

3.1 Cathodic Processes

Almost all of the cathodic (reduction) processes used for waste removal are metal recovery processes. Although electrodialysis, gas treatment, and some oxidant synthesis processes make use of cathodic reactions, these will be discussed later under other headings.

Electrolytic recovery of metals is an alternative to precipitation where metallic impurities are removed at the point of origin. Electrodeposition of metals has distinct benefits over precipitation and ion exchange methods: the metals are recovered at lower capital and operating costs, no additional chemicals are needed, and sludge formation is eliminated.

In the past, electrochemical metal recovery techniques have been limited by low efficiencies in recovering low concentrations of metal ions from a process effluent. Recent advances in cell design, coupled with the availability of new cathode materials, now make it possible to achieve higher current efficiencies.

Coeuret and Paulin [9] studied the recovery of copper in a pulsed granular fixed-bed cathode using copper-plated graphite spheres as the cathode bed. The spheres

were supported on a copper screen which in turn served as the current feeder. Periodic pulsation (fluidization) of the electrolyte flowrate put particles in suspension, thus avoiding bed blockage which was found to occur in a fixed-bed cathode, and allowed for continuous metal recovery on the particles. Two modes of operation were studied; pulsed flow with constant current density, and pulsed flow with pulsed current. The pulsed current operation yielded higher current efficiencies ($\approx 90\%$), which were 25% higher than that obtained with a fluidized-bed electrode.

Avci [10] used a rotating tubular bed reactor to recover copper from both an acidic copper solution and an alkaline cyanide solution using 10 mm copper particles as a cathode with a total surface area of 40 dm^2. Applying a current of 4 A, a current efficiency of 80% was reported for copper recovery from the acidic solution. The current efficiency decreased with increasing current. A cyano-cuprate complex, formed during reduction of the alkaline cyanide solutions, led to lower copper recoveries. Addition of an oxidzing agent (NaOCl) and a complexing agent (NH_4Cl) was found to significantly enhance copper recovery as well as cyanide destruction.

Scott [11] compared three types of circulating particulate electrodes for copper recovery from dilute solutions (Fig. 1): spouted (circulating) beds, vortex beds, and moving beds. The beds contained 500–700 μm spherical copper particles positioned on a stainless steel cathode feeder, and a platinized titanium anode. All electrodes performed similarly in terms of copper recovery current efficiencies. Recovery was found to be more efficient at low pH and high metal concentrations. The spouted bed electrode was preferred on the basis of scaleup.

Tsapakh et al. [12] deposited copper on a fluidized cathode in a diaphragmless electrolyzer at 25 °C using a high concentration (20 kg/m^3) copper sulfate solution. The fluidized bed contained copper particles and the anode was lead dioxide plated

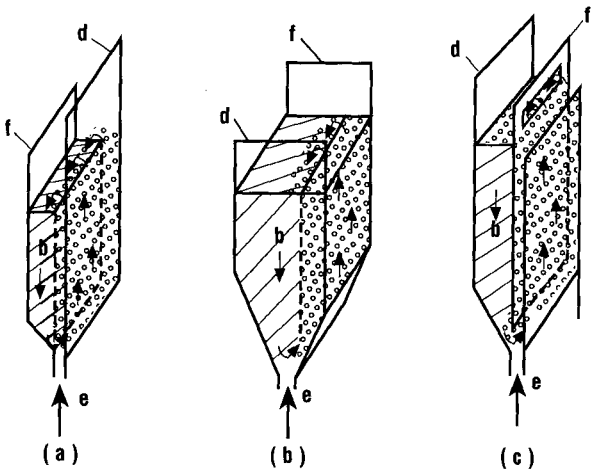

Fig. 1. A schematic of three types of circulating particulate-bed electrodes studied for copper recovery: (a) spouted bed; (b) vortex bed; (c) moving bed. b: bed region; d: diaphragm; f: feeder; e: electrolyte flow. (Adapted from [11]).

on nickel. High current efficiencies (70%) were obtained at high current densities (20000 A/m^2) along with low applied potentials (3–4 V) and specific power consumption (20–40 kWh/kg). Pletcher et al. [13] used reticulated vitreous carbon (RVC) cathodes for the removal of low levels of copper ions from aqueous, acidic sulfate solutions using membrane cells. The most rapid removal rate was attained at a high electrolyte flowrate, with an RVC cathode with the smallest pore size [100 ppi, pores per inch, ($*cm^2/cm^3$)], and largest surface area/volume ratio available. Current efficiency for copper removal was high (>50%), provided the concentration of copper ion was above 5 ppm. The presence of oxygen in the solution had no influence on the copper removal rate although it caused high cell currents, resulting in low current efficiencies. The deposition of copper was mass transport controlled at −0.4 V vs. SCE. Operating the cell at −0.3 V improved the current efficiency, but lowered the copper removal rate. The presence of chloride ions or a decrease in the ionic strength of the solution had no adverse effects on the copper deposition rate.

In a related study, Walsh et al. [14] examined the performance of a reactor divided by a DuPont Nafion® 417 membrane for the removal of copper. The cathode was a 5 cm × 5 cm × 1.2 cm piece of RVC operated under mass transport controlled conditions in a 0.5 M Na_2SO_4 solution (pH 2) containing low levels (<100 ppm) of $CuSO_4$. A lead – 6% antimony anode was used along with a 0.5 M Na_2SO_4 solution as the anolyte.

The $k_L A_e$ value (the product of the mass transfer coefficient and the cathode area per unit electrode volume) was found to depend on the surface area and pore size of the RVC and the electrolyte velocity. For a 100 ppi RVC cathode, $k_L A_e$ values up to 0.23 s^{-1} were obtained. During the reduction of 10 ppm cupric ion levels to less than 0.1 ppm, a current efficiency as high as 69% was attained, even in air-saturated solutions. The cell was scaled up from an electrode length of 50 mm to 400 mm [15]. Values of the mass transfer coefficient obtained from this reactor agreed well with those obtained from the smaller electrode [14]. The Cu(II) content was reduced from 10 to 0.1 ppm in a single pass, with a current efficiency of 69%. RVC cathodes were found to be useful for streams having low metal ion concentrations since higher concentrations may lead to clogging of the three-dimensional structure, decreasing thereby the cathode performance.

Yen and Yao [16] used a fin-type titanium cathodic current feeder (Fig. 2) in a fluidized-bed electrode to achieve enhanced copper recovery from dilute solutions. Copper particles served as the fluidized-bed cathode and platinized titanium screens were used as the anode, where oxygen evolution occurred. The feeder with the longer fin yielded higher current densities at increasing Reynolds numbers and larger bed expansions as compared with the short fin or the planar current feeder. The increased currents were due to the increased rate of copper deposition on the fluidized particles.

While operating at −1.0 V, and at a bed expansion of 75%, an initial copper concentration of 350 ppm was reduced to 3.5 ppm using the long fin feeder. This exit concentration was found to be lower for the planar or the short fin types of feeders. The enhanced performance of the long fin feeder was due to increased contact between the current feeder and fluidized particles, and the increased number of active monopolar particles in the cell.

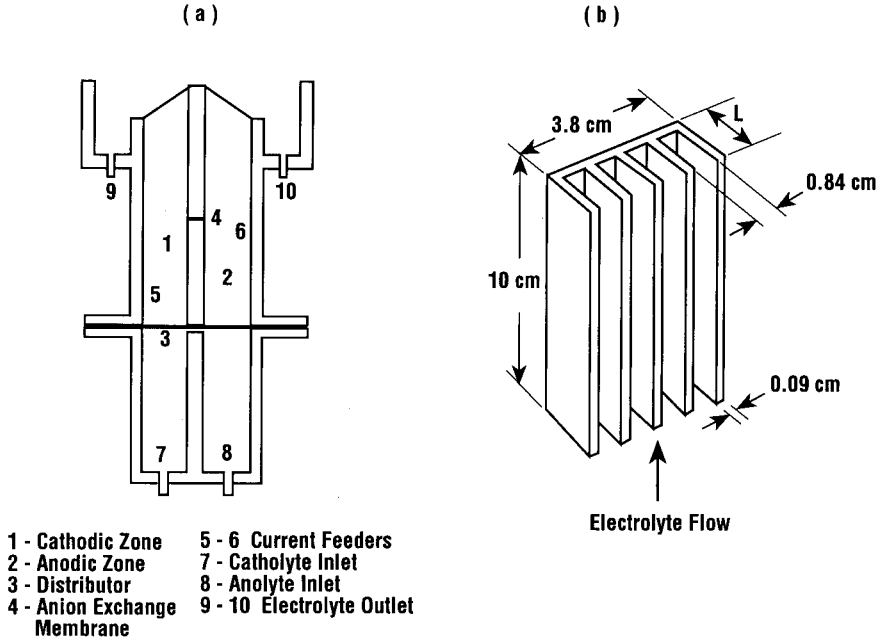

Fig. 2. Schematic of (a) a fluidized-bed cell, and (b) a fin-type current feeder, $L = 0.7$, 1.2 cm. (Adapted from [16]).

Bergmann et al. developed a vertically moving particle bed (VMPB) electrochemical reactor for copper recovery from dilute solutions (0.1 – 10000 ppm) [17]. Although higher rotation rates increased the current efficiency for copper removal at lower cell currents, rotation rates of below 5 min^{-1} were chosen to minimize mechanical wear. Impurities such as chloride ions, citric acid, and surfactants did not seem to interfere with the current efficiency of the process. This reactor was able to bring metal ion concentrations down to 0.5 ppm. A schematic of the VMPB reactor is shown in Fig. 3.

Boyanov et al. studied the removal of copper and cadmium from hydrometallurgical leach solutions using fluidized-bed electrolysis [18]. The electrolytic chamber was partly filled with 0.6 mm glass beads to ensure a high degree of turbulence in the chamber. Titanium or stainless steel expanded mesh was used as the cathode while platinized titanium served as the anode. High current efficiencies (90%) for copper removal were attained at low current densities (30 A/m^2). Although a low current density and high acid concentration were found to aid in the separation, complete electrolytic separation of the two metals was not achieved. Copper removal was more efficient in the absence of cadmium. The presence of 0.1 g/dm^3 Co and 1.0 g/dm^3 Zn did not affect the kinetics of copper deposition, while iron did lower current efficiencies for copper reduction.

Avci [19] developed a rotating tubular-bed reactor with extended cathode surface areas to improve mass transfer for nickel recovery from industrial Watts plating

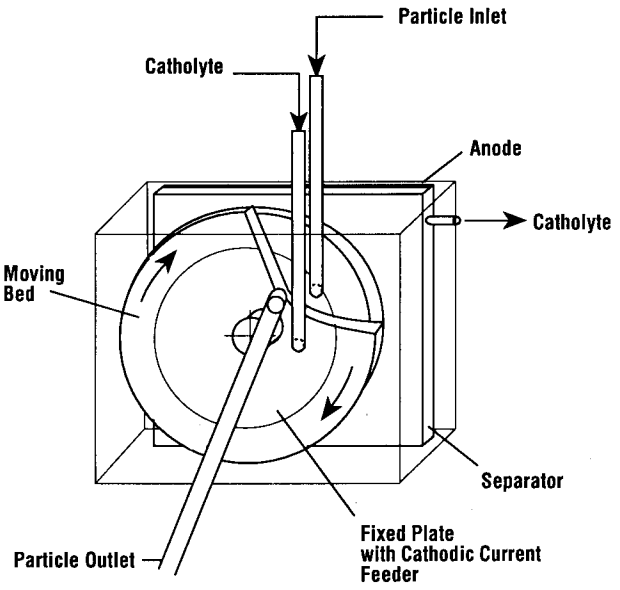

Fig. 3. Schematic of the vertically moving particle bed (VMPB) reactor. (Adapted from [17]).

baths. The electrodes were two perforated tubes, the space between which was filled with 10 mm nickel particles. At a current of 8 A, current efficiencies of up to 75% were attained for inlet nickel concentrations of 1800 to 2000 mg/dm^3 requiring 130 Ah to reduce the nickel concentration to 2.5 mg/dm^3. The current efficiency was a function of nickel concentration in solution and was higher at higher nickel concentrations. Increasing the current from 8 to 15 A, however, lowered the current efficiency.

Hu and Bautista used a fluidized-bed electrochemical reactor to recover chromium from dilute solutions [20]. The particulate cathode bed contained chromium particles (20-mesh, 450–600 μm diameter) and carbon rod current feeders which projected into the center of the fluidized bed. The lead tube anode was separated from the cathode by a porous Vycor glass tube which was selective to hydrogen ions. Current efficiency for chromium deposition varied from 8 to 22% and increased with increasing chromium concentrations and current density. The conversion ratio (the ratio of the amount of Cr(III) formed to Cr(VI) consumed) was 0.77.

Abda et al. [21] removed hexavalent chromium from aqueous solutions using graphite felt cathodes. The reduction rate of Cr(VI) to Cr(III) (which precipitated as $Cr(OH)_3$) increased with a decrease in pH. Appropriate pH values were obtained by controlling the water electrolysis rate at the anode and cathode. The location of the $Cr(OH)_3$ precipitate moved toward the outlet port as the current decreased.

Dudek et al. developed an electrolytic process for the one-step stripping of galvanized steel (at the anode) while recovering zinc by electroplating [22]. The zinc separated from the galvanized steel scrap was reused. As shown in Fig. 4, the galvanized

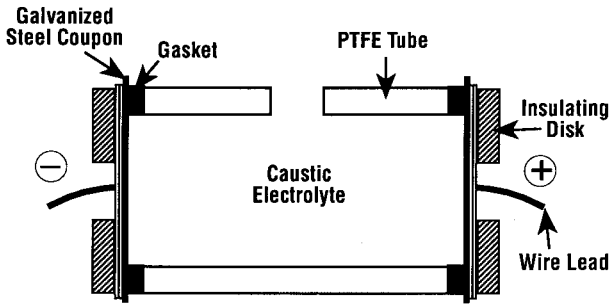

Fig. 4. An electrolytic cell for stripping galvanized steel in 90 °C caustic electrolyte. (Adapted from [22]).

scrap was the anode in a tank filled with warm (70–90 °C) NaOH while steel plates were used as the cathode. Active zinc dissolution occurred at 0.4–0.5 V positive to the zinc rest potential. Zinc deposition efficiencies varied between 70% at 25 mA/cm^2 to 95% at 150 mA/cm^2. The presence of trace metal impurities did not have any measurable effect on the current efficiency.

Electrolytic recovery of iron from pickling solutions using tungsten carbide gas diffusion anodes was studied by Streng et al. [23]. Replacement of Tainton anodes (99% lead and 1% silver) with a gas diffusion tungsten carbide anode led to a 1.5–1.7 V decrease in the cell voltage and a 50% reduction in energy consumption. Unwanted oxidation of ferrous ions to ferric ions did not occur on these gas diffusion anodes, since the cell was operated at a lower potential.

Recovery of silver from spent photographic process streams using a graphite felt cathode in a flow-through reactor (Fig. 5) was studied by Tricoli et al. [24]. Initially, the current increased with time because of the higher exchange current density of silver deposition on silver than on graphite. On the other hand, currents obtained from

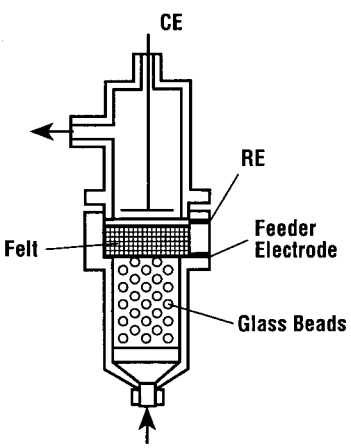

Fig. 5. A flow-through reactor designed for silver recovery from photographic process waste streams: CE, counter electrode; RE, reference electrode. (Adapted from [24]).

a precoated silver cathode decreased with time. At a cathode potential of −650 mV vs. SCE, high current efficiencies (93%) were obtained at high initial silver concentrations (500−550 mg/dm^3). Lower cathode potentials were recommended for lower initial silver concentrations to obtain high current efficiencies ($\approx$100%).

Delanghe et al. studied the removal of mercury(II) from contaminated brines using graphite felt cathodes [25]. A 100% current efficiency for mercury removal was obtained at a potential of −400 mV vs. SCE on a graphite felt 1 cm thick at a flowrate of 1 cm/s. This current efficiency was higher than that obtained on RVC, nickel foam platinum grids, or graphite sphere cathodes.

In the 1960s, fluidized-bed electrodes (FBEs) were considered to be a major breakthrough in metal recovery, primarily because of high mass transfer rates and continuous metal removal capability (as opposed to batch operations). However, low interparticle contact of the fluidized cathode caused ohmic losses resulting in high energy consumption. The high energy consumption, as well as problems associated with scaleup, resulted in only a few commercial applications, mainly in Europe [10]. To obtain higher current efficiencies for metal removal, a number of alternative reactor designs with moving particulate electrodes (as reviewed above) are under study. Although some of these designs scale up reasonably well [11, 17], most of the studies are on a benchtop scale.

Porous, three-dimensional cathodes that can be used in flow-by reactors have advantages for metal removal from dilute streams. These advantages include high electrode surface area per unit volume of electrode, and high mass transfer coefficients. The RVC cathodes used by Pletcher and his coworkers [13−15] have the additional benefit of a low pressure drop due to a high porosity. The RVC electrode was shown to scale-up well with increase in electrode length [15]. Unlike planar two-dimensional electrodes, however, RVC cathodes are brittle and need careful handling. There are also difficulties in removing or stripping the metals off the porous electrodes. However, since most waste streams tend to have low metal ion concentrations to begin with, stream cleanup will be more important than metal recovery. If metal reclamation is important (as in most electrowinning processes), a two-dimensional electrode could be used at first to recover most of the metal ions, followed by a three-dimensional electrode for cleaning up the waste stream prior to discharge.

Metal removal and recovery could be carried out by depositing on a three-dimensional cathode until most of the active surface area of the porous cathode is occupied by the plated metal. The "used" cathode would then be sent to an electrowinning cell where it would be regenerated by anodically stripping the metal which is deposited onto stainless steel sheets. The metal is then peeled off the sheets as a nontoxic, salable product. Baker Brothers/Systems (Stoughton, MA, USA) currently use this process in their high-surface-area metal recovery systems.

An alternative scheme would involve reversing the direction of current flow in a reactor after the porous cathode has become completely clogged by the recovered metal. The current reversal strips the metal off the plugged cathode and the metal is recovered in an independent, contaminant-free stream fed to the stripping chamber. This stream can be sent directly to the plating bath as a concentrated metal solution. This process, however, requires the use of an ion exchange membrane to separate the anode and cathode chambers.

2.2 Anodic Processes

While cathodic processes may produce positive payoffs by recovering metals from waste streams, anodic processes are essentially destructive in nature. Positive payoffs may occur if it is possible to carry out an anodic process which destroys toxic species at the same time that the cathode is recovering metals. For example, during the treatment of a cyanide plating bath, heavy metals are recovered at the cathode while cyanide is destroyed at the anode along with any organic additives and brighteners.

Anodic processes may occur by direct electrochemical reaction of the waste at the anode, or by indirect oxidation when an oxidizing agent is generated in the waste stream. For example, oxygen and ozone may be generated from water in the waste stream, or the addition of sodium chloride to the waste stream can be used to generate free chlorine or hypochlorite at the anode. In addition, metal ions of higher valence states can be produced at the anode to oxidize wastes.

2.2.1 Direct Electrochemical Oxidation

Direct electrochemical oxidation of organics present in waste streams faces an inherent problem in that the species that need to be oxidized may be present at very low concentrations (organics, typically at $5-1000\,mg/dm^3$) compared with water ($\approx 55\,mol/dm^3$). However, the ultimate goal is not necessarily to mineralize the organics (i.e., convert them to CO_2 and H_2O), but to detoxify the hazardous components in the waste water. Electrochemical oxidation may achieve this objective in a nonpolluting fashion by making use of the electron directly while eliminating the use of extraneous oxidizing agents.

The anodic oxidation of phenol (dissolved in sodium sulfate) was studied by De Sucre and Watkinson using two types of lead dioxide anodes [26]. The first was made of 2 mm lead shot that was oxidized for 12 h at $526\,mA/cm^2$ in 20% sulfuric acid while the second anode, electrodeposited lead dioxide flakes, was supplied by a commercial manufacturer. The phenol oxidized faster on the electrodeposited PbO_2, which also turned out to be more corrosion-resistant than the oxidized lead shot. While all of the phenol oxidized rapidly (1.5 h) on the electrodeposited anode, not all of it formed CO_2. It was found that 80% of the total organic carbon remained in solution after the phenol was completely oxidized. Phenol destruction increased with an increase in current density, and decreased as electrolyte flowrate, pH, and anode particle size were increased.

The oxidation of aniline in sulfuric acid was studied by Kirk et al. on a packed-bed anode made up of 1 mm spherical lead pellets in contact with a pure lead anode collector plate [27]. The lead pellets were oxidized to lead dioxide for an hour in sulfuric acid (pH = 2) at $300\,A/m^2$. No mention was made of the corrosion resistance of these anodes. The anodic destruction of aniline to CO_2 was found to occur through the formation of benzoquinone and maleic acid. At a current of 2 A, the initial rate of aniline (2.7 mM) oxidation was very rapid with more than 90% of the initial aniline being oxidized within one hour. After 5 h of operation, 72.5% of the

aniline was converted to CO_2. The amount of aniline oxidized increased with increasing current density and decreased with increasing aniline concentration and pH. Current efficiencies for complete oxidation to CO_2 ranged from 15 to 40%. A schematic of the packed-bed reactor is shown in Fig. 6.

Ho et al. completely oxidized simple sugars (sucrose, maltose, and 1.0% glucose in 0.5% NaCl or Na_2SO_4) on PbO_2-coated titanium mesh anodes [28]. At 0.5 A, the electrodestruction, measured in terms of chemical oxygen demand (COD) remaining, followed a linear relationship with time; all of the sugars were destroyed at a rate of $375-400\ mg/dm^3\ h$. Negligible electrode corrosion occurred; no Pb^{2+} ions were found in solution, even after prolonged use of the electrode.

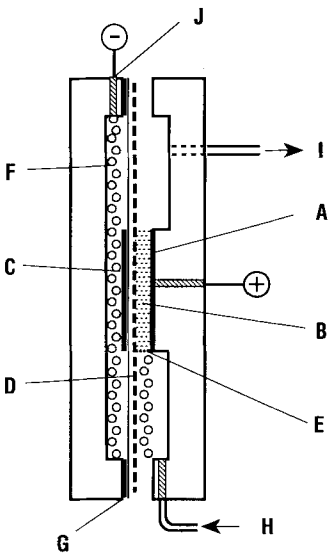

Fig. 6. An electrochemical reactor used for aniline oxidation on a lead dioxide packed-bed anode: (A) lead anode; (B) 1 mm lead pellets; (C) stainless steel cathode; (D) Nafion®427 membrane; (E) stainless steel retaining screen; (F) glass beads; (G) gasket; (H) inlet; (I) outlet; (J) cathode gas vent. (Adapted from [27]).

Patzer et al. studied the anodic oxidation of urea in a closed-loop hemodialysis system [29]. While urea was completely oxidized to ammonia and CO_2 on platinum surfaces at 0.5 – 1.1 V vs. Ag/AgCl, these reaction products were thought to be adsorbed to the electrode surface, leading to electrode deactivation and subsequent increase in electrode potentials. An optimal constant constant-current strategy, voltage polarity relay (VPR), appeared to accomplish simultaneous urea oxidation and electrode regeneration. The VPR control method reversed the polarity of the working and the counter electrode when the working electrode reached 1.1 V.

The electrochemical incineration of synthetic sewage waste in 12 M H_2SO_4 or urine was studied by Kaba et al. [30]. At a potential of 1.8 V vs. NHE, a 95% reduction in total organic carbon (TOC) occurred on lead dioxide electrodes after 90 h of operation. The addition of a Ce^{3+}/Ce^{4+} redox couple to the electrolyte caused a fivefold increase in the current density but only a 1.5-fold increase in the destruction rate. The use of ultrasound also resulted in an increase in the current density and destruction rate.

Electrolysis of a urine-waste biomass mixture at 800 mA on a PbO_2 anode showed an 82% decline in TOC after 96 h of operation. The destruction process occurred through the generation of ClO^- ions at the anode from Cl^- within the urine. Noxious gases such as carbon monoxide, nitrogen dioxide, nitrous oxide, ammonia, and methane were not detected in the gaseous effluent, while Cl_2 which was formed during the process constituted only 0.1% of the evolved gases.

Disinfection of municipal water contaminated with coliforms and fecal streptococci was the subject of a study by Patermarkis and Fountoukidis [31]. Disinfection was achieved using titanium electrodes and direct current. The polarity was alternated every minute to eliminate titanium oxide buildup. No additives or supporting electrolytes were used in this room-temperatures process. At a current density of 2.5 mA/cm^2 and an applied voltage of 45 V, no microbial activity was detected after 30 min of operation. Noncontaminated, electrochemically treated water possessed a residual disinfection capacitiy; addition of treated water to a contaminated sample destroyed the microbial life in the sample.

Matsunaga et al. studied the disinfection of drinking water at room temperature using *Escherichia coli* as a model microorganism. As shown in Fig. 7, the carbon cloth electrodes were interwoven with ion exchange membranes and rolled around a glass tube [32]. At an applied potential of 0.7 V vs. SCE, an initial cell suspension of 10^5 cells/dm^3 was reduced to $< 10^2$ cells/dm^3 at a residence time of 10 min. The disinfection was thought to be based on the electrochemical oxidation of intracellular coenzyme A.

Comninellis formulated the "electrochemical oxidizability index" (EOI) and the "electrochemical oxygen demand" (EOD) to quantify the anodic mineralization or

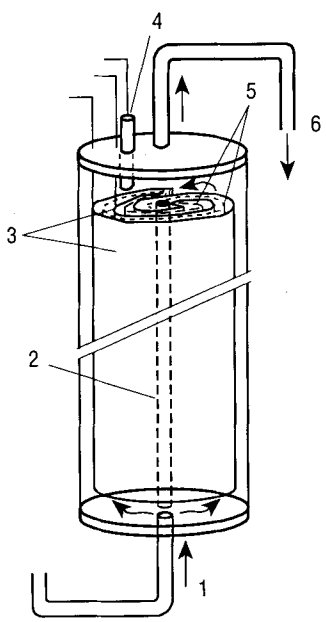

Fig. 7. Electrochemical sterilization reactor used for drinking water disinfection: (1) feedwater; (2) glass jar; (3) carbon-cloth electrode; (4) SCE; (5) ion exchange membrane, (6) treated water. (Adapted from [32]).

destruction of organic species in wastewaters [33, 34]. Studies on the destruction of substituted groups, such as $-COOH$, $-NO_2$, $-SO_3H$, etc., had low EOI values while substituents which were electron-donating, such as $-NH_2$, had high EOI values.

The oxidation of phenol on a platinum anode was studied by the same author [34]. At a current density of 50 mA/cm^2, 70 °C, and a pH of 3, the initial phenol concentration of 21 mmol/dm^3 completely disappeared in 2 h. Apart from CO_2, other organic intermediates such as hydroquinone, benzoquinone, maleic acid, fumaric acid, and oxalic acid were identified. An analysis of the reaction intermediates and a carbon balance showed that the destruction reaction occurred by two parallel pathways; chemical oxidation with electrogenerated hydroxyl radicals, and direct oxidation of phenol and/or its aromatic intermediates to CO_2.

Kotz et al. used an SnO_2 anode doped with antimony to oxidize 1000 ppm phenol in 0.25 M Na_2SO_4 [35]. It required 1 Ah to destroy phenol completely and 8 Ah for the total disappearance of organic carbon from the system, suggesting that all of the phenol had been converted to CO_2. The SnO_2 anode was superior to Pt and PbO_2 anodes, as the latter two electrodes failed to eliminate organic carbon completely. The enhanced performance of these SnO_2 anodes was attributed to the availability of holes at the surface of the doped electrode which would allow the oxidation of organics to proceed via a hole mechanism.

In a related study, Comninellis and Pulgarin [36] showed that only small amounts of intermediates were formed during the destruction of phenol on doped SnO_2 anodes while larger concentrations were observed on platinum anodes. Aliphatic acids that were formed as intermediates during phenol oxidation were rapidly oxidized at the SnO_2 anode while they were electrochemically inactive at Pt anodes.

Stucki et al. studied the destruction of benzoic acid [37] on an SnO_2 anode. It required 2Ah to destroy the benzoic acid completely and a little over 10 Ah for the total disappearance of organic carbon from the system, once again suggesting that all of the benzoic acid had been converted to CO_2. A similar comparison with Pt and PbO_2 anodes revealed that both these electrodes failed to eliminate organic carbon completely.

The electrochemical oxidation of 1,4-benzoquinone, a toxic organic compound found in photographic process wastewater streams, was investigated by Pulgarin et al. [38]. The electrochemical cell designed for this purpose is shown in Fig. 8. At an anodic current density of 50 mA/cm^2, the rate of oxidation depended on the type of anode used. Complete mineralization of benzoquinone to CO_2 was observed on an SnO_2 anode deposited on a titanium substrate at 40 Ah/dm^3 while an IrO_2 anode, also deposited on a titanium substrate, needed 80 Ah/dm^3 of charge before all of the benzoquinone was destroyed. Only 60% of the organic carbon was completely mineralized to CO_2, and a number of organic intermediates such as maleic, fumaric, and oxalic acids were found in solution. No explanation was offered for the differences in the activity of these two electrodes.

Murphy et al. used a proton exchange membrane (Nafion® 117) as a solid electrolyte to oxidize a mixture of 12 low-concentration (50–60 ppm TOC) organic compounds contained in deionized water [39]. Platinum 10% iridium mesh anodes and cathodes were hot-pressed onto the surface of the membrane. This membrane elec-

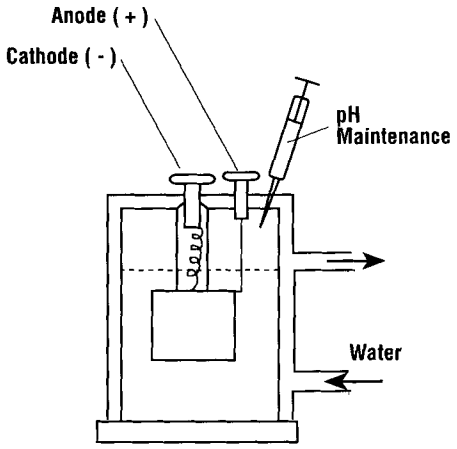

Fig. 8. Electrochemical cell used for 1,4-benzoquinone oxidation. (Adapted from [38]).

trode assembly was in turn "sandwiched" between two current collectors as shown in the schematic of the proton exchange membrane (PEM) reactor in Fig. 9. At a current density of 1.2 A/cm^2, it required 60 h to bring the TOC levels to zero. The oxidation of the organics was found to occur by the same reaction mechanism at different applied potentials and was under kinetic control. The oxidation reactions occurring were assumed to be proceeding through a heterogeneous bimolecular mechanism where the disappearance of the organics was directly proportional to the concentration of the organic species as well as to the concentration of the surface-active sites consisting of metal oxide films formed *in situ*.

The anodic destruction of low-concentration cyanide solutions was studied using nine different lead dioxide anodes which were plated from lead nitrate solutions con-

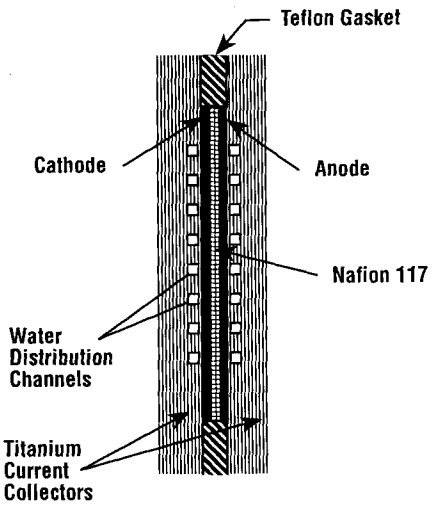

Fig. 9. Single-cell PEM reactor used to destroy organic waste streams. (Adapted from [39]).

taining different surfactants or organic additives [40]. All of the lead dioxide anodes were able to reduce the cyanide concentration from an initial value of 800 ppm to 0 ppm in 1.5–3 h, while a graphite anode was not able to achieve complete degradation even after 4 h. The surfactants or derivatives used in electrode fabrication altered the porosity of the lead dioxide anode, which in turn appeared to affect the decomposition efficiency.

Ho et al. used a packed-bed reactor and a series of 316 stainless steel fiber anode/cathode pairs to decompose cyanide-containing effluent [41]. The cyanide destruction process was enhanced by the presence of metal ions, which led the authors to treat a copper cyanide effluent. The cyanide concentration was decreased from an initial concentration of 1400 ppm to less than 20 ppm within a 4–20 h time period at an energy consumption of 5–13 kW h/kg CN. At a CN/Cu ratio of 4.6 most of the copper was deposited on the cathode while some was converted to the divalent form and deposited on the anode surface as an oxide.

In a related study, Lin et al. [42] used a bipolar arrangement of the same reactor and electrode system mentioned above to compare the performance of the two configurations. The bipolar design was shown to yield higher current efficiencies for cyanide destruction at the expense of a higher power consumption. Nonuniform copper deposition on various cathodes showed that the reactions were not occurring uniformly with the bipolar arrangement.

Most studies on electrochemical oxidation were performed using added acids or salts as supporting electrolytes; these create a secondary waste stream that needs to be treated. In contrast, the proton exchange membrane electrolyte used by Murphy et al. [39] eliminates extraneous addition of acids and salts and does not create a secondary waste. However, "real" waste streams which contain dissolved inorganics in addition to organic compounds could foul the membrane, the electrode, or both. One approach to circumvent this problem would be to treat and remove inorganics from the waste stream (possibly by electrochemical methods) before oxidizing the organics in membrane cells. Alternatively, the waste stream could be treated first in a cell without a membrane, since the presence of inorganics will enhance conductivity of the waste stream where the removal of inorganics occurs simultaneously with the oxidation of the organics. Once the solution conductivity begins to drop to an unacceptable level, a membrane cell can be used to "polish up" the waste stream, since then the low concentration of the waste species should not poison the membrane and/or electrode.

Mechanistic studies have shown that hydroxyl radicals formed at the anode, as a precursor to oxygen evolution, can chemically oxidize dissolved organics in the waste stream [34]. In such cases, current efficiencies for organic destruction could be improved by suppressing unwanted side reactions such as oxygen evolution. Metal oxide anodes which typically have high oxygen overvoltages work well in this area. Doped SnO_2 anodes [35–38] even outperform PbO_2 in completely mineralizing organic compounds.

A majority of the studies on electrochemical oxidation were performed on single organic compounds. While this provides fundamental kinetic and mechanistic data, further studies need to be done using streams containing a mixture of compounds (such as the one studied by Murphy et al. [39]) to simulate actual waste streams.

Much like metal recovery from dilute streams, the use of three-dimensional electrodes will enhance the oxidation rates of low-concentration organics by increasing the surface area available for reaction. Moreover, porous electrodes which could be incorporated into cells using solid electrolytes can draw upon technologies developed for other electrochemical systems such as PEM-based water electrolyzers and fuel cells.

2.2.2 Indirect Electrochemical Oxidation

Indirect electrochemical oxidation encompasses all those processes in which the pollutant is indirectly oxidized, either by the generation of oxidants (e.g., Cl_2, ClO^-, O_3) or by the presence of a redox couple (Ag^+/Ag^{2+}, Fe^{2+}/Fe^{3+}, Co^{2+}/Co^{3+}) that is used as an electron carrier for oxidation.

The indirect oxidation of dilute cyanide solutions using electrolytically generated chlorine or hypochlorite from NaCl in the electrolyte was examined by Yen et al. [43]. Packed layers of platinized titanium screens were used as the anode. The cyanide destruction rate increased with increasing current density, but decreased with increasing pH. The presence of NaCl in the electrolyte enhanced the CN destruction rate. The optimum amount of NaCl increased with increasing current density. Increasing the electrolyte flowrate did not affect the destruction rate of cyanide, which led the authors to believe that the presence of oxygen and hydrogen bubbles at the anode and cathode respectively allowed for increased mixing, resulting in no mass transfer limitations. The presence of cuprous ions accelerated the destruction rate of cyanide, although no explanation was offered for this phenomenon.

Poon and Soscia demonstrated a process for the destruction of cyanide from a metal-finishing waste solution with simultaneous removal of cadmium [44]. This was achieved in a reactor (Fig. 10) that electrolyzed seawater below a column of the metal-finishing waste to generate oxidants such as hypochlorite which was brought to the top, into the metal-finishing waste column, by ascending gases (O_2, H_2, Cl_2) generated during electrolysis. The hypochlorite reacted with the cyanide to form

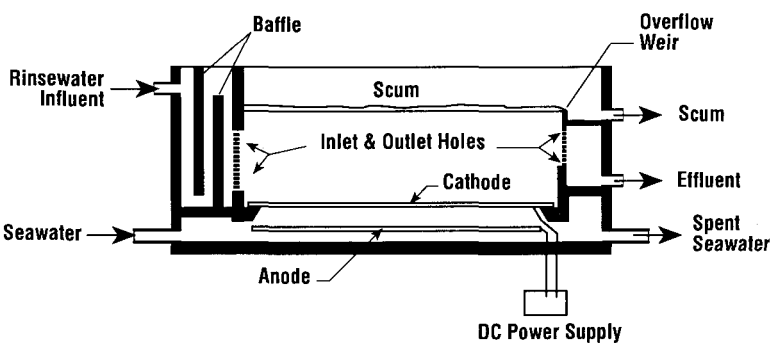

Fig. 10. Electrochemical reactor used for the simultaneous treatment and removal of cyanide and cadmium from a metal-finishing waste stream. (Adapted from [44]).

CO_2 and N_2. Excess chlorine gas (i.e., chlorine which did not form hypochlorite) converted the cyanide to cyanate, which was subsequently oxidized by hypochlorite. Cadmium was precipitated from the water due to an increase in the solution pH. A platinum-plated niobium screen was the anode and a stainless steel screen was used as the cathode. At an applied potential of 6.0 V, resulting in a current of 6.0 A, the cadmium concentration decreased from 17.4 mg/dm^3 to 0.01 mg/dm^3, while the cyanide concentration declined from 54 mg/dm^3 to zero in 80 min of cell operation.

Franklin et al. studied the *in-situ* anodic oxidation of barium peroxide (BaO_2) in aqueous sodium chloride solutions containing cationic surfactants. An active intermediate, barium superoxide (BaO_2^+), was formed which in turn converted carbon tetrachloride to soluble barium chloride and barium carbonate precipitate [45]. This work was extended to the destruction of 1,2-dibromomethane in aqueous solutions [46]. Destruction of 1,2-dibromomethane was increased by increasing the amount of barium peroxide, electrolysis time, current density, and temperature of the solution. Using a graphite anode, a destruction efficiency of 86–89% was achieved at a potential of 0.9 V vs. SCE and a current density of 16.6 mA/cm^2, when the solution was maintained at 25 °C. The authors postulated that the superoxide acted as a nucleophile which in turn displaced the halide from dibromomethane. The resulting compound was then oxidized electrolytically and chemically. No oxidation was found to occur when the barium peroxide was replaced with hydrogen peroxide, which suggests that the barium ion helps to stabilize the superoxide ion. The surfactant was thought to aid in suspending the insoluble organic compound and the barium peroxide, while also helping to stabilize the superoxide ion.

Although the superoxide ion was also successful in destroying some aliphatic and aromatic halogenated hydrocarbons, resulting in the formation of barium carbonate, soluble halides, and water, it was unsuccessful in destroying nitroaromatic compounds, or aliphatic compounds having an amine or a nitrile group attached to them [47]. This led the authors to believe that the superoxide ion was not a strong enough nucleophile to displace nitro, amine, or cyanide groups.

The combined use of nonelectrochemically generated ozone and electrolytic oxidation using ferrite anodes to oxidize ethylene glycol was studied by Takahashi and Katsuki [48]. At a current density of 2.1 A/dm^2, an O_3 feed gas concentration of 15.6 mg/dm^3, and an initial ethylene glycol concentration of 4×10^{-3} mol/dm^3, the complete removal of organic carbon, while not achievable by either of the two methods separately (i.e., ozonation alone, or electrochemical oxidation alone) was attained when both methods were used in combination. The authors inferred that the formation of reactive free radicals was responsible for TOC removal. Glycolaldehyde, glyoxal, glyoxylic acid, and formaldehyde were detected as the reaction products of ethylene glycol decomposition: this led the authors to conclude that TOC removal proceeded via the temporary formation and rapid decomposition of formic acid.

The conversion of ethylene glycol to CO_2 by reaction with Co(III), Fe(III), or Ag(II) in HNO_3 using a gold rotating-cylinder anode was studied by Farmer et al. [49]. At temperatures between 28 and 47 °C, ethylene glycol and its intermediates (formaldehyde and formic acid) were completely converted to CO_2 using Co(III). At 673 mA, current efficiencies between 55 and 64% were observed using Co(III), in contrast to 88% observed using Ag(II) under similar experimental conditions. Poor

conversion and current efficiencies were observed using Fe(III), which led the authors to conclude that the strongest oxidizing agents served as the most efficient mediators in the oxidation of organic compounds.

In a related study, Farmer et al. studied the destruction of benzene by Ag(II) [50]. Unlike in the case of ethylene glycol, a maximum conversion of 60% was achieved after 5 h of electrolysis at 336 mA. The authors attributed the failure to achieve 100% conversion to the volatilization of benzene or one of its intermediates from the anolyte. Of the three separator materials, porous ceramic, Vycor microporous glass, and Nafion® 117, which were investigated, the latter two were found to be effective barriers to HNO_2 (formed by the reduction of HNO_3 at the cathode) migration from the catholyte to the anolyte.

Farmer and his coworkers [51] modified their earlier process by replacing the HNO_3 electrolyte with H_2SO_4, the gold anode with platinum, eliminating the membrane separator, and replacing the Ag(II) mediator with Co(III). These changes were made because the earlier process suffered from precipitation of Ag as a halide, leakage of Ag through the membrane separator, fouling of the membrane, anode corrosion in the presence of HNO_3, and generation of HNO_2 and NO_x at the cathode. While 20–50% of the organics studied were volatilized during the process, the remaining organics were completely converted to CO_2. A schematic of the electrolytic cell with the rotating cylindrical anode is shown in Fig. 11.

Sudoh et al. demonstrated the destruction of phenol via electrolytically generated Fenton's reagent in a ferrous sulfate/sodium sulfate electrolyte. These studies were performed in an H-type electrolyzer (Fig. 12) on a graphite plate cathode [52]. At an operating potential of −0.6 V vs. Ag/AgCl, a solution pH of 3, and a ferrous concentration of 2 mol/m^3, a phenol degradation current efficiency of 60% was reported for initial phenol values ranging from 260 to 2600 ppm.

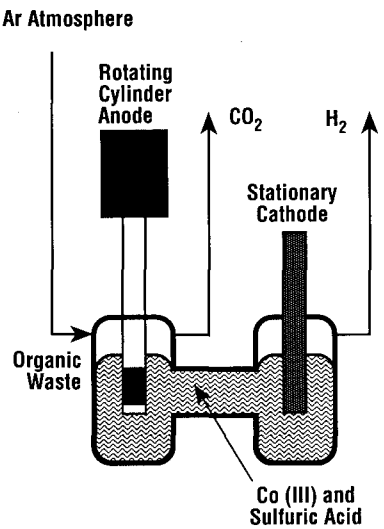

Fig. 11. Schematic of an electrochemical cell and gold rotating-cylinder anode (RCA) for the indirect destruction of chlorinated organics using Co(III). (Adapted from [51]).

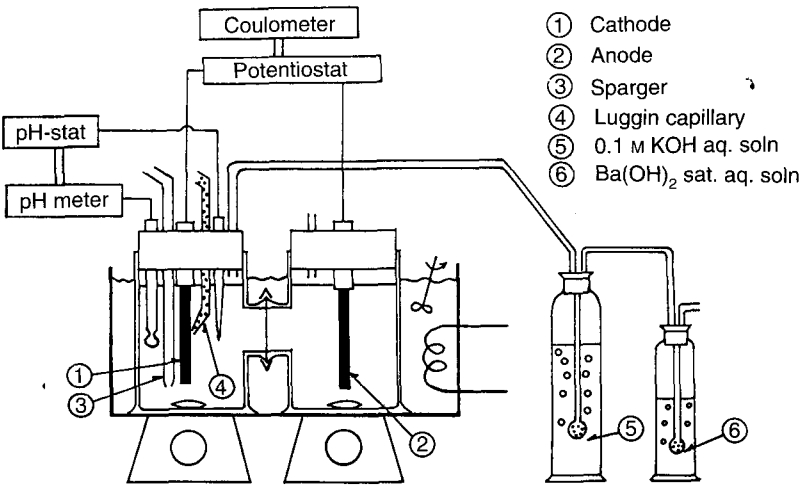

Fig. 12. H-type electrolyzer for the electrogeneration of Fenton's reagent [52]. (By permission from Society of Chemical Engineers, Japan).

Unlike the above process, which was operated in the acidic range, Do and Chen showed that formaldehyde could be destroyed *in situ* using electrolytically generated alkaline hydrogen peroxide on a graphite plate cathode [53]. At a current density of 0.5 mA/cm^2, a pH of 13, and an operating temperature of 45 °C, 99.9% of the initial formaldehyde (1000 ppm) was degraded at a current efficiency of 81.1%.

All the above processes involved the anodic formation of oxidizing agents in aqueous media. Kalu and White, however, generated superoxide ions $O_2^{\bullet -}$ at the cathode by the reduction of oxygen in aprotic solvents such as dimethylformamide and/or dimethylsulfoxide containing 0.2 M tetraethylammonium perchlorate supporting electrolyte [54]. Studies were conducted in a once-through flow reactor (Electrocell Co., Sweden) to determine the feasibility of destroying hexachlorobenzene on a graphite gas diffusion electrode loaded with 0.3 mg/cm^2 platinum. The extent of C_6Cl_6 degradation increased with current density. At 4.5 mA/cm^2, the degradation efficiency was higher at low solvent flowrates, reaching values close to 100% at a solvent flowrate of < 1 cm^3/min. The type of solvent also appeared to affect the degradation efficiency, as did the purity of the substrate. These differences in performance were attributed to conductivity differences of the solvents used as well as the physical properties of oxygen in the media. The contaminants in the impure substrate either inhibited superoxide formation or competed with C_6Cl_6 for the superoxide ions.

The use of electrochemically generated oxidants for the indirect oxidation of organic wastes has an inherent advantage in that direct electrochemical oxidation of the wastes can occur simultaneously. However, the use of chlorine and hypochlorite has raised concern because of the formation of chlorinated organics. Fortunately, ecologically desirable oxidants such as ozone and hydrogen peroxide (which decom-

pose to oxygen and water) can be prepared on site, electrochemically, and are just as effective as chlorine or hypochlorite.

The use of redox couples for the destruction of organic compounds has its basis in electroorganic synthesis. An advantage of this process is that the redox reagent is recycled, thus eliminating the production of unwanted solids or an effluent solution. However, unless complete mineralization of the organics occurs (to CO_2 and H_2O), the redox reagents have to be separated from the waste stream (for them to be reused), which may not be possible. If the redox couple is immobilized within the electrode (in the form of a coating), separation of the couple from the waste products will not be a problem.

2.2.3 Miscellaneous Anodic Processes

This section reviews additional anodic processes in water cleanup, leaching pure metals from ores, cleaning contaminated metallic surfaces, and anode behavior in harsh electrolytic environments.

Pretorius et al. proposed the electrolytic dissolution of iron in a tapwater/NaCl electrolyte using mild steel electrodes as a means of producing ferrous ions that could be used to precipitate phosphorus from wastewater [55]. The cost of this electrolytically produced iron was found to compare favorably with commercially available iron salts which tend to contaminate water supplies.

Lee et al. studied the oxidation of ferrous ions in sulfuric acid using graphite particle packed-bed anodes [56]. The resulting ferric ions are used as oxidizing agents for the leaching of copper and iron from metal ores, and for sulfur dioxide removal from sulfuric acid solutions. Current densities of 100 mA/cm^2 were achieved in 3 M H_2SO_4 with 0.5 M $FeSO_4$.

Chaudry and Bhide [57] demonstrated a process for cleaning metallic surfaces contaminated by a spent-fuel radioactive wastewater stream. Using an aluminum cathode and tapwater as the electrolyte, a current density of 15 $\mu A/cm^2$ on a contaminated pipe wrench made of mild steel (rendered anodic) reduced the radioactivity from 26 $\mu Gy/h$ to 0.26–0.39 $\mu Gy/h$ in 15 min. Similar results were obtained when studies were performed on contaminated aluminium plates.

Harnsberger and Ramoda compared the relative performance of platinum-clad niobium, iridium-oxide-coated titanium, and iridium-oxide-coated titania suboxide ceramic anodes to assess their stability in fluoride-containing metal-finishing effluents [58]. The anodes were polarized in a sulfuric-acid-based fluoride-containing solution at 100 mA/cm^2. The ceramic anode showed the highest degree of resistance by lasting for 3500 h before it ceased to function. The Pt/Nb and the IrO_2/Ti electrodes, in comparison, lasted for 1500 and 48 h, respectively. The authors believed that the superior performance of the ceramic electrode was due to a lower solubility of the substrate in HF as well as its higher porosity, which may have provided a reservoir for the IrO_2 coating.

2.3 Electrochemical Synthesis of Oxidizing Agents

Electrochemical routes to synthesizing oxidizing agents for waste treatment practices can offer a number of advantages over conventional processes: close control product output and purity; elimination and/or minimization of by-product co-generation; elimination of transport of toxic and hazardous oxidants through on-site generation at concentrations proportional to the waste needing to be treated; possible economic advantages over traditional routes, especially for small-scale applications.

Oxidants can be synthesized either at the anode or the cathode, and in some instances simultaneously at both the electrodes. Synthesis can also take place in either divided or undivided cells; in some cases, the presence or lack of a separator dictates the type of oxidant formed.

2.3.1 Ozone

Ozone is the second most powerful oxidant molecule, exceeded in its oxidizing capacity only by fluorine. However, the nonpolluting nature of ozone (ozone is reduced to oxygen during oxidation) makes it far more useful than fluorine for waste treatment purposes. The current technology for ozone synthesis (corona discharge) tends to yield 2–6 wt.% ozone in the gas phase at a relatively low power consumption (20–40 kW h/kg O_3). However, low transfer efficiencies of ozone from the gas phase (where it is formed) to the liquid phase (where it is needed for wastewater treatment) have restricted the use of this otherwise useful and powerful oxidant. To overcome these difficulties, various electrochemical technologies for ozone evolution have been investigated. Advantages in capital costs, ozone concentrations, and operating characteristics show that electrochemical technologies for ozone synthesis can be economical for small-scale uses.

Since its accidental discovery by electrolysis of sulfuric acid in 1840 [59], electrochemical synthesis of ozone has evolved fairly slowly, primarily because of low current efficiencies observed at practical operating temperatures.

Electrolytically, ozone is formed by the anodic decomposition of water:

$$O_3 + 6\,H^+ + 6\,e^- \rightarrow 3\,H_2O \qquad E^0 = 1.51\ V \tag{1}$$

where the oxidation of evolved oxygen could also contribute to ozone synthesis:

$$O_3 + 2\,H^+ + 2\,e^- \rightarrow O_2 + H_2O \qquad E^0 = 2.07\ V \tag{2}$$

Oxygen evolution occurs preferentially to ozone evolution as it is a lower-potential process:

$$O_2 + 4\,H^+ + 4\,e^- \rightarrow 2\,H_2O \qquad E^0 = 1.23\ V \tag{3}$$

To obtain ozone at significant current efficiencies, the rate of the oxygen evolution reaction must be reduced. Some of the requirements for practical ozone genera-

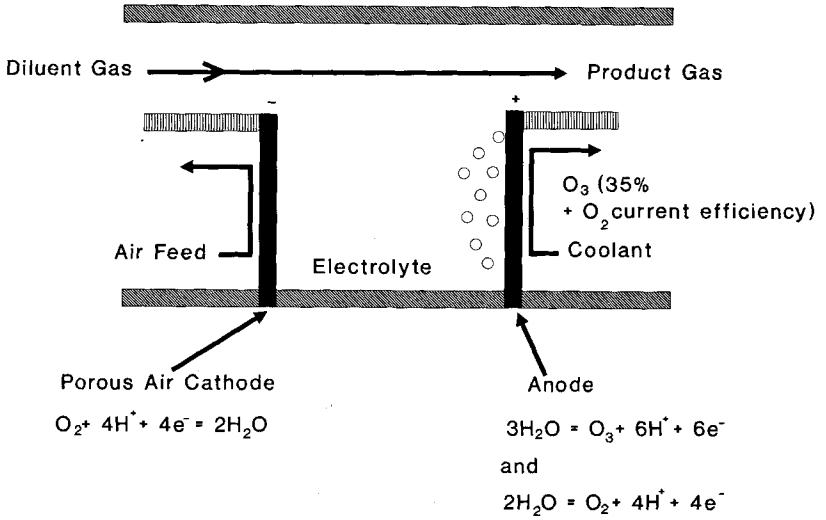

Fig. 13. Electrochemical cell for ozone synthesis using the HBF_4/glassy carbon route. (Adapted from [66]).

tion include the use of: high oxygen overvoltage (poor oxygen evolution kinetics) anodes; electrolytes whose anions and cations engage in no competitive oxidation or reduction; anodes present in their highest oxidation state or kinetically resistant to further oxidation and; anodes which are stable in highly acidic environments produced by the anodic decomposition of water.

Most laboratory studies on the evolution of ozone were performed at low temperatures using Pt and PbO_2 electrode materials and H_2SO_4, $HClO_4$, or H_3PO_4 electrolytes [60–65]. A lower-temperature operation was necessary to reduce ozone decomposition at higher operating temperatures.

Based on these early studies, two current approaches have evolved for generating ozone electrolytically. One of them, shown in Fig. 13, uses glassy carbon anodes, a specialized electrolyte, tetrafluoboric acid (HBF_4), and an air cathode [66]. At a current density of 400 mA/cm^2, 35 vol% of ozone was obtained from 48 wt.% HBF_4 maintained at -5 to 0 °C, with a cell potential of 3.2–3.4 V vs. NHE. The ozone gas formed within the cell was immediately diluted with air to lower the ozone concentration to 15 wt.%, a value below explosion limits. The electrodes were not attacked at these current densities and in the presence of this electrolyte.

This approach offers relatively high current efficiencies (35%), a low cell voltage, and elimination of the requirement for hydrogen management through the use of an air cathode. However, a disadvantage of this process is that wastewater treatment processes will be limited by the rate of mass transfer of ozone from the gas phase (where it is formed) to the liquid phase (where it is needed for reaction).

The second approach to synthesizing ozone electrochemically uses deionized water fed from the rear of a three-dimensional porous inert anode (lead dioxide) in contact with a solid polymer electrolyte at room temperature [67, 68]. The synthesis

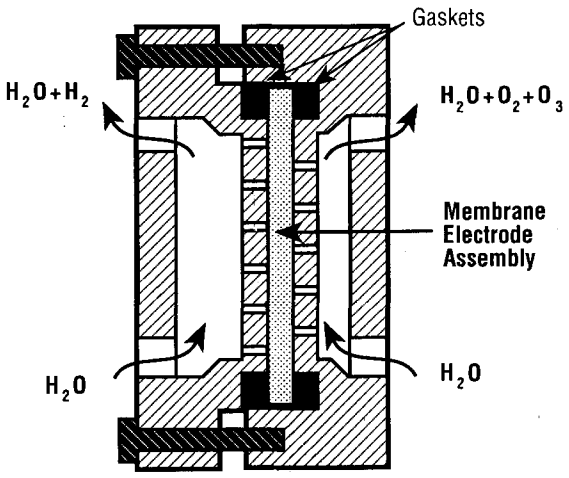

Fig. 14. Electrochemical reactor for ozone synthesis using the lead dioxide/solid polymer electrolyte route. (Adapted from [67]).

takes place in a cell (Fig. 14) whose anodic section is made of titanium and the cathodic section of stainless steel. A Nafion® membrane acts as the electrolyte and as the separator between the anode and cathode chambers. This membrane is sandwiched between the ozone- and oxygen-evolving anode (lead dioxide) and a hydrogen-evolving cathode (platinum). Electrolysis takes place at 25 °C and a total cell voltage of 3–5 V yields 0.5–2.0 A/cm^2. High concentrations of dissolved ozone (20 mg/dm^3) were obtained at a current density of 1 A/cm^2. Current efficiencies, however, were low (14%).

This method produces ozone in electrolyte-free water, making the system more desirable for wastewater treatment. Higher concentrations of dissolved ozone can be achieved by pressurizing the system [68], which eliminates the need for low-efficiency gas-liquid contact spargers. However, some of the disadvantages of this process are: low current efficiencies (< 15%); high dependence on the type of lead dioxide used (α- or β-forms), its morphology, and method of preparation; the substrate used for the lead dioxide (titanium); and the change in electrode morphology with time.

Tatapudi and Fenton [69] explored the synthesis of ozone in a proton exchange membrane (PEM) electrochemical flow reactor as part of an overall scheme to study the paired synthesis of ozone and hydrogen peroxide in the same PEM reactor. A mixture of commercially available lead dioxide powder and Teflon®, deposited on a Nafion® 117 membrane, was used as the anode. Current efficiencies ranged from 2.5% at an applied potential of 3.0 V to 5.5% at 4.0 V. The low current efficiencies were attributed to inefficient reactor design. A decrease in ozone concentrations, observed at higher applied potentials (> 4.0 V) was attributed to the disintegration of lead dioxide at high anodic potentials.

Graves et al. showed that the current efficiency for ozone evolution on PbO_2-plated Ebonex® (conducting ceramic material composed of Magneli phase titanium

oxides) in tetrafluoboric acid at 0 °C was comparable with that on lead dioxide on other substrates and in other media [70]. While a bare Ebonex® anode had current efficiencies ranging from 0 to 0.6%, the current efficiency for a PbO_2-plated Ebonex® anode had a current efficiency of 15% at 0.8 A/cm^2. Unfortunately, the PbO_2 was found not to be stable at this current density.

Interest in electrolytic techniques for generating ozone will depend on the nature of the application, since higher specific energy consumption is required for electrochemical methods as compared with the traditional corona discharge technology. Electrochemical techniques will work for small-scale applications such as on-site wastewater treatment where high ozone concentrations are needed in water streams, at concentrations proportional to the waste present. Therefore, processes involving ozone synthesis in pure water (as demonstrated by Stucki and coworkers [67, 68] are likely to have applications such as sterilization of drinking and swimming-pool water, disinfection of pharmaceutical equipment, or generation of contaminant-free water for the microelectronics industry. The simultaneous synthesis of ozone at the anode and hydrogen peroxide at the cathode, as demonstrated by Tatapudi and Fenton [71], could further increase the dual use of ozone and hydrogen peroxide in wastewater treatment.

2.3.2 Hydrogen Peroxide

The use of hydrogen peroxide as a bleaching agent in the pulp and paper industry and as a nonpolluting oxidant (hydrogen peroxide is reduced to water) in wastewater treatment has been increasing steadily. It is rapidly replacing chlorine and hypochlorite as a bleaching agent for paper pulp. On an industrial scale, hydrogen peroxide is predominantly manufactured by the autooxidation of anthraquinone. Electrochemical processes which have existed for a long time can compete with the anthraquinone process only for small-scale, on-site applications.

Hydrogen peroxide can be produced electrochemically by reducing oxygen at the cathode. The following reaction occurs in acidic electrolytes:

$$O_2 + 2\,H^+ + 2\,e^- \rightarrow H_2O_2 \qquad E^0 = 0.68\ V \tag{4}$$

At higher cathodic potentials, oxygen is reduced by a four-electron process, and water is formed as the end-product:

$$O_2 + 4\,H^+ + 4\,e^- \rightarrow H_2O \qquad E^0 = 1.23\ V \tag{5}$$

At even higher potentials, hydrogen peroxide reduces to water:

$$H_2O_2 + 2\,H^+ + 2\,e^- \rightarrow H_2O \qquad E^0 = 1.78\ V \tag{6}$$

In alkaline electrolytes, the following reactions are involved:

$$O_2 + H_2O + 2\,e^- \rightarrow OH^- + HO_2^- \qquad E^0 = -0.076\ V \tag{7}$$

$$HO_2^- + H_2O + 2\,e^- \rightarrow 3\,OH^- \qquad E^0 = 0.87\ V \tag{8}$$

The perhydroxyl ion, HO_2^-, is formed by hydrogen peroxide dissociation in base:

$$H_2O_2 \rightarrow H^+ + HO_2^- \tag{9}$$

Reaction (8) and the reverse of Reaction (7) result in hydrogen peroxide decomposition and lower current efficiencies. Decomposition of hydrogen peroxide can also be catalyzed by trace metal ions [72]:

$$2\,H_2O_2 \rightarrow 2\,H_2O + O_2 \tag{10}$$

Reaction (10) may occur homogeneously (in bulk solution) or heterogeneously (at the electrode surface). Although Reaction (8) is thermodynamically favored over Reaction (7), it is much slower kinetically, so that cathodic loss of peroxide may be insignificant [72].

The synthesis of hydrogen peroxide, therefore, depends upon electrolyte composition, and the type of electrode used. Studies on the cathodic synthesis of hydrogen peroxide in significant amounts have mostly been performed in alkaline electrolytes using carbon cathodes (i.e., Reaction (7)).

Davison et al. [73] produced hydrogen peroxide in a trickle-bed cell design (Fig. 15) with graphite chips and reticulated vitreous carbon (RVC) cathodes in 2 M NaOH electrolyte. Using graphite chips as the cathode, the current efficiency was 100% for H_2O_2 evolution at potentials more positive than -0.7 V vs. SCE. Under identical conditions the RVC cathodes exhibited similar behavior up to -0.7 V.

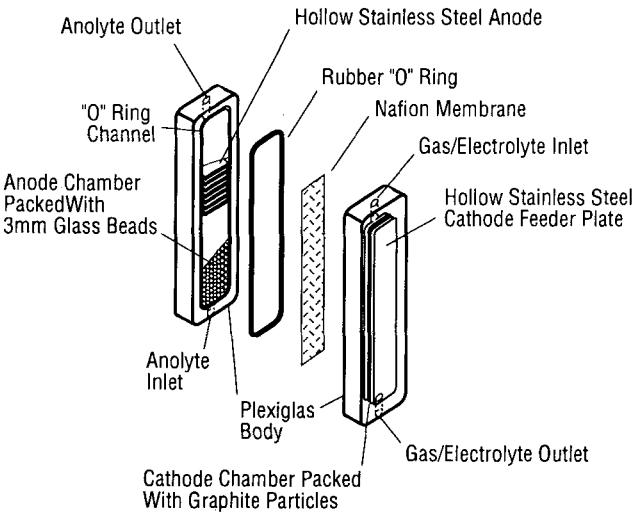

Fig. 15. Two-compartment trickle-bed cell used for hydrogen peroxide synthesis. (Adapted from [73]).

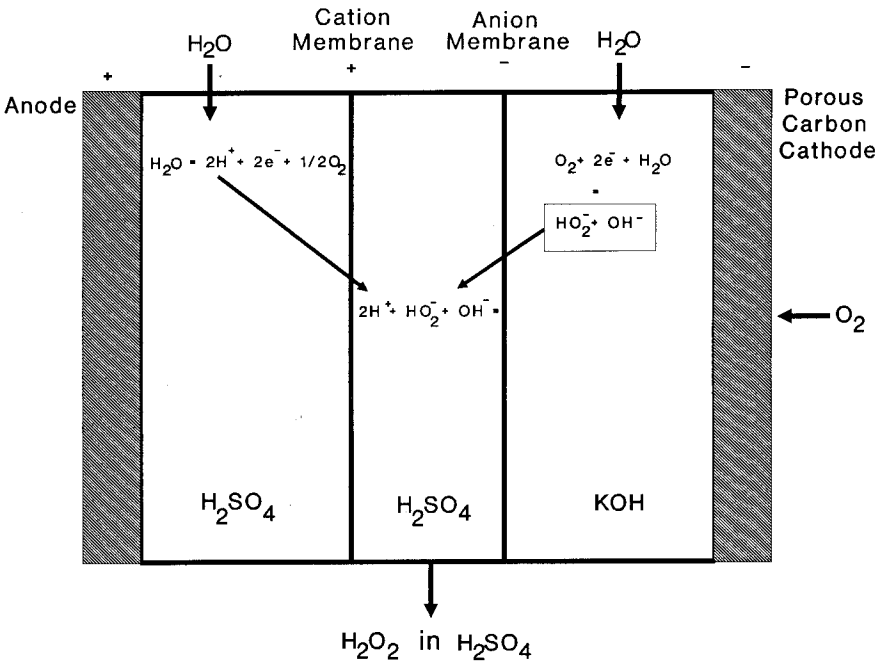

Fig. 16. Schematic representation of the operations involved in the production of acidic hydrogen peroxide. (Adapted from [74]).

However, unlike the graphite electrodes, RVC was able to maintain a higher current efficiency and produce higher hydrogen peroxide concentrations at more negative potentials. The performance of the RVC cathode was significantly better than graphite chips at lower flowrates.

Hydrogen peroxide was synthesized in caustic potash by Kuehn et al. and concentrated as an acidic product by electrodialysis in a dual-membrane batch cell containing three chambers [74]. A carbon black gas diffusion cathode was used to synthesize hydrogen peroxide in a cathodic chamber by bubbling oxygen through 0.5 M KOH. As shown in Fig. 16, the anode chamber contained sulfuric acid electrolyte, where water was oxidized to oxygen. A central chamber, separated by an anion exchange membrane on the cathode side and a cation exchange membrane on the anode side, contained 0.1 M sulfuric acid. Perhydroxyl and hydroxide ions generated at the cathode migrated through the anion exchange membrane into the middle chamber and combined with the protons migrating from the anode. Acidic hydrogen peroxide accumulated in the central chamber for over 6 h, resulting in a final concentration of 3.3 M (11 wt.%) in a 200 ml volume. The anion exchange membranes used broke down after a few hours of operation although the Nafion® cation membranes remained stable during the same period.

Dow Chemical developed a modification of the trickle-bed cell, in which a liquid permeable membrane separated two chambers [72]. As shown in Fig. 17, a packed-

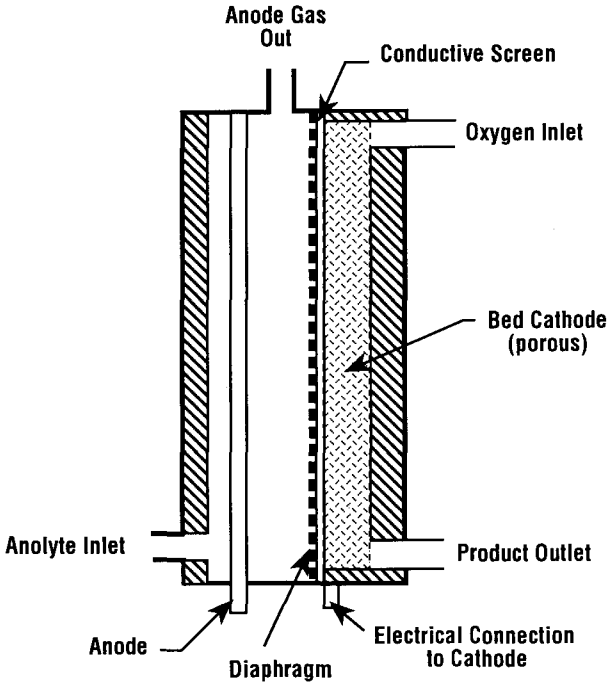

Fig. 17. Diaphragm flow controlled trickle-bed cell used by Dow Chemical Co. for the alkaline synthesis of hydrogen peroxide. (Adapted from [72]).

bed cathode, made of graphite chips coated with a Teflon®/carbon black matrix, was wetted by a caustic electrolyte seeping from the anode chamber through the membrane while the bed was kept essentially dry. Oxygen gas was pumped through the cathode from the top and product was drawn off at the cell bottom. The product was 2% hydrogen peroxide in 1 M NaOH at a current efficiency of 67% in a single-pass operation at a cell voltage of 2 V.

Kalu and Oloman [75] studied the simultaneous synthesis of alkaline hydrogen peroxide and sodium chlorate in a bench-scale "flow-by" single-cell electrochemical reactor. A schematic of the electrode conditions is shown in Fig. 18. Graphite felt was used as the cathode to synthesize peroxide from 0.5–2.0 M NaOH; chlorate was the product at a dimensionally stable anode (DSA). The anodic and cathodic reactions were as follows:

$$ClO_3^- + 3\,H_2O + 6\,e^- \rightarrow Cl^- + 6\,OH^- \qquad E^0 = 0.62\ V \tag{11}$$

$$3\,O_2 + 3\,H_2O + 6\,e^- \rightarrow 3\,HO_2^- + 3\,OH^- \qquad E^0 = -0.076\ V \tag{12}$$

The two chambers were separated by a Raipore® 1035 anion membrane covered with an asbestos diaphragm. The peroxide current efficiency varied from 20 to 86%

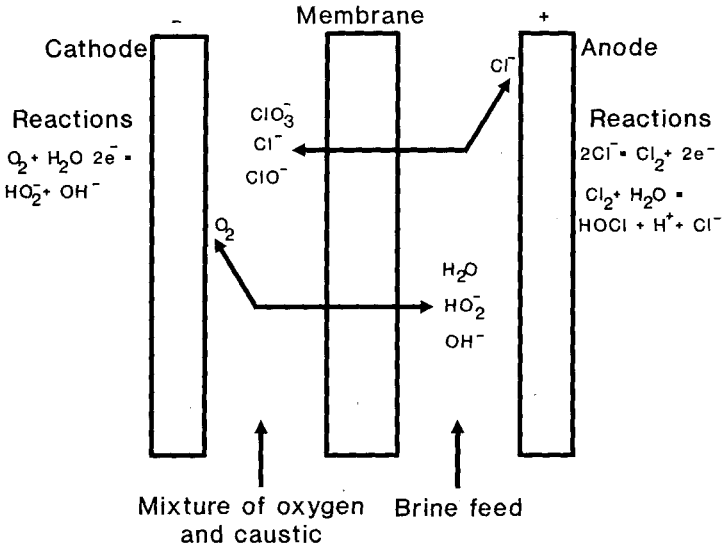

Fig. 18. Membrane cell for the paired synthesis of hydrogen peroxide and sodium chlorate showing electrode conditions and transport processes. (Adapted from [75]).

(0.069 – 0.80 M), while the sodium chlorate current efficiency varied from 51 to 81%. No membrane degradation was observed (in terms of a change in product current efficiency with time) at a cell voltage of 4.2 V (2.4 kA/m^2).

Grasso investigated the continuous production of hydrogen peroxide in a perpendicular flow-through reactor equipped with a porous RVC electrode [76]. Artificial seawater was used as the electrolyte. Using single-phase flow (oxygen dissolved in the electrolyte), 100% conversion of oxygen to peroxide was attained in the potential range of -0.6 to -0.9 V vs. SCE at a maximum hydrogen peroxide concentration of 16 ppm. The reactor design prohibited studies on two-phase flow.

Production of hydrogen peroxide in a KCl/NaOH mixture was studied by Sudoh et al. [77] using graphite particles or graphite felt as the cathode (Fig. 19). For a one-pass operation, sparging oxygen gas to the cathode bed was found to increase the overall yield of hydrogen peroxide. Current efficiencies which decreased with increasing peroxide concentration were also higher for the felt cathode. Peroxide concentrations increased with increasing bed depth. A maximum current efficiency (100%) was obtained at potentials less than -1.0 V vs. Ag/AgCl and resulted in a peroxide concentration of 294 mol/m^3.

On the basis of this study, Sudoh et al. [78] proceeded to generate hydrogen peroxide in an acidic solution (1 M H_2SO_4) for use in Fenton's reagent oxidation of wastewater streams (Fig. 20). The peroxide, produced at the cathode in an alkaline KOH electrolyte, was transferred by electrodialysis to a central chamber, separated by anion exchange membrane (ACLE-5P, Tokuyama Soda, Japan) on the cathode side and a cation exchange membrane (CM-2, Tokuyama Soda, Japan) on the anode side. At a current of 4 A, 2.2 kmol/m^3 of H_2O_2 was found to accumulate in the cen-

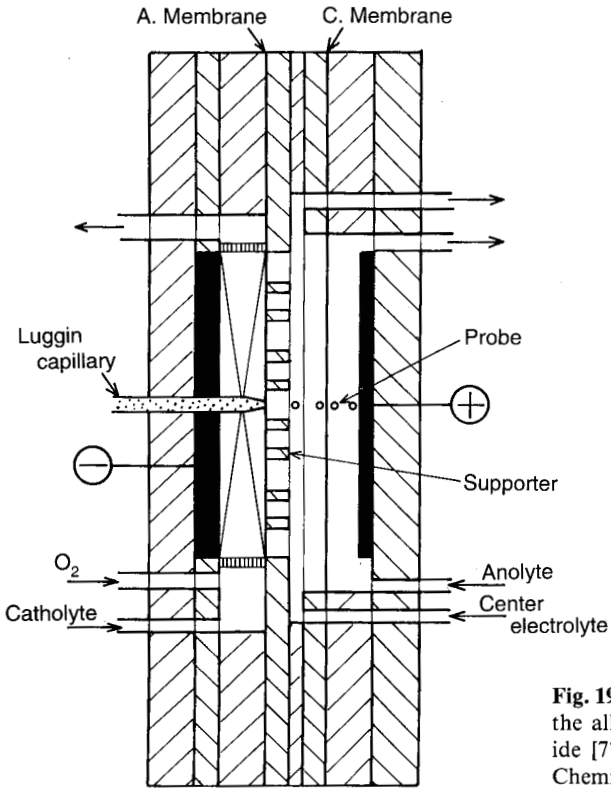

Fig. 19. Packed-bed electrode reactor for the alkaline synthesis of hydrogen peroxide [77]. (By permission from Society of Chemical Engineers, Japan).

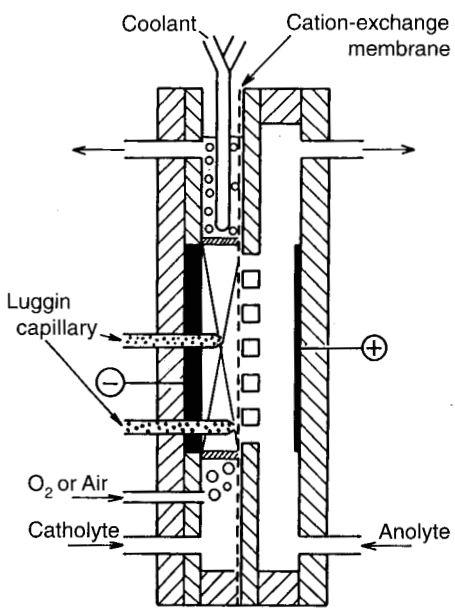

Fig. 20. Three-compartment packed-bed electrode reactor for the acidic production of hydrogen peroxide [78]. (By permission from Society of Chemical Engineers, Japan).

ter compartment. The ohmic potential drop was found to be the highest across the anion exchange membrane which increased with increasing charge passed. While no mention was made of membrane stability, this increase in ohmic resistance suggests a decrease in the anion exchange membrane performance with time.

Otsuka and Yamanaka [79] generated acidic H_2O_2 at the cathode in a fuel cell while oxidizing hydrogen at the anode. A variety of gas diffusion electrodes, immersed in 0.1 M HCl, were investigated at an oxygen partial pressure of 100 kPa. The electrodes included platinum, palladium, gold, and graphite powders, all of which were mechanically bonded onto a Nafion® 117 membrane using Teflon® as a binder. In addition, a gold mesh was also tested as a potential electrode material for peroxide synthesis. This mesh was in physical contact with the membrane. Graphite and the gold mesh showed better performances for peroxide synthesis. A 60% current efficiency was obtained at pH 2.2 in HCl solutions using a gold mesh electrode.

Tatapudi and Fenton [80] investigated the continuous production of hydrogen peroxide by oxygen reduction in a proton exchange membrane (PEM) electrochemical flow reactor using commercially available powders of gold, activated carbon, and graphite. This study was undertaken as part of an overall scheme to study the simultaneous synthesis of ozone and hydrogen peroxide in the same PEM reactor. It was shown that catalysts containing 20% Teflon® binder yielded slightly higher concentrations than those with 10% Teflon®. This phenomenon was attributed to the hydrophobic nature of Teflon®. A 6% current efficiency was obtained at 2.5 V using the graphite powder catalyst at a loading of 10 mg/cm^2 with 20% Teflon® binder.

The same authors also demonstrated the feasibility of synthesizing ozone and hydrogen peroxide simultaneously using pure water and oxygen as the reactants [71]. Commercially available β lead dioxide and graphite powders were used as the anode and cathode, respectively. While the lead dioxide was deposited directly onto a solid polymer electrolyte (Nafion® 117), the graphite powder was deposited onto a carbon fiber paper and pressed against the membrane. At an applied potential of 4.5 V, with a current density of 2 A/cm^2, a 4.5% current efficiency was obtained for ozone evolution while the current efficiency for peroxide production was 0.8%.

The future of the hydrogen peroxide industry looks promising, especially since the use of chlorine-based oxidizing agents (except chlorine dioxide) is declining. Electrolytic techniques for large-scale hydrogen peroxide synthesis, however, continue to remain hampered by low yields, high power consumption, and membrane fouling. Energy consumption for peroxide synthesis will be of secondary importance for small-scale, on-site pollution treatment applications. However, anion membranes needed for peroxide transfer from alkaline electrolytes (in which current efficiencies for peroxide synthesis are relatively high) to an acidic medium (for use as Fenton's reagent) or a neutral medium are unstable [72]. Continued reasearch in the development of stable anion exchange membranes may produce a membrane that allows the system developed by Kuehn et al. [74] to be studied at the pilot plant stage.

Synthesis of pure hydrogen peroxide using solid polymer electrolytes (SPE) could eliminate the need to separate the product from liquid electrolytes (basic or acidic). Designs of the (SPE) fuel cell type of reactor could be investigated for such a process. Tatapudi and Fenton [71, 80] demonstrated the basic feasibility of this process (with or without concurrent anodic ozone evolution). However, new cathode materials and

a better reactor design are required to increase the current efficiency of peroxide synthesis, thereby leading to economic feasibility.

2.3.3 Chlorine and Hypochlorite

Chlorine and hypochlorite are the traditional oxidizing agents used widely in sewage treatment, paper pulp bleaching, and sterilization of drinking and swimming pool water.

Chlorine gas is synthesized by the oxidation of the chloride ion present in aqueous sodium chloride. The electrode reactions are:

$$Cl_2 + 2\,e^- \rightarrow 2\,Cl^- \quad E^0 = 1.36\ V \quad \text{(anode)} \tag{13}$$

$$2\,H_2O + 2\,e^- \rightarrow H_2 + 2\,OH^- \quad E^0 = -0.827\ V \quad \text{(cathode)} \tag{14}$$

Application of membrane technology has led to the replacement of mercury or diaphragm cells in low-tonnage chlorine production [81].

The synthesis of hypochlorite involves the same reactions found in chlorine synthesis. The major difference is in reactor design. A separator which partitions the cathodic and anodic products in chlorine formation is eliminated, which results in the anodically formed chlorine reacting with the cathodically formed hydroxide to form hypochlorite:

$$Cl_2 + 2\,OH^- \rightarrow H_2O + ClO^- + Cl^- \tag{15}$$

The cathode material is usually stainless steel, a nickel alloy, or titanium. Graphite, lead dioxide, platinized titanium, and DSA are some of the materials that have been used as an anode. The cells are operated at a current density of between 0.1 and 0.5 A/cm^2. The majority of the cells used to produce hypochlorite have the parallel-plate type of geometry [81].

The use of chlorine and hypochlorite in the effluent treatment industry, and chlorine as a bleaching agent in the paper and pulp industry, is declining because of concern over the formation of chlorinated organics such as dioxin. The pulp and paper industry, in particular, has been substituting chlorine dioxide in place of chlorine.

2.3.4 Chlorine Dioxide

While the use of chlorine as a bleaching agent continues to decline, demand for sodium chlorate ($NaClO_3$), the raw material for large-scale production of chlorine dioxide gas (ClO_2), is rising. In the manufacture of chlorine dioxide, the chlorate ion is chemically reduced in the presence of a strong acid. Small-scale generators of chlorine dioxide (< 2000 kg/day), used for water treatment and disinfection applications, prefer sodium chlorite over sodium chlorate as the starting material. Both the large- and small-scale processes for chlorine dioxide generation result in the co-gen-

eration of chlorine gas from which ClO_2 has to be separated. These chemical processes also result in the formation of by-products such as sodium chloride and/or sodium sulfate.

The need for chlorine dioxide with little or no chlorine present and the impetus to reduce/eliminate by-product formation have led to the development of a variety of electrochemical technologies to produce chlorine dioxide. The starting material for these processes is usually an alkali metal chlorate or chlorite.

Lipsztajn et al. produced chlorine dioxide gas from a sodium chlorate, sodium chloride, and hydrochloric acid electrolyte [82]. A cation exchange membrane separated the two electrode compartments. The hydrogen ions, generated by water electrolysis on a dimensionally stable anode, migrate through the cation exchange membrane to the cathode, where they react chemically with sodium chlorate and chloride ions to form chlorine dioxide.

$$NaClO_3 + 2\,H^+ + 2\,Cl^- \rightarrow ClO_2 + 1/2\,Cl_2 + NaCl + H_2 \tag{16}$$

Chlorine gas, co-produced with chlorine dioxide, is removed by selective reduction on the graphite felt cathode. At 70 °C, a cathode potential of −0.7 V vs SCE and a current density of 1.97 kA/m^2 produced chlorine dioxide which had a purity of 90.2% at a chemical efficiency of 82.2%.

Kaczur et al. [83] electrolytically produced an aqueous solution of chlorine dioxide using a cation exchange resin bed separated from the electrodes by two cation exchange membranes. Hydrogen ions formed at the anode passed into the cation exchange resin compartment through the adjacent cation exchange membrane. For each hydrogen ion that enters the compartment, a sodium ion passes through the other cation exchange membrane to maintain electrical neutrality. An aqueous solution of alkali metal chlorite, fed to the ion exchange compartment, reacts with the hydrogen ions producing chlorine dioxide. This ion exchange process and subsequent chlorine dioxide formation are represented by the following reactions:

$$4\,H^+ + 4\,NaClO_2 \rightarrow 4\,HClO_2 + 4\,Na^+ \tag{17}$$

$$4\,HClO_2 \rightarrow 2\,ClO_2 + HClO_3 + HCl + H_2O \tag{18}$$

If additives such as alkali metal chlorides, phosphates, tartrates, or citrates are added to the chlorite solution, chlorate ion (ClO_3^-) formation is suppressed and chlorine dioxide is formed by the reaction:

$$5\,HClO_2 \rightarrow 4\,ClO_2 + H^+ + Cl^- + 2\,H_2O \tag{19}$$

A variety of electrodes, including a platinum-plated metal mesh and perforated stainless steel, were used over a temperature range of 50–70 °C at a current density of 0.05–3 kA/m^2.

In a similar three-compartment cell, chloric acid was electrochemically produced from sodium chlorate. The chloric acid was in turn reduced by water, in a separate reactor, to form chlorine dioxide [84, 85]. The anode compartment was filled with

2.0 wt.% sulfuric acid, the cathode compartment with 2.0 wt.% sodium hydroxide, and 20 wt.% sodium chlorate was fed through the ion exchange compartment at 7.0 – 14.4 g/min. The hydrogen ions liberated at the anode during electrolysis migrated to the ion exchange compartment through the cation exchange membrane, converting sodium chlorate to chloric acid:

$$NaClO_3 + H^+ \rightarrow HClO_3 + Na^+ \quad (20)$$

The sodium ions migrated into the cathode chamber where they formed sodium hydroxide, 52.6% of the sodium chlorate was converted to chloric acid at an operating temperature of 54 °C and a current density of 1.2 kA/m^2.

To reduce production of chlorinated organics during bleaching, the pulp and paper industry has replaced chlorine with chlorine dioxide. Chlorine dioxide or its primary precursor, sodium chlorate, can be produced by the low-tonnage chlorine industry with the same hardware that is used for synthesis of chlorine and hypochlorite. This simple transition from chlorine to chlorine dioxide synthesis may be the reason for the less-than-anticipated usage of hydrogen peroxide in the pulp and paper industry. Increasing use of chlorine dioxide could also lead to its applications in other effluent treatment areas such as industrial wastewater remediation.

2.4 Electrodialysis

Electrodialysis is a membrane-based process which can be used for separation, removal, or concentration of ionic species present in aqueous solutions. These operations are accomplished by the selective transport of ions through an ion exchange membrane under the influence of a direct current. One of the earliest applications of electrodialysis was the desalting of brackish water. However, since the 1970s, extensive studies have been performed on the application of electrodialysis for wastewater treatment, especially in the electroplating and metal-finishing industries.

A typical electrodialysis stack (Fig. 21) consists of a series of anion and cation exchange membranes arranged in an alternating pattern between an anode and a cathode to form individual compartments. An ionic solution is pumped through these compartments and, under the influence of an electric potential difference, the positively charged cations in the solution migrate toward the cathode. These ions pass through the cation exchange membrane containing fixed negative charges, but are rejected by the anion exchange membrane containing fixed positive charges. The anions in solution migrate toward the positively charged anode, pass through the anion exchange membrane, but are rejected by the cation exchange membrane. The overall result is an ion concentration increase in alternating compartments with a depletion of ions in other compartments.

Gering and Scamehorn [86] studied the removal of $CdCl_2$ and $CdSO_4$ from water by electrodialysis using a platinum-coated columbium anode and a Hastelloy cathode. Ionics (Watertown, MA) cation and anion exchange membranes were used in the electrodialysis stack. The effective cell pair area, defined as half the area of

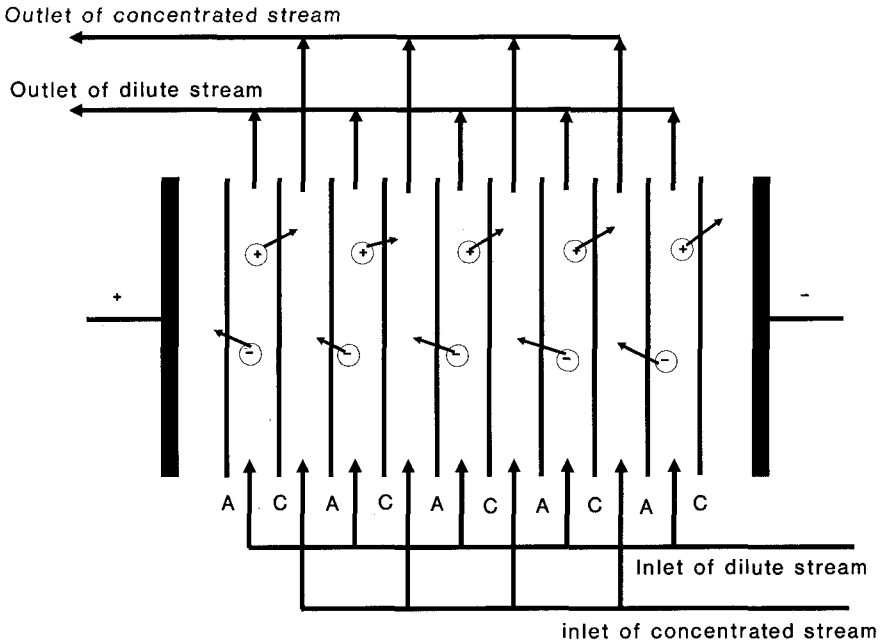

Fig. 21. Schematic configuration of an electrodialysis stack used for metal removal.

a cell pair available for ion transfer, was 220 cm^2. A voltage of 4 V/cell pair (8 V total) was applied to the cell stack producing current densities ranging from 0.1 to 45 mA/cm^2. The cell was operated at 15 psig (103 kPa) and at room temperature.

Cadmium removal was obtained at high current efficiencies ($\approx 100\%$) over a wide range of $CdCl_2$ and $CdSO_4$ concentrations. The current efficiency was a function of the concentration gradient between the diluate (feed) and concentrate, and decreased with an increase in this gradient. The stack resistance was also found to be a function of the electrolyte concentration. The current efficiency for $CdCl_2$ was higher than that of $CdSO_4$ electrolyte. An increase in the stream temperature and a decrease in pH were shown to decrease current efficiencies. Neither membrane degradation nor concentration polarization was observed in this study.

Shah and Scamehorn [88] studied the deionization of an acidic process water stream containing HCl or NaCl. The cells were operated at an applied potential of 3–4 V/cell stack. At higher electrolyte concentrations (2.5–3.0 mol/dm^3), current efficiencies for HCl removal (12%) were lower than for NaCl removal (80%). At lower acid concentrations (0.01–0.35 mol/dm^3), however, the current efficiencies were comparable, so that neutralizing the acidic process stream with NaCl was not necessary. The reason for the poor performance of high-concentration HCl systems was caused by hydrogen ion leakage through the anion exchange membrane. As in the previous study, no membrane deterioration was observed.

Deming et al. [88] studied the electrodialytic treatment of cupric chloride solutions discharged as wastewater after an etching process, using cationic and anionic

membranes manufactured "in house". The membrane area was 640 cm^2 and the membrane stack contained 30 cell pairs. A maximum cell voltage of 18.0 V was needed to reduce the cupric concentration in the wastewater from 2000 mg/dm^3 to less than 1 mg/dm^3. The energy consumption was found to be less than 3 kWh/t water treated. No copper deposition occurred at the cathode at these operating potentials. Based on the operating time of the cell, the membrane area, and the cell voltage, the current density to treat one tonne (1000 kg) of the water stream was inferred to be 0.17 A/cm^2.

Raghava Rao et al. [89] selectively removed neutral salts contained in spent chromium tanning solutions to achieve a more efficient technique for recycling the unused chromium and process water. The electrodialysis unit contained Neosepta CL-25T and ACH-45T membranes. An application of 13–30 V to a 5 dm^3 solution over a period of 5–6 h produced currents between 2 and 4 A; 90% of the sodium chloride and 50% of the sodium sulfate were selectively removed with minimal transport of Cr(III) species across the membranes. Addition of EDTA to the spent liquor as well as periodic reversal of electrode polarities eliminated membrane fouling.

Enoch et al. [90] used electrodialysis reversal (EDR) to prepare boiler makeup water for Dutch power stations from several types of surface waters. EDR uses automatic reversal of electrode polarity at regular time intervals to minimize membrane scaling. The EDR unit contained 200 anion and cation exchange membrane pairs, each with a surface area of 0.47 m^2. Polarity reversal occurred every 15, 20, or 25 min. Samples of surface water were desalted by 96% at an energy consumption of 1 kWh/m^3 of product water and at a current density (8.3 A/cm^2) that was 80% of the limiting current density (current density when the surface water cation concentration at the membrane surface drops to zero).

Walker and Pennline [91] have described a process for the simultaneous removal of SO_2 and NO_x from flue gas by a combination of adsorption, electrodialysis, and additional regeneration of the scrubbing liquor. The process consisted of scrubbing the flue gas with either a solution of ammonium sulfate and iron(II) ethylenediaminetetraacetic acid (Fe-EDTA) or sodium sulfate and Fe-EDTA. The SO_2 gas converts the ammonium sulfate to the bisulfite which is then passed through an electrodialysis unit to further dilute the bisulfite stream, which is eventually converted to the sulfate downstream by the addition of ammonia. The size of the Fe-EDTA-NO species formed from the adsorption of NO gas does not allow it to pass through either of the permselective membranes.

Rockstraw et al. [92] studied an integrated electrodialysis-evaporation process for the treatment of electrolytic aqueous streams. Using a 3000 mg/dm^3 Na_2SO_4 solution as the electrolyte feed and with an outlet concentration of 375 mg/dm^3, the optimum conditions for operation required the electrodialysis unit to produce 55% of the purified product. At higher feed concentrations it became more economical to produce less of the purified product by the electrodialysis unit.

Chiapello and Gal [93] studied the recovery of cyanide electroplating rinse waters by electrodialysis. The transfer rates of the ionic species present in a copper or zinc cyanide rinse bath was limited by the high resistance of the anion exchange membrane used. The presence of highly charged cyano complexes of copper increased the resistance of the anion exchange membrane. The transfer of zinc was easier at higher

pH values, although the transfer rate was found to be very low when compared with that of copper.

Xue et al. [94] used electrodialysis to purify and recover spent alkaline process streams containing potassium hydroxide, lithium hydroxide and potassium carbonate using nickel-plated steel cathodes and a stainless steel anode. A potential of 3 – 5 V was required at operating temperatures of 80-105 °F (26.7 – 40.6 °C) to obtain current densities between 170 and 200 mA/cm^2 with current efficiencies of 75 – 60%.

Dobrevsky and Pavlova [95] removed humic acids and desalinated water under a variety of operating conditions using electrodialysis. An 86% degree of desalination and simultaneous humic acid decrease were achieved at 30 °C and at an applied voltage of 200 V (0.54 A).

Cherif et al. [96] separated cations from a mixture of low-concentration electrolytes (0.01 M $AgNO_3$, $Zn(NO_3)$, and $Cu(NO_3)_2$) using electrodialysis. Raipore (RAI) 5035 was used as the anion exchange membrane, and C.M.S. Neosepta (which was developed for the separation of monovalent ions from bivalent ions) and RAI 5010 were used as cation exchange membranes. The separation was performed by adding either ammonia or nitric acid to this salt mixture to prevent precipitation of metal hydroxides on the membrane surface. At 10 mA/cm^2, the current efficiencies for Ag^+ recovery were low (10% using nitric acid and 55% using ammonia) because of competitive transport of ammonium ions and protons through the membrane.

The current efficiencies for the separation of silver from zinc and copper (in the presence of acid or ammonia) were found to improve by using EDTA as a complexing agent. Cupric and zinc ions formed negatively charged complexes with EDTA and were transferred to the anode side while the monovalent silver ions migrated to the cathode. The low mobility of Cu^{2+} and Zn^{2+} complexes in the membrane decrease current efficiency for metal removal, overall but, the separation using EDTA had a higher current efficiency than without using EDTA.

The future for electrodialysis-based wastewater treatment processes appears bright. The dilute concentrations of metals in the waste streams do not degrade or foul the cation or anion exchange membranes. The concentrate streams are recirculated to build up their metal content to a level that is useful for further recovery or direct return to the process stream. Ongoing research in the development of cheaper cation exchange membranes, and stable anion exchange and bipolar membranes will allow electrodialysis-based applications to become more competitive with other treatments.

2.5 Electromembrane Processes

Unlike electrodialysis, which tends to concentrate and remove or recover species, electromembrane processes transform species present in waste streams by electrolysis and the use of cation and anion exchange membranes. These processes offer chemical cost reduction (by recovery), water consumption reduction, and discharge or reuse of contaminant-free waters. Supplementary gains are also obtained by identifying a market for products obtained from the recovery and transformation processes.

Buckley, Simpson and coworkers recovered sodium hydroxide from textile scour effluent [97] and from bottling plant effluent [98]. The NaOH was first converted to sodium bicarbonate by passing CO_2 through it. This pretreated effluent was fed to the anodic section of a cation exchange membrane cell. A dilute NaOH solution was fed to the catholyte compartment. The electrolytic process took place at 40–60 °C and at a current density of 300–1000 A/m^2. Sodium ions from the anode compartment migrated to the cathode compartment through a cation exchange membrane and combined with the hydroxide ions generated at the cathode from the reduction of water, resulting in the formation of concentrated, purified, NaOH. The carbonate species in the anode compartment reacted with the protons formed at the anode during oxidation of water to form H_2O and CO_2. The CO_2 was then recycled for effluent conversion to sodium bicarbonate.

Simpson and Buckley [99] also removed sulfuric acid from acid minewater by reaction with calcium hydroxide to form calcium sulfate. Minewater containing sulfuric acid was fed to the cathode compartment. The anode compartment, which contained a saturated solution of calcium hydroxide, was separated from the cathode compartment by an anion exchange membrane. At a current density of 500 A/m^2, the hydroxide ions produced at the cathode neutralized the H^+ in the acid minewater. Oxidation of water at the anode resulted in O_2 and H^+ formation and required a high $Ca(OH)_2$ concentration to counterbalance the production of these protons. $CaSO_4$ was produced in the anode compartment as a result of the migration of sulfate ions. Precipitation of $CaSO_4$ salt crystals on the anode was avoided by circulating $CaSO_4$ seed crystals.

Voortman et al. [97] converted ammonium nitrate, present in an aqueous effluent, to reusable calcium nitrate and ammonia gas. At a current density of 1000 A/m^2, the ammonium ions in the ammonium nitrate effluent reacted with the hydroxide ions produced at the cathode. Ammonia gas was recovered from the solution by adjusting the pH of the solution, and heating the catholyte. The nitrate ion migrated through an anion exchange membrane to form calcium nitrate.

Speranzini studied the treatment of boiler chemical cleaning wastes containing chelated metals such as copper and iron, and recovered EDTA, the chelating agent [100]. This approach combined electrochemical reduction, electrodialysis, and precipitation. Using a "flow by" electrochemical reactor operating at an applied current density of 23 mA/cm^2, with the inlet waste stream adjusted to pH 2, the copper was removed by deposition on the cathode. The EDTA was precipitated as H_4EDTA, and the ferrous ions which were released into solution migrated through a cation exchange membrane into a basic solution where the iron precipitated out as $Fe(OH)_2$.

The use of electrolysis in conjunction with ion exchange membranes is bound to find increased interest and wider application for wastewater treatment. Not only do these processes offer closed-loop recycling of materials, they also permit various useful products to be produced at the counter electrode (as opposed to *sacrificial* oxygen or hydrogen evolution) while treating a waste stream at the working electrode. Increasing restrictions on effluent discharge for chemical manufacturing processes coupled with continued work on the manufacture of cheaper and more efficient ion exchange membranes will reduce economic barriers for the use of electromembrane processes and encourage further development.

2.6 Electrochemical Effluent Gas Treatment

Anthropogenic emissions for sulfur and nitrogen oxides, known to be acid rain precursors and smog promoters, represent an appreciable fraction of the gases released to the atmosphere. Furthermore, hydrogen sulfide, a product from coal gasifiers, is also known to be a source of SO_2 formation. Increasing emissions of carbon dioxide, a greenhose gas, continue to be a global concern.

Studies on the electrochemical treatment and removal of these gaseous pollutants have increased considerably since the 1970s. In many cases, the electrochemical routes may be cleaner than currently existing technologies, and/or more economically viable. Furthermore, reaction products from gas treatment may be salable by-products. A review on electrochemical separation of gases has been published in an earlier volume of this series [101].

2.6.1 SO_2 Removal

Townley and Winnick [102] studied the removal of SO_x gases at the cathode from simulated coal-burning power plant stack gases. The cell functioned in two modes, used a molten sulfate electrolyte and 10 cm^2 $LiCrO_2$ electrodes, and operated at 512 °C. In the first mode, the electrochemical cell was driven electrolytically by applying 0.7 V across the two electrodes. The following reactions were thought to take place at the cathode (information on the equilibrium potentials for SO_2 and SO_3 reduction can be obtained from [101]:

$$SO_3 \rightarrow 1/2\,O_2 + 2\,e^- \rightarrow SO_4^{2-} \tag{21}$$

$$SO_2 + O_2 + 2\,e^- \rightarrow SO_4^{2-} \tag{22}$$

The sulfate ions were reoxidized at the anode to yield SO_3, thus concentrating the dilute sulfur oxides while purifying the cathode stream.

$$SO_2^{4-} \rightarrow SO_3 + 1/2\,O_2 + 2\,e^- \tag{23}$$

More than 95% of the SO_x was reduced at the cathode while up to 2.0% SO_3 was produced at the anode. The removal of SO_x at the cathode was limited by mass transfer in the gas phase.

In the second mode, an electrochemical driving force was provided by passing a reducing gas (H_2) into the anode and oxidizing the sulfate ion, to form H_2S and H_2O.

$$SO_4^{2-} + 4\,H_2 \rightarrow 4\,H_2O + S^{2-} \tag{24}$$

$$S^{2-} + H_2 \rightarrow H_2S + 2\,e^- \tag{25}$$

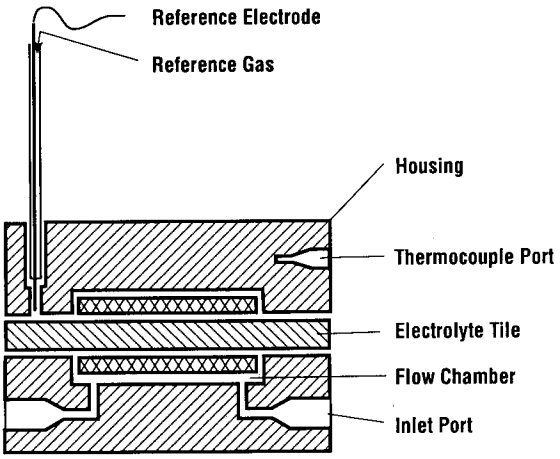

Fig. 22. Electrochemical cell used for SO_2 removal from power plant stack gases. (Adapted from [103].

Using a cell that was designed along the lines of a molten carbonate fuel cell (Fig. 22), the removal rates of SO_x varied from 78% at 600 ppm of SO_x at the cathode to 24% at 2100 ppm of SO_x at the cathode. The same authors [103] also reported an improvement over their earlier study by using a ternary eutectic of lithium, potassium, and sodium sulfates as the electrolyte together with $Li_2O \cdot 9CrO_3$ electrodes, which were found to be stable in the molten electrolyte.

Scott et al. [104] studied the cathodic removal of SO_2 from a simulated flue gas stream using pure $K_2S_2O_7$ (potassium pyrosulfate), as well as a mixture of $K_2S_2O_7$ and K_2SO_4, as the molten electrolyte, with V_2O_5 added in both cases as an oxidant enhancer. The studies were performed at 300 °C. They found that pure potassium pyrosulfate actually produced sulfur dioxide at the cathode. However, a combination of 1% V_2O_5 and 99% $K_2S_2O_7$ increasingly removed sulfur dioxide as the cathodic current was raised. Addition of potassium sulfate further increased the rate of sulfur dioxide removal at the cathode.

Franke and Winnick [105], using a $K_2S_2O_7$ based electrolyte dispersed within the interstices of an inert $K_2Mg_2(SO_4)_3$ matrix, were able to achieve removal efficiencies of SO_2 greater than 99% at current efficiencies near 100%. A porous electrode constructed of a perovskite-type compound, $La_{0.8}Sr_{0.2}CoO_3$, was found to be conductive and stable in the corrosive cell environment.

To diminish electrode pore flooding, McHenry and Winnick [106] studied new membrane formulations which included borosilicate glass and zeolites. These showed improved electrolyte retention and polarization behavior as compared with MgO-based membranes. The reduction in flooding allowed the cell to handle three times the current for the same applied overpotential. The same authors [107] also found that $La_{0.8}Sr_{0.2}CoO_3$ electrodes reacted with the molten pyrosulfate electrolyte. Lithium-doped nickel oxide replacement electrodes, however, were not degraded.

Card et al. [108] oxidized dissolved sulfur dioxide gas to sulfuric acid, at room temperature, using packed bed anodes. The corresponding cathodic reaction was oxygen reduction to water. A variety of electrodes and electrode systems were studied,

including platinum composite gas diffusion electrodes, platinum deposited on a graphite bed, a graphite packed bed, and a graphite packed bed in which iodide ions were dissolved in the sulfuric acid-sulfur dioxide solution to serve as an electron transfer mediator.

The platinum-graphite packed-bed electrode and the iodide-mediated electrode provided currents in the region of 100 mA/cm^2. The single-pass conversion of SO_2 to H_2SO_4 was about 20% using platinum deposited on graphite as the electrode.

Aurousseau et al. [109] electrochemically scrubbed SO_2-containing waste gas. The sulfur dioxide (0.7%) was dissolved in 0.5 M sulfuric acid, transported to the electrode, and finally oxidized at the graphite anode. The oxidation was limited by the transport of sulfur dioxide to the electrode as well as by poor reaction kinetics at the electrode. The use of three-dimensional electrodes was suggested to alleviate these problems.

2.6.2 H_2S Removal

Lim and Winnick [110] examined removal of H_2S from a simulated hot coal-gas stream fed to the cathode while elemental sulfur gas was evolved at the anode. This process was performed in a cell that was similar in construction to a molten carbonate fuel cell (Fig. 23). The electrolyte was a mixture of Na_2S and Li_2S retained in a porous inert matrix material (MgO). The cathodic reaction involved the two-electron reduction of hydrogen sulfide to hydrogen (information on the equilibrium potential for H_2S reduction can be obtained from [111]:

$$H_2S + 2\,e^- \rightarrow H_2 + S^{2-} \tag{26}$$

The sulfide ion migrates across the membrane-electrolyte matrix to the anode, where either elemental sulfur vapor is generated or, if hydrogen gas is present at the anode hydrogen sulfide is formed.

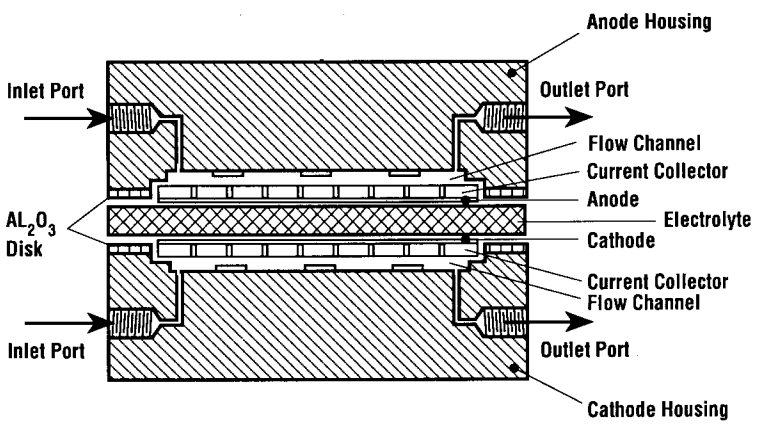

Fig. 23. Electrochemical cell used for H_2S removal from hot coal-gas streams. (Adapted from [110]).

$$S^{2-} \rightarrow 1/2\,S_2 + 2\,e^- \quad (27)$$

$$S^{2-} + H_2 \rightarrow H_2S + 2\,e^- \quad (28)$$

Porous carbon electrodes were used as the anode and cathode and the operating temperatures varied from 700 to 920 °C. A 98.8% removal efficiency of 0.65% H_2S was reported at current densities around 35 mA/cm^2.

Weaver and Winnick [111] studied the performance of a nickel/nickel sulfide cathode for the electrochemical removal of hydrogen sulfide gas from a gas stream. At 650 °C, the porous nickel cathode was converted *in situ* to $Ni_{3\pm x}S_2$ by the H_2S in the feed gas stream. The exact composition of the nickel sulfide was found to be a function of the H_2S/H_2 ratio in the gas stream. A current density of 150 mA/cm^2 was attained at an *iR* free cathodic overpotential of 300 mV. A maximum H_2S removal of 40% was reported. The low removal percentage was due to mass transport limitations of the reactant gas to the electrode.

Alexander and Winnick [112] investigated the electrochemical removal of hydrogen sulfide from contaminated natural gas, using carbon and CoS_2 electrodes and a molten carbonate electrolyte encapsulated in a membrane with a 50/50 weight ratio of electrolyte to matrix material. The electrolyte was 62 mol% $LiCO_3$ and 38 mol% K_2CO_3 while the matrix material was $LiAlO_2$. The feed gas to the cathode contained specified levels of H_2S, CO_2, and H_2O, with the remainder being CH_4. At 607 °C, using a feed gas containing 2000 ppm H_2S, 1% CO_2, and the remainder methane, it was shown that 80% of the hydrogen sulfide and 70% of the CO_2 gas were removed at an applied current of 300 mA. Gas-phase mass transfer resistance was seen as the limiting factor on the cell performance.

Weaver and Winnick [113] tested several transition-metal sulfides as well as metal oxide semiconductors as potential cathode materials for the electrochemical separation of H_2S from hot gas streams. Several of the metal sulfides tested were highly conductive, showed low cathodic polarization, and displayed kinetics favoring the reduction of H_2S over unwanted side-reactions involving other gaseous species. Among all the metal sulfides tested, cobalt sulfide Co_9S_8 appeared to have the best electrochemical properties. Among the metal oxide semiconductor cathodes, lanthanum chromite doped with strontium showed the best results. However, the metal oxide compounds had higher ohmic and activation polarization as compared with the cobalt sulfide cathodes.

The same authors [114] also demonstrated the performance of the separator used in references [112, 113] over a wide range of gas compositions and operating temperatures, as well as different cathode and anode materials. The H_2S concentration was reduced from 6500 ppm at the cell inlet to 180 ppm at the cell outlet (98.8% removal), at a current density of 70 mA/cm^2, and at applied potentials of 2 V or less. At temperatures of 973 K or higher, mass transport of H_2S from the bulk gas to the cathode was the rate-limiting step; while at lower temperatures, ionic transport of sulfide ions through the membrane was thought to limit the process. Concurrent removal of CO_2 was also observed and was attributed to poor electrolyte morphology, leading to gas crossover.

Mao et al. [115] mathematically modeled a high-temperature H_2S electrolyzer which was similar in design to a molten-carbonate fuel cell. The maximum current

density that can be obtained is determined solely by the transport rate of sulfide ions through the separator. A large part of the cell voltage was used to overcome the concentration polarization in the anodic region. The authors mention that the maximum current density for this type of electrolyzer cannot be improved beyond 10 mA/cm^2. In this mode, the authors used a sintered porous Ni-Cr plate as the cathode, a tape-cast lithium aluminate matrix which acts as the membrane, and a porous graphite anode.

Mao et al. [116] also demonstrated, on a laboratory scale, a process to recover hydrogen and sulfur by electrochemical decomposition. A scrubber solution (NaOH), saturated with H_2S, is pumped into the anode compartment of an electrochemical cell. The cathode compartment, containing pure alkaline solution, is separated from the anode compartment by a cation exchange membrane. Scrubbing H_2S dissociates in NaOH forming HS^- and S^{2-}, which apparently provides the optimum pH balance for electrolysis to occur while minimizing anode passivation and unwanted chemical and electrochemical reactions. Oxidation of HS^- and S^{2-} at the anode results in sulfur formation and migration of Na^+ ions from the anode compartment to the cathode compartment through a cation exchange membrane. Water is reduced in the cathode compartment to form hydrogen gas. Advantages of this process include improved current efficiencies because of minimal blocking of the anode surface resulting from precipitation of sulfur in the bulk electrolyte, as opposed to deposition; and elimination of the need for organic solvent for sulfur removal.

2.6.3 CO_2 Removal

Increasing levels of CO_2 emitted into the atmosphere could prove detrimental to the environment in the future. Transforming CO_2 electrochemically and recovering and utilizing its carbon has been an area of interest for a number of years.

Mahmood et al. [117] studied the electrochemical reduction of carbon dioxide using gas diffusion electrodes. The reduction was performed on metal (lead, indium, and tin)-impregnated Teflon®-bonded carbon gas diffusion electrodes in a sulfuric acid electrolyte over a 1–5 pH range. A schematic of the cell is shown in Fig. 24. The following reactions occurred:

$$CO_2 + 2\,H^+ + 2\,e^- \rightarrow HCOOH \qquad E^0 = -0.2\ V \qquad \text{(cathode)} \tag{29}$$

$$1/2\,O_2 + 2\,H^+ + 2\,e^- \rightarrow H_2O \qquad E^0 = 1.23\ V \qquad \text{(anode)} \tag{30}$$

The lead-impregnated electrodes produced formic acid with 100% current efficiency at 115 mA/cm^2 and a potential of −1.8 V vs. SCE, at room temperature and atmospheric pressure. The electrodes bonded with indium and tin produced formic acid at rates comparable with those on lead electrodes, but small concentrations of carbon monoxide were also produced. The evolution of hydrogen was also more significant on these electrodes.

The same authors [118] reduced CO_2 using carbon gas diffusion electrodes impregnated with metal (cobalt(II), copper, zinc, or manganese) phthalocyanine. High

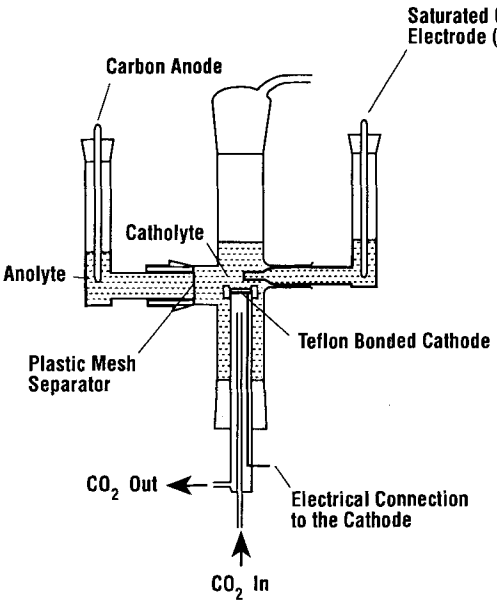

Fig. 24. Electrochemical cell used for carbon dioxide reduction using gas diffusion electrodes. (Adapted from [117]).

reduction rates of carbon dioxide to carbon monoxide were observed on electrodes containing cobalt(II) phthalocyanine, while formic acid was produced at low current efficiencies (5–38%) and low current densities (1–22 mA/cm^2) on electrodes containing the phthalocyanine of either manganese, copper, or zinc.

Cook et al. [119] studied the reduction of CO_2 at 0 °C and atmospheric pressure in 0.5 M $KHCO_3$ (pH 9.2) using a copper cathode. At a CO_2 flowrate of 12.75 cm^3/min and at current densities ranging from 15 to 38 mA/cm^2, current efficiencies of 33% were obtained for the formation of methane from CO_2 reduction. The reduction step was reported to be controlled by mass transfer in the electrolyte.

The same authors [120] also studied the gas-phase reduction of CO_2 at ambient temperature using solid polymer electrolyte (SPE) cells with copper cathodes deposited on the Nafion® 117 membrane. The deposition was performed for 15–30 min using a 0.5 M K_2SO_4/0.05 $CuSO_4$ solution. Two different configurations were used on the anode side of the cell. In the first, aqueous 0.5 M K_2SO_4 (pH 8.67) was used in the counter electrode compartment with a platinum anode. In the second configuration, platinum was initially deposited directly onto a Nafion® 117 membrane from a 0.05 M H_2PtCl_6 solution; this was followed by copper deposition on the other side of the membrane. Using the first configuration, C_2H_4 and C_2H_6 were observed as CO_2 reduction products but no CH_4 was observed. In the second configuration, however, all three hydrocarbon gases were detected; CO was also identified as an intermediate.

Cook et al. also reduced CO_2 using *in-situ* deposited copper on glassy carbon electrodes [121] and on electrodes of the gas diffusion type consisting of copper

deposited on carbon black spread on copper gauze [122]. In the former case, at 25 mA/cm^2, CH_4 and C_2H_4 were observed as the reaction products with an overall efficiency of 79% in a 0.5 M $KHCO_3$ electrolyte. A reaction mechanism was proposed in which weakly adsorbed CO_2 was thought to react with electrochemically generated chemisorbed hydrogen at the copper surface. Subsequent reduction of the adsorbed CO_2 led to formation of bridged CO groups which could desorb to form carbon monoxide or reduce further to form CH_4 and C_2H_4. In the latter case, by operating the system in a 1 M KOH electrolyte at 2 °C current efficiencies of 71.3% were achieved at current densities higher than 500 mA/cm^2.

Azuma et al. [123] reduced CO_2 on 32 metal electrodes in low-temperature aqueous $KHCO_3$ electrolyte. The current efficiency for CO_2 reduction was a strong function of temperature and increased with a decrease in temperature on Ni, Ag, and Pd cathodes. Formation of CH_4 and C_2H_4 was observed on all 32 metal cathodes although, except for the copper cathode, current efficiencies for the production of these hydrocarbon gases were low. A periodic table of the 32 metal cathodes used for CO_2 was developed, based on the reduction products. The table provides a systematic rule for CO_2 reduction on these surfaces.

2.6.4 Natural Gas Treatment

Ogura et al. [124] studied the photochemical and electrochemical oxidation of methane to methyl chloride and methanol. This room-temperature process evolved chlorine at a platinum anode followed by photochemical generation of $Cl^{\bullet}$ (chloride radical) from Cl_2. The chloride radical subsequently oxidized methane gas (fed to the anode) to the methyl radical ($CH_3^{\bullet}$). The methyl radical reacted with chlorine gas to form methyl chloride which was immediately hydrolyzed to methanol. The formation of methyl chloride and methanol began at 1.1 V vs. SCE, which corresponds to the onset of chlorine evolution.

Kuchynka et al. [125] studied the electrochemical oxidative dimerization of methane to C_2 hydrocarbon species using perovskite anode electrocatalysts. Three designs of solid oxide fuel cells were used, including tubular and flat plate solid electrolytes. The maximum current density for the dimerization reaction at these electrocatalysts was related to the oxygen binding energies on the catalyst surface. The anodic reaction was:

$$2\,CH_4 + 2\,O^{2-} \rightarrow C_2H_4 + 2\,H_2O + 4\,e^- \tag{31}$$

while at the cathode, the following reaction occurred:

$$O_2 + 4\,e^- \rightarrow 2\,O^{2-} \tag{32}$$

Since the overall electrochemical process is thermodynamically spontaneous, the free energy change associated with the electrochemical reaction is directly converted to dc electrical energy.

Electrochemical studies on SO_2 and H_2S removal at high temperature, using molten electrolytes, were limited by the transport of gases from the bulk to the cathode. Studies on SO_2 oxidation at room temperature using sulfuric acid as the solvent electrolyte also encountered gas-phase transport problems. To overcome mass transfer limitations of gaseous pollutants to the electrode, alternative reactor configurations with three-dimensional electrode structures such as packed beds and expanded metal meshes should be considered. For high-temperature operations, reactor designs similar to solid oxide fuel cells or molten carbonate fuel cells could improve mass transport.

The electrocatalytic behavior of cathodes appears to play a crucial role in the reduction of carbon dioxide. To find more efficient catalysts, detailed mechanistic studies of CO_2 reduction are needed. Further studies could also concentrate on the investigation of different electrolytes as well as different catalysts delivering products of choice, such as alcohols.

2.7 Electrochemical Soil Treatment

Corrosion of underground storage and gasoline tanks leading to discharge of toxic chemicals has led to severe contamination of soils and groundwaters. Previous practice of discharging waste streams to settling lagoons has also contributed to soil and groundwater pollution.

One of the more recent technologies in pollution treatment and remediation is based on the electrokinetic decontamination of soils [126–128], in which a dc potential (a few volts per centimeter) is applied across two inert electrodes embedded in a soil mass. This applied potential causes decomposition of the soil water to occur at the two electrodes. The migration of contaminants in the electric field, water transport, and reactions at the electrodes, as well as reactions caused by the induced pH gradient, can effectively clean soils. Acar et al. [127] reviewed electrokinetic remediation for the removal of metals and other inorganic contaminants from soil as well as its use in the extraction of organics from contaminated soils.

The principal electrode reactions involved in electrochemical soil remediation are:

$$2\,H_2O \rightarrow O_2 + 4\,H^+ + 4\,e^- \qquad \text{(anode)} \tag{33}$$

$$4\,H_2O + 4\,e^- \rightarrow 2\,H_2 + 4\,OH^- \qquad \text{(cathode)} \tag{34}$$

In addition the metal deposition reaction can also occur:

$$M^{n+} + n e^- \rightarrow M \qquad \text{(cathode)} \tag{35}$$

where M is the metal that is being removed from solution.

For a given passage of charge, twice as many water molecules are broken down at the cathode as at the anode, causing a gradient for the transport of water. This phenomenon, also known as electroosmosis, is one of the ways in which contami-

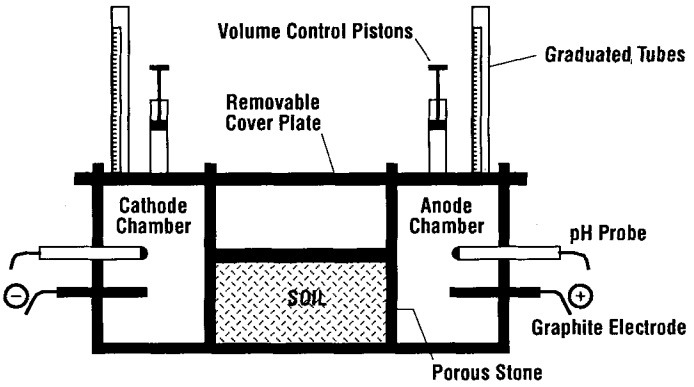

Fig. 25. Electrochemical cell used for zinc removal from groundwater in low-permeability soils. (Adapted from [130]).

nants in the soil are transported from one region to another. Furthermore, the pH imbalance produced at the electrodes by the generation of H^+ and OH^- ions also may lead to increased contaminant solubility and/or precipitation near one of the electrodes. Metallic contaminants may also be removed by direct deposition of the metal on the cathode.

Acar et al. [128] studied the development of pH gradients during electroosmosis in kaolinite clay which had a 50% water content. A current of 1 mA applied for 120 h on 21 cm^2 carbon electrodes decreased the pH at the anode from 5.0 to 2.5, while the pH at the cathode increased to 12.5. For the same time period, the water content at the anode decreased by 8% when compared with the water content at the cathode.

Pamukcu et al. [130] selectively removed zinc from groundwater in low-permeability soils (kaolinite clay) using graphite electrodes that were placed 25 cm apart (Fig. 25). A potential difference of 30 V was applied intermittently across the soil sample. This periodic application of the dc potential enabled the authors to study the difference in the zinc movement during electromigration and diffusion. At the end of the experiment, the zinc concentration in the anode chamber had increased from 275 to 745 mg/dm^3 and from 200 to 440 mg/dm^3 in the cathode chamber. The authors proposed the formation and migration of negatively charged complexes such as $Zn(OH)_3^-$ and $Zn(OH)_4^{2-}$ to the anode to explain the increased zinc concentrations in the anode chamber. No mention was made of the magnitude of the currents used or the electrode area.

Hamed et al. [131] removed Pb(II) from kaolinite specimens using graphite electrodes. The Pb loadings varied from 118–145 μg/g of dry soil. A current density of 0.037 mA/cm^2 was used and the total charge passed varied between 1400 and 2000 Ah/m^3 soil. The removal, 75–90%, was directly related to the pH gradients developed in the process. The energy requirement for lead removal varied between 29 and 60 kWh/m^3 soil processed.

Acar et al. [132] removed phenol from kaolinite clays using graphite electrodes. At a current density of 0.037 mA/cm^2 (at which the maximum voltage was 20 V),

the acid front produced at the anode swept across the soil specimen, neutralizing the base generated at the cathode. A 85–95% phenol removal from an initial concentration of 500 μg/g dry kaolinite occurred; the phenol removed was near the cathode. Energy requirements for this removal varied from 18 to 39 kWh/m^3.

Pamukcu and Wittle [133] investigated the feasibility of electrokinetic treatment at 30 V of different clay mixtures containing a number of heavy metals including Cd, Co, Ni, and Sr. The metal removal success ranged between 85–95% and appeared to depend on the soil matrix, the metal, and the pore fluid composition. At low initial metal concentrations, electroosmosis appeared to be the dominant mechanism for metal removal. At higher concentrations, electrolytic migration of the ionic species played a more dominant role. Of the three soil types tested, kaolinite had the highest electroosmotic efficiency.

Alshawabkeh and Acar [134] developed a theoretical model describing contaminant transport during electrokinetic remediation, based on the equilibrium chemistry of the solution and the electrochemical properties of the contaminants within the soil. The model demonstrates that the removal of ions from soils is caused by a combined effect of electrical, hydraulic, and concentration potential gradients that exist in the soil. The factors controlling the rate of change of these potential gradients included the volume compressibility and electrical capacitance of the soil, and the conductivities of the ions.

Lindgren et al. examined the removal of chromium from unsaturated 50–100-mesh sand containing 10% water [135]. Studies were performed in a rectangular cell containing the soil sample into which graphite electrodes of 0.64 cm diameter were embedded, spaced 21 cm apart. The centerline of the cell was spiked with 100 ppm sodium chromate. The application of 10.3 A for 22 h resulted in the initially contaminated region being cleansed of the chromate ions. Chromate anions near the anode surface were found to migrate at 0.4 cm/h. The electroosmotic rate, 0.02 cm/h, was considerably lower, showing that electromigration was the dominant transport mechanism for chromium.

Shapiro et al. [136] removed acetic acid and phenol from kaolin clay using carbon or perforated 316 stainless steel electrodes (Fig. 26). A 94% removal occurred at a current density of 6 A/m^2. Predictions of a one-dimensional theoretical model that takes into account electroosmotic convection, diffusion, electromigration, chemical reactions in the electrolyte, and electrode reactions of oxygen and hydrogen evolution were compared with the experimental results. The neglect of adsorption effects in the model did not allow the evaluation of phenol removal, although acetic acid removal was well predicted by the model. In a later study [137] using the same set of electrodes, contaminants, and clay matrix, the energy cost for contaminant removal, based on an average applied electric field of 60 V/m, was estimated to be $2.00/ton of effluent removed.

Pamukcu and Wittle [138] removed radioactive metals (Sr, Cs, and U) in clay or clay–sand mixtures. An 80% removal was observed at the cathode chamber for Sr and Cs for 24–48 h durations of treatment. Only 20% of the uranium was transferred to the cathode compartment because of precipitation and speciation of this metal in the soil. Chromium, which was present as an anionic species, migrated to the anode, where a 30% removal was achieved.

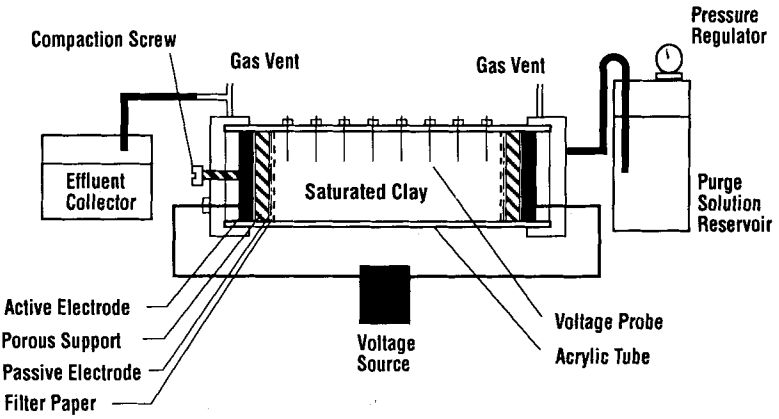

Fig. 26. Reactor design used for the removal of acetic acid and phenol from kaolin clay. (Adapted from [136]).

While electrokinetic treatment of soils looks promising, most of the work performed was bench-scale, under carefully controlled laboratory conditions. For electrokinetic remediation to be a viable alternative for *in-situ* cleanup of waste sites, a number of factors will have to be investigated. All of the work to date has dealt with uniformly contaminated soil samples. Studies performed on partially saturated soils will yield different results. Further studies on the removal of mixed metal contaminated soils, using different soil types, are needed. The presence of organic compounds in the soil will also influence successful treatment of "real" contaminated soils. The use of reagents which could increase desorption and/or solubilization (without further contaminating the soil matrix) may also be areas of future investigation. Finally, field tests need to be performed to substantiate studies accomplished on the bench scale.

2.8 Electroflotation

Electrolytic formation of finely dispersed bubbles (usually H_2 and O_2, from water electrolysis) can remove suspended particles from a liquid by floating them to the top. This "solid" matter can then be skimmed off from the top and subsequently treated. Much like electrodialysis, electroflotation is a process that concentrates the waste, which eventually needs to be treated and/or reused. It was estimated in 1980 that 20 electroflotation plants existed in the UK for treating industrial effluent [139]. Little to no information is available on the use of electroflotation for the decontamination of waste effluents in the USA.

Matis studied the separation of a paint–water suspension by electroflotation using seawater as the electrolyte [139]. At 300 A/m^2, the paint concentration dropped from 1000–1500 mg/dm^3 to 100–150 mg/dm^3, a 90% reduction. The horizontal

sets of electrodes were separated by a cation exchange membrane to examine the individual effect of oxygen and hydrogen on the flotation process. The oxygen gas could accomplish flotation only when a coagulant (alum) was used. Oxygen contributed mostly to the transfer of the already coagulated matter to the surface. Hydrogen gas on the other hand, was capable of breaking up the emulsion by itself.

Costaz et al. investigated the simultaneous electroflotation and disinfection of sewage in the presence of chloride ions (used to form hypochlorite ions) [140]. The solid–liquid separation was improved, compared with static clarification alone. The disinfection efficiency of the sludge was equal to or better than that obtained using gaseous clorine only.

Ho and Chan used a PbO_2-coated titanium anode for the electroflotation of palm oil mill effluent [141]. The electroflotation of suspended particles and anodic destruction of soluble substances such as sugars and phenolics occurred simultaneously. At 0.5 A and after 20 hours of operation, 86% of the suspended matter was found to be removed by flotation while 50% of the dissolved substances were destroyed. The lead dioxide anode was not corroded during the course of operation.

Electroflotation is unlikely to compete economically with air flotation (using compressed air and an air-sprager) to achieve large-scale separation of solid suspensions. However, the use of high oxygen overvoltage anodes such as lead dioxide [141] could generate hydroxyl radicals during gas generation, causing not only separation of suspended particles but oxidation of the wastes as well. This type of separation/oxidation unit could find on-site wastewater treatment applications where the ease of operation outweighs consideration of power consumption.

2.9 Electrochemical Ion Exchange

Electrochemical ion exchange is a relatively new technology for treating waste streams. Two distinct types seem to be emerging. One method uses a two-phase mixture of particulate ion exchange materials and the dilute aqueous metal waste solution to enhance the reclamation of metals at the cathode. The ion exchange resin is used to enhance the conductivity of the dilute aqueous solutions, thus increasing the reaction rate and improving current distribution. Although the addition of dissolved electrolytes can improve solution conductivity, these electrolytes require replacement and may cause additional contamination.

Tison [142] reclaimed metals from dilute copper and nickel solutions using this method. Studies were performed at 20–23 °C in 267 cm^3 Hull cells using five proprietary ion exchange resins (weakly and strongly acidic cationic and strongly basic anionic). The strongly acidic cation exchangers with sulfonate functional groups improved plating performance and enhanced the conductivity of the solution. The performance improvements included lower electrical energy requirements, higher current efficiencies, and improved throwing power.

A second method incorporates an ion exchange material (weak acid cation exchangers and basic anion exchangers) into an electrode structure using a suitable binder (Fig. 27). Bridger et al. [143] used such a system to remove ionic species from

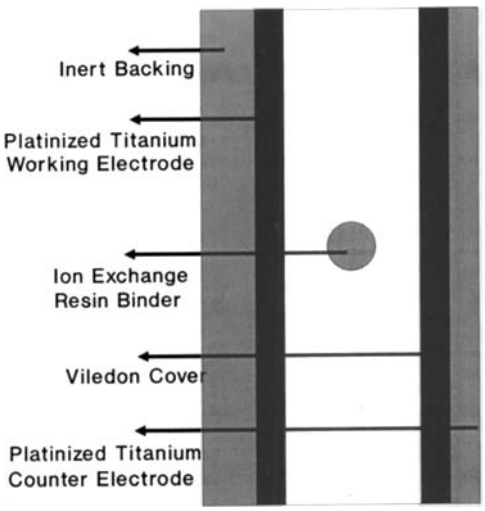

Fig. 27. Cross-sectional view of the electrochemical ion exchange (EIX) electrode. (Adapted from [143]).

aqueous waste streams. The ion exchange materials were ground to a fine powder and mixed with a suitable rubber binder dissolved in 1,1,1-trichloroethane (a volatile solvent). This dispersion was poured into molds containing platinized titanium mesh electrodes and the solvent was allowed to evaporate. Studies were performed using a zirconium phosphate cation electrochemical ion exchange unit with anion exchange units to remove radionuclides from low-level radioactive waste, the bulk of which were Co isotopes. Cobalt activity decreased by a factor of 50 using the cation electrochemical ion exchange unit. The major anion present in the waste stream, borate, was removed to below the detection limit using the anion exchange unit.

Adams and Hudson [144] used the water splitting reaction to promote ion exchange properties of materials incorporated into electrodes. The authors extracted Co(II) using alpha-zirconium hydrogenphosphate mixed in an unreactive polymer matrix which was embedded in a platinized titanium cathode. The cobalt removal process occurred solely by ion exchange into the matrix, i.e., neither cobalt precipitation nor cobalt plating was observed. The rates of ion exchange by this electrochemical method were found to be 100 times faster than normal ion exchange. Cobalt elution was achieved by reversing the applied potential at a low solution pH of 2.3.

Hobro et al. are currently utilizing the concept of electrochemical ion exchange to remove chromium from metal finishing waste [145]. In this process, a three-compartment cell is filled with anion exchange resins and separated by two anion exchange membranes. Solution containing chromate ($Cr_2O_7^{2-}$) is fed into the middle compartment, where it is adsorbed by the resin. The adsorbed ions, under the influence of an electric field, migrate to the anode across the anion exchange membrane. These ions are concentrated in the anode chamber and returned to the plating bath. Hydroxide ions produced at the cathode migrate to the middle compartment to regenerate the ion exchange resin continuously. Increasing the chromate mass loading

(a product of the solution volumetric flowrate and chromate concentration) was limited because of co-migration of hydroxyl ions into the anode compartment. Analysis of process streams revealed complete "on line" regeneration of resin without the need for extraneous chemicals.

A modification of the above process, also under study, involves *ex-situ* regeneration of the ion exchange resin. This process has an ion exchange resin bed saturated with a metal cation which is regenerated using an H^+-based solution. This solution, containing a high concentration of the metal ions, is sent into a metal recovery cell where the metal is plated onto a planar cathode. Water splitting at the anode releases protons into the solution, which is reused for regenerating the resin.

DiMascio et al. are developing an electrochemical deionization process (EDP) [146] for deionizing pretreated water to high purity levels, similar to that attained by mixed bed demineralizers, without the need for chemical regeneration. The EDP module is made up of a series of alternating cation and anion exchange membranes placed between two electrodes. A specific arrangement of cation and anion exchange resin layers is placed between each membrane pair to increase electrical conductivity and enable the process to treat low-conductivity water.

The feedwater is fed downward between the parallel ion-selective membranes and through the ion exchange resins, enabling the cations and anions to be adsorbed by the resins. A dc potential applied across the electrodes results in the migration of the adsorbed ions and continuous regeneration of the ion exchange resins. Each compartment alternately becomes more dilute and concentrated in ions, the contents of which are then continuously withdrawn.

Electrochemical ion exchange appears to be especially suitable for dilute waste streams having low ionic conductivities. The addition of ion exchange resins reduces electrolyte resistance by providing a conductive pathway between the electrodes. This results not only in reduced cell potential (and therefore lower operating cost), but also in increased metal recovery, and high feed throughputs. Unlike conventional ion exchange, the resins used in electrochemical ion exchange need not be chemically regenerated, thus eliminating the need for regenerating reagents and reducing the volume of resin required at a given time. These features make electrochemical ion exchange more acceptable than traditional processes such as evaporation and filtration; it may replace electrodialysis and traditional chemical regeneration in several applications.

3 Conclusions

Our desire to protect the environment (i.e. air, water, and soil) has increased considerably since the 1980s and will continue to do so in the future. This has steered industry to develop optimum waste treatment and/or minimization processes which are compatible with their needs and requirements. A variety of factors need to be considered in the development of an optimum waste management approach, including the type and size of waste stream (organic or inorganic), the phase in which the contaminant

is present, and the direct and indirect costs (recovery of waste or conversion to a salable by-product) associated with the choice of a treatment process.

Apart from metal recovery from metal finishing wastes and a few oxidant generation systems, electrochemical treatment techniques are practiced only on a laboratory scale or, at best, on a small scale. For larger-scale electrochemical treatment technologies to be established, the electrochemical route will have to compete more effectively with established and emerging physicochemical and biological treatment processes. Fortunately, the increased availability of ion exchange membranes coupled with recent advances in electrocatalysis and electrochemical reactor design will lead to an increasing number of applications in the area of waste treatment and minimization. One way for electrolytic treatment processes to gain increasing access to the marketplace is to combine or include an electrochemical step along with another treatment process. As the waste treatment industry becomes more familiar with the benefits of electrochemical processes, the number of applications involving electrochemistry will increase.

Traditionally, return on investment calculations of a manufacturing operation were the sole factor for its development. The process economics of a manufacturing operation will undergo an adjustment (in most cases for the worse) when effluent treatment steps are included. Electrochemical technologies, either for treatment or manufacturing, can be cleaner than pure chemical technologies, even after taking into account utility power plant emissions (needed for generating electricity). This is because chemical change in an electrochemical process is brought about by the ability to add or remove electrons, thus eliminating the use of redox agents. Redox reactions without spent streams, coupled with recovery or recycling of valuable chemicals and metals, permit electrochemical techniques not only to treat pollutants, but also to aid the environment through long-term pollution prevention.

4 References

1. B. Fleet in Electrochemistry Past and Present, J.T. Stock, M.V. Orna (eds), ACS Symp. Ser., 390, 544 (1989).
2. D. Pletcher, N.L. Weinberg, Chemical Engineering (London) (Aug. 1992).
3. D. Pletcher, N.L. Weinberg, Chemical Engineering (Nov. 1992).
4. J.D. Gender, N.L. Weinberg (eds), Electrochemistry for a Cleaner Environment. Electrosynthesis Co., East Amherst, New York (1992).
5. C.A.C. Sequeira (ed) Environmentaly Oriented Electrochemistry. Elsevier, Amsterdam (1994).
6. J.O'M. Bockris, R.C. Bhardwaj, C.K. Tennakoon, J. Serb. Chem. Soc. 57, 799 (1992).
7. A.T. Kuhn in Modern Aspects of Electrochemistry, J.O'M Bockris, B.E. Conway (eds), Academic Press, New York (1972), No. 8, p. 273.
8. A.T. Kuhn in Electrochemistry of Cleaner Environments, J.O'M Bockris (ed). Plenum Press, New York (1972), p. 98.
9. F. Coeuret, M. Paulin, J. Appl. Electrochem. 18, 162 (1988).
10. E. Avci, J. Appl. Electrochem. 18, 288 (1988).
11. K. Scott, J. Appl. Electrochem. 18, 504 (1988).
12. S.L. Tsapakh, E.M. Shalygina, B.S. Krasikov, I.V. Rzhevskii, Zh Prikl Khim 61, 2131 (1988).

13. D. Pletcher, I. White, F.C. Walsh, J.P. Millington, J. Appl. Electrochem. 21, 667 (1991).
14. F.C. Walsh, D. Pletcher, I. White, J.P. Millington, J. Chem. Tech. Biotechnol. 55, 147 (1992).
15. D. Pletcher, I. White, F.C. Walsh, J.P. Millington, J. Appl. Electrochem. 23, 82 (1993).
16. S. Yen, C. Yao, J. Electrochem. Soc. 138, 2344 (1991).
17. H. Bergmann, H. Hertwig, F. Nieber, Chem. Eng. Proc. 31, 195 (1992).
18. B.S. Boyanov, J.D. Donaldson, S.D. Grimes, J. Chem. Tech. Biotechnol. 41, 317 (1988).
19. E. Avci, Sep. Sci. Tech. 24, 317 (1989).
20. X. Hu, R.G. Bautista, Sep. Sci. Tech. 23, 1989 (1988).
21. M. Abda, Z. Gavra, Y. Oren, J. Appl. Electrochem. 21, 734 (1991).
22. F.J. Dudek, E.J. Daniels, Z. Nagy, S. Zaromb, R.M. Yonco, Sep. Sci. Tech. 25, 2109 (1990).
23. B. Streng, A. Mobius, K. Wiesner, V. Nikolova, I. Nikolova, T. Vitanov, J. Appl Electrochem. 20, 317 (1990).
24. V. Tricoli, N. Vatistas, P.F. Marconi, J. Appl. Electrochem. 23, 390 (1993).
25. B. Delanghe, S. Tellier, M. Astruc, Environ. Tech. 11, 999 (1990).
26. V.S. DeSucre, A.P. Watkinson, Can. J. Chem. Eng. 59, 52 (1981).
27. D.W. Kirk, H. Sharifian, F.R. Foulkes, J. Appl. Electrochem. 15, 285 (1985).
28. C.C. Ho, C.Y. Chan, K.H. Khoo, J. Chem. Tech. Biotechnol. 36, 7 (1986).
29. J.F. Patzer, S.K. Wolfson, S.J. Yao, Chem. Eng. Sci. 45, 2777 (1990).
30. L. Kaba, G.D. Hitchens, J.O'M Bockris, J. Electrochem. Soc. 137, 1341 (1990).
31. G. Patermarkis, E. Fountoukidis, Water Res. 24, 1491 (1990).
32. T. Matsunaga, S. Nakasono, T. Takamuku, J.G. Burgess, N. Nakamura, K. Sode, Appl. Environ. Biol. 58, 686 (1992).
33. Ch. Comninellis in Proc. Symposia on Electrochemical Engineering and Small Scale Electrolytic Processing, C.W. Walton, J.W. Van Zee, R.D. Varjian (eds). The Electrochemical Society Pennington, NJ, USA, (1990), Vol. 90–10, p. 971.
34. Ch. Comninellis, C. Pulgarin, J. Appl. Electrochem. 21, 703 (1991).
35. R. Kotz, S. Stucki, B. Carcer, J. Appl. Electrochem. 21, 14 (1991).
36. Ch. Comninellis, C. Pulgarin, J. Appl. Electrochem. 23, 108 (1993).
37. S. Stucki, R. Kotz, B. Carcer, W. Suter, J. Appl Electrochem. 21, 99 (1991).
38. C. Pulgarin, N. Adler, P. Peringer, Ch. Comninellis, Water Res. 28, 887 (1994).
39. O.J. Murphy, G.D. Hitchens, L. Kaba, C.E. Verostko, Water Res. 26, 443 (1992).
40. T.C. Wen, Plating and Surface Finishing (Nov. 1990).
41. S.P. Ho, Y.Y. Wang, C.C. Wan, Water Res. 24, 1317 (1990).
42. M.L. Lin, Y.Y. Wang, C.C. Wan, J. Appl. Electrochem. 22, 1197 (1992).
43. S. Yen, C. Wang, J. Wang, Chem. Eng. Commun. 109, 167 (1991).
44. C.P.C. Poon, K.P. Soscia, Ind. Water Eng. 17, 28 (1980).
45. T.C. Franklin, J. Darlington, W.K. Adeniyi, J. Electrochem. Soc. 137, 2124 (1990).
46. T.C. Franklin, J. Darlington, T. Solouki, J. Electrochem. Soc. 138, 747 (1991).
47. T.C. Franklin, J. Darlington, T. Solouki, N. Tran, J. Electrochem. Soc. 138, 2285 (1991).
48. N. Takashi, O. Katsuki, Ozone Sci. Eng. 12, 115 (1990).
49. J.C. Farmer, F.T. Wang, P.R. Lewis, L.J. Summers, Trans. Instr. Chem. Eng. 70, 158 (1992).
50. J.C. Farmer, F.T. Wang, R.A. Fedder, P.R. Lewis, L.J. Summers, L. Foiles, J. Electrochem. Soc. 139, 654 (1992).
51. J.C. Farmer, F.T. Wang, P.R. Lewis, L.J. Summers, J. Electrochem. Soc. 139, 3025 (1992).
52. M. Sudoh, T. Kodera, K. Sakai, J. Zhang, K. Koide, J. Chem. Engl. Jpn. 19, 513 (1986).
53. J.S. Do, C.P. Chen, J. Electrochem. Soc. 140, 1632 (1993).
54. E.E. Kalu, R.E. White, J. Electrochem. Soc. 138, 3656 (1991).
55. W.A. Pretorius, W.G. Johannes, G.G. Lempert, Water SA, 17, 133 (1991).
56. J. Lee, B. Darus, S.H. Langer, J. Appl. Electrochem. 23, 745 (1993).
57. P.B. Chaudry, M.g. Bhide, Nuclear Tech. 98, 242 (1992).
58. S.K. Harnsberger, I. Ramoda, Plating and Surface Finishing (Juli 1990).
59. C.F. Schobein, C.R. Hebd. Seances Acad. Sci. 10, 706 (1840).
60. F. Fischer, K. Massenez, Anorg. Chem. 52, 202 (1907).

61. J.D. Seader, C.W. Tobias, Ind. Eng. Chem. 44, 9 (1952).
62. E. Briner, R. Haefeli, H. Paillard, Helv. Chim. Acta 120, 1510 (1937).
63. D.P. Semchenko, E.T. Lyubushkina, Y. Lyubushkin, Electrochimiya 9, 1744 (1973).
64. D.P. Semchenko, E.T. Lyubushkina, V. Lyubushkin, Izv. Sev-Kuk. Nauch. Tsentra Vyssh. Shk., Ser. Tekn. Nauk, 3, 98 (1975).
65. P.C. Foller, C.W. Tobias, J. Electrochem. Soc. 129, 506 (1982).
66. P.c. Foller, M.L. Goodwin, Ozone Sci. Eng. 6, 29 (1984).
67. S. Stucki, G. Theis, R. Kotz, H. Devantay, H.J. Christen, J. Electrochem. Soc. 132, 367 (1985).
68. S. Stucki, H. Baumann, H.J. Christen, R. Kotz, J. Appl. Electrochem. 17, 773 (1987).
69. P. Tatapudi, J.M. Fenton, J. Electrochem. Soc. 140, 3527 (1993)
70. J.E. Graves, D. Pletcher, R.L. Clarke, F.C. Walsh, J. Appl. Electrochem. 22, 200 (1992).
71. P. Tatapudi, J.M. Fenton, J. Electrochem. Soc. 141, 1174 (1994).
72. J.A. McIntyre, R.F. Phillips, Proc. Symposium on Electrochemical Process and Plant Design, R.C. Alkire, T.R. Beck, R.D. Varjian (ed). The Electrochemical Society Pennington, NJ, USA, (1983), Vol. 83–6, p. 79.
73. J.B. Davison, J.M. Kacsir, P.J. Peerce-Landers, R. Jasinski, J. Electrochem. Soc. 130, 1497 (1983).
74. C. Kuehn, F. Leder, R. Jasinski, K. Gunt, J. Electrochem. Soc. 130, 1117 (1983).
75. E.E. Kalu, C. Oloman, J. Appl. Electrochem. 20, 932 (1990).
76. D. Grasso, M.S. Thesis, University of Connecticut (1989).
77. M. Sudoh, T. Kodera, T. Ichino, J. Chem. Eng. Jpn. 24, 165 (1991).
78. M. Sudoh, K. Minamoto, T. Makino, H. Hakamada, J. Chem. Eng. Jpn. 24, 165 (1991).
79. K. Otsuka, I. Yamanaka, Electrochim. Acta 35., 319 (1990).
80. P. Tatapudi, J.M. Fenton, J. Electrochem. Soc. 140, L55 (1993).
81. D. Pletcher, F.C. Walsh, Industrial Electrochemistry, (2nd. ed.), Chapmann and Hall, New York (1990).
82. M. Lipsztajn et al. US Patent 4853096 (Aug 1, 1989) (to Tenneco Canada, Inc.).
83. J.J. Kaczur et al. US Patent 5106465 (Apr. 21, 1992) (to Olin Chemical Corporation).
84. J.J. Kaczur et al. US Patent 5084189 (Jan. 28, 1992) (to Olin Chemical Corporation).
85. D.W. Cawlfield et al. US Patent 5248397 (Sept. 28, 1993) (to Olin Chemical Corporation).
86. K.L. Gering, J.F. Scamehorn, Sep. Sci. Tech. 23, 2231 (1988).
87. P.M. Shah, J.F. Scamehorn, Ind. Eng. Chem. Res. 26, 269 (1987).
88. X. Deming, S. Dezheng, L. Xiaoying, Desalination 62, 251 (1987).
89. J. Raghava Rao, B.G.S. Prasad, V. Narasimhan, T. Ramaswsami, P.R. Shah, A.A. Khan, J. Membrane. Sci 46, 215 (1989).
90. G.D. Enoch, P. Tigchelaar, J. de Niet, J.B. Lefers, Sep. Sci. Tech. 25, 1387 (1990).
91. R.J. Walker, H.W. Pennline, Environ. Prog. 7, 215 (1988).
92. D.A. Rockstraw, J.F. Scamehorn, E.A. O'Rear III, J. Membrane Sci. 52, 43 (1990).
93. J.M. Chiapello, J.Y. Gal, J. Membrane Sci. 68, 283 (1992).
94. Z. Xue, Z. Hua, N. Yao, Water Sci. Tech. 26, 2305 (1992).
95. I. Dobrevesky, S. Pavlova, Desalination 86, 43 (1992).
96. A.T. Cherif, A. Elmidaoui, C. Gavach, J. Membrane Sci. 76, 39 (1993).
97. W.J. Voortman, A.E. Simpson, C.A. Kerr, C.A. Buckley, Water Sci. Tech. 25, 329 (1992).
98. A.E. Simpson, F.G. Neytzell-De Wilde, C.A. Buckley, Water SA. 14, 99 (1988).
99. A.E. Simpson, C.A. Buckley, Desalination 70, 431 (1988).
100. D.J. Speranzini, M.S. Thesis, University of Connecticut (1990).
101. J. Winnick in Advances in Electrochemical Science and Engineering, H. Gerischer, C.W. Tobias (eds), VCH, New York (1990), Vol. 1, p. 205.
102. D. Townley, J. Winnick, Ind. Eng. Chem., Process. Res. 20, 435 (1981).
103. D. Townley, J. Winnick, Electrochim. Acta 283, 389 (1983).
104. K. Scott, T. Fannon. J. Winnick, J. Electrochem. Soc. 1353, 573 (1988).
105. M. Franke, J. Winnick, Ind. Eng. Chem. Res. 28, 1352 (1989).
106. D. McHenry, J. Winnick, Sep. Sci. Tech. 25, 1523 (1990).

107. D. McHenry, J. Winnick, AIChE Journal 40, 143 (1994).
108. J.C. Card, M.J. Foral, S.H. Langer, Environ. Sci. Tech. 22, 1499 (1988).
109. M. Aurousseau, T. Hunger, A. Storck, F. Lapicque, Chem. Eng. Sci. 48(3), 541 (1993).
110. H.S. Lim, J. Winnick, J. Electrochem. Soc. 131, 562 (1984).
111. D. Weaver, J. Winnick, J. Electrochem. Soc. 134, 2451 (1987).
112. S. Alexander, J. Winnick, Sep. Sci. Tech. 25, 2057 (1990).
113. D. Weaver, J. Winnick, J. Electrochem. Soc. 138, 1626 (1991).
114. D. Weaver, J. Winnick, J. Electrochem. Soc. 139, 492 (1992).
115. Z. Mao, P. Adanuvor, R.E. White, J. Electrochem. Soc. 137, 2116 (1990).
116. Z. Mao, A. Anani, R.E. White, S. Srinivasan, A.J. Appleby, J. Electrochem. Soc. 138, 1299 (1991).
117. M.N. Mahmood, D. Masheder, C.J. Harty, J. Appl. Electrochem. 17, 1159 (1987).
118. M.N. Mahmood, D. Masheder, C.J. Harty, J. Appl. Electrochem. 17, 1223 (1987).
119. R.L. Cook, R.C. MacDuff, A.f. Sammells, J. Electrochem. Soc. 134, 1873 (1987).
120. R.L. Cook, R.C. MacDuff, A.F. Sammells, J. Electrochem. Soc. 135, 1470 (1988).
121. R.L. Cook, R.C. MacDuff, A.F. Sammels, J. Electrochem. Soc. 135, 1320 (1988).
122. R.L. Cook, R.C. MacDuff, A.F. Sammells, J. Electrochem. Soc. 137, 607 (1990).
123. M. Azuma, K. Hashimoto, M. Hiramoto, J. Electrochem. Soc. 137, 1772 (1990).
124. K. Ogura, C.T. Migita, Y. Ito, J. Electrochem. Soc. 137, 500 (1990).
125. D.J. Kuchynka, R.L. Cook, A.F. Sammells, J. Electrochem. Soc. 138, 1284 (1991).
126. D.C. Guzman, J.T. Scwartzbaugh, A.W. Weisman, J. Air Waste Man. Assoc. 40, 1670 (1990).
127. Y.B. Acar, A.N. Alshawabkeh, R.J. Gale, Waste Management, 13, 141 (1993).
128. Y.B. Acar, J. Hamed, Transportation Research Record, No. 1312 (1991), p. 153.
129. Y.B. Acar, R.J. Gale, G.A. Putnam, J. Hamed, R.L. Wong, J. Environ. Health A25, 687 (1990).
130. S. Pamukcu, L.I. Khan, H.Y. Fang, Transportation Research Record, No. 1288, (1990), p. 41.
131. J. Hamed, Y.B. Acar, R.J. Gale, J. Geotech. Eng. 117, 241 (1991).
132. Y.B. Acar, H. Li, R.J. Gale, J. Geotech. Eng. 118, 1837 (1992).
133. S. Pamukcu, J.K. Wittle, Environ. Prog. 11, 241 (1992).
134. A.N. Alshawabkeh, Y.B. Acar, J. Environ. Sci. Health A27(7), 1835 (1992).
135. E.R. Lindgren, M.W. Kozak, E.D. Mattson, Electrokinetic remediation of contaminated soils: an update, Proc. Waste Management '92, Conf., March 1–5, at Tucson, AZ. (1992).
136. A.P. Shapiro, P.C. Renaud, R.F. Probstein, Physico Chem. Hydrodyn. 11, 785 (1989).
137. A.P. Shapiro, P.C. Renaud, R.F. Probstein, Environ. Sci. Technol 27, 283 (1993).
138. S. Pamukcu, J.K. Wittle, Electrokinetics for removal of low-level radioactivity from soil, presented at 14th Annu Department of Energy Low-Level Radiative Waste Management Conf., Phoenix, AZ (November 18–20 1992).
139. K.A. Matis, Water Pollut. Control 136 (1980).
140. P. Costaz, J. Miquel, M. Reinbold, Water Res 17, 255 (1983) (in French).
141. C.C. Ho, C.Y. Chan, Water Res 20, 1523 (1986).
142. R.P. Tison, Plating and Surface Finishing, 114 (May 1988).
143. N.J. Bridger, C.P. Jones, M.D. Neville, J. Chem. Tech. Biotechnol. 50, 469 (1991).
144. R.J.W. Adams, M.J. Hudson, Solvent Extraction Ion Exchange, 9, 497 (1991).
145. D. Hobro, J.M. Fenton, F. DiMascio, A. Jha, Proc. Symposium on Water Purification by Photocatalytic, Photoelectrochemical, and Electrochemical Processes, T.L. Rose, O.J. Murphy, E. Rudd, B.E. Conway (eds.) The Electrochemical Society, Pennington, NJ, USA, (1994), Vol. 94–19, p. 173.
146. F. DiMascio, A. Jha, D. Hobro, J.M. Fenton, D. Hobro, Proc. Symposium on Water Purification by Photocatalytic, Photoelectrochemical, and Electrochemical Processes, T.L. Rose, O.J. Murphy, E. Rudd, B.E. Conway (eds.) The Electrochemical Society, Pennington, NJ, USA, (1994), Vol. 94–19, p. 164.

Advances in Electrochemical Science and Engineering
Edited by Heinz Gerischer and Charles W. Tobias

Index